frontiers | Research Topics

Animal biomechanics: Application of the biomedical engineering to the veterinary sciences for the animal healthcare

Edited by
Mauro Malvè, Alessia Di Giancamillo, Rocío Fernández-Parra and Christian Peham

Published in
Frontiers in Veterinary Science
Frontiers in Bioengineering and Biotechnology

ISSN 1664-8714
ISBN 978-2-8325-4720-5
DOI 10.3389/978-2-8325-4720-5

About Frontiers

Frontiers is more than just an open access publisher of scholarly articles: it is a pioneering approach to the world of academia, radically improving the way scholarly research is managed. The grand vision of Frontiers is a world where all people have an equal opportunity to seek, share and generate knowledge. Frontiers provides immediate and permanent online open access to all its publications, but this alone is not enough to realize our grand goals.

Frontiers journal series

The Frontiers journal series is a multi-tier and interdisciplinary set of open-access, online journals, promising a paradigm shift from the current review, selection and dissemination processes in academic publishing. All Frontiers journals are driven by researchers for researchers; therefore, they constitute a service to the scholarly community. At the same time, the *Frontiers journal series* operates on a revolutionary invention, the tiered publishing system, initially addressing specific communities of scholars, and gradually climbing up to broader public understanding, thus serving the interests of the lay society, too.

Dedication to quality

Each Frontiers article is a landmark of the highest quality, thanks to genuinely collaborative interactions between authors and review editors, who include some of the world's best academicians. Research must be certified by peers before entering a stream of knowledge that may eventually reach the public - and shape society; therefore, Frontiers only applies the most rigorous and unbiased reviews. Frontiers revolutionizes research publishing by freely delivering the most outstanding research, evaluated with no bias from both the academic and social point of view. By applying the most advanced information technologies, Frontiers is catapulting scholarly publishing into a new generation.

What are Frontiers Research Topics?

Frontiers Research Topics are very popular trademarks of the *Frontiers journals series*: they are collections of at least ten articles, all centered on a particular subject. With their unique mix of varied contributions from Original Research to Review Articles, Frontiers Research Topics unify the most influential researchers, the latest key findings and historical advances in a hot research area.

Find out more on how to host your own Frontiers Research Topic or contribute to one as an author by contacting the Frontiers editorial office: frontiersin.org/about/contact

Animal biomechanics: Application of the biomedical engineering to the veterinary sciences for the animal healthcare

Topic editors

Mauro Malvè — Public University of Navarre, Spain

Alessia Di Giancamillo — University of Milan, Italy

Rocío Fernández-Parra — Catholic University of Valencia San Vicente Mártir, Spain

Christian Peham — University of Veterinary Medicine Vienna, Austria

Citation

Malvè, M., Di Giancamillo, A., Fernández-Parra, R., Peham, C., eds. (2024). *Animal biomechanics: Application of the biomedical engineering to the veterinary sciences for the animal healthcare*. Lausanne: Frontiers Media SA.

doi: 10.3389/978-2-8325-4720-5

Table of contents

frontiers | Frontiers in Veterinary Science

TYPE Editorial
PUBLISHED 25 March 2024
DOI 10.3389/fvets.2024.1390136

OPEN ACCESS

EDITED AND REVIEWED BY
Carmel T. Mooney,
University College Dublin, Ireland

*CORRESPONDENCE
Mauro Malvè
✉ mauro.malve@unavarra.es

RECEIVED 22 February 2024
ACCEPTED 11 March 2024
PUBLISHED 25 March 2024

CITATION
Fernández-Parra R, Di Giancamillo A, Peham C and Malvè M (2024) Editorial: Animal biomechanics: application of the biomedical engineering to the veterinary sciences for the animal healthcare. *Front. Vet. Sci.* 11:1390136. doi: 10.3389/fvets.2024.1390136

Editorial: Animal biomechanics: application of the biomedical engineering to the veterinary sciences for the animal healthcare

Rocío Fernández-Parra[1], Alessia Di Giancamillo[2], Christian Peham[3] and Mauro Malvè[4,5]*

[1]Department of Veterinary Medicine and Surgery, Catholic University of Valencia (UCV) San Vicente Mártir, Valencia, Spain, [2]Department of Biomedical Sciences for Health, University of Milan, Milan, Italy, [3]Department of Companion Animals and Horses, University of Veterinary Medicine, Vienna, Austria, [4]Department of Engineering, Public University of Navarra (UPNA), Pamplona, Spain, [5]Biomedical Research Networking Center in Bioengineering, Biomaterials and Nanomedicine (CIBER-BBN), Madrid, Spain

KEYWORDS

respiration physiology and drug delivery, animal orthopedics, animal kinematics, animal biomechanics, biomechanical test, medical devices and endoprosthesis, electrical impedance tomography, finite element analysis

Editorial on the Research Topic
Animal biomechanics: application of the biomedical engineering to the veterinary sciences for the animal healthcare

Biomedical engineering is a discipline that combines engineering, biology and medicine. Within biomedical engineering, biomechanics uses the equations and laws of mechanics to solve problems and study phenomena relevant to the biomedical field. Traditionally, biomedical engineering has been used extensively in human medicine to improve human health and clinical outcomes. For example, it has been used to study pathologies and understand the function of cardiovascular and pulmonary mechanics, among other organs. It has enabled virtual surgical planning and the improvement of medical devices. More recently, considerable research has been devoted to mechanobiology, to study the motility and behavior of cells in different environments, with several applications in the study of human pathologies and tissue regeneration. Today, artificial intelligence is expected to drive future sophisticated applications.

The extensive research carried out over the last 30 years in this area has led to an increase in knowledge of a considerable number of aspects related to human health. With the increase in the power of computers and the parallel development of experimental set-ups, the complexity of numerical and experimental models that reproduce natural phenomena in human medicine and health care has increased considerably, allowing further improvements in related fields of research.

Surprisingly, biomedical engineering remains relatively underused in veterinary medicine. Despite its extensive applications in biology and human health, biomedical engineering has only occasionally been applied to veterinary medicine. However,

the knowledge gained from previous applications of biomedical engineering in human medicine is readily available and suitable for direct implementation in veterinary medicine using similar technologies, protocols and workflows. For example, computational modeling based on patient-specific images can provide insights that are otherwise unattainable *in vivo* in both animals and humans. Artificial intelligence can analyze animal kinematics and stability to help diagnose disease. Experimental tests on animal tissue, originally intended for human health research, can be applied to animal health. In addition, three-dimensional (3D) additive printing for orthopedic purposes can facilitate the creation of customized endo- and exoprostheses uniquely tailored to the needs of animals.

This Research Topic therefore focuses on the application of biomedical engineering to veterinary science with the specific and precise aim of improving veterinary medicine and animal health. In this Research Topic, there is a collection of 14 papers that include some of the commented aspects and applications in different animals and techniques.

In the field of experimental animal orthopedics, Brabon et al. propose a Bayesian network model to study condylar fractures in horses. As these are commonly repaired with cortical screws, inadequate interfragmentary compression can lead to postoperative complications. Their investigation attempts to assess the relationships between several different fixation techniques and interfragmentary compression. They found moderate evidence that triangular repairs result in greater interfragmentary compression than linear repairs. Mendaza-DeCal et al. present and test a new 3D-printed endoprosthetic device with a specific protocol to mimic normal canine loading during walking, trotting and galloping. The research is a first step in the development of a valuable alternative to the well-known complex exo-endoprosthetic procedure for animals. Shi et al. examined the qualitative and quantitative morphological features of the porcine knee and anterior cruciate ligaments, comparing human and animal data reported in the literature. They found similar locations, orientations and basic morphology to humans, but different structure and dimensions. Lundin et al. develop a biomechanical test model of partial tarsal arthrodesis to determine whether a novel resorbable bone adhesive, phosphoserine-modified cement, provides measurable fixation strength in canine calcaneal arthrodesis without orthopedic implants. This work attempts to provide an alternative to arthrodesis. This invasive surgical procedure is used to treat canine and feline joints associated with a high incidence of complications. The results obtained in a cadaveric biomechanical test model showed that the resorbable adhesive can potentially contribute to the stability of arthrodesis surgery and can be evaluated as an alternative or complement to traditional fixation with metal implants.

Studies of large animal populations can help understand the effectiveness of pharmaceuticals. Huang conducts a comprehensive analysis of 131 metagenomic sequencing datasets from five species of non-human primates, including different regions and lifestyles, to analyze their resistance to antibiotics. As antibiotic resistance is a serious threat to animal health, the proposed comprehensive research will increase the knowledge of antibiotic management and disease prevention in a bidirectional way for both animal and human health.

Computational animal models using numerical algorithms and three-dimensional geometric discretisation have been widely used in human medicine, but few studies have focused on animal health. Xue et al. proposed a finite element analysis to study biomechanical changes in the rabbit knee joint. The computational results suggest that horizontal meniscal tears may not have a significant effect on the rabbit knee joint, and that different resection strategies may result in different biomechanical environmental changes.

The aim of this paper is to provide a reference for the future selection of experimental studies and clinical surgical strategies. Fernández-Parra et al. propose a computational fluid dynamics study focused on the treatment of asthma in cats. They evaluate the inhalation, deposition and transport of drug microparticles using discrete phase modeling and considering flows and particle sizes of salbutamol in a healthy cat model. The results suggest that therapy in animals differs from that in humans. In the same line, Zamora-Perarnau et al. investigated the effects of different airway management devices in cats under general anesthesia. They proposed a comparison of the performance of endotracheal tubes and supraglottic airway devices, showing that the correct size should be chosen carefully to avoid obstruction and reduce resistance. In their methods article, Burgos et al. introduce the in-house software Flowgy to the veterinary community. This software is a semi-automated tool designed to simulate human and animal airflow through the nasal passage to detect changes in flow. In this study, the authors tested the use and accuracy of Flowgy in lions with the aim of understanding the dynamics of nasal airflow in large felids for their health care and conservation.

Brabant et al. used non-invasive experimental methods for obtaining images of pulmonary ventilation in cattle to evaluate whether electrical impedance tomography variables could detect a difference in ventilation homogeneity between healthy and respiratory diseased cattle. Electrical impedance is a non-invasive imaging technique used to detect impedance changes where there is a change in the electrical conductivity of the body. Such changes are usually due to changes in the regional distribution of ventilation within the lung or changes in blood flow. The authors demonstrated that the proposed method, based on a belt with sensors connected to a computer, is a useful tool for the diagnosis of respiratory disease in cattle.

Animal kinematics and stability is also an important topic in this Research Topic. Non-invasive measurements can help in the early diagnosis of orthopedic diseases. Lutonsky et al. investigate the effect of external mechanical perturbations on stability in dogs using the body's center of pressure and demonstrate the effects of a balance training device in dogs. They show that the wobble amplitude of the platform controls the intensity of training programmes on motorized equipment. Virag et al. measured the center of pressure and ground reaction forces of 32 Labrador Retrievers and 17 Golden Retrievers at 4, 8, and 12 months of age to improve knowledge of canine hip dysplasia. The results showed significantly higher values for the center of pressure in the affected limb groups in both breeds at each measurement point during gait. The differences in measured parameters between limbs with healthy and diseased hip joints can be interpreted in terms of possible biomechanical adaptations and as an indicator of reduced stability. Mielke et al. apply semi-automatic deep learning digitization to a multivariate kinematic dataset in piglets to

calculate joint angle profiles. The proposed workflow has potential for automated, accurate screening in livestock management. The overall aim of the study is to provide accurate diagnostic measurements, generated at high throughput, to improve animal welfare. Finally, Charalambous et al. investigate changes in vertical ground reaction forces, center of pressure and paw pressure in Belgian Malinois participating in obedience competitions during heelwork walking using a sensor-based experimental set-up. The measured variables are closely related and can be used to describe the effects of various factors such as aging, orthopedic, and neurological diseases.

In summary, the findings of the aforementioned papers underline a significant collection of pertinent applications of biomedical engineering in animal healthcare. However, they also indicate that numerous aspects remain ready for investigation concerning the intersection of these two disciplines.

Author contributions

RF-P: Conceptualization, Writing—original draft, Writing—review & editing. AD: Writing—review & editing. CP: Writing—review & editing. MM: Conceptualization, Writing—original draft, Writing—review & editing.

Funding

The author(s) declare that financial support was received for the research, authorship, and/or publication of this article. RF-P and MM are supported by grants PID2021-125731OB-C33 and PID2021-125731OB-C31 from the Spanish Ministry of Science and Innovation MCIN/AEI/10.13039/501100011033/ and FEDER ("A way to build Europe").

Acknowledgments

The editors thank all the authors for presenting their research through their excellent scientific publications. This Research Topic is the result of their dedication and expertise.

Conflict of interest

The authors declare that the research was conducted in the absence of any commercial or financial relationships that could be construed as a potential conflict of interest.

The author(s) declared that they were an editorial board member of Frontiers, at the time of submission. This had no impact on the peer review process and the final decision.

Publisher's note

frontiers | Frontiers in Veterinary Science

ORIGINAL RESEARCH
published: 30 June 2022
doi: 10.3389/fvets.2022.887676

Biomechanical Test of a New Endoprosthesis for Cylindrical Medullary Canals in Dogs

Rosa Mendaza-DeCal[1,2], Yolanda Ballesteros[3], Salvador Peso-Fernandez[2], Eva Paz[3], Juan Carlos del Real-Romero[3] and Jesus Rodriguez-Quiros[1]*

[1] Animal Medicine and Surgery Department, Veterinary Faculty, Complutense University of Madrid, Madrid, Spain, [2] ABAX Innovation Technologies, Villanueva de la Cañada, Madrid, Spain, [3] Institute for Research in Technology/Mechanical Engineering Department, Universidad Pontificia Comillas, Madrid, Spain

Exo-endoprosthesis is a limb salvage procedure for animals, although only expensive metal devices have been described. Now-a-days, new materials for this type of implant could be considered due to novel and affordable manufacturing techniques. However, a factor of safety (FoS) should be considered. There are kinetic and kinematic studies of canine natural gaits, which can be used to establish an FoS for mechanical tests for new non-metallic devices. Polyetheretherketone (PEEK) is used in different specialties in human medicine. Its mechanical properties (and its close mechanical stiffness to that of bone) make this polymer an alternative to metals in veterinary traumatology. PEEK could also be used in 3D printing. The suitability of a novel inner part of an exo-endoprosthesis manufactured by fuse deposition modeling (FDM) was presented in this study for long canine bones. Mechanical characterization of 3D-printed PEEK material and *ex vivo* mechanical tests of a customized endoprosthesis were performed to address it. Young's modulus of 3D-printed PEEK suffered a reduction of 30% in relation to bulk PEEK. Customized 3D-printed PEEK endoprostheses had promising outcomes for the tibiae of 20 kg dogs. Pure compression tests of the non-inserted endoprostheses showed a maximum force of 936 ± 199 N. In the bending tests of non-inserted endoprostheses, the PEEK part remained intact. Quasistatic mechanical tests of bone-inserted endoprostheses (compression-bending and pure compression tests) reached a maximum force of 785 ± 101 N and 1,642 ± 447 N, respectively. In fatigue tests, the samples reached 500,000 cycles without failure or detriment to their quasistatic results. These outcomes surpass the natural weight-bearing of dogs, even during a galloping pace. In conclusion, the 3D-printed PEEK part of the endoprosthesis for an exo-endoprosthesis can withstand loading, even during a galloping pace.

Keywords: biomechanical test, patient-specific implant, FDM, PEEK, exo-endoprosthesis, *ex vivo*, tibia, canine

OPEN ACCESS

Edited by:
Mauro Malvè,
Public University of Navarre, Spain

Reviewed by:
Caitlyn J. Collins,
Virginia Tech, United States
Feihu Zhao,
Swansea University, United Kingdom

****Correspondence:***
Rosa Mendaza-DeCal
rmendaza@ucm.es

Specialty section:
This article was submitted to Veterinary Surgery and Anesthesiology, a section of the journal Frontiers in Veterinary Science

Received: *01 March 2022*
Accepted: *02 June 2022*
Published: *30 June 2022*

Citation:
Mendaza-DeCal R, Ballesteros Y, Peso-Fernandez S, Paz E, del Real-Romero JC and Rodriguez-Quiros J (2022) Biomechanical Test of a New Endoprosthesis for Cylindrical Medullary Canals in Dogs. Front. Vet. Sci. 9:887676. doi: 10.3389/fvets.2022.887676

INTRODUCTION

Exo-endoprosthesis is a limb salvage procedure in humans and, to a lesser extent, in animals (1–5). Because the implant is inserted into the medullary canal of a long bone, its advantages are no pain, no delay in load transfer, energetic efficiency, and good proprioception. However, complications have been reported, such as infection, skin breakdown, aseptic loosening, device failure, and

avulsion (2, 5, 6). The two last complications can be related to stress-shielding phenomena (7). Therefore, aseptic loosening and stress-shielding are related to the higher stiffness of metals as compared to bone (7, 8) and metallic debris. A rigid material is reluctant to deform and difficult to adapt when it is inserted in a flexible object, like the medullary canal of a bone. So perfect fitting of the rigid material to the bone cannot be expected. This mismatch produces a lack of stress transmission between rigid material and bone, which is one of the reasons for stress-shielding. In the same way, it is the flexible material, the bone, which is deformed because of the rigid material in case of irregular stress transmission. Thus, these phenomena are related to the chosen material of a medical device, and their effect could be reduced by selecting other materials with a stiffness closer to the bone. Now-a-days, all veterinary implants are individualized, and made in metal. These characteristics make them an expensive solution that few owners can afford for their pets.

Seeking price reduction and avoiding the aforementioned complications related to metal stiffness, other materials could be considered for implants. The stiffness is directly related to the elastic properties of a material, such as Young's modulus, tensile strength, and bending strength among others (9). Materials with a much higher Young's modulus, such as metals, when compared with bone, could be prone to stress-shielding of the host bone due to their rigidity (7, 10). Therefore, a non-metallic material with bone-like elastic properties could be considered to reduce the aseptic loosening and stress-shielding of a medical device on a bone.

Polyetheretherketone (PEEK) is one of those alternative non-metallic materials for medical devices. PEEK is a thermoplastic of the polyaryletherketone family that is generally used for different specialties in human medicine, such as neurosurgery, traumatology, and dental and craniomaxillofacial surgery (11, 12). PEEK is also bioinert in the physiological environment and has good biocompatibility (11). It is one of the polymers with good mechanical properties, such as its weight-bearing and strength properties (11). Furthermore, its stiffness is closer to that of bone than to that of metal (11). All of these specific characteristics make it a candidate for the avoidance of stress-shielding as is assessed on ovine or canine specimens in experimental studies for different traumatological devices (11–14).

Now-a-days, thanks to additive manufacturing (AM), quite a range of materials can be considered for manufacturing small productions of final devices with a minimum cost (15, 16). There are different technologies in the field of AM, although only direct metal laser sintering (DMLS) has been reported in papers in the field of veterinary medicine as a manufacturing method for endoprosthesis or intraosseous implants (5, 6, 17, 18). This type of technology is cheaper than traditional manufacturing (15). However, it is still quite expensive when compared with fused deposition modeling (FDM) (16). Currently, there are a few patents for 3D-printed exo-endoprostheses that are manufactured in FDM, such as ES2736410A1 (19) or US10925755B2 (20). Nevertheless, the mechanical properties of polymers manufactured by FDM should be evaluated, as these properties are usually inferior to those obtained by the injection molding process (21–23). Thus, preliminary tests are recommended with tensile test samples of the studied polymers. Tensile test samples are shaped according to ISO 527-1 (24).

To assess a new material for a load-bearing device, a factor of safety (FoS) should be determined to endorse the feasibility of the material for that activity and situation. Currently, the FoS and working load have not been determined for veterinary limb salvage devices. Working load is the applied load on the device during the activity. FoS is a ratio defined for any mechanical device to avoid failure during its work, expressed as the ratio of the maximum load (failure load) to the working load. As a working load, these devices will withstand different body weights (BWs) according to the type of pace and moment of the stance phase (25–27) during the gait cycle. Each canine pelvic limb bears approximately 0.44 times its BW during walking (28, 29), around 0.71 times its BW during trotting (25), and 1.5 times its BW while dogs are in a steady gallop (26, 30). To compare the aforementioned weight-bearing forces, data have been normalized to the BW of animals using the BW equation described by Krotscheck et al. (31). Hence, these values could be considered as working load for determining the FoS for *ex vivo* mechanical testing of new load-bearing implants. Currently, published quasistatic and dynamic mechanical tests of other veterinary implants (5, 32, 33) just expected device failure without relating it to an actual canine weight-bearing force. In addition, the mechanical tests will need the placement of the bone specimens as close as possible to the real positions during canine paces. Kinematic studies can be used as a reference for this issue. A range of 126° to 147.2° is collected for a stifle joint during walking at a stance stage (34), while a range of 107° to 159° is registered at trotting, galloping, and acceleration (27, 30). These data give an average stifle angle of 135°, which is the assumed value of this joint for dogs in veterinary medicine. In a dynamic test, the stride per second of each pace can be used as a reference for adjusting frequency values (35). Strides per second range approximately from 3 to 1 depending on galloping to walking pace, respectively.

The aim of this study is to determine if PEEK material in contact with the bone could be a possible weight-bearing option for canine patients during their regular gaits. This work describes initial *ex vivo* research on the use of a PEEK sleeve to interface between the bone and inner part of an exo-endoprosthesis in the context of limb-sparing surgery. The 3D-printed endoprosthetic element was tested by new loading protocols to mimic normal canine loads during walking, trotting, and galloping. To our knowledge, no evidence of mechanical tests was found for other exo-endoprostheses in veterinary medicine.

METHODS

Endoprosthesis Design

The assessed endoprosthesis was patented by Mendaza et al. (19) and was composed of two main elements: (i) the PEEK sleeve, composed of a base, "umbrella", neck, and stem (36), which will be in contact with bone tissue, and (ii) surgical metal threaded rod, made of AISI 316 austenitic stainless steel, which will be attached to an exoprosthesis (**Figure 1**).

The PEEK sleeve of the endoprosthesis was designed with a CAD program (SolidWorks, SolidWorks Corp., Waltham, MA).

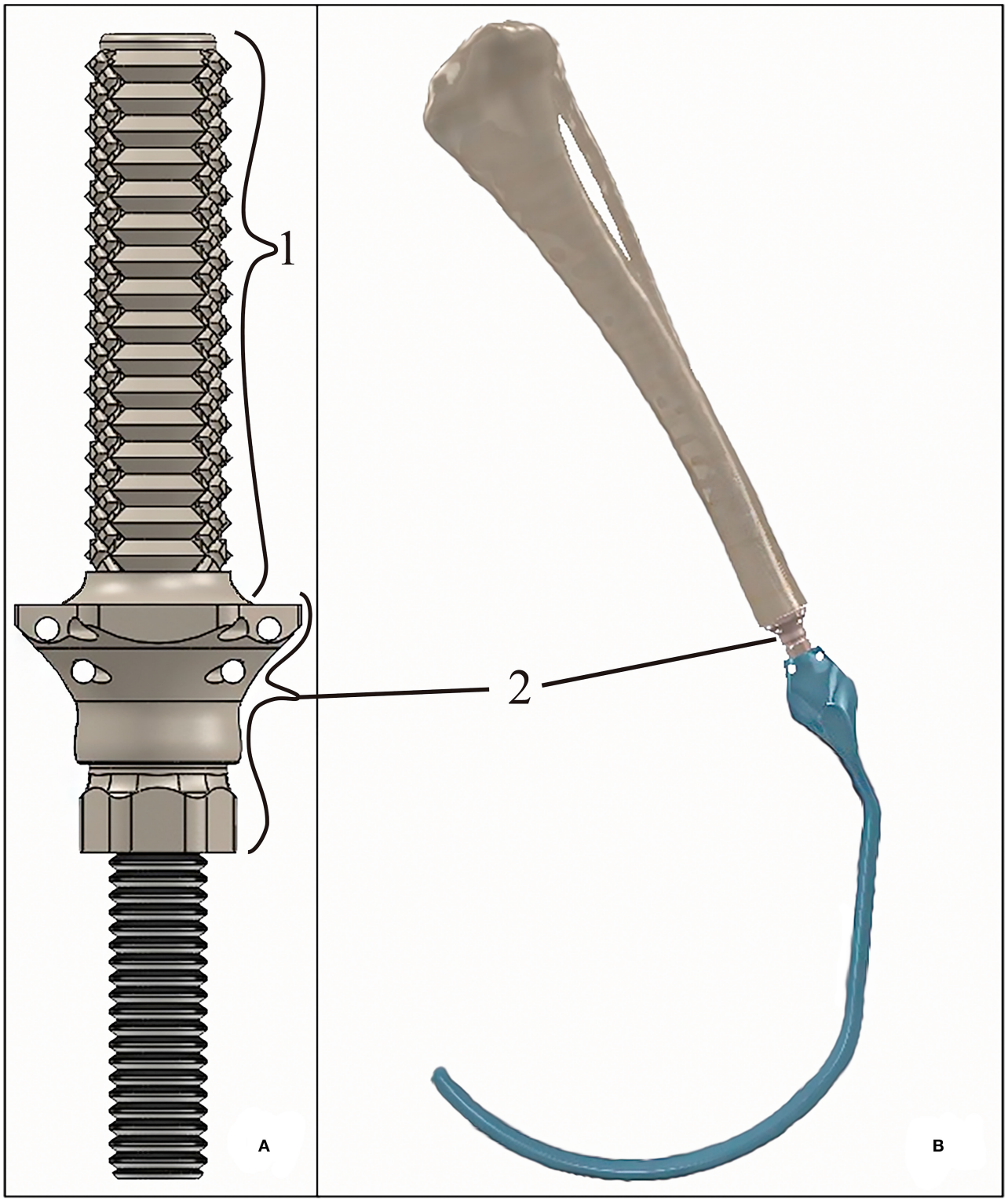

FIGURE 1 | (A) 3D-rendered model of the tibial endoprosthesis and **(B)** 3D-rendered assembly of the exo-endoprosthesis inserted into a tibia. The exo-prosthesis part (blue) is an example of the ideal construct. Where (1) represents the stem; and (2) represents an approximation base- "umbrella" section.

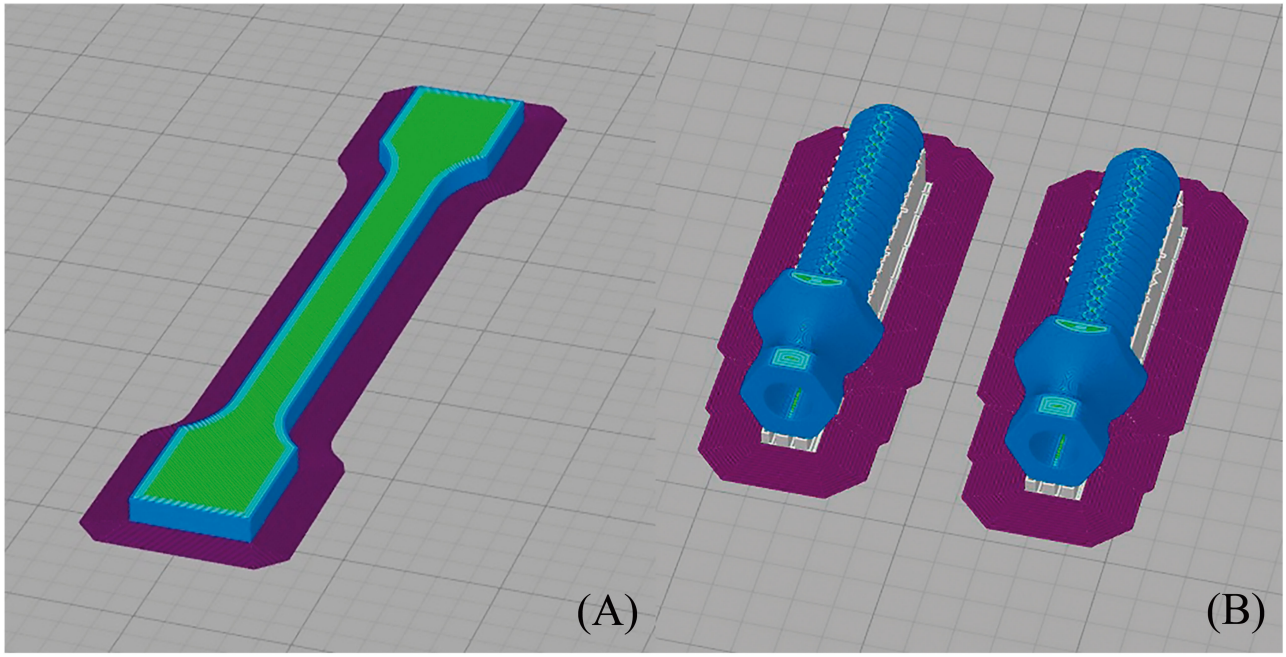

FIGURE 2 | Printing simulation of **(A)** dog bone sample (its dimensions were 75 ± 0.5 mm length, 5 ± 0.2 mm width, and 3.5 ± 0.2 mm thickness, with a gauge length of 25 ± 0.5 mm) and **(B)** endoprosthesis (its dimensions were 16.54*50.21*14.72 mm^3, which are width, length, and thickness of the printing bed, respectively) in Simplify 3D.

TABLE 1 | Characteristics of FDM printings at Simplify 3D slicer. DB- and RB-samples, are tensile test and bending test samples.

		Tibial endo-prosthesis	DB- and RB-samples
N° Models each printing		2 (40 mm distance between them)	1
Extrusion multiplier		0.92	0.92
Layer height (mm)		0.05	0.05
Skirt	*Layer*	1	1
	Skirt outlines	15	15
Infill (%)		50	50
Speed	*Default (mm/s)*	30	30
	Outline underspeed (%)	50	50
	Solid infill underspeed (%)	80	80
	Supports underspeed (%)	80	80

The external diameter of the stem was 0.40 mm larger than the drilled medullary canal of a tibia (9 mm). Thus, all external diameters of the stems measured 9.40 mm. The diameter of the inner cavity of the PEEK sleeve was 6 mm just like the diameter of the threaded rod. This cavity was slightly reduced at the level of the stem for applying extra-radial compression to the bone, such as that described by Mendaza-DeCal et al. (36).

3D Printing Material

Tibia endoprostheses and tensile and bending test samples were printed in PEEK (3D4Makers, Amsterdam, Netherlands). Filaments were stored in a special ziplock multi-layered bag with a special EVOH barrier film and silica desiccant sachets provided by the filament supplier. Otherwise, following the recommended protocols in the literature (22) and by filament manufacturers, spools were dried at 150 °C for 3 h in a dry heat oven before printing with PEEK.

3D Printing Manufacturing Parameters

Tensile and bending test samples and endoprostheses were printed by FunMat HT (INTAMSYS, Shanghai, China) based on FDM technology, with a build volume of 260 mm × 260 mm × 260 mm (x, y, and z). The printer has a hardened steel nozzle of 0.4 mm diameter. This printer reaches a nozzle temperature of up to 450 °C, bed temperature of up to 160 °C, and chamber temperature of up to 90 °C. Before printing, 3D virtual models were sliced by Simplify 3D software (Cincinnati, USA).

All 3D models were horizontally oriented with respect to the printing bed (36). The largest axes of the endoprostheses and tensile test samples with dog bone shapes were oriented parallel to the printing bed (**Figure 2**). Endoprosthesis dimensions were 16.54*50.21*14.72 mm^3, which are x, y, and z of the printing bed, respectively. Also, the bending test samples were printed like rectangular bars, with the same printing orientation as the other 3D models. A horizontal orientation was carried out to take into account the main mechanical forces borne inside the medullary canal. The general printing parameters were constant for all 3D models, which are shown in **Table 1**. Also, the temperature parameters were the same for both 3D models: nozzle temperature of 410 °C, bed temperature of 130 °C,

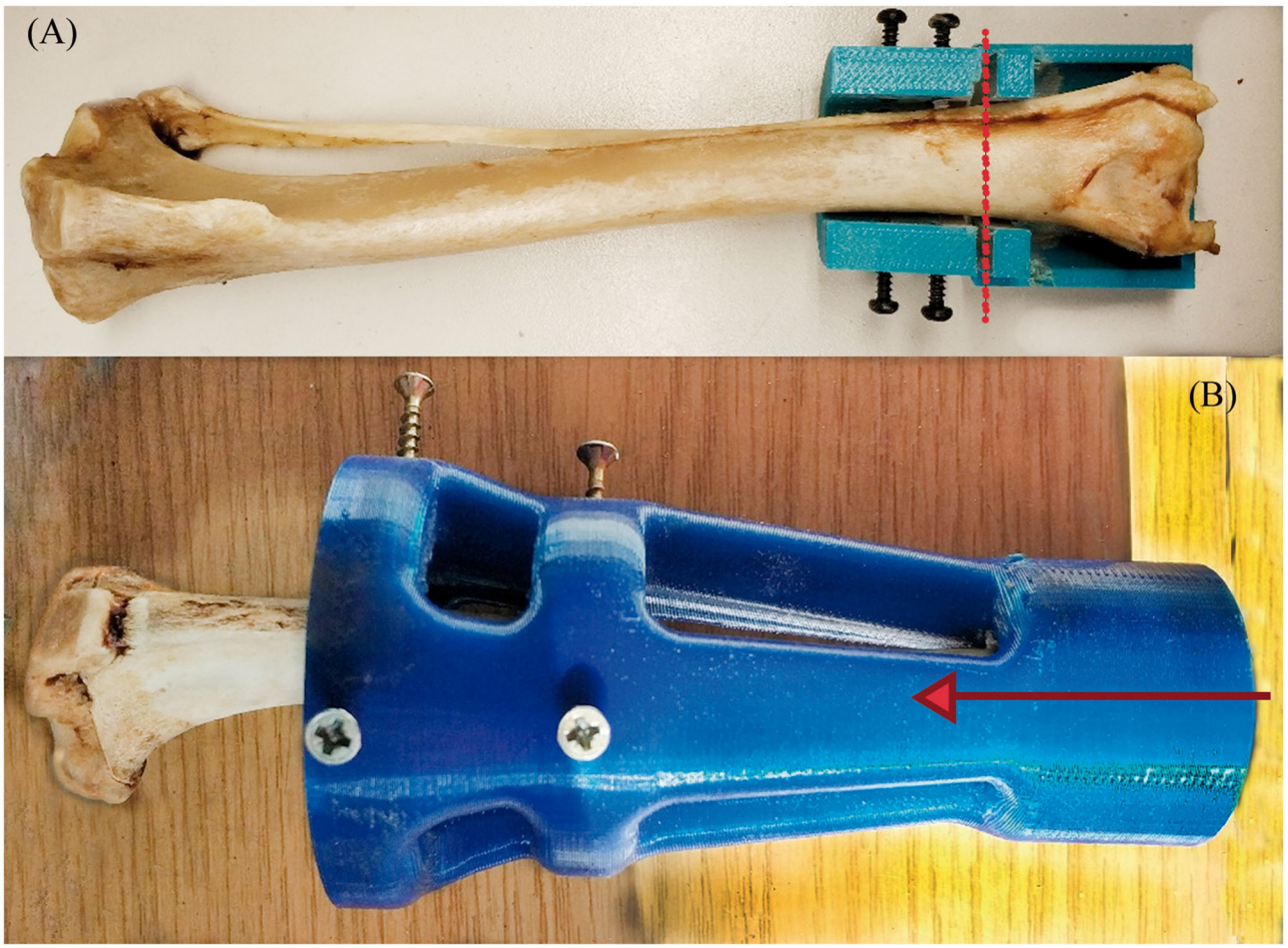

FIGURE 3 | Transverse cut **(A)** and MC-concentric drill **(B)** guides. Both self-designed and printed at PLA. At **(A)**, the red dash line represents where the transversal cut was made on the distal tibia. At **(B)**, the red arrow represents the drilling direction of the MC to homogenize the MC diameter.

chamber temperature of 90 °C, and the cooling fan speed of 50%. All these parameters were set without variants between the 3D models because it has been proven that the mechanical properties of 3D-printed models varied due to printing conditions (21, 23, 37).

Furthermore, immediately before each printing, a specific liquid fixative (Dimafix, DIMA 3D, Valladolid, Spain) for 3D printing was applied to the cold print bed for better adhesion of the material during printing. A preheat of the chamber and build bed temperatures were set and allowed to stabilize for at least for 30 min before starting any printing.

Preparation of the Endoprosthesis-Tibia Construct

The endoprosthesis-tibia interface will be referred to as endoprosthesis-tibia construct in this article. The construct was assessed by mechanical tests. *Ex vivo* fresh tibiae were used to insert the endoprostheses. The 33 tibiae used for this study belonged to canine specimens (20.85 ± 1.25 kg BW) that were euthanized for reasons unrelated to this study. The longitudinal length of tibiae was 208.51 ± 40.27 mm. The fresh bones were immediately stored inside a vacuum bag in a freezer until the insertion of the endoprosthesis. Bones were perpendicularly cut to the longitudinal axes above the distal epiphysis. Immediately, the medullary canals of the tibiae were measured on the cut plane by a metric digital caliper. Tibiae with an average medullary canal diameter of 9.48 ± 0.29 mm were selected. This average medullary canal diameter was observed on the selected canine specimens. After measure, the medullary canal was drilled with a 9 mm bit to homogenize the canal. Two PLA 3D-printed self-designed surgical guides were used to make perpendicular cuts and to align drilling (**Figure 3**) (36). Insertion of the endoprosthesis was made by soft blows with a hammer. Later, an AISI 316 austenitic stainless steel threaded rod with a diameter of 6 mm was gently inserted using a locknut, with a length of 30 mm being left outside the PEEK sleeve. Cutting, drilling, and insertion were carried out by the same operator.

Once the endoprostheses were inserted, 25 tibiae were attached with a two-component epoxy resin (Resoltech 1050/1058S, Eguilles, France) in aluminum holders. Tibiae

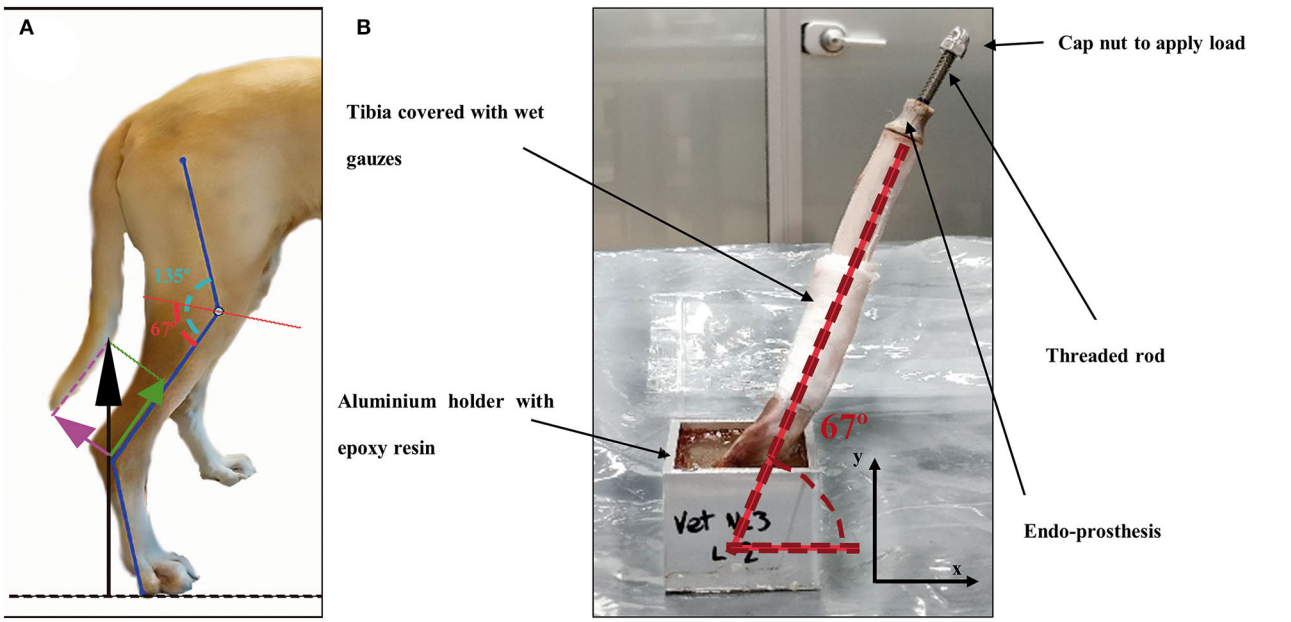

FIGURE 4 | (A) Schematic figure of the decompounded ground reaction force (black arrow) on the canine tibia in compression (green arrow) and bending forces (pink arrow). Angle of the stifle joint (135°) was split in half by a red line as a reference for testing. **(B)** Endoprosthesis-tibia construct at 67° to the testing table for compression-bending and fatigue testing.

TABLE 2 | Elastic properties of bulk PEEK, stainless steel, titanium, and canine tibia obtained from the literature.

Material	Tensile strength (MPa)	Young's modulus (GPa)	Bending strength (MPa)
Bulk PEEK (41)	97–117	3.76–3.95	105–116
316L-SS (41–43)	90–1,100	193–210	170–310
Ti (46,47)	240–1,100	110	130–1,280
Canine Tibia (44, 45)	107.7–199.12	8.85–15.59	142–193

were cured in the holders at half the average angle of the stifle joint when the dog is standing (**Figure 4A**), as described by Holler et al. (38). The angle value of attachment was 67° of the tibial axis to the test table (**Figure 4B**) for compression-bending and fatigue tests. This angle is consistent with the average angle in maximum weight-bearing during trotting, acceleration, and galloping, as it has been described in the introduction section. The remaining eight tibiae were perpendicularly clamped to the test table for a pure compression test.

Mechanical Testing

Mechanical Characterization of the 3D-Printed PEEK

The tensile properties of the 3D-printed PEEK were determined using tensile test samples with dog bone shapes (DB-samples) (39) (**Figure 2A**). The dimensions for each sample were 75 ± 0.5 mm in length, 5 ± 0.2 mm in width, and 3.5 ± 0.2 mm in thickness, with a gauge length of 25 ± 0.5 mm. All these measurements were according to the Spanish standard UNE 116005:2012 (39). Tests were performed according to ISO 527-1 (24) using the universal testing machine Elib 20W (SAE Ibertest Madrid, Spain) with a load cell of 2 kN, which operated at a crosshead speed of 1 mm/min.

A three-point bending load arrangement was used to determine the bending properties in accordance with ISO 178 (40). The tests were conducted using the universal testing machine IBTH/500 (Ibertest, Madrid, Spain) with a load cell of 500 N, which operated at a crosshead speed of 5 mm/min. For the bending tests, the samples were rectangular bars (RB-samples) with dimensions of 80.0 ± 0.1 mm length, 10.0 ± 0.1 mm width, and 4.0 ± 0.1 mm thickness [dimensions according to the Spanish standard UNE 116005:2012 (39)]. Eight samples were tested for each kind of test.

The results of the elastic properties were compared with those of canine tibiae, bulk PEEK, 316L stainless steel (316L-SS), and titanium (Ti) obtained from the literature (**Table 2**).

Quasistatic Mechanical Testing of the Endoprosthesis

Pure compression (**Figure 5A**) and bending (**Figure 5B**) tests were carried out onto endoprostheses themselves (E-samples) using the universal testing machine Elib 20W with a load cell of 2 kN, which operated at a crosshead speed of 500 mm/min. Five samples were tested for each kind of test. The aim of these tests was to find the weakest zone of the endoprosthesis and estimate if the mechanical strength of the endoprosthesis in the main load direction (vertical position) was enough to support the BW of the dog.

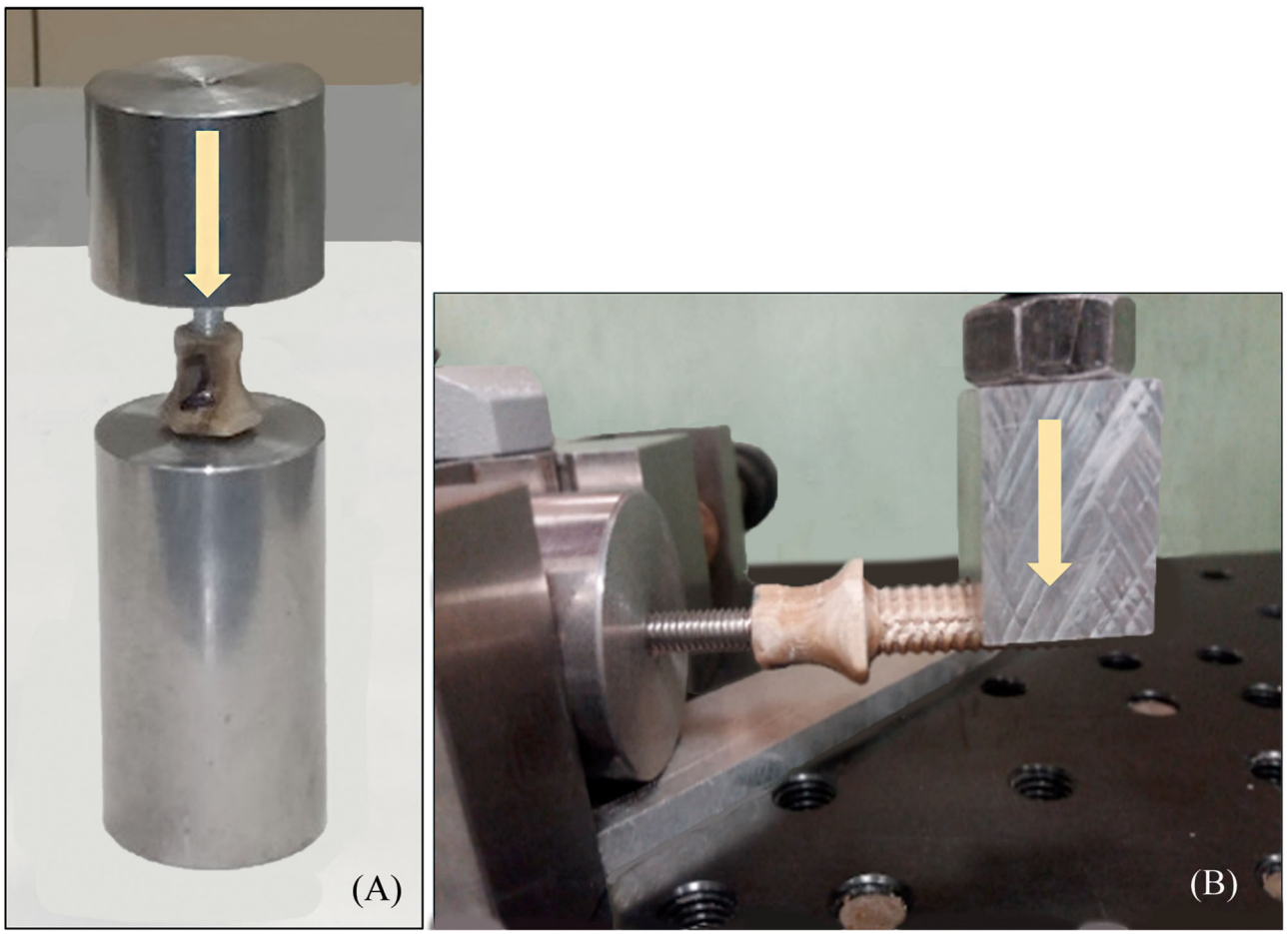

FIGURE 5 | (A) Pure compression (endoprosthesis at vertical position) and **(B)** bending test (endoprosthesis at horizontal position) of the endoprosthesis. Yellow arrows represent the direction of the applied force.

Pure Compression and Compression–Bending Testing of the Endoprosthesis-Tibia Construct

To obtain a more realistic result about the mechanical behavior of the endoprosthesis-tibia construct, samples (ET-samples) were prepared as described in section 2.4 above for pure compression (90°) and compression-bending test (67°). Each of the ET samples was assessed using the universal testing machine Elib 20 W (SAE Ibertest Madrid, Spain) with a load cell of 2 kN (**Figure 6A**). Tests were conducted under room conditions (22 ± 1 °C). Bones of ET-samples were covered with a gauze soaked in phosphate buffer solution (PBS) to maintain the correct pH and degree of humidity, simulating the *in vivo* conditions. Eight ET-samples were evaluated by pure compression testing (**Figure 6A**) and 15 ET-samples by compression-bending testing (**Figure 6B**) at a crosshead speed of 500 mm/min.

Fatigue Compression-Bending Testing of the Endoprosthesis-Tibia Construct

Fatigue tests are particularly important to study the long-term behavior of the endoprosthesis-tibia construct. The load to be supported by the tibia can be approximated by equation 1 (26, 30). For a theoretical 20 kg dog, if we consider the most unfavorable circumstances (dog at galloping), the maximum load to support would be approximately 300 N. This value was also considered as a working load to determine the FoS.

$$Maximum\ load\ (N) = 1.5\ x\ DW\ \left(dog\ weight\ in\ kg\right)\ x\ 9.8 \quad (1)$$

Fatigue testing was conducted under room conditions (22 ± 1 °C) using an electrodynamic testing machine with a load cell of 3 kN (ElectroPlus E3000, Instron, Norwood, MA, USA). ET-samples were prepared as described in section 2.4 (**Figure 6B**) for compression-bending testing. These samples were assessed until failure or until 500,000 cycles, using a sinusoidal force cycle with a maximum load of 300 N and a load ratio of $R = 0.1$. A frequency of 2 Hz was used for the test, which is similar to the pacing frequency when the dog is trotting. Under these conditions, 10 ET-samples were evaluated.

Statistical Analysis

Data from pure compression of E-samples and ET-samples tests were analyzed by analysis of variance (ANOVA) using

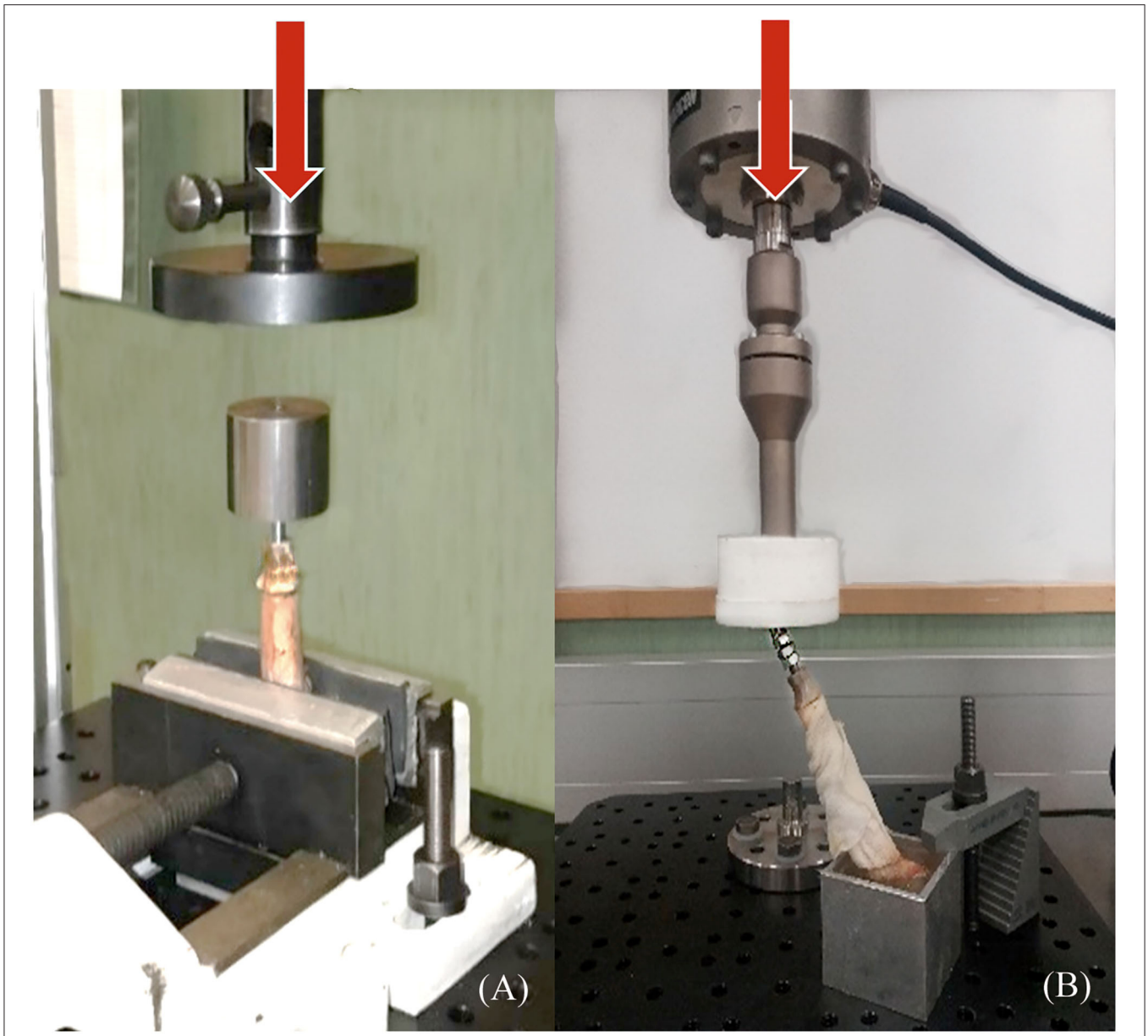

FIGURE 6 | Pure compression **(A)** and compression-bending **(B)** tests of endoprosthesis-tibia construct. **(A)** samples were tested clamped directly to the bone, and **(B)** samples were potted at 67° to the ground before testing. Red arrows represent the direction of the applied force.

the STATGRAPHICS program (XVII Centurion. Ver. 17.2.00, StatPoint, Inc., Herndon, VA, USA). Also, compression-bending data with or without fatigue tests were analyzed by analysis of variance (ANOVA). Significant differences were observed ($p \leq 0.05$) by the *F*-test for both comparisons.

RESULTS

Mechanical Testing of 3D-Printed PEEK Samples

Tensile strength, Young's modulus, and bending strength of the DB- and RB- samples, as described in section 2.5.1, were 36–52 MPa, 2.1–2.9 GPa, and 46–70 MPa, respectively. These results were compared with those of Ti, 316L-SS, bulk PEEK, and canine tibiae obtained from the literature. 3D-printed PEEK exhibited a reduction of tensile strength of 2- to 16-fold compared with the other materials. Comparing 3D-printed PEEK with bulk PEEK, the reduction was 2.5-fold. Young's modulus of 3D-printed PEEK was closer to that of bone than to that of metal. 3D-printed PEEK was 0.2-fold inferior to that of bone, while 316L-SS and Ti alloys exhibited Young's modulus 9- and 16-fold higher, respectively (**Supplementary File 1**).

3D-printed PEEK exhibited a reduction of bending strength of 1.9- to 12.2-fold compared with that of

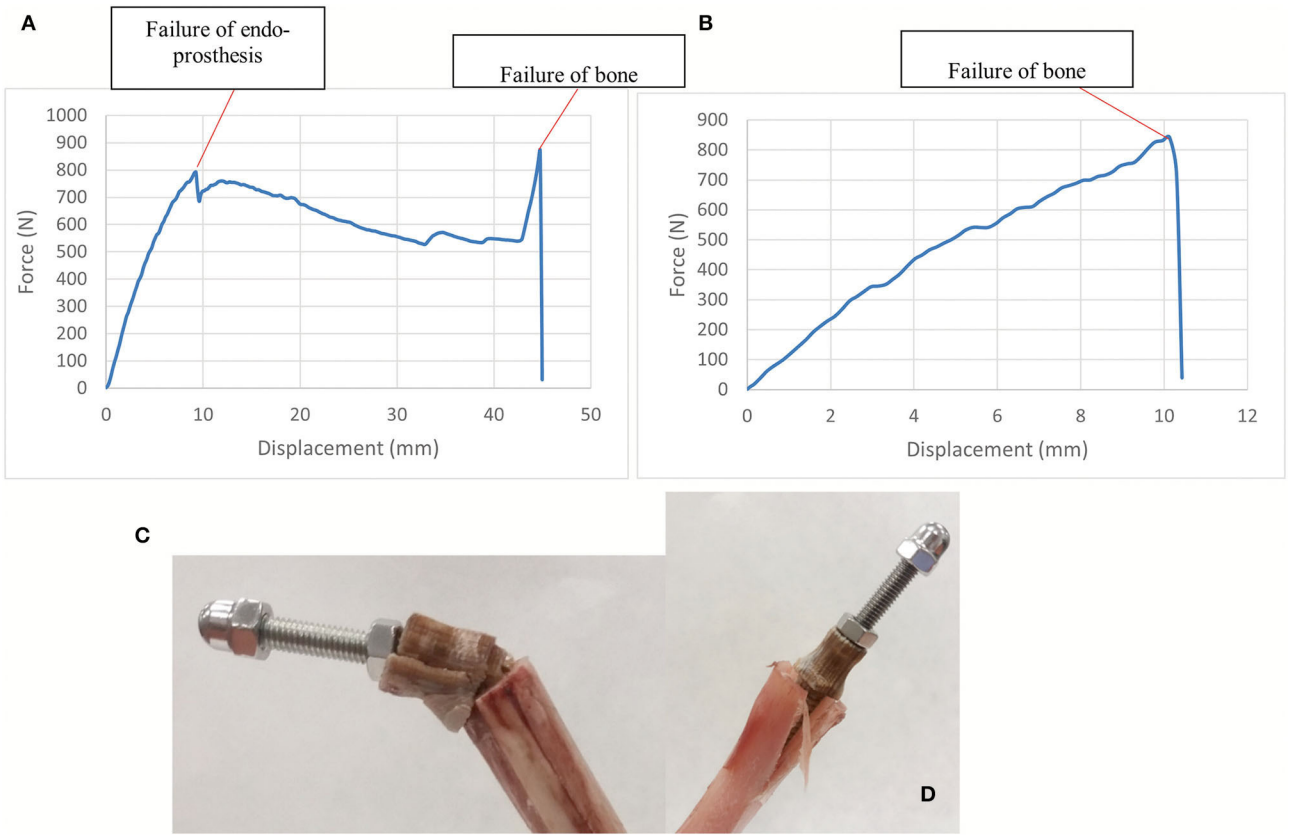

FIGURE 7 | (A,C) show force-displacement curve and ET-samples after endoprosthesis failure in a long tibia. **(B,D)** show force-displacement curve and ET-samples after bone failure in a short tibia. Compression-bending test of the tibia-endoprosthesis constructs at 67° to the ground.

other materials. Additionally, its bending strength was closer to that of bone than to that of metal, especially compared to Ti.

Mechanical Testing of the Endoprosthesis

Mechanical Testing of the Non-inserted Endoprosthesis

In all the bending tests, the endoprosthesis remained intact, while the steel rod showed plastic deformation. In the compression tests, the failure occurred between the umbrella and stem of the endoprosthesis, with a maximum load of 936 ± 199 N (**Supplementary File 2**).

Compression-Bending and Pure Compression Testing of the Endoprosthesis-Tibia Construct

The compression-bending test (67°) was assessed for the 15 ET-samples (**Supplementary File 3**). The tested samples showed two different types of failure. In eight of them, the endoprosthesis broke, leading to a force-displacement graph with a first peak load due to endoprosthesis failure and a second peak that indicates the fracture of the tibia (**Figures 7A,C**). The bone failure occurred in the seven remaining samples, without any damage to the endoprosthesis after testing. In these cases, the force-displacement curves only showed the peak of the tibia fracture (**Figures 7B,D**). Considering only the breaking data of the eight endoprostheses, the average failure force is 785 ± 101 N. The calculated FoS was 2.6 ± 0.3 for ET-samples at the compression–bending test.

The results of the pure compression test reached a maximum force of 1,642 ± 447 N before failure (**Supplementary File 2**). For higher forces, the endoprostheses failed between the umbrella and distal tibia (**Figure 8**). The calculated FoS was 5.8 ± 1.4 for ET-samples at pure compression.

Fatigue Testing of the Endoprosthesis-Tibia Construct at 67°

Upon fatigue test, the assessed ET-samples reached 500,000 cycles without failure. To analyze the effect of fatigue, the survivor samples were evaluated for failure by means of the quasistatic compression-bending test described in section 2.5.3. The samples could stand 764 ± 62 N upon static compression-bending test after fatigue before breaking (**Supplementary File 3**). No statically significant differences were observed between the maximum force at the compression–bending test with or without the previous fatigue test with a $p \leq 0.05$. The calculated FoS was 2.5 ± 0.2 for ET-samples at the compression–bending test after fatigue.

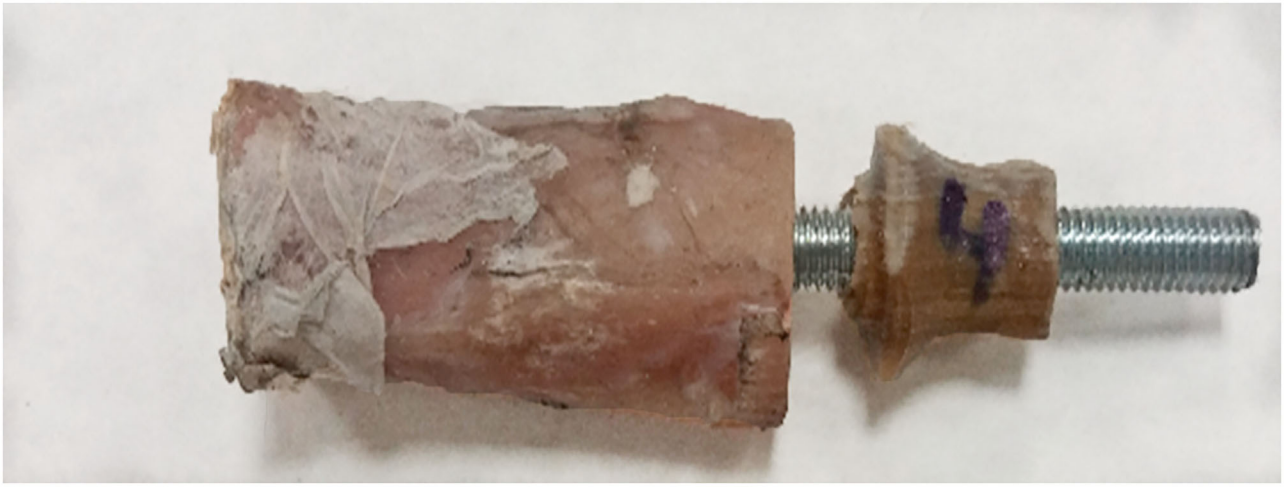

FIGURE 8 | Failure example of the tibia-endoprosthesis constructs observed after pure compression test.

DISCUSSION

The 3D-printed endoprosthetic element can withstand normal weight-bearing loads reported in dogs at walk and trot. Additionally, we demonstrate that the behavior of the construct with acute loading to failure is not significantly different if the endoprosthesis is pre-fatigued with 500,000 cycles of pre-loading. The PEEK part of the endoprosthesis bore higher flexion and compression forces than canine tibiae during galloping (26, 30). All obtained results during our tests were more than two times the vertical load that the endoprosthesis will have to support during the life of the canine. Thus, PEEK could be an interesting option for weight-bearing implants in quadrupedal animals because a single limb would support the entire weight of the animal.

The ET-samples showed a maximum load at failure of more than 2-fold the selected working load (300 N for a 20 kg dog) in the compression–bending test. These results are even more promising considering that we only used a wet canine tibia without the remaining skeletal system components of the pelvic limb. Besides, we are comparing compression-bending results with the force borne by the whole pelvic limb, which is another handicap for the studied endoprosthesis. In addition, it should be considered that the compression-bending tests were carried out in a standing-like position, imitating the canine stifle angle (38). It means that the endoprosthesis suffered bending and compression load, at the same time, during our compression-bending test. Taking into consideration that all tibiae had a medullary canal of 9 mm and the inserted endoprostheses had the same size, two types of failure have been described in the ET-samples during this test. In eight samples, failure occurred in both the prosthesis and bone, and in seven samples, the endoprosthesis remained intact while bone failure occurred. These failure modes could be explained due to the lengths of the assessed tibiae. Thus, if the ET-sample is considered as a cantilever, with more bone length, more bending moments would suffer the endoprosthesis (9). Thus, in longer tibiae, both failure of bone and the PEEK part will be expected. We can confirm that these facts are disadvantages for the endoprosthesis because, during the bending test of the E-samples, the PEEK part remained intact while the steel rod showed plastic deformation.

The fatigue test shows the long-term behavior of a device. The results of fatigue and the following compression-bending test indicate that the endoprosthesis can withstand 500,000 cycles with a trotting-like frequency and the total BW during galloping without detriment of its strength. The fatigue parameters, cycles, and frequencies were set based on other papers where fatigue resistance was evaluated for different metal implants (32, 33) and assuming that trotting is the dog's pace with more step frequency. These test conditions were considered the most unfavorable scenario. No significant differences were observed between the maximum force at the compression–bending test with or without the previous fatigue test. Therefore, the FoS after fatigue indicated that the endoprosthesis designed for this work would not experience dangerous levels of load during normal activity.

Pure compression results confirm that force-bearing data from only pure compression of the E-samples or from pure compression of ET-samples are significantly different. The ET-samples could stand 1,642 ± 447 N on pure compression (5-fold increase in the dog's weight-bearing), in contrast to 936 ± 199 N in the E-samples. This means that the endoprosthesis has better results in an environment closer to a real one, such as using wet bones (46) as receptacles for the endoprosthesis. Bone is considered an anisotropic material that has different elastic behavior and strength according to the percentage of humidity, the forces applied, and the force speed application (46–48). Thus, achieving a test environment close to a real situation for medical application is essential for bone. Likewise, this increase in force-bearing results was because of the lateral compression exerted by

the tibia during the endoprosthesis since part of the load applied to the endoprosthesis is transmitted to the tibia.

When a 3D printer is used to obtain solid pieces, the resultant material shows anisotropic behavior (49). Therefore, the 3D-printed PEEK properties will be different in each direction and will depend on the printing conditions. For this reason, mechanical characterization was carried out on 3D-printed PEEK samples (under the same printing conditions as the endoprostheses) to determine the mechanical properties of the PEEK material used for the endoprosthesis and to compare them with those of the tibiae. The differences observed in the mechanical properties between 3D-printed PEEK and bulk PEEK are due to the small spaces between the printed layers, which is typical in FDM technology, and to the infill parameter of 50% for the dog bone shape samples. This infill parameter was the same as that of the endoprostheses, which causes a drop in the mechanical properties (49) of 3D-printed PEEK. Nevertheless, its elasticity was still within canine cortical bone ranges and closer than those of metallic materials (21, 22). Young's modulus especially was in the same order of magnitude as that of bone. In addition, the tensile and bending strengths of 3D-printed PEEK are enough to guarantee that the endoprosthesis will deform similarly to the bone. Besides, the lower stiffness and strength of 3D-printed PEEK with respect to that of bone allows for a good transfer of the loads from the implant to the tibia, minimizing the probability of peri-implant bone loss due to stress-shielding (7, 10, 42). Also, using no annealed 3D-printed PEEK permits anisotropic material behavior (22, 23, 49). This makes the force transmission between PEEK and bone more interesting because putting two anisotropic materials in contact with a similar elastic modulus and transmitting the bearing forces through them could be a potential solution to the stress-shielding phenomenon. In addition, the interaction of PEEK and canine tibia can be evaluated by comprehending the mechanical characterization of 3D-printed PEEK, mechanical properties of the canine tibia, and force-bearing results of pure compression of ET-samples. The interaction of two materials with similar elastic properties, such as PEEK and canine tibia, made a similar deformation of both materials. Once the endoprosthesis is inserted on the tibia, it adapts its shape to the medullary canal. This deformation would allow the reduction or elimination of dead spaces between the internal part of the exo-endoprosthesis and the bone. This PEEK-bone interface seems to permit a better stress transmission, as pure compression data of ET-samples had been probed. This increment of stress transmission would reduce the possibilities of stress-shielding phenomenon in a real situation. Nonetheless, more studies about it should be done.

In conclusion, the evaluated endoprosthetic part of an exo-endoprosthesis can largely withstand a dog's weight during a galloping pace and at a higher frequency than this pace without detriment to its maximum weight-bearing. This makes the 3D-printed PEEK exo-endoprostheses a suitable mechanical choice for medical devices in veterinary medicine.

DATA AVAILABILITY STATEMENT

The original contributions presented in the study are included in the article/**Supplementary Material**, further inquiries can be directed to the corresponding author.

AUTHOR CONTRIBUTIONS

Conceptualization: RM-D, YB, JR-R, and JR-Q. Data curation, methodology, resources, and writing—original draft: RM-D, YB, and JR-R. Formal analysis and validation: RM-D and JR-R. Funding acquisition and project administration: JR-Q and SP-F. Investigation: RM-D, YB, JR-R, and EP. Software: RM-D, SP-F, EP, YB, and JR-R. Supervision: JR-Q, SP-F, and JR-R. Writing—review and editing: RM-D, YB, JR-R, and JR-Q. All authors contributed to the article and approved the submitted version.

FUNDING

This work was supported by the regional government of Madrid, Spain [Grant IND2017/BMD-7726]. RM-D received a PhD fellowship from this grant. The regional government of Madrid was not involved in any decision about the development of this study.

ACKNOWLEDGMENTS

We would like to thank Abax Innovation Technologies and the Veterinary Anatomy and Embryology Department of the Faculty of Veterinary Medicine at Complutense University of Madrid for their technical support and knowledge. In addition, we are sincerely thankful to all the people of the Industrial Testing Laboratory at the ICAI School of Engineering of Comillas Pontifical University, especially to Gonzalo García Galán and Susana Guzmán.

SUPPLEMENTARY MATERIAL

The Supplementary Material for this article can be found online at: https://www.frontiersin.org/articles/10.3389/fvets.2022.887676/full#supplementary-material

Supplementary File 1 | PEEK_tests.xlsx. Tested 3D-printed PEEK samples and their corresponding dimensions and strength results are shown. Characteristics of the tests, mean and standard deviation (SD) are also described.

Supplementary File 2 | Compression_Tests.xlsx. Strength results of the endoprosthesis and bone-endoprosthesis assembly are described. Also, characteristics of the tests, mean, and standard deviation (SD) are also described.

Supplementary File 3 | C-B_Tests.xlsx. Number of ET-samples and their corresponding results at compression-bending test before and after fatigue test are shown. Also, characteristics of the tests, mean, and standard deviation (SD) are also described.

REFERENCES

1. Thesleff A, Brånemark R, Håkansson B, Ortiz-Catalan M. Biomechanical characterisation of bone-anchored implant systems for amputation limb prostheses: a systematic review. *Ann Biomed Eng.* (2018) 46:377–91. doi: 10.1007/s10439-017-1976-4
2. Fitzpatrick N, Smith TJ, Pendegrass CJ, Yeadon R, Ring M, Goodship AE, et al. Intraosseous Transcutaneous Amputation Prosthesis (ITAP) for limb salvage in 4 dogs. *Vet Surg.* (2011) 40:909–25. doi: 10.1111/j.1532-950X.2011.00891.x
3. Farrell BJ, Prilutsky BI, Kistenberg RS, Dalton JF, Pitkin M. An animal model to evaluate skin–implant–bone integration and gait with a prosthesis directly attached to the residual limb. *Clin Biomech.* (2014) 29:336–49. doi: 10.1016/j.clinbiomech.2013.12.014
4. Drygas KA, Taylor R, Sidebotham CG, Hugate RR, Mcalexander H. Transcutaneous tibial implants: a surgical procedure for restoring ambulation after amputation of the distal aspect of the tibia in a dog. *Vet Surg.* (2008) 37:322–7. doi: 10.1111/j.1532-950X.2008.00384.x
5. DeVasConCellos P, Balla VK, Bose S, Fugazzi R, Dernell WS, Bandyopadhyay A. Patient specific implants for amputation prostheses: design, manufacture and analysis. *Vet Comp Orthop Traumatol.* (2012) 25:286–96. doi: 10.3415/VCOT-11-03-0043
6. Golachowski A, Al Ghabri MR, Golachowska B, Al Abri H, Lubak M, Sujeta M. Implantation of an intraosseous transcutaneous amputation prosthesis restoring ambulation after amputation of the distal aspect of the left tibia in an arabian Tahr (Arabitragus jayakari). *Front Vet Sci.* (2019) 6:182. doi: 10.3389/fvets.2019.00182
7. Huiskes R, Weinans H, Rietbergen BV. The relationship between stress shielding and bone resorption around total hip stems and the effects of flexible materials. *Clin Orthop Relat Res.* (1992) 274:124–34. doi: 10.1097/00003086-199201000-00014
8. Wooley P, Schwarz E. Aseptic loosening. *Gene Ther.* (2004) 11:402–7. doi: 10.1038/sj.gt.3302202
9. Sharir A, Barak MM, Shahar R. Whole bone mechanics and mechanical testing. *Vet J.* (2008) 177:8–17. doi: 10.1016/j.tvjl.2007.09.012
10. Sumner DR. Long-term implant fixation and stress-shielding in total hip replacement. *J Biomech.* (2015) 48:797–800. doi: 10.1016/j.jbiomech.2014.12.021
11. Kurtz SM. *PEEK Biomaterials Handbook*. 2nd ed. Amsterdam: Elsevier (2019). p. 465.
12. Maté Sánchez de Val JE, Gómez-Moreno G, Pérez-Albacete Martínez C, Ramírez-Fernández MP, Granero-Marín JM, Gehrke SA, et al. Peri-implant tissue behavior around non-titanium material: experimental study in dogs. *Ann Anat.* (2016) 206:104–9. doi: 10.1016/j.aanat.2016.03.005
13. Wang N, Xie H, Xi C, Zhang H, Yan J. A study to compare the efficacy of polyether ether ketone rod device with titanium devices in posterior spinal fusion in a canine model. *J Orthop Surg Res.* (2017) 12:40. doi: 10.1186/s13018-017-0543-x
14. Shimizu T, Fujibayashi S, Yamaguchi S, Otsuki B, Okuzu Y, Matsushita T, et al. *In vivo* experimental study of anterior cervical fusion using bioactive polyetheretherketone in a canine model. *PLoS ONE.* (2017) 12:e0184495. doi: 10.1371/journal.pone.0184495
15. Atzeni E, Salmi A. Economics of additive manufacturing for end-usable metal parts. *Int J Adv Manuf Technol.* (2012) 62:1147–55. doi: 10.1007/s00170-011-3878-1
16. Hopkinson N, Dicknes P. Analysis of rapid manufacturing—using layer manufacturing processes for production. *Proc Inst Mech Eng C J Mech Eng Sci.* (2003) 217:31–9. doi: 10.1243/095440603762554596
17. Popov VV, Muller-Kamskii G, Katz-Demyanetz A, Kovalevsky A, Usov S, Trofimcow D, et al. Additive manufacturing to veterinary practice: recovery of bony defects after the osteosarcoma resection in canines. *Biomed Eng Lett.* (2019) 9:97–108. doi: 10.1007/s13534-018-00092-7
18. Bray JP, Kersley A, Downing W, Crosse KR, Worth AJ, House AK, et al. Clinical outcomes of patient-specific porous titanium endoprostheses in dogs with tumors of the mandible, radius, or tibia: 12 cases (2013–2016). *J Am Vet Med Assoc.* (2017) 251:566–79. doi: 10.2460/javma.251.5.566
19. Mendaza De Cal RM, Peso Fernández S, Rodríguez Quirós J. Endoprótesis a medida para huesos largos de animales (2020). Available online at: https://patentimages.storage.googleapis.com/0c/f4/54/d74e23ec379b45/ES2736410A1.pdf (accessed April 27, 2020).
20. Steven Lathers, Jeffrey La Belle. Osseointegratable prosthetic device and manufacturing method. US 2018/0049897 Al, 2018. p. 49.
21. Arif MF, Kumar S, Varadarajan KM, Cantwell WJ. Performance of biocompatible PEEK processed by fused deposition additive manufacturing. *Mater Des.* (2018) 146:249–59. doi: 10.1016/j.matdes.2018.03.015
22. Wu WZ, Geng P, Zhao J, Zhang Y, Rosen DW, Zhang HB. Manufacture and thermal deformation analysis of semicrystalline polymer polyether ether ketone by 3D printing. *Mat Res Innov.* (2014) 18:S5-12–6. doi: 10.1179/1432891714Z.000000000898
23. Yang C, Tian X, Li D, Cao Y, Zhao F, Shi C. Influence of thermal processing conditions in 3D printing on the crystallinity and mechanical properties of PEEK material. *J Mat Process Technol.* (2017) 248:1–7. doi: 10.1016/j.jmatprotec.2017.04.027
24. *Plastics—Determination of Tensile Properties. Part 1: General Principles*. Report No.: ISO 527-1:2019. Geneva: International Organization for Standardization (2019).
25. Voss K, Wiestner T, Galeandro L, Hässig MR, Montavon PM. Effect of dog breed and body conformation on vertical ground reaction forces, impulses, and stance times. *Vet Comp Orthop Traumatol.* (2011) 24:106–12. doi: 10.3415/VCOT-10-06-0098
26. Walter RM, Carrier DR. Ground forces applied by galloping dogs. *J Exp Biol.* (2007) 210:208–16. doi: 10.1242/jeb.02645
27. Colborne GR, Walker AM, Tattersall AJ, Fuller CJ. Effect of trotting velocity on work patterns of the hind limbs of Greyhounds. *Am J Vet Res.* (2006) 67:1293–8. doi: 10.2460/ajvr.67.8.1293
28. Corbee RJ, Maas H, Doornenbal A, Hazewinkel HAW. Forelimb and hindlimb ground reaction forces of walking cats: assessment and comparison with walking dogs. *Vet J.* (2014) 202:116–27. doi: 10.1016/j.tvjl.2014.07.001
29. Schwarz N, Tichy A, Peham C, Bockstahler B. Vertical force distribution in the paws of sound labrador retrievers during walking. *Vet J.* (2017) 221:16–22. doi: 10.1016/j.tvjl.2017.01.014
30. Walter RM, Carrier DR. Rapid acceleration in dogs: ground forces and body posture dynamics. *J Exp Biol.* (2009) 212:1930–9. doi: 10.1242/jeb.023762
31. Krotscheck U, Todhunter RJ, Nelson SA, Sutter NB, Mohammed HO. Precision and accuracy of ground reaction force normalization in a heterogeneous population of dogs: ground reaction force normalization. *Vet Surg.* (2014) 43:437–45. doi: 10.1111/j.1532-950X.2014.12176.x
32. Schmierer PA, Smolders LA, Zderic I, Gueorguiev B, Pozzi A, Knell SC. Biomechanical properties of plate constructs for feline ilial fracture gap stabilization. *Vet Surg.* (2019) 48:88–95. doi: 10.1111/vsu.13124
33. Chao P, Conrad BP, Lewis DD, Horodyski M. Pozzi A. Effect of plate working length on plate stiffness and cyclic fatigue life in a cadaveric femoral fracture gap model stabilized with a 12-hole 24 mm locking compression plate. *BMC Vet Res.* (2013) 9:125. doi: 10.1186/1746-6148-9-125
34. Kim J, Rietdyk S, Breur GJ. Comparison of two-dimensional and three-dimensional systems for kinematic analysis of the sagittal motion of canine hind limbs during walking. *Am J Vet Res.* (2008) 69:1116–22. doi: 10.2460/ajvr.69.9.1116
35. Fischer MS, Lilje KE. Dogs in motion. 2nd ed. Paderborn: VDH (2020).p. 207.
36. Mendaza-DeCal R, Peso-Fernandez S, Rodriguez-Quiros J. Test of designing and manufacturing a polyether ether ketone endoprosthesis for canine extremities by 3D printing. *Front Mech Eng.* (2021) 7:693436. doi: 10.3389/fmech.2021.693436
37. Vaezi M, Yang S. Extrusion-based additive manufacturing of PEEK for biomedical applications. *Virtual Phys Prototyp.* (2015) 10:123–35. doi: 10.1080/17452759.2015.1097053
38. Holler PJ, Brazda V, Dal-Bianco B, Lewy E, Mueller MC, Peham C, et al. Kinematic motion analysis of the joints of the forelimbs and hind limbs of dogs during walking exercise regimens. *Am J Vet Res.* (2010) 71:734–40. doi: 10.2460/ajvr.71.7.734
39. Manufacturing by additive of caps on plastics. *Additive Manufacturing. Preparation of Test Pieces*. Report No.: UNE 116005:2012. Madrid: Asociación Española de Normalización y Certificación (2012).
40. *Plastics—Determination of Flexural Properties*. Report No.: ISO 178:2019. Geneva: International Organization for Standardization (2019).
41. Swanson J. *Ansys Granta EdoPack Software*. Cambridge: Ansys Inc.

42. Geetha M, Singh AK, Asokamani R, Gogia AK. Ti based biomaterials, the ultimate choice for orthopaedic implants—a review. *Prog Mater Sci.* (2009) 54:397–425. doi: 10.1016/j.pmatsci.2008.06.004
43. Dewidar MM, Yoon HC, Lim JK. Mechanical properties of metals for biomedical applications using powder metallurgy process: a review. *Met Mater Int.* (2006) 12:193–206. doi: 10.1007/BF03027531
44. Saha S, Martin DL, Phillips A. Elastic and strength properties of canine long bones. *Med Biol Eng Comput.* (1977) 15:72–4. doi: 10.1007/BF02441578
45. Kemp TJ, Bachus KN, Nairn JA, Carrier DR. Functional trade-offs in the limb bones of dogs selected for running *versus* fighting. *J Exp Biol.* (2005) 208:3475–82. doi: 10.1242/jeb.01814
46. Lee KL, Sobieraj M, Baldassarri M, Gupta N, Pinisetty D, Janal MN, et al. The effects of loading conditions and specimen environment on the nanomechanical response of canine cortical bone. *Mater Sci Eng C.* (2013) 33:4582–6. doi: 10.1016/j.msec.2013.07.018
47. Sammarco GJ, Burstein AH, Davis WL, Frankel VH. The biomechanics of torsional fractures: the effect of loading on ultimate properties. *J Biomech.* (1971) 4:113–7. doi: 10.1016/0021-9290(71)90021-2
48. Sielman E. Mechanical properties of long bones in dogs. *Am J Vet Res.* (1994) 55:3.
49. Pu J, McIlroy C, Jones A, Ashcroft I. Understanding mechanical properties in fused filament fabrication of polyether ether ketone. *Addit Manuf.* (2020) 37:101673. doi: 10.1016/j.addma.2020.101673

Conflict of Interest: RM-D and SP-F were employed by ABAX Innovation Technologies.

The remaining authors declare that the research was conducted in the absence of any commercial or financial relationships that could be construed as a potential conflict of interest.

frontiers | Frontiers in Veterinary Science

TYPE Original Research
PUBLISHED 18 November 2022
DOI 10.3389/fvets.2022.1045785

OPEN ACCESS

EDITED BY
Christian Peham,
University of Veterinary Medicine
Vienna, Austria

REVIEWED BY
Georgi P. Georgiev,
Medical University Sofia, Bulgaria
Balazs Gerics,
University of Veterinary Medicine
Vienna, Austria

*CORRESPONDENCE
Huizhi Wang
wang_huizhi8866@163.com
Cheng-Kung Cheng
ckcheng2020@sjtu.edu.cn

SPECIALTY SECTION
This article was submitted to Comparative and Clinical Medicine, a section of the journal Frontiers in Veterinary Science

RECEIVED 16 September 2022
ACCEPTED 03 November 2022
PUBLISHED 18 November 2022

CITATION
Shi Q, Wang H, He K, Tao M and Cheng C-K (2022) Comparison of the morphology of the anterior cruciate ligament and related bony structures between pigs and humans. *Front. Vet. Sci.* 9:1045785. doi: 10.3389/fvets.2022.1045785

Comparison of the morphology of the anterior cruciate ligament and related bony structures between pigs and humans

Qinyi Shi, Huizhi Wang*, Kaixin He, Mingzhu Tao and Cheng-Kung Cheng*

Engineering Research Center of Digital Medicine, School of Biomedical Engineering and Med-X Research Institute, Ministry of Education, Shanghai Jiao Tong University, Shanghai, China

Introduction: Pigs are widely used for clinical research on the anterior cruciate ligament (ACL) because of the similarity of the knee structure to the human knee. But evidence to support the suitability of using porcine samples to guide clinical practices is limited. This study aims to explore the qualitative and quantitative morphological features of the porcine knee and ACL, and to compare these with data on humans reported in literature.

Methods: Nineteen porcine knees were used for this study. The bone structures were measured on coronal X-ray images. The length of the ACL was measured using a caliper. The ACL bone insertion sites were marked and measured on a digital photograph. The lengths of the long and short axis of the ACL isthmus were measured on the X-ray microscopy reconstructed images. The outcomes were compared with previously reported data on humans using an abstract independent-samples *T* test.

Results: Qualitative observation indicated a similar location, orientation and general morphology of the porcine ACL to human ACLs. The major difference was the location of the ACL tibial insertion with respect to the anterior horn of the lateral meniscus (AHLM). The porcine ACL was split into AM and PL bundles by the AHLM, while the AHLM was adjacent to the anterolateral border of the ACL tibial insertion in human knees. The quantitative comparison showed no significant difference between the human and porcine ACL in terms of the length of the ACL, the width of the femoral condyle and tibial plateau, and the tibial interspinal width. However, the CSA, the lengths of the long and short axis of the ACL isthmus, and the femoral and tibial insertion areas of the porcine ACL were all significantly larger than the reported features in human knees.

Conclusion: The location, orientation and basic morphology of the porcine ACL and knee are similar to humans. However, the two-bundle structure is more distinct in a porcine ACL, and the dimensions of the porcine ACL are generally larger. This study may provide useful information to researchers when assessing the feasibility and limitations of using porcine samples for research on the human ACL and knee.

KEYWORDS

anterior cruciate ligament (ACL), pig, joint anatomy, knee morphology, comparative medicine

Introduction

The anterior cruciate ligament (ACL) is an important ligament in the knee joint for maintaining the stability of articular movement (1). However, rupture of the ACL is increasingly common, probably due to the increasing popularization of sports. Research on the anatomy and biomechanical function of the ACL is beneficial for preventing injury and improving clinical treatment.

In vivo human studies are often more difficult to perform than *in vitro* laboratory research using cadaveric knees, mainly because of the invasive methods required and considerable ethical constraints. The acquisition of human cadaveric samples for performing *in vitro* studies is also restricted for both ethical reasons and a scarcity of samples. In this context, animal samples have become a popular substitute, among which pigs are one of the most widely used species for exploring clinical problems related to the ACL. Proper use of porcine samples can reduce the research budget and ease the complicated process of applying for ethical approval. Porcine knees have been used extensively in biomechanical research to understand the role of the ACL in knee functionality (2), constraining the knee (3), to investigate ACL healing after surgery (4–6), and the microstructure of ACL enthesis (7).

Among the aforementioned studies, only a few discussed the suitability of using porcine samples for guiding clinical practice on humans. Proffen et al. (8) compared the general anatomy of the intra-articular structures between humans and six animal species (cow, sheep, goat, dog, pig, and rabbit). The tibial insertion of the human ACL is adjacent to the AHLM, but for the porcine knee, the AM and PL bundles of the ACL are split by the ALM (8–10). Porcine knees also have a longer ACL than humans, and thus are not suggested as the best choice for ACL research. In contrast, Bascuán et al. (11) assessed the anatomy and biomechanics of the ACL in five large laboratory animals and compared those against the human ACL. Bascuán concluded that goats and pigs were most similar to humans in terms of the number of bundles, location of insertion sites, vascular supply, topography of the tibial plateau, mechanical function and ultimate load. Xerogeanes et al. (10) measured the *in situ* force of the ACL in humans, goats, pigs, and sheep and found that porcine knees may be the most suitable for mechanical studies on the human ACL. However, in contrast to the two bundles reported by other investigators, Kato et al. (2) divided the porcine ACL into three bundles and tested *in situ* forces in each bundle and concluded that the AM and PL bundles of the porcine ACL have similar roles to the corresponding bundles in the human knee.

These studies and related publications have improved knowledge on the mechanical function and morphology of the porcine knee and ACL and discussed similarities and differences to the function of the human ACL. However, controversy remains around the number of bundles and location of the bone insertions for the porcine ACL. There is a lack of comprehensive and quantitative measurements of the three-dimensional morphology of the porcine ACL and related bony structures, which is important for understanding its biomechanical role and the suitability as a substitute for research on the human ACL. The purpose of this study was to qualitatively and quantitatively explore the morphological features of the porcine ACL and related bony structures in the knee, including the widths of femoral and tibial condyles, width and height of the femoral notch, width of the tibial interspinal fossa, location and areas of ACL bone insertion sites, shape of the ACL and its bone insertion sites, and cross-sectional area of the ACL isthmus and ACL length. The recorded measurements would be compared to data for the human knee from literature. It was hypothesized that all of the measured morphological parameters of the porcine knees were within the range of the human knee, demonstrating the suitability of porcine models for research on the anatomy and function of the human knee and ACL. This study may help with research planning to determine the feasibility and clinical suitability of using porcine samples for conducting scientific research on the anatomy, biomechanics and pathologies of the human ACL.

Materials and methods

Samples

The research protocol was approved by the university's Institutional Animal Care and Use Committee. Nineteen porcine knees (Duroc-landrace-yorkshire crossbred, male, and 1 year) were harvested from a licensed slaughterhouse and preserved at −20°C at our laboratory within 24 hours of slaughter. The samples were thawed at room temperature for 12 hours prior to use. Soft tissues were removed approximately 12 cm proximal and distal to the joint line and the samples were kept hydrated in gauze wetted with saline. Previous studies measured the dimensions of the human knee joint from anteroposterior X-ray images (12–15). As such, anteroposterior X-ray images were taken of the porcine knees to determine the corresponding morphological parameters of bony structures.

Measurement of bone structures in porcine knee joint from anteroposterior X-ray images

As shown in Figure 1, the most distal points of the medial and lateral femoral condyles were defined as point A and point B, respectively. Point C was the most proximal point of the femoral notch. A line perpendicular to line AB passing through point C was defined as the notch height (length of line CD). Line EF was

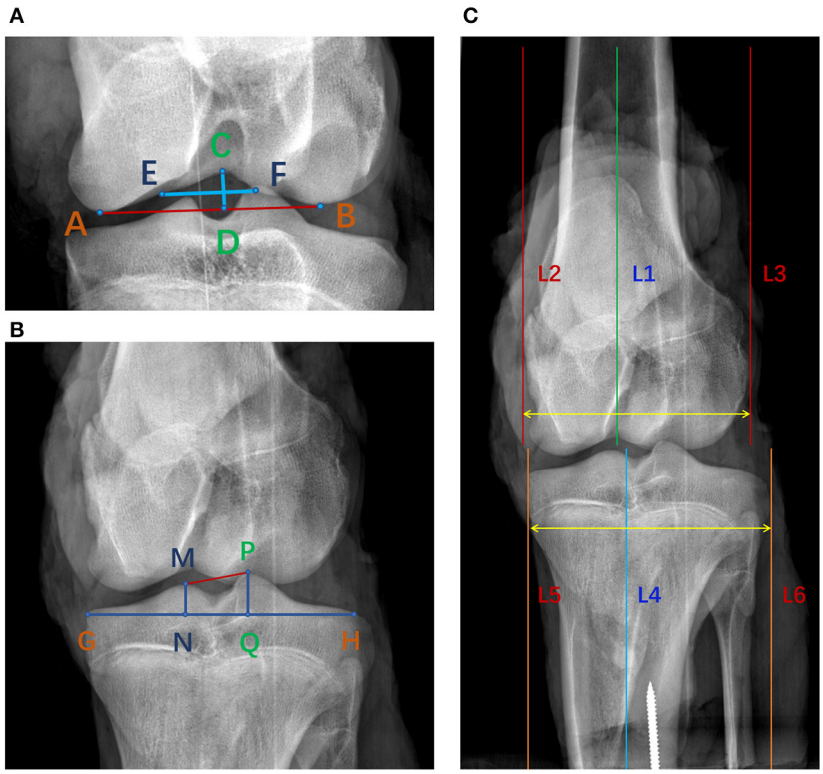

FIGURE 1
Measurement of bony parameters on coronal radiographs of porcine knee. **(A)** Line CD was the notch height and line EF was the notch width. S1 was the area of the femoral notch. **(B)** Line NQ was the width of the tibial interspinal fossa. S2 was the area of the tibial interspinal fossa. **(C)** The distance between line 2 and line 3 was the width of the femoral condyle and the distance between line 5 and line 6 was the width of the tibial condyle.

perpendicular line CD and passed through its center, and defined the notch width (12). Similar to the femoral notch, line GH was plotted tangent to the tibial plateau. The vertex of the tibial ridges was defined as points M and *P*. The perpendiculars to the line GH passing through points M and *P* respectively intersected GH at point N and point Q. The line NQ was defined as the width of tibial interspinal fossa (13). In Figure 1C, lines 1 and 4 were the anatomical axes of the femoral and tibial shafts. Lines 2 and 3, plotted parallel to line 1, were the medial and lateral margins of the femoral condyle. Lines 5 and 6, parallel to line 4, were the medial and lateral margins of the tibial condyle. The distance between line 2 and line 3 was defined as the width of the femoral condyle and the distance between line 5 and line 6 was defined as the width of the tibial condyle (14, 15).

Qualitative observation of the macro-morphology of the porcine ACL

The porcine knee joints were fixed at full extension in 10% formalin at room temperature for 48 hours, after which the patella and soft tissues surrounding the knee were removed to expose the intracapsular structures for qualitative observation. The removal of soft tissues was performed by one of the authors who is familiar with the standard process to expose the ACL and performed several similar studies in the past. Next, the medial femoral condyle and the menisci were carefully removed to allow for a better viewing of the whole ACL. During the dissection, the relative position, macromorphology and connectivity of the ACL with adjacent tissues were observed. Specifically, the shape of the ACL, location of its bone insertions, the general size of the ACL relative to the femoral notch and condyles, the number of ACL bundles, and the mode of twisting of the bundles were observed for further comparison with those from human ACLs published in literature.

Measurement of morphological parameters of the ACL

With the knee in full extension, an electrical caliper with an accuracy of 0.01 mm was used to measure the length of the ACL

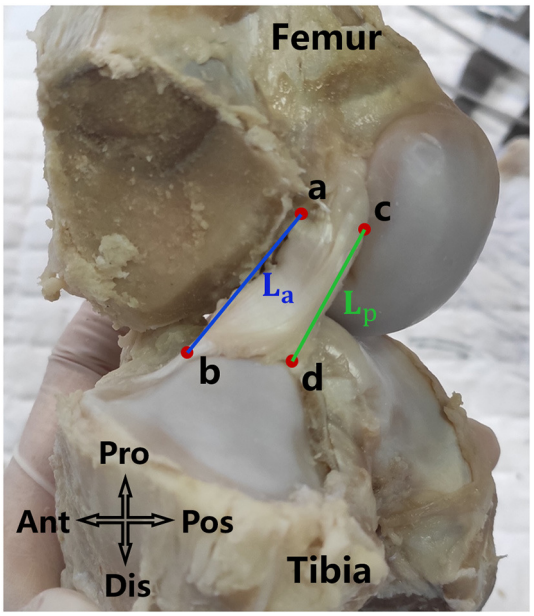

FIGURE 2
La and Lp were respectively the anterior and posterior length of the ACL. The average of *La* and *Lp* was defined as the length of the ACL.

in a sagittal view. As shown in Figure 2, points a and c were the most distal points of the femoral origin of the ACL and points b and d were the most proximal points of the tibial insertion of the ACL. *La* and *Lp* represent the anterior and posterior lengths of the ACL, and were averaged to represent the effective length of the whole ACL (Figure 2).

Then, the ACL substance was cut off along its femoral and tibial bone insertion sites. The circumferences of the femoral and tibial insertion sites were circumscribed with a marker pen which was further divided into direct and indirect parts according to whether the ligament had a direct connection to the mid-substance fibers of the ACL (Figures 3A,C). The indirect part is not directly attached to the mid-substance fibers of the ACL but is a broader fan-like extension of the direct part. Digital photographs were taken to obtain the largest projected area of the marked regions which represent the best approximation of the surface area of the insertion sites. While photographing, a vernier caliper was placed near the circumferences of the insertion sites to allow the measurements to be calibrated. The total area and the areas of the direct and indirect insertion sites of the ACL were respectively measured on the photographs using Creo Parametric 7.0 (PTC, Massachusetts, USA) (precision 0.001 mm) (Figure 3).

The ACL substances were enveloped with plastic film and scanned by X-ray microscopy (Zeiss Xradia 520 Versa, Carl Zeiss AG, Germany) at a resolution of 30 × 30 × 30 μm to acquire the accurate morphology of the ACL. One thousand one hundred one projections were measured with an exposure of 1 s at 70 kV and 6 W. The sample-source distance was 81.8 mm and the sample-detector distance was 104.0 mm. The projected images were imported into Dragonfly software (ORS, Montréal, Canada) to measure the cross-sectional area (CSA) and the lengths of the long and short axis of the ACL isthmus (Figure 4). Firstly, a cross-sectional plane was defined to be perpendicular to the isthmus of the ACL. The CSA was measured on this plane with the freehand shape tool in Dragonfly. To measure the long axis and short axis of the ACL, a circumscribed ellipse of the CSA and its long and short axis was drawn. Then, lines were drawn parallel to the long and short axis of the ellipse and tangent to the border of the ACL isthmus on the plane. The length of the lines between the parallel lines were respectively defined as the long axis and short axis of the ACL isthmus.

All measurements were conducted by two independent observers, and the first observer measured twice. The intra- and inter- observer reliabilities were calculated using the intraclass correlation coefficient (ICC) with a 2-way random model of absolute agreement. The ICC can assume any value from 0 to 1, where a value greater than 0.80 represents good agreement, between 0.60 and 0.79 signifies moderate agreement, and 0.59 signifies poor agreement.

Comparison of morphological features of the porcine ACL and knee joint to human

Qualitative observation and quantitative measurements on the porcine knee and ACL were compared with those previously reported for humans (12, 13, 16–20). Related publications were searched through the Web of Science with the following search terms: ACL, insertion, attachment, knee, tibial spine, femoral notch with measurement, morphology, anthropometry, shape, width, length, and height. Those published from 2000 to 2020 were selected. The most recent and highly cited publications which used similar measurement methods to this study were preferentially referred to for the comparison. According to how results were presented in the previous studies, the average values, the values of standard deviation, or the minimum and maximum values for the measurements were correspondingly chosen to facilitate the comparison. The location, shape, and morphological characteristics of the porcine ACLs and the bone insertion points were compared against the human ACL data (12, 13, 16–20). The morphological parameters recorded in this current study, including the ACL length, cross-sectional area of ACL, area of bone insertion points, width of femoral and tibial condyles, and the width and area of the femoral notch and tibial spines, were compared with the corresponding measurements reported in previous studies. According to the outcome of the comparison, the suitability of using the porcine model for

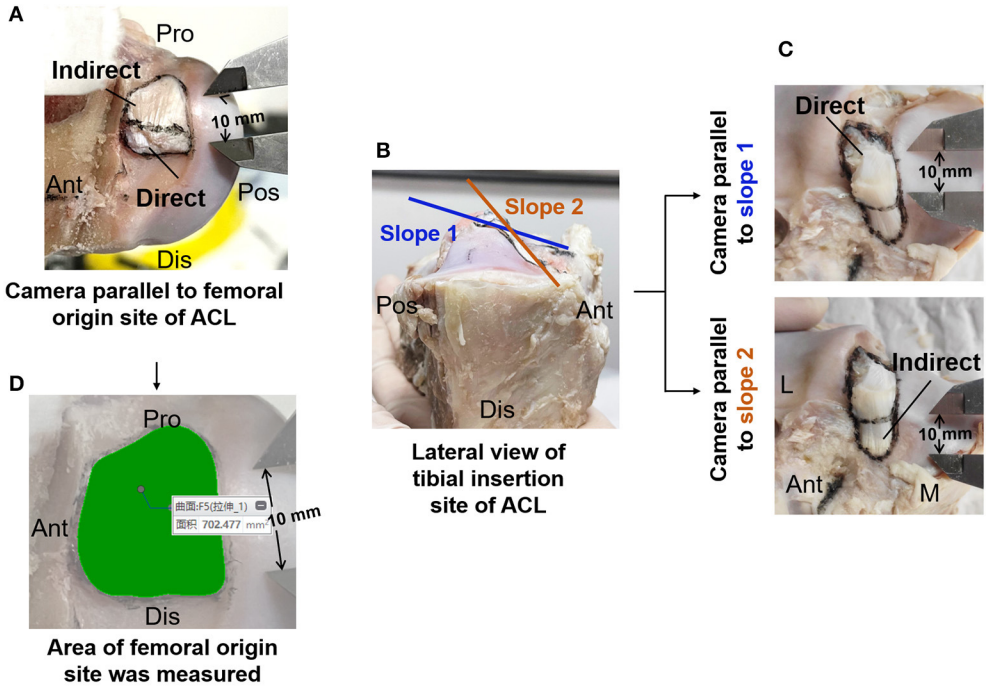

FIGURE 3
Measurement of insertion site of ACL. **(A)** Image of femoral origin site of ACL divided into direct and indirect part. **(B)** Double-sloped tibial insertion site of ACL with the slopes shown parallel to the direct and indirect part. **(C)** Image of tibial insertion site of ACL. **(D)** Area of femoral origin site measured in Creo Parametric 7.0 software (PTC, Massachusetts, USA) (precision 0.001 mm). M, medial; L, lateral; Ant, anterior; Pos, posterior; Pro, proximal; Dis, distal.

different types of studies on the human knee and ACL were analyzed and discussed.

Statistical analysis

All statistical analyses were performed in IBM SPSS Statistics 25 (SPSS Inc, Chicago, USA). A single sample Kolmogorov-Smirnov test was used to ensure that all the measurement results were normally distributed and the sample size was sufficient. An abstract independent-samples *T*-test was used to evaluate whether the recorded parameters for the porcine knee and ACL were significantly different to the reported human data. Equal variances were not assumed. Statistical significance was assumed when $P < 0.05$ for the Kolmogorov-Smirnov test and $P < 0.01$ for the abstract independent-samples *T*-test.

Results

Macroscopic comparison of porcine ACL to human ACL

Through dissection, the macroscopic shape of the porcine ACL and its relative position to the knee were observed. In the knee joint, synovial membranes connect adjacent fibrous connective tissues to form a semifixed structure. Therefore, when cutting the posterior cruciate ligament, it is important to be mindful not to damage of the ACL.

At full knee extension, the porcine ACL extended from the medial side of the lateral condyle of the femur, then went medially, and inserted into the anterior edge of the tibial plateau (Figures 5A,C). It is known that the human ACL attaches lateral and anterior to the medial intercondylar spine of the tibia, and to the medial aspect of the lateral femoral condyle (21–23) (Figures 5B,D,F). The femoral origin of the porcine ACL was located on the posterosuperior part of the medial side of the lateral condyle of the femur, with its posterior border clinging to the posterior articular margin of the lateral femoral condyle and its anterior border clinging to the lateral intercondylar ridge. The femoral origin of the human ACL is generally described as traveling obliquely from anteroproximal to posterodistal and is located on the posterior part of the medial surface of the lateral condyle (18, 21, 24) (Figures 5, 7). The porcine tibial insertion was located on the anterior medial section of the tibial spines and extended anteriorly to form an indirect part (Figures 5A,C,E, 6A,C). The human tibial insertion is described as beginning behind the anterior border of the tibia and extending to the medial and lateral tibial spine (21, 22, 25) (Figures 5B,D,F,

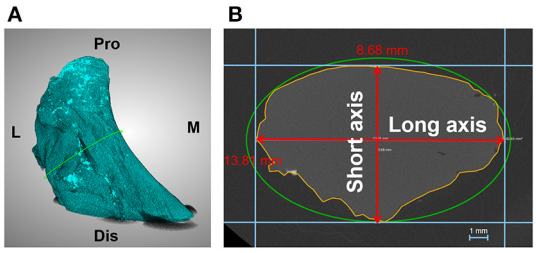

FIGURE 4
Measurement of dimensions of the ACL isthmus. **(A)** ACL substance reconstructed in Dragonfly. **(B)** Cross sectional area and long axis and short axis of the ACL isthmus (enclosed by yellow line) was measured on the isthmus plane. M, medial; L, lateral; Pro, proximal; Dis, distal.

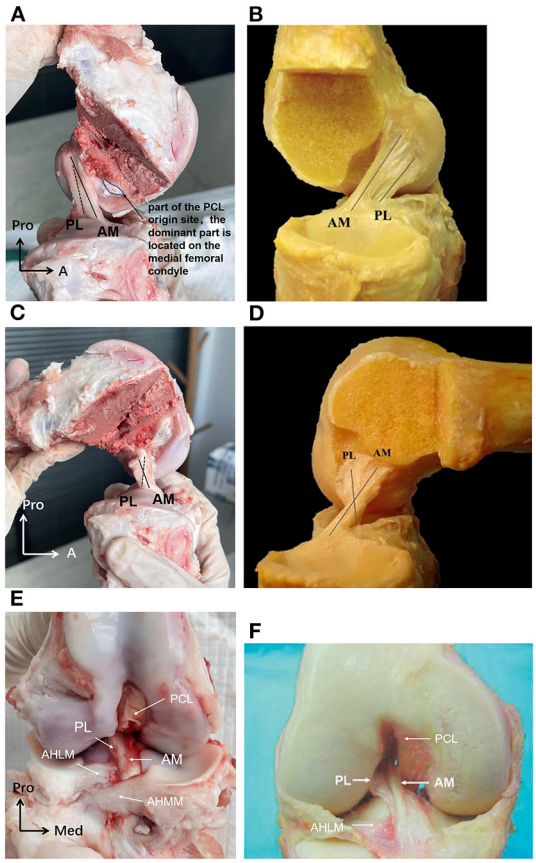

FIGURE 5
(A) The porcine ACL at full knee extension in sagittal view. The AM bundle was lax while the PL bundle was tight, and the two bundles were almost parallel. **(B)** The human ACL at full knee extension in sagittal view. **(C)** The porcine ACL with knee flexed to around 90. The AM bundle was tight while the PL bundle was lax, and the two bundles formed an intersecting structure. **(D)** The human ACL with knee flexed to around 90. **(E)** The porcine ACL in the coronal plane. The AM bundle of the porcine ACL was anterior and medial to the PL bundle at the tibial insertion. The AHLM (anterior horn of the lateral meniscus) split the porcine ACL into AM and PL bundles. **(F)** The human ACL in the coronal plane. The AM bundle of the human ACL was anterior and medial to the PL bundle at the tibial insertion. The AHLM borders on the lateral side of the human ACL (23).

6B,D). Therefore, the gross anatomical location of the ACL bone insertions is similar in pigs and humans.

The porcine ACL presented as an hourglass shape with fan-like insertions on the femur and tibia (Figures 5A,C,E). The ACL substance appeared as a ribbon shape rather than column. After removing the synovial membranes that wrapped the ACL fibers, a distinct double-bundle structure could be observed. One bundle was anterior and medial to the other bundle at the tibial insertion and was proximal and posterior to the other bundle at the femoral origin (Figures 5A,C). Correspondingly, the human ACL is widely reported as being divided into anteromedial (AM) and posterolateral (PL) fiber bundles (21–23, 26). In addition, the AM bundle of the porcine ACL was longer and wider than the PL bundle. When the knee was extended, the two bundles were almost parallel (Figure 5A). When the knee was flexed, the AM bundle which was originally at the proximal femoral origin turned posteriorly, thus forming an intersecting structure with the PL bundle (Figure 5C). These changes in orientation of the AM and PL bundles in the porcine ACL were similar to the orientations reported for human ACLs (21–23, 26) (Figure 5).

Part of the bone insertion of the porcine ACL was directly connected to the mobile mid-substance fibers of the ACL (called direct insertion, Figures 6C, 7A), while the other part was an extended fan-like section from the direct part (called indirect insertion, Figures 6C, 7A) and attached to the bone at a sharp angle. Fibers in the direct insertion were flexible in changing directions along with the sway of the mid-substance fibers, while the fibers in the indirect insertion were relatively immobile.

The tibial insertion had a cashew shaped attachment to the anterior medial section of the tibial spines and extended along the anterior part of the medial tibial spine. The AM bundle was anterior to the medial tibial spine and extended to the anterior border of the tibia, while the indirect insertion of the PL bundle lay beneath the AM bundle and extended posterior and lateral to the tibial spine. As shown in Figure 6A, in the porcine knee, the anterior horn of the lateral meniscus (AHLM) split the ACL into AM and PL bundles on the lateral side. But the two bundles were still connected to the medial side, making the whole structure appear like a folded page. The indirect insertion of the PL bundle was covered by the posterior half of the AHLM, and the anterior edge of the AHLM marked the boundary of the direct and indirect insertion of the AM bundle. Indirect insertion of the AM bundle was covered by the anterior horn of the medial meniscus (Figure 5E).

In humans, most tibial insertions have an oval shape. The anterior edge of the tibial insertion is covered by the transverse meniscal ligament. And the AHLM is adjacent to

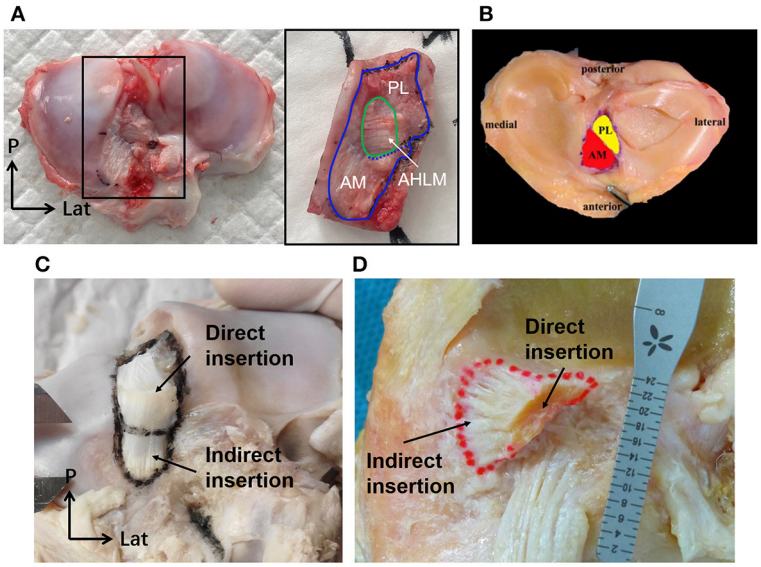

FIGURE 6
The tibial insertion of porcine and human ACLs. **(A)** The AHLM split the porcine tibial insertion into AM and PL bundles. **(B)** The AM and PL bundle of the tibial insertion for a human ACL. **(C)** The direct and indirect tibial insertion pattern of a porcine ACL. **(D)** The direct and indirect tibial insertion pattern of a human ACL.

the anterolateral border of the ACL tibial insertion. In human knees, only a few fibers of the ACL are blended with the anterior attachment of the AHLM as well as with the posterior attachment of the posterior horn of the lateral meniscus (18). The anterior edge of the AHLM is also identifiable to distinguish the AM and PL bundles. However, the AHLM doesn't spilt the ACL in human knees, which appears to be different to the porcine ACL (Figures 2B, 5F). In humans. the ACL indirect tibial insertion extends from the direct insertion site anteriorly and broadly spreads toward the anterior rim of the tibial plateau (17) (Figure 6D).

As shown in Figure 7A, the porcine ACL femoral origin had an open umbrella-shaped insertion and was located posterior and proximal to the PCL origin (Figures 5A,E). The AM bundle lay proximal to the PL bundle. But the two bundles were only split at the anterior portion and merged at the posterior (Figure 7C). The direct origin was raindrop-shaped at the distal side of the femoral origin and the indirect part was the proximal extension (Figure 7A). For human ACLs, the AM bundle is more anterior than the PL bundle, and the indirect origin is on the proximal and posterior side of the femoral origin and borders on the margin of the articular cartilage (18) (Figures 7B,D).

From macroscopic observation, the major difference between the porcine and human ACL is that the AHLM splits the porcine ACL into AM and PL bundles on the lateral side at the tibial attachment. However, the porcine ACL is similar to the human ACL in terms of overall shape and positioning of the ACL and its insertions.

Quantitative comparison of dimensions of the ACL and bony structures between porcine and human knees

Dimensions of the ACL and bony structures from the porcine knees in this study and those from human knees reported in literature are presented in Table 1.

The results show that the difference in length between the porcine and human ACL is not statistically significant ($p = 0.032$). But the CSA of the porcine ACL (67.4 mm^2) is significantly larger than the human ACL (38.7 mm^2) ($p = 0$), and the long and short axis are both significantly longer in pigs ($p = 0$). The minimum value of the porcine short axis (5.4 mm) is longer than the maximum value of the ACL short axis in humans (4.9 mm). Similarly, it was found that the porcine ACL insertions are significantly larger than human ACL insertions on both the femoral and tibial side ($p = 0$). Particularly, the mean value of the total area of the porcine tibial insertion (301.2 mm^2) is nearly triple that in humans (110.9 mm^2).

Peng et al. (12) measured the height and width of the femoral notch on X-ray images of human knees with the knee flexed to 45°, while the current study on pigs recorded measurements at full knee extension. It was shown that the height and width of the porcine femoral notch (6.94 mm and 14.4 mm) are significantly smaller than humans (28.0 and 19.8 mm). However, there was no significant difference in femoral condyle width (69.9 vs. 73.8 mm), tibial interspinal width (13.9 vs. 13.9 mm), and tibial plateau width (72.9 vs. 72.0 mm) between the porcine and

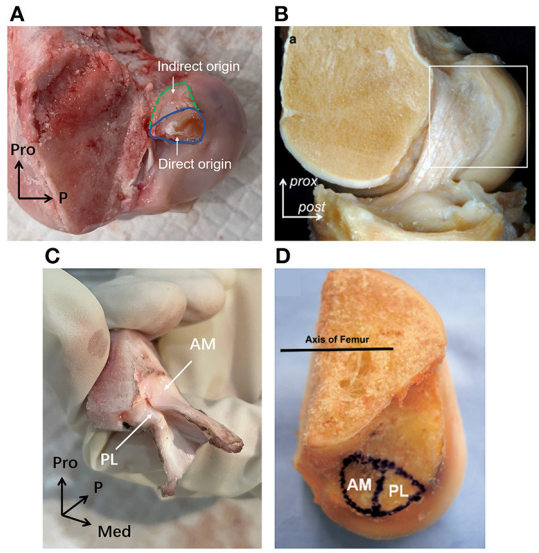

FIGURE 7
The femoral origin of porcine and human ACLs. **(A)** The direct and indirect origin regions of porcine femoral ACL insertion. **(B)** The mid-substance and fan-like extension of human ACL femoral origin. **(C)** The AM and PL bundle femoral origin of porcine ACL. **(D)** The AM and PL bundle femoral origin of human ACL.

human knees ($p = 0.022$, 1, 0.455, respectively). In addition, the mean values of femoral condyle width, tibial interspinal width, and tibial plateau width for humans were all within the range of values from porcine knees in this study.

Discussion

This study compared the macroscopic morphology of the ACL and related bone structures between pigs and humans to determine the suitability of using porcine samples for research on the knee joint and ACL. The qualitative observation indicated a high degree of similarity between the porcine and human ACL, including the overall shape and the position and orientation of the insertions relative to the femur and tibia. However, at the tibial attachment, the anterior horn of the lateral meniscus (AHLM) split the porcine ACL into AM and PL bundles. That was the most distinct difference in the gross anatomy of the porcine ACL compared to humans. The quantitative comparison showed that the CSA and the lengths of the long and short axis of the ACL isthmus, as well as the femoral and tibial insertion areas of the porcine ACL, were all significantly larger than a human ACL. However, there was no significant difference in the length of ACL, the width of the femoral condyle and tibial plateau, and the tibial interspinal width.

The gross anatomical location of the ACL bone insertions is similar between porcine and human knees, which is supported by earlier studies (8, 9, 27, 28). However, Fuss (9) compared the ACL of domestic pigs with humans and considered the femoral origin point in porcine knees to be more posteroproximal. This current study found the posterior border of the femoral origin of the porcine ACL to be tightly clung to the posterior articular margin of the lateral femoral condyle, which was similar to the arrangement depicted in human studies. The dispute over whether the porcine femoral origin is more proximal may be related to its larger area and differences in the definition of the boundary for the indirect region. The double bundle (AM and PL bundles) structure of porcine ACLs is consistent with the findings of Proffen et al. (8) on adult female Yorkshires pigs and Zhao et al. (7), who didn't mention the breed of pigs used. And the observation of the double bundle structure in pigs is similar to that previously reported for humans (29). However, Tantisricharoenkul et al. (27), Maeyama et al. (30), and Kato et al. (31) observed three bundles in the porcine ACL: anteromedial (AM) bundle, posterolateral (PL) bundle and intermediate (IM) bundle (Hampshire, 7–8 months). It is not known why some studies found two bundles while others reported three bundles, but the difference may be related to the breed of pigs used. Similarly, some studies have argued for three fiber bundles in the human ACL, but it is more widely accepted that the human ACL consists of two AM and PL bundles. Observation in this current study showed that the porcine ACL insertion can be divided into two parts, namely the direct insertion and indirect insertion. Yamauchi et al. (32) also observed in mature porcine knees that the anterior attachment of the femoral ACL site was a direct insertion and the posterior attachment could be characterized as an indirect insertion. This finding is consistent with the current study, and with previous studies on human knees (17, 18, 33). However, the indirect part of the porcine ACL femoral origin was located proximally on the knee while it was reported to be more posterior in humans. Nevertheless, this current study found that lines connecting the centers of the direct and indirect insertions in both porcine and human knees were aligned with the direction of ACL longitudinal fibers.

The finding that the AHLM separates the AM and PL bundles into two distinct bundles in porcine knees has also been reported in previous studies on pigs and other large mammals such as cows and sheep (8, 9). In humans, the AHLM is adjacent to the anterolateral border of the ACL tibial insertion and does not split the insertion. We suspect that this may be related to differences in gait between quadruped and bipedal mammals. Also, the mid-substance fibers in the porcine ACL can be further separated along the AHLM fissure through blunt dissection. However, it was observed that the porcine ACL cannot be totally separated into two independent bundles since the bundles are connected at the back, presenting like a folded page with the opening at the front. A membranous tissue between the two fiber bundles on the open side acts to bind them together to achieve cooperative but distinguishable functions. These features have not been reported in previous studies.

TABLE 1 Quantitative comparison of the ACL and bone features in porcine and human knees.

	Porcine		Human			*N*	*P*	Acquisition method
	Mean ± sd	Range	Mean ± sd	Range	Study			
Length (mm)	26.1 ± 3.5	21.0–35.9	29.4 ± 4.7	22.2–36.5	Hashemi et al. (16)	15	0.032	Calipers
CSA (mm^2)	67.4 ± 10.4	44.7–87.2	38.7 ± 7.7	20.3–51.5	Siebold et al. (17)	20	0	Digital camera and calipers
Long axis (mm)	12.8 ± 1.9	10.2–18.1	9.9 ± 1.5	7.0–12.7			0	
Short axis (mm)	7.5 ± 1.0	5.4–9.2	3.9 ± 0.7	2.8–4.9			0	
F-total (mm^2)	227.7 ± 22.4	188.1–258.4	142.2 ± 24.4	110.5–188.8	Mochizuki et al. (18)	24	0	Digital photograph
F-direct (mm^2)	138.7 ± 24.9	92.92–177.56	91.4 ± 23.7	54.3–142.3			0	
F-indirect (mm^2)	88.9 ± 16.7	66.3–127.7	50.8 ± 12.6	28.8–74.4			0	
T-total (mm^2)	301.2 ± 48.1	233.6–412.0	110.9 ± 14.7	80.1–133.1	Siebold et al. (17)	20	0	Digital photograph and calipers
T-direct (mm^2)	114.3 ± 37.9	65.1–214.6	31.4 ± 7.2	18.5–45.0			0	
T-indirect (mm^2)	186.9 ± 42.9	124.5–304.7	79.6 ± 12.7	53.7–107.7			0	
NH (mm)	6.94 ± 1.5	4.9–9.6	28.0 ± 3.1		Peng et al. (12)	67	0	X–ray
NW (mm)	14.4 ± 2.3	9.5–18.3	19.8 ± 2.4				0	
FW (mm)	69.9 ± 3.4	64.3–76.9	73.8 ± 3.9		Lipps et al. (19)	9	0.022	MRI
SW (mm)	13.9 ± 1.3	11.6–17.1	13.9 ± 2.1		Iriuchishima et al. (13)	37	1	X–ray
TW (mm)	72.9 ± 2.7	69.2–78.8	72.0 ± 6.4		Yahagi et al. (20)	39	0.455	Digital photograph and calipers

N, sample size; *Length*, ACL length; *CSA*, the cross sectional area of the ACL isthmus; *Long axis*, the long axis of the ACL isthmus; *Short axis*, the short axis of the ACL isthmus; *F-total*, area of total ACL femoral origin; *F-direct*, area of direct ACL femoral origin; *F-indirect*, area of indirect ACL femoral origin; *T-total*, area of total ACL tibial insertion; *T-direct*, area of direct ACL tibial insertion; *T-indirect*, area of indirect ACL tibial insertion; *NH*, the height of femoral intercondylar notch; *NW*, the width of femoral intercondylar notch; *FW*, the width of femoral condyle; *SW*, the width of tibial interspinal fossa; *TW*, width of the tibial condyle.

In terms of the quantitative results, the difference in length between the porcine and human ACL was not significant ($p = 0.032$), but the CSA of the mid-substance of the porcine ACL was significantly larger. In other words, the human ACL was thinner than the porcine ACL. This may be due to several reasons, one of which may be the human knee being more flexible in extension-flexion with the ability to move to 0° in extension, while the porcine knee can only extend to around 30° (8, 9). The valley in the femoral notch becomes shallower as the knee extends, meaning that the greater extension of the human knee may result in a smaller space for accommodating the ACL and so evolved to have a narrower CSA. In addition, the ACL in both bipedal and quadrupeds becomes tensed and more vulnerable during knee extension (34, 35), and mainly functions to prevent posterior sliding of the femur against the tibia (34, 35). Previous studies found that the anterior tibial load (which forces the femur to glide posteriorly against the tibia) during daily activities is proportional to the body weight (36), and thus the load on the ACL would also depend on the body weight. Considering that pigs are more massive (200–240 kg) than humans, the larger ACL may have evolved to resist these forces.

The results also showed a wide range of values for the CSA of the mid-substance and insertion area for both the porcine and human samples. While the statistical analysis in this study shows that porcine ACLs are significantly larger than human ACLs, the crossover between the ranges for pigs and humans indicates that the dimensions of a specific porcine ACL may not be larger than the native human ACL. Accordingly, studies should consider how individual differences in the size of the ACL may affect the outcome and whether a specific porcine ACL is representative.

The shape of the femoral and tibial insertions of the porcine ACL were similar to insertions reported for human subjects in literature. Most human tibial insertions were reported to have an oval shape, but there are also triangular or "C"-shaped types (37). This current study found that the tibial insertion of the porcine ACL has a cashew shape when the AHLM inserts medially. This was similar to the reported "C" shape in human knees (37, 38). On the other side, the femoral origin of human ACLs is commonly described as having a crescent or ribbon shape (39). This is similar to the porcine ACL femoral origin, but the porcine samples were thicker in the proximal-distal direction and had an open umbrella-shaped area that may be related to the pigs having an overall thicker ACL. The indirect part of the porcine femoral origin was mainly proximal while the indirect part of the human femoral origin was further posterior. However, lines connecting the centers of the direct and indirect insertions followed the direction of the ACL longitudinal fibers for both humans and pigs. This unique feature may facilitate the fibers in the direct insertion to move easily in flexion-extension but keep the fibers in the indirect area firmly fixed to resist tangential forces along the fiber direction. The different direction of longitudinal fibers in the human and porcine ACL may be a result of the different physiological knee flexion angles. Porcine knees cannot fully extend and are limited to a physiological extension angle of about 30° (8, 9). Therefore, although the indirect part of the porcine femoral origin was proximal to the flexion-extension

axis, it was still posterior and proximal to the knee joint at full extension, which is similar to the orientation in human knees when at full knee extension. This would result in a similar force direction in both human and porcine ACLs at the same knee flexion angle. In terms of size, the porcine ACL insertion area is significantly larger than the human ACL insertion area, which is consistent with the larger mid-substance of the porcine ACL.

The height and width of the porcine femoral notch measured were significantly smaller than in human knees (12) when the human knee is flexed to 45°. The height of the femoral notch in human knees is almost four times greater than in pigs. Proffen et al. (8) also reported a narrower femoral notch in pigs than in humans, but the knee flexion angle at which the measurements were taken was not clearly described. We propose that it is possible the height and width of the porcine femoral notch are not necessarily smaller in pigs than in humans when measured at the same knee flexion angle. Greater knee flexion angles often result in a larger projected height and width of the femoral notch on the coronal plane, and thus flexing a human knee to 45° may show a larger projected dimension of the femoral notch than a porcine knee at full extension. This current study also did not measure the dimensions of the porcine femoral notch at the same knee flexion angle as the referenced literature for human knees because there is no scientific criteria for matching the flexion angle of porcine knees to humans. The results showed no significant difference between the porcine and human knees in terms of the width of the femoral condyle, width of the tibial plateau, and the tibial interspinal width. Thus, in general, the dimensions of the porcine knee are similar to human knees, except for the size of the femoral notch. The results of this study suggest that when porcine knees are used to represent human knees for scientific research, differences in dimensional features may have a negligible effect on the outcome.

Given the similarities and differences in the general shape and quantitative dimensions between the porcine and human ACL, researchers should carefully consider the feasibility of using porcine subjects, and there might be limitations to extrapolating the results to human applications. This study suggests that porcine samples may be suitable for studying the general biomechanical mechanisms of load transmission and for assessing functional differences between the two bundles of the ACL or two types of bone insertions (direct and indirect), since the general orientation, morphology and function are similar between porcine and human ACLs. However, considering the significant differences in ACL dimensions and the relative location of the bone insertion sites to the bone shaft, porcine subjects may not be suitable for studies investigating the size and positioning of the ACL. Future studies may consider exploring differences in the morphological and mechanical features between pigs and humans with respect to age, gender, and physical environment.

The main limitations of this study are (1) the human data from referenced literature used subjects of different ages, races, and sexes and that difference may influence the comparison results. However, these variables have been controlled as well as possible. Data from young, mature subjects were prioritized for comparison with the porcine subjects in the current study. (2) The measurement methods used in previous studies may not be identical to the methods used in this study, but any differences have been stated and discussed. (3) The largest projected area of the marked areas on the digital photographs was measured as the surface area of the insertion sites. However, the insertion is not flat, and thus the actual value may be slightly larger than the measured value. But this measurement method is same as that used in previous studies referenced, and so will have a negligible impact on the comparison results.

Conclusion

This study found that the location, orientation, and general morphology of the porcine ACL and related bony structures in the knee joint are similar to humans. However, the two bundles in the porcine ACL were more distinguishable than in humans because they are split by the AHLM, and the dimensions of the ACL are generally larger in the porcine knee, except for the length of the ACL. The outcomes of this study can guide researchers when determining the feasibility and limitations of using porcine samples for research on the ACL and knee joint.

Data availability statement

The original contributions presented in the study are included in the article/supplementary material, further inquiries can be directed to the corresponding author/s.

Ethics statement

The animal study was reviewed and approved by Institutional Animal Care and Use Committee, Shanghai Jiao Tong University.

Author contributions

QS performed the dissection experiments, data measurement and the statistical analysis, and wrote the first draft of the manuscript. HW contributed to conception and design of the study, performed the dissection experiments, and revised the manuscript. KH and MT performed

data measurement and the statistical analysis. C-KC contributed to conception and design of the study. All authors contributed to manuscript revision, read, and approved the submitted version.

Funding

This work was supported by the National Natural Science Foundation of China (Grant No. 32101050), the China Postdoctoral Science Foundation (Grant No. 2021M702129) and the SJTU Global Strategic Partnership Fund (2021 SJTU-UoM).

Acknowledgments

We would like to thank Mr. McClean for his assistance with editing this manuscript.

Conflict of interest

The authors declare that the research was conducted in the absence of any commercial or financial relationships that could be construed as a potential conflict of interest.

Publisher's note

References

1. Wang HZ, Zhang M, Cheng CK. Changing the diameter of the bone tunnel is more effective than changing the tunnel shape for restoring joint functionality after ACL reconstruction. *Front Bioeng Biotechnol.* (2020) 8:173. doi: 10.3389/fbioe.2020.00173

2. Kato Y, Ingham SJM, Linde-Rosen M, Smolinski P, Horaguchi T, Fu FH. Biomechanics of the porcine triple bundle anterior cruciate ligament. *Knee Surg Sports Traumatol Arthrosc.* (2010) 18:20–5. doi: 10.1007/s00167-009-0893-y

3. Boguszewski DV, Shearn JT, Wagner CT, Butler DL. Investigating the effects of anterior tibial translation on anterior knee force in the porcine model: is the porcine knee ACL dependent? *J Orthop Res.* (2011) 29:641–6. doi: 10.1002/jor.21298

4. Biercevicz AM, Murray MM, Walsh EG, Miranda DL, Machan JT, Fleming BC. T-2* MR relaxometry and ligament volume are associated with the structural properties of the healing ACL. *J Orthop Res.* (2014) 32:492–9. doi: 10.1002/jor.22563

5. Murray MM, Fleming BC. Use of a bioactive scaffold to stimulate anterior cruciate ligament healing also minimizes posttraumatic osteoarthritis after surgery. *Am J Sports Med.* (2013) 41:1762–70. doi: 10.1177/0363546513483446

6. Sawyer GA, Anderson BC, Paller D, Heard WMR, Fadale PD. Effect of interference screw fixation on ACL graft tensile strength. *J Knee Surg.* (2013) 26:155–9. doi: 10.1055/s-0032-1324808

7. Zhao L, Thambyah A, Broom ND. A multi-scale structural study of the porcine anterior cruciate ligament tibial enthesis. *J Anat.* (2014) 224:624–33. doi: 10.1111/joa.12174

8. Proffen BL, McElfresh M, Fleming BC, Murray MM. A comparative anatomical study of the human knee and six animal species. *Knee.* (2012) 19:493–9. doi: 10.1016/j.knee.2011.07.005

9. Fuss FK. Anatomy and function of the cruciate ligaments of the domestic pig (Sus scrofa domestica): a comparison with human cruciates. *J Anat.* (1991) 178:11–20.

10. Xerogeanes JW, Fox RJ, Takeda Y, Kim HS, Ishibashi Y, Carlin GJ, et al. A functional comparison of animal anterior cruciate ligament models to the human anterior cruciate ligament. *Ann Biomed Eng.* (1998) 26:345–52. doi: 10.1114/1.91

11. Bascunan AL, Biedrzycki A, Banks SA, Lewis DD, Kim SE. Large animal models for anterior cruciate ligament research. *Front Vet Sci.* (2019) 6:292. doi: 10.3389/fvets.2019.00292

12. Peng L, Meng Z, Kang Z, Zou Y. Clinical significance of width and height of femoral intercondylar notch measured by using knee tunnel view radiograph for patients with knee osteoarthritis. *Chin J Med Phys.* (2016) 33:930. doi: 10.3969/j.issn.1005-202X.2016.09.012

13. Iriuchishima T, Goto B, Fu FH. The occurrence of ACL injury influenced by the variance in width between the tibial spine and the femoral intercondylar notch. *Knee Surg Sports Traumatol Arthrosc.* (2020) 28:3625–30. doi: 10.1007/s00167-020-05965-y

14. van Zyl R, van Schoor AN, du Toit PJ, Louw EM. Clinical anatomy of the anterior cruciate ligament and pre-operative prediction of ligament length. *SA Orthop J.* (2016) 15:47–52. doi: 10.17159/2309-8309/2016/v15n4a7

15. Park YB, Ha CW, Kim HJ, Park YG. Preoperative prediction of anterior cruciate ligament tibial footprint size by anthropometric variables. *Knee Surg Sports Traumatol Arthrosc.* (2017) 25:1638–45. doi: 10.1007/s00167-016-4164-4

16. Hashemi J, Chandrashekar N, Cowden C, Slauterbeck J. An alternative method of anthropometry of anterior cruciate ligament through 3-D digital image reconstruction. *J Biomech.* (2005) 38:551–5. doi: 10.1016/j.jbiomech.2004.04.010

17. Siebold R, Schuhmacher P, Fernandez F, Smigielski R, Fink C, Brehmer A, et al. Flat midsubstance of the anterior cruciate ligament with tibial "C"-shaped insertion site. *Knee Surg Sports Traumatol Arthrosc.* (2015) 23:3136–42. doi: 10.1007/s00167-014-3058-6

18. Mochizuki T, Fujishiro H, Nimura A, Mahakkanukrauh P, Yasuda K, Muneta T, et al. Anatomic and histologic analysis of the mid-substance and fan-like extension fibres of the anterior cruciate ligament during knee motion, with special reference to the femoral attachment. *Knee Surg Sports Traumatol Arthrosc.* (2014) 22:336–44. doi: 10.1007/s00167-013-2404-4

19. Lipps DB, Oh YK, Ashton-Miller JA, Wojtys EM. Morphologic characteristics help explain the gender difference in peak anterior cruciate ligament strain during a simulated pivot landing. *Am J Sports Med.* (2012) 40:32–40. doi: 10.1177/0363546511422325

20. Yahagi Y, Horaguchi T, Iriuchishima T, Suruga M, Iwama G, Aizawa S. Correlation between the mid-substance cross-sectional anterior cruciate ligament size and the knee osseous morphology. *Eur J Orthop Surg Traumatol.* (2020) 30:291–6. doi: 10.1007/s00590-019-02552-x

21. Kopf S, Musahl V, Tashman S, Szczodry M, Shen W, Fu FH, et al. systematic review of the femoral origin and tibial insertion morphology of the ACL. *Knee Surg Sports Traumatol Arthrosc.* (2009) 17:213–9. doi: 10.1007/s00167-008-0709-5

22. Petersen W, Zantop T. Anatomy of the anterior cruciate ligament with regard to its two bundles. *Clin Orthop Relat Res.* (2007) (454):35–47. doi: 10.1097/BLO.0b013e31802b4a59

23. Zantop T, Petersen W, Fu FH. Anatomy of the anterior cruciate ligament. *Oper Tech Orthop.* (2005) 15:20–8. doi: 10.1053/j.oto.2004.11.011

24. Ferretti M, Ekdahl M, Shen W, Fu FH. Osseous landmarks of the femoral attachment of the anterior cruciate ligament: An anatomic study. *Arthroscopy.* (2007) 23:1218–25. doi: 10.1016/j.arthro.2007.09.008

25. Dye SF, Cannon WD Jr. Anatomy and biomechanics of the anterior cruciate ligament clinics in sports medicine. *Clin Sports Med.* (1988) 7:715–25.

26. Colombet P, Robinson J, Christel P, Franceschi JP, Djian P, Bellier G, et al. Morphology of anterior cruciate ligament attachments for anatomic reconstruction: a cadaveric dissection and radiographic study. *Arthroscopy.* (2006) 22:984–92. doi: 10.1016/j.arthro.2006.04.102

27. Tantisricharoenkul G, Linde-Rosen M, Araujo P, Zhou JB, Smolinski P, Fu FH. Anterior cruciate ligament: an anatomical exploration in humans and in a selection of animal species. *Knee Surg Sports Traumatol Arthrosc.* (2014) 22:961–71. doi: 10.1007/s00167-013-2463-6

28. Schulze-Tanzil G, Silawal S, Hoyer M. Anatomical feature of knee joint in Aachen minipig as a novel miniature pig line for experimental research in orthopaedics. *Ann Anat Anatom Anzeiger.* (2020) 227:151411. doi: 10.1016/j.aanat.2019.07.012

29. Girgis FG, Marshall JL, Monajem A. The cruciate ligaments of the knee joint. Anatomical, functional and experimental analysis. *Clin Orthop Relat Res.* (1975) (106):216–31.

30. Maeyama A, Hoshino Y, Debandi A, Kato Y, Saeki K, Asai S, et al. Evaluation of rotational instability in the anterior cruciate ligament deficient knee using triaxial accelerometer: a biomechanical model in porcine knees. *Knee Surg Sports Traumatol Arthrosc.* (2011) 19:1233–8. doi: 10.1007/s00167-010-1382-z

31. Kato Y, Ingham SJM, Kramer S, Smolinski P, Saito A, Fu FH. Effect of tunnel position for anatomic single-bundle ACL reconstruction on knee biomechanics in a porcine model. *Knee Surg Sports Traumatol Arthrosc.* (2010) 18:2–10. doi: 10.1007/s00167-009-0916-8

32. Yamauchi S, Ishibashi K, Sasaki E, Sasaki S, Kimura Y, Ishibashi Y. Failure load of the femoral insertion site of the anterior cruciate ligament in a porcine model: comparison of different portions and knee flexion angles. *J Orthop Surg Res.* (2021) 16:526. doi: 10.1186/s13018-021-02676-z

33. Iwahashi T, Shino K, Nakata K, Otsubo H, Suzuki T, Amano H, et al. Direct anterior cruciate ligament insertion to the femur assessed by histology and 3-dimensional volume-rendered computed tomography. *Arthroscopy.* (2010) 26:S13–20. doi: 10.1016/j.arthro.2010.01.023

34. Livesay GA, Rudy TW, Woo SLW, Runco TJ, Sakane M, Li G, et al. Evaluation of the effect of joint constraints on the in situ force distribution in the anterior cruciate ligament. *J Orthop Res.* (1997) 15:278–84. doi: 10.1002/jor.1100150218

35. Sakane M, Fox RJ, Woo SLY, Livesay GA Li G, Fu FH. *In situ* forces in the anterior cruciate ligament and its bundles in response to anterior tibial loads. *J Orthop Res.* (1997) 15:285–93. doi: 10.1002/jor.1100150219

36. Kutzner I, Heinlein B, Graichen F, Bender A, Rohlmann A, Halder A, et al. Loading of the knee joint during activities of daily living measured *in vivo* in five subjects. *J Biomech.* (2010) 43:2164–73. doi: 10.1016/j.jbiomech.2010.03.046

37. Guenther D, Irarrazaval S, Nishizawa Y, et al. Variation in the shape of the tibial insertion site of the anterior cruciate ligament: classification is required. *Knee Surg Sports Traumatol Arthrosc.* (2017) 25:2428–32. doi: 10.1007/s00167-015-3891-2

38. Zhang JH, Ren S, Shao JY, Niu XY, Hu XQ, Ao YF. Anatomical and finite element analysis of anterior cruciate ligament reconstruction within biomechanical insertion. *Beijing da xue xue bao Yi xue ban = J Pek Univ Health Sci.* (2019) 51:586–90. doi: 10.19723/j.issn.1671-167X.2019.03.031

39. Smigielski R, Zdanowicz U, Drwiega M, Ciszek B, Ciszkowska-Lyson B, Siebold R. Ribbon like appearance of the midsubstance fibres of the anterior cruciate ligament close to its femoral insertion site: a cadaveric study including 111 knees. *Knee Surg Sports Traumatol Arthrosc.* (2015) 23:3143–50. doi: 10.1007/s00167-014-3146-7

frontiers | Frontiers in Veterinary Science

TYPE Original Research
PUBLISHED 18 November 2022
DOI 10.3389/fvets.2022.1020276

OPEN ACCESS

EDITED BY
Mauro Malvè,
Public University of Navarre, Spain

REVIEWED BY
Gregorio Iraola,
Institut Pasteur de Montevideo, Uruguay
Zuofu Xiang,
Central South University Forestry and Technology, China

*CORRESPONDENCE
Hongli Huang
15296536692@163.com

SPECIALTY SECTION
This article was submitted to Comparative and Clinical Medicine, a section of the journal Frontiers in Veterinary Science

RECEIVED 16 August 2022
ACCEPTED 02 November 2022
PUBLISHED 18 November 2022

CITATION
Huang H (2022) Captivity and geography influence the antibiotic resistome of non-human primates. *Front. Vet. Sci.* 9:1020276. doi: 10.3389/fvets.2022.1020276

Captivity and geography influence the antibiotic resistome of non-human primates

Hongli Huang[1,2]*

[1]Clinical Biological Specimen Bank, Discipline Construction Office, The First Affiliated Hospital of Guangxi Medical University, Nanning, China, [2]Life Sciences Institute, Guangxi Medical University, Nanning, China

Introduction: Antibiotic resistance poses a serious threat for animals and humans health worldwide. Yet a comprehensive exploration of the influence of captivity and geography on non-human primate (NPH) gut antibiotic resistance remains incomplete.

Methods: In this study, 131 metagenomic sequencing datasets of five species of NHPs included different regions and lifestyles were selected to perform the antibiotic resistance analysis.

Results: Nineteen related resistance antibiotics and 325 antibiotic resistance genes (ARGs) were obtained. A significantly higher abundance and diversity index of ARGs in the captive NHPs than in the wild was found but not for all of the samples. The biomarker-tracking of ARGs analysis identified key ARGs related to aminoglycoside resistance genes and tetracycline resistance genes.

Discussion: These results suggest that captivity and geography changes associated with human activities can lead to marked changes in the ecology of the NHP gut flora ARGs.

KEYWORDS

antibiotic resistance genes, captivity, geography, metagenome, non-human primate fecal

Introduction

Antibiotic resistance genes (ARGs) existed before antibiotics were reported and did not pose a threat to humans at that time. However, the widely used antibiotics in clinical, aquaculture, animal husbandry, and planting accelerated the propagation and dissemination of ARGs (1). Nowadays, antibiotic resistance has been recognized as a vital global threat to human and public health by World Health Organization (2). The World Bank warned that antibiotic resistance would cause 10 million deaths and 100 trillion dollars losses in global economic by 2050 if unchecked (3, 4). European Antimicrobial Resistance Surveillance Network (http://www.ecdc.europa.eu/en/activities/surveillance/EARS-Net) and the US National Antimicrobial Resistance Monitoring System for Enteric Bacteria (http://www.cdc.gov/narms/) focus on the clinical and public dosage of antibiotics and the isolation of drug-resistant bacteria in public health laboratories, also illustrating that antibiotic resistance has been a wide concern (5). In almost all environments, sediment (6), surface water (7, 8), sewage (9–11), sludge (12), medical waste (13), and animal feces (14–16) serve as important reservoirs of ARGs that provide for reproduction and propagation conditions.

At the same time, ARGs can transmit by horizontal gene transfer (17–20) between pathogen or host (21) *via* mobile genetic elements (4, 22, 23), which will increase the difficulty of environmental governance and disease treatment. Thus, under the One-Health concept, effective measures should be researched to understand and control ARGs transmission.

Non-human primates, as close living relatives of human beings in the world, have a high degree of genetic and physiological similarity to humans (24). They are considered as the best model animal to explore the occurrence and development of human disease in medicine. However, due to the study of animals referred to ethical issues and part of the NPHs being endangered or protected animals, samples of them are hard to get. The high-throughput sequencing-based metagenomic analysis is a powerful tool that provided conveniences for rare animal samples microbiota analysis. Thus, systematic research on the resistome of NPHs by metagenomic analysis will provide us with the prevention of human diseases. Gut microbial communities, affected by several factors, including host lifestyle, host species, and geography (25), can generally shape the resistome (26, 27). Therefore, hypothesis that NHPs in wild might harbor more diverse ARGs and lower abundance than that in captivity were put forward since their surroundings were varied and they almost free from antibiotic selection pressure. Comparison of the gut resistome of NHPs in wild and in captivity can help us have a deep understanding of how the lifestyles influence the gut resistome. Besides, geography may also be an important factor that influences the ARGs abundance and diversity. To uncover these mysteries, five species of NHPs from different regions and lifestyles were included in our study.

Studies that looked at ARGs in gut microbiota of human or other animals have usually been performed at a local scale, which reduced the statistical power of the analyses. To break through this limitation, ARGs abundance and diversity of NHPs from a large scale were obtained. In this study, *Macaca mulatta* (*M. mulatta*) datasets sampled and sequenced in previous studies were included. Metagenomic datasets of NHPs worldwide including white-faced capuchins (*Cebus capucinus*), *Macaca sp, Macaca fascicularis* (*M. fascicularis*), and *Rhinopithecus roxellana* (*R. roxellana*) that held in the Sequence Read Archive (SRA, https://www.ncbi.nlm.nih.gov/sra) were download. Metagenomic data of white-faced capuchins, *Macaca sp.*, *M. mulatta* and *M. fascicularis* could be classified by the host, lifestyle, and geography and datasets for *R. roxellana* were classified into captive, semi-wild, and wild groups. Hence, this research aimed to (1) investigate the distribution of gut resistome from large-scale NHPs; (2) analyze the biomarker ARGs of captive NHPs by Linear discriminant analysis (LDA) effect size (LEfSe) algorithm; (3) speculate the influence of captivity and geography on the abundance and diversity of NHPs gut resistome.

Materials and methods

Dataset collection

A total of 131 metagenome datasets were included in this study. Among them, 34 *M. mulatta* (Guangxi) were from the datasets of samples collected in the early stage sequenced by Illumina X-ten strategies, and 19 white-faced capuchins (PRJNA485217, Costa Rica), 23 *Macaca sp.* (PRJNA478556, USA, Minneapolis), 17 *M. fascicularis* (PRJEB22765, China, Beijing), and 38 *R. roxellana* (PRJNA436633, China, Hubei) were downloaded from the SRA database of National Center for Biotechnology Information (NCBI) (https://www.ncbi.nlm.nih.gov/sra/?term=) (1, 28). The sample ID, sequencing platform, reads length, reads number, data size, and accession numbers of the downloaded datasets were listed in Supplementary Table S1. The datasets of SRA format were converted to the fastq format by the fastq-dump module integrated in the NCBI SRA Toolkit (http://www.ncbi.nlm.nih.gov/Traces/sra/view5software) for subsequent analysis.

Bioinformatics analysis

The sequencing reads were aligned to a hierarchical structured Structured Antibiotic Resistance Genes (SARG) database (containing 24 ARG types and 1209 ARG subtypes) to characterize the resistance structure by the ARGs-OAP pipeline (version 2.0) (29). Specifically, 131 metagenomic datasets were searched against the integrated structured ARG database by the Usearch sequence analysis tool with the default parameter (25 aa, *E*-value of 1 × 107, identity of 80%). Potential ARG-like reads obtained from the Usearch results were searched against the integrated structured ARG database [ARDB (Antibiotic Resistance Genes Database), CARD (The Comprehensive Antibiotic Resistance Database), and NCBI-NR] by the Basic Local Alignment Search Tool to ensure accurate annotation. A sequence was annotated as an ARG-like read by meeting the following standards: an E-value cutoff of 1e-7, amino acid similarity of 80%, and minimum alignment length of 25 amino acids. The ARGs-OAP pipeline provided three standardized information including total read number, 16S rRNA gene copy number, and cell number. The abundance of ARG profiles of different sample groups was compared at the type level, the subtype level, and the gene level (the reference sequence level). Results of 16S rRNA gene copy number were selected for the following analysis.

Antibiotic resistance mechanisms analysis

The CARD database (30) (http://arpcard.mcmaster.ca) was download to classified ARGs detected in the 131 NHPs gut

microbiota into different mechanism categories. We mapped the detected ARGs were mapped to CARD database to obtain the resistance mechanism of each ARG. Remarkably, the 15 unassigned subtypes were named 'others' in this study.

Statistical analysis

Principal Components Analysis (PCA) and heatmap analysis were performed by STAMP v2.0. Histogram and unpaired t-test analysis were performed by GraphPad v7.0. Alpha-diversity indexes were calculated to estimate microbial diversity between *Macaca sp., M. mulatta, M. fascicularis*, and white-faced capuchins groups. Differences in the relative abundance of the gut microbial ARG features were determined by LEfSe (http://huttenhower.sph.harvard.edu/lefse/).

Results

The ARG diversity of *Macaca sp.*, white-faced capuchins, *M. mulatta*, and *M. fascicularis*

Except for goods_coverage index, all the other 7 indexes showed that white-faced capuchins had the highest index, followed by the wild *M. mulatta* (Figure 1). *Macaca sp.* in captive and *M. fascicularis* had the lowest index. This indicated that the diversity of ARGs in white-faced capuchins was the highest (Figures 1B,C). However, the goods_coverage indexes showed that *M. fascicularis* and *Macaca sp.* in captive had the highest index, and white-faced capuchins and *M. mulatta* in wild had a relatively low index (Figures 1D,E). The Shannon index, Simpson index, Pielou index, Chao index and ACE index of the *M. mulatta* were higher than the captive *Macaca sp.* (Figures 1B–D,F,G).

The ARG profiles of white-faced capuchins, *Macaca sp., M. fascicularis,* and *M. mulatta*

In the study, 19 ARG types were annotated from 131 samples by using the ARGs-OAP pipeline. Seventeen ARG types were identified in white-faced capuchins and *R. roxellana* (Supplementary Figure S1, Figures 2A,B). Sixteen ARG types were found in the wild *M. mulatta* and 12 ARG types were annotated in the captive *Macaca sp.* (Figure 3B). *M. fascicularis* was resistant to 15 ARG types (Figure 3B). The top 10 antibiotic resistance types of white-faced capuchins, *Macaca sp., M. fascicularis*, and *M. mulatta* were presented in Figures 4A–D, respectively. Tetracycline resistance genes had the highest relative abundance in 131 samples, followed by macrolides-lincosamids-streptogramins (MLS), multidrug, and beta-lactam. At the subtype level, 325 ARGs were annotated in 131 samples. Among them, 310 subtypes were classified into four mechanism categories based on the CARD database, of which 145 subtypes belonging to antibiotic inactivation, 110 subtypes to antibiotic efflux, 48 subtypes to antibiotic target alteration, and 7 to antibiotic target replacement (Supplementary Table S2). The top 10 ARGs were presented in Figures 4E–H. *Tet*Q had the highest relative abundance in 131 samples, followed by *tet*W, multidrug_transporter, and *Cfx*A2. The major ARGs of the 3 NHPs differed from one another.

Influence of captivity on *R. roxellana* gut ARGs

Thirty-eight datasets of *R. roxellana* were downloaded from the NCBI SRA database, including captive group, semi-wild group, and wild group. Seventeen ARG types were found in 38 samples, and the relative abundance of the top 10 ARG types were shown by a heat map (Figures 2A,B). The relative abundance of ARGs in the captive group was significantly higher than that in the semi-wild and wild groups (2.063 ± 0.025 vs. 0.002 ± 0.004, $P < 0.0001$, and 2.063 ± 0.025 vs. 0.0007 ± 0.001, $P < 0.0001$), consistent with the result of our datasets (Figure 2C). The relative abundance of ARGs in the captive group was up to 14-fold higher than that in the wild group. In the captive group, tetracycline was the primary ARG, with relative abundance ranging from 0 to 0.145, followed by 0–0.030 in semi-wild and 0–0.007 in wild. In semi-wild and wild *R. roxellana*, vancomycin, bacitracin, and multidrug had high relative abundance (Figures 2A,B). The PCA analysis confirmed that the three lifestyles clustered separately (Figure 2D). The similar result was seen in the heatmap (Supplementary Figure S3). Diversity analysis found that apart from Pielou index, the diversity index of the captive *R. roxellana* and semi-wild were higher than the wild *R. roxellana* (Supplementary Figure S2). Besides, the marker-ARG of captive *R. roxellana* were tetracycline resistance genes, *tet*W, *tet*Q, tetracycline resistance protein, and *tet*O (Supplementary Figures S4, S5).

Influence of geographic location on *Macaca sp., M. fascicularis,* and *M. mulatta* gut ARGs

Macaca spp. from three places were included to explore whether ARGs were associated with geographic factors (the wild *M. mulatta* from Hezhou, Guangxi, the captive *M.*

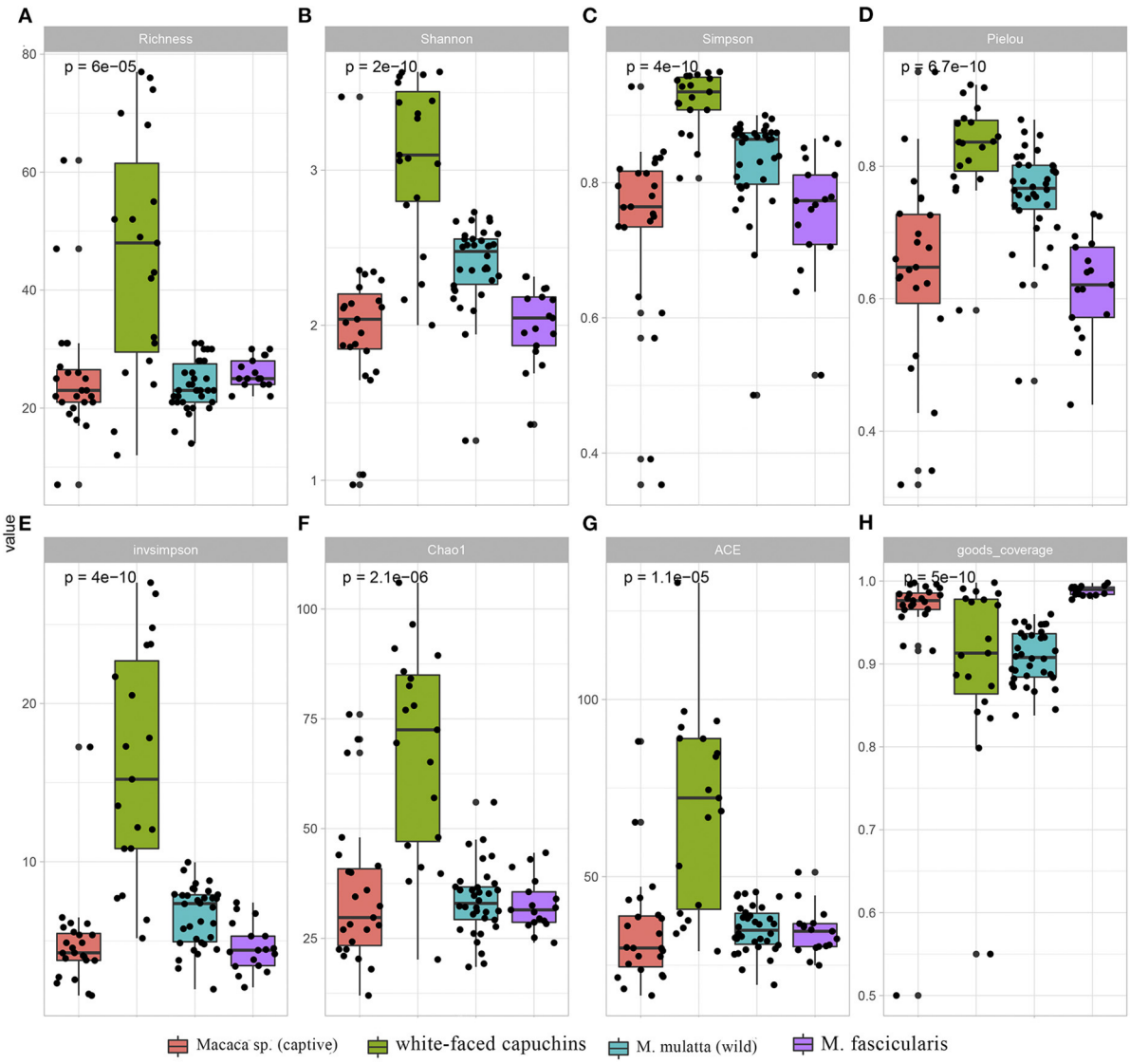

FIGURE 1
Comparison of ARGs diversity index and richness index across *Macaca sp.* (captive), *M. mulatta* (wild), white-faced capuchins and *M. fascicularis*. **(A)** Richness index **(B)** Shanno index **(C)** Simpson index **(D)** Pielou index **(E)** invsimpson index **(F)** Chao1 **(G)** ACE **(H)** goods_coverage.

fascicularis from Beijing, China, and the captive *Macaca sp.* from Minneapolis, USA). At last, 17 ARG types were annotated. The dominant antibiotic resistance of *M. mulatta* and *M. fascicularis* in China were tetracycline, which accounted for 65.71% and 81.27%, respectively. The primary ARG abundance in captive *Macaca sp.* from USA was beta-lactam, accounting for 56.99% (Figures 3A,B). The total relative abundance of ARGs in captive *Macaca spp.* was significantly higher than the wild (unpaired *t*-test, $P < 0.0001$) (Figure 3C), consistent with the result above. PCA analysis was used to evaluate the similarities of the compositions of ARG types in the three groups of *Macaca spp.* (Figure 3D). The samples from the same place clustered more closely, and *M. fascicularis* from China and *Macaca sp.* from USA formed different clusters. Additionally, the captive *Macaca sp.* from the USA was different from those in China, reflecting that the diversity of ARG type was also related to host geography.

Identification of discriminative ARG relative to captivity and geography

LEfSe is an algorithm for high-dimensional biomarker discovery and explanation that identifies genomic features

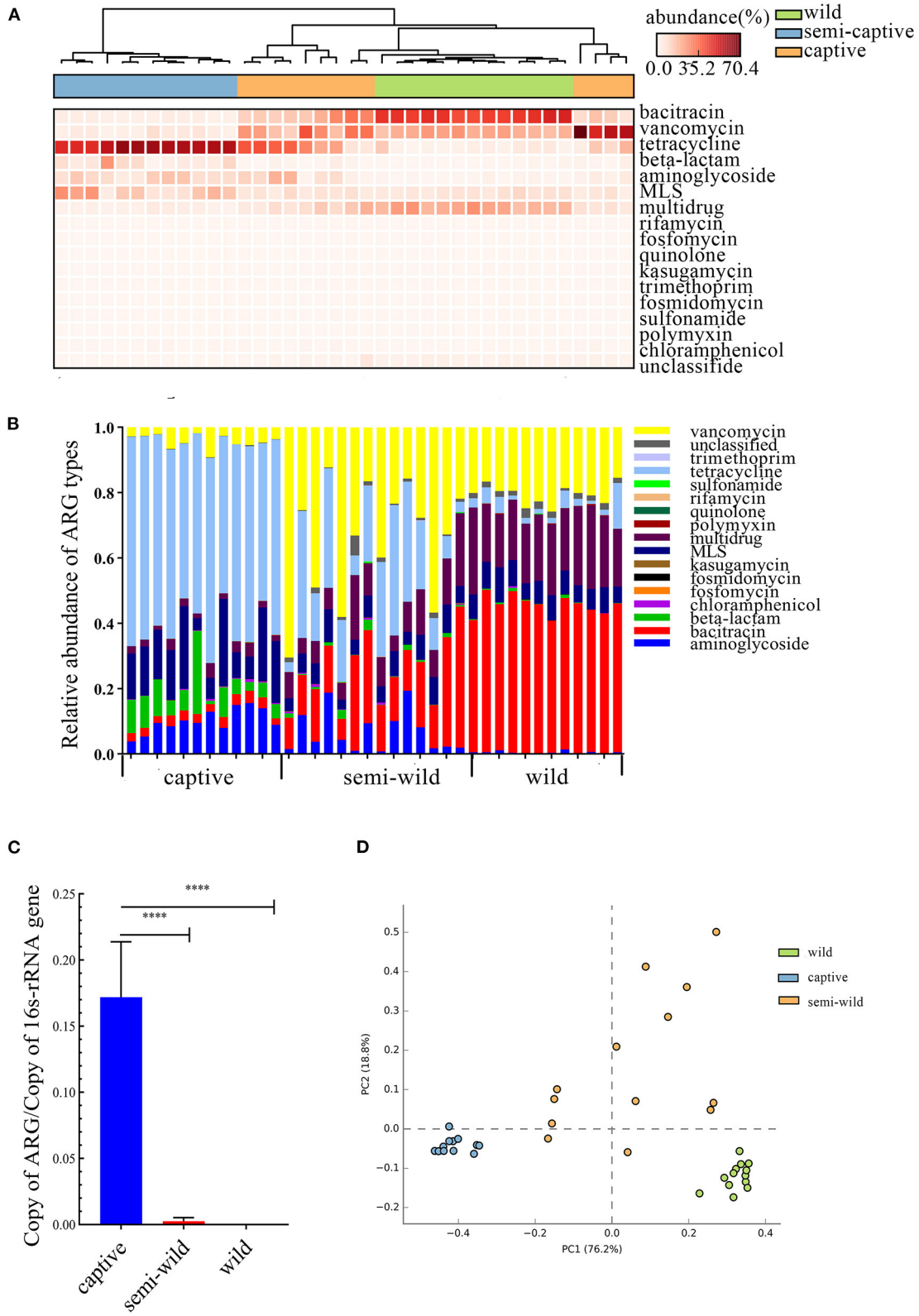

FIGURE 2
Comparison of *R. roxellana* gut microbiota ARGs between captive, semi-wild, wild. **(A)** Clustering heat map of antibiotics with high relative abundance in 38 samples. **(B)** Relative abundance of ARG types of *R. roxellana*. **(C)** Barplot of total ARG relative abundance of 38 *R. roxellana* (*t*-test, ****$P < 0.0001$). **(D)** PCA plot of ARG relative abundance of 38 *R. roxellana*.

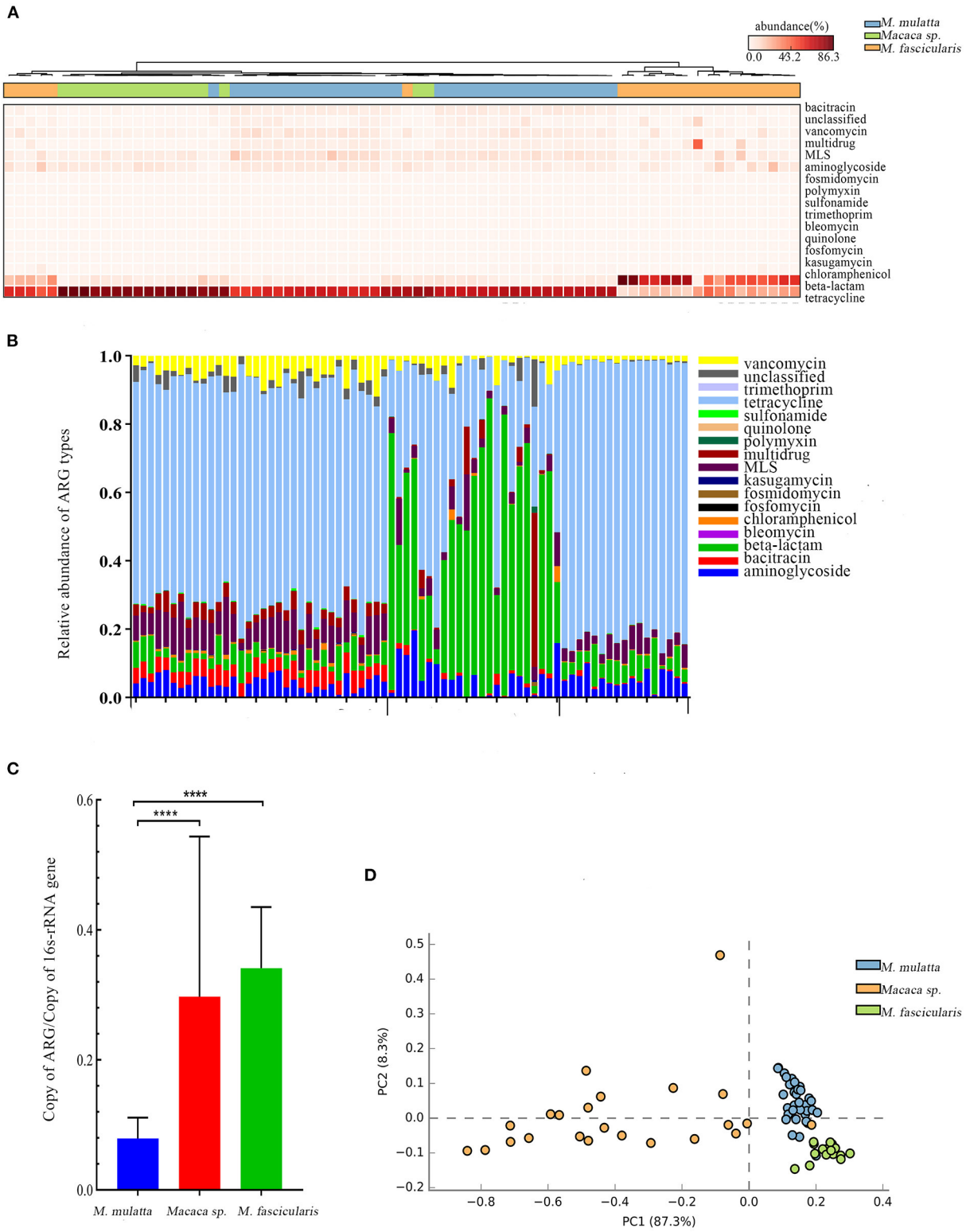

FIGURE 3
Comparison of Macaca spp. gut microbiota ARGs from three regions. **(A)** Heat map clustering 17 antibiotics of 74 samples. **(B)** Relative abundance of 17 antibiotics of 74 samples. **(C)** Barplot of total ARG relative abundance of 74 samples (*t*-test, ****$P < 0.0001$). **(D)** PCA plot of ARG relative abundance of 74 samples.

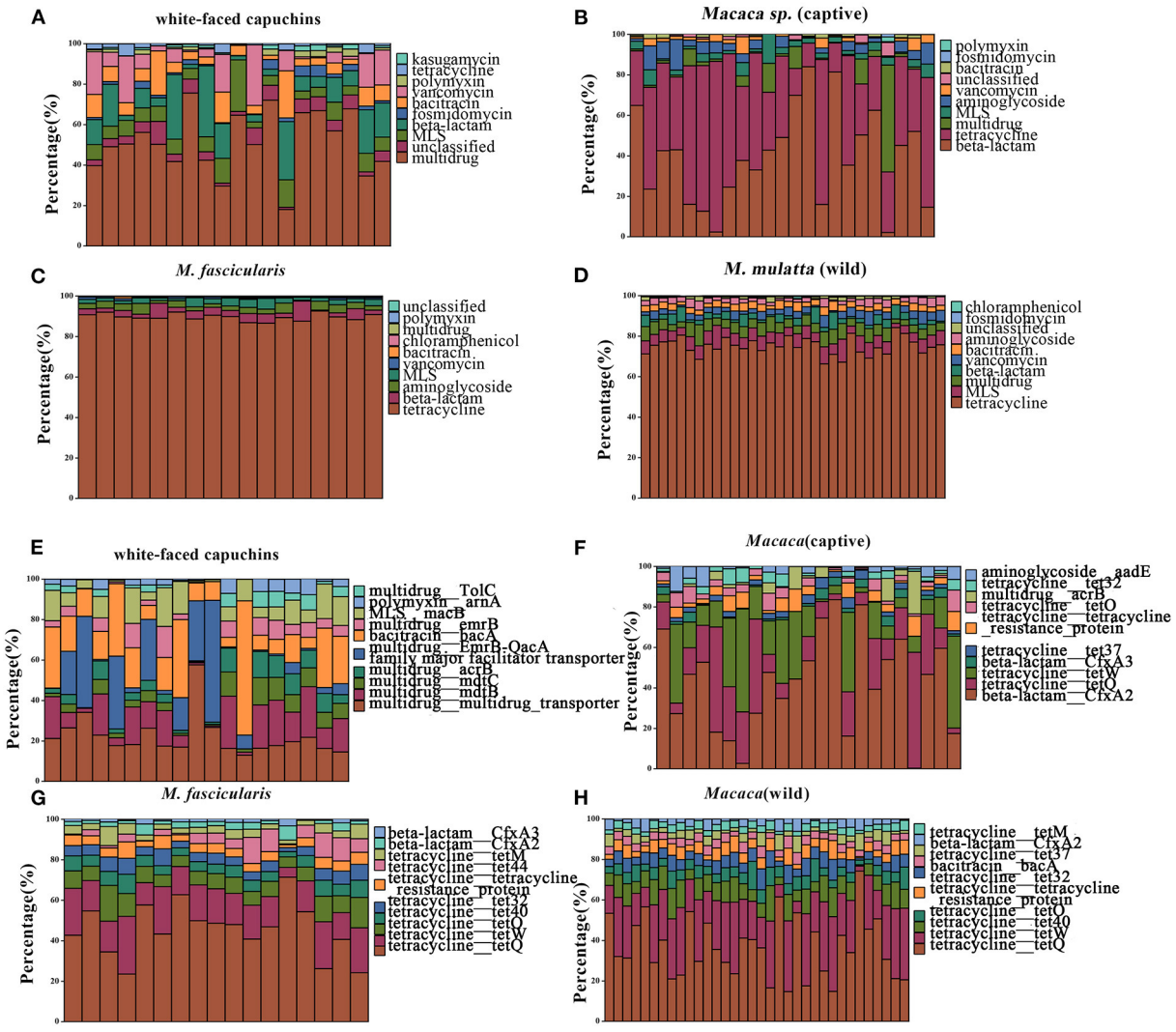

FIGURE 4
Relative abundances of top 10 type and subtype ARGs. **(A)** The top 10 antibiotic resistance class of white-faced capuchins. **(B)** The top 10 antibiotic resistance class of *Macaca* sp. (captive). **(C)** The top 10 antibiotic resistance class of *M. fascicularis*. **(D)** The top 10 antibiotic resistance class of *M. mulatta* (wild). **(E)** The top 10 antibiotic resistance gene of white-faced capuchins. **(F)** The top 10 antibiotic resistance gene of *Macaca* sp. **(G)** The top 10 antibiotic resistance gene of *M. fascicularis*. **(H)** The top 10 antibiotic resistance gene of *M. mulatta* (wild).

(genes, pathways, or taxa) characterizing the differences between two or more biological conditions (or classes). Thus, this tool enables the characterization of specific ARG profiles and identifies ARG biomarkers in different gut microbial communities. These results showed that the key ARGs in *M. fascicularis* were aac-3-II, aac(3)-IIIa, aac(3)-IV, and aac(3)-VI, which belong to the aminoglycoside resistance gene. The key ARGs in white-faced capuchins were aac-6-II, aac-6-Ib, aac-3-X, and ant-3-Ih-aac-6-IId, which also belong to the aminoglycoside resistance gene. Aminoglycoside resistance genes aac(3)-I, aac(3)-IX, and aac(6')-I were enriched in captive *Macaca sp.* whereas tetracycline resistance genes *tet*Q, *tet*W, and *tet*37 were enriched in wild *M. mulatta* (Figures 5, 6).

Discussion

Non-human primates are closely genetically related to humans and share many cognitive, physiological and morphological similarities with humans (31). In this study, a total of 131 NHPs were selected, including *Macaca sp.*, *M. mulatta*, *M. fascicularis*, white-faced capuchins, and *R. roxellana*, to study the impact of captivity and geographic location on the distribution of the NHPs gut resistome.

Researches noted that there were 19 related resistance antibiotics and 325 ARGs in the fecal microbiota of 131 NHPs. Study reveals that both the *M. mulatta* in captive and wild were resistant to tetracycline and with higher abundance compared

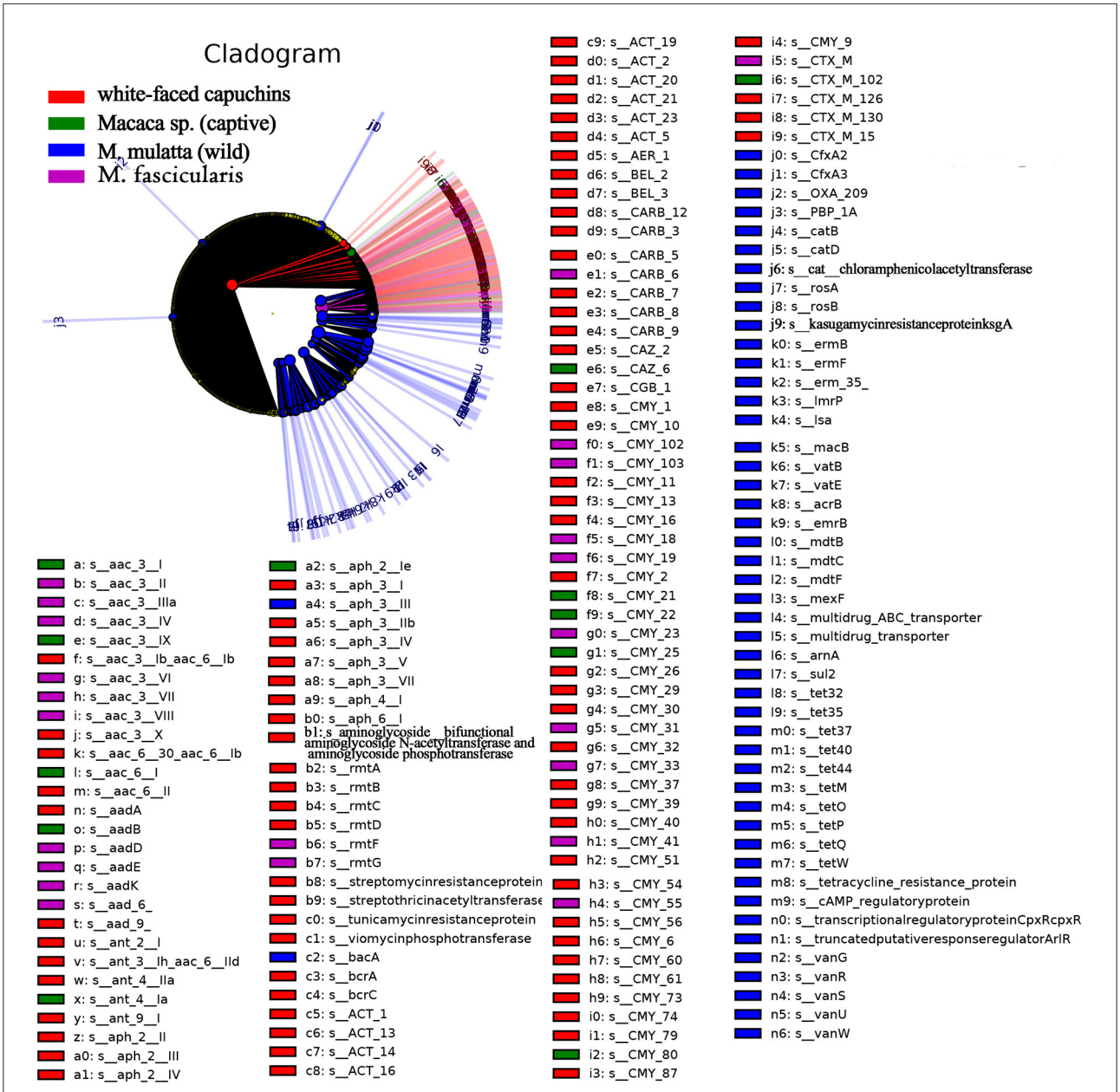

FIGURE 5
Cladogram of the significantly different ARGs between white-faced capuchins, *Macaca sp.* (captive), *M. mulatta* (wild) and *M. fascicularis* samples. The inner circles are at the ARG type level, while the outer circles are at the subtype level.

with other groups. The major resistance of *M. fascicularis* was tetracycline, too. Tremendous tetracycline resistance genes were found in the above three kinds of NHPs, liking *tet*Q, *tet*W, *tet*O, and *tet*40. Yang et al. (32) uncovered that the most abundant ARGs of the gut microbiota of the *M. mulatta* were tetracycline resistance genes and verified by isolation and culture experiments (32). This was also consistent with this study. Aminoglycosides, tetracyclines, and macrolides are the most widely used antibiotics in veterinary medicine worldwide for animal growth promotion and disease control (33, 34). Especially, tetracyclines are broad-spectrum antibiotics and popular first-line antibiotics in human infectious disease treatment (25). The habitat of *M. mulatta* Gupo Mountain in Hezhou is a tourist attraction that produces a lot of human activities. Although tetracycline antibiotics were not used in the wild *M. mulatta*, long-term human activities and widespread use of tetracycline antibiotics in other species have caused an extensive global tetracycline resistance (31, 35, 36). It may be explained the prevalence of tetracycline resistance genes in NPHs. Besides, this study found that 145 subtypes belong to

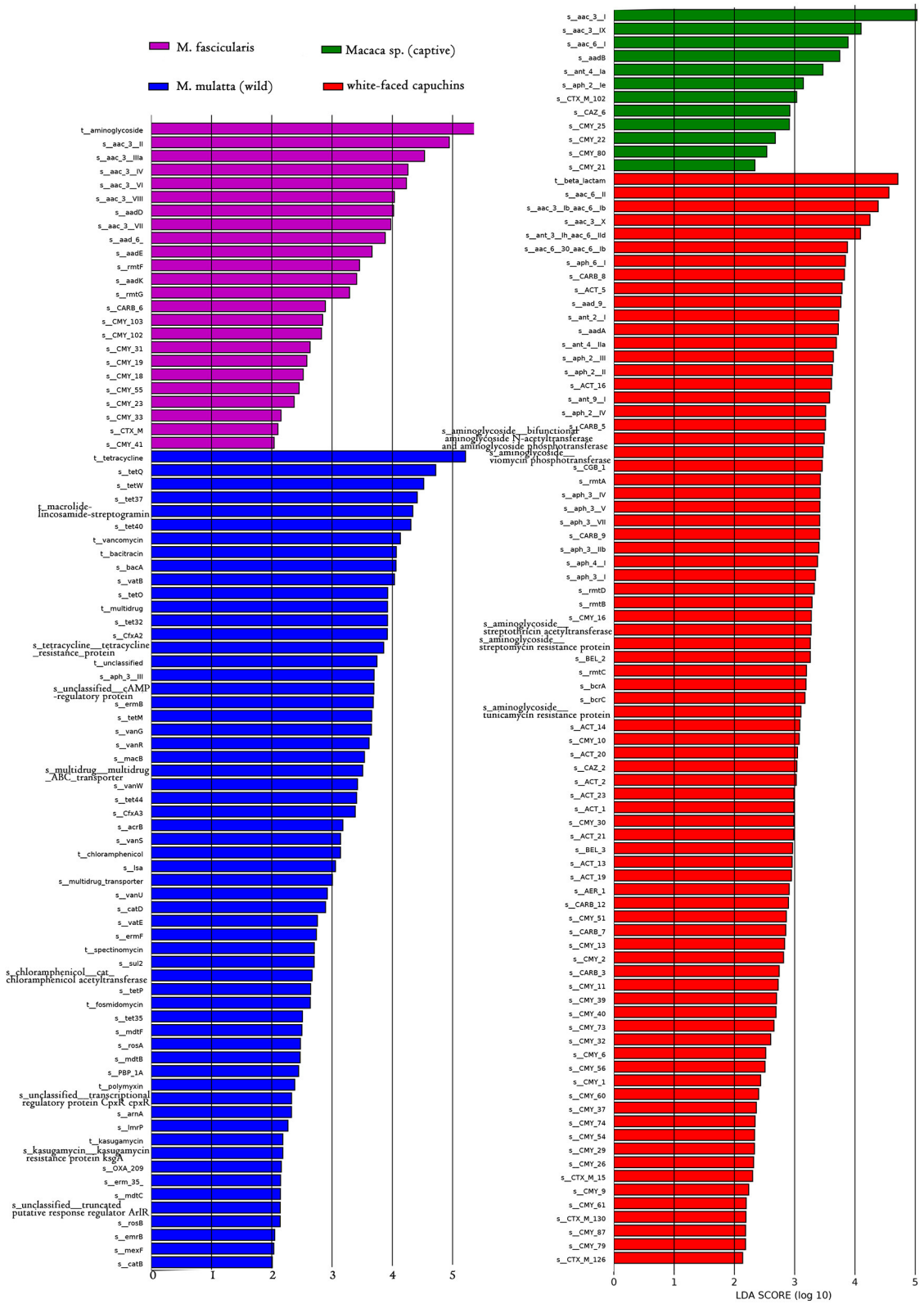

FIGURE 6
LDA score distribution of the discriminative ARGs between white-faced capuchins, *Macaca sp.* (captive), *M. mulatta* (wild) and *M. fascicularis* fecal microbiomes determined by LEfSe analysis. The red rectangle, green rectangle, blue rectangle, purple rectangle represent white-faced capuchins, *Macaca sp.* (captive), *M. fascicularis* samples, and *M. mulatta* (wild), respectively, of which ARGs' LDA score are more than 2.

antibiotic inactivation. Similar results have been reported that antibiotic inactivation was the dominant resistance mechanism in swine and humans (37).

The effect of captivity on intestinal microbial resistance in animals is still unclear. Previous researches show that captivity influences the gut resistome structure by altering the gut microbiota composition. Thus, comparison with wild animals, captive breeding may affect the diversity/abundance of resistant genes by affecting their own intestinal microbial structure in a variety of ways, such as dietary changes, drug treatment, and reducing contact with other individuals, species, and variable environmental substrates as a source of bacterial diversity (16, 38, 39). Previous research also reveals that semi-captive wildlife might harbor a higher diversity of antimicrobial-resistant genes (40). Research on captive and wild baboon gut microbiota and their resistome found that exposure to humans is associated with changes in gut microbiota composition and resistome expansion compared (15). Rolland et al. (41) found that compared with baboons that do not contact humans, baboons that directly contact humans can detect a higher level of antibiotic resistance (41). In these results, both white-faced capuchinsand *M. mulatta* in wild had high diversity index. Further analysis of *R. roxellana* found that captive *R. roxellana* had significantly higher diversity and abundance than wild and semi-wild. Therefore, diversity index analysis can not tell the direct relationship between captive and wild NHPs. It is certain that lifestyle is an important factor that influences the ARGs diversity of NHPs. Besides, a comparison of *M. mulatta* in China and the USA revealed that ARG was also influenced by geography but to a lesser extent. Consequently, a concluded that gut resistome of NHPs were more substantially affected by the captive environment than geography or host.

Compared with the gut microbiota ARGs of *M. mulatta* and *M. fascicularis*, the diversity of gut microbiota ARGs of white-faced capuchins was the highest. Various ARGs of white-faced capuchins that were significantly different from *M. mulatta* and *M. fascicularis* in this study, indicating that the ARGs may have spread to the habitats of white-faced capuchins. Strangely, tetracycline resistance genes *tet*Q, *tet*W and *tet*37 were found in the wild gut microbiota of *M. mulatta*. The spread of ARGs in wild NHPs is more worrisome because it may lead to a large-scale environment polluted that increasingly animal antibiotic-resistant infections cannot be treated including endangered animals. Research showed that the frequent use of antibiotics has led to antibiotic selection pressure causing the prevalence of antibiotic-resistant bacteria (42). Therefore, antibiotics must be used reasonably to reduce the selection pressure. Measures should be taken to reduce resistance development and spreading of resistant bacteria. Under the one-health approach, a holistic perspective on antibiotic resistance, including humans, animals, and the external environment needs to take on Bengtsson-Palme et al. (43). Furthermore, models should be built to demonstrate and predict how resistance emerges and disseminates by increasing knowledge of influence factors and the mechanism of transmission of drive resistance. All in all, these results provide references for NHPs' gut resistome studies.

Conclusion

The study described a comprehensive *R. roxellana*, *M. mulatta*, *Macaca sp*. *M. fascicularis*, and white-faced capuchins gut resistance gene catalog and revealed the abundance and diversity of ARGs of them. The total ARGs relative abundance in the captive animal was higher than in the wild and tetracycline was the predominant resistance in both captive and wild NHPs. Captivity was considered to be the primary influence factor of host gut microbiota ARGs abundance and diversity. This study helps to improve the knowledge and understanding of NHPs' gut flora ARGs and strengthen the management of antibiotics and the prevention of human diseases.

Data availability statement

Publicly available datasets were analyzed in this study. The names of the repository/repositories and accession number(s) can be found in the article/Supplementary material.

Author contributions

HH designed and constructed the manuscript, downloaded and analyzed of the datasets, generated the major figures and tables, and completed the writting.

Acknowledgments

HH acknowledge the providers who submitted the metagenomics-seq data to the public databases. HH also acknowledge Lei Yu for technical support during the conduct of the experimental analysis. HH sincerely thank the editors and reviewers for their insightful and constructive feedback that helped to improve this manuscript.

Conflict of interest

The author declares that the research was conducted in the absence of any commercial or financial relationships that could be construed as a potential conflict of interest.

Publisher's note

All claims expressed in this article are solely those of the authors and do not necessarily represent those

of their affiliated organizations, or those of the publisher, the editors and the reviewers. Any product that may be evaluated in this article, or claim that may be made by its manufacturer, is not guaranteed or endorsed by the publisher.

Supplementary material

The Supplementary Material for this article can be found online at: https://www.frontiersin.org/articles/10.3389/fvets.2022.1020276/full#supplementary-material

References

1. Yang Y, Li Z, Song W, Du L, Ye C, Zhao B, et al. Metagenomic insights into the abundance and composition of resistance genes in aquatic environments: influence of stratification and geography. *Environ Int.* (2019) 127:371–80. doi: 10.1016/j.envint.2019.03.062

2. Nathan C, Cars O. Antibiotic resistance - problems, progress, and prospects. *New Engl J Med.* (2014) 371:1761–3. doi: 10.1056/NEJMp1408040

3. He LY, He LK, Liu YS, Zhang M, Zhao JL, Zhang QQ, et al. Microbial diversity and antibiotic resistome in swine farm environments. *Sci Total Environ.* (2019) 685:197–207. doi: 10.1016/j.scitotenv.2019.05.369

4. Qian X, Gunturu S, Guo J, Chai B, Cole JR, Gu J, et al. Metagenomic analysis reveals the shared and distinct features of the soil resistome across tundra, temperate prairie, and tropical ecosystems. *Microbiome.* (2021) 9:1–13. doi: 10.1186/s40168-021-01047-4

5. Li B, Yang Y, Ma L, Ju F, Guo F, Tiedje JM, et al. Metagenomic and network analysis reveal wide distribution and co-occurrence of environmental antibiotic resistance genes. *ISME J.* (2015) 9:2490–502. doi: 10.1038/ismej.2015.59

6. Zhu YG, Zhao YI, Li B, Huang CL, Zhang SY, Yu S, et al. Continental-scale pollution of estuaries with antibiotic resistance genes. *Nat Microbiol.* (2017) 2:1–7. doi: 10.1038/nmicrobiol.2016.270

7. Xu Y, Xu J, Mao DQ, Luo Y. Effect of the selective pressure of sub-lethal level of heavy metals on the fate and distribution of ARGs in the catchment scale. *Environ Pollut.* (2017) 220:900–8. doi: 10.1016/j.envpol.2016.10.074

8. Zheng J, Gao R, Wei Y, Chen T, Fan J, Zhou Z, et al. High-throughput profiling and analysis of antibiotic resistance genes in East Tiaoxi River, China. *Environ Pollut.* (2017) 230:648–54. doi: 10.1016/j.envpol.2017.07.025

9. Chen H, Zhang MM. Effects of advanced treatment systems on the removal of antibiotic resistance genes in wastewater treatment plants from Hangzhou, China. *Environ Sci Technol.* (2013) 47:8157–63. doi: 10.1021/es401091y

10. Karkman A, Do TT, Walsh F, Virta MPJ. Antibiotic-resistance genes in waste water. *Trends Microbiol.* (2018) 26:220–8. doi: 10.1016/j.tim.2017.09.005

11. Fresia P, Antelo V, Salazar C, Giménez M, D'Alessandro B, Afshinnekoo E, et al. Urban metagenomics uncover antibiotic resistance reservoirs in coastal beach and sewage waters. *Microbiome.* (2019) 7, 1–9. doi: 10.1186/s40168-019-0648-z

12. Huang K, Xia H, Zhang Y, Li J, Cui G, Li F, et al. Elimination of antibiotic resistance genes and human pathogenic bacteria by earthworms during vermicomposting of dewatered sludge by metagenomic analysis. *Bioresource Technol.* (2020) 297:122451. doi: 10.1016/j.biortech.2019.122451

13. Chi T, Zhang A, Zhang X, Li AD, Zhang H, Zhao Z, et al. Characteristics of the antibiotic resistance genes in the soil of medical waste disposal sites. *Sci Total Environ.* (2020) 730:139042. doi: 10.1016/j.scitotenv.2020.139042

14. Zhu YG, Johnson TA, Su JQ, Qiao M, Guo GX, Stedtfeld RD, et al. Diverse and abundant antibiotic resistance genes in Chinese swine farms. *P Natl Acad Sci USA.* (2013) 110:3435–40. doi: 10.1073/pnas.1222743110

15. Tsukayama P, Boolchandani M, Patel S, Pehrsson EC, Gibson MK, Chiou KL, et al. Characterization of wild and captive baboon gut microbiota and their antibiotic resistomes. *Msystems.* (2018) 3: e00016-18. doi: 10.1128/mSystems.00016-18

16. Joyce A, McCarthy CGP, Murphy S, Walsh F. Antibiotic resistomes of healthy pig faecal metagenomes. *Microb Genomics.* (2019) 5:5. doi: 10.1099/mgen.0.000272

17. Sun Y, Qiu T, Gao M, Shi M, Zhang H, Wang X, et al. Inorganic and organic fertilizers application enhanced antibiotic resistome in greenhouse soils growing vegetables. *Ecotox Environ Safe.* (2019) 179:24–30. doi: 10.1016/j.ecoenv.2019.04.039

18. Zheng J, Zhou Z, Wei Y, Chen T, Feng W, Chen H, et al. High-throughput profiling of seasonal variations of antibiotic resistance gene transport in a peri-urban river. *Environ Int.* (2018) 114:87–94. doi: 10.1016/j.envint.2018.02.039

19. Fang H, Huang K, Yu J, Ding C, Wang Z, Zhao C, et al. Metagenomic analysis of bacterial communities and antibiotic resistance genes in the *Eriocheir sinensis* freshwater aquaculture environment. *Chemosphere.* (2019) 224:202–11. doi: 10.1016/j.chemosphere.2019.02.068

20. Zhang G, Guan Y, Zhao R, Feng J, Huang J, Ma L, et al. Metagenomic and network analyses decipher profiles and co-occurrence patterns of antibiotic resistome and bacterial taxa in the reclaimed wastewater distribution system. *J Hazard Mater.* (2020) 400:123170. doi: 10.1016/j.jhazmat.2020.123170

21. Wang C, Li P, Yan Q, Chen L, Li T, Zhang W, et al. Characterization of the pig gut microbiome and antibiotic resistome in industrialized feedlots in China. *Msystems.* (2019) 4:e00206–19. doi: 10.1128/mSystems.00206-19

22. Rizzo L, Manaia C, Merlin C, Schwartz T, Dagot C, Ploy MC, et al. Urban wastewater treatment plants as hotspots for antibiotic resistant bacteria and genes spread into the environment: a review. *Sci Total Environ.* (2013) 447:345–60. doi: 10.1016/j.scitotenv.2013.01.032

23. Guo JH, Li J, Chen H, Bond PL, Yuan ZG. Metagenomic analysis reveals wastewater treatment plants as hotspots of antibiotic resistance genes and mobile genetic elements. *Water Res.* (2017) 123:468–78. doi: 10.1016/j.watres.2017.07.002

24. Yan YY, Li H, Fayyaz A, Gai YP. Metagenomic and network analysis revealed wide distribution of antibiotic resistance genes in monkey gut microbiota. *Microbiol Res.* (2022) 254:126895. doi: 10.1016/j.micres.2021.126895

25. Campbell TP, Sun X, Patel VH, Sanz C, Morgan D, Dantas G, et al. The microbiome and resistome of chimpanzees, gorillas, and humans across host lifestyle and geography. *ISME J.* (2020) 14:1584–99. doi: 10.1038/s41396-020-0634-2

26. Qiu Q, Wang J, Yan Y, Roy B, Chen Y, Shang X, et al. Metagenomic analysis reveals the distribution of antibiotic resistance genes in a large-scale population of healthy individuals and patients with varied diseases. *Front Mol Biosci.* (2020) 7:590018. doi: 10.3389/fmolb.2020.590018

27. Forsberg KJ, Patel S, Gibson MK, Lauber CL, Knight R, Fierer N, et al. Bacterial phylogeny structures soil resistomes across habitats. *Nature.* (2014) 509:612. doi: 10.1038/nature13377

28. Feng J, Li B, Jiang X, Yang Y, Wells GF, Zhang T, et al. Antibiotic resistome in a large-scale healthy human gut microbiota deciphered by metagenomic and network analyses. *Environ Microbiol.* (2018) 20:355–68. doi: 10.1111/1462-2920.14009

29. Yin X, Jiang XT, Chai B, Li L, Yang Y, Cole JR, et al. ARGs-OAP v2.0 with an expanded SARG database and Hidden Markov Models for enhancement characterization and quantification of antibiotic resistance genes in environmental metagenomes. *Bioinformatics.* (2018) 34:2263–70. doi: 10.1093/bioinformatics/bty053

30. Alcock BP, Raphenya AR, Lau TT, Tsang KK, Bouchard M, Edalatmand A, et al. CARD 2020: antibiotic resistome surveillance with the comprehensive antibiotic resistance database. *Nucleic Acids Res.* (2020) 48:D517–25. doi: 10.1093/nar/gkz935

31. Thaker M, Spanogiannopoulos P, Wright GD. The tetracycline resistome. *Cell Mol Life Sci.* (2010) 67:419–31. doi: 10.1007/s00018-009-0172-6

32. Yang S, Liu Y, Yang N, Lan Y, Lan W, Feng J, et al. The gut microbiome and antibiotic resistome of chronic diarrhea rhesus macaques (*Macaca mulatto*) and its similarity to the human gut microbiome. *Microbiome.* (2022) 10:1–13. doi: 10.1186/s40168-021-01218-3

33. Zhang RM, Liu X, Wang SL, Fang LX, Sun J, Liu Y, et al. Distribution patterns of antibiotic resistance genes and their bacterial hosts in pig farm wastewater treatment systems and soil fertilized with pig manure. *Sci Total Environ.* (2021) 758:143654. doi: 10.1016/j.scitotenv.2020.143654

34. Tong C, Xiao D, Xie L, Yang J, Zhao R, Hao J, et al. Swine manure facilitates the spread of antibiotic resistome including tigecycline-resistant tet(X)

variants to farm workers and receiving environment. *Sci Total Environ.* (2022) 808:152157. doi: 10.1016/j.scitotenv.2021.152157

35. Allen SE, Boerlin P, Janecko N, Lumsden JS, Barker IK, Pearl DL, et al. Antimicrobial resistance in generic *Escherichia coli* isolates from wild small mammals living in swine farm, residential, landfill, and natural environments in southern Ontario, Canada. *Appl Environ Microb.* (2011) 77:882–8. doi: 10.1128/AEM.01111-10

36. Allen SE, Boerlin P, Janecko N, Lumsden JS, Barker IK, Pearl DL, et al. Associations between antimicrobial use and the faecal resistome on broiler farms from nine European countries. *J Antimicrob Chemoth.* (2019) 74:2596–604.

37. Qian X, Gu J, Sun W, Wang XJ, Su JQ, Stedfeld R, et al. Diversity, abundance, and persistence of antibiotic resistance genes in various types of animal manure following industrial composting. *J Hazard Mater.* (2018) 344:716–22. doi: 10.1016/j.jhazmat.2017.11.020

38. McKenzie VJ, Song SJ, Delsuc F, Prest TL, Oliverio AM, Korpita TM, et al. The Effects of Captivity on the Mammalian Gut Microbiome. *Integr Comp Biol.* (2017) 57:690–704. doi: 10.1093/icb/icx090

39. Wang X, Wang Z, Pan H, Qi J, Li D, Zhang L, et al. Captivity influences the gut microbiome of *Rhinopithecus roxellana*. *Front Microbiol.* (2021) 12:3841. doi: 10.3389/fmicb.2021.763022

40. Jia T, Chang WS, Marcelino VR, Zhao S, Liu X, You Y, et al. Characterization of the gut microbiome and resistomes of wild and zoo-captive macaques. *Front Vet Sci.* (2022) 8:778556. doi: 10.3389/fvets.2021.778556

41. Rolland RM, Hausfater G, Marshall B. Antibiotic-resistant bacteria in wild primates: increased prevalence in baboons feeding on human refuse. *Appl Environ Microbiol.* (1985) 49:791–4. doi: 10.1128/aem.49.4.791-794.1985

42. Schechner V, Temkin E, Harbarth S, Carmeli Y, Schwaber MJ. Epidemiological interpretation of studies examining the effect of antibiotic usage on resistance. *Clin Microbiol Rev.* (2013) 26:289–307. doi: 10.1128/CMR.00001-13

43. Bengtsson-Palme J, Kristiansson E, Larsson DGJ. Environmental factors influencing the development and spread of antibiotic resistance. *Fems Microbiol Rev.* (2018) 42:68–80. doi: 10.1093/femsre/fux053

frontiers | Frontiers in Veterinary Science

TYPE Original Research
PUBLISHED 22 December 2022
DOI 10.3389/fvets.2022.1087693

OPEN ACCESS

EDITED BY
Muhammad Saqib,
University of Agriculture,
Faisalabad, Pakistan

REVIEWED BY
Mário Ginja,
University of Trás-os-Montes and Alto Douro, Portugal
Anu Katriina Lappalainen,
University of Helsinki, Finland
Sofia Alves-Pimenta,
Universidade de Trás-os-Montes e Alto, Portugal

*CORRESPONDENCE
Barbara Bockstahler
✉ barbara.bockstahler@vetmeduni.ac.at

SPECIALTY SECTION
This article was submitted to Comparative and Clinical Medicine, a section of the journal Frontiers in Veterinary Science

RECEIVED 02 November 2022
ACCEPTED 06 December 2022
PUBLISHED 22 December 2022

CITATION
Virag Y, Gumpenberger M, Tichy A, Lutonsky C, Peham C and Bockstahler B (2022) Center of pressure and ground reaction forces in Labrador and Golden Retrievers with and without hip dysplasia at 4, 8, and 12 months of age.
Front. Vet. Sci. 9:1087693.
doi: 10.3389/fvets.2022.1087693

Center of pressure and ground reaction forces in Labrador and Golden Retrievers with and without hip dysplasia at 4, 8, and 12 months of age

Yvonne Virag[1], Michaela Gumpenberger[2], Alexander Tichy[3], Christiane Lutonsky[1], Christian Peham[4] and Barbara Bockstahler[1]*

[1]Section of Physical Therapy, Small Animal Surgery, Department of Companion Animals and Horses, University Clinic for Small Animals, University of Veterinary Medicine, Vienna, Austria, [2]Diagnostic Imaging, Department of Companion Animals and Horses, University of Veterinary Medicine, Vienna, Austria, [3]Department of Biomedical Sciences, Bioinformatics and Biostatistics Platform, University of Veterinary Medicine Vienna, Vienna, Austria, [4]Department of Companion Animals and Horses, Movement Science Group, University Clinic for Horses, University of Veterinary Medicine, Vienna, Austria

Canine hip dysplasia (CHD) is a common orthopedic disease. Owing to the importance of CHD in affected dogs, both clinically and for their use in breeding or work, increasing attention is being given to early diagnosis. Therefore, early clinical and radiological examination of young animals is increasingly in demand, whereas common CHD screening according to the Fédération Cynologique Internationale (FCI) is usually performed at the age of 12 months or even older in Europe. One way to objectively evaluate gait pattern is to measure the ground reaction forces (GRFs) and center of pressure (COP). In this study, we used a pressure plate to evaluate the GRF and COP parameters for 32 Labrador Retrievers and 17 Golden Retrievers at 4, 8, and 12 months of age. The dogs also underwent radiological examination of the hip joints following the FCI rules at the age of at least 12 months, which were grouped as sound (FCI grade A or B) and diseased (FCI grade C or worse). The results revealed significantly higher COP values in both breeds in the diseased limb groups at any measurement point during walking, with the most pronounced results obtained at 8 months of age. Furthermore, COP values during walking were significantly higher at 4 months than at 8 and 12 months in both the sound and diseased limb groups, indicating an increased stability of the gait pattern. Except for COP-Speed, the values of all COP parameters were higher during walking than during trotting at 4 months of age (i.e., COP-Speed was higher when trotting), indicating that the 4-beat gait in walk is more difficult to control for puppies than the 2-beat gait in trot. Overall, our results support the early evaluation of CHD in growing animals using non-invasive methods.

KEYWORDS

center of pressure, ground reaction forces, canine hip dysplasia, Labrador Retriever, Golden Retriever

1. Introduction

Canine hip dysplasia (CHD) is one of the most common orthopedic diseases in young dogs without a traumatic background, especially in large and predisposed breeds. This condition leads to significant orthopedic effects and pain in aging animals through the development of osteoarthritis (OA) (1, 2).

According to the rules of the Fédération Cynologique Internationale (FCI), radiographic examination for CHD screening should be performed at the age of 12 months (or even 18 months for large-breed dogs). However, owing to the importance of CHD in affected dogs, both clinically and for their use in breeding or work, increasing attention is being given to early diagnosis (3). Clinical and radiological examinations of young animals, even before official radiographic FCI hip scoring, are increasingly in demand. Clinical evaluation methods include the Ortolani, Bardens, and Barlow tests, (3), whereas the Penn Hip method is preferred for radiographs, in which a distraction index (DI) is used to determine hip joint laxity (4). In addition, other radiological parameters, such as dorsal acetabular rim slope and center edge angle, and qualitative parameters, such as sclerosis of the cranial acetabular rim, location of the center of the femoral head, grading of the degenerative joint disease, and grading of the dorsal acetabular rim, are also used (5). A total score that includes different parameters can be used as an early detection method to distinguish dogs that are later classified as CHD-free (according to the FCI guidelines) and dogs with a transitional hip (FCI-B) (6). Furthermore, the combination of the Norberg angle, distraction recording, and laxity index presents a reliable prediction of whether a dog will develop an FCI-grade A, B, or C hip (7). However, at present, there is no consensus on the best methodology for the early evaluation or conclusive assessment of the usefulness of various evaluable parameters (6, 8). Additionally, the evaluation of parameters is complicated by breed differences and the corresponding cutoff values that delineate a "healthy" hip joint from a "diseased" hip joint with increased laxity (7, 9, 10).

Kinetic motion analysis has become increasingly important in recent years to objectively describe the clinical effects of orthopedic diseases. Using this method, the ground reaction forces (GRF) are evaluated using force- or pressure-measurement plates. Numerous studies have used this non-invasive method to describe, for example, the compensatory effects of lameness (11–13) and therapeutic results (14–16). Additionally, the pressure distribution within the paws can be described by pedobarography with the help of pressure-measurement plates. Using this method, significant changes in the distribution of forces in the paws of orthopedically diseased dogs have been documented (17–20). Another more recently applied parameter is the center of pressure (COP), which is the location where the GRF vector acts on the ground (i.e., the application point of the force). The COP constantly changes its position to control the stability of the upright posture and gait pattern. This parameter can be evaluated when standing (statokinesiogram) and when in motion. Crucially, COP analysis reveals disturbances in postural control in human patients with hip dysplasia (HD) (21). Likewise, orthopedically diseased dogs show a significant increase in COP parameters, and COP parameter measurements are, therefore, considered useful in the evaluation of lameness (12, 18, 22). Furthermore, dogs with coxarthrosis show a significant increase in mediolateral COP deviation and COP-Area in the hindlimbs (12). While age-related changes in various COP parameters in horses have been documented between the first and the 5th months of life (23), few studies have evaluated the kinetic parameters of growing dogs. One study investigated whether the DI correlated with different kinetic variables, but no association was found, although this may reflect high data variability possibly linked to incompletely developed neuromuscular function and coordination of the puppies (24).

Based on the existing literature from both human and veterinary medicine, in this study, we aimed first time to obtain GRF and COP parameters for retriever dogs aged 4, 8, and 12 months. We hypothesized that even in clinically non-lame dogs, the COP parameter values of limbs with a CHD grade C or worse based on radiographic FCI hip scores would be increased compared to CHD grade A or B limbs. Results of the study could have potential of the early, non-invasive evaluation of future CHD risk in puppies and, thus, allowing early intervention.

2. Materials and methods

2.1. Dogs

The total number of participants included 51 puppies (Labrador Retrievers, $n = 33$; Golden Retrievers, $n = 18$) from the Austrian Retriever Club (ÖRC). For inclusion in the study, the breeding parents of a puppy had to have a breeding license with the ÖRC, and the owners had to have the intention to have an FCI hip and elbow radiograph as defined by the ÖRC, to be performed at the earliest age of 12 months. Puppies with disorders not related to the hip joint, such as osteochondrosis dissecans (OCD) of the shoulder joint and elbow dysplasia, were excluded from the study.

The dogs were presented at 4 (M1), 8 (M2), and 12 (M3) months of age. At each time point, the animals underwent clinical, orthopedic, and neurological examinations. Subsequently, the dogs underwent motion analysis on a Zebris pressure plate (FDM Type 2, Zebris Medical GmbH, Allgäu, Germany) with a measurement area of 203.2 × 54.2 cm containing 15,360 sensors with a sampling rate of 100 Hz. The plate was mounted in the middle of a 9-m runway and covered with a rubber mat (1 mm thickness) to hide the measurement area and prevent slipping. A camera (Panasonic NV-MX500)

was used to obtain the measurements. The collected data were analyzed using custom software (Pressure Analyzer 4.3.3; Michael Schwanda).

2.2. Measurement procedure

The measurements were performed while walking and trotting. In each case, the dog and owner were allowed to familiarize themselves with the measuring room and explore it playfully. As soon as the dog felt comfortable, the measurement and data collection began. To ensure that the animal moved straight across the force plate with the head in a straight and forward position, an assistant stood directly at the opposite end of the force plate and encouraged the animal to walk or trot toward them while keeping eye contact with the dog. If free movement without a leash due to the individual behavior of the animal was not possible, the measurements were performed with a leash. To minimize the influence of leashes, dogs were trained to walk or trot in a smooth and harmonious gait pattern without pulling on the leash before the analysis began. At least five passes with valid steps over the pressure plate were performed during walking and trotting. Valid measurements were performed if the animal walked or trotted in a straight line with the head in a straight and forward position, without an apparent change in speed. In cases where the dog was led over the plate with a leash, the leash must have swung freely without pulling to be counted as a valid pass. Passes were judged as failed when the study participant did not move straight across the measurement plate (e.g., when it left the plate or entered it obliquely from the side) or held its head to the side, up, or down relative to the floor. Passes where the dog stopped, slowed down, sped up, or sat down, were also excluded. To be included, the speed at which a dog crossed the plate had to be within $\pm$ 0.3 m/s when walking, with a maximum of 0.5 m/s when trotting and with an acceleration of $\pm$ 0.5 m/s^2 (25–27).

Radiological assessment was performed from the age of 12 months (M3), and this followed the FCI standard. Radiographic analysis was performed approximately 2 weeks before or after M3. The dog owners were allowed to have the examination performed at the veterinarian of their choice, but all of the resulting radiographs were sent to us for evaluation. Evaluation of the hip and elbow joints was performed by a certified radiologist (MG) according to the standard procedure of the FCI. The radiologist had no information about the results of the gait analysis. A symmetric ventrodorsal view of the coxofemoral joints and pelvis with caudally extended hind legs positioned parallel to the table (position I) was used for screening. Congruity of the joint space, shape and (abnormal) sclerosing of the cranial acetabular rim, shape, and density of the femoral head and neck, femoral head center in relation to the dorsal acetabular rim, radiographic signs of arthrosis, and, finally, the Norberg angle, were used to grade each hip joint as grade A (free of CHD), B (borderline), C (mild), D (moderate) to E (severe CHD). Furthermore, the presence or absence of a lumbosacral transitional vertebra was verified. Mediolateral and craniocaudal radiographs of both elbows were monitored for new bone formation, isolated anconeal processes, fractured medial coronoid processes, incongruity, osteochondrosis (dissecans), contact lesions, and incomplete humeral condyle ossification to obtain a final grade ranging from ED 0 (free of elbow dysplasia) to ED III (grade 3, severe elbow dysplasia).

2.3. Data evaluation

Through video analysis, the footprints displayed on the custom Pressure Analyzer software (version 4.3.3, Michael Schwanda) were manually assigned to the corresponding hindlimb. For data analysis, the limbs were divided into two groups—those that were evaluated at the FCI examination with HD grade A or B (sound limb) and those with a HD grade of C or worse (diseased limb).

Subsequently, the following parameters were obtained (12, 28, 29):

- Speed (m/s) and acceleration (m/s^2) for the left hindlimb.
- Peak vertical force (PFz, N) and vertical impulse (IFz, Ns) for each hind limb normalized to the total force exerted by the hindlimbs (PFz %, IFz %), using the following formula:

$$Value\ in\ \%\ of\ total\ force\ = \left(\frac{XFz\_LR\ or\ LL}{XFz\_LR + XFz\_LL}\right) \times 100$$

  where XFz = mean value of PFz or IFz of the valid steps, LR = right hindlimb, and LL = left hindlimb.
- Stance phase duration (SPD): The mean duration of the stance phase(s) of each limb was normalized to the total duration of the stance phase (SPD %) following the previous formula.
- Time of occurrence of PFz (TPFz) as a percentage (%) of the stance phase of the respective limb.
- Paw contact area (cm^2): The area of force application.
- Center of pressure area (COP-Area): The surface that includes all points of the COP normalized to the paw contact area and expressed as a percentage (%).
- Mediolateral (COP-Med-lat) and craniocaudal COP (COP-Cran-caud) displacements: The difference between the maximum positive and negative excursions along the craniocaudal and mediolateral axes, respectively, expressed as a percentage (%) of the maximum width or length of the paw contact area.
- COP-Radius (mm): The mean of the distance of all COP points to the center point of all COP points, normalized to the paw contact area and expressed as a percentage (%).

TABLE 1 Demographic data of the studied dogs at three measurement points (M1 = 4 months, M2 = 8 months, and M3 = 12 months of age).

	Labrador Retriever (n = 32)			Golden Retriever (n = 17)		
Evaluation	M1	M2	M3	M1	M2	M3
Body mass (kg ± SD)	13.34 ± 3.17	23.62 ± 4.23	26.35 ± 4.80	16.54 ± 3.84	27.64 ± 5.22	29.07 ± 5.32
Mean age (weeks ± SD)	18.41 ± 2.17	34.69 ± 1.00	59.09 ± 9.30	19.00 ± 1.80	34.82 ± 1.19	60.76 ± 11.32

- COP-Speed: The mean speed (distance/time) of the movement of the COP (mm/s).

2.4. Statistical analysis

All statistical analyses were performed using IBM SPSS v28. For every single parameter, the difference between hips (sound with FCI scoring A and B and diseased with FCI scoring C and worse), speed (walk and trot), and time (4, 8, and 12 months) were analyzed separately for each of the two breeds using a linear mixed effect model. Specific *post-hoc* comparisons were performed using Sidak's alpha correction procedure. The assumption of normal distribution was assessed using the Shapiro–Wilk test. A p-value of $< 5\%$ ($p < 0.05$) was considered statistically significant.

3. Results

The demographic data of the dogs at the time of measurement are shown in Table 1. Based on the inclusion criteria, one Labrador Retriever in the 8th month of life had to be excluded because of OCD in one shoulder, and one Golden Retriever was excluded because he displayed elbow dysplasia grade 2, as detected by the FCI investigation. Therefore, data were evaluated based on a total of 49 dogs [98 hip joints from 32 Labrador (17 female, 15 male) and 17 Golden Retrievers (10 females, 7 males).

3.1. Linear mixed effect model

The linear mixed effect model showed that except for COP-Med-lat ($p = 0.065$), the healthy or diseased status of the dogs had a significant effect on all the COP parameters for the entire population ($p < 0.001$). Regarding the GRF parameters, health status had a significant effect on IFz ($p = 0.040$) and TPFz ($p = 0.028$). There were also significant effects of breed on COP-Cran-caud, COP-Radius, and COP-Speed ($p < 0.001$). Speed of gait (at walk and trot) had a significant influence on all the COP parameters and TPFz ($p < 0.001$). The time of measurement (4, 8, and 12 months) also had a significant influence on all of the COP parameters ($p < 0.001$) but not GRF. Breed influenced three out of the five COP parameters (COP-Cran-caud, COP-Radius, and COP-Speed; $p < 0.001$) and TPFz ($p = 0.046$).

TABLE 2 Speed (v) and acceleration (a) (mean ± SD) (calculated for the left hind limb) when walking and trotting for Labrador Retrievers (n = 32) at the three measurement points (M1 = 4 months, M2 = 8 months, and M3 = 12 months of age).

Measurement		M1	M2	M3
Walk	a (m/s²)	0.00 ± 0.02	−0.01 ± 0.04	0.01 ± 0.03
	v (m/s)	1.03 ± 0.09	1.17 ± 0.10	1.23 ± 0.12
Trot	a (m/s²)	0.01 ± 0.08	0.01 ± 0.12	0.07 ± 0.20
	v (m/s)	2.01 ± 0.17	2.28 ± 0.18	2.41 ± 0.26

v = speed (m/s) and a = acceleration (m/s²) for the left hindlimb.

Thus, subsequent evaluations were performed separately for the two breeds.

3.2. Labrador Retrievers

3.2.1. Clinical, orthopedic, and neurological examination

Clinical, orthopedic, and neurological examinations of the 32 Labradors did not reveal any abnormalities. As previously noted, one dog was excluded because of an OCD at M2.

3.2.2. Hip scoring

FCI examination of the 64 hip joints revealed the following results: 31 were rated as grade A, 16 as B, 12 as C, 2 as D, and 3 as E. Therefore, 47 hip joints were scored as sound and 17 as diseased. Among the 17 diseased hips 5 animals had unilateral and 6 bilateral CHD. Eight dogs displayed a lumbosacral transitional vertebra, 5 in dogs with sound hip joints (3 type 1 and 2 type 3) and 3 dogs with bilateral FCI scoring C (all type 1).

3.2.3. Speed and acceleration

The speed and acceleration data are presented in Table 2. All values were within the acceptable ranges described in Section 2.2.

3.2.4. Differences between sound and diseased limbs

With regard to GRF and SPD, no differences were found in any of the measurements between limbs classified as sound

TABLE 3 Descriptive statistics (mean ± SD) for walking and trotting Labrador Retrievers ($n = 32$) at three measurement points (M1 = 4 months, M2 = 8 months, and M3 = 12 months of age) in sound and diseased limb groups.

Measurement		M1		M2		M3	
Gait	Parameter	Sound	Diseased	Sound	Diseased	Sound	Diseased
Walk	COP-Area (%)	$1.84 \pm 0.44^{*\#¥}$	$2.24 \pm 0.66^{*\#¥}$	$0.97 \pm 0.27^{*\#}$	$1.20 \pm 0.37^{*\#}$	$0.84 \pm 0.23^{(*)¥}$	$0.98 \pm 0.33^{(*)¥}$
	COP-Cran-caud (%)	$35.23 \pm 5.17^{*\#¥}$	$38.32 \pm 6.87^{*\#¥}$	$23.26 \pm 3.36^{*\#}$	$25.99 \pm 4.52^{*\#}$	$21.87 \pm 3.26^{*¥}$	$24.76 \pm 3.56^{*¥}$
	COP-Med-lat (%)	$8.19 \pm 1.82^{\#¥}$	$8.60 \pm 1.65^{\#¥}$	$5.80 \pm 1.20^{*\#}$	$6.98 \pm 1.00^{*\#}$	$5.44 \pm 1.37^{¥}$	$6.11 \pm 2.29^{¥}$
	COP-Radius (%)	$0.22 \pm 0.03^{*\#¥}$	$0.25 \pm 0.07^{*\#¥}$	$0.13 \pm 0.02^{*\#}$	$0.15 \pm 0.03^{*\#}$	$0.12 \pm 0.02^{¥}$	$0.13 \pm 0.02^{¥}$
	COP-Speed (mm/s)	$96.92 \pm 10.07^{*\#¥}$	$109.24 \pm 21.63^{*\#¥}$	$68.84 \pm 8.72^{*\#}$	$78.99 \pm 15.00^{*\#}$	$68.08 \pm 10.39^{*¥}$	$76.16 \pm 9.65^{*¥}$
	IFz (%TF)	50.00 ± 1.32	49.99 ± 1.46	49.98 ± 0.88	50.04 ± 0.63	50.06 ± 0.98	49.83 ± 1.51
	PFz (%TF)	50.05 ± 1.47	49.85 ± 1.17	49.98 ± 1.39	50.07 ± 1.15	50.08 ± 1.36	49.77 ± 1.85
	SPD (%)	49.99 ± 0.71	50.03 ± 0.79	50.00 ± 0.57	50.00 ± 0.38	49.99 ± 0.52	50.03 ± 0.78
	TPFz (%SPD)	22.01 ± 2.43	22.62 ± 3.47	23.99 ± 4.68	23.70 ± 3.08	$23.73 \pm 2.96^{*}$	$25.37 \pm 3.39^{*}$
Trot	COP-Area (%)	0.70 ± 0.30	0.80 ± 0.24	0.75 ± 0.34	0.85 ± 0.30	$0.64 \pm 0.34^{*}$	$0.92 \pm 0.34^{*}$
	COP-Cran-caud (%)	$25.46 \pm 4.48^{*\#¥}$	$28.22 \pm 4.63^{*\#¥}$	$21.62 \pm 3.77^{\#£}$	$22.76 \pm 3.90^{\#}$	$18.86 \pm 5.39^{*¥£}$	$22.68 \pm 5.08^{*¥}$
	COP-Med-lat (%)	4.94 ± 1.47	5.65 ± 1.85	5.27 ± 1.44	5.74 ± 1.41	5.93 ± 2.48	6.31 ± 1.98
	COP-Radius (%)	$0.15 \pm 0.02^{(*)\#¥}$	$0.16 \pm 0.03^{(*)\#¥}$	$0.12 \pm 0.02^{\#£}$	$0.12 \pm 0.02^{\#}$	$0.11 \pm 0.02^{*¥£}$	$0.12 \pm 0.02^{*¥}$
	COP-Speed (mm/s)	$238.60 \pm 32.52^{\#¥}$	$244.48 \pm 22.42^{\#¥}$	$178.94 \pm 29.26^{\#}$	$186.47 \pm 22.70^{\#}$	$171.64 \pm 30.14^{¥}$	$183.92 \pm 26.08^{¥}$
	IFz (%TF)	50.08 ± 1.20	49.79 ± 1.78	50.17 ± 1.89	49.52 ± 1.89	50.27 ± 1.85	49.24 ± 2.25
	PFz (%TF)	50.07 ± 0.87	49.81 ± 1.30	50.07 ± 1.23	49.80 ± 1.63	50.17 ± 1.50	49.53 ± 1.34
	SPD (%)	50.00 ± 0.89	50.00 ± 1.18	50.07 ± 1.18	49.81 ± 0.51	50.02 ± 0.85	49.94 ± 0.80
	TPFz (%SPD)	$41.51 \pm 1.85^{\#¥}$	$42.00 \pm 2.10^{¥}$	$41.85 \pm 1.85^{\#}$	40.61 ± 2.02	$42.50 \pm 2.27^{*¥}$	$41.34 \pm 2.11^{*¥}$

*Significant difference between groups ($p < 0.05$), (*) $p = 0.06$; #significant difference between M1 and M2, ¥ significant difference between M1 and M3, £significant difference between M2 and M3.

and diseased. The only exception was TPFz, which was reached earlier by the sound limbs at M3 during walking ($p = 0.023$) and later in trot ($p = 0.051$) (Table 3).

At M1, COP values were increased for three of the five parameters in the diseased legs (COP-Area, $p = 0.033$; COP-Radius, $p = 0.023$; and COP-Speed, $p = 0.004$) in walking and one of the five parameters in trot (COP-Cran-caud, $p = 0.022$; COP-Radius was just short of significance, $p = 0.06$). At M2, all of the parameters showed increased values during walking (COP-Area, $p = 0.016$; COP-Cran-caud, $p = 0.004$; COP-Med-lat, $p = 0.002$; COP-Radius, $p = 0.001$; COP-Speed, $p < 0.001$), but no differences were detected In trot. At M3, significant differences between limbs were identified for two parameters during walking (COP-Cran-caud, $p = 0.002$; COP-Speed, $p = 0.006$; COP-Area was just short of significance, $p = 0.064$) and three parameters when trotting (COP-Area, $p < 0.001$; COP-Cran-caud, $p = 0.002$; COP-Radius, $p = 0.002$; Table 3; Figure 1).

3.2.5. Development over time

For both sound and diseased limbs, there were no significant differences in PFz, IFz, and SPD between the measurement periods. TPFz occurred significantly later during walking in M2 ($p = 0.023$) and M3 ($p = 0.010$) than in M1 in the sound limbs, and between M1 and M3 in the diseased limbs ($p = 0.008$) (Table 3).

Considering the development of the COP over time during walking, all of the five COP parameters had significantly higher values at M1 than at M2 and M3 (both limb groups, $p < 0.001$), while there were no differences between M2 and M3. When trotting, COP-Area and COP-Med-lat showed stable values over time, while the sound limb group showed significantly higher values for the other three parameters at M1 than at M2 and M3 ($p < 0.001$). In contrast, COP-Cran-caud ($p = 0.006$) and COP-Radius ($p = 0.008$) decreased between M2 and M3. While the diseased legs showed similar overall trends, the decrease in COP-Cran-caud and COP-Radius values between M2 and M3 was not observed ($p < 0.000$–0.004) (Table 3, Figure 1).

3.2.6. Comparison of walk and trot

In both the sound and diseased limb groups, PFz, IFz, and SPD did not show significant differences between walking and trotting, but TPFz occurred significantly later during trotting in both limb types ($p < 0.001$) (Table 3).

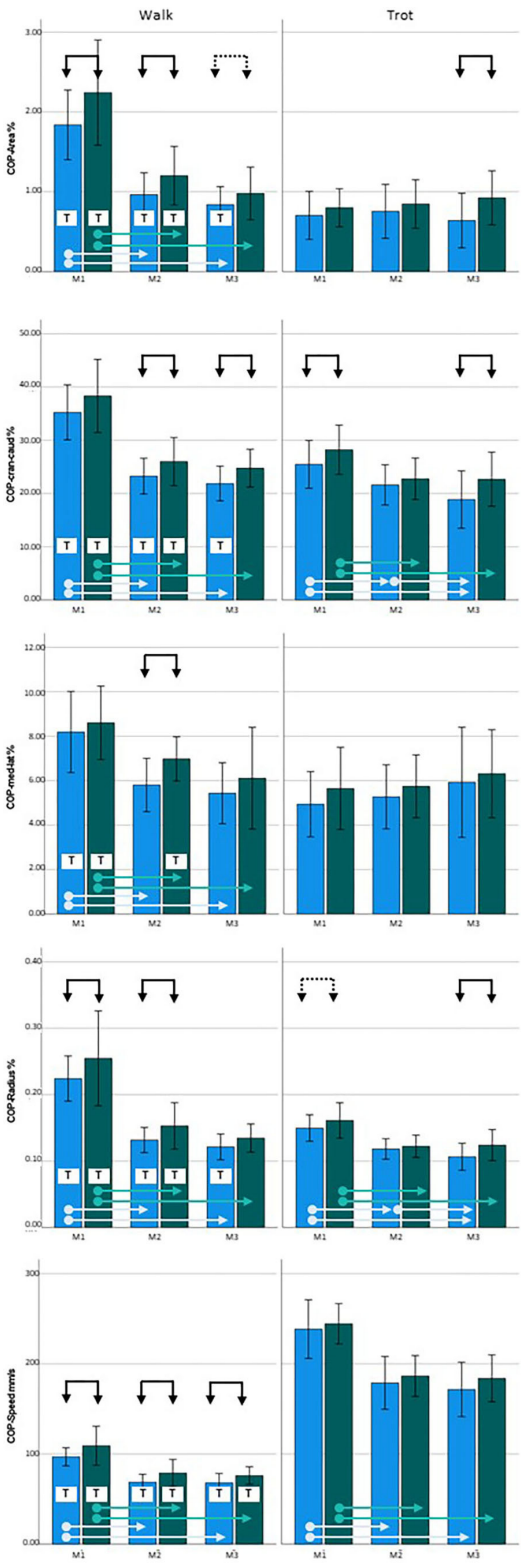

FIGURE 1
Center of pressure (COP) data for Labrador Retrievers: **Left** = walking, **right** = trotting; **blue** = sound limbs, **green** = diseased *(Continued)*

FIGURE 1 (Continued)
limbs; M1 = 4 months; M2 = 8 months; M3 = 12 months. Black arrows indicate significant differences between sound and diseased limb groups; dotted black arrows indicate $p = 0.06$; light blue and green arrows indicate significant differences between measurement points in the sound and diseased limb groups, respectively. T = significant difference between walking and trotting.

Almost all of the COP values of the sound legs were significantly higher when walking than when trotting at each of the measurement points (COP-Area, $p < 0.001$, $p = 0.005$, and $p = 0.001$; COP-Cran-caud, $p = < 0.001$, $p = 0.036$, and $p = 0.001$; and COP-Radius $p < 0.001$, $p = 0.001$, and $p = 0.008$ at M1, M2, and M3, respectively). COP-Med-lat was higher during walking only at M1 ($p < 0.001$). COP-Speed, was lower during walking than during trotting (all three points, $p < 0.\ 001$). In the diseased limb groups, COP-Speed was lower during walking than during trotting at each measurement period ($p < 0.001$). The values of all the other COP parameters were higher during walking than when trotting at M1 and M2 (COP-Area $p < 0.001$ and $p = 0.005$; COP-Cran-caud $p < 0.001$ and $p = 0.015$; COP-Med-lat $p < 0.001$ and $p = 0.023$; and COP-Radius $p < 0.001$ and $p < 0.001$, respectively) but not at M3 (Table 3, Figure 1).

3.3. Golden Retrievers

3.3.1. Clinical, orthopedic, and neurological examination

The clinical, orthopedic, and neurological examinations of the 17 Golden Retrievers did not reveal any abnormalities. However, as previously noted, one dog was excluded because of elbow dysplasia seen in radiographs at M3.

3.3.2. Hip scoring

The FCI examination of the 34 hip joints revealed the following results: 11 were rated as grade A, 11 as B, 8 as C, and 4 as D. Therefore, 22 hip joints were scored as sound and 12 as diseased. Among the 12 diseased hips 4 animals had unilateral and 4 bilateral CHD. No lumbosacral transitional vertebras were detected.

3.3.3. Speed and acceleration

The speed and acceleration data are presented in Table 4. All values were within the acceptable ranges described in Section 2.2.

3.3.4. Differences between sound and diseased limbs

None of the GRF parameters showed significant differences between diseased and sound legs (Table 5) except for TPFz, which was significant later at M3 in the sound limbs when trotting ($p = 0.009$).

At M1, three of the COP parameters showed significantly higher values in the diseased limb group when walking (COP-Area, $p < 0.001$; COP-Cran-caud, $p = 0.001$; COP-Speed, $p = 0.023$). When trotting, higher values were also obtained for COP-Cran-caud ($p = 0.004$) and COP-Speed ($p = 0.004$). At M2, all of the COP parameters showed higher values in the diseased limb group during walking (COP-Area, $p < 0.001$; COP-Cran-caud, $p < 0.001$; COP-Med-lat, $p = 0.020$; COP-Radius, $p = 0.005$; COP-Speed, $p < 0.001$) and two parameters had higher values when trotting (COP-Cran-caud, $p = 0.035$; COP-Speed, $p = 0.020$). At M3, three of the COP parameters had higher values when walking (COP-Aare, $p = 0.003$; COP-Cran-caud, $p < 0.001$; COP-Speed, $p = 0.001$) and two had higher values when trotting (COP-Cran-caud, $p = 0.011$; COP-Speed, $p = 0.007$; Table 5; Figure 2).

TABLE 4 Speed (v) and acceleration (a) (mean ± SD) (calculated for the left hind limb) when walking and trotting for Golden Retrievers ($n = 17$) at the three measurement points (M1 = 4 months, M2 = 8 months, and M3 = 12 months of age).

Measurement		M1	M2	M3
Walk	a (m/s²)	0.00 ± 0.03	0.01 ± 0.02	0.01 ± 0.02
	v (m/s)	1.00 ± 0.10	1.10 ± 0.12	1.17 ± 0.10
Trot	a (m/s²)	−0.03 ± 0.11	0.04 ± 0.12	0.00 ± 0.08
	v (m/s)	1.96 ± 0.22	2.18 ± 0.17	2.18 ± 0.23

v = speed (m/s) and a = acceleration (m/s²) for the left hindlimb.

3.3.5. Development over time

In both the sound and diseased limb groups, PFz, IFz, and SPD did not significantly differ between the measurement points. In the diseased limb group, TPFz occurred significantly earlier when trotting at M2 ($p = 0.011$) and M3 ($p = 0.002$) than at M1 (Table 5).

During walking, all of the COP parameters for the sound limb group had significantly higher values at M1 than at M2 and M3 ($p < 0.001$) but remained constant between M2 and M3. Similar results were observed in the diseased limb group

TABLE 5 Descriptive statistics (mean ± SD) for walking and trotting Golden Retrievers ($n = 17$) at three measurement points (M1 = 4 months, M2 = 8 months, and M3 = 12 months of age) in sound and diseased limb groups.

Measurement		M1		M2		M3	
Gait	Parameter	Sound	Diseased	Sound	Diseased	Sound	Diseased
Walk	COP-Area (%)	1.62 ± 0.75*#¥	2.47 ± 1.09*#¥	0.89 ± 0.42*#	1.38 ± 0.52*#	0.82 ± 0.38*¥	1.14 ± 0.31*¥
	COP-Cran-caud (%)	36.15 ± 6.46*#¥	43.55 ± 7.50*#¥	24.76 ± 4.06*#	30.80 ± 4.63*#	23.35 ± 3.95*¥	29.47 ± 4.54*¥
	COP-Med-lat (%)	9.02 ± 1.92#¥	8.87 ± 1.74¥	6.36 ± 1.74*#	7.50 ± 2.11*	5.85 ± 2.24¥	6.40 ± 1.58¥
	COP-Radius (%)	0.22 ± 0.05#¥	0.24 ± 0.04#¥	0.14 ± 0.02*#	0.17 ± 0.03*#	0.15 ± 0.06¥	0.15 ± 0.02¥
	COP-Speed (mm/s)	102.17 ± 16.40*#¥	114.24 ± 14.87*#¥	73.53 ± 11.73*#	86.44 ± 10.01*#	73.59 ± 12.20*¥	86.96 ± 9.75*¥
	IFz (%TF)	49.88 ± 0.96	50.22 ± 1.43	49.98 ± 0.83	50.05 ± 0.61	50.15 ± 1.29	49.72 ± 0.92
	PFz (%TF)	49.83 ± 1.53	50.32 ± 2.35	49.95 ± 0.76	50.10 ± 1.25	50.11 ± 1.15	49.80 ± 0.96
	SPD (%)	49.96 ± 0.78	50.08 ± 0.38	49.98 ± 0.43	50.03 ± 0.43	50.04 ± 0.64	49.92 ± 0.76
	TPFz (%SPD)	24.23 ± 2.17	24.21 ± 4.11	25.80 ± 2.67	23.26 ± 2.24	26.40 ± 2.31	24.83 ± 1.68
Trot	COP-Area (%)	0.88 ± 0.48	0.95 ± 0.33	0.89 ± 0.47	1.01 ± 0.43	0.73 ± 0.34	0.84 ± 0.28
	COP-Cran-caud (%)	28.06 ± 3.95*¥	32.68 ± 4.31*#¥	25.53 ± 4.15*	28.50 ± 4.53*#	22.54 ± 3.68*¥	26.85 ± 4.15*¥
	COP-Med-lat (%)	5.95 ± 2.94	5.25 ± 1.61	5.62 ± 2.11	5.43 ± 2.40	5.38 ± 2.07	4.61 ± 0.95
	COP-Radius (%)	0.16 ± 0.02#¥	0.17 ± 0.02#¥	0.14 ± 0.02#	0.14 ± 0.02#	0.13 ± 0.02¥	0.13 ± 0.02¥
	COP-Speed (mm/s)	251.94 ± 38.41*#¥	286.94 ± 40.21*#¥	182.16 ± 27.89*#	210.41 ± 54.31*#	172.97 ± 22.53*¥	200.15 ± 37.11*¥
	IFz (%TF)	50.16 ± 1.03	49.71 ± 0.96	50.19 ± 1.82	49.65 ± 1.29	50.08 ± 2.04	49.85 ± 3.40
	PFz (%TF)	50.02 ± 0.76	49.97 ± 0.75	50.00 ± 1.29	49.99 ± 0.97	49.92 ± 1.23	50.15 ± 3.09
	SPD (%)	50.12 ± 0.78	49.77 ± 0.84	50.12 ± 1.38	49.78 ± 1.18	50.14 ± 0.90	49.75 ± 2.70
	TPFz (%SPD)	40.71 ± 1.78	40.66 ± 1.95#¥	39.45 ± 4.18	37.53 ± 5.83#	39.86 ± 1.79*	37.87 ± 1.51*¥

*Significant difference between groups ($p < 0.05$), #significant difference between M1 and M2, ¥ significant difference between M1 and M3.

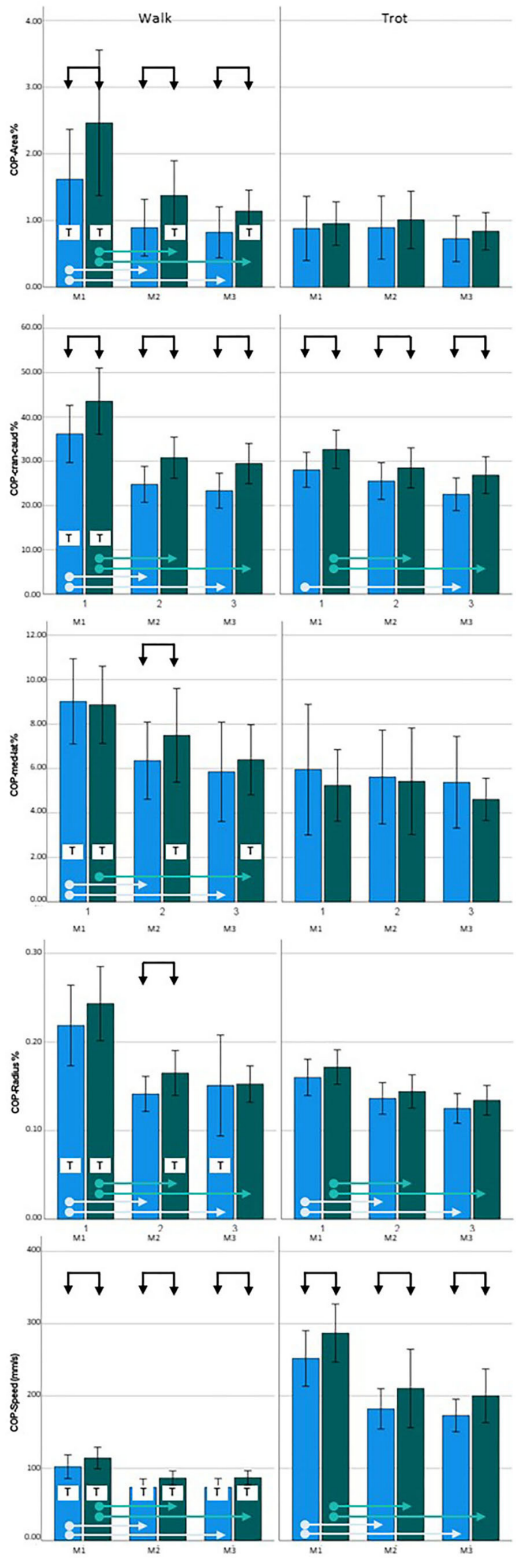

FIGURE 2
Center of pressure (COP) data for Golden Retrievers. **Left** = walking, **right** = trotting; **blue** = sound limbs, **green** = diseased *(Continued)*

FIGURE 2 (Continued)
limbs; M1 = 4 months; M2 = 8 months; M3 = 12 months. Black arrows indicate significant differences between sound and diseased limb groups; dotted black arrows indicate $p = 0.06$; light blue and green arrows indicate significant differences between measurement points in the sound and diseased limb groups, respectively. T = significant difference between walking and trotting.

($p < 0.001$), except the COP-Med-lat was only significantly different between the M1 and M3 measurements ($p = 0.003$). When trotting, COP-Area and COP-Med-lat did not change over time in either the sound or diseased limb group. In the sound limb group, COP-Radius and COP-Speed values at M1 were higher than those at M2 and M3 ($p < 0.001$), and COP-Cran-caud differed only when comparing M1 to M3 ($p < 0.001$). In the diseased limb group, the three of the COP parameters were consistently higher at M1 than at M2 and M3 (COP-Cran-caud, $p = 0.034$ and $p = 0.005$; COP-Radius, $p = 0.001$ and < 0.001; COP-Speed, $p < 0.001$ and $p < 0.001$, respectively; Table 5; Figure 2).

3.3.6. Comparison of walk and trot

For both the sound and diseased limb groups, PFz, iFz, and SPD did not significantly differ between walking and trotting, while TPFz occurred significantly later during trotting in both groups ($p < 0.001$) (Table 5).

COP-Speed values when walking were significantly lower than when trotting for both limb groups and at all three measurement points ($p < 0.001$). All of the other measured parameters showed significantly higher values for both limb groups at M1 when walking compared to trotting ($p < 0.001$). At M2, there were no differences for cop-Area; COP-Cran-caud, COP-Med-lat and COP-Radius in the sound limb group, while in the diseased limb group, the COP-Area ($p = 0.015$), COP-Med-lat ($p = 0.002$), and COP-Radius ($p = 0.010$) values were higher during walking. At M3, the sound limb group had higher COP-Radius values when walking compared to trotting ($p = 0.002$), and in the diseased limb group, the COP-Area ($p = 0.013$) and COP-Med-lat ($p = 0.029$) values were significantly higher when walking (Table 5, Figure 2).

3.4. Synthesis

At the age of 8 months (M2), in both breeds, all of the examined COP-Parameters had significantly higher values for the diseased limb group during walking. At 4 (M1) and 12 (M3) months of age, this difference was less pronounced, but three of the five measured parameters were still affected when walking. As COP-Area and COP-Speed were affected at all three measurement points when walking, these represent

the most reliable parameters for early detection of CHD. In contrast, we found few differences in COP parameters between the sound and diseased limb groups of Labrador Retrievers when trotting: at 4 months, COP-Cran-caud values were different (and COP-Radius was just short of significance); at 8 months, none of the parameters were different; and at 12 months, three parameters (COP-Area, COP-Cran-caud, and COP-Radius) were affected. In the Golden Retrievers, the COP-Radius values when walking and trotting, and the COP-Speed when trotting, were consistently higher in the diseased limb group at all measurement points.

4. Discussion

We evaluated the COP and GRF parameters of Labrador and Golden Retrievers at 4, 8, and 12 months of age using a pressure plate. We hypothesized that even in non-lame dogs, the COP parameter values of limbs assessed with a HD grade of C or worse (i.e., diseased according to the FCI radiographic standards) would be higher than those of HD grade A or B (i.e., sound). Our results confirm this hypothesis.

The differences in COP parameters between limbs with sound and diseased hip joints can be interpreted with respect to possible biomechanical adaptations (18, 22) as well as being an indicator of reduced stability (18, 21). Comparisons with the existing literature are difficult because veterinary studies have typically used only adult lame animals when examining COP. Additionally, in some studies (18, 22), measurements were performed while the animal was standing and not walking/trotting, with three measurements of 20 s each performed when the dogs were not permitted to move. Because this is very difficult to achieve with puppies, we made our measurements while the dogs were in motion.

Nevertheless, the changes in outcome parameters presented in our study can be related to the existing literature. In particular, the findings of Poy et al. (30) provide insight into why differences in COP parameters and TPFz were observed. Dogs with CHD show greater adduction, a greater range of motion in abduction-adduction, and greater lateral movement of the pelvis. CHD leads to complex changes in the kinematics of the affected joint and the other joints of the limb. Additionally, changes in angularities and angular velocities in diseased individuals have been described (31–34). Those kinematic changes explain the differences in COP-Area and mediolateral COP displacement, as already described for lame dogs (12). The increased abduction-adduction seems to cause a greater excursion of the COP in mediolateral direction (and thus also of the COP-Area). It is noteworthy that these changes (especially of the COP-Area) also occurred without a lameness in the animals of our study. Here, it is additionally striking that we could also present increases in COP-Cran-caud, which certainly also contributed to the increased COP-Area, but probably also to the COP-Radius. However, it is unclear why this change in COP-Cran-caud was not also presented in lame dogs (12). Several considerations can be used as a basis for discussion. Dysplastic dogs show increased extension of the hip joint at the end of the stance phase with a concomitant faster extension during the stance phase. The stifle joint is more flexed during and flexed faster at the end of the stance phase. The tarsal joint is more flexed at the beginning of the stance phase and its extension at the end of the stance phase is slowed down. This compensatory interaction of the joints may lead to the fact that in lame dogs the craniocaudal excursion of the COP is not altered. In the young animals used in this study, it could be assumed that the lameness-free gait caused kinematic changes that led to increases in COP-Cran-Caud. This conclusion could be supported by the significant difference in TPFz, which was only observed at M3. Possibly, this change indicates increased adaptations of the gait pattern, especially since this has not been described before (34). The relationship between kinematics and COP is also supported by Lopez et al. (22). These authors interpreted the altered COP values of dogs with elbow joint disease as a result of modified kinematics, especially in the case of the larger caudal margin (i.e., the distance between the most caudal limit of the paw print and the most caudal limit of the limb COP path); notably, we did not measure this parameter in our study. To prove all these assumptions, kinematic studies with growing dogs should be performed in the future.

Notably, in one study, postural changes in human patients with osteoarthritis of the hip joints due to pathologies of the joint structures impair proprioception and postural stability (21), although patients were measured in the standing position, which limits kinematic changes in the motion sequence. Thus, our results may reflect a combination of the hip joint not developing normally (and, correspondingly, disturbed proprioceptive input) and altered kinematics. Further studies are now needed to address this. Muscling of the affected limb may also have influenced our results, which increases in the growing animal alongside possible muscular adaptions. This was supported by evidence that the longissimus dorsi muscle shows increased activity contralateral to the affected limb, and that lame animals rotate their limbs mediolaterally (35). To address this further, the extent to which alterations in muscle activity are observed in lameness-free growing dogs should be investigated.

In addition to the significant differences between the diseased and sound limb groups, we found striking differences in the COP parameter values between the measurement time points. Especially when walking, the COP values were significantly lower from M2 (8 months of age). This likely indicates increased stability of the gait pattern of developing puppies, with similar observations reported for horses; newborn foals show a relative increase in craniocaudal COP, which decreases rapidly in the first week of life and slowly stabilizes over the following months (23). In our dogs, this phenomenon also occurred when trotting, but not for all of the measured parameters. It may be that the two-beat trot is easier for animals to control than the more complicated footing pattern of walking.

Indeed, this was supported by the fact that the COP values were higher during walking (with the logical exception of COP-Speed) than during trotting. However, further studies are needed to investigate the extent to which the shape of the paws also changes during growth, as this may influence COP.

As with previous studies, our study demonstrates that the homogeneity of the cohort group is a critical factor (36, 37). Specifically, the breed had a statistically significant effect on some of the measured parameters, although the results may have been influenced by different group sizes. To date, no studies have been dedicated to comparing the COP in different breeds, which may be an interesting area of future research.

While our results indicate that even in very young dogs, limbs later classified as CHD show detectable changes in COP parameters, several limitations should be acknowledged. First, the number of dogs examined was relatively small, and more limbs were judged to be healthy than diseased, meaning that different degrees of CHD could not be examined separately. Although grouping hips rated C or worse is not uncommon (6), it is unfortunate that we could not determine the extent to which hips assessed as HD grades D and E contributed to the results. Further studies should therefore seek to obtain data from more animals to further build on our results.

Indeed, compensatory mechanisms may occur between limbs that influence COP measurements, and even in studies with larger sample sizes, interpretations will be complicated by bilateral disease. In our study, 50% of affected animals had bilateral disease and 50% had unilateral disease. The interpretation of our results is further complicated by the inability to examine the diseased and sound contralateral sides of the same animals. It can be assumed that bilateral disease leads to compensatory mechanisms that are different from those in animals with unilateral disease. To verify this in further studies animals with unilateral and bilateral disease should be compared. Furthermore, the presence of transitional vertebrae in the Labrador Retrievers may have influenced the COP parameters. However, more transitional vertebrae occurred in the dogs with healthy hip joints. In any case, this issue should be addressed in further studies and COP measurements should be performed in dogs with different types of transitional vertebrae and healthy dogs.

Additionally, the rather small differences (despite statistically significant differences) in the COP parameters of the healthy and diseased hip joints should be considered. This makes it difficult to establish cut-off values that allow a tentative diagnosis. It should be considered whether further clinical examination methods, such as the flexion test (38), could be used to allow a clearer distinction between healthy and diseased joints.

One way to achieve deeper insight into the biomechanics of dogs would be to implement early diagnostic radiological procedures, as the evaluation of the distraction index (4). This could yield correlations between measured COP values and the current status of the hip joint. And, if studies with more animals confirm our results, COP measurements together with early radiological diagnostics the distraction index could further improve the prediction of CHD.

Another possibility for early diagnosis is ultrasonography, which can be performed without sedation. However, this method is not recommended due to a lack of correlation of the measurement results with the final CHD grade in the adult dog (39, 40). However, it should be investigated whether a combination of COP measurements and ultrasound would provide further indicators that could contribute to early diagnosis.

Overall, we suggest that COP measurements could be used to obtain useful indicators of potential CHD development in very young dogs. This could guide further early diagnosis based on radiological examination.

Data availability statement

The original contributions presented in the study are included in the article/supplementary material, further inquiries can be directed to the corresponding author.

Ethics statement

The animal study was reviewed and approved by Ethics and Animal Welfare Committee. Written informed consent was obtained from the owners for the participation of their animals in this study.

Author contributions

BB and YV contributed to the study's conception and design. YV, BB, and CL performed measurements and evaluated the data. AT performed statistical analyses. MG evaluated and graded the radiographs. YV wrote the draft of the manuscript. MG, AT, CL, and BB wrote the manuscript. All authors contributed to manuscript revision and read and approved the submitted version.

Acknowledgments

The authors thank the owners and their dogs for their contributions to this study.

Conflict of interest

The authors declare that the research was conducted in the absence of any commercial or financial relationships that could be construed as a potential conflict of interest.

Publisher's note

References

1. Baldinger A, Genevois JP, Moissonnier P, Barthélemy A, Carozzo C, Viguier É et al. Prevalence of canine hip dysplasia in 10 breeds in France, a retrospective study of the 1997–2017 radiographic screening period. *PLoS ONE.* (2020) 15:e0235847. doi: 10.1371/journal.pone.0235847

2. Harper TAM. Conservative management of hip dysplasia. *Vet Clin North Am Small Anim Pract.* (2017) 47:807–21. doi: 10.1016/j.cvsm.2017.02.007

3. Vidoni B, Bauer V, Bockstahler B, Gumpenberger M, Tichy A, Aghapour M. Early diagnosis of canine hip laxity: correlation between clinical orthopedic examinations and the FCI scoring method in a closed cohort of rottweilers. Animals. (2021) 11:20416. doi: 10.3390/ani11020416

4. Guilliard M. The Penn. HIP method of predicting canine hip dysplasia. *In Pract.* (2014) 36:66–74. doi: 10.1136/inp.f7486

5. Vidoni B, Aghapour M, Kneissl S, Vezzoni A, Gumpenberger M, Hechinger H et al. Inter-observer agreement in radiographic diagnosis of coxofemoral joint disease in a closed cohort of 4-month-old Rottweilers. *Animals.* (2022) 12:1269. doi: 10.3390/ani12101269

6. Merca R, Bockstahler B, Vezzoni A, Tichy A, Boano S, Vidoni B. Canine hip dysplasia screening: comparison of early evaluation to final grading in 231 dogs with Federation Cynologique Internationale A and B. *PLoS ONE.* (2020) 15:e0233257. doi: 10.1371/journal.pone.0233257

7. Taroni M, Genevois JP, Viguier E, Pillard P, Livet V, Cachon T et al. Comparison of early measurements of the distraction index, Norberg angle on distracted view and the official radiographic evaluation of the hips of 215 dogs from two guide dog training schools. *Vet Comp Orthop Traumatol.* (2018) 31:445–51. doi: 10.1055/s-0038-1668087

8. Santana A, Alves-Pimenta S, Franco-Gonçalo P, Gonçalves L, Martins J, Colaço B et al. Early hip laxity screening and later canine hip dysplasia development. *Vet World.* (2022) 15:679–84. doi: 10.14202/vetworld.2022.679-684

9. Bertal M, Vezzoni A, van der Vekens E, Polis I, Saunders JH, Broeckx BJG. Analysis of a laxity index database and comparison with the fédération cynologique internationale grades of this population. *Vet Comp Orthop Traumatol.* (2021) 34:108–14. doi: 10.1055/s-0040-1719062

10. Vezzoni A, Dravelli G, Corbari A, de Lorenzi M, Cirla A, Tranquillo V. Early diagnosis of canine hip dysplasia. *EJCAP.* (2005) 3:173–84.

11. Bockstahler BA, Vobornik A, Müller M, Peham C. Compensatory load redistribution in naturally occurring osteoarthritis of the elbow joint and induced weight-bearing lameness of the forelimbs compared with clinically sound dogs. *Vet J.* (2009) 180:202–12. doi: 10.1016/j.tvjl.2007.12.025

12. Reicher B, Tichy A, Bockstahler BA. Center of pressure in the paws of clinically sound dogs in comparison with orthopedically diseased dogs. *Animals.* (2020) 10:81366. doi: 10.3390/ani10081366

13. Wagmeister P, Steigmeier-Raith S, Reese S, Meyer-Lindenberg A. Compensatory changes in ground reaction forces in small and large breed dogs with unilateral hindlimb lameness in comparison to healthy dogs. *Vet Comp Orthop Traumatol.* (2022) 35:105–11. doi: 10.1055/s-0041-1736218

14. Caterino C, Aragosa F, Della Valle G, Costanza D, Lamagna F, Piscitelli A et al. Clinical efficacy of Curcuvet and boswellic acid combined with conventional nutraceutical product: an aid to canine osteoarthritis. *PLoS ONE.* (2021) 16:e0252279. doi: 10.1371/journal.pone.0252279

15. Budsberg SC, Kleine SA, Norton MM, Sandberg GS, Papich MG. Comparison of the effects on lameness of orally administered acetaminophen-codeine and carprofen in dogs with experimentally induced synovitis. *Am J Vet Res.* (2020) 81:627–34. doi: 10.2460/ajvr.81.8.627

16. Knebel J, Eberle D, Steigmeier-Raith S, Reese S, Meyer-Lindenberg A. Outcome after tibial plateau levelling osteotomy and modified Maquet procedure in dogs with cranial cruciate ligament rupture. *Vet Comp Orthop Traumatol.* (2020) 33:189–97. doi: 10.1055/s-0040-1701502

17. Moreira JPL, Tichy A, Bockstahler BA. Comparison of the vertical force distribution in the paws of dogs with coxarthrosis and sound dogs walking over a pressure plate. Animals. (2020) 10:60986. doi: 10.3390/ani10060986

18. Carrillo JM, Manera ME, Rubio M, Sopena J, Santana A, Vilar JM. Posturography and dynamic pedobarography in lame dogs with elbow dysplasia and cranial cruciate ligament rupture. *BMC Vet Res.* (2018) 14:108. doi: 10.1186/s12917-018-1435-y

19. Braun L, Tichy A, Peham C, Bockstahler BA. Comparison of vertical force redistribution in the pads of dogs with elbow osteoarthritis and healthy dogs. *Vet J.* (2019) 250:79–85. doi: 10.1016/j.tvjl.2019.06.004

20. López S, Vilar JM, Rubio M, Sopena JJ, Santana A, Rodríguez O et al. Pedobarography: a novel approach to test the efficacy of treatments for lameness; an experience with mavacoxib in dogs with elbow osteoarthritis. *BMC Vet Res.* (2019) 15:193. doi: 10.1186/s12917-019-1946-1

21. Slomka B, Rongies W, Sierdzinski J, Dolecki W, Worwag M, Trzepla E. Assessment of postural stability in women with hip osteoarthritis: a case-control study. *Acta Orthop Traumatol Turc.* (2019) 53:56–60. doi: 10.1016/j.aott.2018.07.006

22. López S, Vilar JM, Rubio M, Sopena JJ, Damiá E, Chicharro D et al. Center of pressure limb path differences for the detection of lameness in dogs: a preliminary study. *BMC Vet Res.* (2019) 15:138. doi: 10.1186/s12917-019-1881-1

23. Nauwelaerts S, Malone SR, Clayton HM. Development of postural balance in foals. *Vet J.* (2013) 198(Suppl 1):e70–4. doi: 10.1016/j.tvjl.2013.09.036

24. Lopez MJ, Quinn MM, Markel MD. Evaluation of gait kinetics in puppies with coxofemoral joint laxity. *Am J Vet Res.* (2006) 67:236–41. doi: 10.2460/ajvr.67.2.236

25. Hans EC, Zwarthoed B, Seliski J, Nemke B, Muir P. Variance associated with subject velocity and trial repetition during force platform gait analysis in a heterogeneous population of clinically normal dogs. *Vet J.* (2014) 202:498–502. doi: 10.1016/j.tvjl.2014.09.022

26. Roush JK, McLaughlin RM. Effects of subject stance time and velocity on ground reaction forces in clinically normal greyhounds at the walk. *Am J Vet Res.* (1994) 55:1672–6.

27. Conzemius MG, Torres BT, Muir P, Evans R, Krotscheck U, Budsberg S. Best practices for measuring and reporting ground reaction forces in dogs. *Vet Surg.* (2022) 51:385–96. doi: 10.1111/vsu.13772

28. Bieber B, Reicher B, Tichy A, Bockstahler B. Changes in ground reaction forces and center of pressure parameters of paws when wearing dog boots in dogs. *Front Vet Sci.* (2022) 9:906277. doi: 10.3389/fvets.2022.906277

29. Charalambous D, Strasser T, Tichy A, Bockstahler B. Ground reaction forces and center of pressure within the paws when stepping over obstacles in dogs. *Animals.* (2022) 12:31702. doi: 10.3390/ani12131702

30. Poy NS, DeCamp CE, Bennett RL, Hauptman JG. Additional kinematic variables to describe differences in the trot between clinically normal dogs and dogs with hip dysplasia. *Am J Vet Res.* (2000) 61:974–8. doi: 10.2460/ajvr.2000.61.974

31. Bockstahler BA, Henninger W, Müller M, Mayrhofer E, Peham C, Podbregar I. Influence of borderline hip dysplasia on joint kinematics of clinically sound Belgian Shepherd dogs. *Am J Vet Res.* (2007) 68:271–6. doi: 10.2460/ajvr.68.3.271

32. Miqueleto NSML, Rahal SC, Agostinho FS, Siqueira EGM, Araújo FAP, El-Warrak AO. Kinematic analysis in healthy and hip-dysplastic German Shepherd dogs. *Vet J.* (2013) 195:210–5. doi: 10.1016/j.tvjl.2012.06.021

33. Bennett RL, DeCamp CE, Flo GL, Hauptman JG, Stajich M. Kinematic gait analysis in dogs with hip dysplasia. *Am J Vet Res.* (1996) 57:966–71.

34. Madore E, Huneault L, Moreau M, Dupuis J. Comparison of trot kinetics between dogs with stifle or hip arthrosis. *Vet Comp Orthop Traumatol.* (2007) 20:102–7. doi: 10.1160/vcot-06-06-0052

35. Fischer S, Nolte I, Schilling N. Adaptations in muscle activity to induced, short-term hindlimb lameness in trotting dogs. *PLoS ONE.* (2013) 8:e80987. doi: 10.1371/journal.pone.0080987

36. Voss K, Galeandro L, Wiestner T, Haessig M, Montavon PM. Relationships of body weight, body size, subject velocity, and vertical ground reaction forces in trotting dogs. *Vet Surg.* (2010) 39:863–9. doi: 10.1111/j.1532-950X.2010.00729.x

37. Voss K, Wiestner T, Galeandro L, Hässig M, Montavon PM. Effect of dog breed and body conformation on vertical ground reaction forces, impulses, and stance times. *Vet Comp Orthop Traumatol.* (2011) 24:106–12. doi: 10.3415/VCOT-10-06-0098

38. Grosjean D, Van Rysse B, Samoy Y. Flexion test applied on dogs: a 10 years retrospective study on lameness clinical cases. In *Proceedings of the 3th ECVSMR Scientific Meeting.* Pula (2022) 35. ISSN: 2510-8093

39. Fischer A, Flöck A, Tellhelm B, Failing K, Kramer M, Thiel C. Static and dynamic ultrasonography for the early diagnosis of canine hip dysplasia. *J Small Animal Practice.* (2010) 51:582–8. doi: 10.1111/j.1748-5827.2010.00995.x

40. Adams WM, Dueland RT, Meinen J, O'Brien RT, Giuliano E, Nordheim EV. Early detection of canine hip dysplasia: comparison of two palpation and five radiographic methods. *J Am Anim Hosp Assoc.* (1998) 34:339–47. doi: 10.5326/15473317-34-4-339

frontiers | Frontiers in Veterinary Science

TYPE Original Research
PUBLISHED 10 February 2023
DOI 10.3389/fvets.2023.1106170

OPEN ACCESS

EDITED BY
Mauro Malvè,
Public University of Navarre, Spain

REVIEWED BY
Chiara Caterino,
University of Naples Federico II, Italy
Emanuel Andrada,
Friedrich Schiller University Jena, Germany
John E. A. Bertram,
University of Calgary, Canada

*CORRESPONDENCE
Danae Charalambous
✉ danaecharalam@hotmail.com

SPECIALTY SECTION
This article was submitted to Comparative and Clinical Medicine, a section of the journal Frontiers in Veterinary Science

RECEIVED 23 November 2022
ACCEPTED 24 January 2023
PUBLISHED 10 February 2023

CITATION
Charalambous D, Lutonsky C, Keider S, Tichy A and Bockstahler B (2023) Vertical ground reaction forces, paw pressure distribution, and center of pressure during heelwork in working dogs competing in obedience.
Front. Vet. Sci. 10:1106170.
doi: 10.3389/fvets.2023.1106170

Vertical ground reaction forces, paw pressure distribution, and center of pressure during heelwork in working dogs competing in obedience

Danae Charalambous[1]*, Christiane Lutonsky[1], Stefan Keider[1], Alexander Tichy[2] and Barbara Bockstahler[1]

[1]Department of Companion Animals and Horses, University Clinic for Small Animals, Small Animal Surgery, Section of Physical Therapy, University of Veterinary Medicine, Vienna, Austria, [2]Department of Biomedical Sciences, Platform of Bioinformatics and Biostatistics, University of Veterinary Medicine, Vienna, Austria

Heelwork walking is a command that competitive obedience and working dogs are trained to perform. Unlike other canine sports, the research for competitive obedience sport is limited and no research regarding biomechanical gait adaptions during heelwork walking has been published. The aim of the study was to investigate the changes in vertical ground reaction forces, paw pressure distribution (PPD), and center of pressure (COP) of Belgian Malinois during heelwork walking. Ten healthy Belgian Malinois were included in the study. The dogs walked first without heeling (normal walk) and then while heeling on a pressure platform. The comparison between normal and heelwork walking was performed using mixed-effects models. *Post-hoc* analyses were performed using Sidak's alpha correction procedure. During heelwork walking, a significant decrease in the vertical impulse and stance phase duration (SPD) and a significant increase in the craniocaudal index and speed of COP was observed in the forelimbs compared to normal walking. At the hindlimbs, a significant increase in vertical impulse and SPD was observed during heelwork walking. Regarding PPD, a significant decrease of vertical impulse was observed at the cranial quadrants of the right forelimb and craniolateral quadrant of the left forelimb during heelwork. The area was significantly decreased at the craniolateral quadrant of the left forelimb and the time for the peak vertical force was prolonged significantly at the caudal quadrants of the right forelimb during heelwork walking. The vertical impulse was significantly increased in all quadrants of the hindlimbs except the craniolateral quadrant of the left hindlimb. The effect of these changes on the musculoskeletal system of working dogs should be investigated in further studies, using electromyography and kinematic analysis.

KEYWORDS

heelwork, kinetics, obedience, working dogs, ground reaction forces, center of pressure, paw pressure distribution

1. Introduction

Police, military, search and rescue, and security dogs are some examples of working dogs, which, alongside with the handler, provide vital support to the society (1). The financial investment to acquire, train, and maintain working police and military dogs makes them very valuable. Understanding causes of injury can provide optimal care and preventive measures that could prolong the working life of a service dog and improve animal welfare (2, 3). Police and military dogs are at an increased risk of orthopedic disease compared to dogs living as

pets (2, 4, 5). In a study investigating the causes of loss from active duty among German Shepherd police dogs, the single most important cause was the inability to cope with the physical demands of the job (61/94 dogs or 65%). The median age of retirement was 6.6 years of age and only 40% reached the desired age of retirement of 8 years, most commonly due to orthopedic diseases (3). Given the high prevalence of musculoskeletal diseases, such as hip dysplasia, lumbosacral stenosis (6), semitendinosus myopathy (7–10) and supraspinatus tendinopathy (11) in working dogs investigations should be conducted to determine how each training affects the animal's body.

Certain areas of working dog training paved the way for dog sports. Competitive obedience was first introduced in 1930 as an adaptation of the military dog's work. Originally, the purpose of this competition was to show that the dog can work with their owner and follow specific commands which ensure a good compliance in daily life (11). Over the years, competitive obedience has evolved and more commands have been included in the competition trials. According to the Federation Cynologique Internationale (FCI), three main classes exist for competitive obedience (12).

Heelwork is a basic command and is included in all levels. This should not be confused with normal walking at the handler's side, where the dog usually faces forward (Figure 1A). Dogs are trained to walk close to the handler's left leg, with their head looking up and to the right toward the handler (Figure 1B) while performing a series of commands (11). The guidelines regarding heelwork include the following: the dog's shoulder should be approximately level with and reasonably close to the handler's leg at all times (13) and that the dog's head position should in no way compromise its top line or impair the natural movement of the dog. Moreover, the FCI states that "the dog should move naturally but what is seen as a natural neck and backline depends also on the breed" (12).

The heelwork position observed in obedience sports and other working dogs differs greatly from the physiological posture observed during normal walking (14)—due to the lifting of the head and its rotation to the right. Although research in this specific sport is limited, it has been proposed in textbooks that competitive obedience dogs experience chronic strain injuries to the shoulders, such as supraspinatus tendinopathy, especially at the left shoulder due to heeling (11).

Due to the increased awareness of preventive medicine, the specific posture that these dogs adapt has attracted research interest. The apparent neck angle of competitive obedience dogs shows a wide variation from 97.2° (±2.0) to 169.7° (±2.8) (mean 123.4°). However, there is no significant correlation between the apparent neck angle and the judges' scores, nor between the duration and neck angle. This suggests that it does not create an advantageous speed when working in heelwork position (14). While further research investigated the human preferences for heelwork positions during competitive obedience in the United Kingdom (15), the effect of the changed head position on the animals body has not been evaluated using kinetic and kinematic analysis nor electromyography.

The evaluation of the ground reaction forces (GRFs) has gained interest in the last decade due to the non-invasive and relatively easy to perform measurements. These are used to assess normal motion in healthy individuals (16–19) to evaluate efficacy of treatments (20–23) and as an objective diagnostic tool (24, 25). Evaluation of the GRFs provides data on the forces generated between the limb and the ground during the stance phase. Numerous values can be obtained during a gait analysis, including PFz and IFz for each limb. Moreover, each paw can be further divided in quadrants (cranio-medial, cranio-lateral, caudo-medial, and caudo-lateral) to examine the distribution of the pressure within the paw (PPD, paw pressure distribution). Important findings include the normal forces exerted on each digit or pad during walking and other activities in sound animals (24, 25) and changes in the affected and other limbs in orthopedically diseased animals (26, 27).

In recent years, there has been additional interest in veterinary research in the center of pressure (COP) which has been studied in humans for decades. The COP is the instantaneous vector where the GRFs act and reflects the trajectory of the center of mass (COM) of the body. During ground contact, the position of the COP changes continuously, thus creating the COP path. Displacements of the

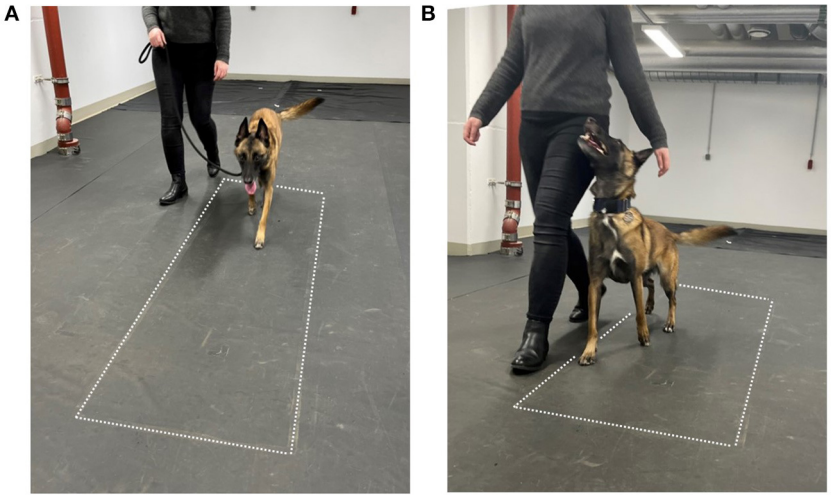

FIGURE 1
Measurement setup. **(A)** Normal walking, **(B)** heel work position. The dotted lines indicate the position of the pressure measurement plate.

COM lead to a displacement of the COP, which can be easily measured by for example force plates or pressure plates. In human medicine, the COP is used as an indirect way to measure the postural sway (28). A variety of COP are used in research, which can be derived from the measured COP path. Typical examples are (a) the COP-area (also called statokinesiogram), determined by the recorded points of the COP trajectory; (b) the mean speed of the movement of the COP (COP-speed, mm/s); (c) the mean distance of all COP points to the center point of all COP points (COP-radius); (d) the COP excursion index and the craniocaudal index, quantifying the mediolateral and craniocaudal displacement of the COP respectively (29–33).

It should be noted that both the body COP (e.g., in humans between the legs) and the COP under the legs (limb COP) can be evaluated as well during standing (static posturography) as well during motion (dynamic posturography). If the COP is evaluated during standing it is generally assumed, that lower values of the mentioned values are indicative for better stability (28, 29, 33–39). In humans such measurements are widely used in different conditions. As a few examples: it was shown that in patients with knee osteoarthritis COP-parameters correlated with the severity of the osteoarthritis (40) and in such with hip osteoarthritis significant differences occurred in numerous COP parameters (41). Further, there is a wide body of evidence that impairment of postural stability is associated with aging and Alzheimer's Disease (42, 43). In veterinary medicine, newborn foals showed a higher amplitude and velocity of COP movements compared data collected during the following months, which was interpreted as an increased stability during the growth (44) and senior dogs showed a higher COP displacement compared to younger dogs (39). Also lame dogs with elbow osteoarthrosis showed a significant increase in COP-area and greater and asymmetric oscillations in mediolateral and craniocaudal direction (33). Similarly, lame horses showed a significantly higher mediolateral COP displacement (30).

When the COP measured in motion, as recently done in veterinary medicine, it can also be used to describe the foot dynamics and lame dogs show significant differences in COP parameters compared to sound dogs. A significant increase in COP-area was found in lame dogs in the in the affected limb (31, 32) as well as in the hindlimbs in dogs with elbow osteoarthrosis (31), indicating an increased instability (32). Furthermore, affected dogs show a significant increase in the caudal margin (the distance between the most caudal point of the paw and the most caudal point of the COP path) and a significant decrease in craniocaudal excursion index and mediolateral COP excursion (31, 32), while the latter has been interpreted as a sign for an increased pad deformation (32). A lateral migration of the COP, which was also found in lame dogs with elbow osteoarthrosis, was interpreted as a sign of joint instability and body posture modification (38). Similar findings, in the sense of an increases mediolateral displacement of the COP was found in dogs with coxarthrosis (31).

Further also connections can be made between the PPD and the COP. In human medical research, the interaction between the size of the foot contact area and the plantar pressure distribution and stability has been investigated using the COP excursion (45–47), where again a larger COP excursion was interpreted as a sign of reduced stability. It has been proposed that even little changes in the support surface result in instability due to a reduction in sensory information (45). In veterinary medicine, research has not focused on the influence of PCA nor PPD on stability, and therefore COP parameters yet.

In summary, GRF, COM, and COP are closely related and can be used to describe the effects of various factors, such as aging, orthopedic and neurological diseases.

Due to the specific body position during heelwork, it can be assumed that heelwork leads to changes in the above-mentioned parameters. While there is no information on the influence of the head- and neck position on vertical GRF (vGRF) in dogs, research in equines found an effect of the head position on the vertical impulse (IFz), stride length, and stance duration of the forelimbs. A higher degree of collection of the head and neck in horses results in a pronounced shift in impulse toward the hindlimbs [without a similar increase of the peak vertical force (PFz)] (48). However, veterinary medical research does not provide information regarding the effect on COP parameters.

The aim of the present study was to investigate the changes in vGRFs, COP, and PPD of Belgian Malinois participating in competitive obedience during heelwork walking. First aim was to measure the GRF, assuming that lifting the head leads to increased forces in both hindlimbs and that turning the head to the right additionally leads to an increased force in the left forelimb, resulting in an asymmetrical loading on the contralateral limb pair as shown by the SI. Second aim was to investigate whether the altered vGRF also lead to changes in PPD, or whether the loading on the paw quadrants is unchanged. Since COP is affected by changes in PPD as described in human medicine (47), the 3rd aim was to investigate whether altered PPD is also reflected in changes in COP parameters.

2. Material and methods

2.1. Ethics

The study was approved by the Ethics and Animal Welfare Committee of the University of Veterinary Medicine, Vienna, in accordance with the university's guidelines for "Good Scientific Practice" (Ref. No. 18/03/97/2014 and ETK-133/08/2022).

2.2. Animals and inclusion criteria

Based on a preliminary master thesis (49), sample size was determined using GPower (Version 3.1.9.6, University Kiel, Germany). The IFz (normalized to total force) of the values of Malinois collected in this study during normal walking and heelwork were used as baseline data. The IFz showed significantly higher values in the hind legs during heelwork (HL 22.35 ± 3.10%, HR 22.98 ± 2.94%) than during normal walking (HL 19.46 ± 1.02% $p = 0.03$, HR 19.56 ± 1.58% $p = 0.02$). With α error probability 0.05 and a power of 0.90 we calculated based on that a sample size of $n = 10$ for HL and $n = 7$ for HR.

Twelve to ten-year-old Belgian Malinois were included in the study. The animals should present with normal orthopedic and neurological examination results to be included. The orthopedic examination included visual assessment of lameness and palpation of joints. Furthermore, an SI < 3% was required, as an SI of up to 3% is considered normal for dogs and values higher than 3% are interpreted as lameness (26, 27, 31).

10.3389/fvets.2023.1106170

Twelve Belgian Malinois dogs were examined for the study. Two dogs were excluded, one due to pain at the palpation of the hip joint and one dog due to a SI of 3.08%. Seven females and three males were evaluated for the present study. The mean age was 4.67 ± 1.26 years (median = 4.95 years, minimum = 3 years, maximum = 7 years) and the mean body mass was 27.46 ± 6.58 kg (median = 26 kg, minimum = 20.6 kg, maximum = 41 kg).

2.3. Equipment

A 203- × 54.2-cm pressure measurement plate [FDM Type 2 from Zebris Medical GmbH, Allgäu, Germany (27, 31, 50–55)] was used, which measures the pressure of the dog's paws through 15,360 piezoelectric sensors and a sampling rate of 100 Hz. The plate was covered with a black, 1-mm-thick rubber mat composed of polyvinyl chloride to avoid slipping. To assign the measured values to the correct limb of the respective test during data evaluation, each measurement run was filmed with a Panasonic camera, model NV-MX500.

2.4. Measurement procedure

Same-day measurements were acquired for each dog. The dogs were first allowed to become accustomed to the examination room and the people involved. For this purpose, they were allowed to move freely in the room. As soon as the animal became accustomed to the environment, they were subjected to a standard analysis of the vGRFs during a normal walk, as described by Reicher et al. (31), including an afterward analysis of the vGRFs while heeling. The animals were on the left side of the owner, which is the side that they usually walk next to the owner. This was repeated until a minimum of four valid steps had been collected for each limb and gait (normal walk and heelwork walk). Valid passes during normal walk included those where the dog had crossed the plate without changing pace, turning its head, pulling on the lead, and touching the owner. During heelwork walk, valid passes were those in which the dog performed the command without interruption. Moreover, if the dog had body contact with the handler, those measurements were excluded for both gaits. Heelwork was achieved in the same way as in obedience competitions. The difference in speed at which the dogs crossed the plate had to be within a range of ±0.3 m/s and an acceleration of ±0.5 m/s^2 (56, 57). The values obtained during a normal walk were compared with the values obtained during a heelwork walk.

2.5. Data analysis

The data were analyzed with the custom software Pressure Analyzer (Michael Schwanda, version 4.6.5.0) and then exported to Microsoft® Excel® 2016. The individual pawprints recorded during the valid passes were manually assigned to the corresponding limb with the help of the recorded video. The standard method of assessment includes the identification and assignment of each limb as left forelimb (FL), right forelimb (FR), left hindlimb (HL), and right hindlimb (HR).

2.6. Parameters under investigation

The following parameters were used for the evaluation of the vGRFs and temporo-spatial parameters:

- Mean speed (m/s) and acceleration (m/s^2) which were calculated based on the left forelimb;
- Peak vertical force (PFz in N);
- Vertical impulse (IFz in N/s);
- The PFz and the IFz were normalized with the following formula and expressed as a percentage of total forces:

$$\textbf{Value in \% of total force} = \frac{\textbf{XFzLx}}{(\textbf{XFzFL} + \textbf{XFzFR} + \textbf{XFzHL} + \textbf{XFzHR})} * \textbf{100}$$

Where: XFz is the mean value of PFz or IFz of the valid steps, Lx is the limb under investigation, FL is the left forelimb, FR is the right forelimb, HL is the left hindlimb, and HR is the right hindlimb.

- SI expressed as a percentage (SI%) was calculated for both parameters (PFz and IFz) according to the following equation:

$$\textbf{SIXFz}\ (\%) = \textbf{abs}\left(\frac{(\textbf{XFzLLx} - \textbf{XFzRLx})}{(\textbf{XFzLLx} + \textbf{XFzRLx})}\right) * \textbf{100}$$

Where XFz is the mean value of PFz or IFz of the valid steps, LLx is the left fore- or hindlimb, and RLx is the right fore–hindlimb; perfect symmetry between the right and left fore- or hindlimbs was assigned a value of 0%.

- Mean stance phase duration (SPD) in seconds.

The mean duration of the stance phase was normalized with the following formula, expressed as the percentage of the total SPD (SPD%).

TABLE 1 Mean values, standard deviation, and *p*-values of the speed and acceleration based on the left forelimb between normal walking and heelwork walking.

	Speed			Acceleration		
	Mean ± SD		*p*-value	Mean ± SD		*p*-value
	Normal walk	Heelwork walk	Normal walk	Heelwork walk	Normal walk	
FL	1.34 ± 0.21	1.41 ± 0.24	0.495	−0.04 ± 0.10	0.01 ± 0.09	0.218

FL, left forelimb; mean ± SD, mean and standard deviation.

10.3389/fvets.2023.1106170

TABLE 2 Mean values, standard deviation, and significant differences of the ground reaction forces and temporo-spatial parameters for each limb between normal walking and heelwork walking.

	PFz (%)			IFz (%)			TPFz (%)			SPD (%)		
	Mean ± SD		*p*-value	Mean ± SD		*p*-value	Mean ± SD		*p*-value	Mean ± SD		*p*-value
	Normal walk	Heelwork walk		Normal walk	Heelwork walk		Normal walk	Heelwork walk		Normal walk	Heelwork walk	
FL	29.18 ± 1.40	29.57 ± 1.69	0.582	30.59 ± 0.92	26.76 ± 2.69	0.001*	36.17 ± 8.17	40.82 ± 7.12	0.192	25.90 ± 0.65	22.88 ± 2.39	0.003*
FR	29.51 ± 1.29	30.37 ± 2.51	0.351	31.16 ± 1.04	26.47 ± 3.44	0.002*	37.73 ± 10.02	41.11 ± 8.16	0.418	25.85 ± 0.61	22.23 ± 2.39	0.001*
HL	20.86 ± 1.13	19.86 ± 1.41	0.095	19.27 ± 0.98	23.20 ± 2.46	0.001*	31.22 ± 11.26	31.02 ± 7.76	0.965	24.22 ± 0.70	27.11 ± 1.88	0.001*
HR	20.45 ± 1.50	20.20 ± 2.34	0.785	18.97 ± 0.98	23.57 ± 3.49	0.002*	30.34 ± 10.78	30.28 ± 7.13	0.989	24.03 ± 0.54	27.79 ± 2.77	0.003*
	PCA (%)			SL (m)			Reach (cm)					
	Mean ± SD		*p*-value	Mean ± SD		*p*-value	Mean ± SD		*p*-value			
	Normal walk	Heelwork walk		Normal walk	Heelwork walk		Normal walk	Heelwork walk				
FL	26.66 ± 0.46	26.44 ± 0.98	0.540	0.88 ± 0.10	0.79 ± 0.17	0.159						
FR	26.94 ± 0.37	26.43 ± 1.39	0.287	0.89 ± 0.11	0.81 ± 0.15	0.198						
HL	23.24 ± 0.47	23.41 ± 1.10	0.664	0.89 ± 0.11	0.88 ± 0.12	0.768	6.48 ± 5.16	3.31 ± 6.43	0.241			
HR	23.15 ± 0.43	23.70 ± 1.28	0.222	0.89 ± 0.11	0.90 ± 0.14	0.803	4.49 ± 8.93	3.02 ± 6.36	0.676			

FL, left forelimb; FR, right forelimb; HL, left hindlimb; HR, right hindlimb; mean ± SD, mean and standard deviation; PFz%, peak vertical force as a percentage of total force; IFz%, vertical impulse as a percentage of total force; TPFz%, time to PFz as a percentage of stance phase duration; SPD%, stance phase duration as a percentage of total stance phase duration; PCA%, paw contact area; SL(m), step length. Significant differences within the groups are marked with *.

$$\mathbf{SPD}\ (\%) = \frac{\mathbf{XmDStPhLx}}{(\mathbf{XmDStPhFL}+\mathbf{XmDStPhFR}+\mathbf{XmDStPhHL}+\mathbf{XmDStPhHR})} * \mathbf{100}$$

Where XmDStPh is the value of the mean duration of the stance phase of the valid steps, Lx is the limb under investigation, FL is the left forelimb, FR is the right forelimb, HL is the left hindlimb, and HR is the right hindlimb.

- Time of occurrence of PFz as a percentage of the stance phase of the respective limb (TPFz%).
- Paw contact area (PCA) of each limb as a percentage of the contact area (cm^2).
- Step length (SL) of each limb in meters.
- Reach which is the distance between the center of the forelimb and the center of the hindlimb on the same side in the direction of movement in cm.

The evaluation of the vertical force distribution in the paws was performed according to Moreira et al. (26) as follows.

Each paw was equally divided into four quadrants, craniomedial (CrM), craniolateral (CrL), caudomedial (CdM), and caudolateral (CdL). This was achieved by calculating the midpoint of the maximum length in the cranial/caudal and medial/lateral directions of each paw by the software. The parameters under investigation were the PFz, IFz, TPFz, and area. The PFz and IFz were normalized to the total force and presented as % (i.e., PFz% and IFz%), in which the sum of PFz% and IFz% of the 16 quadrants was equal to 100%.

The formula used for the above values was:

$$\mathrm{TFnk}\ (\%) = \frac{\mathbf{100} * \mathbf{X_{nk}}}{\sum_{k=1}^{4}\sum_{n=1}^{4} X_{nk}}$$

Where X represents PFz% or IFz%, n represents a limb (FL, FR, HL, and HR), and k represents one quadrant (CrL, CrM, CdL, and CdM).

The TPFz was normalized to the duration of the stance phase and the area was normalized to the contact area.

For the statistical analysis, each quadrant was compared for the two walks (normal and heelwork walk).

The evaluation of the COP was conducted according to Reicher et al. (31) and Lopez et al. (32) as follows:

- COP-area: The COP-area is a measurement of the area covered by the COP movement. It was normalized to the PCA and expressed as a percentage (COP-area%).
- COP-speed: The COP-speed is the mean speed of the movement of the COP (COP-Sp, mm/s).
- COP-radius: The COP-radius is the mean distance of all COP points to the center point of all COP points. This parameter was also normalized to the PCA and given as a percentage (COP-radius%).
- Caudal margin (mm): Caudal margin is the distance between the most caudal point of the paw and the most caudal point of the COP path.

TABLE 3 Mean values of PFz and symmetry index of PFz of the forelimbs and hindlimbs during normal walk and heelwork walk for each dog and all dogs.

Dog	Normal walk				Heelwork walk				Normal walk				Heelwork walk			
	PFz%		SI% of PFz		PFz%		SI% of PFz		PFz%		SI% of PFz		PFz%		SI% of PFz	
	FL	FR	Forelimbs		FL	FR	Forelimbs		HL	HR	Hindlimbs		HL	HR	Hindlimbs	
1	29.79	30.46	1.11		29.06	30.97	3.18		19.87	19.89	0.05		20.72	19.25	3.68	
2	31.28	30.69	0.95		31.82	29.17	4.34		19.54	18.49	2.76		19.4	19.61	0.54	
3	27.58	29.22	2.89		31.93	32.19	0.41		21.91	21.29	1.44		18.26	17.62	1.78	
4	30.01	30.46	0.74		28.77	32.75	6.47		19.93	19.6	0.83		20.09	18.39	4.42	
5	29.87	28.97	1.53		30.8	32.85	3.22		21.17	19.99	2.87		18.48	17.87	1.68	
6	28.29	29.2	1.58		28.7	28.42	0.49		21.19	21.31	0.28		20.98	21.91	2.17	
7	28.92	29.98	1.80		27.7	30.71	5.15		21.04	20.06	2.38		20.69	20.9	0.50	
8	30.8	30.98	0.29		31.17	30.86	0.50		19.36	18.86	1.31		17.67	20.3	6.93	
9	26.99	26.77	0.41		27.72	24.46	6.25		22.6	23.64	2.25		22.22	25.59	7.05	
10	28.26	28.34	0.14		28.01	31.33	5.59		22.04	21.36	1.57		20.05	20.61	1.38	
Mean ± SD	29.18 ± 1.40	29.51 ± 1.29	1.15 ± 0.84		29.57 ± 1.69	30.37 ± 2.51	3.56 ± 2.40		20.86 ± 1.13	20.45 ± 1.50	1.58 ± 0.99		19.86 ± 1.41	20.20 ± 2.34	3.01 ± 2.43	

Black boxes indicate which forelimb or hindlimb has higher values. Green indicates decrease and red indicates increase of the values during heelwork walk compared to normal walk. Orange indicates increase of the values during heelwork walk compared to normal walk but not above 3% (normal).

FL, left forelimb; FR, right forelimb; HL, left hindlimb; HR, right hindlimb; PFz, peak vertical force; SI%, symmetry index; SD, standard deviation.

- Craniocaudal index (%): Craniocaudal index is the COP length (the distance between the first and the last COP point in the craniocaudal axis) in relation to the paw length. It was calculated with the following formula:

$$\textbf{Craniocaudal index } (\%) = \frac{\textbf{COP length}}{\textbf{paw length}} * \textbf{100}$$

- COP excursion index (%): COP excursion index is the lateromedial excursion (the distance between the first and the last COP point in the mediolateral axis) of the COP related to the paw width. It was calculated with the following formula:

$$\textbf{COP excursion index } (\%) = \frac{\textbf{lateromedial excursion}}{\textbf{paw width}} * \textbf{100}$$

2.7. Statistical analysis

All statistical analyses were performed using IBM SPSS, version 28. The difference between normal walk and heelwork in the investigated parameters was evaluated using linear mixed-effects models, where the condition (normal walk vs. heelwork) was added to the model as a fixed within subjects effect *Post-hoc* analyses were performed using Sidak's alpha correction procedure. A p-value below 5% ($p < 0.05$) was seen as significant.

3. Results

3.1. Speed and acceleration

No significant differences were found for the speed and acceleration between normal walk (1.34 ± 0.21 m/s, −0.04 ± 0.10 m/s^2) and heelwork (1.41 ± 0.24 m/s, 0.01 ± 0.09 m/s^2) (Table 1) and they were within the defined ranges (Chapter 2.4).

3.2. Vertical ground reaction forces and temporo-spatial parameters

No significant differences were found between heelwork and normal walk regarding PFz, TPFz, reach, SL, and PCA (Table 2).

During heelwork, eight dogs increased their SI of PFz where 7/10 dogs reached an SI of PFz >3% (range 3.18–6.47%), with five dogs displaying a higher PFz in the FR, and two on the FL (Table 3). Although this resulted in comparable mean values for FL and FR PFz, without a significant difference to a normal walk, a significantly higher SI of PFz (3.56%) during heelwork than in the normal walk (1.15%, $p = 0.012$, Table 4) was observed. In the hindlimbs (Table 3), six dogs displayed a higher SI of PFz than in normal walk, but only four dogs had an SI of PFz >3% (range 3.68–7.05%) (two dogs with higher PFz values on the HL and two on the HR). Neither PFz nor SI of PFz showed a significant difference in comparing a normal walk and heelwork (Tables 2, 4). Significant differences between heelwork and normal walk are displayed in Figure 2.

TABLE 4 Mean values, standard deviation, and significant differences of the symmetry index for the peak vertical force and vertical impulse between normal walking and heelwork walking.

	Symmetry PFz (%)			Symmetry IFz (%)		
	Mean ± SD		*p*-value	Mean ± SD		*p*-value
	Normal walk	Heelwork walk		Normal walk	Heelwork walk	
Forelimbs	1.15 ± 0.84	3.56 ± 2.40	0.012*	1.25 ± 0.61	3.62 ± 2.89	0.030*
Hindlimbs	1.58 ± 0.99	3.01 ± 2.43	0.110	1.62 ± 0.81	3.61 ± 2.36	0.028*

Mean ± SD, mean and standard deviation; PFz%, peak vertical force as a percentage of total force; IFz%, vertical impulse as a percentage of total force. Significant differences within the groups are marked with *.

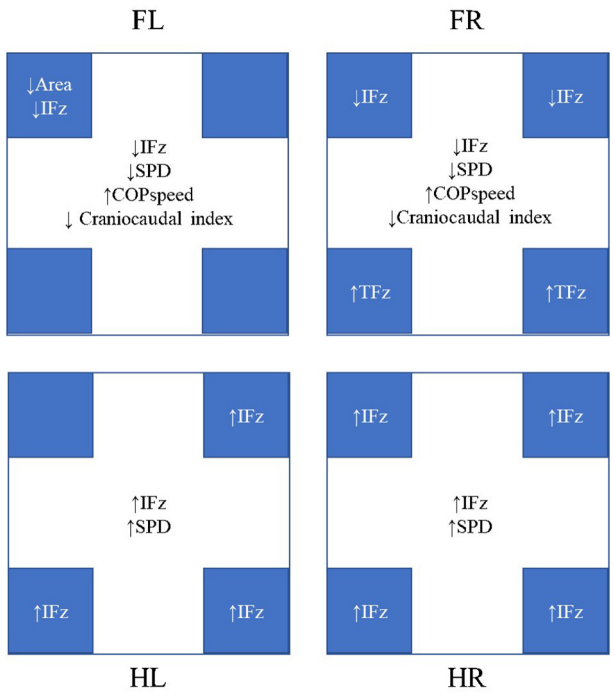

FIGURE 2
Significant differences were observed during heelwork walking compared to normal walking. The results in the center of each box represent the changes in each limb, whereas the results in the blue boxes represent the changes in the quadrants. FL, left forelimb; FR, right forelimb; HL, left hindlimb; HR, right hindlimb; IFz, vertical impulse; SPD, stance phase duration; TPFz, time to peak vertical force. All mean values, standard deviations, and *p*-values are given in Tables 2, 4, 6, 7.

IFz decreased significantly at the forelimbs (FL: $p = 0.001$, FR: $p = 0.002$). The SI of IFz of the forelimbs (Table 4) during heelwork was increased in eight dogs, with five dogs displaying values >3% (range 3.11–9.9%); here, three dogs had higher IFz on the FL (Table 5). The SI of IFz of the forelimbs during heelwork (3.62%) was significantly increased compared to a normal walk (1.25%, $p = 0.030$). IFz increased in both hindlimbs (HL: $p = 0.001$, HR: $p = 0.002$). Seven dogs increased their SI of IFz, with six dogs displaying an SI of IFz > 3% (range 3.19–6.45%), with four of them displaying higher values in the HR and two in the HL (Table 5). The SI of IFz of the forelimbs and hindlimbs during heelwork (3.61%) was significantly increased compared to a normal walk (1.62%, $p = 0.028$, Table 4).

SPD was significantly decreased at the FL and FR ($p = 0.003$ and $p = 0.001$, respectively) and increased at the HL and HR ($p = 0.001$ and $p = 0.003$, respectively).

3.3. Vertical force distribution in the paw quadrants

No significant differences of the PFz were found between the normal walk and heelwork walk. IFz was significantly decreased at the CrL quadrant of the FL ($p = 0.002$) and CrL and CrM quadrants of the FR ($p = 0.038$, $p = 0.009$, respectively) and significantly increased in all the quadrants of the hindlimbs except the CrL quadrant of the HL. TPFz was significantly increased at the CdM and CdL quadrant of the FR ($p = 0.046$ and $p = 0.020$, respectively). The area of the CrL quadrant of the FL ($p = 0.029$) was significantly decreased during heelwork walk (Table 6, Figure 2).

3.4. Center of pressure

The COP-radius, COP-area, excursion index, and caudal margin were not significantly different between the heelwork walk and normal walk. The craniocaudal index was significantly decreased at the forelimbs during heelwork walk (FL: $p = 0.037$, FR: $p = 0.003$). The COP-speed was significantly increased at the FL ($p = 0.012$) and FR ($p = 0.003$) during heelwork walk (Table 7, Figure 2).

4. Discussion

Our hypothesis was that due to the changed head position (lifted and tilted to the right side) during heelwork, higher vGRF will be applied on the left forelimb (due to the tilting to the right) and both hind limbs (due to the lifting) compared to a normal walk This hypothesis was partially confirmed: IFz increased in the hindlimbs. However, the higher loading of the FL did not occur, on the contrary, both forelimbs showed a decreased IFz. Nevertheless, the SI was significantly higher during heelwork than during normal walking, although only slightly above the value that is often used as a cutoff value to differentiate lame from sound dogs (26, 27, 31). Interestingly, when the mean values of PFz and IFz were considered, there were no obvious differences in the values between the right and left forelimb. The SI used nevertheless showed an increasing asymmetry in the load (although not in all animals and within animals also to different extents). This shows the importance of the choice of formula used to

10.3389/fvets.2023.1106170

TABLE 5 Mean values of IFz and symmetry index of IFz of the forelimbs and hindlimbs during normal walk and heelwork walk for each dog and all dogs.

Dog	Normal walk			Heelwork walk			Normal walk			Heelwork walk		
	IFz%		SI% of IFz	IFz%		SI% of IFz	IFz%		SI% of IFz	IFz%		SI% of IFz
	FL	FR	Forelimbs	FL	FR	Forelimbs	HL	HR	Hindlimbs	HL	HR	Hindlimbs
1	30.55	32.01	2.33	27.2	31.2	6.85	19.21	18.23	2.62	22.04	19.56	5.96
2	30.58	31.46	1.42	23.77	22.03	3.82	19.13	18.83	0.79	27.38	26.82	1.03
3	30.8	32.05	1.99	28.12	27.46	1.19	18.95	18.21	1.99	22.48	21.95	1.19
4	31.92	32.39	0.73	29.8	27.23	4.51	17.59	18.1	1.43	22.72	20.26	5.72
5	31.15	31.92	1.22	29.26	30.77	2.52	18.93	17.99	2.55	19.8	20.18	0.95
6	30.67	31.37	1.13	24.79	25.84	2.08	19.27	18.69	1.53	25.01	24.37	1.30
7	31.62	31.2	0.67	28.05	28.01	0.07	18.37	18.81	1.18	21.27	22.67	3.19
8	29.31	29.54	0.39	29.12	27.88	2.18	21.1	20.05	2.55	20.64	22.36	4.00
9	28.93	29.88	1.62	25.92	21.25	9.90	20.33	20.87	1.31	24.71	28.12	6.45
10	30.42	29.82	1.00	21.6	22.99	3.11	19.85	19.92	0.18	25.96	29.45	6.30
Mean ± SD	30.59 ± 0.92	31.16 ± 1.04	1.25 ± 0.61	26.76 ± 2.69	26.47 ± 3.44	3.62 ± 2.89	19.27 ± 0.98	18.97 ± 0.98	1.62 ± 0.81	23.20 ± 2.46	23.57 ± 3.49	3.61 ± 2.36

Black boxes indicate which forelimb or hindlimb had higher values. Green indicates decrease and red indicates increase of the values during heelwork walk compared to normal walk. Orange indicates an increase of the values during heelwork walk compared to normal walk but below 3% (normal).

FL, left forelimb; FR, right forelimb; HL, left hindlimb; HR, right hindlimb; IFz, vertical impulse; SI%, symmetry index; SD, standard deviation.

calculate the SI, because as described above, some dogs showed higher values on the right and others on the left during heelwork. The study design does not allow further conclusions regarding the differing results between the dogs. However, our results indicate that in further studies, kinematic measurements should be included, which examine the head/neck posture and the back line of the animals. It is likely that the differences in the neck angle described by Harris et al. (14) led to the inconsistent results. The lack of literature on this topic indicates that further studies are needed to develop best practice guidelines for GRFs measurements to obtain an accurate and repeatable results (58).

Due to the lack of scientific studies investigating the influence of head/neck position on the GRFs in dogs, a literature comparison is difficult. However, gait and jump analysis in healthy cats revealed an increase in the PFz of the forelimb to which the head is turned during the measurements by a factor of 1.73 ± 0.53 (59), which was not shown in our study. Furthermore, changes in IFz, stride length, and stance duration of the forelimbs of horses are evident during different positions of the head and neck. A higher degree of collection of the head and neck in horses results in a pronounced shift in impulse toward the hindlimbs (without a similar increase of the PFz) (48). However, a lateral flexion, as seen in dogs during heelwork (11), was not assessed in horses (48). Although the comparisons between different species are difficult due to the different anatomy, we can see some similarities between the biomechanical adaptations when the head and neck position deviates from the natural position. In horses, it has been suggested that a "prolonged stance duration and positive diagonal advanced placement can be indicative of a good balance and self-carriage and interpreted as expression of a greater reliance of the hindlimbs for support" (60). Further studies are needed to investigate if the same applies to dogs.

Regarding the second aim of the study, it could be shown that the particular body position also led to changes in PPD in the forelimbs: the reduction of the forces in the forelimbs was caused by a decrease of IFz in the CrL quadrants of both forelimbs and the CrM quadrant of the FR. Furthermore, a correlation between PPD and COP within the paws could be shown: the reduced loading of the cranial quadrants led to shortened craniocaudal index during heelwork, indicating a changed paw roll over dynamic. This change was accompanied by an increased COP speed in the forelimbs. Although the walking speed of the dogs did not differ between the conditions, a shorter SPD was observed in the front limbs, which together with the shortened craniocaudal index led to a significant increase in COP-speed. In the hindlimbs, on the contrary, the SPD was longer than during normal walk, which, however, did not lead to a change in this parameter due to the unchanged PPD.

In contrast the PPD during heelwork and normal walk was similar in the hindlimbs, leading to no statistically significant changes in COP parameters. This supports our interpretation that craniocaudal index changes are the result adaptations in the pressure distribution within the paw. Similar to our findings, the displacement of COP in human patients with high-arched feet was explained by the differences in pressure distribution (47, 61).

The results of the study can be discussed under different aspects. First, in humans, it is known that the spatial progression of the COP on the craniocaudal foot axis is seen as a function of the articular mobility of the joints in craniocaudal direction in human patients (62), with lower craniocaudal indices indicating reduced joint mobility. To verify whether the changes in COP parameters found here in dogs also lead to changes in joint kinematics, for

TABLE 6 Mean values, standard deviation, and significant differences of the ground reaction forces in the quadrants between normal walking and heelwork walking.

	PFz (%)			IFz (%)			TPFz (%)			Area (%)		
	Mean ± SD		*p*-value	Mean ± SD		*p*-value	Mean ± SD		*p*-value	Mean ± SD		*p*-value
	Normal walk	Heelwork walk		Normal walk	Heelwork walk		Normal walk	Heelwork walk		Normal walk	Heelwork walk	
FLCaudoLateral	7.28 ± 0.95	7.55 ± 1.41	0.627	6.54 ± 1.36	6.02 ± 1.24	0.386	32.12 ± 6.29	36.01 ± 6.43	0.188	6.94 ± 0.54	7.28 ± 0.71	0.246
FLCaudoMedial	5.57 ± 1.18	5.72 ± 1.23	0.786	4.46 ± 1.17	4.28 ± 0.97	0.716	27.95 ± 5.67	35.17 ± 10.06	0.068	6.41 ± 0.73	6.71 ± 0.67	0.348
FLCranioLateral	8.74 ± 0.98	7.83 ± 1.17	0.075	10.43 ± 1.32	8.13 ± 1.43	0.002*	62.39 ± 11.16	60.91 ± 14.30	0.799	6.65 ± 0.63	5.91 ± 0.75	0.029*
FLCranioMedial	8.30 ± 0.75	8.14 ± 0.58	0.591	9.17 ± 0.97	8.32 ± 1.10	0.086	69.06 ± 8.82	63.25 ± 13.26	0.266	6.79 ± 0.53	6.55 ± 0.62	0.357
FRCaudoLateral	7.54 ± 1.15	8.20 ± 0.95	0.177	6.67 ± 1.58	6.28 ± 0.93	0.510	30.58 ± 5.94	37.64 ± 6.43	0.020*	7.21 ± 0.57	7.40 ± 0.54	0.467
FRCaudoMedial	5.56 ± 0.78	5.60 ± 0.88	0.915	4.77 ± 0.97	3.99 ± 0.66	0.053	29.89 ± 7.34	35.14 ± 7.74	0.046*	6.41 ± 0.69	6.40 ± 0.48	0.950
FRCranioLateral	8.62 ± 1.44	7.95 ± 1.24	0.279	10.28 ± 1.76	8.41 ± 1.96	0.038*	63.33 ± 10.29	59.34 ± 14.22	0.482	6.55 ± 0.89	6.13 ± 0.79	0.277
FRCranioMedial	8.41 ± 0.88	7.82 ± 1.04	0.188	9.44 ± 1.11	7.78 ± 1.38	0.009*	68.53 ± 9.57	62.14 ± 11.87	0.202	6.67 ± 0.80	6.34 ± 0.68	0.337
HLCaudoLateral	4.15 ± 0.77	4.00 ± 0.57	0.629	3.05 ± 0.64	3.64 ± 0.57	0.042*	26.47 ± 6.70	24.00 ± 6.53	0.414	5.54 ± 0.60	5.55 ± 0.46	0.954
HLCaudoMedial	4.02 ± 0.73	4.39 ± 0.88	0.318	2.45 ± 0.49	3.45 ± 0.73	0.002*	25.03 ± 5.16	21.66 ± 5.95	0.193	5.77 ± 0.45	6.02 ± 0.42	0.225
HLCranioLateral	6.73 ± 1.18	6.42 ± 0.65	0.488	7.89 ± 1.27	8.63 ± 0.94	0.153	57.59 ± 14.19	60.35 ± 9.42	0.615	6.21 ± 0.47	6.17 ± 0.29	0.816
HLCranioMedial	5.36 ± 0.66	5.87 ± 0.60	0.091	5.89 ± 0.86	7.47 ± 1.45	0.010*	53.61 ± 17.41	63.12 ± 11.04	0.165	5.77 ± 0.47	5.88 ± 0.35	0.537
HRCaudoLateral	3.99 ± 0.62	4.22 ± 0.98	0.531	2.84 ± 0.49	3.78 ± 0.97	0.017*	24.90 ± 4.70	24.08 ± 5.18	0.714	5.51 ± 0.56	5.65 ± 0.75	0.650
HRCaudoLateral	3.99 ± 0.62	4.22 ± 0.98	0.531	2.84 ± 0.49	3.78 ± 0.97	0.017*	24.90 ± 4.70	24.08 ± 5.18	0.714	5.51 ± 0.56	5.65 ± 0.75	0.650
HRCaudoMedial	3.82 ± 0.83	4.33 ± 1.29	0.306	2.38 ± 0.60	3.46 ± 1.38	0.042*	25.19 ± 5.31	21.78 ± 5.08	0.160	5.57 ± 0.43	5.90 ± 0.51	0.131
HRCranioLateral	6.34 ± 1.12	6.52 ± 1.04	0.716	7.51 ± 1.14	9.20 ± 2.01	0.036*	51.32 ± 15.79	58.55 ± 12.82	0.276	5.99 ± 0.60	6.29 ± 0.85	0.374
HRCranioMedial	5.57 ± 0.56	5.44 ± 0.52	0.589	6.24 ± 0.75	7.13 ± 1.07	0.047*	56.83 ± 15.40	60.59 ± 14.32	0.579	6.00 ± 0.43	5.82 ± 0.36	0.327

Mean ± SD, mean and standard deviation; PFz%, peak vertical force; IFz%, vertical impulse; TPFz%, time to PFz. Significant differences within the groups are marked with *.

10.3389/fvets.2023.1106170

TABLE 7 Mean values, standard deviation, and significant differences between normal walking and heelwork walking of the center of pressure.

	COP-area (%)			COP-speed (mm/s)			COP-radius (%)		
	Mean ± SD		*p*-value	Mean ± SD		*p*-value	Mean ± SD		*p*-value
	Normal walk	Heelwork walk		Normal walk	Heelwork walk		Normal walk	Heelwork walk	
FL	1.28 ± 0.38	1.32 ± 0.69	0.890	95.61 ± 15.59	129.02 ± 32.66	0.012*	0.13 ± 0.02	0.13 ± 0.02	0.427
FR	1.16 ± 0.39	1.26 ± 0.60	0.672	92.68 ± 16.56	126.41 ± 25.27	0.003*	0.13 ± 0.02	0.13 ± 0.01	0.320
HL	0.82 ± 0.50	1.07 ± 0.47	0.263	86.67 ± 21.51	102.21 ± 16.31	0.087	0.15 ± 0.03	0.16 ± 0.02	0.383
HR	0.80 ± 0.36	1.12 ± 0.62	0.173	86.39 ± 18.66	101.04 ± 16.04	0.076	0.15 ± 0.02	0.16 ± 0.02	0.269
	Caudal margin (mm)			Craniocaudal index (%)			Excursion index (%)		
	Mean ± SD		*p*-value	Mean ± SD		*p*-value	Mean ± SD		*p*-value
	Normal walk	Heelwork walk		Normal walk	Heelwork walk		Normal walk	Heelwork walk	
FL	32.04 ± 4.05	35.11 ± 3.16	0.076	32.09 ± 7.93	25.06 ± 5.74	0.037*	5.12 ± 2.06	7.05 ± 3.55	0.157
FR	32.07 ± 4.15	35.29 ± 2.92	0.062	32.52 ± 7.00	23.10 ± 5.23	0.003*	4.21 ± 1.58	5.78 ± 2.18	0.082
HL	31.92 ± 6.12	32.15 ± 2.11	0.909	32.24 ± 7.88	37.12 ± 7.74	0.179	3.14 ± 1.54	3.47 ± 1.62	0.647
HR	32.05 ± 4.60	31.69 ± 2.51	0.834	32.06 ± 8.65	38.10 ± 9.03	0.144	3.30 ± 1.54	3.21 ± 1.81	0.908

FL, left forelimb; FR, right forelimb; HL, left hindlimb; HR, right hindlimb; mean ± SD, mean and standard deviation; COP, center of pressure; Significant differences within the groups are marked with *.

example in the carpal joint, kinematic measurements would have to be performed in further studies. While the studies on injuries in obedience dogs do not indicate an increased risk for injuries of the pads, it should still be further investigated, if the excessive pressure under the caudal quadrants of the forelimbs contribute to soft tissue injuries, as described in human medicine (63). Furthermore, in human patients, a decreased foot contact area and changes in plantar pressure distribution result in impairments in stability which is explained by a reduction in sensory information (45). While the PCA was not significantly different between heelwork and normal walk, the adaptations in PPD could have a similar effect as described in human medicine, indicating an increased instability.

The caudal margin of the COP and the COP excursion index did not show alterations during heelwork. This is of interest as in lame dogs with elbow dysplasia a larger caudal margin is interpreted as a sign of decreased extension of the limb and consequently an incorrect load takeover of the paw during the beginning of the stance phase (32). If the caudal margin is taken as descriptor of the load takeover, the sound dogs in our study did not displayed a changed load takeover at the beginning of the stance phase during heelwork, but conclusions on changed kinematics of the joints can only be drawn by further studies, as already noted above.

Numerous orthopedic diseases are described in working dogs (6), such as the semitendinosus myopathy (8–10). This disease is of particular interest, since a secondary fibrosis and contracture of the muscle lead to functional impairments and early retirement (9). While the definitive etiology of this disease is still unknown, recurrent microtraumas are discussed as a possible cause (64). The extent to which increased forces acting on the hind legs may contribute to these traumas could be investigated, for example, with parallel measurement of electromyography during work. Furthermore, heelwork could contribute to the progression of existing diseases such as hip dysplasia or worsen the symptoms of lumbosacral stenosis. However, multiple factors play a role here (type of training, training frequency, other required tasks, such as jumping, A-wall, etc.). Nevertheless, the observed changes of vGRF, COP and PPD could contribute to the development of biomechanical pathologies due to altered balance of moments acting across the joint axis, as proposed in human medicine (65–67). However, as mentioned before, simultaneous kinetic and kinematic measurements and electromyography should be performed to achieve a better insight.

One of the limitations of our study was the small sample size. Since this study included only Belgian Malinois and differences exist during gait analysis between different breeds (68–70), we cannot extrapolate our results in other breeds participating in competitive obedience. For example, Della Valle et al. (70) observed that GRFs cannot be compared between breeds with different morphological types. Likewise, Fischer et al. (69) found significant differences in the kinematics of the hindlimbs of Malinois compared to other breeds. This issue complicates the interpretation of the results, since the above-mentioned publication about different neck angles during heelwork included a high percentage of Border Collies (14).

5. Conclusion

In conclusion, heelwork leads to specific changes in vGRF, PPD, and COP compared to normal walk, indicating that the COM and consequently the PFz is shifted caudally, the paw rollover dynamics of the front legs display less forces in the cranial quadrants and that the craniocaudal displacement of the COP reacts accordingly. These findings could be also a sign of changed joint kinematics, altered muscle activation and joint reaction forces, which should be investigated in further studies. Such further studies could be used to investigate if these changes contribute to the development of biomechanical pathologies, which are often seen in working dogs.

Data availability statement

The raw data supporting the conclusions of this article will be made available by the authors, without undue reservation.

Ethics statement

The animal study was reviewed and approved by Ethics and Animal Welfare Committee of the University of Veterinary Medicine, Vienna. Written informed consent was obtained from the owners for the participation of their animals in this study.

Author contributions

Conceptualization, methodology, and validation: BB. Formal analysis: AT. Data curation: SK, CL, and DC. Writing—original draft preparation: DC. Writing—review and editing: CL and BB. All authors have read and agreed to the published version of the manuscript.

Acknowledgments

The authors would like to thank all participating dogs and their owners for their contribution.

Conflict of interest

The authors declare that the research was conducted in the absence of any commercial or financial relationships that could be construed as a potential conflict of interest.

Publisher's note

All claims expressed in this article are solely those of the authors and do not necessarily represent those of their affiliated organizations, or those of the publisher, the editors and the reviewers. Any product that may be evaluated in this article, or claim that may be made by its manufacturer, is not guaranteed or endorsed by the publisher.

References

1. Carnevale M, Jones J, Li G, Sharp J, Olson K, Bridges W. Computed tomographic evaluation of the sacroiliac joints of young working Labrador retrievers of various work status groups: detected lesions vary among the different groups and finite element analyses of the static pelvis yields repeatable measures of sacroiliac ligament joint strain. *Front Vet Sci.* (2020) 7:528. doi: 10.3389/fvets.2020.00528

2. Parr JR, Otto CM. Emergency visits and occupational hazards in German Shepherd police dogs (2008–2010). *J Vet Emerg Crit Care.* (2013) 23:591–7. doi: 10.1111/vec.12098

3. Worth AJ, Sandford M, Gibson B, Stratton R, Erceg V, Bridges J, et al. Causes of loss or retirement from active duty for New Zealand police German shepherd dogs. *Animal Welfare.* (2013) 22:166–73. doi: 10.7120/09627286.22.2.167

4. Moore GE, Burkman KD, Carter MN, Peterson MR. Causes of death or reasons for euthanasia in military working dogs: 927 cases (1993–1996). *J Am Vet Med Assoc.* (2001) 219:209–14. doi: 10.2460/javma.2001.219.209

5. Takara MS, Harrell K. Noncombat-related injuries or illnesses incurred by military working dogs in a combat zone. *J Am Vet Med Assoc.* (2014) 245:1124–8. doi: 10.2460/javma.245.10.1124

6. von und zur Mühlen M, Schnabl-Feichter E, Bockstahler B. *Eine Literaturübersicht über die Effekte der Diensthundearbeit und des Obedience-Trainings auf den Bewegungsapparat von Hunden*. University of Veterinary Medicine, Vienna (2022).

7. Vaughan LC. Muscle and tendon injuries in dogs. *J Small Anim Pract.* (1979) 20:711–36. doi: 10.1111/j.1748-5827.1979.tb06688.x

8. Moore RW, Rouse GP, Piermattei DL, Ferguson HR. Fibrotic myopathy of the semitendinosus muscle in four dogs. *Vet Surg.* (1981) 10:169–74. doi: 10.1111/j.1532-950X.1981.tb00654.x

9. Steiss JE. Muscle disorders and rehabilitation in canine athletes. *Vet Clin N Am Small Anim Pract.* (2002) 32:267–85. doi: 10.1016/S0195-5616(03)00088-3

10. Lewis DD, Shelton GD, Piras A, Dee JF, Robins GM, Herron AJ, et al. Gracilis or semitendinosus myopathy in 18 dogs. *J Am Anim Hosp Assoc.* (1997) 33:177–88. doi: 10.5326/15473317-33-2-177

11. Zink C, van Dyke JB, editors. *Canine Sports Medicine and Rehabilitation*. Hoboken, NJ: John Wiley & Sons, Inc (2018). p. 594. doi: 10.1002/9781119380627

12. FCI. *Obedience*. Cumberland: FCI (2022). Available online at: https://www.fci.be/en/Obedience-46.html (accessed September 25, 2022)

13. The Kennel Club. *Kennel Club Obedience Show Regulations* (2023). Available online at: https://www.thekennelclub.org.uk/media/3467/obedience-show-g-regulations.pdf (accessed March, 2022).

14. Harris H, Birch E, Boyd J. An examination of neck angle in obedience dogs whilst completing competition heelwork. *Comp Exerc Physiol.* (2017) 13:31–6. doi: 10.3920/CEP160023

15. Harris H, Birch E, Boyd J. Human preferences for heelwork positions during UK competitive obedience. *Comp Exerc Physiol.* (2018) 14:199–207. doi: 10.3920/CEP180025

16. Schnabl-Feichter E, Tichy A, Gumpenberger M, Bockstahler B. Comparison of ground reaction force measurements in a population of Domestic Shorthair and Maine Coon cats. *PLoS ONE.* (2018) 13:e0208085. doi: 10.1371/journal.pone.0208085

17. Budsberg SC, Jevens DJ, Brown J, Foutz TL, DeCamp CE, Reece L. Evaluation of limb symmetry indices, using ground reaction forces in healthy dogs. *Am J Vet Res.* (1993) 54:1569–74.

18. Humphries A, Shaheen AF, Gómez Álvarez CB. Biomechanical comparison of standing posture and during trot between German shepherd and Labrador retriever dogs. *PLoS ONE.* (2020) 15:e0239832. doi: 10.1371/journal.pone.0239832

19. Bertram JE, Lee DV, Case HN, Todhunter RJ. Comparison of the trotting gaits of Labrador Retrievers and Greyhounds. *Am J Vet Res.* (2000) 61:832–8. doi: 10.2460/ajvr.2000.61.832

20. Amimoto H, Koreeda T, Ochi Y, Kimura R, Akiyoshi H, Nishida H, et al. Force plate gait analysis and clinical results after Tibial Plateau levelling osteotomy for cranial cruciate ligament rupture in small breed dogs. *Vet Comp Orthop Traumatol.* (2020) 33:183–8. doi: 10.1055/s-0039-1700990

21. Della Valle G, Caterino C, Aragosa F, Micieli F, Costanza D, Di Palma C, et al. Outcome after modified Maquet procedure in dogs with unilateral cranial cruciate ligament rupture: evaluation of recovery limb function by use of force plate gait analysis. *PLoS ONE.* (2021) 16:e0256011. doi: 10.1371/journal.pone.0256011

22. Budsberg SC, Kleine SA, Norton MM, Sandberg GS, Papich MG. Comparison of the effects on lameness of orally administered acetaminophen-codeine and carprofen in dogs with experimentally induced synovitis. *Am J Vet Res.* (2020) 81:627–34. doi: 10.2460/ajvr.81.8.627

23. Amimoto H, Koreeda T, Wada N. Evaluation of recovery of limb function by use of force plate gait analysis after Tibial plateau leveling osteotomy for management of dogs with unilateral cranial cruciate ligament rupture. *Am J Vet Res.* (2019) 80:461–8. doi: 10.2460/ajvr.80.5.461

24. Schwarz N, Tichy A, Peham C, Bockstahler B. Vertical force distribution in the paws of sound Labrador retrievers during walking. *Vet J.* (2017) 221:16–22. doi: 10.1016/j.tvjl.2017.01.014

25. Souza AN, Tatarunas AC, Matera JM. Evaluation of vertical forces in the pads of Pitbulls with cranial cruciate ligament rupture. *BMC Vet Res.* (2014) 10:51. doi: 10.1186/1746-6148-10-51

26. Moreira JP, Tichy A, Bockstahler B. Comparison of the vertical force distribution in the paws of dogs with coxarthrosis and sound dogs walking over a pressure plate. *Animals.* (2020) 10:986. doi: 10.3390/ani10060986

27. Braun L, Tichy A, Peham C, Bockstahler B. Comparison of vertical force redistribution in the pads of dogs with elbow osteoarthritis and healthy dogs. *Vet J.* (2019) 250:79–85. doi: 10.1016/j.tvjl.2019.06.004

28. Palmieri RM, Ingersoll CD, Stone MB, Krause BA. Center-of-pressure parameters used in the assessment of postural control. *J Sport Rehabil.* (2002) 11:51–66. doi: 10.1123/jsr.11.1.51

29. Carrillo JM, Manera ME, Rubio M, Sopena J, Santana A, Vilar JM. Posturography and dynamic pedobarography in lame dogs with elbow dysplasia and cranial cruciate ligament rupture. *BMC Vet Res.* (2018) 14:108. doi: 10.1186/s12917-018-1435-y

30. Pitti L, Oosterlinck M, Díaz-Bertrana ML, Carrillo JM, Rubio M, Sopena J, et al. Assessment of static posturography and pedobarography for the detection of unilateral forelimb lameness in ponies. *BMC Vet Res.* (2018) 14:151. doi: 10.1186/s12917-018-1462-8

31. Reicher B, Tichy A, Bockstahler B. Center of pressure in the paws of clinically sound dogs in comparison with orthopedically diseased dogs. *Animals.* (2020) 10:81366. doi: 10.3390/ani10081366

32. López S, Vilar JM, Rubio M, Sopena JJ, Damiá E, Chicharro D, et al. Center of pressure limb path differences for the detection of lameness in dogs: a preliminary study. *BMC Vet Res.* (2019) 15:138. doi: 10.1186/s12917-019-1881-1

33. Manera ME, Carrillo JM, Batista M, Rubio M, Sopena J, Santana A, et al. Static posturography: a new perspective in the assessment of lameness in a canine model. *PLoS ONE.* (2017) 12:e0170692. doi: 10.1371/journal.pone.0170692

34. Ickenstein GW, Ambach H, Klöditz A, Koch H, Isenmann S, Reichmann H, et al. Static posturography in aging and Parkinson's disease. *Front Aging Neurosci.* (2012) 4:20. doi: 10.3389/fnagi.2012.00020

35. Clayton HM, Nauwelaerts S. Is a single force plate adequate for stabilographic analysis in horses? *Equine Vet J.* (2012) 44:550–3. doi: 10.1111/j.2042-3306.2011.00458.x

36. Asseman F, Caron O, Crémieux J. Is there a transfer of postural ability from specific to unspecific postures in elite gymnasts? *Neurosci Lett.* (2004) 358:83–6. doi: 10.1016/j.neulet.2003.12.102

37. Baratto L, Morasso PG, Re C, Spada G, A. new look at posturographic analysis in the clinical context: sway-density vs. other parameterization techniques. *Motor Control.* (2002) 6:246–70. doi: 10.1123/mcj.6.3.246

38. López S, Vilar JM, Rubio M, Sopena JJ, Santana A, Rodríguez O, et al. Pedobarography: a novel approach to test the efficacy of treatments for lameness; an experience with mavacoxib in dogs with elbow osteoarthritis. *BMC Vet Res.* (2019) 15:193. doi: 10.1186/s12917-019-1946-1

39. Mondino A, Wagner G, Russell K, Lobaton E, Griffith E, Gruen M, et al. Static posturography as a novel measure of the effects of aging on postural control in dogs. *PLoS ONE.* (2022) 17:e0268390. doi: 10.1371/journal.pone.0268390

40. Kul-Panza E, Berker N. Pedobarographic findings in patients with knee osteoarthritis. *Am J Phys Med Rehabil.* (2006) 85:228–33. doi: 10.1097/01.phm.0000200377.52610.cd

41. Truszczyńska A, Trzaskoma Z, Białecki J, Drzał-Grabiec J, Dadura E, Rapała K, et al. The effect of unilateral osteoarthritis of the hip on postural balance disorders. *Hip Int.* (2016) 26:567–72. doi: 10.5301/hipint.5000395

42. Lorbach ER, Webster KE, Menz HB, Wittwer JE, Merory JR. Physiological falls risk assessment in older people with Alzheimer's disease. *Dement Geriatr Cogn Disord.* (2007) 24:260–5. doi: 10.1159/000107101

43. Kido T, Tabara Y, Igase M, Ochi N, Uetani E, Nagai T, et al. Postural instability is associated with brain atrophy and cognitive impairment in the elderly: the J-SHIPP study. *Dement Geriatr Cogn Disord.* (2010) 29:379–87. doi: 10.1159/000255106

44. Nauwelaerts S, Malone SR, Clayton HM. Development of postural balance in foals. *Vet J.* (2013) 198:e70–4. doi: 10.1016/j.tvjl.2013.09.036

45. Cote KP, Brunet ME, Gansneder BM, Shultz SJ. Effects of pronated and supinated foot postures on static and dynamic postural stability. *J Athl Train.* (2005) 40:41–6.

46. Hertel J, Gay MR, Denegar CR. Differences in postural control during single-leg stance among healthy individuals with different foot types. *J Athl Train.* (2002) 37:129–32.

47. Li B, Xiang Q, Zhang X. The center of pressure progression characterizes the dynamic function of high-arched feet during walking. *J Leather Sci Eng.* (2020) 2:1–15. doi: 10.1186/s42825-019-0016-6

48. Waldern NM, Wiestner T, von Peinen K, Gómez Alvarez CG, Roepstorff L, Johnston C, et al. Influence of different head-neck positions on vertical ground reaction forces, linear and time parameters in the unridden horse walking and trotting on a treadmill. *Equine Vet J.* (2009) 41:268–73. doi: 10.2746/042516409X397389

49. Keider S. *Änderung der Extremitätenbelastung beim Fuß gehen in der bei Obedience geforderten Körperhaltung.* New York, NY: Magister Medicinae Veterinariae (2015).

50. Schnabl-Feichter E, Tichy A, Bockstahler B. Evaluation of a pressure plate for detection of hind limb lameness in cats. *PLoS ONE.* (2020) 15:e0231904. doi: 10.1371/journal.pone.0231904

51. Schnabl-Feichter E, Tichy A, Bockstahler B. Coefficients of variation of ground reaction force measurement in cats. *PLoS ONE.* (2017) 12:e0171946. doi: 10.1371/journal.pone.0171946

52. Bieber B, Reicher B, Tichy A, Bockstahler B. Changes in ground reaction forces and center of pressure parameters of paws when wearing dog boots in dogs. *Front Vet Sci.* (2022) 9:906277. doi: 10.3389/fvets.2022.906277

53. Häusler KA, Braun D, Liu N-C, Penrose F, Sutcliffe MP, Allen MJ. Evaluation of the repeatability of kinetic and temporospatial gait variables measured with a pressure-sensitive treadmill for dogs. *Am J Vet Res.* (2020) 81:922–9. doi: 10.2460/ajvr.81.12.922

54. Charalambous D, Strasser T, Tichy A, Bockstahler B. Ground reaction forces and center of pressure within the paws when stepping over obstacles in dogs. *Animals.* (2022) 12:702. doi: 10.3390/ani12131702

55. Strasser T, Peham C, Bockstahler BA, A. comparison of ground reaction forces during level and cross-slope walking in Labrador Retrievers. *BMC Vet Res.* (2014) 10:241. doi: 10.1186/s12917-014-0241-4

56. Roush JK, McLaughlin RM. Effects of subject stance time and velocity on ground reaction forces in clinically normal greyhounds at the walk. *Am J Vet Res.* (1994) 55:1672–6.

57. Hans EC, Zwarthoed B, Seliski J, Nemke B, Muir P. Variance associated with subject velocity and trial repetition during force platform gait analysis in a heterogeneous population of clinically normal dogs. *Vet J.* (2014) 202:498–502. doi: 10.1016/j.tvjl.2014.09.022

58. Conzemius MG, Torres BT, Muir P, Evans R, Krotscheck U, Budsberg S. Best practices for measuring and reporting ground reaction forces in dogs. *Vet Surg.* (2022) 51:385–96. doi: 10.1111/vsu.13772

59. Stadig SM, Bergh AK. Gait and jump analysis in healthy cats using a pressure mat system. *J Feline Med Surg.* (2015) 17:523–9. doi: 10.1177/1098612X14551588

60. Weishaupt MA, Byström A, von Peinen K, Wiestner T, Meyers H, Waldern N, et al. Kinetics and kinematics of the passage. *Equine Vet J.* (2009) 41:263–7. doi: 10.2746/042516409X397226

61. Fernández-Seguín LM, Diaz Mancha JA, Sánchez Rodríguez R, Escamilla Martínez E, Gómez Martín B, Ramos Ortega J. Comparison of plantar pressures and contact area between normal and cavus foot. *Gait Posture.* (2014) 39:789–92. doi: 10.1016/j.gaitpost.2013.10.018

62. Pan X, Bai J, Sun J, Ming Y, Chen L, Wang Z. The characteristics of walking strategy in elderly patients with type 2 diabetes. *Int J Nurs Sci.* (2016) 3:185–9. doi: 10.1016/j.ijnss.2016.05.002

63. Nakhaee Z, Rahimi A, Abaee M, Rezasoltani A, Kalantari KK. The relationship between the height of the medial longitudinal arch (MLA) and the ankle and knee injuries in professional runners. *Foot.* (2008) 18:84–90. doi: 10.1016/j.foot.2008.01.004

64. Johnston SA, Tobias KM, editors. *Veterinary Surgery: Small Animal.* St. Louis: Elsevier (2018).

65. Kirby KA. Biomechanics of the normal and abnormal foot. *J Am Podiatr Med Assoc.* (2000) 90:30–4. doi: 10.7547/87507315-90-1-30

66. Shelburne KB, Torry MR, Steadman JR, Pandy MG. Effects of foot orthoses and valgus bracing on the knee adduction moment and medial joint load during gait. *Clin Biomech.* (2008) 23:814–21. doi: 10.1016/j.clinbiomech.2008.02.005

67. Duarte M, Freitas SM. Revision of posturography based on force plate for balance evaluation. *Rev Bras Fisioter.* (2010) 14:183–92. doi: 10.1590/S1413-35552010000300003

68. Carr BJ, Canapp SO, Zink MC. Quantitative comparison of the walk and trot of Border Collies and Labrador Retrievers, breeds with different performance requirements. *PLoS ONE.* (2015) 10:e0145396. doi: 10.1371/journal.pone.0145396

69. Fischer MS, Lehmann SV, Andrada E. Three-dimensional kinematics of canine hind limbs: *in vivo*, biplanar, high-frequency fluoroscopic analysis of four breeds during walking and trotting. *Sci Rep.* (2018) 8:16982. doi: 10.1038/s41598-018-34310-0

70. Della Valle G, Caterino C, Aragosa F, Balestriere C, Piscitelli A, Di Palma C, et al. Relationship between ground reaction forces and morpho- metric measures in two different canine phenotypes using regression analysis. *Vet Sci.* (2022) 9:325. doi: 10.3390/vetsci9070325

frontiers | Frontiers in Veterinary Science

TYPE Original Research
PUBLISHED 07 March 2023
DOI 10.3389/fvets.2023.1111140

OPEN ACCESS

EDITED BY
Rocio Fernandez-Parra,
Catholic University of Valencia San Vicente Mártir, Spain

REVIEWED BY
Suresh Neethirajan,
Farmworx Research Institute, Netherlands
Madonna Benjamin,
Michigan State University, United States

*CORRESPONDENCE
Falk Mielke
✉ falkmielke.biology@mailbox.org

SPECIALTY SECTION
This article was submitted to Comparative and Clinical Medicine, a section of the journal Frontiers in Veterinary Science

RECEIVED 29 November 2022
ACCEPTED 13 February 2023
PUBLISHED 07 March 2023

CITATION
Mielke F, Van Ginneken C and Aerts P (2023) A workflow for automatic, high precision livestock diagnostic screening of locomotor kinematics. *Front. Vet. Sci.* 10:1111140. doi: 10.3389/fvets.2023.1111140

A workflow for automatic, high precision livestock diagnostic screening of locomotor kinematics

Falk Mielke[1,2]*, Chris Van Ginneken[2] and Peter Aerts[1]

[1]Functional Morphology, Department of Biology, Faculty of Science, University of Antwerp, Antwerp, Belgium, [2]Comparative Perinatal Development, Department of Veterinary Sciences, University of Antwerp, Antwerp, Belgium

Locomotor kinematics have been challenging inputs for automated diagnostic screening of livestock. Locomotion is a highly variable behavior, and influenced by subject characteristics (e.g., body mass, size, age, disease). We assemble a set of methods from different scientific disciplines, composing an automatic, high through-put workflow which can disentangle behavioral complexity and generate precise individual indicators of non-normal behavior for application in diagnostics and research. For this study, piglets (*Sus domesticus*) were filmed from lateral perspective during their first 10 h of life, an age at which maturation is quick and body mass and size have major consequences for survival. We then apply deep learning methods for point digitization, calculate joint angle profiles, and apply information-preserving transformations to retrieve a multivariate kinematic data set. We train probabilistic models to infer subject characteristics from kinematics. Model accuracy was validated for strides from piglets of normal birth weight (i.e., the category it was trained on), but the models infer the body mass and size of low birth weight (LBW) piglets (which were left out of training, out-of-sample inference) to be "normal." The age of some (but not all) low birth weight individuals was underestimated, indicating developmental delay. Such individuals could be identified automatically, inspected, and treated accordingly. This workflow has potential for automatic, precise screening in livestock management.

KEYWORDS

locomotion, kinematics, probabilistic modeling, Fourier Series, precision livestock farming, diagnostics, piglets, low birth weight

1. Introduction

Veterinary diagnostics have struggled with a methodological trade-off between high precision and high through-put. In the era of genomics, proteomics, and the like, the strive for accurate diagnostics of livestock diseases has directed considerable attention to the development of modern laboratory tests (1, 2). Conventional imaging techniques also play a role, but usually require special equipment and measurement techniques [e.g., radiography, microscopy, ultrasound, *cf.* (3)]. These methods are high precision tools, but low through-put or expensive, some potentially invasive, and therefore not generally suitable for broad monitoring of farm animals. On the other hand, computational techniques are increasingly available to mine extensive data sets collected with sensors or cameras for diagnostically relevant signals (4–8). "Precision Lifestock Farming," an application of

integrated management systems, might be the desired economic model. These techniques complement the high precision tools by enabling broad screening and early detection of abnormalities, often preceding manual, veterinary intervention. Precision Lifestock Farming is promising in terms of its impact on animal welfare and economic success, but pitfalls remain (9, 10). The term "precision" might be misleading. In an animal management context, it refers to the availability of individual animal data, and the reduction of inefficient and thereby non-sustainable management. However, in practice, the use of sensors and cameras often still is restricted to superficial measures such as the overall activity or the mere occurrence or frequency of certain behaviors of individuals. For example, in swine farming, conventional video cameras can be used to monitor activity, and reduction can be associated with disease (11–13); specificity and precision of these methods deserve further validation.

One class of behaviors that is typically monitored with such cameras is locomotion. Locomotion involves multiple subsystems, and one of the major challenges is to understand how exactly locomotor patterns are altered by conditions of the animal or by external circumstances. The involved subsystems are the musculoskeletal apparatus, energy supply, metabolism, and multiple levels of neuro-motor control. The kinematic and dynamic measurements obtainable by cameras and measurement equipment represent the collective output of interacting variables of the ensemble of subsystems (14). In normal function, all of them are potentially affected in different, non-trivial ways by characteristics of the animal (15), e.g., age (due to individual development), weight (due to body segment inertia), and size and morphology (due to allometrics in general and specific muscle lever relations in particular). In non-normal conditions or disease, another dimension of complexity is added. In consequence, studying alterations in specific locomotor patterns holds more diagnostic potential than activity measurement alone. Kinematic measurements have enabled the inference of many aspects of the locomotion of domestic animals [e.g., (8, 16–18)]; even individual recognition is possible in well-studied domestic species [e.g., (19, 20)]. However, the cross-influence of the more or less correlated systems and co-variates mentioned above, and thus the superimposed effects of multiple factors, complicate data analysis, and diagnostics. Most studies have relied on derived measures, such as speed or duty factor, as performance indicators, which neglects most of the individual movements of the joints and their temporal orchestration. For precision diagnostics, it would be desirable to have an automated system which tracks the locomotion of an individual, extracts and quantifies kinematics in all available detail, takes into account possible co-factors (such as age, size, and external physical conditions), and compares these observations to a reference for the species. Implicitly, this is what "a medieval husbandman," i.e., a human classifier, would do with "his house cow or sow" (9).

At the technical core of diagnostics is thus a classification problem: finding a diseased subset in a population of observations. Correct classification is complicated when there are multiple influence factors, but even more when the observation is subject to substantial intrinsic variability.[1] Variability is a central feature of motor behavior: even for identical external conditions and in a single individual, it can be noted that "successive movements [...] never exactly repeat themselves" (21). Could a putatively abnormal or pathological behavior actually fall "within the bell curve" of normal variability? How likely is that? Which of the many "input factors" is responsible, and how, for a given (temporary) alteration in the collective output? These analysis questions are common in research on bipeds [e.g., (22–24)] and quadrupeds [e.g., (25–27)], and the solution is not novel. Multivariate models are capable of handling complex situations, given sufficient data. Multivariate *probabilistic* models (see below) are suited to also capture intra-individual variability and yield effect likelihoods. However, the high dimensionality of kinematic data sets, the multi-parameter, multi-level (hierarchical) covariate situations, and the high digitization workload have often been a limiting factor for the generation of quantitative models of vertebrate locomotion (28–30).

Several recent technological advances have enabled researchers to tackle scientific questions on locomotion in a more efficient way. Firstly, the past few years have brought huge leaps in terms of computer vision, deep learning, and thereby semi-automatic video digitization methods (30–34). These tools typically require a manually digitized subset of the data as the "training set" for a neural network, which is then able to digitize further videos in high through-put, hopefully with reasonable accuracy. A second field of technological advance are the aforementioned probabilistic models, which build on an elegant computational implementation of Bayesian theory [Markov Chain Monte Carlo / MCMC sampling, *cf.* (35–37)]. Such models can naturally incorporate hierarchical parameter interrelations and intrinsic variability. The main reason for this is that probabilistic models work on data distributions, and their outcome are distributions and "effect likelihoods," rather than point estimates. This can be informative on an intrinsically varying process such as locomotion (38). Machine learning methods for video digitization are validly advancing to be the standard in kinematic analysis, whereas probabilistic models still lack recognition in the field, despite their potential. To summarize, the mentioned advances in computer vision and statistical modeling enable us to (1) acquire a lot of quantitative data with minimal to no workload, and (2) model them in a suitable way. It would be desirable to adapt those technological advances for veterinary use, generating a classifier which could identify systematic alterations in the locomotion of domestic animals, and thereby enabling the computer-supported diagnostic screening for deficiencies, pathological states, and diseases.

Domestic pigs are a well-studied model system in which scientific interest joins the economic interest of commercial breeding. These animals have been subject to a variety of locomotor studies, including paradigms to test the effects of breed (39), birth weight (40–42), surface friction (43), welfare (44), various pathologies (45–47), and more [*cf.* (8)]. Of particular interest has been the occurrence of a subset of individuals which are born

1 Whether "intrinsic" just describes variability for which no influence factor has yet been determined is a valid, but philosophical question beyond the scope of this study.

with lower weight (LBW, low birth weight) than their "normal" (NBW) littermates. There are multiple standards to classify these birth weight categories, using absolute mass, litter quantile criteria, or asymmetry of body proportions (48–54). A possible cause of low birth weight is intra-uterine growth restriction, and LBW phenotype seems often, but not always, to correlate with low vitality and a reduced chance of survival (55–58). Locomotor maturation after birth is quick (40, 59), yet crushing by the sow constitutes one of the major causes of piglet mortality (60, 61). The likelihood of being crushed is directly reduced by more agile locomotion. Thus, locomotor capabilities are crucial for piglet survival, and delayed development might be fatal.

Previous studies from our group (40, 42) raised the hypothesis that the apparent difference in LBW and NBW individuals can be attributed to delayed development. They measured spatiotemporal gait variables (e.g., stride frequency and distance, speed, duty factor), which are collective variables of the actual kinematics [*cf.* (14, 62, 63)]. This strategy has the advantage that it requires only five landmarks (four limbs, one reference) to be digitized, which used to be a crucial trade-off to handle large data sets. However, the collective variables cannot capture full information on intra-limb coordination (i.e., the relative timing of segmental movements within a limb; as opposed to inter-limb coordination, i.e., the relative timing of the cycling of the different limbs). This complicates disentangling effects such as those of size, age, (birth) weight, and disease. It is expected that animals adapt their gait to the physical constraints of motor behavior, which are depending on the weight and other characteristics of the subject. However, the changes to kinematics might be more subtle, and collective variables might not be altered in a distinct way. For example, an animal might learn to move its joint angles in a more efficient way by adapting clearance to substrate conditions (43), which could in principle be achieved without changing the speed of voluntary locomotion on those substrates. Hence, targeting automated gait analysis and diagnostic classification of swine, it would be desirable to include full kinematic information.

Using the semi-automatic, machine-learning digitization techniques mentioned above, one can extend the analysis of gait variables to quantities of intra-limb coordination with manageable workload. However, using the whole set of raw point coordinates of joint points of interest raises the issue of dimensionality (two to three coordinates per reference point, simply too many data variables). Statistical modeling requires a minimum number of observations for being able to infer effects of the different variables (64–67). The common solution is to reduce the dimensionality with an appropriate transformation. To choose a transformation, it can be exploited that common analysis procedures in locomotor biomechanics require steady state locomotion. "Steady state" implies that the behavior consists of repetitive blocks of kinematics, i.e., stride cycles. And one of the most common sets of techniques in physics and engineering to handle cyclic data is Fourier analysis, or more specifically Fourier Series Decomposition [FSD; (26, 68–72)]. With FSD, joint angle profiles are transformed into their representation in the frequency domain, i.e., an array of harmonics. Some of the characteristics of the profiles (namely mean angle, amplitude, and phase) are more readily captured by those harmonics and can optionally be removed. This is most intuitive in the case of phase: removing phase differences enables a mathematically optimal temporal alignment of the profiles. By isolating the other characteristics, mean and amplitude, the joint angle profiles can be transformed to meaningful quantities such as dynamic posture [mean joint angle and effective range of motion (eROM)], and coordination *sensu stricto* [relative phase/joint timing and residual kinematics, *cf.* (68)]. Harmonics are independent of temporal sampling and duration: the coefficient array is of fixed size, which is useful for subsequent multivariate analysis methods, such as Principal Component Analysis (PCA). Another advantage of this transformation procedure is that it is reversible because all mathematical information is retained in the process (which is not the case when using collective variables alone). This means that joint angle profiles can be reconstructed for any observed or hypothetical point in parameter space, which enables in-sample and out-of-sample predictive sampling.

To summarize, the Fourier Series decomposition provides a mathematically convenient and biomechanically meaningful representation of the kinematic data, which opens up new options for data analysis and modeling.

In this study, we establish a workflow which can be automated and used to identify individual animals locomoting differently from the "normal" reference, based on video recordings, deep learning digitization, mathematical transformations, and probabilistic modeling. A conventional, 2D kinematics data set is extracted with the aid of deep learning tools from lateral videos of walking piglets. By applying multivariate analysis and FSD, we separate spatiotemporal gait variables, dynamic posture, and coordination, and model their relation to subject characteristics (mass, size, age, and birth weight category). Crucially, this constitutes the complete information captured by locomotor kinematics, and all parameters are submitted to an inclusive, probabilistic model. As a test case, we tackle the question of whether low birth weight in domestic piglets is an indication of delayed development, and attempt to quantify the delay with an inverse modeling strategy as follows. Intuitively, and conventionally, joint kinematics are considered the output of the locomotor system. Therefore, conventional statistical models might consider them on the "outcome" side; on the "input" side, the effects of birth weight, age, speed, or other parameters are quantified. Herein, we use a different approach, and invert the model. We construct a probabilistic computer model which describes "age" and other subject characteristics as a function of all available kinematic parameters. The rationale is similar to that in subject recognition tasks: given a certain kinematic profile, can we infer (characteristics of) the subject? We split our data set into birth weight classes (LBW, NBW), and train the model on only the strides from NBW observations. This NBW model is our "kinematic reference" model, quantitatively capturing the expectation of what would be "normal" by inferring the plausible age range for a given kinematic observation. We then use that trained model to compute out-of-sample inference of individual LBW observations.

Our hypothesis is that, if LBW were at the same stage of postnatal locomotor development as their NBW siblings, then the model should accurately infer the age of the LBW animals. Conversely, if the LBW piglets are delayed in development, the model would underestimate their age. Thus, by applying this inverse modeling strategy and comparing the computer-inferred

age to the actual age of the LBW piglets, we can quantify and potentially falsify a hypothesized delay in locomotor development.

The components of this classification workflow are not novel, and commonly used in physics and engineering. We use available machine learning tools to digitize videos, apply a series of well-known transformations, and train a probabilistic model classifier. We demonstrate that a set of individual locomotor events can be used to distinguish individuals which develop slower than expected, in a temporal accuracy of four to eight hours (which is a considerable timespan for neonate animals). These are precise diagnostic measurements, generated at high through-put, with the overall aim of improving animal welfare, all of which is in line with the prototypical ideal of precision livestock farming.

2. Materials and methods

2.1. Data acquisition

Recordings were done at a local farm in Belgium during several trips in October and November 2017. Farrowing was monitored to select Topigs × PIC piglets for another experiment (73). Piglets from selected litters were weighed at birth and numbered with non-toxic skin markers. Low birth weight (LBW) was classified by birth weight quantile [lowest 10% of each litter] and by a maximum mass of (800) g (49–51, 74); all other piglets are assigned the NBW category. At variable time points afterwards [ages (1–10) h], piglets were briefly taken from their pen and brought to a separate room for video recording (see below). Animals were recorded in pairs [as in (38)], which drastically reduced anxiety and increased their motivation to cooperate. A few animals were recorded repeatedly, usually with a changing partner. Animals were ear-tagged and followed up: recording was repeated at approximately 4 and 10 days of age. That data was part of the digitization procedure (i.e., "deeplabcut" network training), but excluded from further analysis (i.e., probabilistic modeling, see below). The subject characteristics documented for analysis are birth weight (continuous, and categories "LBW"/"NBW"), mass at recording, age at recording (i.e., hours since farrowing), sex, and size. The size of the animal was approximated by a Principal Component Analysis (PCA) of digitization landmark distances along all segments ("size PCA," only first PC used, 93% of variability). Size and mass are expected to correlate, yet deviations would indicate animals of particularly slender or rotund habitus. All procedures followed ethical regulations and guidelines, and were approved by the Ethical Committee for Animal Testing of the University of Antwerp, Belgium (ECD 2015-26).

The recording room contained an elevated runway (150 × 50 cm), covered with a rubber mat to increase friction, and visible through a transparent frontal shield. Color videos were recorded (camera model: GC-PX100BE, JVC, Japan) at a temporal sampling rate of 50 frames per second and a spatial resolution of 1,920 × 1,080 pixels (later cropped to 500 pixels height), from a distance at which the field of view would exactly capture the entire runway. A chess board at the back wall enabled spatial calibration. Video surveillance was permanent during the presence of the animals and stopped only in between recording sessions. Animals were able to move freely on the enclosed platform. To stimulate locomotion, the two animals were repeatedly placed on opposite ends of the runway. Gentle tickling on the back and grunting vocalization of the researcher were other successful strategies to induce targeted locomotion in the direction perpendicular to the camera axis. After recording sessions the piglets were returned to their litter and remained with the sow. The workflow herein involved handling of the animals as a consequence of the research setting. However, note that the procedure could easily be automated for continuous data collection by a suitable pen arrangement (8, 27, 75).

2.2. Digitization

We used the software DeepLabCut [DLC, (76)] for digitization of all video material. In addition, a custom made point tracking software (34) was used to generate a training set. In total, our dataset contained 180 videos (more than 11 h, 169 animals) of video. Our goal was to prepare a general DLC network which is capable of automatically tracking piglets at multiple ages, and which can be shared and re-used for subsequent research questions. This is why the full data set was used for digitization and for the calculation of some derived measures (size PCA). However, the analysis focus of this study (see below) was only a subset of the data (i.e., the 58 animals of the youngest age class). The video processing workflow, applied to the full data set, was as follows. To get a balanced training set, one stride of each of the animals was selected, and the video was cut, cropped to runway height, and optionally mirrored horizontally so that movement would always be rightwards. All videos were concatenated and submitted to the DLC training set generation. DLC was set to select 2,552 frames from these videos, which were tracked in an external software and re-imported for training (80% training fraction). Seventeen landmarks (i.e., points of interest or "key-points"; usually joint centers, Figure 1) were digitized, representing all body parts visible on the lateral perspective (head: snout, eye, ear; back line: withers, croup, tail base; forelimb: scapula, shoulder, elbow, carpal/wrist, fetlock, forehoof; hindlimb: hip, stifle/knee, tarsal/ankle, hind fetlock, hindhoof). We selected a "resnet 152" network architecture and trained for 540,672 iterations (16 days of computer workload). The network was then applied to digitize the continuous, full video recordings twice: once in default direction and once horizontally mirrored, because training set was always rightward movement.

The next step is to find the relevant temporal sequences of walking in the continuous videos. Naturally, the trained network would only extract potentially useful landmark traces for episodes which resembled the training set, i.e., in episodes with a piglet moving perpendicular to the image axis, in lateral aspect and rightward direction. We automatically extracted 2,597 of such sequences by filtering for high digitization "likelihood" provided by DLC, low noise (i.e., steady landmark movement) and consistent, plausible landmark distances. We further applied an automatic algorithm to find footfalls and label stride cycles in the candidate episodes (4,730 cycles). This procedure involved a start-end-matching optimization (using Procrustes superimposition) to ensure that strides were indeed cyclical. To further assess digitization quality, gait variables were automatically extracted.

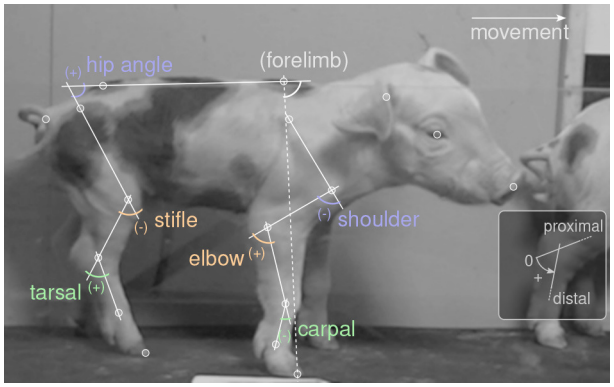

FIGURE 1
Video digitization and joint angle definitions. White circles mark points of interest ("landmarks"). Movement was always rightwards. Labels show joint angles, defined as shown in the inset: straight joint (parallel segments) corresponds to zero; counter-clockwise angles are positive. Forelimb angle was used as a reference for temporal alignment, but did not enter the analysis.

Definition of these variables was chosen to simplify the automatic procedure, as follows. Stride distance, frequency, and speed are trivial measures of the animal movement. Duty factor is available for fore- and hindlimb, and measures the fraction of stride time in which the respective hoof is in ground contact. Clearance is approximated by quantifying the ratio of flexion of each limb (one minus the quotient of minimum and maximum absolute hip-toe-distance during the stride). Head and torso angle are the stride-average angles of the snout-ear or withers-croup lines with respect to the coordinate system. Hindlimb phase measures the time between hind- and forehoof touchdown, divided by the stride cycle duration. Where applicable, gait variables were prepared for analysis (see below) by converting them to dimensionless values (77, 78) using the cumulated distance of landmarks along the snout-to-tailbase line of the animal as reference, extracted as stride average from the digitized landmarks. Only strides with plausible values (i.e., those which lie within the theoretical distribution of each parameter; 1,862 cycles) where processed. Manual inspection further boiled down the data set to 897 stride cycles (the others excluded for digitization errors, multi-animal confusion, non-walking gait, intermittent or sidewards locomotion, or incompleteness).

Finally, 368 of the remaining strides from 58 animals were in the youngest age category (<10 h) and thus selected for the present analysis, the data table is available online (see below).

2.3. Data processing

The landmark data provided by DLC was further processed for analysis. Python code for the whole procedure is available (https://git.sr.ht/~falk/piglet_fcas, Python version 3.10.8 at time of model calculation, https://www.python.org). First, joint angle profiles (i.e., joint angle values over time) were extracted for all relevant joints and for the total forelimb angle (croup-withers-hoof). Shoulder, elbow, carpal, hip, stifle, and tarsal were the six joints sufficiently well-digitized and therefore considered relevant for analysis. We then applied Fourier Series decomposition in the framework we previously termed Fourier Coefficient Affine Superimposition [FCAS, (68)], a flexible procedure which subsumes the following steps. Joint angle profiles are cyclic, i.e., periodical, and can therefore be transformed to the frequency domain with a Fourier Series decomposition (eight harmonics were deemed sufficient by visual comparison of raw and transformed/retransformed profiles). In the frequency domain, the affine components (mean, amplitude, phase) of a joint angle profile are easily accessible [*cf.* (68)]. The forelimb angle served as reference to temporally align all cycles in the data set (removal of phase differences between different cycles; forelimb angle was not used further). Then, mean and amplitude of the joint oscillations were isolated for all joint angles and are categorized as "dynamic posture" parameters. Mean joint angle is the temporal average, whereas amplitude is related to effective range of motion (eROM). The residual, i.e., differences captured by non-affine Fourier coefficients, can be categorized as "coordination" *sensu stricto* (it measures the precise temporal succession of joint configurations). In our case, there were 96 variables of coordination (six angles, eight harmonics, real and imaginary) which were submitted to a PCA. Only the first 12 coordination components (*CC*) were used for statistical analysis, capturing 80.2% of the variability in coordination.

To summarize, FSD and FCAS served three purposes: (i) temporal alignment of the cyclic traces, (ii) separation of meaningful parameter categories (dynamic posture and coordination), and (iii) preparation for multivariate analysis *via* PCA. Basic script code (Python, Matlab, and R) to perform FCAS can be found on a dedicated git repository (https://git.sr.ht/~falk/fcas_code).

Information retention is generally a strength of this method. FCAS and PCA are mathematical transformations, which means that the information content after transformation is theoretically identical to that prior to transformation (theoretically, because only a finite number of harmonics can be used, yet this is of little concern for continuous, smooth joint angle profiles). The neglected PCs and the residual not captured by eight harmonics were the only information from kinematics of the given joints to be lost in this procedure, and by definition these contain the least information. Apart from that, all information present in the raw joint angle profiles enters the analysis. Though we used a 2D dataset herein, the procedure could be applied equally well to angles measured from 3D coordinate data (79).

Furthermore, all transformations are reversible, hence any analysis outcome can be translated back to kinematics with high accuracy. Reversibility bares a lot of herein unused potential, for example for interpolating unobserved subject states or for inferring kinematics of fossil species by phylogenetic and morphometric bracketing. Reversibility can also be of use when presenting raw joint angle profiles and their averages, as follows. One crucial aspect of the FCAS procedure is temporal alignment of the joint angle profiles in the frequency domain. In conventional temporal alignment, a single characteristic point in the stride cycle is chosen as a reference, wherein this is only "characteristic" for a certain part of one limb (e.g., left hindlimb hoof touchdown). Temporal alignment to the hindhoof touchdown might cause distinct peaks in the forelimb angle joint profiles to occur at

different relative points in the stride cycle (e.g., tarsal joint profiles in Figure 3 below, lower half, green traces). If profiles show such variable peak positions, then their average will have a wider, less pronounced (i.e., lower amplitude), and potentially unnatural peak. For illustration, this is analogous to averaging two sine-waves of identical amplitude, but phase shifted: in the worst case, they cancel each other out (as in "destructive interference"). The problem is not restricted to pronounced peaks, but generally occurs if the temporal intra-limb coordination varies within a data set. Using FCAS, it is possible to get a more representative average of the raw traces which has its amplitude conserved, but phase and mean angle averaged. This is enabled by transformation to the frequency domain, separation of affine components, removal of phase differences by shifting to average phase, profile averaging, followed by inverse transformation back to the time domain. Because a set of profiles and phases may be calculated for each angle individually, and because phase relations can differ between joints, there are the options to align based on one reference angle (e.g., the whole forelimb, as done herein) or minimize all phase differences across all joints. Choosing the first option herein has implications: when plotting hindlimb joints aligned by a forelimb reference (as in Figure 3, lower half), phases still differ, and the "destructive interference" problem might hamper averaging. In such cases it is possible to apply an extra, joint-wise FCAS alignment for the sole purpose of generating meaningful averages.

2.4. Statistical modeling

To summarize, four categories of variables were used for analysis:

- subject characteristics: age, sex, mass, birth weight category, size
- spatiotemporal gait variables: distance, frequency, speed, clearance (fore-/hindlimb), duty factor (fore-/hindlimb), head angle, hindlimb phase
- dynamic posture: mean joint angles and eROM for six joints
- coordination: the residual after extraction of dynamic posture (see above).

Our guiding question for model design is whether a probabilistic, linear model is able to infer subject characteristics (specifically: age, mass, and size) from raw kinematics (expressed as dynamic posture and coordination) and gait variables (collective variables). Given the common conception that kinematics are a complex output of an individual motor system, this might be considered an "inverse" modeling approach. The present analysis focused on three outcome variables (Figure 2): mass (*kg*), size (*arb. units*, from a PCA of marker distances), and age (*h*). Though these outcome variables were specific per individual and recording session, we analyzed them "per stride" (i.e., there were multiple strides with identical subject measures on the outcome side).

The model formula is:

$$\theta \sim \nu_1 \cdot \alpha + \nu_s \cdot \beta_s + \sum_G \nu_g \cdot \beta_g + \sum_P \nu_p \cdot \beta_p + \sum_C \nu_c \cdot \beta_c + \nu_1 \cdot \epsilon \quad (1)$$

Herein, θ is either of the outcome subject characteristics, β are slopes associated with the model parameters (s sex, G gait variables, P dynamic posture, C coordination), ν are data vectors (e.g., ν_1 is a vector of ones for the intercept α and model residual ϵ, and ν_s is a boolean vector coding for subjects of "sex == male"). The models have a total number of 36 degrees of freedom. Priors (i.e., *a priori* assigned distributions) for all slopes were Normal distributions with mean and standard deviation corresponding to the mean and two times standard deviation of all observed values of each parameter; logarithmic transform was applied where necessary. The observable ("likelihood") prior for θ was a Student's t-distribution (allows for wider-than-normal tails and robust regression) with a Gamma distributed ν (degrees of freedom); ϵ was modeled to be a Half Cauchy distribution. The model was implemented using the Python library "PyMC" [version 4.2.2, (80)].

To re-emphasize, dynamic posture and coordination together effectively capture all the kinematic information of the stride. Hence, we train the predictor model with all kinematics, gait variables, and sex. Birth weight category (LBW, NBW) is a filter parameter: we split our data set into LBW strides and two NBW subsets (training and validation). Training is performed by MCMC sampling ("sample" function in PyMC), and a No U-Turn sampler was set to sample with 32 chains, each 2^{14} tuning and equally many sampling steps. All *post-hoc* model checks confirmed convergence (inspection of traces, $bfmi > 0.94$ for all chains, Gelman-Rubin statistics ≈ 1 for all parameters, sufficient effective sample size). Model comparison was performed, iteratively leaving out model parameters or replacing some by meaningful combinations (e.g., duty factor combined for fore- and hindlimb). However, because we follow an "all in" strategy, the results have little instructive value for model construction: we might thus have retained parameters which are numerically unimportant for the NBW-only models.

The data set of N=368 strides was split into three categories: (i) the NBW training set as reference with N=294 strides, (ii) the NBW validation set (N=35 strides), which is a random subset of NBW strides, approximately equal in size to (iii) the LBW test set with N=39 strides.

The model was thus trained with a set of 294 NBW training strides (i). Inferences (model "predictions") were then done per stride, for all observed strides (NBW training, NBW validation, and LBW test), iteratively using the "pymc.sample_posterior_predictive" function in PyMC after setting all the data arrays to the actual observed values for one given stride (using "pymc.set_data"). The number of predictions usually matches the number of training samples, which means that all posterior information is used to construct the prediction distributions. We would thus retrieve mass, size, and age predictions (i.e., probabilistic inference) for each stride in the data set, which were then compared to the known, actual mass, size, and age.

All procedures, code, data, and this manuscript are available online (https://git.sr.ht/~falk/piglet_fcas).

3. Results

The present analysis is centered around a linear model which is designed to infer mass, size, and age (subject characteristics)

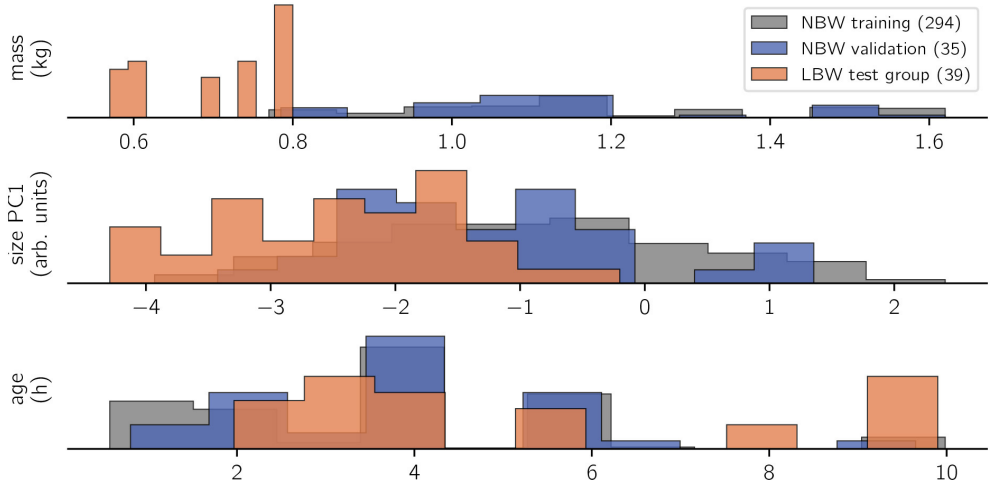

FIGURE 2
Histogram of observations. Trivially, the LBW group measured the lowest body masses in the data set. This correlated with a lower body size, whereas age is rather uniformly sampled for all study groups. Recordings happened opportunistically within the first 10 life hours of the animals, repeated measurements were possible. Number of strides per class are indicated in brackets on the legend. Bar heights are scaled by sample size to show relative value distributions.

from an extensive set of kinematic parameters from 2D videos. The numbers provided by the model sampling are equally extensive, and will only be reported in brief. The key purpose of the model is posterior predictive sampling of the LBW strides which were left out of the model, and which are analyzed in detail below.

To assess whether there are qualitative differences between the birth weight categories, one can compare the joint angle profiles (i.e., raw, angular kinematics) on which the present analysis was performed (Figure 3). The intra-group variability clearly exceeds the differences between groups, although it must be emphasized that groups are inhomogeneous (with regard to age, speed, etc.), which might lead to a bias if composition of LBW and NBW data differs. Low birth weight piglets walk with a more flexed hindlimb posture, as indicated by the parallel offset average hip, stifle, and tarsal profiles. Additionally, NBW individuals on average seem to set the shoulder at a more extended angle. No differences in coordination are apparent (which would manifest in altered temporal structure of the profiles). These findings indicate that LBW kinematics are hardly distinguishable from NBW kinematics by qualitative, visual assessment, which is at least in part be due to high variability.

A quantitative comparison of variable kinematic measurements can be achieved with probabilistic linear models. For the purpose of predictive sampling (see below), we train models to describe the interrelations of kinematic parameters and subject characteristics in NBW piglets. The outcome of MCMC sampling of a linear model are value distributions for slopes, which in our case indicated how certain kinematic parameters are associated with a change in mass, size, and age (Supplementary Table S1). Of the gait- or coordination parameters, only hindlimb clearance was correlated with differences in animal mass. Mass was also associated with changes in the dynamic posture of the hip and tarsal. For size, the model inferred associations with head angle, hindlimb duty factor and clearance, and one coordination component (CC3), as well as changes in the fore- and hindlimb posture and an effect of sex. Finally, age was associated with an increase in forelimb clearance, potential changes at the hip and carpal, and several coordination components (CC9, CC11). Some eROM slope distributions for age were high in average magnitude, but variable (the "credible interval" contained zero). These model results provide detailed insight into parameter interrelations in the present data set and indicate which of the parameters are the relevant ones to infer a given subject attribute in predictive sampling.

Performing in-sample and out-of-sample predictive inference with the models trained on NBW strides elucidated if and how left-out strides differed from NBW model expectation (Figure 4). Note that, to capture variance (i.e., uncertainty in the prediction), each stride was sampled repeatedly.

Out-of-sample inferences for the *NBW validation set* matched those of in-sample NBW inference in terms of average values and standard deviation for all modeled outcome variables, which confirms that inference of subject characteristics from kinematics is possible. In contrast, inferences for *LBW strides* did not match those of the NBW training set. Low birth weight animals were inferred to be on average 0.44 kg heavier than actual, and their size was overestimated (+ 1.71 units). Both faults matched the actual differences in magnitude (*cf.* methods, Figure 2). In contrast, the age inference for the low birth weight subjects were not normally distributed: most ages were correctly inferred from stride-wise kinematics, but ages for some strides were underestimated. The underestimation of those strides quantified to just below 5 h.

In summary, the NBW-trained model "guesses" the size and mass of the animals producing LBW strides to be "normal" (although they are not), which indicates that these defining features of LBW do not reflect in altered kinematics. However, age inference is non-normal, i.e., some strides are classified as typical for animals of younger than actual age.

To find out whether the offset age inference was related to certain individuals, or certain strides from different individuals,

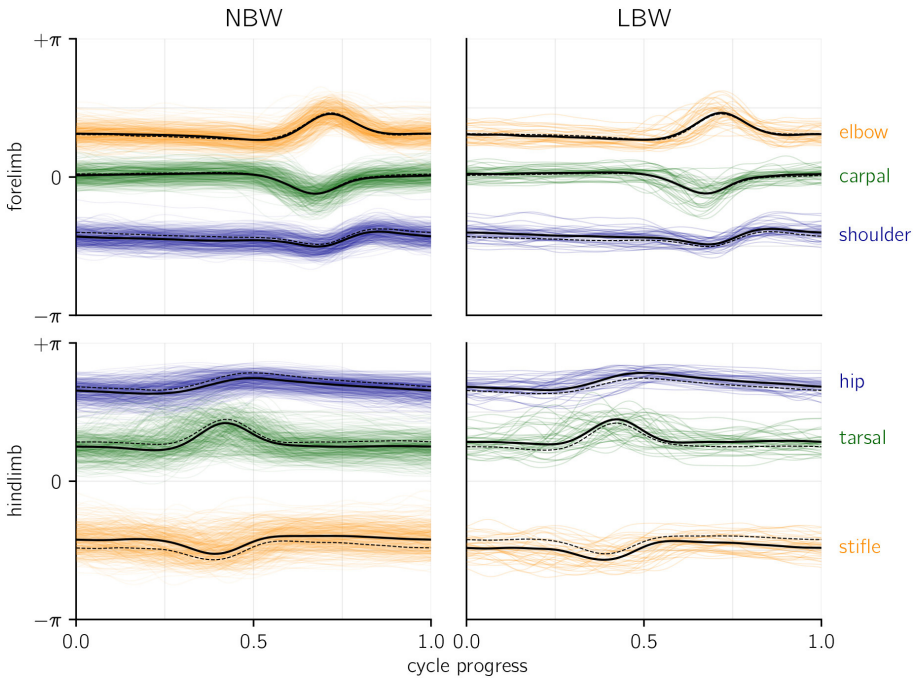

FIGURE 3
Joint angle profiles per joint, grouped by birth weight category. An angle of zero would be a fully extended (i.e., straight) joint. Thick lines represent the average profiles, dashed lines indicate the average of the opposite birth weight group for comparison. Colored, shaded lines show all raw profiles available for the present analysis. Temporal alignment was done based on total forelimb angle (see methods), yet for the shown hindlimb averages (but not for the raw profiles), a separate alignment of the hindlimb was performed.

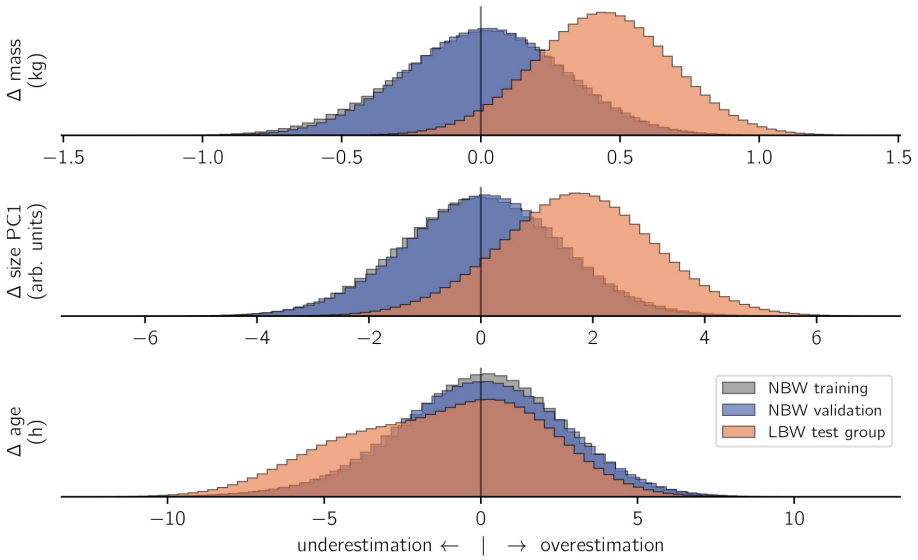

FIGURE 4
Model inference. For all included subject characteristics, models which were trained on NBW strides correctly inferred the training data (gray) and values from the validation set (blue). In contrast, the same models wrongly inferred the characteristics of LBW subjects (orange). The *x*-axes show the difference (Δ) between actual and predicted values per prediction. To facilitate comparison, histogram heights are again normalized per category.

we grouped the inferences per stride or subject and calculated the chance of over- or underestimating age. Of the 8 low birth weight subjects who contributed 39 strides, 4 individuals were consistently underestimated (Table 1). Consistently means that more than 75% of all predictive samples were below actual age, and that the ages for a majority of strides were on average underestimated. The magnitude of underestimation was between 2 and 5 h. Curiously, those were the individuals recorded at a slightly higher age (>5 h). Overestimation in the other four LBW individuals was also consistent, but less so (less extreme

TABLE 1 Age inference per LBW animal (compared to NBW average, last row).

Piglet	Age h	Strides	Underestimation count	Underestimation ratio	Pred. mean Δ h	Pred. std h
b23	2.0	6	0	0.29	1.13	2.00
b15	2.9	5	0	0.37	0.68	1.96
b76	3.1	4	0	0.39	0.57	2.01
b74	4.2	7	1	0.40	0.52	1.97
1794.5	5.6	5	5	0.90	-2.57	1.99
b58	7.8	3	3	0.91	-2.85	2.00
b19v2	9.8	1	1	1.00	-6.14	1.99
b56	9.9	8	8	0.99	-4.58	1.96
All NBW	< 3.8 >	329	158	0.49	-0.03	1.95

Δ, "inferred - actual" difference. Underestimation is defined as $\Delta < 0$, "count", per stride; "rate", per predictive sample; *h*, hours; *std*, standard deviation.

underestimation rate, mean $\Delta < 2\ h$). Standard deviation of the estimates did not vary across individuals or birth weight categories.

We conclude that underestimation of age is consistent over multiple strides of the same individual, and thus individual-specific.

4. Discussion

Quadruped terrestrial locomotion is the collective output of an ensemble of organismal subsystems, which is both reason and challenge for its usefulness in veterinary diagnostics. On one side, the kinematics can be quantified in multidimensional data sets, capturing the many degrees of freedom of the limb joints. On the other side, kinematic quantities are context dependent and affected by numerous subject characteristics (age, weight, pathologies, …) which also cross-influence each other. The challenge emerges to find the right trace of a given (or unknown) condition in the multidimensional observation on the background of kinematic variability. Deep Learning methods for video digitization have become available, and probabilistic computational models offer a flexible framework to mirror complex parameter relations. Once trained to a given question, these computer tools can achieve comparative diagnostic classification with minimal human interaction, e.g., for continuous screening in a farm setting. Multivariate systems have been a challenge to integrated management and precision farming, and the presented locomotor analysis workflow highlights a possible way to succeed in that challenge.

In this study, we have demonstrated a test case for generating a probabilistic model of piglet locomotion which incorporates all kinematic information.

Our example model was trained on a high number of observations which are considered "normal," and applied to classify untrained observations in terms of deviation from normal behavior. The data stems from laterally filmed videos of normal (NBW) and low birth weight (LBW) piglet locomotor behavior from unrestricted walking gait (an inexpensive, high-throughput arrangement, and a common behavior). Low birth weight is often associated with low vitality (55–57), and this supposedly correlates with deficient locomotion. Hence, the obvious first research question is whether birth weight has an influence on the locomotor behavior. Top-down, direct, visual assessment could justify the hypothesis that LBW walking kinematics are somehow different from "normal" (81). Yet that is (i) hard to assess due to high behavioral variability and (ii) trivially expected given the adaptation to different physical properties of their body: gravitational force is a predominant constraint of locomotion, and it simply scales with animal weight. Our results showed that the eight LBW individuals we submitted to the weight-kinematics model were all over-estimated in terms of their weight, by the amount that matched LBW–NBW weight difference (Figure 4). The same is true for the size model. This indicates that LBW, at least all those in our data set, are capable of walking as if they were of normal birth weight and size. This is the first example of a diagnostic model application: the model confirms quantitatively normal locomotor behavior despite occurrence of a given non-normal co-variate (weight).

A second diagnostic application is the identification of individuals (or even strides) which systematically deviate from an expectation or norm. Probabilistic models do not only classify "normal" or "not": they yield a distribution of plausible values, and thereby a likelihood that a given observation is indicative of a problem. The same model architecture as above, but configured to infer age from a kinematic measurement, estimated some (but not all) individuals to be of lower than actual age (Table 1). Those were specifically the older of the LBW individuals, whereas the youngest ones (<4 h) walked as expected for neonates. Though we cannot fully rule out chance with our limited sample size, this provides evidence that the quick postnatal development was halted in those individuals. Our interpretation is that, at birth, LBW individuals putatively had the same capabilities as their NBW siblings, yet at least some "fell behind" regular development in the first hours. We can think of two possible reasons for this: (1) the birth process as a trauma might mask the actual capabilities of all neonates alike, concealing actual, pre-existing differences (74); (2) development is impeded by depleted energy reserves and a failure in (kin) competition and the perinatal struggle for teats and warmth (82). We found little support for the first possible reason:

top-down locomotor development is quick for both groups (40, 41), and muscular architecture shows no differences (83). On the other hand, there is evidence for quick depletion of energy levels in the low birth weight individuals, which rectifies within a period of 10 h (84). This finding is consistent with the present study and supports the perinatal struggle hypothesis. Delayed development does not necessarily corroborate the hypothesis of locomotor deficiency in LBW. We would expect truly deficient strides to be substantially different from the data trained to the model, thus be either excluded or misclassified. Exclusion means that the used Deep Learning implementation could not capture deficient strides, or only in a way which led to exclusion in subsequent (automatic) quality checks (see below). We acknowledge that there currently still is room for refinement in the Deep Learning digitization procedure. Yet in the likely case that some deficient strides passed quality checks and were subjected to the model, we would expect them to be more "unpredictable" (i.e., higher variance of posterior samples). Instead, in our data set, inferences were consistent for repeated measures of an individual, without notable increase in variance across inferences per stride. For the affected subjects, we can even quantify a plausible delay of less than 5 h, which could nevertheless be critical given the rapid maturation of locomotor behavior in this species (40) and the importance of postnatal competition. Such detailed information is valuable when evaluating the success of different mitigation strategies [e.g., supplementing energy to piglets, (85)]. It must be emphasized that, just like other computational diagnostic tools, the method outlined herein is not intended for standalone use. Instead, it is complementary to or can facilitate the in-depth inspection. Nevertheless, the specificity of the presented gait analysis supersedes mere activity analysis: to our knowledge, being able to automatically retrieve an individual, probabilistic measure for developmental delay in swine has not been achieved before. Information retention is a feature of the presented workflow which we think can enable researchers and veterinaries to differentiate a multitude of potential influences on locomotor behavior, given sufficient reference data and an appropriate model design.

These observations are specific to the present test case, and the question remains whether the method is generally suited to diagnose animal pathologies. In the proposed workflow, data transformations (e.g., Fourier Series, PCA) are preparing the kinematic data for diagnostics. Diagnostics are the classification of "non-normal" observation, herein achieved by comparison of the probabilistic predictive samples and the actual observation (Figure 4 and Table 1). In the present example, there is no pathology, which was surprising to us: when observing NBW and LBW piglets (human classifier), one tends to see differences in how they walk. However, there are confounding factors: first and foremost, their weight and body proportions, age (locomotor maturation), sex, etc. In other words: they walk differently, but this is expected, given the biomechanical and physical constraints of the phenomenon. These are general complications in diagnostics. Our models provide evidence that, when accounting for potentially confounding factors (e.g., by working on "dynamically similar" joint angle profiles), no difference remains. Given the high level of detail that could be extracted for the present case, we would expect it to be as accurate as a human classifier in cases where pathologies can be visually identified. Whether the workflow could even outperform human diagnosis in other cases, for example because confounding factors are accounted for, remains to be evaluated.

There are other limits imposed by the present test case. Our data set is limited and potentially biased in terms of LBW observations. There are much fewer valid LBW strides in our data set, in absolute numbers: only 39 of 368 observations are LBW. This could be interpreted as evidence for a lower capacity (despite equal potential) of LBW to produce normal locomotion. Yet there are proximal, trivial explanations: for this study, the 10% lower quantile of birth weights in a litter is considered LBW, and there is a hard cap of 800 g. The resulting share is equal in our training set for video digitization, and in the final data set, because of pseudo-random, opportunistic sampling on-site (i.e., recording work was permanent, yet determined by farrowing and feeding of the subjects). The minority of LBW training videos might lead to an under-learning of those animals in the digitization network, which could lead to reduced digitization quality and therefore an exclusion bias for "non-normal" individuals. Though it seems unlikely, we cannot rule out reduced locomotor capacity in LBWs: the present data set is unsuited to count the occurrence of locomotor behavior due to its automatic generation. On the other hand, the strict stride filtering criteria for "good" kinematics may have involuntarily filtered out deficient individuals. Our conclusion that low birth weight individuals are non-deficient is strictly tied to the definition of the low birth weight category, which is herein based on weight criteria and did not regard phenotypical indicators of intra-uterine growth restriction [which we did not record, *cf.* (54)].

A corollary question is which patterns in the kinematic variables cause the different age inferences. We report high magnitude (but also highly variable, i.e., "non-significant") slopes inferred from the age model (Supplementary Table S1). Note that these slopes solely reflect effects within the NBW data subset. We also observed slight differences in the average hindlimb dynamic posture (Figure 3). In fact, a more flexed hindlimb is typical for the youngest animals of both birth weight categories. We emphasized potential differences in group composition to explain that (e.g., sex effect in the "size" model), and different age per group might be a proximal explanation for the non-normal age inference in LBW. However, the average age of LBW animals (5.3 h) in our data set is nominally above that of NBW (3.8 h), which is a discrepancy with the age underestimation. Yet if we assume that the hypothesis of delayed locomotor development is correct, the nominal age would be misleading, and LBW effectively behave similar to younger animals. This can explain the apparent discrepancy in age group composition and age inferences from kinematics. It also suggests that dynamic posture might be the major proxy for perinatal maturation, though many other parameters also entered the probabilistic model and influenced the model outcome.

To summarize, we herein assembled state-of-the-art computer techniques for the purpose of individual diagnostics in quadruped locomotion, which we think constitute a valuable workflow for livestock screening and management. All components require some manual and computational efforts for initialization (network training, model regression). However, once that is done, the workflow is as follows:

- generate more video recordings (e.g., in an instrumented runway)
- apply the trained Deep Learning network for automated digitization
- identify stride cycles (automatic with framewise Procrustes comparison)
- stride cycle quality filtering by automatic criteria (end-start difference, constant speed, . . .)
- Fourier Series decomposition, temporal alignment, and parameter transformation (PCA)
- probabilistic classification (i.e., posterior predictive sampling) with an inverted model structure
- validation of above-threshold classifications.

Except for the last (crucial) step, all of this can be fully automated, and the whole workflow is readily available for precision livestock farming. Modules of the workflow can be altered: for example, Probabilistic Deep Learning models could be applied instead of the currently implemented classification. Monitoring can happen automatically [as in (8, 74)], which reduces delay in identifying individuals in need of intervention. Multiple models can be tested in parallel: in the present test case, the "weight" and "size" models found LBW locomotion indistinguishable from the "normal" reference group, whereas the "age" model specifically identified those animals which likely experience a delay in locomotor development. Likewise, tests for specific diseases could be set up. A more extensive (longitudinal) data set and more specific models are required to bring this tool into "clinical" or economical/commercial use, and one purpose of the present study was also to give sufficient explanations and references for readers unfamiliar with the mentioned methods. Nevertheless, we demonstrated that the modeling workflow is able to provide a high precision, high throughput method for domestic pig locomotor diagnostics.

Data availability statement

The datasets presented in this study can be found in online repositories. The names of the repository/repositories and accession number(s) can be found below: git repository https://git.sr.ht/~falk/piglet_fcas.

Ethics statement

The animal study was reviewed and approved by Ethical Committee for Animal Testing of the University of Antwerp, Belgium (ECD 2015-26). Written informed consent from the owners for the participation of their animals in this study was not required in accordance with the national legislation and the institutional requirements. Naturally, the owner of the animals was consulted on this application. The Ethics Committee on animal experimentation has indicated that no additional and specific requests were needed including that no consent was to be filled out. Moreover, biosecurity on a pig farm is strict, which means that any access to the farm must be approved and checked. Therefore, because we were able to carry out the in the manuscript mentioned on-site observations, the owner declares his agreement with the procedures and use of the piglets.

Author contributions

FM acquired and analyzed the data and wrote the initial draft of the manuscript. All authors conceptualized the study and refined the manuscript. All authors contributed to the article and approved the submitted version.

Funding

This study was funded by a grant from the special research fund of the University of Antwerp (BOF-GOA 2016 33927).

Acknowledgments

The authors would like to thank Miriam Ayuso for organizing and participating in the recording sessions, as well as Laura Buyssens, Georgios Petrellis, Gunther Vrolix, Charlotte Vanden Hole, Denise Vogel, and all students who joined for help during recordings. Maja Mielke provided valuable comments on the manuscript text.

Conflict of interest

The authors declare that the research was conducted in the absence of any commercial or financial relationships that could be construed as a potential conflict of interest.

Publisher's note

Supplementary material

The Supplementary Material for this article can be found online at: https://www.frontiersin.org/articles/10.3389/fvets.2023.1111140/full#supplementary-material

References

1. Howson ELA, Soldan A, Webster K, Beer M, Zientara S, Belak S, et al. Technological advances in veterinary diagnostics: opportunities to deploy rapid decentralised tests to detect pathogens affecting livestock. *Rev Sci Tech.* (2017) 36:479–98. doi: 10.20506/rst.36.2.2668

2. Lamy E, Mau M. Saliva proteomics as an emerging, non-invasive tool to study livestock physiology, nutrition and diseases. *J Proteomics.* (2012) 75:4251–8. doi: 10.1016/j.jprot.2012.05.007

3. Yitbarek D, Dagnaw GG. Application of advanced imaging modalities in veterinary medicine: a review. *Vet Med.* (2022) 13:117. doi: 10.2147/VMRR.S367040

4. Neethirajan S. The role of sensors, big data and machine learning in modern animal farming. *Sens Bio Sens Res.* (2020) 29:100367. doi: 10.1016/j.sbsr.2020.100367

5. Wurtz K, Camerlink I, D'Eath RB, Fernández AP, Norton T, Steibel J, et al. Recording behaviour of indoor-housed farm animals automatically using machine vision technology: a systematic review. *PLoS ONE.* (2019) 14:1–35. doi: 10.1371/journal.pone.0226669

6. Piñeiro C, Morales J, Rodríguez M, Aparicio M, Manzanilla EG, Koketsu Y. Big (pig) data and the internet of the swine things: a new paradigm in the industry. *Anim Front.* (2019) 9:6–15. doi: 10.1093/af/vfz002

7. Gómez Y, Stygar AH, Boumans IJMM, Bokkers EAM, Pedersen LJ, Niemi JK, et al. A systematic review on validated precision livestock farming technologies for pig production and its potential to assess animal welfare. *Front Vet Sci.* (2021) 8:660565. doi: 10.3389/fvets.2021.660565

8. Netukova S, Duspivova T, Tesar J, Bejtic M, Baxa M, Ellederova Z, et al. Instrumented pig gait analysis: state-of-the-art. *J Vet Behav.* (2021) 45:51–9. doi: 10.1016/j.jveb.2021.06.006

9. Wathes CM, Kristensen HH, Aerts JM, Berckmans D. Is precision livestock farming an engineer's daydream or nightmare, an animal's friend or foe, and a farmer's panacea or pitfall? *Comput Electr Agric.* (2008) 64:2–10. doi: 10.1016/j.compag.2008.05.005

10. Azarpajouh S, Díaz JAC, Taheri H. Precision livestock farming: automatic lameness detection in intensive livestock systems. *CABI Rev.* (2020). doi: 10.1079/PAVSNNR202015031

11. Fernández-Carrión E, Martínez-Avilés M, Ivorra B, Martínez-López B, Ramos AM, Sánchez-Vizcaíno JM. Motion-based video monitoring for early detection of livestock diseases: the case of African swine fever. *PLoS ONE.* (2017) 12:e0183793. doi: 10.1371/journal.pone.0183793

12. Benjamin M, Yik S. Precision livestock farming in swine welfare: a review for swine practitioners. (2019). *Animals (Basel).* (2019) 9:133. doi: 10.3390/ani9040133

13. Vranken E, Berckmans D. Precision livestock farming for pigs. *Anim Front.* (2017) 7:32–7. doi: 10.2527/af.2017.0106

14. Nishikawa K, Biewener AA, Aerts P, Ahn AN, Chiel HJ, Daley MA, et al. Neuromechanics: an integrative approach for understanding motor control. *Integr Comp Biol.* (2007) 47:16–54. doi: 10.1093/icb/icm024

15. Young JW, Shapiro LJ. Developments in development: What have we learned from primate locomotor ontogeny? *Am J Phys Anthropol.* (2018) 165:37–71. doi: 10.1002/ajpa.23388

16. Schlageter-Tello A, Bokkers EAM, Groot Koerkamp PWG, Van Hertem T, Viazzi S, Romanini CEB, et al. Manual and automatic locomotion scoring systems in dairy cows: a review. *Prevent Vet Med.* (2014) 116:12–25. doi: 10.1016/j.prevetmed.2014.06.006

17. Serra Bragança FM, Rhodin M, van Weeren PR. On the brink of daily clinical application of objective gait analysis: What evidence do we have so far from studies using an induced lameness model? *Vet J.* (2018) 234:11–23. doi: 10.1016/j.tvjl.2018.01.006

18. Qiao Y, Kong H, Clark C, Lomax S, Su D, Eiffert S, et al. Intelligent perception-based cattle lameness detection and behaviour recognition: a review. *Animals.* (2021) 11:3033. doi: 10.3390/ani11113033

19. Figueiredo J, Santos CP, Moreno JC. Automatic recognition of gait patterns in human motor disorders using machine learning: a review. *Med Eng Phys.* (2018) 53:1–12. doi: 10.1016/j.medengphy.2017.12.006

20. Patua R, Muchhal T, Basu S. Gait-based person identification, gender classification, and age estimation: a review. In: Panigrahi CR, Pati B, Mohapatra P, Buyya R, Li KC, editors. *Progress in Advanced Computing and Intelligent Engineering*. Singapore: Springer Singapore (2021) p. 62–74.

21. Bernstein NA. Chapter II: The problem of the interrelation of co-ordination and localization. *Adv Psychol.* 17:77–119. doi: 10.1016/S0166-4115(08)61370-9

22. Ganley KJ, Powers CM. Gait kinematics and kinetics of 7-year-old children: a comparison to adults using age-specific anthropometric data. *Gait Posture.* (2005) 21:141–5. doi: 10.1016/j.gaitpost.2004.01.007

23. Stiffler-Joachim MR, Wille C, Kliethermes S, Heiderscheit B. Factors influencing base of gait during running: consideration of sex, speed, kinematics, and anthropometrics. *J Athl Train.* (2020) 55:1300–6. doi: 10.4085/1062-6050-565-19

24. Bruton MR, O'Dwyer N, Adams R. Sex differences in the kinematics and neuromuscular control of landing: Biological, environmental and sociocultural factors. *J Electromyogr Kinesiol.* (2013) 23:747–58. doi: 10.1016/j.jelekin.2013.04.012

25. Irschick DJ, Jayne BC. Comparative three-dimensional kinematics of the hindlimb for high-speed bipedal and quadrupedal locomotion of lizards. *J Exp Biol.* (1999) 202:1047–65. doi: 10.1242/jeb.202.9.1047

26. Pike AVL, Alexander RM. The relationship between limb-segment proportions and joint kinematics for the hind limbs of quadrupedal mammals. *J Zool.* (2002) 258:427–33. doi: 10.1017/S0952836902001577

27. Stavrakakis S, Guy JH, Warlow OME, Johnson GR, Edwards SA. Walking kinematics of growing pigs associated with differences in musculoskeletal conformation, subjective gait score and osteochondrosis. *Lives Sci.* (2014) 165:104–13. doi: 10.1016/j.livsci.2014.04.008

28. Seethapathi N, Wang S, Saluja R, Blohm G, Kording KP. Movement science needs different pose tracking algorithms. *arXiv.* (2019) 1907.10226. doi: 10.48550/arXiv.1907.10226

29. Michelini A, Eshraghi A, Andrysek J. Two-dimensional video gait analysis: a systematic review of reliability, validity, and best practice considerations. *Prosthet Orthot Int.* (2020) 44:245–62. doi: 10.1177/0309364620921290

30. Jackson BE, Evangelista DJ, Ray DD, Hedrick TL. 3D for the people: multi-camera motion capture in the field with consumer-grade cameras and open source software. *Biol. Open.* (2016) 5:1334–42. doi: 10.1242/bio.018713

31. Karashchuk P, Rupp KL, Dickinson ES, Walling-Bell S, Sanders E, Azim E, et al. Anipose: a toolkit for robust markerless 3D pose estimation. *Cell Rep.* (2021) 36):109730. doi: 10.1016/j.celrep.2021.109730

32. Mathis A, Schneider S, Lauer J, Mathis MW. A primer on motion capture with deep learning: principles, pitfalls, and perspectives. *Neuron.* (2020) 108:44–65. doi: 10.1016/j.neuron.2020.09.017

33. Corcoran AJ, Schirmacher MR, Black E, Hedrick TL. ThruTracker: open-source software for 2-D and 3-D animal video tracking. *bioRxiv.* (2021). doi: 10.1101/2021.05.12.443854

34. Mielke M, Aerts P, Van Ginneken C, Van Wassenbergh S, Mielke F. Progressive tracking: a novel procedure to facilitate manual digitization of videos. *Biol Open.* (2020) 9:bio055962. doi: 10.1242/bio.055962

35. McElreath R. *Statistical Rethinking: A Bayesian Course With Examples in R and Stan*. New York, NY: Chapman and Hall/CRC (2018).

36. Gelman A, Carlin J, Stern H, Dunson D, Vehtari A, Rubin D. *Bayesian Data Analysis*. 3rd ed. (2020). Available online at: http://www.stat.columbia.edu/~gelman/book/ (accessed February 19, 2023).

37. van de Schoot R, Depaoli S, King R, Kramer B, Märtens K, Tadesse MG, et al. Bayesian statistics and modelling. *Nat Rev Methods Primers.* (2021) 1:1. doi: 10.1038/s43586-020-00001-2

38. Mielke F, Schunke V, Wölfer J, Nyakatura JA. Motion analysis of non-model organisms using a hierarchical model: influence of setup enclosure dimensions on gait parameters of Swinhoe's striped squirrels as a test case. *Zoology (Jena).* (2018) 129:35–44. doi: 10.1016/j.zool.2018.05.009

39. Mirkiani S, Roszko DA, O'Sullivan CL, Faridi P, Hu DS, Fang D, et al. Overground gait kinematics and muscle activation patterns in the Yucatan mini pig. *J. Neural Eng.* (2022) 19:026009. doi: 10.1088/1741-2552/ac55ac

40. Vanden Hole C, Goyens J, Prims S, Fransen E, Ayuso Hernando M, Van Cruchten S, et al. How innate is locomotion in precocial animals? A study on the early development of spatio-temporal gait variables and gait symmetry in piglets. *J Exp Biol.* (2017) 220:2706–16. doi: 10.1242/jeb.157693

41. Vanden Hole C, Aerts P, Prims S, Ayuso M, Van Cruchten S, Van Ginneken C. Does intrauterine crowding affect locomotor development? A comparative study of motor performance, neuromotor maturation and gait variability among piglets that differ in birth weight and vitality. *PLoS ONE.* (2018) 13:1–21. doi: 10.1371/journal.pone.0195961

42. Vanden Hole C, Ayuso M, Aerts P, Van Cruchten S, Thymann T, Sangild PT, et al. Preterm birth affects early motor development in pigs. *Front Pediatr.* (2021) 9:731877. doi: 10.3389/fped.2021.731877

43. von Wachenfelt H, Pinzke S, Nilsson C, Olsson O, Ehlorsson CJ. Gait analysis of unprovoked pig gait on clean and fouled concrete surfaces. *Biosyst Eng.* (2008) 101:376–82. doi: 10.1016/j.biosystemseng.2008.09.002

44. Guesgen MJ, Bench CJ. What can kinematics tell us about the affective states of animals? *Anim Welf.* (2017) 26:383–97. doi: 10.7120/09627286.26.4.383

45. Abell CE, Johnson AK, Karriker LA, Rothschild MF, Hoff SJ, Sun G, et al. Using classification trees to detect induced sow lameness with a transient model. *Animal.* (2014) 8:1000–9. doi: 10.1017/S1751731114000871

46. LaVallee KT, Maus TP, Stock JD, Stalder KJ, Karriker LA, Murthy NS, et al. Quantitation of gait and stance alterations due to monosodium iodoacetate–induced knee osteoarthritis in Yucatan swine. *Comp Med.* (2020) 70:248–57. doi: 10.30802/AALAS-CM-19-000075

47. Benasson I, Wagnac E, Diotalevi L, Moore D, Mac-Thiong JM, Petit Y. Gait analysis of a post induced traumatic spinal cord injury porcine model. *Annu Int Conf IEEE Eng Med Biol Soc.* (2020) 2020:3803–6. doi: 10.1109/EMBC44109.2020.9175280

48. Quiniou N, Dagorn J, Gaudré D. Variation of piglets' birth weight and consequences on subsequent performance. *Livest Prod Sci.* (2002) 78:63–70. doi: 10.1016/S0301-6226(02)00181-1

49. Van Tichelen K, Prims S, Ayuso M, Van Kerschaver C, Vandaele M, Degroote J, et al. Handling associated with drenching does not impact survival and general health of low birth weight piglets. *Animals.* (2021) 11:404. doi: 10.3390/ani11020404

50. Wang J, Yang M, Cao M, Lin Y, Che L, Duraipandiyan V, et al. Moderately increased energy intake during gestation improves body condition of primiparous sows, piglet growth performance, and milk fat and protein output. *Livestock Sci.* (2016) 194:23–30. doi: 10.1016/j.livsci.2016.09.012

51. D'Inca R, Gras-Le Guen C, Che L, Sangild PT, Le Huërou-Luron I. Intrauterine growth restriction delays feeding-induced gut adaptation in term newborn pigs. *Neonatology.* (2011) 99:208–16. doi: 10.1159/000314919

52. Feldpausch JA, Jourquin J, Bergstrom JR, Bargen JL, Bokenkroger CD, Davis DL, et al. Birth weight threshold for identifying piglets at risk for preweaning mortality. *Transl Anim Sci.* (2019) 3:633–40. doi: 10.1093/tas/txz076

53. Roehe R, Kalm E. Estimation of genetic and environmental risk factors associated with pre-weaning mortality in piglets using generalized linear mixed models. *Anim Sci.* (2000) 70:227–40. doi: 10.1017/S1357729800054692

54. Amdi C, Krogh U, Flummer C, Oksbjerg N, Hansen CF, Theil PK. Intrauterine growth restricted piglets defined by their head shape ingest insufficient amounts of colostrum. *J Anim Sci.* (2013) 91:5605–13. doi: 10.2527/jas.2013-6824

55. Baxter EM, Jarvis S, D'Eath RB, Ross DW, Robson SK, Farish M, et al. Investigating the behavioural and physiological indicators of neonatal survival in pigs. *Theriogenology.* (2008) 69:773–83. doi: 10.1016/j.theriogenology.2007.12.007

56. Hales J, Moustsen VA, Nielsen MBF, Hansen CF. Individual physical characteristics of neonatal piglets affect preweaning survival of piglets born in a noncrated system. *J Anim Sci.* (2013) 91:4991–5003. doi: 10.2527/jas.2012-5740

57. Muns R, Manzanilla EG, Sol C, Manteca X, Gasa J. Piglet behavior as a measure of vitality and its influence on piglet survival and growth during lactation. *J Anim Sci.* (2013) 91:1838–43. doi: 10.2527/jas.2012-5501

58. Van Ginneken C, Ayuso M, Van Bockstal L, Van Cruchten S. Preweaning performance in intrauterine growth-restricted piglets: characteristics and interventions. *Mol Reprod Dev.* (2022) 1–11. doi: 10.1002/mrd.23614

59. Andersen AD, Sangild PT, Munch SL, van der Beek EM, Renes IB, Ginneken Cv, et al. Delayed growth, motor function and learning in preterm pigs during early postnatal life. *Am J Physiol Regul Integr Comp Physiol.* (2016) 310:R481–92. doi: 10.1152/ajpregu.00349.2015

60. Marchant JN, Rudd AR, Mendl MT, Broom DM, Meredith MJ, Corning S, et al. Timing and causes of piglet mortality in alternative and conventional farrowing systems. *Vet Rec.* (2000) 147:209–14. doi: 10.1136/vr.147.8.209

61. Edwards SA, Baxter EM. Chapter 11. Piglet mortality: causes and prevention. In: Farmer C, editor. *The Gestating and Lactating Sow* (2015) p. 253–78. doi: 10.3920/978-90-8686-803-2_11

62. Newell KM, Liu YT. Collective variables and task constraints in movement coordination, control and skill. *J Mot Behav.* (2021) 53:770–96. doi: 10.1080/00222895.2020.1835799

63. Aerts P, Van Damme R, Van Elsacker L, Duchêne V. Spatio-temporal gait characteristics of the hind-limb cycles during voluntary bipedal and quadrupedal walking in bonobos (*Pan paniscus*). *Am J Phys Anthropol.* (2000) 111:503–17. doi: 10.1002/(SICI)1096-8644(200004)111:4<503::AID-AJPA6>3.0.CO;2-J

64. Frick RW. The appropriate use of null hypothesis testing. *Psychol Methods.* (1996) 1:379. doi: 10.1037/1082-989X.1.4.379

65. Maxwell SE, Delaney HD, Kelley K. *Designing Experiments and Analyzing Data: A Model Comparison Perspective*. New York, NY: Routledge (2017).

66. Riley RD, Ensor J, Snell KIE, Harrell FE, Martin GP, Reitsma JB, et al. Calculating the sample size required for developing a clinical prediction model. *BMJ.* (2020) 368:m441. doi: 10.1136/bmj.m441

67. Austin PC, Steyerberg EW. The number of subjects per variable required in linear regression analyses. *J Clin Epidemiol.* (2015) 68:627–36. doi: 10.1016/j.jclinepi.2014.12.014

68. Mielke F, Van Ginneken C, Aerts P. Quantifying intralimb coordination of terrestrial ungulates with Fourier coefficient affine superimposition. *Zool J Linn Soc.* (2019) 189:1067–83. doi: 10.1093/zoolinnean/zlz135

69. Webb D, Sparrow WA. Description of joint movements in human and non-human primate locomotion using Fourier analysis. *Primates.* (2007) 48:277–92. doi: 10.1007/s10329-007-0043-4

70. Fourier J. *Theorie Analytique de la Chaleur, par M. Fourier*. Paris: Chez Firmin Didot, père et Fils (1822).

71. Bracewell RN. *The Fourier Transform and its Applications*. 3rd ed. McGraw-Hill Series in Electrical and Computer Engineering. Circuits and Systems. New York, NY: McGraw Hill (2000).

72. Gray RM, Goodman JW. *Fourier Transforms: An Introduction for Engineers.* 1st ed. The Springer International Series in Engineering and Computer Science. Vol. 322. New York, NY: Springer US (1995).

73. Ayuso M, Irwin R, Walsh C, Van Cruchten S, Van Ginneken C. Low birth weight female piglets show altered intestinal development, gene expression, and epigenetic changes at key developmental loci. *FASEB J.* (2021) 35:e21522. doi: 10.1096/fj.202002587R

74. Litten J, Drury P, Corson A, Lean I, Clarke L. The influence of piglet birth weight on physical and behavioural development in early life. *Neonatology.* (2003) 84:311–8. doi: 10.1159/000073640

75. Meijer E, Bertholle CP, Oosterlinck M, van der Staay FJ, Back W, van Nes A. Pressure mat analysis of the longitudinal development of pig locomotion in growing pigs after weaning. *BMC Vet Res.* (2014) 10:1–37. doi: 10.1186/1746-6148-10-37

76. Mathis A, Mamidanna P, Cury KM, Abe T, Murthy VN, Mathis MW, et al. DeepLabCut: markerless pose estimation of user-defined body parts with deep learning. *Nat Neurosci.* (2018) 21:1281–9. doi: 10.1038/s41593-018-0209-y

77. Hof AL. Scaling gait data to body size. *Gait Posture.* (1996) 4:222–3. doi: 10.1016/S0966-6362(01)00097-2

78. Alexander RM, Jayes AS. A dynamic similarity hypothesis for the gaits of quadrupedal mammals. *J Zool.* (1983) 201:135–52. doi: 10.1111/j.1469-7998.1983.tb04266.x

79. Scott B, Seyres M, Philp F, Chadwick EK, Blana D. Healthcare applications of single camera markerless motion capture: a scoping review. *PeerJ.* (2022) 10:e13517. doi: 10.7717/peerj.13517

80. Salvatier J, Wiecki TV, Fonnesbeck C. Probabilistic programming in Python using PyMC3. *PeerJ Comput Sci.* (2016) 2:e55. doi: 10.7717/peerj-cs.55

81. D'Eath R. Repeated locomotion scoring of a sow herd to measure lameness: consistency over time, the effect of sow characteristics and inter-observer reliability. *Anim Welf.* (2012) 21:219–31. doi: 10.7120/09627286.21.2.219

82. Le Dividich J, Charneca R, Thomas F. Relationship between birth order, birth weight, colostrum intake, acquisition of passive immunity and pre-weaning mortality of piglets. *Span J Agric Res.* (2017) 15:e0603. doi: 10.5424/sjar/2017152-9921

83. Vanden Hole C, Cleuren S, Van Ginneken C, Prims S, Ayuso M, Van Cruchten S, et al. How does intrauterine crowding affect locomotor performance in newborn pigs? A study of force generating capacity and muscle composition of the hind limb. *PLoS ONE.* (2018) 13:e0209233. doi: 10.1371/journal.pone.0209233

84. Vanden Hole C, Ayuso M, Aerts P, Prims S, Van Cruchten S, Van Ginneken C. Glucose and glycogen levels in piglets that differ in birth weight and vitality. *Heliyon.* (2019) 5:e02510. doi: 10.1016/j.heliyon.2019.e02510

85. Schmitt O, Baxter EM, Lawlor PG, Boyle LA, O'Driscoll K. A single dose of fat-based energy supplement to light birth weight pigs shortly after birth does not increase their survival and growth. *Animals (Basel).* (2019) 9:227. doi: 10.3390/ani9050227

frontiers | Frontiers in Bioengineering and Biotechnology

TYPE Original Research
PUBLISHED 22 June 2023
DOI 10.3389/fbioe.2023.1164922

OPEN ACCESS

EDITED BY
Christian Peham,
University of Veterinary Medicine Vienna, Austria

REVIEWED BY
Gregorio Marchiori,
Rizzoli Orthopedic Institute (IRCCS), Italy
Masoud Aghapour,
University of Veterinary Medicine Vienna, Austria
Andreas Martin Seitz,
Ulm University Medical Center, Germany

*CORRESPONDENCE
Dong Jiang,
bysyjiangdong@126.com
Yubo Fan,
yubofan@buaa.edu.cn
Feng Zhao,
fzhao@buaa.edu.cn

†These authors have contributed equally to this work and share first authorship

RECEIVED 13 February 2023
ACCEPTED 13 June 2023
PUBLISHED 22 June 2023

CITATION
Xue A, Mao Z, Zhu X, Yang Q, Wang P, Mao Z, Du M, Ma X, Jiang D, Fan Y and Zhao F (2023), Biomechanical effects of the medial meniscus horizontal tear and the resection strategy on the rabbit knee joint under resting state: finite element analysis.
Front. Bioeng. Biotechnol. 11:1164922.
doi: 10.3389/fbioe.2023.1164922

Biomechanical effects of the medial meniscus horizontal tear and the resection strategy on the rabbit knee joint under resting state: finite element analysis

Anqi Xue[1,2†], Zuming Mao[1†], Xiaoyu Zhu[1], Qiang Yang[1], Peichen Wang[2], Zimu Mao[3], Mingze Du[3], Xu Ma[1], Dong Jiang[3]*, Yubo Fan[1]* and Feng Zhao[1]*

[1]Key Laboratory for Biomechanics and Mechanobiology of Ministry of Education, Beijing Advanced Innovation Center for Biomedical Engineering, School of Biological Science and Medical Engineering, Beihang University, Beijing, China, [2]Beijing Institute of Medical Device Testing, Beijing, China, [3]Department of Sports Medicine, Peking University Third Hospital, Institute of Sports Medicine of Peking University, Beijing Key Laboratory of Sports Injuries, Beijing, China

The biomechanical changes following meniscal tears and surgery could lead to or accelerate the occurrence of osteoarthritis. The aim of this study was to investigate the biomechanical effects of horizontal meniscal tears and different resection strategies on a rabbit knee joint by finite element analysis and to provide reference for animal experiments and clinical research. Magnetic resonance images of a male rabbit knee joint were used to establish a finite element model with intact menisci under resting state. A medial meniscal horizontal tear was set involving 2/3 width of a meniscus. Seven models were finally established, including intact medial meniscus (IMM), horizontal tear of the medial meniscus (HTMM), superior leaf partial meniscectomy (SLPM), inferior leaf partial meniscectomy (ILPM), double-leaf partial meniscectomy (DLPM), subtotal meniscectomy (STM), and total meniscectomy (TTM). The axial load transmitted from femoral cartilage to menisci and tibial cartilage, the maximum von Mises stress and the maximum contact pressure on the menisci and cartilages, the contact area between cartilage to menisci and cartilage to cartilage, and absolute value of the meniscal displacement were analyzed and evaluated. The results showed that the HTMM had little effect on the medial tibial cartilage. After the HTMM, the axial load, maximum von Mises stress and maximum contact pressure on the medial tibial cartilage increased 1.6%, 1.2%, and 1.4%, compared with the IMM. Among different meniscectomy strategies, the axial load and the maximum von Mises stress on the medial menisci varied greatly. After the HTMM, SLPM, ILPM, DLPM, and STM, the axial load on medial menisci decreased 11.4%, 42.2%, 35.4% 48.7%, and 97.0%, respectively; the maximum von Mises stress on medial menisci increased 53.9%, 62.6%, 156.5%, and 65.5%, respectively, and the STM decreased 57.8%, compared to IMM. The radial displacement of the middle body of the medial meniscal was larger than any other part in all the models. The HTMM led to few biomechanical changes in the rabbit knee joint. The SLPM showed minimal effect on joint stress among all resection strategies. It is recommended to preserve the posterior root and the remaining peripheral edge of the meniscus during surgery for an HTMM.

KEYWORDS

knee, meniscus injury, meniscectomy, biomechanics, finite element

1 Introduction

The meniscus is an important component of the knee joint, and its main functions are to absorb shock, transmit load, lubricate the joint, and improve the matching degree of the femur and tibia (Lau et al., 2018; Kani et al., 2021; Patsch et al., 2021). The biomechanical changes following meniscal tears and surgery could lead to osteoarthritis (Lau et al., 2018). Recent reports have indicated that the maximum shear stress of cartilage increases as the resection volume of a meniscectomy increases (Bedi et al., 2010; Zhang et al., 2021; Liu et al., 2022) and further leads to joint pain, swelling, and even osteoarthritis (Bedi et al., 2010; Beamer et al., 2017; Bedrin et al., 2021; Ozeki et al., 2022). Horizontal tears account for 12%–35% of all tear patterns (Shanmugaraj et al., 2019) and usually occur in the medial menisci (especially the posterior horn of the medial meniscus (Yim et al., 2013; Brown et al., 2016)) due to joint degeneration (Lee et al., 2016; Jiang et al., 2017; Posadzy et al., 2020). Due to the limited healing capacity and tissue weakness of meniscal horizontal tears following meniscal repair (Kurzweil et al., 2014; Kurzweil et al., 2018; Ogawa et al., 2020) or conservative or nonsurgical methods (Haemer et al., 2007; Herrlin et al., 2013; Brown et al., 2016), the dominant clinical treatment for horizontal meniscal tears is arthroscopic meniscectomy to remove the single-leaf, double-leaf, subtotal body or total body of a meniscus (Seil et al., 2010; Yang et al., 2021). To date, there is no systematic research on the impact of meniscal horizontal tears and all the clinically used resection strategies on joint mechanics (Haemer et al., 2007; Brown et al., 2016), which is important for the selection of meniscectomy strategies during surgery (Feucht et al., 2015).

Rabbits, as a relatively inexpensive animal model, have been commonly used to study meniscal injury and surgery (Narita et al., 2012; Zhang et al., 2015; Civitarese et al., 2016; Jiang et al., 2018), despite certain differences in cellularity, and vascularity (Chevrier et al., 2009). Meanwhile, the progressive rate of degenerative changes of knee cartilage in rabbits is faster than that in large animals or humans, which can be used as a reference for long-term results of future clinical applications (Roland et al., 1973; Jiang et al., 2018). However, the biomechanics of the rabbit knee joint has not been quantified, and its mechanical changes have not been fully studied. The purpose of this study was to construct models more in line with clinical meniscal horizontal tears and different resection strategies by the finite element analysis method and to study the relative biomechanical changes in the rabbit knee joint. Based on static analyses, a hypothesis was proposed that meniscal horizontal tears may not have a significant impact on the rabbit knee joint, and different resection strategies may result in different biomechanical environment changes. These results can improve our understanding of the relationship between meniscal horizontal tears, meniscectomies, and osteoarthritis and provide a reference for the future selection of experimental studies and clinical surgery strategies.

2 Materials and methods

The research was approved by the IRB Medical Ethics Committee of Peking University Third Hospital (A2022019). Magnetic resonance images (MRI) were obtained from the right hind limb of a healthy New Zealand rabbit (male, 6 months, 4 kg). The MR scanning was 3.0 T with T2 weighting, the layer thickness was 0.1 mm, and 349 images were obtained. All image data were from Peking University Third Hospital. The volumetric image data from MRI were imported into Mimics 21.0 software (Materialise, Leuven, Belgium), and the contours of knee bones and soft tissue were manually reconstructed under the guidance of an experienced orthopedist, including femur, tibia, fibula, articular cartilages, menisci, and major knee ligaments (anterior cruciate ligament (ACL), posterior cruciate ligament (PCL), medial collateral ligament (MCL), and lateral collateral ligament (LCL)). Then, a complete model of the rabbit knee joint (Figures 1A,B) and a model of an intact medial meniscus (IMM, Figure 1C) were generated by ABAQUS 2021 (SIMULIA, Rhode Island, United States). Finally, by resecting the medial meniscal body in ABAQUS, different rabbit knee joint models of posterior root horizontal tears and different meniscectomies were established, including a horizontal tear of the medial meniscus (HTMM, Figure 1D), a superior leaf partial meniscectomy (SLPM, Figure 1E), an inferior leaf partial meniscectomy (ILPM, Figure 1F), a double-leaf partial meniscectomy (DLPM, Figure 1G), a subtotal meniscectomy (STM, Figure 1H), and a total meniscectomy (TTM).

Each part of the rabbit knee joint was meshed by tetrahedral elements. For better observing and calculating the biomechanical changes between cartilage and meniscus, as well as between cartilages, and effectively reduce computational costs, an improved 10 nodes tetrahedral element (C3D10M) is used for cartilage and meniscus. And the element type of the femur, tibia, and fibula was C3D4. Ligaments used the T3D2 truss grid type. The mesh of the model had undergone convergence verification. Bone, cartilage, and menisci were defined as linear elastic isotropic materials. The Young's moduli of bone, cartilage, and menisci were 15,000 MPa, 20 MPa, and 120 MPa, and their Poisson's ratios were 0.30, 0.46, and 0.45, respectively (Sweigart and Athanasiou, 2005; Zhang et al., 2019). Ligaments were defined as nonlinear hyperelastic isotropic material because they only bear tension but not pressure, and the constitutive relation was neo-Hookean (Li et al., 2020). Table 1 shows the attribute assignment of the neo-Hookean model for the different ligaments.

Although there are studies about the dynamic loading curves of rabbit knee joints, which are more suitable for highlighting the role of meniscus horizontal tears, their data are difficult to apply to our model (Gushue et al., 2005). Most of the time the rabbits are in a resting state, and the meniscus of the rabbit knee joint also plays a role in transmitting loads, buffering, and so on under such condition. Therefore, the mechanical behavior of the rabbit knee joint in the resting state was simulated, and the load was an axial force. Considering the anatomical characteristics of the rabbit knee joint, the femur flexion was 45° (Mansour et al., 1998), and the load was 40 N, which was approximately the weight of a whole rabbit (Anderson et al., 1990). The femur was coupled to a reference point, which was set on the midpoint of the farthest point of the femoral condyle on the medial and lateral sides (Figure 1A), to control the freedom of the femur. For the motion of the tibia and femur is relative, the axial and internal/external rotation degrees of the femur were released, and the

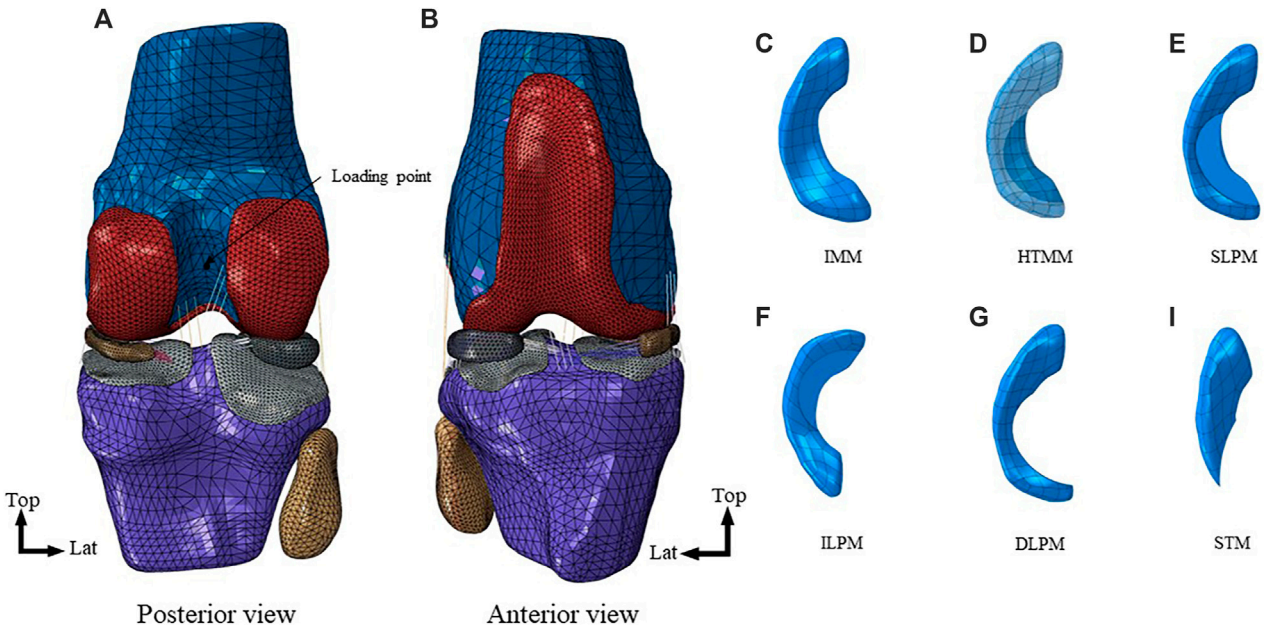

FIGURE 1
Finite element models of the rabbit knee joint: **(A)** Posterior view of the right knee; **(B)** Anterior view of the right knee; **(C)** intact medial meniscus (IMM); **(D)** horizontal tear of medial meniscus (HTMM); **(E)** superior leaf partial meniscectomy (SLPM); **(F)** inferior leaf partial meniscectomy (ILPM); **(G)** double-leaf partial meniscectomy (DLPM); **(H)** subtotal meniscectomy (STM).

TABLE 1 The attribute assignment of Neo-Hookean of major ligaments.

ligaments)	C10 (MPa)	C3 (MPa)	C4 (-)	C5 (MPa)	D1 (MPa-1)	Λ(-)
ACL	1.95	0.0139	116.22	535.039	0.00683	1.046
PCL	3.25	0.1196	87.178	431.063	0.0041	1.035
LCL	1.44	0.57	48.0	467.1	0.00126	1.036
MCL	1.44	0.57	48.0	467.1	0.00126	1.036

Abbreviation: ACL-anterior cruciate ligament, PCL-posterior cruciate ligament, MCL-medial collateral ligament, LCL-lateral collateral ligament.

other degrees of the femur and tibia were constrained. Due to the lubrication function of the knee joint fluid, we set the tangential contact to "frictionless" and normal contact to "hard contact" in ABAQUS. The analysis used the Standard solver. The output of the load in the axial direction between cartilage to menisci and cartilage to cartilage was exported. By simulating the rabbit knee joint in the static state, the axial load transmitted from femoral cartilage to menisci and tibial cartilage, the maximum von Mises stress and the maximum contact pressure on the menisci and cartilages, the contact area between cartilage to menisci and cartilage to cartilage, and absolute value of the meniscal displacement were evaluated.

3 Results

3.1 Axial load

The axial load on the medial tibial cartilages and medial menisci was redistributed in the medial compartment (Figure 2A). After the HTMM, SLPM, and ILPM, the medial menisci bore 2.0 N, 1.3 N, and 1.5 N, which was 11.4%, 41.9%, and 35.4% lower than the IMM, respectively. After the STM, the load on the medial menisci was only 0.1 N, which was similar to the TTM. Furthermore, after the DLPM and TTM, the axial load of the medial tibial cartilage was 6.2% and 12.9% higher than that on the IMM (16.3 N), respectively. There was little effect on the axial load distribution of the medial and lateral compartments of the rabbit knee joint among the IMM, HTMM, and different resections.

3.2 Maximum von Mises stress

As shown in Figure 2B, it is worth noting that the maximum von Mises stress of the six models in the medial menisci (MM) (except TTM (0 MPa) due to the resection of the whole medial menisci) varied significantly. After the SLPM, ILPM, and DLPM, the maximum von Mises stress on the medial menisci was 8.3 MPa, 13.1 MPa, and 8.4 MPa, respectively. After the ILPM, the maximum

10.3389/fbioe.2023.1164922

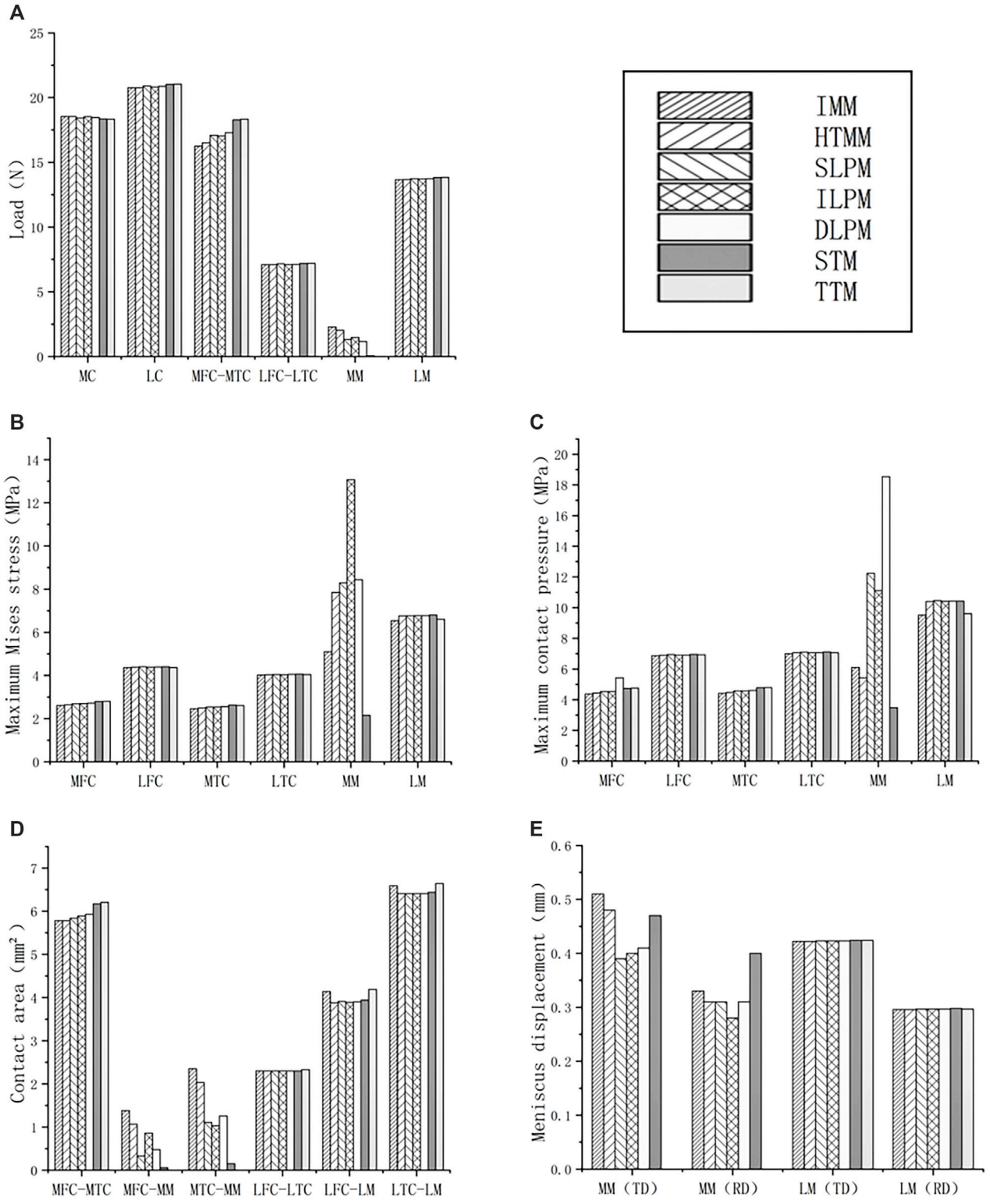

FIGURE 2
Results of comparison of axial load, maximum von Mises stress, maximum contact pressure, contact area and meniscus displacement between IMM, HTMM, SLPM, ILPM, DLPM, STM, and TTM: **(A)** Axial load of medial and lateral compartment (MM here means the axial load transmitted from medial femoral cartilage to medial menisci, so as the LM); **(B)** Maximum von Mises stress of medial and lateral compartment; **(C)** Maximum contact pressure of medial and lateral compartment; **(D)** Contact area of the medial and lateral compartment; **(E)** Meniscus displacement. Abbreviation: MC-medial compartment, LC-lateral compartment, MFC-medial femoral cartilage, MTC-medial tibial cartilage, LFC-lateral femoral cartilage, LTC-lateral tibial cartilage, MM-medial meniscus, LM-lateral meniscus, TD-total displacement, RD-radial displacement, IMM-intact medial meniscus, HTMM-horizontal tear of medial meniscus, SLPM-superior leaf partial meniscectomy, ILPM-inferior leaf partial meniscectomy, DLPM-double-leaf partial meniscectomy, STM-subtotal meniscectomy, TTM-total meniscectomy. Here "-" means the contact between two parts, for example, "MFC-MTC" means the contact between MFC and MTC.

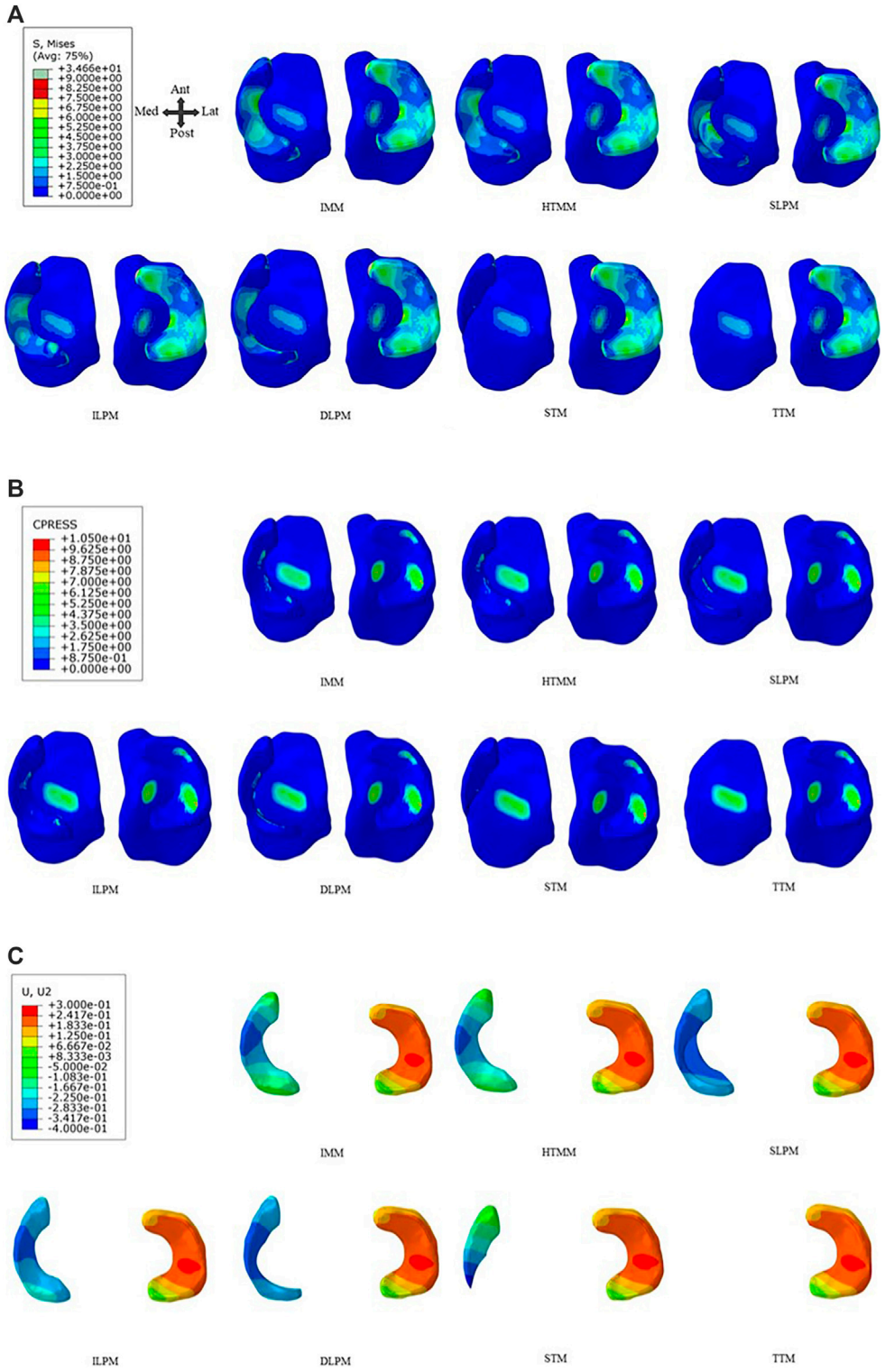

FIGURE 3
IMM, HTMM, and different resections on the tibial plateau of **(A)** Von Mises stress distribution, **(B)** Contact pressure distribution, and **(C)** Radial displacement of the medial meniscus. Abbreviation: IMM-intact medial meniscus, HTMM-horizontal tear of medial meniscus, SLPM-superior leaf partial meniscectomy, ILPM-inferior leaf partial meniscectomy, DLPM-double-leaf partial meniscectomy, STM-subtotal meniscectomy, TTM-total meniscectomy.

von Mises stress increased the most among the five resections by 156.5% compared with the IMM (5.1 MPa). After the STM, the maximum von Mises stress was 2.2 MPa, which decreased by 57.9% compared with the IMM. There was little difference in the magnitude of the maximum von Mises stress on the medial femoral cartilage (MFC), lateral femoral cartilage (LFC), medial

tibial cartilage (MTC), lateral tibial cartilage (LTC) and lateral menisci (LM). Figure 3A also shows little difference in the von Mises stress distribution on the LTC and LM. After the HTMM, the distribution was similar to that on the IMM. The maximum von Mises stress was concentrated at the remaining edge of the medial meniscus, which contacted the articular cartilage after the SLPM, ILPM, and DLPM.

3.3 Maximum contact pressure and contact area

After the SLPM, ILPM, and DLPM, the maximum contact pressure of the medial menisci was 12.2 MPa, 11.1 MPa, and 18.5 MPa, which increased by 100.8%, 82.2%, and 202.7%, respectively, compared with the IMM (6.1 MPa), respectively (Figure 2C). In addition, the maximum contact pressure on the medial menisci of the HTMM (5.4 MPa) and STM (3.5 MPa) decreased by 11.2% and 42.8% compared with the IMM, respectively. However, the maximum contact pressure on LM did not change significantly (approximately 10%) among the seven models. As shown in Figure 3B, there was little difference in the distribution of contact pressure in the lateral compartment. In the medial compartment, the distribution of contact pressure was more on the MTC than on the MM. The contact pressure was also mainly located in the remaining edge of the medial meniscus, which contacted the articular cartilage.

For the contact area, the difference between the MFC-MM and MTC-MM varied greatly among the seven models (Figure 2D). After the ILPM, SLPM, and DLPM, the contact areas of MFC-MM were 0.9 mm^2, 0.3 mm^2 and 0.5 mm^2, which were 37.7%, 76.1%, and 65.2% lower than that of the IMM (1.4 mm^2), respectively. The contact areas of the MTC-MM were 1.0 mm^2, 1.1 mm^2, and 1.3 mm^2, which were 56.2%, 52.8%, and 46.4% lower than that of the IMM (2.4 mm^2), respectively. In the lateral compartment, the contact areas of the LFC-LM and LTC-LM were 3.9 mm^2 and 6.4 mm^2 after the STM, which decreased by 4.8% and 2.3% compared with the IMM, respectively. In addition, the contact area after the TTM was similar to that of the intact rabbit knee joint.

3.4 Meniscal displacement

After the HTMM, the total and radial displacements of the medial menisci were 5.9% and 6.1% lower than those after the IMM, respectively (Figure 2E, Figure 3C). Both the removal of the single-leaf and double-leaf meniscectomies reduced the total and radial displacements. After the SLPM, the radial displacement of the medial menisci was 23.4% less than that after the IMM. Because of the lack of posterior root connections of the menisci, the maximum radial displacement was 0.4 mm after the STM, which increased by 21.7% compared to the IMM. Among the seven models, there was no significant difference in the radial displacements on the lateral menisci (Figure 3C). The radial displacement of the medial meniscal middle body was larger than that of any other part in all the models, and the radial displacement after the ILPM was the minimum, while after the STM, the radial displacement was the most obvious.

4 Discussion

The most important findings of the present study included that horizontal tears not reaching the edge of the medial meniscus had little effect on the biomechanics of the knee joint under the resting state and that there were fewer biomechanical changes when performing a superior leaf partial meniscectomy than when performing an inferior leaf partial meniscectomy and double-leaf meniscectomy. A partial meniscectomy with an intact posterior root achieved fewer biomechanical changes than a subtotal meniscectomy. These results suggested the importance of preserving the posterior root and the remaining peripheral meniscal tissue.

The present study constructed a detailed finite element model of the rabbit knee joint, including bones, cartilages, menisci, and major ligaments, to evaluate the biomechanical changes after a horizontal tear of the medial meniscus (HTMM) and different resection strategies. There is no similar reported finite element study to simulate the resting state (45°) of the rabbit knee joint. Therefore, additional simulations were performed, one of which followed the study of Tan et al. (Tan et al., 2020). The intact knee joint was flexed to the degree consistent with Tan's model, and the axial load was 80 N. The results showed that the maximum von Mises stress on the femoral cartilage was 5.7 MPa, which was basically consistent with Tan's research (7.9 ± 2.5 MPa). The other simulated the stance phase of hopping (30°) under static analysis, and the ratio of the total force on medial to lateral compartments was 0.97. The result was also consistent with Gushue's study that at the stance phase of hopping, the ratio of peak contact force of medial tibia to lateral was 0.89 ± 0.25 (Gushue et al., 2005). These results demonstrated the reliability of the model used in this study.

For a horizontal tear not spreading to the outer edge, the contact pressure and contact area of the articular cartilage changed slightly compared with the IMM. The results indicated that horizontal tears may not promote the progression of knee joint degeneration. This was consistent with some clinical results of joint degeneration after an HTMM. Cho et al. found that discoid menisci with horizontal tears were less associated with articular cartilage injury even if the tear lasted for a relatively long time (Cho et al., 2019). In Koh's study, fresh-frozen human cadaveric knees were tested, and they also found that there was no significant change in the contact area and contact pressure after medial meniscal horizontal tears compared with intact menisci (Koh et al., 2016). The reason might be that the HTMM did not break the hoop stress of the meniscus, so it did not affect the maintenance of the meniscal basic biomechanical function and performed the same functions as the IMM (Kedgley et al., 2019). The results could also explain why most patients with horizontal tears are clinically asymptomatic and do not require surgery unless there are obstructive symptoms (Yim et al., 2013). After an HTMM, Amano et al. (Amano et al., 2015) established a finite element model and found that the tear would further expand and deform during knee joint flexion movement. However, most reported studies, including the present study, were basically static analyses, and whether an HTMM in the dynamic state increases joint stress and accelerates joint degeneration needs further research.

It should be noted that although the contact pressure was not increased significantly after an HTMM, the stress on the meniscus becomes nonhomogeneous and mainly concentrated on the outer

edge. The reason might be that the superior and inferior leaves of the inner two-thirds were squeezed together, spreading the stress to the outer edge. This vicious cycle could cause the horizontal tear to develop into larger and more complex tears, ultimately bringing about greater biomechanical changes. Therefore, although the clinical symptoms and biomechanical changes caused by an HTMM are not obvious, early management and promotion of meniscal tear healing are important. More animal experiments and long-term clinical studies need to be carried out to investigate the effect of an HTMM on the meniscus and knee joint.

In terms of meniscectomy strategies, resecting different parts of the meniscus showed different biomechanical consequences. After a superior leaf partial meniscectomy (SLPM), the maximum von Mises and contact pressure on the medial tibial cartilage changed slightly compared with an intact medial meniscus (IMM), while that on the medial meniscus increased significantly. Since an HTMM generally occurs in the middle and posterior parts of the meniscus, after the medial meniscus is resected with one or both leaves, the remaining medial meniscus can still bear a certain axial load. In addition, the outer edge of the meniscus can partially retain the ability of hoop stress and play a certain role in supporting and cushioning the articular cartilage (Haemer et al., 2007; Brown et al., 2016). Lee et al. (Lee et al., 2016) found that removing a single leaf of the meniscus and retaining the outer edge of the meniscus was an effective treatment when there was a horizontal tear. Haemer et al. (Haemer et al., 2007) studied superior leaf and double-leaf meniscectomies on sheep knees after horizontal tears and found that there was a biomechanical advantage in retaining the superior leaf when a horizontal tear occurred on 1/3 of the posterior of the meniscus. Based on the results of the present study, which highlighted that there are fewer biomechanical changes when performing an SLPM than an inferior leaf partial meniscectomy (ILPM) and double-leaf partial meniscectomy (DLPM), the SLPM could be recommended in the case of good quality of both the superior and inferior leaves.

The present study also showed the importance of the posterior root in meniscectomy strategy selection after an HTMM. After a subtotal meniscectomy (STM), the axial load, the maximum von Mises stress, and the maximum contact pressure on the tibial cartilage increased compared with a partial meniscectomy with root retention. The reason was that the posterior root and outer edge of the meniscus were destroyed, and the hoop stress function was lost after the STM (Kedgley et al., 2019). The meniscus lost support for the femur and only bore a 0.1 N axial load, and the contact area between the medial femoral cartilage and medial meniscus (MFC-MM) and the contact area between the medial tibial cartilage and medial meniscus (MTC-MM) were reduced. The total and radial displacement was also higher than that of single-leaf and double-leaf resections, and the remaining meniscus could not form stable support for the femoral cartilage. Sung et al. also found that root tears caused a greater degree of spontaneous osteonecrosis of the knee (Sung et al., 2013). Thus, it is strongly recommended to preserve the outer edge and posterior root of the meniscus to reduce the impact on the biomechanics of the knee joint despite higher technical requirements.

Although rabbits are typically used as animal models for the human knee joint, there are some differences in morphology, axial load distribution, and von Mises stress distribution between rabbits and humans (Messner et al., 2000; Chevrier et al., 2009; Esrafilian et al., 2022). In humans, the load ratio between the medial and lateral compartments of the knee joint is approximately 2:1, and approximately 70.9% of the total axial load is transmitted to the meniscus (Wang et al., 2022). The present study found that more axial load is transmitted to the lateral compartment of the rabbit knee joint, where the load ratio between the medial and lateral compartments is 0.97, and the ratio of the axial load on the menisci in the intact compartment is approximately 40.6%. However, as a relatively inexpensive animal model (Civitarese et al., 2016), the variation trend of the axial load, von Mises stress, contact pressure, contact area, and meniscal displacement in rabbits could be used as a reference for studying human knee joint HTMM and different meniscectomies. The construction of finite element models of the rabbit knee joint can reduce the number of animal trials and is in accordance with the 3R-principles in animal research. This may enhance our understanding of the influence of biomechanics on the development of osteoarthritis. Considering the need for future research, it is necessary to further compare the biomechanical similarities and differences in meniscal tears and surgical strategies between different species to provide a better animal model for relevant research on menisci.

The present study has some limitations. First, the linear elastic material model was adopted for menisci and cartilage, while the nonlinear model would better describe the actual behavior of knee joint tissues. Fortunately, the results could basically meet the requirements to simulate the mechanics of the knee joint, and they could obtain support from similar studies (Bell et al., 2009). Second, soft tissues, including the joint capsule, nonmajor ligament, fat, and muscle, were not included in the model, which might lead to some deviations in the simulation. Third, the study only carried out the static analysis of rabbit knee joints in the resting state. Kinetic loading applications like walking, running, and stair-climbing are more suitable for highlighting the role of meniscus horizontal tears and surgical treatments. Further studies on static analysis or dynamic analysis of different rabbit activities in the rabbit knee joint are necessary. Furthermore, the study still requires comparative verification of related experiments of the rabbit knee joint.

5 Conclusion

A horizontal tear of the medial meniscus (HTMM) led to few biomechanical changes in a rabbit knee joint. A superior leaf partial meniscectomy (SLPM) showed a minimal effect on joint stress among all resection strategies under a resting state. It is recommended to preserve the posterior root and the remaining peripheral edge of the meniscus during surgery for an HTMM.

Data availability statement

The original contributions presented in the study are included in the article/supplementary material, further inquiries can be directed to the corresponding authors.

Ethics statement

The animal study was reviewed and approved by the research was approved by the IRB Medical Ethics Committee of Peking

University Third Hospital (A2022019). Written informed consent was obtained from the owners for the participation of their animals in this study.

Author contributions

AX, ZM: Methodology, Investigation, Formal analysis, Writing–original draft. XZ, QY, and PW: Methodology, Investigation, Data curation. ZM, MD, XZ, and XM: Methodology, Validation, Writing–review & editing. DJ, YF, and FZ: Supervision, Writing–review & editing. All authors contributed to the article and approved the submitted version.

Funding

This work was supported by the National Natural Science Foundation of China (11072021, 82072428, 11772038), the National Key Research and Development Program (2016YFC1103202, 2019YFB1706900).

Conflict of interest

The authors declare that the research was conducted in the absence of any commercial or financial relationships that could be construed as a potential conflict of interest.

Publisher's note

All claims expressed in this article are solely those of the authors and do not necessarily represent those of their affiliated organizations, or those of the publisher, the editors and the reviewers. Any product that may be evaluated in this article, or claim that may be made by its manufacturer, is not guaranteed or endorsed by the publisher.

References

Amano, H., Iwahashi, T., Suzuki, T., Mae, T., Nakamura, N., Sugamoto, K., et al. (2015). Analysis of displacement and deformation of the medial meniscus with a horizontal tear using a three-dimensional computer model. *Knee Surg. Sports Traumatol. Arthrosc.* 23 (4), 1153–1160. doi:10.1007/s00167-014-2931-7

Anderson, D. D., Brown, T. D., Yang, K. H., and Radin, E. L. (1990). Dynamic finite element analysis of impulsive loading of the extension-splinted rabbit knee. *J. Biomech. Eng.* 23 (2), 711. doi:10.1016/0021-9290(90)90171-X

Beamer, B. S., Walley, K. C., Okajima, S., Manoukian, O. S., Viloria, M. P., DeAngelis, J. P., et al. (2017). Changes in contact area in meniscus horizontal cleavage tears subjected to repair and resection. *Arthroscopy-the J. Arthrosc. Relat. Surg.* 33 (3), 617–624. doi:10.1016/j.arthro.2016.09.004

Bedi, A., Kelly, N. H., Baad, M., Fox, A. J. S., Brophy, R. H., Warren, R. E., et al. (2010). Dynamic contact mechanics of the medial meniscus as a function of radial tear, repair, and partial meniscectomy. *J. Bone & Jt. Surgery-american Volume* 92 (6), 1398–1408. doi:10.2106/JBJS.I.00539

Bedrin, M. D., Kartalias, K., Yow, B. G., and Dickens, J. F. (2021). Degenerative joint disease after meniscectomy. *Sports Med. Arthrosc. Rev.* 29 (3), e44–e50. doi:10.1097/jsa.0000000000000301

Bell, J. S., Winlove, C. P., Smith, C. W., and Dehghani, H. (2009). Modeling the steady-state deformation of the solid phase of articular cartilage. *Biomaterials* 30 (31), 6394–6401. doi:10.1016/j.biomaterials.2009.08.026

Brown, M. J., Farrell, J. P., Kluczynski, M. A., and Marzo, J. M. (2016). Biomechanical effects of a horizontal medial meniscal tear and subsequent leaflet resection. *Am. J. Sports Med.* 44 (4), 850–854. doi:10.1177/0363546515623782

Chevrier, A., Nelea, M., Hurtig, M. B., Hoemann, C. D., and Buschmann, M. D. (2009). Meniscus structure in human, sheep, and rabbit for animal models of meniscus repair. *J. Orthop. Res.* 27 (9), 1197–1203. doi:10.1002/jor.20869

Cho, W. J., Kim, J. M., Lee, B. S., Kim, H. J., and Bin, S. I. (2019). Discoid lateral meniscus: A simple horizontal tear was associated with less articular cartilage degeneration compared to other types of tear. *Knee Surg. Sports Traumatol. Arthrosc.* 27 (10), 3390–3395. doi:10.1007/s00167-019-05363-z

Civitarese, D., Donahue, T. L., Laprade, C. M., Saroki, A. J., Laprade, R. F., Schon, J. M., et al. (2016). Qualitative and quantitative measurement of the anterior and posterior meniscal root attachments of the New Zealand white rabbit. *J. Exp. Orthop.* 3 (1), 10. doi:10.1186/s40634-016-0046-4

Esrafilian, A., Stenroth, L., Mononen, M. E., Vartiainen, P., Tanska, P., Karjalainen, P. A., et al. (2022). Toward tailored rehabilitation by implementation of a novel musculoskeletal finite element analysis pipeline. *IEEE Trans. Neural Syst. Rehabilitation Eng.* 30, 789–802. doi:10.1109/TNSRE.2022.3159685

Feucht, M. J., Salzmann, G. M., Bode, G., Pestka, J. M., Kühle, J., Südkamp, N. P., et al. (2015). Posterior root tears of the lateral meniscus. *Knee Surg. Sports Traumatol. Arthrosc.* 23 (1), 119–125. doi:10.1007/s00167-014-2904-x

Gushue, D. L., Houck, J., and Lerner, A. L. (2005). Rabbit knee joint biomechanics: Motion analysis and modeling of forces during hopping. *J. Orthop. Res.* 23 (4), 735–742. doi:10.1016/j.orthres.2005.01.005

Haemer, J. M., Wang, M. J., Carter, D. R., and Giori, N. J. (2007). Benefit of single-leaf resection for horizontal meniscus tear. *Clin. Orthop. Relat. Res.* 457 (457), 194–202. doi:10.1097/BLO.0b013e3180303b5c

Herrlin, S. V., Wange, P. O., Lapidus, G., Hållander, M., Werner, S., and Weidenhielm, L. (2013). Suzanne werner, lars weidenhielm. Is arthroscopic surgery beneficial in treating non-traumatic, degenerative medial meniscal tears? A five year follow-up. *Knee Surg. Sports Traumatol. Arthrosc.* 21 (2), 358–364. doi:10.1007/s00167-012-1960-3

Jiang, D., Luo, X., Ao, Y., Gong, X., Wang, Y. J., Wang, H. J., et al. (2017). Risk of total/subtotal meniscectomy for respective medial and lateral meniscus injury: Correlation with tear type, duration of complaint, age, gender and ACL rupture in 6034 asian patients. *BMC Surg.* 17 (1), 127. doi:10.1186/s12893-017-0324-9

Jiang, D., Zhang, Z. Z., Zhao, F., Wang, S. J., Qi, Y. S., Zhao, L. H., et al. (2018). The radiated deep-frozen xenogenic meniscal tissue regenerated the total meniscus with chondroprotection. *Sci. Rep.* 8 (1), 9041. doi:10.1038/s41598-018-27016-w

Kani, K. K., Porrino, J. A., and Chew, F. S. (2021). Meniscal allograft transplantation: A pictorial review. *Curr. Problems Diagnostic Radiology* 51 (5), 779–786. doi:10.1067/j.cpradiol.2021.09.008

Kedgley, A. E., Saw, T. H., Segal, N. A., Hansen, U. N., Bull, A. M. J., and Masouros, S. D. (2019). Predicting meniscal tear stability across knee-joint flexion using finite-element analysis. *Knee Surg. Sports Traumatol. Arthrosc.* 27 (1), 206–214. doi:10.1007/s00167-018-5090-4

Koh, J. L., Yi, S. J., Ren, Y., Zimmerman, T. A., and Zhang, L. Q. (2016). Tibiofemoral contact mechanics with horizontal cleavage tear and resection of the medial meniscus in the human knee. *J. Bone & Jt. Surg. Am. Volume* 98 (21), 1829–1836. doi:10.2106/JBJS.16.00214

Kurzweil, P. R., Cannon, W. D., and Dehaven, K. E. (2018). Meniscus repair and replacement. *Sports Med. Arthrosc. Rev.* 26 (4), 160–164. doi:10.1097/JSA.0000000000000224

Kurzweil, P. R., Lynch, N. M., Coleman, S., and Kearney, B. (2014). Repair of horizontal meniscus tears: A systematic review. *Arthrosc. J. Arthrosc. Relat. Surg.* 30 (11), 1513–1519. doi:10.1016/j.arthro.2014.05.038

Lau, B. C., Conway, D., Mulvihill, J., Zhang, A. Z., and Feeley, B. T. (2018). Biomechanical consequences of meniscal tear, partial meniscectomy, and meniscal repair in the knee. *Jbjs Rev.* 1, e3. doi:10.2106/JBJS.RVW.17.00125

Lee, S. W., Chun, Y. M., Choi, C. H., Kim, S. J., Jung, M., Han, J. W., et al. (2016). Single-leaf partial meniscectomy in extensive horizontal tears of the discoid lateral meniscus: Does decreased peripheral meniscal thickness affect outcomes? (Mean four-year follow-up). *Knee* 23 (3), 472–477. doi:10.1016/j.knee.2015.11.019

Li, L., Yang, L., Zhang, K., Zhu, L., Wang, X., and Jiang, Q. (2020). Three-dimensional finite-element analysis of aggravating medial meniscus tears on knee osteoarthritis. *J. Orthop. Transl.* 20, 47–55. doi:10.1016/j.jot.2019.06.007

Liu, W., Sun, X., Liu, W., Liu, H., Zhai, H. Y., Zhang, D. D., et al. (2022). Finite element study of a partial meniscectomy of a complete discoid lateral meniscus in adults. *Med. Eng. Phys.* 107, 103855. doi:10.1016/j.medengphy.2022.103855

Mansour, J. M., Wentorf, F. A., and Degoede, K. M. (1998). *In vivo* kinematics of the rabbit knee in unstable models of osteoarthrosis. *Ann. Biomed. Eng.* 26 (3), 353–360. doi:10.1114/1.133

Messner, K., Fahlgren, A., Ross, I., and Andersson, B. (2000). Simultaneous changes in bone mineral density and articular cartilage in a rabbit meniscectomy model of knee osteoarthrosis. *Osteoarthr. Cartil.* 8 (3), 197–206. doi:10.1053/joca.1999.0290

Narita, A., Takahara, M., Sato, D., Ogino, T., Fukushima, S., Yu, K., et al. (2012). Biodegradable gelatin hydrogels incorporating fibroblast growth factor 2 promote healing of horizontal tears in rabbit meniscus. *Arthroscopy* 28 (2), 255–263. doi:10.1016/j.arthro.2011.08.294

Ogawa, H., Matsumoto, K., Sengoku, M., Yoshioka, H., and Akiyama, H. (2020). Arthroscopic repair of horizontal cleavage meniscus tears provides good clinical outcomes in spite of poor meniscus healing. *Knee Surg. Sports Traumatol. Arthrosc.* 28 (11), 3474–3480. doi:10.1007/s00167-019-05782-y

Ozeki, N., Koga, H., and Sekiya, I. (2022). Degenerative meniscus in knee osteoarthritis: From pathology to treatment. *Life* 12 (4), 603. doi:10.3390/life12040603

Patsch, C., Dirisamer, F., and Schewe, B. (2021). Relevance of meniscus loss for the progression of osteoarthritis and treatment options for early arthritis. *Der Orthopade* 50 (5), 366–372. doi:10.1007/s00132-021-04101-z

Posadzy, M., Joseph, G. B., McCulloch, C. E., Nevitt, M. C., Lynch, J. A., Lane, N. E., et al. (2020). Natural history of new horizontal meniscal tears in individuals at risk for and with mild to moderate osteoarthritis: Data from osteoarthritis initiative. *Eur. Radiol.* 30 (11), 5971–5980. doi:10.1007/s00330-020-06960-0

Roland, W. M., Wirt, D., James, S., Mark, M., Jack, B., Michaael, M., et al. (1973). Experimentally induced degenerative joint lesions following partial meniscectomy in the rabbit. *Arthritis & Rheumatology* 16 (3), 397–405. doi:10.1002/art.1780160317

Seil, R., and Pape, D. (2010). "Meniscal repair: Biomechanics," in *The meniscus*. Editors P. Beaufils, and R. Verdonk (Berlin, Heidelberg: Springer). doi:10.1007/978-3-642-02450-4_15

Shanmugaraj, A., Tejpal, T., Ekhtiari, S., Gohal, C., Bhandari, M., Hanson, B., et al. (2019). The repair of horizontal cleavage tears yields higher complication rates compared to meniscectomy: A systematic review. *Knee Surg. Sports Traumatol. Arthrosc.* 28 (1), 915–925. doi:10.1007/s00167-019-05557-5

Sung, J. H., Ha, J. K., Lee, D. W., Seo, W. Y., and Kim, J. G. (2013). Meniscal extrusion and spontaneous osteonecrosis with root tear of medial meniscus: Comparison with horizontal tear. *Arthroscopy* 29 (4), 726–732. doi:10.1016/j.arthro.2012.11.016

Sweigart, M. A., and Athanasiou, K. A. (2005). Tensile and compressive properties of the medial rabbit meniscus. *Proc. Institution Mech. Eng. Part H J. Eng. Med.* 219 (5), 337–347. doi:10.1243/095441105X34329

Tan, Z. W., Wang, B. A., Yao, Y. M., Chen, J. L., Duan, X., Liu, M., et al. (2020). Finite element analysis of cartilage stress of rabbits in the knee joints and establishment of a model for cartilage defects in different weight-bearing sites. *J. biomaterials tissue Eng.* 10 (6), 757–762. doi:10.1166/jbt.2020.2326

Wang, S., Hase, K., Kita, S., and Ogaya, S. (2022). Biomechanical effects of medial meniscus radial tears on the knee joint during gait: A concurrent finite element musculoskeletal framework investigation. *Front. Bioeng. Biotechnol.* 10, 957435. doi:10.3389/fbioe.2022.957435

Yang, W. Z., Shi, T., Du, H. B., and Yan, G. H. (2021). Effect of arthroscopic operation on meniscus injury of knee joint and functional recovery of patients. *Med. Forum* 25 (10), 3. [in chinese]. doi:10.19435/j.1672-1721.2021.10.036

Yim, J. H., Seon, J. K., Song, E. K., Choi, J. I., Kim, M. C., Lee, K. B., et al. (2013). A comparative study of meniscectomy and nonoperative treatment for degenerative horizontal tears of the medial meniscus. *Am. J. Sports Med.* 41 (7), 1565–1570. doi:10.1177/0363546513488518

Zhang, K., Li, L., Yang, L., Shi, J., Zhu, L. Y., Liang, H. X., et al. (2019). Effect of degenerative and radial tears of the meniscus and resultant meniscectomy on the knee joint: A finite element analysis. *J. Orthop. Transl.* 18, 20–31. doi:10.1016/j.jot.2018.12.004

Zhang, X. H., Yuan, S., Wang, J., Liao, B. G., and Liang, D. (2021). Biomechanical characteristics of tibio-femoral joint after partial medial meniscectomy in different flexion angles: A finite element analysis. *BMC Musculoskelet. Disord.* 22 (1), 322. doi:10.1186/s12891-021-04187-8

Zhang, Z. Z., Jiang, D., Wang, S. J., Qi, Y. S., Zhang, J. Y., and Yu, J. K. (2015). Potential of centrifugal seeding method in improving cells distribution and proliferation on demineralized cancellous bone scaffolds for tissue-engineered meniscus. *ACS Appl. Mater Interfaces* 7 (28), 15294–15302. doi:10.1021/acsami.5b03129

frontiers | Frontiers in Veterinary Science

TYPE Original Research
PUBLISHED 18 July 2023
DOI 10.3389/fvets.2023.1176757

OPEN ACCESS

EDITED BY
Claire Rebecca Sharp,
Murdoch University, Australia

REVIEWED BY
Cord Brundage,
University of Wisconsin-La Crosse, United States
Elizabeth Anne Rozanski,
Tufts University, United States

*CORRESPONDENCE
Rocio Fernández-Parra
✉ rocio.f.parra@ucv.es

RECEIVED 28 February 2023
ACCEPTED 03 July 2023
PUBLISHED 18 July 2023

CITATION
Fernández-Parra R, Pey P, Reinero C and Malvè M (2023) Salbutamol transport and deposition in healthy cat airways under different breathing conditions and particle sizes.
Front. Vet. Sci. 10:1176757.
doi: 10.3389/fvets.2023.1176757

Salbutamol transport and deposition in healthy cat airways under different breathing conditions and particle sizes

Rocio Fernández-Parra[1]*, Pascaline Pey[2], Carol Reinero[3] and Mauro Malvè[4,5]

[1]Department of Small Animal Medicine and Surgery, Faculty of Veterinary Medicine, Universidad Católica de Valencia San Vicente Mártir, Valencia, Spain, [2]Antech Imaging Services, Irvine, CA, United States, [3]Department of Veterinary Medicine and Surgery, University of Missouri, Columbia, MO, United States, [4]Department of Engineering, Public University of Navarre (UPNA), Pamplona, Spain, [5]Biomedical Research Networking Center in Bioengineering, Biomaterials and Nanomedicine (CIBER-BBN), Madrid, Spain

Salbutamol is a bronchodilatator commonly used for the treatment of feline inflammatory lower airway disease, including asthma or acute bronchospasm. As in humans, a pressurized metered dose inhaler (pMDI) is used in conjunction with a spacer and a spherical mask to facilitate salbutamol administration. However, efficacy of inhalation therapy is influenced by different factors including the non-cooperative character of cats. In this study, the goal was to use computational fluid dynamics (CFD) to analyze the impact of breathing patterns and salbutamol particle size on overall drug transport and deposition using a specific spherical mask and spacer designed for cats. A model incorporating three-dimensional cat airway geometry, a commercially available spherical mask, and a 10 cm spacer, was used for CFD analysis. Two peak inspiratory flows were tested: 30 mL/s and 126 mL/s. Simulations were performed with 30s breathing different inspiratory and expiratory times, respiratory frequencies and peaks. Droplet spray transport and deposition were simulated with different particle sizes typical of the drug delivery therapies (1, 5, 10, and 15 μm). The percentage of particle deposition into the device and upper airways decreased with increasing particle diameter during both flows imposed in this cat model. During increased mean ventilatory rate (MVR) conditions, most of the salbutamol was lost in the upper airways. And during decreased MVR conditions, most of the particles remained in suspension (still in hold-up) between the mask and the carina, indicating the need for more than 30 s to be transported. In both flows the percentage of particles traveling to the lung was low at 1.5%–2.3%. In conclusion, in contrast to what has been described in the human literature, the results from this feline model suggest that the percentage of particles deposited on the upper airway decreases with increasing particle diameter.

KEYWORDS

computational fluid dynamics (CFD), lower airway disease, feline, bronchospasm, inhalation therapy

1. Introduction

Inhalation therapy at-home or at the hospital is commonly used in cats (1). The primary treatment of feline lower airway disease (FLAD) is glucocorticoids with or without bronchodilators (1–3). Oral medication is generally considered to be effective and affordable, but some cats are challenging to medicate by this route and systemic side effects can be problematic (4). Parenteral treatment may be used during hospitalization but inhalational treatment has important advantages including direct application to the site of action (lower respiratory tract), fewer systemic adverse effects, and for certain inhaled bronchodilators, a more rapid onset of action (5). However, inhaled medications are not without their own set of limitations. In a recent online survey study (4) difficulties in administration of glucocorticoid or bronchodilator inhalant therapies were reported in 28% and 31% of owners, respectively. In another study of FLAD in which cats received metered dose inhalant budesonide, 55.8% of owners withdrew therapy due to high cost, lack of time for twice daily treatment, and/or drug ineffectiveness (6). Nebulization of liquid medications has been proposed as an alternative treatment (7, 8), but further studies are needed to test the efficiency of drug delivery with this technique. Furthermore, nebulizers require good hygiene to avoid contamination and some nebulizers are noisy and bulky (9).

In the case of feline asthma, one type of inflammatory FLAD, airways have increased responsiveness to inhaled aeroallergens or irritants provoking bronchoconstriction (10). Clinically, tachypnoea, wheezing, coughing or labored respiration (typically with increased expiratory effort) are observed, which can be treated with bronchodilators (2, 11) such as salbutamol. Clinically, bronchodilators may also be used as a preventive therapy against bronchospasm during bronchoscopy and bronchoalveolar lavage (12) or as an emergency drug during bronchospasm through general anesthesia. Inhaled salbutamol, also known as albuterol, is marketed as a pressurized metered dose inhaler (pMDI) with doses ranging between 25 to 100 µg per actuation (13). In general, the pMDIs are filled with the pressurized drug in the form of either a solution or suspension of drug particles in the micron size ranging between 1 to 100 µm and dispersed within a suitable propellant in its interior (14). The diameter of salbutamol pMDI particles are in the range of microns (15, 16). Most computational studies use particle sizes ranging between 1 and 17 µm to test inhaled particle deposition (17, 18). The transport and distribution of particles are mainly affected by their size and the flow patterns during inhalation in humans (16). But the velocity, relative humidity (19), devices used to apply them, or the anatomy (20, 21) also play roles. Spacers are chamber extensions to the pMDI attached to a mask that allow the inhalation of the drug without synchronization with the actuation of the inhaler (22). However, their efficiency is controversial (23). In a previous study using computational fluid dynamics (CFD), we demonstrated how the choice of different devices to administer salbutamol in cats with pMDIs impact the amount of drug that ultimately reaches the lung (24).

In human medicine, therapeutic effectiveness is strongly related to the correct use of devices and to the inhalation technique (25, 26). Additionally, the respiratory system has developed defense mechanisms against inhaled particles which must be overcome by inhalational therapies (27). In veterinary medicine, devices are not fully optimized to the individual patient or to the underlying pathological condition (28). Veterinarians are able to choose from a large number of commercial devices and masks designed for cats or adapted from humans. Unfortunately, masks are commercially available only in standard dimensions and clinically may not fully conform with a necessary tight seal to the muzzle of an individual cat. Furthermore, it is difficult to assess if the inhalation technique is well or poorly performed. Commands to initially exhale, fully inhale the medication, and breath hold as is done in humans, cannot be performed in cats and likely contributes to suboptimal drug deposition in the lungs (29). Furthermore, any unwillingness of cats to tolerate correct use of the device is a major limitation to its clinical use. Clinically, we have observed that inhalation therapies where restrain of the cat is necessary can be even more challenging leading to drug waste or increased stress of the cat. Acute disease exacerbation may modify the respiratory rate and pattern. There are also scenarios (e.g., critically ill hospitalized cats) where hypoventilation is more common. The deposition of particles of these scenarios is unknown.

The size of aerosolized particles during therapeutic delivery is essential to determine location and amount of drug deposition in the airways (30). The transport mechanism depends on particle diameter, with impaction being the main phenomenon driving micro-particles and diffusion driving nanoparticles. In the human airways, while deposition is small for particles less than 1 µm, it tends to increase in the range of micron (16, 31, 32). Additionally, breathing conditions affect the transport and the deposition of particles in the airways with higher flow rates tending to increase deposition for larger particle sizes (31). In animals, limited studies in rabbits, rats, monkeys and mice have investigated transport and deposition of aerosolized particles in the nasal and upper airways (33–38). Specifically in cats, data on the behavior of different aerosolized particle sizes with different peak inspiratory flows has yet to be reported.

Our previous work was a proof of concept using computed tomographic images based CFD model of upper airways from a single cat, using reasonable inspiratory and expiratory peak flow with a fixed salbutamol particle diameter of 10 µm and different devices. In the present study we have considered two ventilation conditions corresponding to decreased and increased mean ventilatory rate (MVR) or, in other words, minute ventilation that match better with the clinical situation of the animal when inhalant therapy is carried out during hospitalization (critical/sedated or stressed, respectively). Moreover, we have considered and studied the deposition and transport of different salbutamol particle sizes typical of drug delivery with a single device (10 cm length spacer and spherical mask).

The aim of this study was to use CFD to evaluate the distribution of microparticles according to two flows and particle size of salbutamol using a single device and anatomical healthy feline model. We hypothesized that larger particle sizes and increased MVR would enhance particle waste, while decreased MVR would enhance delivery of smaller particles to the lung.

2. Materials and methods

2.1. Animal model and computed tomographic (CT) images

A previous geometrical reconstruction of a CT image from a client-owned domestic shorthair cat of 3 years and 8 months of age that presented to our hospital for otitis media with no other concomitant

respiratory or systemic disease, was used for further simulations. The cat weighed 4.25 kg, was sedated, breathing spontaneously, and placed in sternal recumbency with the head elevated and neck fully extended for a head to thorax CT. The use of images was approved by the Clinical Research Ethical Committee of the École Nationale Vétérinaire d'Alfort (ENVA), France (number: 2020-05-30).

Non-contrast-enhanced multidetector computed tomography (MDCT) examination was carried out using a 64-detector-row CT system (Brilliance 64; Philips, Amsterdam, Netherlands). The CT scan was obtained using a matrix of 768 × 768, tube voltage of 120 kV, tube current of 196 mA and a display field of view of 35 cm and a pitch of 0.5. Images for the study were acquired from the nostrils to the most caudal border of the lungs. One-millimeter-thick images were reconstructed using a high-resolution algorithm. The scan was reviewed using a commercial medical imaging software, DICOM (Digital Imaging and Communications in Medicine) viewer (Horos v.1.1.7., 64-bit, HorosTM, US) using a lung window (window width (WW): 1600; window level (WL): -550).

2.2. Geometrical reconstruction and numerical discretization

The creation and discretization of the model has been extensively described and discussed in a previous study (24). Briefly, using the commercial software MIMICS (Materialise Software, Leuven, Belgium), using the CT images of the cat, a three-dimensional geometry of the upper airways including nasal cavity, naso-pharynx, oropharynx, larynx, and trachea was created (see Figure 1A). The reconstruction was performed manually. The geometry was exported in STL (Stereo Lithography) file and successively imported in the meshing program Ansys IcemCFD of the commercial package Ansys (v.20, Ansys Inc.). The devices (inhaler; Ventolin Evohaler 100 micrograms GlaxoSmithKline, Brentford, UK, spherical mask and 10 cm length spacer without valve; Aerokat™, Trudell Animal Health, ON, Canada) were created in the software package Rhinoceros (Robert McNeel & Associates, Seattle, WA, United States) (Figure 1B) and added to the cat STL file using Boolean union tools and functions. The final geometry is depicted in the Figure 1C. An automatic discretization of the geometry consisting of filling in the volume (composed by all the imported regions) with tetrahedral elements and the surfaces with triangles was carried out. As widely known in computational biomechanics, numerical models comprised of a small number of elements permits short computational costs but provides low precision of the results. On the contrary, models with a large number of discretization elements implies high computational costs with more precise results. For these reasons, prior to the final simulations we performed a mesh independence study to assess the dependency of the results on the number of elements composing the computational geometrical volume. This analysis was described previously (24) and demonstrated that greater than 23.5 million elements provides only higher computational costs without improving the precision of the solution. As a consequence, a grid composed of approximately 23.5 million elements was ultimately chosen. This mesh consisted of 2.5 million elements for the pre-oxygenation mask, 3 million elements for the spacer, and 18 million elements for the cat airways.

2.3. Computational analysis

The software package divided the simulations in two main parts: the continuous phase, consisting of the flow entering and going out to

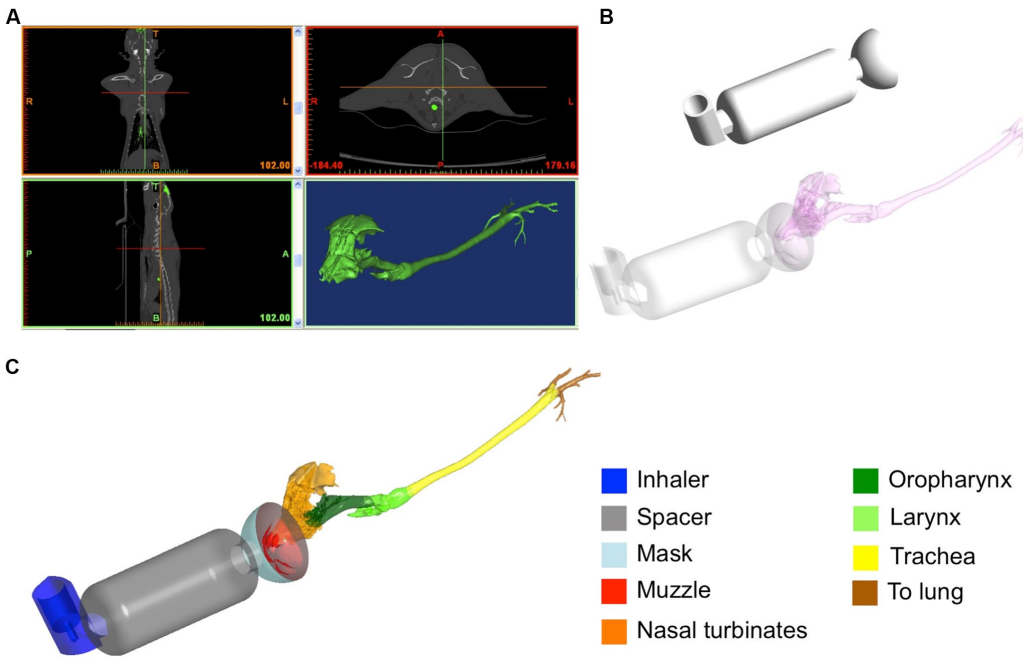

FIGURE 1
Reconstruction of the geometrical model starting from the CT-images of the cat **(A)**. Considered devices designed using CAD software: inhaler, spacer of 10 cm length and spherical pre-oxygenation mask **(B)**. Final geometrical domain considered for the simulations **(C)**.

the computational domain, and the discrete phase consisting of a finite number of particles traveling within the domain and subjected to a specific behavior depending on the continuous phase (flow structure) and on collision with the airways.

2.3.1. CFD modeling (continuous phase)

The mesh obtained after the volume discretization of the cat was imported into a simulation software package (Ansys CFX, v.22, Ansys Inc., Canonsburg, PA, United States).

The governing equations of motion of the gas flow used were the Reynolds averaged Navier-Stokes equations:

$$\nabla \cdot \bar{V} = \mathbf{0}$$

$$\frac{\partial \bar{V}}{\partial t} + \nabla \cdot \left(\bar{V} \times \bar{V}\right) = -\frac{\nabla p'}{\rho} + \left(\nabla \cdot \nu_{eff}\left(\nabla \bar{V} + \left(\nabla \bar{V}\right)^T\right)\right)$$

where $\bar{\boldsymbol{V}}$ is the averaged fluid velocity vector, p′ is modified pressure, ρ is the gas density, ν_{eff} is the effective kinematic viscosity and $\frac{\partial \bar{\boldsymbol{V}}}{\partial t}$ is its partial derivative of the velocity $\bar{\boldsymbol{V}}$ respect to the time t, ∇ is the nabla symbol, $\nabla \bar{V}$ is the gradient of the average fluid velocity and $\left(\nabla \bar{V}\right)^T$ its transposed. The latter can be obtained as sum of the gas kinematic viscosity ν, and the turbulence kinematic viscosity ν_t:

$$\nu_{eff} = \nu + \nu_t.$$

For modeling the turbulence, the Wilcox $k - \omega$ model was selected. This model predicts the turbulence using a partial differential equation for the turbulence kinetic energy k and a partial differential equation for its rate of dissipation ω (39). The general form of the gas dynamics equations, the turbulence equations, the precise definition of all parameters and variables, and the discretization and resolution methods are found in the Ansys manufacturer's manual (40).

The governing equations of the fluid mechanics were recursively solved by this software using the finite volume method applied to the computational domains, i.e., the generated mesh and using boundary conditions such as flow velocity or pressure among others. The exact mathematical formulation and the solving algorithms used by Ansys CFX are given in the software manual (40).

The peak inspiratory flow under conditions of decreased MVR was 30 mL/s and under increased MVR was 126 mL/s (41). The 30 mL/s flow was obtained by means of a variable orifice flow sensor (GE Aestiva 5 Anesthesia Machine – Datex Ohmeda, Madison, WI, United States) in cats under general anesthesia. The peak inspiratory flow was imposed at the top of the pMDI (see Figure 2). As commented before, the flow was considered unsteady and turbulent with an initial turbulence intensity value of 5% (24).

A respiratory cycle of 3 s (1 s inspiration, 2 s expiration) and 10 respiratory cycles were used for the simulation under conditions of decreased MVR. Secondly, a respiratory cycle of 1.19 s (0.48 s inspiration, 0.71 s expiration) and 25 respiratory cycles were used for the increased MVR model (41). Both simulations had a duration of 30 s, divided into 3,000 time steps using a time step size of 0.01 s. The simulations adopted an air density of 1.185 kg/m^3 and a viscosity of 1.83 10^{-5} Pa·s (42).

2.3.2. Particle modeling (discrete phase)

The particle modeling was also computed in Ansy CFX and performed simultaneously with the fluid dynamics simulations. The software uses the discrete phase modeling (DPM) to obtain the trajectories and the fate of the particles injected through the pMDI nozzle. After defining the initial position, velocity and size, each particle is individually followed through the computational model using the force balance and local continuous phase conditions. Ansys CFX computes particle trajectories using Newton's second law considering the drag force and gravity. This equation can be written as:

$$\frac{m_p d\boldsymbol{V}}{dt} = \frac{1}{8}\rho {d_p}^2 c_{Dp}\left|\boldsymbol{V} - \boldsymbol{V_p}\right|\left(\boldsymbol{V} - \boldsymbol{V_p}\right) + \boldsymbol{g}$$

where $\boldsymbol{V}$ is the gas velocity, $d\boldsymbol{V}/dt$ is its derivative respect to the time t, $\boldsymbol{V}_p$ is the particle velocity, m_p is the particle mass, ρ is the gas density, $\boldsymbol{g}$ is the gravitational force, d_p the particle diameter and c_{Dp} is the drag coefficient that is computed through the relation:

$$c_{Dp} = \frac{c_D}{c_S}$$

where c_S is a correction factor of the drag coefficient c_D that takes into account the irregularity of the droplet with respect to a spherical shape and it is function of the particle Reynolds number (Re_p)

$$\mathrm{Re}_p = \frac{\rho\left|V - V_p\right|V_p}{\mu}$$

where μ is the dynamic viscosity of the gas.

The model included 2000 particles that are representative of a dose of 100 μg per actuation (13). Particles are tracked through the fluid domain until one of the following three specific conditions happens: they impact and are trapped on the airways walls (deposition), they escape from the domain through outlets, or they continue in suspension in the flow (they could subsequently be exhaled or impact an airway wall in further breathings). If they escape through the outlets, they are automatically considered as traveling to the lungs. Particles are considered perfectly spherical and dilute and it is assumed that while flow influences the particle trajectories, the particles cannot interfere with the fluid motion (i.e., the continuous phase is not affected by the discrete phase). This hypothesis (also called "one way coupling") is applicable, as the considered particles sizes and the volume fraction are sufficiently small (32). In order to obtain a regional particle deposition, the model was divided into zones, as shown in the Figure 1C. In particular, we specified the device that includes the inhaler, spacer and mask, the muzzle and the upper airways, divided into nasal turbinates that also includes the sinus, oropharynx, larynx, trachea that includes the carina and primary bronchi. Particles getting into the bronchi or exiting through the outlet where considered as traveling "to lung".

Also, for the particle modeling, prior to the simulation a particle number independence study was carried out to find out

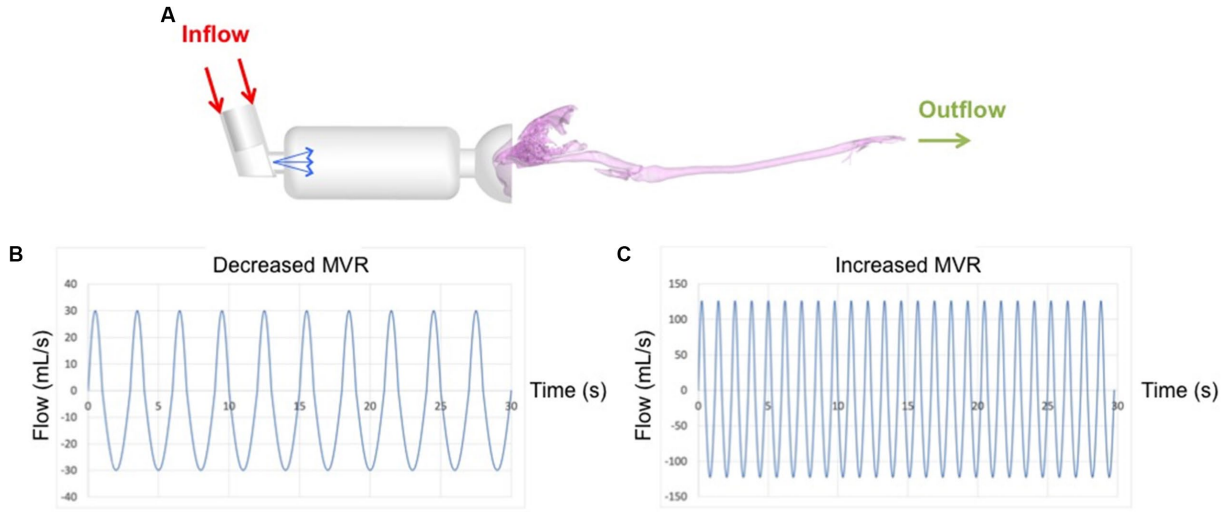

FIGURE 2
Complete computational model with boundary conditions used for the simulations. Red arrows represent location where the flow enters; green arrows represent the location where the flow exits. Blue arrows show the salbutamol spray which entrance velocity was 150 m/s **(A)**. Waveforms of 30s duration applied at the inlet and corresponding to 30 mL/s **(B)** and 126 mL/s **(C)** flows are plotted in the lower part of the figure.

the necessary number of particles to be injected in the fluid domain, i.e., to prove if 2000 particles are representative of a dosage of 100 per actuation. A sensibility analysis with different particle numbers was performed in a previous study (24) and concluded that 2000 particles are effectively representative of the considered actuation dose. The initial droplet diameters considered in this study were 1, 5, 10, and 15 μm, based on previous studies (15, 17, 18). The initial spray velocity was 150 m/s with a cone angle of 15 (43). Furthermore, the pMDI actuation was applied prior to the first breathing cycle in order to simulate clinical conditions.

The salbutamol spray was modelled in CFX using a specific available model called "gas–liquid interactive Enhanced Taylor Analogy Breakup (ETAB) model" (13). This model predicts the formation of droplets caused by the drag force due to the interaction between gas and particle and their different velocities. The droplets formation takes place accordingly to the ratio between the inertia force to surface tension, also called Weber number (We), that combines the droplet deformation and the liquid surface tension as follows:

$$We = \rho \frac{V^2 r}{\sigma_L}$$

where ρ is the gas density, V is the relative velocity between gas and particle, r is the particle radius, and σ_L is the coefficient of liquid surface tension.

The pMDI used in the model consisted of a canister connected to a metering valve capable of producing variable dosages. As commented before, in this study we used 100 µg (13) delivered through an actuator-nozzle of 0.5 mm diameter located at the center line of the canister in a centered position with respect to the mask (Figure 2).

The numerical models allow computation of flow velocity and structures inside the cat airways and devices. The structure of the flow is depicted using 3D streamlines while the flow intensity is represented using a heatmap.

All computations were performed on an Intel Core i9 workstation with 2.3 GHz frequency, 32 GB RAM and parallelized on 8 processors. The computational cost of the simulations under decreased MVR was 254.5 h while during increased MVR condition was 273.2 h.

2.3.3. Validation of the model

The computational model used in the present study was validated in a previous work (24). Briefly, the particle transport and deposition were validated using idealized human airways (including the oral tract through the first 4 bifurcations), classical breathing conditions (15, 30, and 60 L/min) and a particle diameter of 10 µm. In this model, particles were uniformly distributed to the oral entrance and released directly in the oral cavity without using the inhaler. Aerosol delivery was evaluated by means of steady simulations using the aforementioned breathing conditions and turbulent flow. Deposition fractions within the oral tract and the main bifurcations were computed and systematically compared with the results of Zhang and co-workers in 2005 (32). The obtained results confirmed the validity of the model, as the deposition fractions obtained with the present model were the same as those found by Zhang and co-workers (32).

Furthermore, because the spray modeling used in this work is based on those published in the literature (30, 43), using human airways without bifurcations, we have compared the spray performances obtained in the present model with the values obtained in those studies. It was clearly seen that the spray characteristics comply with the necessary requirements as the obtained results match well the findings previously published by Kleinstreuer and co-workers in 2007 (13) and by Yousefi and co-workers (43). For further details please see the paper from Fernandez-Parra et al. (24).

2.4. Data analysis

Airflow streamlines (peak inspiratory flow structures) and droplet deposition were represented using heat maps and described qualitatively for the various conditions in the three models. Percentages of particles deposited to the devices, to the upper airways and transported to the lung as previously defined for all conditions in each model were reported. Further data was analyzed with the statistical program IBM® SPSS® (Statistics software, version 30, Chicago, IL). A Shapiro-Wilk test was used to test for normal distribution of percentages of particles deposited to the aforementioned three regions and in suspension for further comparisons. Results are expressed in median (ranges) with maximum and minimum values. A Mann-Whitney U test was used to compare deposition percentages and a Kruskal Wallis test to compare differences in particle sizes between flow conditions. Values of $p < 0.05$ were considered statistically significant.

3. Results

3.1. Airflow patterns

The airflow structure within the cat airways is represented in Figure 3. Streamlines (lines indicating the direction of the flow) were colored with the velocity intensity for decreased and increased MVR during inhalation and exhalation in the last breathing cycle.

Comparing the two breathing conditions, there were obvious differences in intensity of the velocity, more marked during increased MVR (light blue in Figure 3B representing higher velocity in comparison with dark blue in Figure 3A). Additionally, there was a visible and consistent difference inside the spacer. A low breathing rate led to more ordinate and parallel streamlines in this device whereas for a higher breathing rate, the streamlines inside the spacer were more chaotic. These flow patterns likely influence salbutamol deposition as the particles are transported by airflow that presents changes in direction much more enhanced for 126 mL/s versus 30 mL/s.

High flow velocity is visible in both cases and for both inhalation and exhalation near the nasal region, where the flow entrance suddenly reduces from the spacer (during inhalation) and from the oropharynx (during exhalation). On the contrary, the laryngeal region shows lower velocity intensity compared to the nasal region. Although the larynx normally acts as a nozzle, decreased MVR seems to promote a uniform intensity through the larynx; under conditions of increased MVR there is only a slight high-speed region visible (see Figure 3).

Figure 4 shows the trajectories followed by particles of 1, 5, 10, and 15 µm during entire breathing cycles. The Figure depicts the aerosolized salbutamol flow of particles injected through the MDPI orifice and reaching the lung (the model outlet of the computational domain). A marked difference is visible in both ventilation conditions between particles of 1 µm with respect to the other sizes. One-µm particles are less influenced by the airflow inside the spacer compared to 5, 10, and 15 µm particles. Comparing the two flow rates for particles bigger than 1 µm, the trajectories follow the airflow structure in the spacer providing a higher number of particles in suspension for decreased MVR (compare with Figure 3A). Additionally, increased MVR leads to more chaotic trajectories in the spacer compared to decreased model (for example, compare the density of trajectories inside the spacer for particle >1 µm represented in Figures 4A,B).

3.2. Particle transport and deposition

All values in this section, deposition, reaching the lung and suspension refer to the entire cycles lasting 30s. The total percentage (%) of particles reaching the lung after 30 s of breathing flows of 30 mL/s (A) and 126 mL/s (B) are represented in Figure 5.

Particle deposition percentage was computed after 30s as ratio of deposited and injected particles times 100. These percentages of particles deposited at the device are summarized in Table 1. They represent the amount of drug, which is not able to reach the upper airways or the lungs.

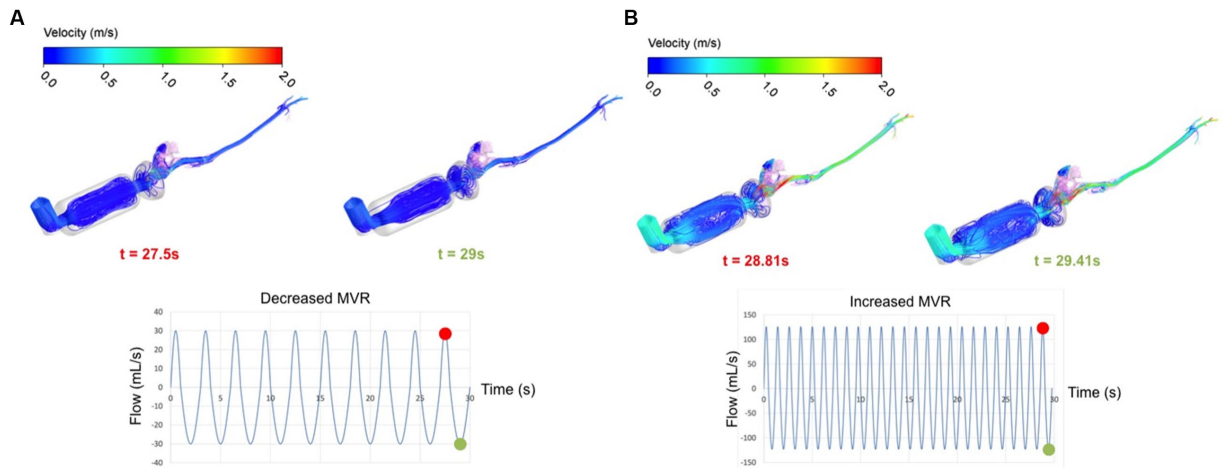

FIGURE 3
3D view of the flow structure colored using the velocity intensity for both breathing flows 30 mL/s **(A)** and 126 mL/s **(B)** at specified instants of time: at inhalation, t = 27.50s and 28.81 s, respectively (red circle on the curve) and at exhalation, t = 29.00s and 29.41 s, respectively (green circle on the curve).

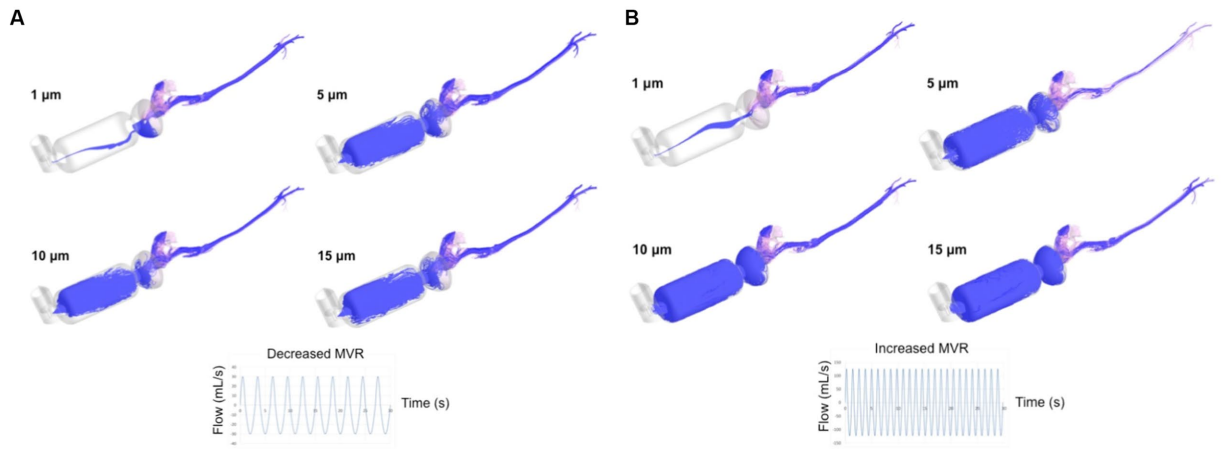

FIGURE 4
Time evolution of the salbutamol particles trajectories (depicted in purple) after 30s of both breathing flows, 30 mL/s **(A)** and 126 mL/s **(B)**. MVR: mean ventilatory rate. The trajectories represent the aerosolized salbutamol flow of particle injected through the MDPI orifice in the computational domain (devices + upper airways) and reaching the lung (model outlet).

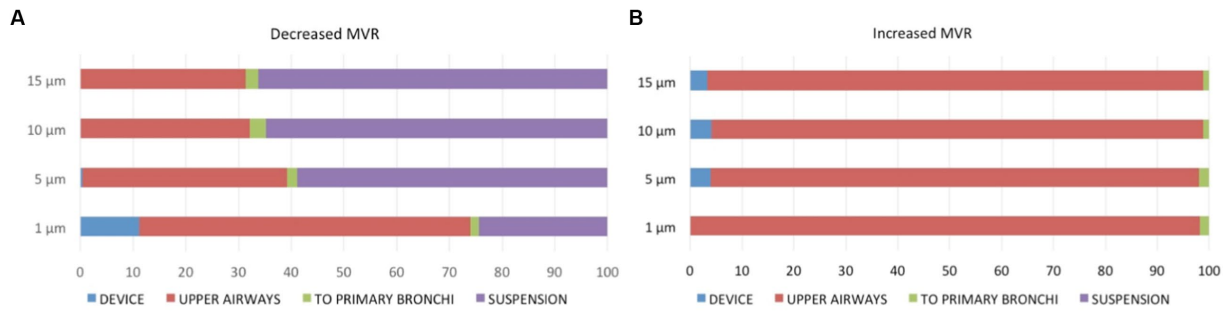

FIGURE 5
Percentage of particle distribution after 30 s of breathing flows of 30 mL/s **(A)** and 126 mL/s **(B)** into the three regions [device (blue), upper airways (red), to primary bronchi (green), as well as remaining in suspension (purple)].

Taking into account all particles sizes, similar particle waste due to deposition into the device was noted during decreased (11.7%) and increased (11.4%) MVRs. No particle deposition in any part of the device was noted during decreased MVR for particles of 15 μm size or during increased MVR for particles of 1 μm size.

Deposition of particles of different sizes deposited on the muzzle or in the upper airways (nasal turbines, oropharynx, larynx, and trachea) during 30 and 126 mL/s flows are represented in Table 2. Particle deposition in the nasal turbinates was at the highest value compared to other sites in both flows. During decreased MVR, the particle residue in this area was twice as great at a size of 1 μm compared to a size of 15 μm. Similarly, the amount of drug lost in the nasal turbinates during increased MVR was 1.5 as great at a size of 1 μm compared to a size of 15 μm.

Medians and (range) of the percentage of particles deposited into the devices, upper airways, reaching the lungs (i.e., exiting the computational model) and in suspension during both flows are displayed in Table 3. No significant differences were observed between the particles traveling to the primary bronchi or those deposited into the device between both flows. During increased MVR, the deposition of particles in the upper airways was significantly higher compared to decreased MVR. Conversely, during 30 mL/s flow significantly more particles remained in suspension compared to the 126 mL/s flow.

The percentage of particle deposition decreased with increasing particle diameter but there were no statistical differences between the distribution of particles into the device and upper airways ($p = 0.869$ and $p = 0.801$, respectively) or between those traveling to the lung or in suspension ($p = 0.881$ and $p = 0.925$, respectively) between different particle sizes.

4. Discussion

It is well established that the deposition of micro-particles tends to increase with increasing particle diameter, meaning there are wasted particles that will never reach the bronchi (32). In this study and contrary to what we hypothesized, the tendency observed for particle depositing in the upper airways walls decreased when the particle diameter increased, despite a lack of significant difference between location of deposition and particle size. Different to what is described in the human literature, particles of the largest size reached the bronchial area more easily and remained in suspension for a

greater time than smaller ones (Figure 4). Airway bifurcations in the first few generations are subjected to high flow rates and hence, they may receive only small amounts of micro-particles due to largely amount of deposition that takes place upstream. At the flows studied, the percentage of particles traveling to the lung was low, ranging between 1.5%–2.3%. Inhalation in humans is performed through the mouth, with the oral cavity, oropharynx, larynx, and regions just upstream of the glottis being preferred locations for micro-particle deposition. In cats, inhalation is carried out mainly through the nose, and preferred locations for deposition of micro-particles of 10 µm are the muzzle and main airways independent of the type of device used for the therapy (spacer of 10 cm or 20 cm and conical or spherical mask) (24). Smaller particles (1–5um) tended to primarily deposit on the muzzle and in the nasal turbinates with far fewer reaching the lower airways; this pattern was exaggerated during increased MVR. We believe this is due to a more complex and narrowed feline upper airway anatomy compared to humans. We found a smaller amount of particle deposition into the devices in this study compared with the previous study (24). Using geometry derived from a single cat and a single particle diameter of 10 µm, we found a very low amount of drug traveling to the target, independent of the type of spacer or mask (24). However, in that study, different respiratory flow and frequencies were imposed (24).

TABLE 1 Percentage of particles of differing sizes deposited to the different parts of the devices after 30 s of breathing flows of 30 mL/s and 126 mL/s.

Flow	Particle size (µm)	Inhaler*	Spacer*	Mask*	Total*
Decreased MVR 30 mL/s	1	0	0	11.2	11.2
	5	0	0.3	0.1	0.4
	10	0	0	0.1	0.1
	15	0	0	0	0
Increased MVR 126 mL/s	1	0	0	0	0
	5	0.2	3.6	0.2	3.9
	10	0.2	4.0	0	4.2
	15	0.4	2.7	0.2	3.3

*All values are described in percentages (%). MVR: mean ventilatory rate.

Data of the percentage of inhaled salbutamol particle transport and deposition in cats is limited. A scintigraphy study proved an 86% positive rate of deposition into the lungs in 20 cats after nebulization of technetium Tc 99 m-diaminetriaminopentaacetic acid (99mTc-DTPA) into a spacer and fitting facemask (44). Pulmonary functional test evaluating bronchodilatation effectiveness of salbutamol administration has also been done (45). And the effectiveness of inhaled lidocaine in healthy and experimentally asthmatic cats was assessed by studying the flow, pressure and airway resistance and after preforming bronchoalveolar lavage fluid (BALF) analysis (8). Li and co-workers in 2007 demonstrated that deposition of micro-particle is due to impaction, secondary flow convection, and turbulent dispersion (46, 47). For this reason, in humans particles tend to deposit mainly at stagnation points (oral cavity, pharynx, larynx, and trachea) and rarely reach the deep bronchial region (21). In this study, deposition tends to be higher in the muzzle and in the nasal turbinates region due to its complex structure and the deposition was lower in the oropharynx and tracheal region. We also found that some micro-particles may travel and deposit in the sinus area, due to turbulent dispersion and secondary flow as described in rabbits (35). But in humans, the inhaled particles of 1 µm are effectively delivered distally (21), contrary to our results. In rodents, the maxilloturbinate region has been recognized as a very important and highly complex structure, accounting for over 50% airways resistance, bifurcating in several branches, and, in rabbits, acting as a filter for inhaled particles (35, 36). In this study, similarities of the nasal turbinates in cats may explain the large deposition in this region. Delivering therapy through an endotracheal tube (24) increases the percentage of particles traveling to the lung as the muzzle and maxilloturbinate region is bypassed.

Higher flow rates may modify the trajectory and distribution of smaller particles. There is a relatively large body of knowledge of aerosol particle behavior in human airways, including adults and children. In comparison, little is known in domestic animals. Previous studies have not focused on a veterinary clinical application such as the aim of improving efficacy of drug delivery for feline asthma. In the current study, during lowers flows, particles were deposited into nasal turbinates without reaching the oropharynx or remained in suspension after 10 breaths in 30 s. Cats should breathe through the mask and spacer for 7–10 s after each actuation (3). During periods of decreased MVR, it is clear the time needed is considerably longer. Lugo and Ballard in 2004 developed a human neonatal ventilator lung

TABLE 2 Percentage of particles of differing sizes deposited to the different areas of the muzzle or upper airways (defined as the nasal turbinates, oropharynx, larynx, and trachea including primary bronchi) after 30 s of breathing flows of 30 mL/s and 126 mL/s.

Flow	Particle size (µm)	Muzzle*	Nasal turbinates*	Oropharynx*	Larynx*	Trachea*	Total*
Decreased MVR 30 mL/s	1	1.45	54.8	2.9	2.4	1.1	62.5
	5	0.6	33.5	1.2	2.5	0.9	38.6
	10	0.4	28.2	1.2	1.4	0.9	32.0
	15	0.4	27.2	1.6	1.6	0.5	31.3
Increased MVR 126 mL/s	1	5.8	88.9	3.00	0.3	0.3	98.2
	5	6.7	82.5	2.5	1.35	0.8	93.8
	10	32.7	60.1	0.6	0.9	0.5	94.7
	15	35.2	58.7	0.7	0.8	0.1	95.5

*All values are described in percentages (%). MVR: mean ventilatory rate.

TABLE 3 Percentage of total particle deposition into the device and upper airways or traveling to the lungs* and in suspension after 30 s of breathing flows of 30 mL/s and 126 mL/s.

Flow	Device	Upper airways	To the lung	Suspension
Decreased MVR 30 mL/s	0.25 (0.00–11.20)	35.45 (31.30–62.70)	2.3 (1.8–3.1)	61.78 (24.4–66.20)
Increased MVR 126 mL/s	3.58 (0.00–4.15)	95.13 (94.05–98.15)	1.53 (1.15–2.05)	0.00 (0.00–0.00)
Value of *p*	0.686	0.029	0.057	0.029

All values are described in percentages (%). The value of *p* was determined for comparisons between decreased and increased MVR for each location of particle deposition. *Lung refers to lower conducting airways distal to the primary bronchi to the parenchyma. MVR, mean ventilatory rate.

model and described a low albuterol delivery for 5–15 breaths and moderate increases in delivery for 30 breaths during 60s (48). In our study during conditions of decreased MVR, a high number of particles remained in suspension, indicating they have not deposited on any walls or reached the model outlets (meaning traveled to the lungs). In contrast, during increased MVR no particle remained in suspension over the same amount of time. This suggests that due to the low flow rate, a larger time and number of breaths would be necessary promote particle transport. The effect of breathing condition on the distribution and deposition of particles in humans has been standardized to three flow types; 30 L/min for normal, 15 L/min for light and 60 L/min heavy breathing patterns (15, 16, 30, 32). In this study, we have tried to simulate two different flows situations based in the previous literature (41, 49) and spirometry values from anesthetized cats. However, data reporting peak inspiratory flows in cats is scarce. With the respiratory conditions selected for this study, the percentage of salbutamol that travels to the lungs after one actuation during 30s is very low and is independent of the particle size. In human medicine, it is accepted that most inhalers only allow a small amount of the administered dose of drugs in the lungs. However, considering their efficacy and cost, this is not commonly considered problematic (27). As reported previously in a feline model of asthma, Leemans and co-workers in 2009, studied the antispasmodic effects of salbutamol pMDI and justified a single actuation in awake cats (45). Unfortunately, the necessary dose and breathing time in cats under different respiratory conditions is currently unknown.

The main limitations in this study include the assumptions of rigid, non-dynamic, and not deformable airways and the use of a single cat's anatomy to model the airways which cannot take into account interindividual morphologic variability of the pet cat population. Thus, findings of this study may not be representative of the salbutamol inhalant delivery in all cats and clinical situations. However, this model is the first step to understand the influence of different flows and particles sizes in the inhalation therapies in cats. Additionally, the considered geometry did not take into account the entire lung, which would have been complex to image and reconstruct. Furthermore, additional ventilation conditions may be crucial for confirming the main findings of this study. Finally, in all the simulations, perfect fitting of the spherical mask on the cat muzzle has been assumed. However, it is clear that this is an ideal situation, and the unwilling patient may cause drug waste directly from the device. Studies using CT images-based models of asthmatic cats are left for future investigation.

In conclusion, different flow conditions modified particle transport in this model of device and cat airway anatomy. From a clinical point of view, during decreased MVR situations, longer breaths and times for medication delivery than typically recommended are needed. Results of this study suggest that increased MVR induced drug wastage. Further studies including different CT images-based models of asthmatic cats, varied cat anatomies, and different devices, drugs and dosages are necessary to further extend and assess the knowledge of drug delivering therapies.

Data availability statement

The original contributions presented in the study are included in the article/supplementary material, further inquiries can be directed to the corresponding author.

Ethics statement

The animal study was reviewed and approved by Clinical Research Ethical Committee of the École Nationale Vétérinaire d'Alfort (ENVA), France (number: 2020-05-30). Written informed consent was obtained from the owners for the participation of their animals in this study.

Author contributions

RF-P and MM: conceptualization, methodology, formal analysis, investigation, data curation, and funding acquisition. MM: software. MM and PP: validation. RF-P, MM, and CR: writing—original draft preparation. RF-P, MM, PP, and CR: writing—review and editing and visualization. PP and CR: supervision and project administration. All authors contributed to the article and approved the submitted version.

Funding

This study is supported by grants PID2021-125731OB-C31 and PID2021-125731OB-C33 from the Spanish Ministry of Science and Innovation MCIN/AEI/10.13039/501100011033/ and FEDER ("A way to build Europe").

Acknowledgments

The authors acknowledge the support of the Institute of Health Carlos III (ISCIII) through the CIBER-BBN initiative.

Conflict of interest

The authors declare that the research was conducted in the absence of any commercial or financial relationships that could be construed as a potential conflict of interest.

Publisher's note

References

1. Gareis H, Hörner-Schmid L, Zablotski Y, Palić J, Schulz B. Evaluation of barometric whole-body plethysmography for therapy monitoring in cats with feline lower airway disease. *PLoS One*. (2022) 17:e0276927. doi: 10.1371/journal.pone.0276927

2. Reinero CR. Advances in the understanding of pathogenesis, and diagnostics and therapeutics for feline allergic asthma. *Vet J*. (2011) 190:28–33. doi: 10.1016/j.tvjl.2010.09.022

3. Padrid P. Use of inhaled medications to treat respiratory diseases in dogs and cats. *J Am Anim Hosp Assoc*. (2006) 42:165–9. doi: 10.5326/0420165

4. Paulin MV, Caney SM, Cosford KL. Online survey to determine client perceptions of feline chronic lower airway disease management: response to therapy, side effects and challenges encountered. *J Feline Med Surg*. (2022) 24:1219–27. doi: 10.1177/1098612X211070988

5. Cheng YS. Mechanisms of pharmaceutical aerosol deposition in the respiratory tract. *AAPS PharmSciTech*. (2014) 15:630–40. doi: 10.1208/s12249-014-0092-0

6. Galler A, Shibly S, Bilek A, Hirt RA. Inhaled budesonide therapy in cats with naturally occurring chronic bronchial disease (feline asthma and chronic bronchitis). *J Small Anim Pract*. (2013) 54:531–6. doi: 10.1111/jsap.12133

7. Reinero CR, Lee-Fowler TM, Dodam JR, Cohn LA, DeClue AE, Guntur VP. Endotracheal nebulization of N-acetylcysteine increases airway resistance in cats with experimental asthma. *J Feline Med Surg*. (2011) 13:69–73. doi: 10.1016/j.jfms.2010.09.010

8. Nafe LA, Guntur VP, Dodam JR, Lee-Fowler TM, Cohn LA, Reinero CR. Nebulized lidocaine blunts airway hyper-responsiveness in experimental feline asthma. *J Feline Med Surg*. (2013) 15:712–6. doi: 10.1177/1098612X13476705

9. O'Malley CA. Device cleaning and infection control in aerosol therapy. *Respir Care*. (2015) 60:917–30. doi: 10.4187/respcare.03513

10. Lee EA, Johnson LR, Johnson EG, Vernau W. Clinical features and radiographic findings in cats with eosinophilic, neutrophilic, and mixed airway inflammation (2011-2018). *J Vet Intern Med*. (2020) 34:1291–9. doi: 10.1111/jvim.15772

11. Trzil JE. Feline Asthma. *Vet Clin North Am Small Anim Pract*. (2020) 50:375–91. doi: 10.1016/j.cvsm.2019.10.002

12. Kirschvink N, Leemans J, Delvaux F, Snaps F, Clercx C, Gustin P. Bronchodilators in bronchoscopy-induced airflow limitation in allergen-sensitized cats. *J Vet Intern Med*. (2005) 19:161–7. doi: 10.1111/j.1939-1676.2005.tb02677.x

13. Kleinstreuer C, Shi H, Zhang Z. Computational analyses of a pressurized metered dose inhaler and a new drug–aerosol targeting methodology. *J Aerosol Med*. (2007) 20:294–309. doi: 10.1089/jam.2006.0617

14. Deb PK, Abed SN, Maher H, Al-Aboudi A, Paradkar A, Bandopadhyay S, et al. Aerosols in pharmaceutical product development In: RK Tekade, editor. *Drug Delivery Systems*. USA: Academic Press (2020). 521–77.

15. Huang J, Zhang L, Yu S. Modeling micro-particle deposition in human upper respiratory tract under steady inhalation. *Particuology*. (2011) 9:39–43. doi: 10.1016/j.partic.2010.04.003

16. Rahimi-Gorji M, Pourmehran O, Gorji-Bandpy M, Gorji TB. CFD simulation of airflow behavior and particle transport and deposition in different breathing conditions through the realistic model of human airways. *J Mol Liq*. (2015) 209:121–33. doi: 10.1016/j.molliq.2015.05.031

17. Talaat M, Si X, Xi J. Effect of MDI actuation timing on inhalation dosimetry in a human respiratory tract model. *Pharmaceuticals*. (2022) 15:61. doi: 10.3390/ph15010061

18. Malvè M, Sánchez-Matás C, López-Villalobos JL. Modelling particle transport and deposition in the human healthy and stented tracheobronchial airways. *Ann Biomed Eng*. (2020) 48:1805–20. doi: 10.1007/s10439-020-02493-1

19. Ahookhosh K, Saidi M, Mohammadpourfard M, Aminfar H, Hamishehkar H, Farnoud A, et al. Flow structure and particle deposition analyses for optimization of a pressurized metered dose inhaler (pMDI) in a model of tracheobronchial airway. *Eur J Pharm Sci*. (2021) 164:105911. doi: 10.1016/j.ejps.2021.105911

20. Tyfa Z, Jóźwik P, Obidowski D, Reorowicz P, Jodko D, Kapka K, et al. Inhaled drug airflow patterns and particles deposition in the paediatric respiratory tract. *Acta Bioeng Biomech*. (2020) 22:101–10. doi: 10.37190/ABB-01550-2020-02

21. Kadota K, Inoue N, Matsunaga Y, Takemiya T, Kubo K, Imano H, et al. Numerical simulations of particle behaviour in a realistic human airway model with varying inhalation patterns. *J Pharm Pharmacol*. (2020) 72:17–28. doi: 10.1111/jphp.13195

22. Lavorini F, Fontana GA. Targeting drugs to the airways: the role of spacer devices. *Expert Opin Drug Deliv*. (2009) 6:91–102. doi: 10.1517/17425240802637862

23. Newman SP, Newhouse MT. Effect of add-on devices for aerosol drug delivery: deposition studies and clinical aspects. *J Aerosol Med*. (1996) 9:55–70. doi: 10.1089/jam.1996.9.55

24. Fernández-Parra R, Pey P, Reinero C, Malvè M. Salbutamol transport and deposition in the upper and lower airway with different devices in cats: a computational fluid dynamics approach. *Animals*. (2021) 11:2431. doi: 10.3390/ani11082431

25. Usmani OS, Lavorini F, Marshall J, Dunlop WCN, Heron L, Farrington E, et al. Critical inhaler errors in asthma and COPD: a systematic review of impact on health outcomes. *Respir Res*. (2018) 19:10. doi: 10.1186/s12931-017-0710-y

26. Jahedi L, Downie SR, Saini B, Chan H-K, Bosnic-Anticevich S. Inhaler technique in asthma: how does it relate to patients' preferences and attitudes toward their inhalers? *J Aerosol Med Pulm Drug Deliv*. (2017) 30:42–52. doi: 10.1089/jamp.2016.1287

27. Newman SP. Drug delivery to the lungs: challenges and opportunities. *Ther Deliv*. (2017) 8:647–61. doi: 10.4155/tde-2017-0037

28. Rozanski EA, Bach JF, Shaw SP. Advances in respiratory therapy. *Vet Clin North Am Small Anim Pract*. (2007) 37:963–74. doi: 10.1016/j.cvsm.2007.05.009

29. Newman S. Improving inhaler technique, adherence to therapy and the precision of dosing: major challenges for pulmonary drug delivery. *Expert Opin Drug Deliv*. (2014) 11:365–78. doi: 10.1517/17425247.2014.873402

30. Kleinstreuer C, Zhang Z, Li Z. Modeling airflow and particle transport/deposition in pulmonary airways. *Respir Physiol Neurobiol*. (2008) 163:128–38. doi: 10.1016/j.resp.2008.07.002

31. Arsalanloo A, Abbasalizadeh M, Khalilian M, Saniee Y, Ramezanpour A, Islam MS. A computational approach to understand the breathing dynamics and pharmaceutical aerosol transport in a realistic airways. *Adv Powder Technol*. (2022) 33:103635. doi: 10.1016/j.apt.2022.103635

32. Zhang Z, Kleinstreuer C, Donohue JF, Kim CS. Comparison of micro- and nano-size particle depositions in a human upper airway model. *J Aerosol Sci*. (2005) 36:211–33. doi: 10.1016/j.jaerosci.2004.08.006

33. Kolanjiyil AV, Kleinstreuer C, Kleinstreuer NC, Pham W, Sadikot RT. Mice-to-men comparison of inhaled drug-aerosol deposition and clearance. *Respir Physiol Neurobiol*. (2019) 260:82–94. doi: 10.1016/j.resp.2018.11.003

34. Corley RA, Kabilan S, Kuprat AP, Carson JP, Minard KR, Jacob RE, et al. Comparative computational modeling of airflows and vapor dosimetry in the respiratory tracts of rat, monkey, and human. *Toxicol Sci Off J Soc Toxicol*. (2012) 128:500–16. doi: 10.1093/toxsci/kfs168

35. Xi J, Si XA, Kim J, Zhang Y, Jacob RE, Kabilan S, et al. Anatomical details of the rabbit nasal passages and their implications in breathing, air conditioning, and olfaction. *Anat Rec Hoboken NJ*. (2016) 299:853–68. doi: 10.1002/ar.23367

36. Xi J, Talaat M, Si X, Dong H, Donepudi R, Kabilan S, et al. Ventilation modulation and nanoparticle deposition in respiratory and olfactory regions of rabbit nose. *Animals*. (2019) 9:1107. doi: 10.3390/ani9121107

37. Asgharian B, Price O, Kabilan S, Jacob RE, Einstein DR, Kuprat AP, et al. Development of a Zealand white rabbit deposition model to study inhalation anthrax. *Inhal Toxicol*. (2016) 28:80–8. doi: 10.3109/08958378.2016.1140850

38. Kabilan S, Suffield SR, Recknagle KP, Jacob RE, Einstein DR, Kuprat AP, et al. Computational fluid dynamics modeling of Bacillus anthracis spore deposition in rabbit and human respiratory airways. *J Aerosol Sci*. (2016) 99:64–77. doi: 10.1016/j.jaerosci.2016.01.011

39. Wilcox DC. *Turbulence modeling for CFD. 2nd* ed. La Canada, CA, USA: DCW Industries, Inc. (1998).

40. Ansys Inc. *Ansys CFX Theory Manual v.20*. (2020).

41. Caro-Vadillo A, Montoya-Alonso JA, García-Guasch L. Impact of obesity on lung function in cats with bronchoconstriction. *Vet Sci*. (2022) 9:278. doi: 10.3390/vetsci9060278

42. Fernández-Parra R, Pey P, Zilberstein L, Malvè M. Use of computational fluid dynamics to compare upper airway pressures and airflow resistance in brachycephalic, mesocephalic, and dolichocephalic dogs. *Vet J*. (2019) 253:105392. doi: 10.1016/j.tvjl.2019.105392

43. Yousefi M, Inthavong K, Tu J. Effect of pressurized metered dose inhaler spray characteristics and particle size distribution on drug delivery efficiency. *J Aerosol Med Pulm Drug Deliv*. (2017) 30:359–72. doi: 10.1089/jamp.2016.1299

44. Schulman RL, Crochik SS, Kneller SK, McKiernan BC, Schaeffer DJ, Marks SL. Investigation of pulmonary deposition of a nebulized radiopharmaceutical agent in awake cats. *Am J Vet Res*. (2004) 65:806–9. doi: 10.2460/ajvr.2004.65.806

45. Leemans J, Kirschvink N, Bernaerts F, Clercx C, Cambier C, Gustin P. A pilot study comparing the antispasmodic effects of inhaled salmeterol, salbutamol and ipratropium bromide using different aerosol devices on muscarinic bronchoconstriction in healthy cats. *Vet J*. (2009) 180:236–45. doi: 10.1016/j.tvjl.2007.11.008

46. Li Z, Kleinstreuer C, Zhang Z. Simulation of airflow fields and microparticle deposition in realistic human lung airway models. Part II: particle transport and deposition. *Eur J Mech B-Fluids*. (2007) 26:650–68. doi: 10.1016/j.euromechflu.2007.02.004

47. Li Z, Kleinstreuer C, Zhang Z. Simulation of airflow fields and microparticle deposition in realistic human lung airway models. Part I: airflow patterns. *Eur J Mech B-Fluids*. (2007) 26:632–49. doi: 10.1016/j.euromechflu.2007.02.003

48. Lugo RA, Ballard J. Albuterol delivery from a metered-dose inhaler with spacer is reduced following short-duration manual ventilation in a neonatal ventilator-lung model. *Respir Care*. (2004) 49:1029–34.

49. Rozanski EA, Hoffman AM. Pulmonary function testing in small animals. *Pulm Diagn*. (1999) 14:237–41. doi: 10.1016/S1096-2867(99)80017-6

frontiers | Frontiers in Veterinary Science

TYPE Original Research
PUBLISHED 18 September 2023
DOI 10.3389/fvets.2023.1249951

OPEN ACCESS

EDITED BY
Muhammad Saqib,
University of Agriculture, Faisalabad, Pakistan

REVIEWED BY
Alison Wills,
Hartpury University and Hartpury College, United Kingdom
João Carlos Alves,
University of Evora, Portugal

*CORRESPONDENCE
Christiane Lutonsky
✉ christiane.lutonsky@vetmeduni.ac.at

RECEIVED 29 June 2023
ACCEPTED 04 September 2023
PUBLISHED 18 September 2023

CITATION
Lutonsky C, Peham C, Mucha M, Reicher B, Gaspar R, Tichy A and Bockstahler B (2023) External mechanical perturbations challenge postural stability in dogs.
Front. Vet. Sci. 10:1249951.
doi: 10.3389/fvets.2023.1249951

External mechanical perturbations challenge postural stability in dogs

Christiane Lutonsky[1]*, Christian Peham[2], Marion Mucha[1], Bianca Reicher[1], Rita Gaspar[1], Alexander Tichy[3] and Barbara Bockstahler[1]

[1]Department of Companion Animals and Horses, University Clinic for Small Animals, Small Animal Surgery, Section of Physical Therapy, University of Veterinary Medicine, Vienna, Austria, [2]Department of Companion Animals and Horses, University Clinic for Horses, Movement Science Group, University of Veterinary Medicine, Vienna, Austria, [3]Department of Biomedical Sciences, Bioinformatics and Biostatistics Platform, University of Veterinary Medicine, Vienna, Austria

This study aimed to explore the effect of external mechanical perturbations on postural stability (PS) in dogs using the body center of pressure (COP). Thirteen sound adult dogs were included in this study. PS was tested during quiet standing on a pressure measurement plate. The conditions included a standard standing measurement and external mechanical perturbations conducted using six settings on a motorized training platform with different intensities of speed and amplitude. Measurement conditions were compared using linear mixed-effects models, followed by multiple comparisons using Sidak's alpha correction procedure. Compared with the standing measurement, external mechanical perturbations resulted in a significant increase in almost all COP parameters, indicating a challenge for the PS. Furthermore, an increase in amplitude had a greater effect than an increase in speed, whereas the combination of the highest intensities of amplitude and speed was not well tolerated by the dogs. The mediolateral COP displacement was significantly greater than the craniocaudal COP displacement during standing measurement and conditions with a small amplitude, whereas no significant difference was observed during settings with an increased amplitude. To the best of our knowledge, this is the first study to demonstrate the effects of a balance training device in dogs. Therefore, the intensity of the training programs on motorized platforms or similar devices can be controlled by the wobbling amplitude of the platform.

KEYWORDS

canine balance, center of pressure, postural stability, posturography, veterinary rehabilitation, external mechanical perturbations

1. Introduction

Postural stability (PS) is the act of maintaining, achieving, or restoring balance during a posture or activity (1). This is achieved through interactions between the visual, somatosensory, and vestibular systems of the central nervous system (2). Body stabilization results from the transmission of information from the central nervous system to the musculoskeletal system (1).

A typical parameter used to evaluate PS in human patients is the center of pressure (COP) (3–9), which has recently been used in veterinary medicine (10–31). The COP is the location of the instantaneous vector of ground reaction forces and displays the trajectory of the center of mass of the body. During the ground contact, the position of the center of mass, and therefore the COP, changes continuously, resulting in a COP path (9). The COP moves within the base of

support of the body. Balance is maintained by rapid COP movements to maintain the center of mass within the base of support (32, 33). If the COP exceeds the base of support, a protective step is taken to prevent falls (34). Therefore, the ability to restore balance is directly influenced by the position of the COP prior to perturbation (35). The COP can be measured easily using force and pressure measurement plates (10–20).

Previous evaluations in veterinary medicine were performed during static posturography, that is, during quiet standing with (11–16, 22, 24, 31) and without challenging PS (23), and during gait analysis in normal locomotion (10, 20, 21) and different tasks (17, 18). Moreover, the COP of the body (11, 14–16, 22, 23, 31) and that within the paws (10, 12, 13, 17–20) can be measured. Some measurements are conducted with the animal standing on a plate with all feet to calculate the body COP (11, 16, 22, 23, 31), whereas others evaluate it only between the forelimbs (11, 14, 15, 31) or hindlimbs (11, 31). The COP parameters are calculated based on the COP path. During posturography, the following body COP parameters are commonly described: The displacement of the COP in mediolateral (COP-MedLat) and craniocaudal (COP-CranCaud) directions; the support surface, which is the area determined by an ellipse that contains 90% of the points of the COP trajectory; (11) the COP speed; the statokinesiogram length; and length in the function of surface. The statokinesiogram length is the length of the line joining the points of the COP trajectory. It is a measure of the effort needed to maintain an upright position and therefore measures the efficacy of the postural system (36). The length in the function of surface is the correlation between the COP length and its surface. It provides information on the accuracy of the PS and the effort made by the subject to maintain an upright position (15, 37). An increase in the COP parameters is associated with impaired PS (16, 22, 23).

During standard standing measurement, veterinary research has focused on the body COP of sound (28, 31) and lame (15) horses, foals (22), senile (16, 24) and lame (11, 14) dogs, and the COP within the paws of lame dogs (12, 13). In horses, the COP-MedLat was significantly larger than the COP-CranCaud during standing measurement of the forelimbs. Based on suggestions in human medicine, Pitti et al. (15) proposed that the larger craniocaudal diameter of the base of support in horses is responsible for the more profound stability in the craniocaudal direction. While similar comparisons have not yet been performed in dogs, it has been proposed that the support surface has a wider diameter in the mediolateral direction than that in the craniocaudal direction during measurements between the fore (11, 14) and hind limbs (11). Up to this point, according to the authors' knowledge, there have been no investigations into the influence of different body conformations on the support surface. However, COP-parameters are significantly influenced by the weight, height, and length in dogs (16). Increased body COP displacement during static posturography is associated with the age and health status of the animals. In foals, (22), increases in the COP-MedLat and COP-CranCaud were attributed to a poorly developed PS. Similar patterns of COP parameters have been described in senile dogs. Again, these results are discussed as signs of decreased PS (16, 24). This finding is consistent with the results of previous human medical research. Children and elderly individuals show increased support surface and, therefore, decreased PS compared to healthy adults (38). Furthermore, the authors suggested that the significant differences between the senile and younger dogs could be the result of joint pain and other comorbidities associated with aging (16), as described in dogs with osteoarthrosis. Cubarthrosis and gonarthrosis result in a significant increase in COP-MedLat, COP-CranCaud, and support surface compared to a control group (11, 14). Similarly, human medical research has revealed a negative effect of experimentally induced pain on postural stability in healthy adults (39).

Dynamic balance tests challenge the standing postural stability during external perturbations or dynamic conditions, including mechanical, sensory, or combined stimuli (40). Although the loss of visual input in horses results in a significant increase in COP-MedLat, COP-CranCaud, and mediolateral COP velocity (23), dynamic balancing tests during the investigation of COP parameters have not yet been performed in canines. External mechanical perturbations, including different surfaces (41–43), waist pulls (32, 35), mechanical platforms (44–49) and narrowing of the base of support with a single-leg (6, 41, 50–52) and tandem stance (standing in a heel-to-toe position) (53–55), are commonly used in human medical research to challenge PS. Increased base of support by a wider stance resulted in improvements in balance performance, mainly in COP-MedLat in healthy adults (56), while the single-leg stance increased total COP-MedLat, COP-CranCaud, and mean COP-CranCaud (52). In patients with anterior cruciate ligament ruptures, the single-leg stance resulted in a significant increase in the total COP-MedLat compared with the control group (6). Furthermore, the functional base of support, defined as the area used to maintain balance, decreases during the aging process. Therefore, a decrease in functional base of support results in an impaired ability to maintain or restore balance (57, 58). Using a motorized platform, researchers found a significant increase during sinusoidal perturbations at an amplitude of 5° at a high frequency (0.50 Hz) compared to a low frequency (0.25 Hz) in statokinesiogram length, whereas the frequency did not have a significant effect on COP-MedLat and COP-CranCaud. However, a strong correlation between statokinesiogram length and COP-MedLat was observed under both conditions (48). Furthermore, control participants and patients with Parkinson's disease were less challenged by anterior–posterior perturbations than that by lateral perturbations, and diseased patients showed a less efficient postural strategy (49).

As described above, many approaches to challenging PS have been described in humans, most of which cannot be applied to animals. Similar to the single-leg stance, three-legged standing tests are commonly used to assess strength and balance in dogs (59). However, this test is subject to high variability among practitioners (60), and standing measurement is difficult to perform over a sufficient period (16). Therefore, this test condition may lack validity and be difficult to perform in orthopedically and neurologically diseased animals. Dynamic tests, such as walking Figure 8's and stepping over Cavaletti rail obstacles, have been proposed to test dynamic balance and spatial awareness with low variability among patients and practitioners (60). The latter led to significant differences in the COP parameters compared with normal walking (17). However, static posturography during external perturbations has not been addressed in the literature.

Mechanical platforms can be used to measure the PS in animals under challenging conditions. The difficulty can be adjusted to the animal's fitness level by changing the speed and angulation to a horizontal plane (amplitude) of the upward and downward motions. These properties enable the evaluation of PS during repeatable measurements under fixed conditions.

Veterinary research should focus on establishing measurement procedures that assess the influence of external perturbations on the PS in sound and orthopedically or neurologically diseased animals.

As a first step toward evaluating the effect of external perturbations on PS in dogs, this study aimed to assess the effect of external perturbations on COP parameters in sound dogs in different settings on a motorized training platform. In the future, this may serve as an extension of conventional measurements of ground reaction forces, which provide insight into limb loading but are not adequate to describe the sway of the whole-body.

We hypothesized that external mechanical perturbations challenge PS in dogs, which is reflected in the COP parameters of the body. Furthermore, higher amplitude and speed settings of the motorized platform result in signs of increased instability, and an increase in amplitude has a stronger effect than an increase in speed.

2. Materials and methods

2.1. Ethics statement

This study was approved by the Ethics and Animal Welfare Committee of the University of Veterinary Medicine, Vienna, in accordance with the University's guidelines for "Good Scientific Practice" (ETK-131/09/2021).

2.2. Animals and inclusion criteria

The sample size was calculated using G*Power 3.1 based on the results of a pilot study (Ethics and Animal Welfare Committee of the University of Veterinary Medicine approval number ETK-101/06/2020), which resulted in a total of 10 dogs, assuming a power of 80% and a type I error probability of 5%.

Dogs with pre-existing orthopedic and neurological conditions or any other diseases that could negatively impact PS, such as diseases of the inner ear and reduced vision, were preliminarily excluded. Further inclusion criteria were ectomorph or mesomorph conformation, body weight of 15–35 kg, and age of 2–8 years. Additionally, gait analysis was performed using a pressure measurement plate (FDM Type 2; Zebris Medical GmbH, Allgäu, Germany) to obtain an objective lameness assessment (section 2.3.1). The symmetry indices (SI) of peak vertical force (PFz) and vertical impulse (IFz) had to be below 3%, which is a margin that has been repeatedly used to distinguish between sound and lame dogs (10, 61, 62).

Fifteen dogs were initially included in the study. Two dogs were excluded due to their SI for PFz and/or IFz > 3%. The remaining study population included seven female and six male animals (four mixed breeds, four Border Collies, one Australian Shepherd, two Labrador Retrievers, one Belgian Malinois, and one Belgian Laekenois). The mean age and body mass were 4.29 ± 2.15 years (median = 4.33, minimum = 2.00, maximum = 7.83), and 22.18 ± 4.14 kg (median = 21.50, minimum = 16.70, maximum = 29.00), respectively.

2.3. Procedure and equipment

2.3.1. Initial examination

A 203 × 54.2 cm pressure measurement plate (FDM Type 2, Zebris Medical GmbH, Allgäu, Germany) was used during the initial examination for objective gait analysis. The plate was covered with a black, 1-mm thick rubber mat composed of polyvinyl chloride to avoid slipping.

First, the dogs were allowed to move freely to acclimate to the measurement room. The measurements were performed during walking and trotting until at least five valid passes were collected for each gait. A valid pass was defined as a walk or trot in which the dog crossed the plate without changing pace, turning its head, pulling on the leash, or touching the owner. The difference in speed at which the dogs crossed the plate had to be within a range of ±0.3 m/s and an acceleration of ±0.5 m/s^2 (63–65).

2.3.2. Posturography

Static measurements were conducted using a 149 × 54.2 cm pressure measurement plate (FDM-1.5, Zebris Medical GmbH, Allgäu, Germany), which was placed on a motorized platform (Imoove-vet® platform, Allcare Innovations, 26500 Bourg les Valence, France). This platform uses Elispheric® movement that results from a combination of 3 movements (rotation, eccentricity, and inclination) giving an elliptical or spiral outline in 3 dimensions (66). The pressure measurement plate measured the pressure on the dog's paws using 15,360 piezoelectric sensors at a sampling rate of 100 Hz. The plate was covered with a black, 1-mm-thick rubber mat made of polyvinyl chloride. As the plate was longer than the standing surface of the platform, two cavaletti were used to ensure that the dogs did not pass over the edge. Each measurement run was filmed with a camera (Panasonic model NV-MX500) to evaluate head, limb, and tail movements. The movement of the platform during the measurement conditions was measured on the X-, Y-, and Z-axes using an accelerometer (Xsens DOT sensor) placed on the right side of the standing surface (Figure 1).

The owner led the dog onto the pressure measurement plate and halted it in a straight and square position. During data collection, the owner stood close to the dog without physical contact, to discourage movement. All conditions were measured for 1 min and repeated three times. To avoid the effect of fatigue on the data, each dog was tested on three separate days (two conditions per day), with at least 2 days in between. A short break of 1 min was scheduled after each measurement.

First, standard standing measurements (11–14) were conducted in the neutral position of the motorized platform (Figure 1) on all measurement days to accustom the dog to the situation and practice quiet standing. Subsequently, testing conditions with different settings were performed randomly on a motorized platform. The platform allowed a maximum angulation of 8° (100% of amplitude, Figure 1) and maximum speed of 1 Hz or 60 rounds per min (rpm; 100% of speed) (66). The settings used in this study are listed in Table 1. These included settings of increased speed and fixed amplitude (Speed-20%, Speed-30%), increased amplitude and fixed speed (Amplitude-20%, Amplitude-30%), and a combination of speed and amplitude (Combination-20%, Combination-30%). If an animal showed excessive paw or head movement during a condition, the measurement was discontinued and labeled as not well tolerated by the dog.

The motorized platform showed a sinusoidal motion consistent in the craniocaudal and laterolateral directions (Figure 2).

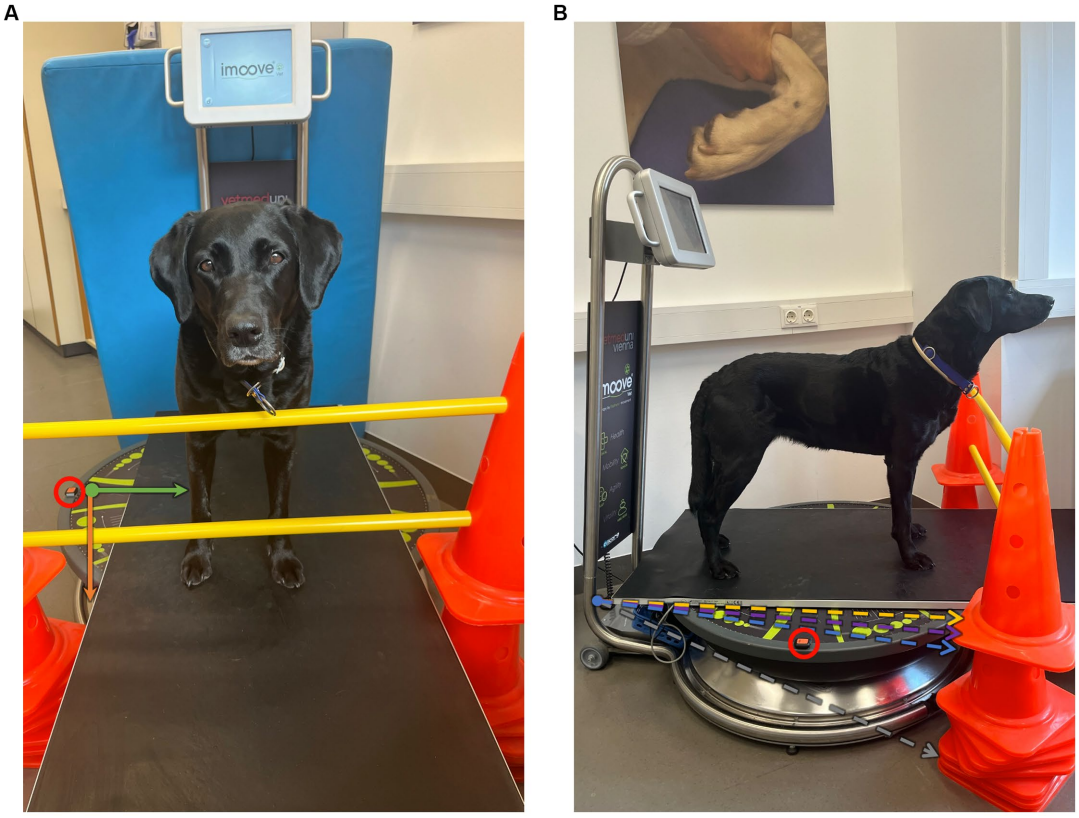

FIGURE 1
Experimental setup: **(A)** frontal and **(B)** lateral views showing the motorized platform in the neutral position, which is used for the standard standing measurement. The accelerometer is placed on the right side of the motorized platform (within the red circle). The movement of the platform is measured on the X- (green), Y- (orange), and Z-axes using Xsens DOT sensor **(A)**. The amplitudes are illustrated in dotted lines to a horizontal plane **(B)**, including 8° in gray (maximal amplitude of the device); 0.8° in yellow (used during Speed-20%, Speed-30%); 1.6° in purple (Amplitude-20%, Combination-20%); and 2.4° (Amplitude-30%, Combination-30%).

TABLE 1 **Overview of the measurement conditions.**

Setting	Speed	Amplitude	Effect of
Speed-20%	20%/12 rpm	10%/0.8°	Speed
Speed-30%	30%/18 rpm	10%/0.8°	
Amplitude-20%	10%/6 rpm	20%/1.6°	Amplitude
Amplitude-30%	10%/6 rpm	30%/2.4°	
Combination-20%	20%/12 rpm	20%/1.6°	Combined settings
Combination-30%	30%/18 rpm	30%/2.4°	

The speed in percentage of total speed (%) and rpm and amplitude in percentage (%) of total amplitude and degrees (°).

2.4. Data analysis

A custom software Pressure Analyzer (Michael Schwanda, version 4.8.5.0) was used for data analysis, which was then exported to Microsoft Excel 2016. Pawprints were manually assigned to the corresponding limbs. Out of each 1-min measurement, a valid period of 20 s, indicating no movements of the head or paws and only minimal tail movements was selected. If a continuous valid period was not achieved, head and paw movements were manually cropped. A measurement was considered insufficient if a valid period of less than 20 s was selected. To assess the different settings, the three-dimensional movements in all directions were included in the selected timeframes. If this was not possible, the measurements were excluded from the data analysis.

2.5. Parameters under investigation

The following parameters were used for the evaluation of the inclusion criteria during the lameness assessment in walk and trot using the pressure measurement plate:

- The mean speed (m/s) and acceleration (m/s^2) were calculated for the left forelimb based on subsequent steps.
- Symmetry index (SI) expressed as a percentage (SI%), was calculated for both parameters (PFz and IFz) according to the following equation:

$$SIXFz\,(\%) = \mathrm{abs}\left(\left[XFzLLx - XFzRLx\right] / \left[XFzLLx + XFzRLx\right]\right) * 100$$

where XFz is the mean value of peak vertical force (PFz) or vertical impulse (IFz) of valid steps, LLx is the left front or

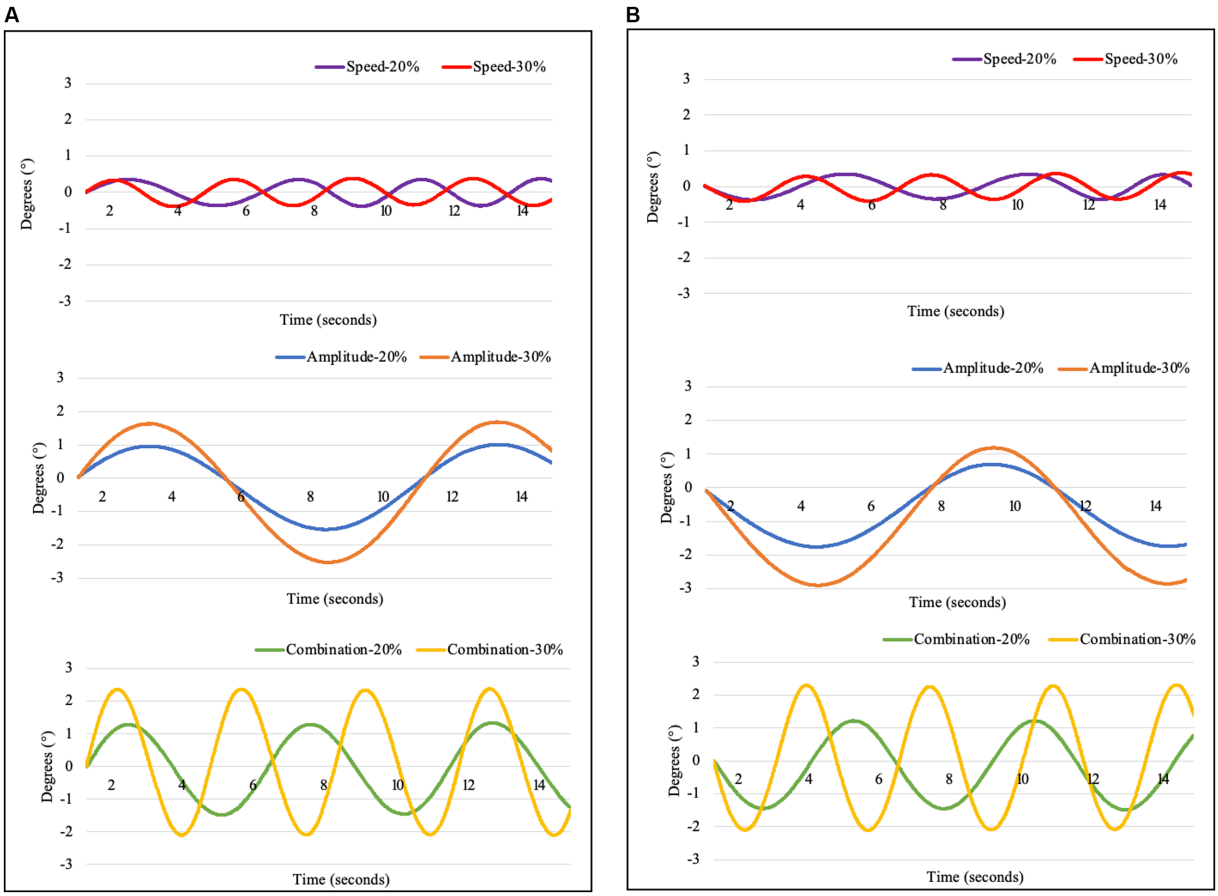

FIGURE 2
Movement of the platform, measured with an Xsens DOT sensor in **(A)** laterolateral (X-axis) and **(B)** craniocaudal (Y-axis) directions during the investigated settings including Speed-20% (purple): Speed 20%, Amplitude 10%; Speed-30% (red): Speed 30%, Amplitude 10%; Amplitude-20% (blue): Speed 10%, Amplitude 20%; Amplitude-30% (orange): Speed 10%, Amplitude 30%; Combination-20% (green): Speed 20%, Amplitude 20%; and Combination-30% (yellow): Speed 30%, Amplitude 30%.

hindlimb, and RLx is the right front or hind; Perfect symmetry between the right and left front or hindlimbs was assigned a value of 0%.

Using the body COP, the following parameters were assessed:

- COP-MedLat: Mean deviation on the lateral axis (mm) measures alterations in the center of mass load distribution on the sagittal axis, and smaller displacement is associated with better stability (16, 24).
- COP-CranCaud: Mean deviation on the craniocaudal axis (mm); a smaller displacement is associated with better stability (16, 24).
- Support surface (mm^2): or statokinesiogram, the area determined by an ellipse that contains 90% of the points of the COP trajectory, gauges the changes in orientation of a standing subject; smaller displacement is associated with better stability (11).
- Statokinesiogram length (path length, m): the length of the line that joins the points of the COP trajectory, a measure of the effort needed to maintain an upright station; and a parameter linked to support surface, which measures the efficiency of the postural system (36). In other words, if support surface is equal, a lower statokinesiogram length indicates a smaller expenditure of energy and, hence, a more efficient PS, and a higher value indicates more instability (14, 15).
- Length as a function of surface: Correlation between COP length and its surface. This provides information on the accuracy of the PS and the effort made by the subject; a higher value indicates greater instability (15, 37).

$$\text{Length as a function of surface} = \text{support surface} / \text{statokinesiogram length}$$

- Mean speed (mm/s) of COP sway (COP-Speed).

2.6. Statistical analysis

All statistical analyses were performed using IBM SPSS v27. The effects of different measurement conditions on the parameters were analyzed using linear mixed-effects models in which the conditions were added as fixed factors to the model. Sidak's alpha correction was applied for multiple comparisons. The assumption of a normal distribution was tested using the Shapiro–Wilk test.

For all analyses, a value of p <5% (p < 0.05) was observed as significant.

3. Results

3.1. Symmetry index

The SI values for PFz and IFz during walking and trotting are listed in Table 2. All dogs included in this study had a SI of PFz and IFz < 3% during walking and trotting.

3.2. Valid measurements

All dogs tolerated conditions Speed-20%, Speed-30%, and Combination-20%; therefore, the data analysis included measurements from 13 dogs. The amplitude settings (Amplitude-20%, Amplitude-30%) were not tolerated by one dog, and condition Combination-30% led to valid measurements in 9 out of 13 dogs.

3.3. Center of pressure

The main results are shown in Figure 3. Compared with standing measurement, all tested conditions led to a significant increase in COP-MedLat, COP-CranCaud, support surface, and length in the function of surface, except for Combination-30% (just out of significance). No significant differences were found between statokinesiogram length and COP-Speed, except for Combination-30%. The mean values, standard deviations, and upper and lower limits of the 95% confidence interval can be found in Table 3, all p-values of the group comparisons are summarized in Table 4.

No significant differences were found in the COP parameters during conditions with the same amplitude (Speed-20% vs. Speed-30%, Amplitude-20% vs. Combination-20%, and Amplitude-30% vs. Combination-30%). Compared with Speed-20% and Speed-30%, all the remaining conditions resulted in a significant increase in COP-MedLat, COP-CranCaud, and support surface. A further increase in COP-MedLat was observed during Amplitude-30% compared to Amplitude-20% and Combination-20%, whereas no significant difference was found in the remaining parameters. The combination of the largest amplitude and fastest speed (Combination-30%) resulted in a significant increase in the COP-MedLat and COP-CranCaud (support surface compared to Amplitude-20%, just out of significance) compared with all other conditions.

TABLE 2 Symmetry index (SI) of peak vertical force (PFz) and vertical impulse (IFz) during the initial examination in walk and trot.

	SI PFz (%)		SI IFz (%)	
	Mean ± SD			
	Walk	Trot	Walk	Trot
Forelimbs	0.67 ± 0.37	0.77 ± 0.79	1.13 ± 0.79	1.33 ± 0.93
Hindlimbs	1.08 ± 0.78	1.21 ± 0.62	1.54 ± 0.65	0.89 ± 0.66

Length in the function of surface was significantly increased during Combination-20% and Amplitude-30% compared to Speed-20%, and Amplitude-30% compared to Speed-30% (Combination-20% just out of significance). No significant differences were found between the statokinesiogram length and speed conditions.

The COP displacement was significantly larger in COP-MedLat than in COP-CranCaud during standing measurement, Speed-20%, and Speed-30%, whereas no significant differences were observed during the remaining conditions (Table 5).

4. Discussion

In the present study, three-dimensional circular movements were used to investigate the effects of external perturbations on the standing balance of sound dogs. We hypothesized that external perturbations challenge PS in dogs, which is reflected in the COP parameters of the body. Further, we hypothesized that higher amplitude and speed settings result in signs of increased instability and that an increase in amplitude has a stronger effect than an increase in speed. Thus, these hypotheses were partially confirmed.

With respect to the first hypothesis, it was possible to show that compared to standing measurement, each setting studied resulted in a significant increase in almost all COP parameters, indicating a challenge to PS. Furthermore, the amplitude setting has a greater effect than the speed setting. An increase in speed did not result in increased instability, because no significant difference was found in the COP parameters between the speed settings. This is partially consistent with what has been found in humans: Similar to our results, the speed of the perturbation on a motorized platform did not have a significant effect on COP-MedLat and COP-CranCaud in healthy individuals. However, statokinesiogram length significantly increased during the higher-speed setting (48). Therefore, future studies should use higher speeds than those used in this study to more precisely investigate this effect in dogs. While no comparable studies using a motorized platform have been performed in veterinary medicine, a similar pattern of results was obtained in blindfolded horses, leading to a significant increase in COP-MedLat and COP-CranCaud compared with measurements during undisturbed vision (23).

Based on the significant increase in COP parameters during settings with an increased amplitude, it can be concluded that, for future research with similar devices, settings with large amplitudes should be preferred over those with high speeds. While the combination of large amplitude and high speed resulted in the largest displacement in both axes, the setting used in this study (Combination-30%) was not well tolerated by the dogs.

Furthermore, the measurement results for condition Combination-30% showed a wide variation in the length in the function of surface. It can be assumed that the width of the confidence interval resulted in a lack of significance. The variation in the length in the function of surface values between dogs indicated that measurement condition Combination-30% was too challenging to obtain reliable data for the evaluation of COP parameters. This assumption is further corroborated by the fact that only nine of 13 dogs could stand still for the required measurement duration. Based on the descriptions of base of support in humans (34), it can be suggested that the COP exceeded the functional base of support in measurements in which the dogs did not stand still for the required

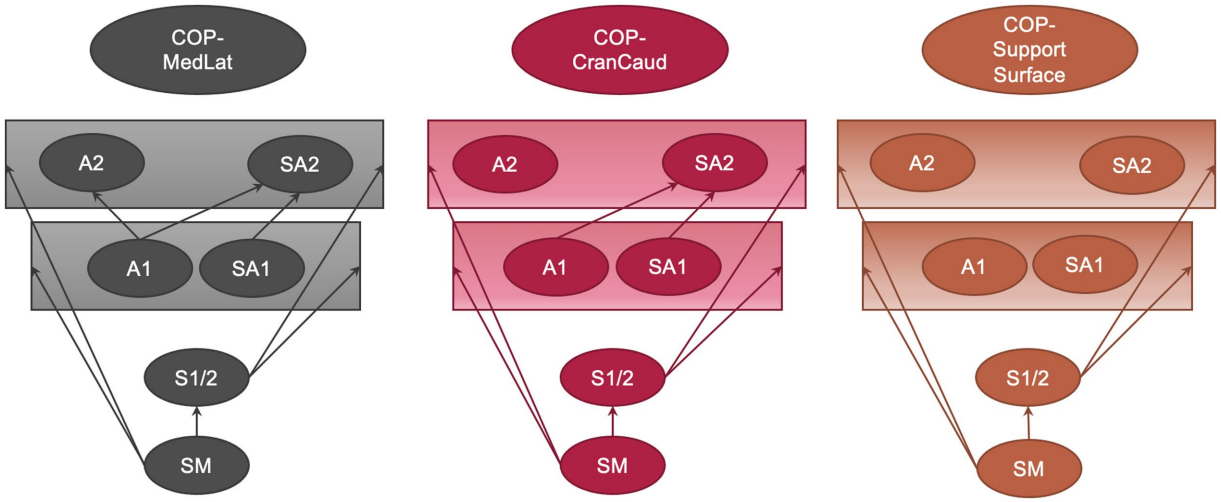

FIGURE 3
Group comparison of the mediolateral (COP-MedLat) and craniocaudal (COP-CranCaud) COP-displacement and the support surface between all measured conditions including standard standing measurement, speed settings (Speed-20%: speed 20%, amplitude 10%; Speed-30%: speed 30%, amplitude 10%); amplitude settings (Amplitude-20%: speed 10%, amplitude 20%; Amplitude-30%: speed 10%, amplitude 30%); and combined setting (Combination-20%: speed 20%, amplitude 20%; Combination-30%: speed 30%, amplitude 30%). The arrows indicate significant differences between the conditions ($p < 0.05$).

time, which resulted in protective steps to prevent falling. Therefore, measurements using settings similar to Combination-30% are not recommended for future research projects.

During the standing measurement and speed conditions (Speed-20% and Speed-30%), the COP displacement was significantly larger in COP-CranCaud than in COP-MedLat. While the COP in humans shows a similar pattern with a larger migration in the craniocaudal direction, the results are contrary to the findings in ponies, which show a larger COP-MedLat than COP-CranCaud during the standing measurement of the forelimbs (15). Similarly, the support surface showed more pronounced migration in the mediolateral direction in dogs during standing measurement of the fore (11, 14) and hind limbs (11). While researchers have found that the fore and hind limbs can be used to determine the body COP in sound horses, the correlation coefficients between the total-body COP and forelimb data were higher than those of the hindlimb data. Therefore, the authors suggested preferring measurements of the forelimbs to assess the body COP in horses (31). In dogs, no data are available regarding the accuracy of these measurement procedures and conflicting outcomes should be viewed with caution because of different measurement techniques. Numerous anatomical differences between horses and dogs may explain the different compensatory mechanisms that maintain stability during standing measurement. Digitization in dogs may offer more stability in the mediolateral direction than that in unguligrade species (67). However, breed-specific compensation mechanisms during standing balance may be observed in dogs owing to differences in pressure distribution in the paws (68–70). Furthermore, the more versatile range of the shoulder and hip joints in dogs (67) may contribute to greater stability in the mediolateral direction. This is also supported by the fact that the mediolateral control of postural stability in humans relies mainly on a hip mechanism (71). The less pronounced abduction and adduction capabilities of the shoulder and hip joints in horses (67) could result in a limited compensatory mechanisms in the mediolateral axis during quiet standing.

More challenging conditions (Amplitude-20%, Amplitude-30%, Combination-20%, and Combination-30%) resulted in the lack of significant differences between COP-MedLat and COP-CranCaud. This can be explained by the rectangular shape of the base of support in dogs. As the mediolateral length of the base of support is smaller, the animals seem to be less stable in this direction, as proposed for ponies. Similarly, lame ponies showed a significantly larger displacement on the X-axis than that in the control group, whereas no difference in COP-CranCaud was observed (15). Therefore, maintaining an upright position on the mediolateral axis is more challenging than in the craniocaudal axis in horses and dogs. It has been proposed that larger forces are necessary to counteract the mediolateral disturbance of the PS, owing to the rectangular shape of the base of support observed in horses (23). This interpretation is in accordance with observations made during the tandem stance in humans. Similar to our results, a narrow base of support in the mediolateral axis compared to the normal standing position resulted in increased instability (53–55). However, a strong correlation between increased statokinesiogram length during sinusoidal external mechanical perturbations and COP-MedLat during a normal standing position has been previously described in human medicine; however, the authors did not include a comparison between COP-MedLat and COP-CranCaud (48). Furthermore, postural stability is challenged more during lateral than craniocaudal perturbations in healthy individuals and patients with Parkinson's disease (49), which is in contrast to the theory that the increased length of the mediolateral axis of the base of support in humans provides better stability (72, 73). Therefore, it can be suggested that postural stability cannot be explained solely based on the shape of base of support, especially during external perturbations. In horses, it has been proposed that the extensor and flexor muscles are better developed than the abductor and adductor muscles and contribute to instability in the mediolateral direction (74), which could also be applied to dogs when PS is challenged.

TABLE 3 Mean values, standard deviation (SD), lower (LL) and upper (UL) limits of the 95% confidence interval (CI) of the conditions standing measurement, speed settings (Speed-20%, Speed-30%), amplitude settings (Amplitude-20%, Amplitude-30%), and combined settings (Combination-20%, Combination-30%) for mediolateral COP-displacement (COP-MedLat), craniocaudal COP-displacement (COP-CranCaud), support surface, statokinesiogram length, length in the function of surface and COP speed.

Condition		Standing measurement	Speed-20%	Speed-30%	Amplitude-20%	Amplitude-30%	Combination-20%	Combination-30%
COP-MedLat (mm)								
Mean value ± SD		5.94 ± 0.32[1,2,3,4,5,6,§]	23.23 ± 0.83*[,3,4,5,6,§]	25.42 ± 1.24*[,3,4,5,6,§]	39.38 ± 1.73*[1,2,5,6]	51.24 ± 2.17*[1,2,3]	41.15 ± 2.13*[1,2,(4),6]	58.77 ± 3.33*[1,2,3,4]
95% CI	LL	5.25	21.42	22.71	35.58	46.46	36.51	51.09
	UL	6.63	25.04	28.12	43.18	56.02	45.79	66.45
COP-CranCaud (mm)								
Mean value ± SD		12.55 ± 0.65[1,2,3,4,5,6,§]	30.26 ± 1.06*[,3,4,5,6,§]	32.24 ± 1.57*[,3,4,5,6,§]	43.85 ± 2.09*[1,2]	50.81 ± 1.67*[1,2]	46.22 ± 2.58*[1,2]	66.92 ± 4.24*[1,2]
95% CI	LL	11.14	27.95	28.82	39.26	47.13	40.61	57.15
	UL	13.97	32.57	35.66	48.45	54.49	51.84	76.69
Support surface (mm^2)								
Mean value ± SD		35.73 ± 4.21[1,2,3,4,5,6]	566.06 ± 52.30*[,3,4,5,6]	701.16 ± 82.59*[,3,4,5,6]	1813.90 ± 196.00*[1,2,(6)]	2836.70 ± 255.31*[1,2]	2062.62 ± 268.25*[1,2]	4044.66 ± 534.26*[1,2]
95% CI	LL	26.57	452.11	521.22	1382.51	2274.77	1478.15	2812.66
	UL	44.89	680.01	881.09	2245.29	3398.63	2647.09	5276.67
Statokinesiogram length (m)								
Mean value ± SD		1.08 ± 0.12	1.63 ± 0.24	1.50 ± 0.26	1.64 ± 0.24	1.53 ± 0.24	1.24 ± 0.24	1.49 ± 0.33
95% CI	LL	0.81	1.11	0.93	1.12	1.00	0.73	0.74
	UL	1.35	2.16	2.08	2.17	2.07	1.76	2.25
Length in the function of surface								
Mean value ± SD		0.05 ± 0.01[1,2,3,4,5,(6)]	0.53 ± 0.11*[,4,5]	0.77 ± 0.13*[,4,(5)]	1.41 ± 0.24*	2.33 ± 0.29*[1,2]	2.54 ± 0.47*[1,(2)]	4.63 ± 1.10 [(*)]
95% CI	LL	0.03	0.29	0.48	0.89	1.69	1.52	2.09
	UL	0.07	0.77	1.05	1.93	2.97	3.57	7.17
COP-Speed (mm/s)								
Mean value ± SD		116.45 ± 3.82[6]	127.87 ± 5.61	136.76 ± 6.38	135.48 ± 6.80	132.09 ± 5.80	133.21 ± 5.56	147.92 ± 6.37*
95% CI	LL	108.13	115.66	122.87	120.51	119.31	121.11	133.22
	UL	124.77	140.09	150.65	150.44	144.86	145.32	162.62

*Significant difference between standard standing measurement and the remaining conditions ($p < 0.05$), [1]significant difference to Speed-20%, [2]significant differences to Speed-30%, [3]significant differences to Amplitude-20%, [4]significant differences to Amplitude-30%, [5]significant difference to Combination-20%, [6]significant difference to Combination-30%, [§] significant differences between COP-MedLat and COP-CranCaud under the same conditions. [0]$p \leq 0.065$.

10.3389/fvets.2023.1249951

TABLE 4 *P*-values of the group comparisons of the conditions standing measurement, speed settings (Speed-20%, Speed-30%), amplitude settings (Amplitude-20%, Amplitude-30%), and combined settings (Combination-20%, Combination-30%) for mediolateral COP-displacement (COP-MedLat), craniocaudal COP-displacement (COP-CranCaud), support surface, Statokinesiogram Length, Length in the function of surface and COP speed.

Condition (I)	Condition (J)	*p-values*					
		COP-MedLat	COP-CranCaud	Support surface	Statokinesiogram length	Length in the function of surface	COP-Speed
Standing measurement	Speed-20%	<0.001*	<0.001*	<0.001*	0.699	0.020*	0.907
	Speed-30%	<0.001*	<0.001*	<0.001*	0.974	0.003*	0.239
	Amplitude-20%	<0.001*	<0.001*	<0.001*	0.674	0.003*	0.421
	Amplitude-30%	<0.001*	<0.001*	<0.001*	0.925	0.000*	0.540
	Combination-20%	<0.001*	<0.001*	<0.001*	1.000	0.004*	0.364
	Combination-30%	<0.001*	<0.001*	0.001*	0.998	0.064(*)	0.018*
Speed-20%	SM	<0.001*	<0.001*	<0.001*	0.699	0.020*	0.907
	Speed-30%	0.973	1.000	0.985	1.000	0.986	1.000
	Amplitude-20%	<0.001*	0.001	0.001*	1.000	0.076	1.000
	Amplitude-30%	<0.001*	<0.001*	<0.001*	1.000	0.001*	1.000
	Combination-20%	<0.001*	0.001*	0.002*	0.998	0.021*	1.000
	Combination-30%	<0.001*	<0.001*	0.004*	1.000	0.114	0.469
Speed-30%	SM	<0.001*	<0.001*	<0.001*	0.974	0.003*	0.239
	Speed-20%	0.973	1.000	0.985	1.000	0.986	1.000
	Amplitude-20%	<0.001*	0.005*	0.002*	1.000	0.449	1.000
	Amplitude-30%	<0.001*	<0.001*	<0.001*	1.000	0.004*	1.000
	Combination-20%	<0.001*	0.003*	0.005*	1.000	0.055(*)	1.000
	Combination-30%	<0.001*	<0.001*	0.005*	1.000	0.153	0.996
Amplitude-20%	Standing measurement	<0.001*	<0.001*	<0.001*	0.674	0.003*	0.421
	Speed-20%	<0.001*	0.001*	0.001*	1.000	0.076	1.000
	Speed-30%	<0.001*	0.005*	0.002*	1.000	0.449	1.000
	Amplitude-30%	0.007*	0.297	0.092	1.000	0.384	1.000
	Combination-20%	1.000	1.000	1.000	0.997	0.627	1.000
	Combination-30%	0.005*	0.008*	0.057(*)	1.000	0.337	0.990
Amplitude-30%	Standing measurement	<0.001*	<0.001*	<0.001*	0.925	< 0.001*	0.540
	Speed-20%	<0.001*	<0.001*	<0.001*	1.000	0.001*	1.000
	Speed-30%	<0.001*	<0.001*	<0.001*	1.000	0.004*	1.000
	Amplitude-20%	0.007*	0.297	0.092	1.000	0.384	1.000
	Combination-20%	0.061(*)	0.968	0.643	1.000	1.000	1.000
	Combination-30%	0.821	0.100	0.755	1.000	0.799	0.838
Combination-20%	Standing measurement	<0.001*	<0.001*	<0.001*	1.000	0.004*	0.364
	Speed-20%	<0.001*	0.001*	0.002*	0.998	0.021*	1.000
	Speed-30%	<0.001*	0.003*	0.005*	1.000	0.055(*)	1.000
	Amplitude-20%	1.000	1.000	1.000	0.997	0.627	1.000
	Amplitude-30%	0.061(*)	0.968	0.643	1.000	1.000	1.000
	Combination-30%	0.011*	0.020*	0.121	1.000	0.911	0.888
Combination-30%	Standing measurement	<0.001*	<0.001*	0.001*	0.998	0.064	0.018*
	Speed-20%	<0.001*	<0.001*	0.004*	1.000	0.114	0.469
	Speed-30%	<0.001*	<0.001*	0.005*	1.000	0.153	0.996
	Amplitude-20%	0.005*	0.008*	0.057(*)	1.000	0.337	0.990
	Amplitude-30%	0.821	0.100	0.755	1.000	0.799	0.838
	Combination-20%	0.011*	0.020*	0.121	1.000	0.911	0.888

*Marks significant differences ($p < 0.05$) between the measurement conditions, (*) highlights comparisons just out of significance ($p \leq 0.065$).

TABLE 5 Mean values, standard deviation, and *p*-values of COP-MedLat and COP-CranCaud during the same measurement condition.

Condition	COP-MedLat (mm)	COP-CranCaud (mm)	*p*-values
Standing measurement	5.94 ± 0.32*	12.55 ± 0.65*	<0.001
Speed-20%	23.23 ± 0.83*	30.26 ± 1.06*	<0.001
Speed-30%	25.42 ± 1.24*	32.24 ± 1.57*	0.002
Amplitude-20%	39.38 ± 1.73	43.85 ± 2.09	0.114
Amplitude-30%	51.24 ± 2.17	50.81 ± 1.67	0.877
Combination-20%	41.15 ± 2.13	46.22 ± 2.58	0.142
Combination-30%	58.77 ± 3.33	66.92 ± 4.24	0.151

*Significant difference between the COP-MedLat and COP-CranCaud groups.

Furthermore, human medical research has found a significant increase in COP displacement when an external perturbation is unpredictable compared to measurement procedures, where an anticipatory postural adjustment is possible owing to a predictable perturbation. These results lead to the conclusion that postural control training plans are valuable for improving the interaction between anticipatory and compensatory PS (75). Similarly, repetitive measurements using predictive forward and backward translation on a motorized platform led to a significant decrease in COP displacement. In conclusion, the human body adapts to predictive and repetitive perturbations by modifying muscle activity (46). Given the sinusoidal movements of the selected settings, the external perturbation used in this study can be classified as predictable. Therefore, future studies using both predictable and unpredictable settings may provide further insights into whether dogs respond similarly to humans when unpredictable external perturbations are applied to an animal's body. These measurements should be supplemented by the analysis of electromyographical activity to investigate prior muscle activation when a perturbation is predictable, as described in human medicine (46, 75). Muscle activation and COP displacements differed between elderly and young individuals (75), and, as previously mentioned, senile (>75% of expected lifespan) (16) and orthopedically diseased dogs (11, 14) showed alterations in COP parameters compared to young and sound dogs during standing measurement. Therefore, alterations in muscle activation strategies in senile and orthopedically diseased dogs should be the focus of future research.

Balancing exercises using wobble boards and cushions are an integral part of the rehabilitation of neurological and orthopedic diseases to improve muscular function and PS (76, 77). Furthermore, a training program that includes PS challenges is recommended in sports dogs to prevent injury risk (77, 78) and in elderly animals to maintain a good quality of life (60). However, the assumption that proprioceptive training programs positively affect PS is based on human medical studies (79). Human research has found that balance recovery effectiveness can be trained or relearned, and perturbation-based exercises have shown positive impacts on reactive balance performance in post-stroke (80, 81), Parkinson's disease (42), and patients with anterior cruciate ligament rupture (7, 8). Therefore, future veterinary medicine studies should focus on the effects of PS training programs on diseased animals.

The investigated settings can be used as an orientation for the implementation of external perturbations in rehabilitation and research on diseases that are considered to negatively impact PS. The following graduated scheme can be suggested: because speed is less challenging for PS than the amplitude, weak dogs should start with a small amplitude (Speed-20%, Speed-30%). This difficulty can be increased by increasing the amplitude (Amplitude-20%, Combination-20%); however, it should be considered that Combination-20% does not have superior effects to Amplitude-20%. The combination of high speed and large amplitude (Combination-30%) further increases the challenge in the mediolateral and craniocaudal directions. However, sound dogs do not perform well under these conditions. Therefore, a further increase should first be performed using a larger amplitude with a slow speed (Amplitude-30%), which is advantageous in the mediolateral direction.

One limitation of our study was the small sample size of 13 dogs. Even though the inclusion criteria were designed to limit this study to healthy, adult dogs with similar body type and weight, it should be mentioned that previous research found a significant correlation between weight, height, and length and the outcomes of COP measurements (16).

5. Conclusion

To the best of our knowledge, this is the first study to demonstrate that external mechanical perturbations challenge PS in dogs. All conditions led to a significant increase in COP-MedLat, COP-CranCaud, and support surface compared with standing measurement. In addition, the extent of displacement positively correlated with the increase in amplitude. All the tested settings, except for Combination-30%, which was not well tolerated by the dogs, are recommended for future research and training programs. While the COP displacement was significantly larger in the craniocaudal direction than that in the mediolateral direction during standing measurement and settings with a low amplitude, no significant difference was found during the more challenging conditions. Therefore, it can be suggested that dogs are less stable during a mediolateral disturbance of PS. Further studies should address the effects of external perturbations on COP parameters in juvenile, senile, and orthopedically or neurologically diseased dogs. These measurements should be supplemented with the determination of muscular activity using electromyographic analysis.

Data availability statement

The raw data supporting the conclusions of this article will be made available by the authors, without undue reservation.

Ethics statement

The animal studies were approved by Ethics and Animal Welfare Committee of the University of Veterinary Medicine, Vienna. The studies were conducted in accordance with the local legislation and institutional requirements. Written informed consent was obtained from the owners for the participation of their animals in this study.

Author contributions

BB, CP, and CL: conceptualization, methodology, and validation. AT: formal analysis. CL and RG: data curation. CL: writing—original draft preparation. BB, MM, CP, BR, and CL: writing—review and

editing. All authors contributed to the article and approved the submitted version.

Funding

Allcare Innovations (111 Rue Carl von Linné, 26500 Bourg les Valence, France) reduced the purchase cost of the Imoove® Vet by 40% to ensure that the study was financially viable.

Acknowledgments

The authors would like to thank all the participating dogs, their owners, and Allcare Innovations for their contributions.

Conflict of interest

The authors declare that the research was conducted in the absence of any commercial or financial relationships that could be construed as a potential conflict of interest.

Publisher's note

All claims expressed in this article are solely those of the authors and do not necessarily represent those of their affiliated organizations, or those of the publisher, the editors and the reviewers. Any product that may be evaluated in this article, or claim that may be made by its manufacturer, is not guaranteed or endorsed by the publisher.

References

1. Pollock AS, Durward BR, Rowe PJ, Paul JP. What is balance? *Clin Rehabil*. (2000) 14:402–6. doi: 10.1191/0269215500cr342oa

2. Faraldo-García A, Santos-Pérez S, Crujeiras-Casais R, Labella-Caballero T, Soto-Varela A. Influence of age and gender in the sensory analysis of balance control. *Eur Arch Otorhinolaryngol*. (2012) 269:673–7. doi: 10.1007/s00405-011-1707-7

3. Bezalel G, Nachoum Arad G, Plotnik M, Friedman J. Voluntary step execution in patients with knee osteoarthritis: symptomatic vs. non-symptomatic legs. *Gait Posture*. (2021) 83:60–6. doi: 10.1016/j.gaitpost.2020.10.006

4. Rambaud AJ, Semay B, Samozino P, Morin J-B, Testa R, Philippot R, et al. Criteria for return to sport after anterior cruciate ligament reconstruction with lower reinjury risk (CR'STAL study): protocol for a prospective observational study in France. *BMJ Open*. (2017) 7:e015087. doi: 10.1136/bmjopen-2016-015087

5. Schweizer N, Strutzenberger G, Franchi MV, Farshad M, Scherr J, Spörri J. Screening tests for assessing arthletes at risk of ACL injury or rseinjury-a scoping review. *Int J Environ Res Public Health*. (2022) 19:19. doi: 10.3390/ijerph19052864

6. Novaes M, Carvalho A, Sauer JF, Brech GC, Helito CP, João SM. Postural control during single leg stance in individuals with clinical indication for combined reconstruction of the anterior cruciate and the anterolateral ligaments of the knee: a cross-sectional study. *BMC Musculoskelet Disord*. (2022) 23:383. doi: 10.1186/s12891-022-05347-0

7. Molka AZ, Lisiński P, Huber J. Visual biofeedback exercises for improving body balance control after anterior cruciate ligament reconstruction. *J Phys Ther Sci*. (2015) 27:2357–60. doi: 10.1589/jpts.27.2357

8. Zemkova E, Vlašič M. The effect of instability resistance training on neuromuscular performance in athletes after anterior cruciate ligament injury. *Sport Sci*. (2009) 2:17–23.

9. Palmieri RM, Ingersoll CD, Stone MB, Krause BA. Center-of-pressure parameters used in the assessment of postural control. *J Sport Rehabil*. (2002) 11:51–66. doi: 10.1123/jsr.11.1.51

10. Reicher B, Tichy A, Bockstahler B. Center of pressure in the paws of clinically sound dogs in comparison with orthopedically diseased dogs. *Animals*. (2020) 10:1366. doi: 10.3390/ani10081366

11. Carrillo JM, Manera ME, Rubio M, Sopena J, Santana A, Vilar JM. Posturography and dynamic pedobarography in lame dogs with elbow dysplasia and cranial cruciate ligament rupture. *BMC Vet Res*. (2018) 14:108. doi: 10.1186/s12917-018-1435-y

12. López S, Vilar JM, Rubio M, Sopena JJ, Damiá E, Chicharro D, et al. Center of pressure limb path differences for the detection of lameness in dogs: a preliminary study. *BMC Vet Res*. (2019) 15:138. doi: 10.1186/s12917-019-1881-1

13. López S, Vilar JM, Rubio M, Sopena JJ, Santana A, Rodríguez O, et al. Pedobarography: a novel approach to test the efficacy of treatments for lameness; an experience with mavacoxib in dogs with elbow osteoarthritis. *BMC Vet Res*. (2019) 15:193. doi: 10.1186/s12917-019-1946-1

14. Manera ME, Carrillo JM, Batista M, Rubio M, Sopena J, Santana A, et al. Static posturography: a new perspective in the assessment of lameness in a canine model. *PLoS One*. (2017) 12:e0170692. doi: 10.1371/journal.pone.0170692

15. Pitti L, Oosterlinck M, Díaz-Bertrana ML, Carrillo JM, Rubio M, Sopena J, et al. Assessment of static posturography and pedobarography for the detection of unilateral forelimb lameness in ponies. *BMC Vet Res*. (2018) 14:151. doi: 10.1186/s12917-018-1462-8

16. Mondino A, Wagner G, Russell K, Lobaton E, Griffith E, Gruen M, et al. Static posturography as a novel measure of the effects of aging on postural control in dogs. *PLoS One*. (2022) 17:e0268390. doi: 10.1371/journal.pone.0268390

17. Charalambous D, Strasser T, Tichy A, Bockstahler B. Ground reaction forces and Center of Pressure within the paws when stepping over obstacles in dogs. *Animals*. (2022) 12:1702. doi: 10.3390/ani12131702

18. Charalambous D, Lutonsky C, Keider S, Tichy A, Bockstahler B. Vertical ground reaction forces, paw pressure distribution, and center of pressure during heelwork in working dogs competing in obedience. *Front Vet Sci*. (2023) 10:1106170. doi: 10.3389/fvets.2023.1106170

19. Bieber B, Reicher B, Tichy A, Bockstahler B. Changes in ground reaction forces and center of pressure parameters of paws when wearing dog boots in dogs. *Front Vet Sci*. (2022) 9:906277. doi: 10.3389/fvets.2022.906277

20. Virag Y, Gumpenberger M, Tichy A, Lutonsky C, Peham C, Bockstahler B. Center of pressure and ground reaction forces in Labrador and Golden retrievers with and without hip dysplasia at 4, 8, and 12 months of age. *Front Vet Sci*. (2022) 9:1087693. doi: 10.3389/fvets.2022.1087693

21. Blau SR, Davis LM, Gorney AM, Dohse CS, Williams KD, Lim J-H, et al. Quantifying center of pressure variability in chondrodystrophoid dogs. *Vet J*. (2017) 226:26–31. doi: 10.1016/j.tvjl.2017.07.001

22. Nauwelaerts S, Malone SR, Clayton HM. Development of postural balance in foals. *Vet J*. (2013) 198:e70–4. doi: 10.1016/j.tvjl.2013.09.036

23. Clayton HM, Nauwelaerts S. Effect of blindfolding on Centre of pressure variables in healthy horses during quiet standing. *Vet J*. (2014) 199:365–9. doi: 10.1016/j.tvjl.2013.12.018

24. Vero AM, Wagner G, Lobaton E, Russell K, Olby N. Age-related changes in posture steadiness in the companion dog. *Innov Aging*. (2021) 5:959–60. doi: 10.1093/geroni/igab046.3461

25. Lewis MJ, Williams KD, Langley T, Jarvis LM, Sawicki GS, Olby NJ. Development of a novel gait analysis tool measuring center of pressure for evaluation of canine chronic thoracolumbar spinal cord injury. *J Neurotrauma*. (2019) 36:3018–25. doi: 10.1089/neu.2019.6479

26. Lee S, Lee J-M, Park H, Cha Y, Cheong J. Balance evaluation after reconstruction of medial patellar luxation in small-sized dogs with Wii balance board. *J Vet Clin*. (2019) 36:301–5. doi: 10.17555/jvc.2019.12.36.6.301

27. Lee S, Lee J-M, Park H, Cha Y, Cheong J. Validity of the Wii balance board for evaluation of medial patellar lsuxation in small sized dog. *J Vet Clin*. (2019) 36:297–300. doi: 10.17555/jvc.2019.12.36.6.297

28. Clayton HM, Bialski DE, Lanovaz JL, Mullineaux DR. Assessment of the reliability of a technique to measure postural sway in horses. *Am J Vet Res*. (2003) 64:1354–9. doi: 10.2460/ajvr.2003.64.1354

29. Dewolf AH, Ivanenko YP, Mesquita RM, Willems PA. Postural control in the elephant. *J Exp Biol*. (2021) 224:648. doi: 10.1242/jeb.243648

30. Chang Y-H, Ting LH. Mechanical evidence that flamingos can support their body on one leg with little active muscular force. *Biol Lett*. (2017) 13:20160948. doi: 10.1098/rsbl.2016.0948

31. Clayton HM, Nauwelaerts S. Is a single force plate adequate for stabilographic analysis in horses? *Equine Vet J*. (2012) 44:550–3. doi: 10.1111/j.2042-3306.2011.00458.x

32. Pai YC, Rogers MW, Patton J, Cain TD, Hanke TA. Static versus dynamic predictions of protective stepping following waist-pull perturbations in young and older adults. *J Biomech*. (1998) 31:1111–8. doi: 10.1016/s0021-9290(98)00124-9

33. Hof AL, Gazendam MG, Sinke WE. The condition for dynamic stability. *J Biomech*. (2005) 38:1–8. doi: 10.1016/j.jbiomech.2004.03.025

34. Horak FB, Shupert CL, Mirka A. Components of postural dyscontrol in the elderly: a review. *Neurobiol Aging*. (1989) 10:727–38. doi: 10.1016/0197-4580(89)90010-9

35. Fujimoto M, Bair W-N, Rogers MW. Center of pressure control for balance maintenance during lateral waist-pull perturbations in older adults. *J Biomech*. (2015) 48:963–8. doi: 10.1016/j.jbiomech.2015.02.012

36. Baratto L, Morasso PG, Re C, Spada G. A new look at posturographic analysis in the clinical context: sway-density versus other parameterization techniques. *Mot Control*. (2002) 6:246–70. doi: 10.1123/mcj.6.3.246

37. Fabbri M, Martoni M, Esposito MJ, Brighetti G, Natale V. Postural control after a night without sleep. *Neuropsychologia*. (2006) 44:2520–5. doi: 10.1016/j.neuropsychologia.2006.03.033

38. van Humbeeck N, Kliegl R, Krampe RT. Lifespan changes in postural control. *Sci Rep*. (2023) 13:541. doi: 10.1038/s41598-022-26934-0

39. Efstathiou MA, Giannaki CD, Roupa Z, Hadjisavvas S, Stefanakis M. Evidence of distorted proprioception and postural control in studies of experimentally induced pain: a critical review of the literature. *Scand J Pain*. (2022) 22:445–56. doi: 10.1515/sjpain-2021-0205

40. Petró B, Papachatzopoulou A, Kiss RM. Devices and tasks involved in the objective assessment of standing dynamic balancing—a systematic literature review. *PLoS One*. (2017) 12:e0185188. doi: 10.1371/journal.pone.0185188

41. Kirsch AN, Bodkin SG, Saliba SA, Hart JM. Measures of agility and single-legged balance as clinical assessments in patients with anterior cruciate ligament reconstruction and healthy individuals. *J Athl Train*. (2019) 54:1260–8. doi: 10.4085/1062-6050-266-18

42. Jöbges M, Heuschkel G, Pretzel C, Illhardt C, Renner C, Hummelsheim H. Repetitive training of compensatory steps: a therapeutic approach for postural instability in Parkinson's disease. *J Neurol Neurosurg Psychiatry*. (2004) 75:1682–7. doi: 10.1136/jnnp.2003.016550

43. Mademli L, Mavridi D, Bohm S, Patikas DA, Santuz A, Arampatzis A. Standing on unstable surface challenges postural control of tracking tasks and modulates neuromuscular adjustments specific to task complexity. *Sci Rep*. (2021) 11:6122. doi: 10.1038/s41598-021-84899-y

44. Brophy RH, Schafer KA, Knapik DM, Motley J, Haas A, Matava MJ, et al. Changes in dynamic postural stability after ACL reconstruction: results over 2 years of follow-up. *Orthop J Sports Med*. (2022) 10:23259671221098989. doi: 10.1177/23259671221098989

45. Dae-Hee L, Jin-Hyuck L, Sung-Eun A, Min-Ji P. Effect of time after anterior cruciate ligament tears on proprioception and postural stability. *PLoS One*. (2015) 10:e0139038. doi: 10.1371/journal.pone.0139038

46. Kennedy A, Bugnariu N, Guevel A, Sveistrup H. Adaptation of the feedforward postural response to repeated continuous postural perturbations. *Neurosci Med*. (2013) 4:45–9. doi: 10.4236/nm.2013.41007

47. Lysholm M, Ledin T, Odkvist LM, Good L. Postural control--a comparison between patients with chronic anterior cruciate ligament insufficiency and healthy individuals. *Scand J Med Sci Sports*. (1998) 8:432–8. doi: 10.1111/j.1600-0838.1998.tb00464.x

48. Grassi L, Rossi S, Cappa P. Dynamic Posturography: perturbed equilibrium assessment on healthy adult subjects. In: *IEEE international symposium on medical measurements and applications (MeMeA) proceedings*, Turin, Italy (2015).

49. Vaugoyeau M, Viel S, Assaiante C, Amblard B, Azulay JP. Impaired vertical postural control and proprioceptive integration deficits in Parkinson's disease. *Neuroscience*. (2007) 146:852–63. doi: 10.1016/j.neuroscience.2007.01.052

50. O'Connell M, George K, Stock D. Postural sway and balance testing: a comparison of normal and anterior cruciate ligament deficient knees. *Gait Posture*. (1998) 8:136–42. doi: 10.1016/S0966-6362(98)00023-X

51. Bodkin SG, Slater LV, Norte GE, Goetschius J, Hart JM. ACL reconstructed individuals do not demonstrate deficits in postural control as measured by single-leg balance. *Gait Posture*. (2018) 66:296–9. doi: 10.1016/j.gaitpost.2018.06.120

52. Lee C-H, Sun T-L. Evaluation of postural stability based on a force plate and inertial sensor during static balance measurements. *J Physiol Anthropol*. (2018) 37:27. doi: 10.1186/s40101-018-0187-5

53. Berg K. Measuring balance in the elderly: preliminary development of an instrument. *Physiother Can*. (1989) 41:304–11. doi: 10.3138/ptc.41.6.304

54. Tesio L, Perucca L, Franchignoni FP, Battaglia MA. A short measure of balance in multiple sclerosis: validation through Rasch analysis. *Funct Neurol*. (1997) 12:255–65.

55. Jonsson E, Seiger A, Hirschfeld H. Postural steadiness and weight distribution during tandem stance in healthy young and elderly adults. *Clin Biomech (Bristol, Avon)*. (2005) 20:202–8. doi: 10.1016/j.clinbiomech.2004.09.008

56. Mouzat A, Dabonneville M, Bertrand P. The effect of feet position on orthostatic posture in a female sample group. *Neurosci Lett*. (2004) 365:79–82. doi: 10.1016/j.neulet.2004.04.062

57. Fujimoto M, Hsu W-L, Woollacott MH, Chou L-S. Ankle dorsiflexor strength relates to the ability to restore balance during a backward support surface translation. *Gait Posture*. (2013) 38:812–7. doi: 10.1016/j.gaitpost.2013.03.026

58. King MB, Judge JO, Wolfson L. Functional base of support decreases with age. *J Gerontol*. (1994) 49:M258–63. doi: 10.1093/geronj/49.6.m258

59. Coates JC. "Evaluation and rehabilitation options for orthopedic disorders of the pelvic limb,". In: C Zink and DykeJB van, editors. *Canine sports medicine and rehabilitation*. Hoboken, NJ: Wiley Blackwell (2018).

60. Frye C, Carr BJ, Lenfest M, Miller A. Canine geriatric rehabilitation: considerations and strategies for assessment, functional scoring, and follow up. *Front Vet Sci*. (2022) 9:842458. doi: 10.3389/fvets.2022.842458

61. Moreira JP, Tichy A, Bockstahler B. Comparison of the vertical force distribution in the paws of dogs with coxarthrosis and sound dogs walking over a pressure plate. *Animals*. (2020) 10:60986. doi: 10.3390/ani10060986

62. Braun L, Tichy A, Peham C, Bockstahler B. Comparison of vertical force redistribution in the pads of dogs with elbow osteoarthritis and healthy dogs. *Vet J*. (2019) 250:79–85. doi: 10.1016/j.tvjl.2019.06.004

63. Roush JK, McLaughlin RM. Effects of subject stance time and velocity on ground reaction forces in clinically normal greyhounds at the walk. *Am J Vet Res*. (1994) 55:1672–6.

64. Hans EC, Zwarthoed B, Seliski J, Nemke B, Muir P. Variance associated with subject velocity and trial repetition during force platform gait analysis in a heterogeneous population of clinically normal dogs. *Vet J*. (2014) 202:498–502. doi: 10.1016/j.tvjl.2014.09.022

65. Conzemius MG, Torres BT, Muir P, Evans R, Krotscheck U, Budsberg S. Best practices for measuring and reporting ground reaction forces in dogs. *Vet Surg*. (2022) 51:385–96. doi: 10.1111/vsu.13772

66. Allcare Innovations *Imoove®vet guide Mise en route & Utilisation: Le soin par le movement*. (2020).

67. Nickel R, Schummer A, Seiferle E. *Lehrbuch der Anatomie der Haustiere*. Berlin, Hamburg: Parey (2004). 625 p.

68. Schwarz N, Tichy A, Peham C, Bockstahler B. Vertical force distribution in the paws of sound Labrador retrievers during walking. *Vet J*. (2017) 221:16–22. doi: 10.1016/j.tvjl.2017.01.014

69. Besancon MF, Conzemius MG, Evans RB, Ritter MJ. Distribution of vertical forces in the pads of greyhounds and Labrador retrievers during walking. *Am J Vet Res*. (2004) 65:1497–501. doi: 10.2460/ajvr.2004.65.1497

70. Souza AN, Pinto AC, Marvulle V, Matera JM. Evaluation of vertical forces in the pads of German shepherd dogs. *Vet Comp Orthop Traumatol*. (2013) 26:06–11. doi: 10.3415/VCOT-11-07-0100

71. Winter DA, Prince F, Frank JS, Powell C, Zabjek KF. Unified theory regarding a/P and M/L balance in quiet stance. *J Neurophysiol*. (1996) 75:2334–43. doi: 10.1152/jn.1996.75.6.2334

72. Suomi R, Koceja DM. Postural sway patterns of normal men and women and men with mental retardation during a two-legged stance test. *Arch Phys Med Rehabil*. (1994) 75:205–9. doi: 10.1016/0003-9993(94)90397-2

73. Błaszczyk JW, Beck M, Sadowska D. Assessment of postural stability in young healthy subjects based on directional features of posturographic data: vision and gender effects. *Acta Neurobiol Exp*. (2014) 74:433–42.

74. Gomes-Costa M, Roupa I, Pequito M, Prazeres J, Gaivão M, Abrantes J, et al. The use of pressure plates for static center of pressure analysis in horses. *J Equine Vet*. (2015) 35:315–20. doi: 10.1016/j.jevs.2015.02.002

75. Kanekar N, Aruin AS. Aging and balance control in response to external perturbations: role of anticipatory and compensatory postural mechanisms. *Age*. (2014) 36:9621. doi: 10.1007/s11357-014-9621-8

76. Wittek K, Bockstahler B. Aktive therapeutische Übungen In: B Bockstahler, K Wittek, D Levine, J Maierl and DL Millis, editors. *Physikalische Medizin, Rehabilitation und Sportmedizin auf den Punkt gebracht: Ein Leitfaden für die Kleintierpraxis*. Babenhausen: VBS (2022)

77. McCauley L, van Dyke JB. "Therapeutic exercise". In: C Zink and DykeJB van, editors. *Canine sports medicine and rehabilitation*. Hoboken, NJ: Wiley Blackwell (2018).

78. Sellon DC, Marcellin-Little DJ. Risk factors for cranial cruciate ligament rupture in dogs participating in canine agility. *BMC Vet Res*. (2022) 18:39. doi: 10.1186/s12917-022-03146-2

79. McKenzie BA, Chen FL. Assessment and management of declining physical function in aging dogs. *Top Companion Anim Med*. (2022) 51:100732. doi: 10.1016/j.tcam.2022.100732

80. Handelzalts S, Kenner-Furman M, Gray G, Soroker N, Shani G, Melzer I. Effects of perturbation-based balance training in subacute persons with stroke: a randomized controlled trial. *Neurorehabil Neural Repair*. (2019) 33:213–24. doi: 10.1177/1545968319829453

81. Mansfield A, Aqui A, Danells CJ, Knorr S, Centen A, DePaul VG, et al. Does perturbation-based balance training prevent falls among individuals with chronic stroke? A randomised controlled trial. *BMJ Open*. (2018) 8:e021510. doi: 10.1136/bmjopen-2018-021510

frontiers | Frontiers in Veterinary Science

TYPE Original Research
PUBLISHED 20 September 2023
DOI 10.3389/fvets.2023.1233921

OPEN ACCESS

EDITED BY
Mauro Malvè,
Public University of Navarre, Spain

REVIEWED BY
Jörg Auer,
University of Zurich, Switzerland
Tanya C. Garcia,
University of California, Davis, United States

*CORRESPONDENCE
Ashley Brabon
✉ abrabon@csu.edu.au

RECEIVED 03 June 2023
ACCEPTED 08 September 2023
PUBLISHED 20 September 2023

CITATION
Brabon A, Hughes KJ and Labens R (2023) Comparison of interfragmentary compression across simulated condylar fractures repaired using four techniques.
Front. Vet. Sci. 10:1233921.
doi: 10.3389/fvets.2023.1233921

Comparison of interfragmentary compression across simulated condylar fractures repaired using four techniques

Ashley Brabon*, Kristopher James Hughes and Raphael Labens

Faculty of Science, School of Agricultural, Environmental and Veterinary Sciences, Charles Sturt University, Wagga Wagga, NSW, Australia

Introduction: Equine condylar fractures are commonly repaired using cortex screws applied in lag fashion. Inadequate interfragmentary compression can lead to post-operative complications.

Methods: Lateral condylar fractures were simulated in 21 cadaver limbs (8 third metatarsals, 13 third metacarpals). In each limb, pressure-sensitive film (Prescale®, Fuji Photo Film Co.) was placed in each osteotomy prior to repair with 4.5 mm diameter cortex screws placed in lag fashion. Screws were placed in linear (L), triangular (T), linear plus a washer (LW) and sequentially tightened triangular configurations (TD1). All screws were tightened to a torque of 4 Nm. Pressure prints obtained were scanned using dedicated software (Fuji FPD-8010E, Fuji Photo Film Co.). A Bayesian Network (BN) model was developed to investigate the impact and interrelationship of each factor on interfragmentary compression. Sixty-three repairs (20*L, 24* T, 11*TD1, and 8*LW) performed on 21 limbs were included in the analysis.

Results: The BN predicted mean contact area (±s.d.) for pressures within the operating range of the prescale film [≥2.5 Megapascals (MPa) ≤ 10 MPa] by L, T, TD1 and LW repairs were 403mm^2 ± (140), 411 mm^2 ± (120), 403 mm^2 ± (120), and 366mm^2 ± (70). The mean contact area (± s.d.) created by L, T, TD1 and LW repairs at pressures >10 MPa were 112 mm^2 ± (48), 167 mm^2 ± (67), 142 mm^2 ± (50), and 100mm^2 ± (27). When pressures ≥2.5 MPA to ≤10 MPa were considered, the construct (T or L), washer and screw tightening sequence variables had a very low effect on interfragmentary contact area. At pressures >10 MPa BN sensitivity findings were 16.3, 5.03, and 0.133% for construct, washer and screw tightening sequence. The BN model indicated that triangular repair configuration had a weak influence in the ≥2.5 MPa ≤ 10 MPa range and a moderate influence in the <10 MPa range, on interfragmentary compression. The addition of a washer and the screw tightening sequence had a weak influence on interfragmentary compression at all pressure ranges.

Discussion: The results show that triangular repairs create larger interfragmentary contact areas at greater interfragmentary pressure in simulated condylar fractures, however it is unknown if this results in improved repair stability in the clinical scenario.

KEYWORDS

configuration, condylar, equine, fracture, repair

1. Introduction

Fractures originating from the distal condyles of the third metacarpal or metatarsal bone (condylar fractures) represent the most frequent long bone fracture in horses and are a common cause of wastage in racehorses, world-wide (1, 2). Internal fixation is the recommended treatment for all but the simplest of condylar fractures (3). Among various fixation techniques, fixation with cortex screws placed in lag fashion is most commonly employed for the treatment of condylar fractures (2). Achieving absolute stability is crucial for primary bone healing in the absence of callus formation, which is essential for optimum healing of articular fractures (2, 4). Lag screw fixation achieves fracture stabilization through compression alone (5). Absolute stability is attained when the interfragmentary friction produced is greater than the traction exerted by the limb's function (4). A screw applied in lag fashion engages the remote cortex only, and the approximation of the screw threads within the remote cortex, and the screw head, results in interfragmentary compression (4). Various methods have been used to assess interfragmentary compression in a variety of osteotomy models, including load cells, pressure sensitive washers, pressure sensitive film and strain gauges (6–9). Despite previous investigations, the optimum interfragmentary compression for repair of condylar fractures is unknown. Although, pressure necrosis, as a result of excessive interfragmentary compression, has not been demonstrated in sheep osteotomy models, and is considered unlikely to occur in horses, it should be considered (2, 5). Common technical errors encountered during the repair of condylar fractures include, inadequate compression of the fracture and imperfect anatomical fracture reduction (10). Inadequate interfragmentary compression along the articular margin and imperfect anatomical reduction can predispose the joint to excessive postoperative osteoarthritis and poor outcomes (10, 11). Increasing the amount of torque applied to a screw head increases the amount of compression achieved across the fracture plane (12). But, inadequate interfragmentary compression cannot be overcome by increased screw torque alone. Because, lag screw fixation has a low tolerance to single overload, and as a screw is tightened the risk of implant or substrate failure increases (13).

Most commonly, condylar fractures are repaired using a single column of lag screws, placed in accordance with principles developed by the AO foundation (2). However, it has been suggested that using two parallel screws through the distal condyle, can improve the strength of repair (10). Recently, an *ex vivo* study showed that two parallel screws placed in the proximal phalanx, adjacent to the metacarpophalangeal joint, provided greater stability under loaded conditions when compared to a single screw (14). Additionally, triangular repair has been demonstrated as a safe and effective treatment option for managing sagittal fractures of the proximal phalanx in racehorses (15). When multiple screws are employed in a lag repair, it has been suggested that an alternate screw tightening technique should be employed to achieve better interfragmentary compression and limit displacement during internal fixation (16).

A washer can be used to distribute the force applied by the screw head to a larger area of cortical bone, subsequently increasing the torque applied before the screw head breaks through the cortical bone (12). The compression applied by a screw affects a small portion of the surrounding bone, and interfragmentary compression reduces as the distance from the screw increases (5). The addition of a washer to internal fixation constructs has been reported to result in increased interfragmentary compression (12).

The primary goals of surgical repair of condylar fractures include re-establishing articular congruency, reduction of the fracture gap and achieving stabilization (2). Increased interfragmentary compression would improve fracture stability and may reduce postoperative arthritis, in turn contributing to improved results for horses undergoing lateral condylar fracture repair. A cadaveric study was conducted to compare the interfragmentary compression achieved by four different repair configurations. The hypothesis was that interfragmentary compression would be greater for triangular (T) vs. linear (L), linear + washer (LW) vs. L and T vs. sequentially tightened triangular (TD1) configurations, respectively.

2. Materials and methods

2.1. Limbs

The study used limbs from mature horses, which were subjected to euthanasia for reasons unrelated to the study or to disease in the metacarpophalangeal region. Horses were of mixed sex and breed, but the horse population which makes up the case load of the clinic being predominantly Thoroughbred and Standardbred racehorses (approximately 35% respectively) with the remainder made up of performance and pleasure horses of a variety of breeds. Thirty-four metacarpi and metatarsi were collected, and all soft tissues were removed before the limbs were wrapped in wet towels and stored at −20°C until use. The collection of cadaveric specimens was approved by the animal care and ethics committee (A21378) at Charles Sturt University. Through a series of trials, the osteotomy, repair and interfragmentary compression measurement processes were established.

2.2. Hole drilling and lateral condyle fracture model

To prepare the samples for hole drilling, bones were thawed, in groups of four, at room temperature in a water bath. To facilitate ease of manipulation and consistent hole placement, the limbs were secured in a custom-made clamp (Figure 1). Following AO guidelines (17) for lag screw fixation, four drill holes were created in a triangular pattern. Holes have been numbered sequentially in a dorsal to palmar/plantar then proximal order, for reference purposes (Figure 2). All glide holes were drilled using an orthopedic aiming device, beginning with an initial 4.5 mm glide hole created in the center of the epicondylar fossa (hole 2). Three additional glide holes were placed. One dorsal (hole 1), one palmar (hole 3), and one 20 mm proximal (hole 4) to, the central hole. The holes created for triangular fixation were 10 mm from the dorsal and palmar/plantar articular surface of the bone. Glide holes were measured as 30 mm deep for the epicondyle and 10 mm deep for the proximal screw hole. The 3.2 mm drill sleeve was used to complete the 3.2 mm thread hole for each screw, and each thread hole was hand tapped using a 4.5 mm tap (vet Tap for Cortex Screws Ø

4.5 mm 311.460; DePuy Synthes Vet). All drilling and tapping procedures were performed with irrigation. After drilling and tapping, the limbs were wrapped in wet towels and re-frozen at −20°C.

To create the osteotomy in the frozen bones, an 800w, 200 mm table saw (TSB-0808, Ozito, Australia) fitted with a saw guide and 200 mm saw blade (200 mm 60 T Marathon, Irwin, Australia) was used. The osteotomy extended from the distal articular surface of the third metacarpal/metatarsal bone, adjacent to the sagittal ridge, and extended proximally for 75 mm. Two proximal osteotomies were performed, 10 mm apart, to complete the simulation of a complete fracture and allow for pressure-film placement and manipulation. Finally, the frozen bone pieces were secured together and wrapped with wet towels before being stored in a freezer at −20°C.

FIGURE 1
Aiming device in place with sample secured in a clamp to stabilize the bone for drilling.

2.3. Repair technique and selection

Six limbs were utilized in preliminary investigations to fine tune the method of bone preparation, pressure film preparation, interfragmentary compression measurement and analysis. This left 28 limbs for investigation. Two screws, placed in screw holes two and four, were used in L and LW repairs. T and TD1 repair techniques employed three screws, placed in holes numbered one, three and four. Repairs were performed in a random order using a cross-over design. The initial repair selection approach was to perform L, LW, T TD1 repair techniques on each limb in a random order. Limbs were numbered one to twenty-eight, and each repair technique was assigned a number of one to four. A free source random number generator (random.org) (18) was used in two stages. The random sequence generator was used to create a random order of numbers between one and twenty-eight. Subsequently the random integer generator was used to select treatment method by generating 28 random integers between the numbers one and four, this process was repeated in case more than four repairs were possible per sample. Cadaver samples were used until screw stripping occurred to make use of cadaver samples. The order in which each repair technique was performed was recorded (Compression cycle), to determine the impact that repeated tightening and sample use had on the interfragmentary contact area measured.

2.4. Testing protocols

To prepare the samples for testing, bones were thawed in groups of four, at room temperature in a water bath. The osteotomy was cleared of debris and moisture to prevent artifacts on the pressure film. Screws were used in groups of five. When burring of the screwdriver seat was noted in one screw, all screws were replaced, resulting in a total of 25 screws being used.

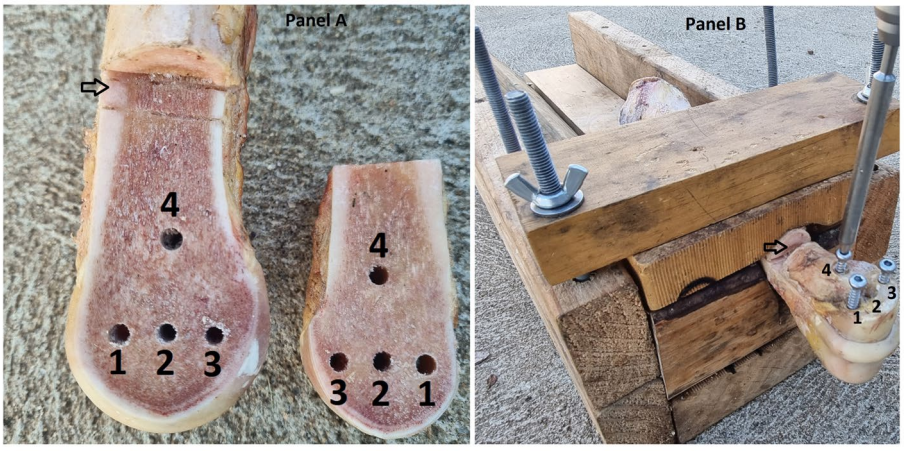

FIGURE 2
(A) Photograph of a left forelimb prepared with the opposing Cis and Trans osteotomy surfaces visible. The holes are numbered 1 = dorsal, 2 = central, 3 = plantar and 4 = proximal screw holes. The proximal osteotomy is indicated by an arrow. **(B)** The same sample with screws in holes 1, 3 and 4 for a triangular repair configuration. The image is labelled as for panel (A).

2.5. Alternate screw tightening

Alternate tightening of 60 mm long, 4.5 mm cortical screws was performed for L, T, LW repairs. The order of screw insertion was dorsal (hole 1), palmar/plantar (hole 3) and proximal (hole 4) for T repairs. For L and LW repairs, the distocentral screw (hole 2) was placed prior to the proximal screw (hole 4; Figure 2). Each screw was tightened, by the primary author, until the screw head contacted the cortical bone or washer before moving on to the next screw. Subsequently, each screw was tightened to 4 Nm with the aid of a surgical screwdriver and quick-release torque limiter (511.771 Synthes, Raynham, MA, U.S.).

2.6. Sequential screw tightening

Sequential tightening of 60 mm long, 4.5 mm cortex screws was employed for TD1 repairs. The dorsal screw (hole 1) was tightened to 4 Nm, before the palmar/plantar (hole 3) and then, proximal (hole 4) screws were tightened to 4 Nm (Figure 2).

2.7. Interfragmentary compression measurement

To measure interfragmentary contact area and pressure, Prescale® pressure-sensitive film (Fuji Photo Film Co., Ltd., Japan) was used. The low-pressure (LLW) Prescale® film was determined through a preliminary experiment, as the most suitable option. The LLW film is 0.2 mm thick and can measure pressures ranging from 2.5 to 10 MPa. The pressure film is not validated for contact pressures of between 0 and <2.5 Mpa or of >10 and ≤12.5 MPa. All contact occurring at pressures of ≤12.5 MPA are recorded as 12.5 MPa. The pressure film consists of two layers labelled "A" and "C." The "A" layer contains microcapsules that rupture at a specific threshold pressure, resulting in red areas following a reaction with the developer solution in the "C" layer. The color density changes according to the pressure exerted.

To prepare the Prescale® film for the experiment, the "A" and "C" layers were cut into 45 mm x 65 mm pieces and punched with holes, corresponding to the screw hole pattern, using a 6 mm paper hole punch. A paper template was used to transfer the hole pattern from each sample, and the lustrous surfaces of each film layer were placed in opposition to prevent any artefactual color leaching during the hole punching process. After punching four holes in each film, the film was correctly opposed and stapled together at a corner.

The pressure film layers were then positioned in the osteotomy, inside two sheets of paper towel, and the initial repair configuration was placed before tracing the outer edge of the cis fragment using a pencil (Figure 3). Temperature and relative humidity readings were recorded, and screws were left in place for 2 min to measure static pressure, ensuring compliance with the recommended parameters outlined in the pre-scale manual. After screw removal, the pressure film was separated, and the "C" film was retained for analysis. This process was repeated for each repair technique, and any pressure film showing signs of moisture leaching or where screws stripped thread holes before reaching 4 Nm torque, were discarded. If a screw stripped before two prints were obtained from that limb, the limb was discarded and any data concerning that limb was removed from the study. All contact pressures of >10 MPa were grouped together, in accordance with the recommended threshold specifications of the pressure sensitive film.

FIGURE 3
Picture of Linear configuration during simulated fracture repair, the paper towel is placed either side of the pressure sensitive film to prevent moisture artifacts.

2.8. Study design revision

Following implementation of the repair selection method in the first 16 limbs, four limbs were discarded for stripping of a thread hole, before two prints were obtained from that limb. Of the 12 limbs that remained in the study, it was possible to apply all four treatments in only four limbs, leaving a success rate of 4/16 limbs. After the high degree of sample dropout was encountered the repair selection process was revised. For the remaining 12 limbs, the L/T repair was randomly applied first, before moving to the LW/TD1 repairs. The order within each pair was determined by sequential digital coin toss (Random.org) (18).

2.9. Image processing

The "C" film prints were trimmed along the pencil outline of the cis fragment. If minor variation occurred between samples following trimming, the largest of the prints was traced and recorded as the measured area, to ensure consistent size for the same sample. The samples were scanned with the recommended scanner and saved at a resolution of 96 Dots Per Inch (DPI) as JPEG images, before analysis with the provided software (Fujifilm Fuji FPD-8010E, Fuji Photo Film Co.). The software analyses the color density of each pixel which is calibrated based on the pressure threshold of the microcapsules in the

pressure sensitive film. The results for total pressure area were categorized based on their values falling within the ranges of ≥2.5 MPA to ≤10 MPa, >2.5 MPa and > 10 MPa. Within the measurement threshold of the pressure sensitive film, further subcategories were created based on pressure values ranging from 2.5–3 MPa, 3–4 MPa, 4–5 MPa, 5–6Mpa, 6–7 MPa, 7–8 MPa, 8–9 MPa, and 9–10Mpa. All values of ≥10 MPa were grouped together and any values below 2.5 MPa were excluded from the final analyses because of the potential for artifacts caused by manipulation at low pressure readings (Figure 4).

2.10. Additional information

Prior to creation of the osteotomy fracture model, measurements of medial and lateral condylar width and diameter across the epicondylar fossa were obtained using a pair of Vernier calipers (ACCUD 300 mm IP67 Dual Scale Digital Vernier Caliper AC-112-012-12; Table 1).

2.11. Statistical analysis

Data were collected and imported into Microsoft Office Excel for further analysis. Descriptive and exploratory statistical analyses were performed using R software (19). To examine the interrelationships among the variables, Bayesian Network (BN) analysis was employed. The BN model was developed using the Netica software package (20). The descriptive data analysis aimed to provide a numerical summary of the sample data, while the BN model sought to quantify the impacts of the investigated influential factors through a what-if analysis. The results are expected to offer objective and quantitative assessment of the evidence supporting the establishment of generalizable research findings. It should be noted that the abbreviation s.d. is used to denote standard deviation. For the development of a BN model, it was technically necessary to discretize the continuous response variable data, a task that was automatically performed in Netica by dividing the range of the sample data into the most suitable intervals or categories. A BN model serves as a graphical representation of the joint probability distribution of all the variables included in the model. Nodes in the model represent the variables and are connected based on probabilistic dependencies (21). The BN approach is rooted in the mathematical formula of Bayes' Theorem, which provides the theoretical foundation for this methodology. The formula is presented as Eq. 1 below (22).

$$\Pr(B|A) = \Pr(A|B)\Pr(B)\Pr(A) = \Pr(A,B)\Pr(A) \quad (1)$$

Where A and B represent random variables, Pr*(A)* and Pr*(B)* denote the marginal probability distributions of A and B, respectively, Pr(B|A) represents the conditional probability distribution of B given A, Pr(A|B) represents the conditional probability of A given B, and Pr(A, B) is the joint probability distribution for A and B. Given that a BN model represents the joint probability of the variables, it allows for inferential analysis by fixing the values of a selected set of variables and predicting or estimating the values of the remaining variables in the model (23). Furthermore, the BN model offers several additional advantages, such as generating estimates and credible intervals for derived parameters or predicted variables. Moreover, it allows for the quantification of support in favor of the null hypothesis, not just against it (24).

A BN model consists of two components: qualitative and quantitative. The qualitative component specifies the network structure by connecting all variables/nodes in the model, while the quantitative component determines the conditional probability tables that quantify the strengths of dependence relations using probability theory (21, 23, 25). In this study, the BN model was developed by determining the optimal model structure using the Tree Augmented Naïve-Bayes-Net (TAN) algorithm, and the model parameters were estimated using the Expectation–Maximization (EM) algorithm in Netica (23). The prediction performance of the resulting BN model was evaluated and compared with the sample data set using Netica's "Testing a Net Using Cases" function. Netica also includes the "Sensitivity to Findings function," which allows ranking of impacts of other variables (referred to as "evidence variables") on a selected target variable (23).

To investigate the most influential variable in determining contact area under pressure, a BN model was constructed by considering the

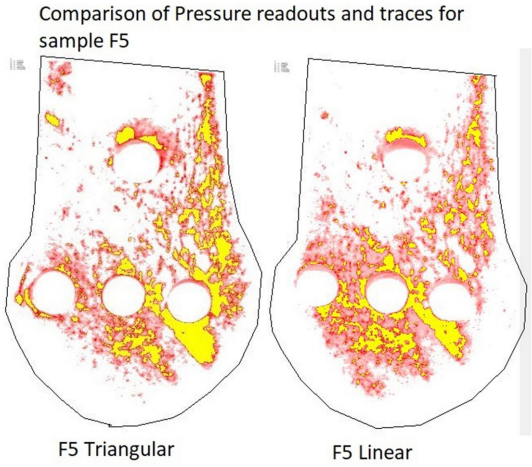

FIGURE 4
Screenshots of the same pressure film sample repaired with a linear and triangular configuration, processed with the Fujifilm software. Red areas correspond to contact area at pressures ≥2.5 MPa < 10 MPa. Yellow areas correspond to contact area at pressures >10 MPa. Pressures <2.5 MPa are below the working range of the pressure film, therefore have been removed.

TABLE 1 Mean measurements of cadaver bones used in experimental investigation.

Limb	Caudal width ± (sd)	Dorsal width ± (sd)	Medial condyle ± (sd)	Lateral condyle ± (sd)	Diameter lateral epicondyle ± (sd)	Diameter medial epicondyle ± (sd)
Front	58.6 mm ± (2.3)	51.5 mm ± (2.1)	29.4 mm ± (1.6)	26.2 mm ± (1.9)	34.1 mm ± (1.6)	35.3 mm ± (3.3)
Hind	59.2 mm ± (2.7)	51.4 mm ± (2.5)	29.7 mm ± (2.9)	27.2 mm ± (2.4)	35.0 mm ± (2.4)	39.2 mm ± (3.0)

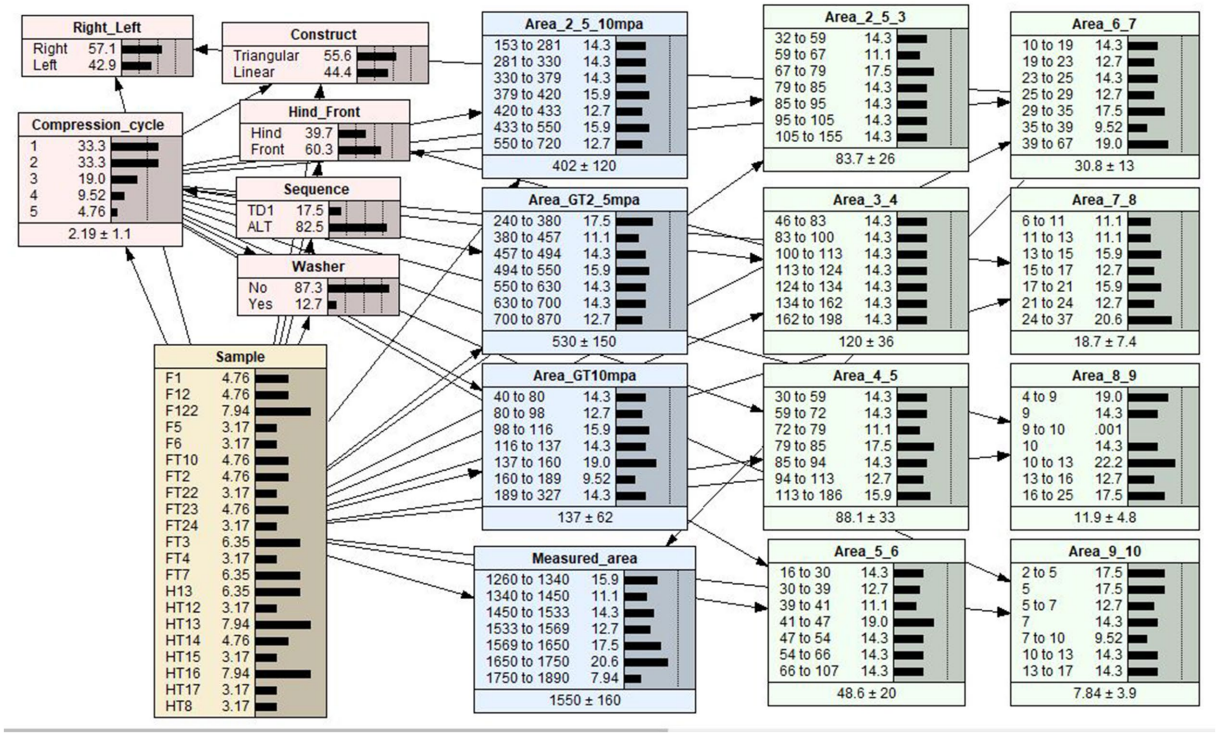

FIGURE 5
A Bayesian network (BN) model of the relationships between effect variables and contact area. Each variable in the BN model is represented by a node. The link between two nodes represents the dependency relationship between two variables. The middle column of each node is a percentage totaling to 100%, which represents the analysis outcomes of each level within a node. The last column is a graphical representation of the percentage values for each level shown as distribution bars. The dotted lines are markers that are equally spaced to aid in visualizing the comparative heights of the distribution bars.

variables Construct (L, T, LW, TD1), Limb (front, hind), Limb (right, left), Compression cycle and Measured area (Cis fragment total area; Figure 5) By selecting different potential variables, the BN model estimated or predicted the mean contact pressure outcomes for L, T, TD1, and LW repairs (Table 2). A table documenting the mean contact areas predicted by the BN model is included as (Supplementary Table 2).

A sensitivity analysis was performed for contact area (the target variable) to quantify the strength of the association between the interrelated variables. Netica inherently includes the *sensitivity to findings* function, allowing for the ranking of impacts of other variables (referred to as "evidence variables") on a selected target variable (23). The outcomes of the sensitivity analysis, for all pressure categories, are presented in Table 3. These sensitivity outcomes represent the strength of association between the evidence variables and the target variable (20). The percentage values obtained from the sensitivity analyses for a selected target variable are broadly analogous to the adjusted R^2, a goodness-of-fit measure used in regression analysis that represents the proportion of the variation explained in the selected variable by fixing the value in one of the evidence variables.

3. Results

3.1. Limbs and repairs

28 limbs obtained from horses of mixed breed underwent fracture simulation and repair. Weight and sex were unknown. Thread holes stripped following the first repair in six limbs and one screw broke through the articular surface during tightening in a further limb. Resulting in a total of Sixty-three repairs (20*L, 24* T, 11*TD1, and 8*LW) performed on 21 (13 front, 8 hind) limbs being included in the analysis. Screw hole stripping occurred most often at the proximal screw hole (18 times), followed by 6 times at the palmar/plantar screw hole and twice each at the central and dorsal screw holes. Average anatomical measurements of the samples included in the final analysis can be found in Table 1. The mean contact area, calculated during descriptive analysis (±s.d.), created at pressures within the operating range of the Prescale® film (≥ 2.5 MPa ≤ 10 MPa) by L, T, TD1 and LW repairs were 406 mm^2 ± (132), 404 mm^2 ± (112), 382 mm^2 ± (119), and 363 mm^2 ± (63) respectively. The mean contact area (±s.d.) created by L, T, TD1 and LW repairs at pressures >10 MPa were 110 mm^2 ± (45), 164 mm^2 ± (67), 144 mm^2 ± (59), and 101 mm^2 ± (23) respectively (Table 2). Median contact areas were greater for T repairs when compared to L repairs at pressures ≥2.5 MPa ≤ 10 MPa and >10 MPa. Median contact areas were greater for L than LW repairs at pressures ≥2.5 MPa ≤ 10 MPa, however at pressures >10 MPa median contact area of LW repairs was greater than L repairs. The median contact areas for T repairs were greater than TD1 repairs at pressures in the >10 MPa category, however at pressures ≥2.5 MPa ≤ 10 MPa the median contact area of TD1 repairs was larger than T repairs (Figures 6, 7). A complete breakdown of mean and median contact areas, calculated during descriptive analysis is available in the (Supplementary Table 1).

10.3389/fvets.2023.1233921

TABLE 2 Mean contact area at all pressures above the minimum working threshold of the pressure sensitive film.

Treatment	Contact area ≥2.5 Mpa ≤10 MPa (sd.)	Contact area >10 MPa (sd.)	≥2.5 Mpa	≥2.5 Mpa ≤3 Mpa	≥3 Mpa ≤4 Mpa	≥4 Mpa ≤5 Mpa	≥5 Mpa ≤6 Mpa	≥6 Mpa ≤7 Mpa	≥7 Mpa ≤8 Mpa	≥8 Mpa ≤9 Mpa	≥9 Mpa ≤10 Mpa
Linear (L)	403 mm^2 ± (140)	112 mm^2 ± (48)	517 mm^2 ± (152)	86 mm^2 ± (26)	86 mm^2 ± (26)	87 mm^2 ± (33)	46 mm^2 ± (19)	28 mm^2 ± (12)	17 mm^2 ± (7)	11 mm^2 ± (4)	7 mm^2 ± (4)
Triangular (T)	411 mm^2 ± (120)	167 mm^2 ± (70)	573 mm^2 ± (156)	80 mm^2 ± (24)	119 mm^2 ± (34)	87 mm^2 ± (25)	49 mm^2 ± (15)	32 mm^2 ± (10)	20 mm^2 ± (7)	13 mm^2 ± (5)	9 mm^2 ± (4)
Linear + washer (LW)	366 mm^2 ± (70)	100 mm^2 ± (27)	465 mm^2 ± (64)	81 mm^2 ± (18)	86 mm^2 ± (26)	77 mm^2 ± (14)	41 mm^2 ± (9)	25 mm^2 ± (5)	14 mm^2 ± (3)	10 mm^2 ± (2)	5 mm^2 ± (1)
Triangular, sequential tightening (TD1)	403 mm^2 ± (120)	142 mm^2 ± (50)	526 mm^2 ± (150)	79 mm^2 ± (23)	113 mm^2 ± (36)	80 mm^2 ± (26)	45 mm^2 ± (16)	28 mm^2 ± (11)	17 mm^2 ± (7)	12 mm^2 ± (5)	8 mm^2 ± (3)

Contact areas were calculated fixing the relevant nodes in the BN model. For example in the linear repair investigation. The Construct, sequence and washer nodes were fixed as Linear, Sequential, and No, respectively.

3.2. Bayesian network model

The goodness-of-fit of the BN model was evaluated using the built-in Netica function *Test with Cases*. The assessment focused on the target variable of contact area in the ≥2.5 Mpa ≤ 10, >10 MPa pressure categories. The model exhibited an error rate of 0% for the ≥2.5 Mpa ≤ 10 and >10 MPa categories.

The sensitivity analysis outlined in Table 3, show that measured area had the strongest model predicted relationship (sensitivity finding of 30.6%) with mean contact area in the ≥2.5 Mpa ≤ 10 Mpa pressure category whereas limb (right or left) had the strongest predicted relationship (sensitivity finding of 23.36%) in the >10 MPa pressure category. The BN model predicted that T repairs resulted in the largest mean contact area in the ≥2.5 Mpa ≤ 10 Mpa and >10 MPa pressure categories. The sensitivity analysis indicated that repair configuration had a weak influence (0.414%) in the ≥2.5 Mpa ≤ 10 Mpa category and a moderate influence (16.3%) in the >10 MPa pressure category on mean interfragmentary contact area. In the ≥2.5 Mpa ≤ 10 Mpa and >10 MPa pressure categories the addition of a washer to a linear configuration explains 1.18and 5.03% of the difference in mean interfragmentary contact area, respectively. The sensitivity analysis indicated that less than 1% of the variation in mean interfragmentary contact area can be attributed to the TD1 repair configuration, indicating a weak influence of sequential tightening on mean interfragmentary compression. The sensitivity analysis indicated repeated use of the same sample (compression cycle) and whether the sample tested was a hind or forelimb had a weak effect on contact area produced (Table 3).

4. Discussion

In this study, the investigation focused on interfragmentary compression achieved by various constructs in the repair of simulated lateral condylar fractures. The BN model showed that T repairs produced a greater mean contact area compared to L repairs. This difference was greatest at pressures greater than10 MPa. Sensitivity analysis indicated that 16.1% of the variation in contact area was attributed to the construct at pressures >10Mpa. The effect of construct on interfragmentary compression in this pressure range is considered moderate. In comparison, 0.414% of the variation in contact area at pressures ≥2.5 Mpa ≤ 10 Mpa could be attributed to the construct. These findings suggest that triangular constructs create larger contact areas at higher pressures compared to linear constructs.

The sensitivity analysis findings presented in Table 3, indicated that the measured area exhibited the highest sensitivity index (30.6%) at pressures between 2.5 and 10 Mpa. This result was expected as the larger surface areas of fragments provide a greater overall area to exert pressure. Additionally, the reduced impact of the measured surface area (sensitivity finding of 12.8%) in the greater than 10 Mpa category aligns with the fact that lag screws have the greatest effect adjacent to the screw (5). Variation in bone size is an obvious contributor to the variation in measured area. However, as the bones were noted to be of similar size (Table 1), the variation in measured area is likely further influenced by the orientation and location of the osteotomy cut. Despite efforts to avoid variation in osteotomy location, because of the tapered anatomy of the condyle, even slight variation in the osteotomy location can result in an appreciable difference in surface area between

TABLE 3 Bayesian network sensitivity findings indicating the effect each variable had on the contact area at respective pressure intervals.

Node	Sensitivity findings (reduction of variance) of the BN model in percent (%). In each pressure category for the respective variable. Percentages given to three significant figures.										
	≥ 2.5 Mpa ≤10 Mpa	>10 Mpa	≥ 2.5 Mpa	≥ 2.5 Mpa ≤3 Mpa	≥ 3 Mpa ≤4Mpa	≥ 4 Mpa ≤5 Mpa	≥ 5 Mpa ≤6 Mpa	≥ 6 Mpa ≤7 Mpa	≥ 7 Mpa ≤8 Mpa	≥ 8 Mpa ≤9 Mpa	≥ 9 Mpa ≤10 Mpa
Limb (right/ left)	5.79	23.3	14.7	0.623	2.13	7.54	7.8	10.2	12.2	8.52	14.9
Construct (T,L)	0.414	16.3	6.97	1.56	0.00518	0.019	3.37	4.11	5.81	9.42	9.06
Measured Area	30.6	12.8	19.1	30.4	29	28.4	20.6	22.1	18.1	18.9	22.5
Washer	1.18	5.03	4.02	0.0171	0.704	1.43	1.38	1.96	4.51	3.01	7.13
Limb (hind/ front)	2.38	2.98	0.386	6.43	2.91	0.998	1.22	0.386	0.65	0.63	0.766
Compression cycle	2.84	2.04	3.49	4.69	3.22	3.65	3.11	3.64	1.57	2.71	0.717
Sequence (Alternate/ TD1)	0.00172	0.133	0.519	0.000657	0.342	0.354	0.0776	0.268	0.017	2.02	0.00645

Sensitivity findings are the percentage reduction of variance. Data is displayed to three significant figures. Shaded area represents the most influential node in each category. Each node corresponds with the nodes of the BN model (Figure 7).

10.3389/fvets.2023.1233921

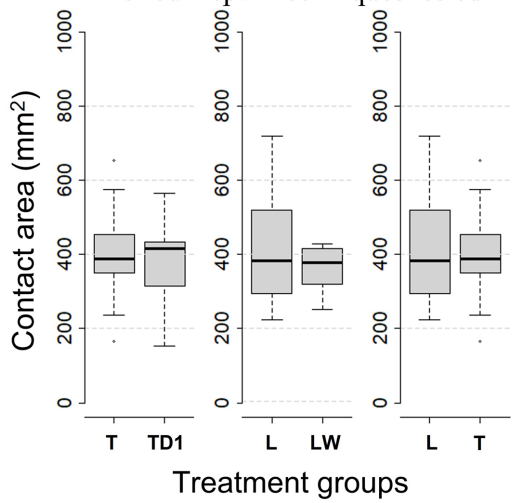

FIGURE 6
Paired Box-whisker plots comparing contact area for pressures of ≥2.5 MPa < 10 MPa between each repair configuration, calculated during descriptive analysis. Box-whisker plots compare the distributions of sample data. Namely, comprehensive comparisons can be made in terms of medians (the bold horizontal bars), the boxes (the middle 50% data points), the minima and maxima, and the extreme cases (outliers) that exceed the 1.5 inter-quartile range (the range of the box).

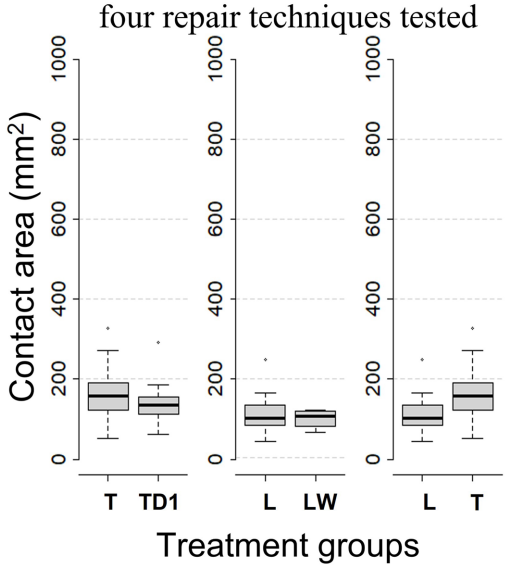

FIGURE 7
Box-whisker plots, calculated during descriptive analysis, comparing mean contact area between repair configurations for pressure > 10Mpa.

samples. The limb (right or left) exhibited the highest sensitivity index at pressures greater than 10 Mpa, which can also be attributed to variation in the measured area.

Interfragmentary compression is an essential element of lag screw fixation, relying on interfragmentary friction to maintain stability across a fracture (5, 26). The results of this study indicate that a T repair creates greater interfragmentary compression than a L repair at higher pressures. Greater interfragmentary compression, as demonstrated in T repairs, may contribute to a more stable repair. Although, interfragmentary compression resulting from linear or triangular repairs of the proximal phalanx has not been assessed, increased interfragmentary compression may contribute to the advantages of T repair over L repair, as observed in a previous experimental model investigating proximal P1 repairs (14). Unlike this study, the aforementioned study assessed triangular and linear repair in maintaining fracture stability in loaded limbs (14). *In vivo*, torque placed on the limb has a greater effect on fracture stability than the force placed perpendicular to the bone's long axis (27). As compression achieved by placement of a lag screw effects only a small region of adjacent bone, the cumulative interfragmentary friction created by an additional screw in T repairs may contribute to their advantages over L repairs under load (5, 14).

In this investigation, the use of a washer was found to reduce the overall mean interfragmentary contact area at pressures of ≥2.5 Mpa ≤ 10 Mpa and >10 Mpa when comparing linear constructs with and without washers. However, the sensitivity analysis indicated that the influence of using a washer on contact area was minor, with findings of 1.08 and 5.11% for the respective ≥2.5 Mpa ≤ 10 Mpa and >10 Mpa pressure categories. Previous studies have suggested that washers can improve interfragmentary compression by reducing screw intrusion into the cortical bone, allowing for greater screw torque before intrusion occurs (28). However, in this investigation, the torque applied to each construct was uniform, and therefore the advantage of using a washer was not apparent. It has been suggested that a larger screw head may result in greater stability compared to a standard 8 mm lag screw head, even without an increase in measurable interfragmentary compression (12). The size of the washer used in this study was the same diameter as the modified screw head (10 mm) used in that previous study. However, it is important to note that the use of a washer cannot be directly compared to the use of a larger screw head since the washer reduces friction between the screw head and the cortical bone interface, while a larger screw head increases friction at this location (12). This study indicates that that addition of a washer does not improve interfragmentary compression, without increased screw torque.

Results of this investigation showed that triangular repairs tightened alternately (T), on average, created greater contact area than sequentially tightened triangular repairs (TD1). However, the sensitivity analysis indicated that tightening sequence has a very weak influence on interfragmentary compression. These results, do not align with reports suggesting that alternate tightening of two lag-screws can reduce fracture displacement during fixation and distribute even compression across the fracture surface (16). When considering engineering applications, uneven tightening of bolted joints can result in bolt cross-talk, where tightening one bolt decreases the preload in another previously tightened bolt (29). The similarity between T and TD1 contact area prints, suggests that tightening the initial screw, did not prevent the second screw from producing comparable contact pressure to those constructs where alternate

tightening was employed. It should be noted that the measurement technique used in this investigation assessed peak pressure, so it is possible that changes in pressure around the initial screw occurred during the tightening process but were not observed. In practice, despite no marked advantages with regards to interfragmentary compression, alternate tightening may allow for even fracture gap reduction (16).

In this study, a screw insertion torque of 4 Nm was used. But, the optimum lag screw insertion torque is not known (12). It should be noted that 4 Nm is less than the perceived maximum torque employed by experienced equine surgeons, as demonstrated in previous research (12). Countersinking was not performed at any of the screw insertion sites in this study, due to spatial limitations within the epicondylar fossa. Opinions on the clinical use of countersinking in the distal-most screw placement differ among surgeons. Some advocate for countersinking in this location, while others argue that the concave structure of the epicondyle allows for satisfactory apposition of the screw head, and countersinking may result in damage to the collateral ligament. Unlike in areas of thin cortical bone such as the proximal phalanx, countersinking contributing to cortical bone failure beneath the screw head is unlikely to occur in the dense bone of the epicondyle (2, 30). In general countersinking improves contact at the screw bone interface and improves interfragmentary compression (2). It is important to emphasize that the primary aim of this investigation was to compare the effect of various treatments on interfragmentary compression, rather than assessing maximum interfragmentary compression. The choice of 4 Nm was based on its frequent use in research and the availability of a recognized orthopedic torque limiter for this value (12). The consistent screw torque placed and the absence of countersinking on all screws allowed an accurate comparison between construct configurations. Investigating the interfragmentary compression achieved by maximal perceived torque and with the use of countersinking, are an obvious target for future investigations.

Various locations have been suggested as the optimal position for the distal screw when repairing condylar fractures. Some authors have recommended placing the distal screw at the level of the epicondylar tubercle to prevent collateral ligament damage, while others proposed placing the screws as close to the articular surface as possible (11). Currently, the recommended location for screw placement is at the center of the epicondylar fossa (10, 26). From a general orthopedic perspective, there is no recommended minimum distance between a screw and the edge of a bone or joint surface. However, in industrial applications, it is recommended to place a lag screw no closer than 1.25 times the screw's diameter to the edge of the material being fastened (31). In orthopedic applications, neighboring screws should be placed no closer than twice the diameter of the screw being used and remain at least one diameter of the screw from a fracture line (32). The epicondylar fossa permits little room for variation in screw placement (2) making triangular repair more difficult when compared to linear repair. In this investigation screws were placed 10 mm from the dorsal and palmar/plantar articular surfaces of the condyle. However, even with the use of an aiming device and the luxury of placing screws in the absence of soft tissue, one screw broke into the articular surface. Placing screws closer than 11.9 (±3.9 mm) to the articular surface of the fetlock joint during condylar fracture repair can result in a reduced rate of successful return to racing (11, 33, 34). In contrast, when repairing fractures of the proximal phalanx, it is recommended to place screws between 5 and 8 mm from the distal extent of the sagittal groove. To date, reduced success rates and complications arising from close placement of implants to the articular surface of the proximal phalanx have not been reported (35). Spatial limitations dictate that meticulous planning, and the use of intraoperative imaging should be considered essential if placing parallel screws in the distal aspect of the third metacarpal or metatarsal bone and the possible negative effects of placing screws closer than 10 mm to the joint surface should be considered.

The cadaver samples used in this investigation were sourced from mixed breed horses euthanized for reasons unrelated to the study. The weight, breed, and sex of the horses used in this study were not available, but the measurements presented in Table 1, indicate that the bones were similar in size. Although a large proportion of the study population was likely to be racehorses, the lack of information regarding cadaver samples should be accounted for when considering generalization of the results of this study.

To ensure bicortical engagement, 60 mm screws were selected for this investigation. The tapered anatomy of the condyle, documented by the anatomical measurements in Table 1, dictates different screw lengths are required for parallel screw placement. A longer palmar/plantar screw will be necessary when compared to the dorsal screw, whereas the dorsal screw length approximates the screw length required in centrally placed distal screws of linear repairs.

The initial study design was deemed unrealistic because of the significant loss of samples caused by thread hole stripping. Thread hole stripping predominantly occurred at the proximal screw hole (hole 4), which was utilized for all constructs. Moreover, the cortical bone at this location is thinner and has a lower density compared to the corresponding bone within the epicondyle region (2, 36). To achieve the cleanest possible cut, following a trial-and-error approach, a table saw was employed in frozen bones. To mitigate the impact of surgical technique on fracture reduction and subsequent interfragmentary compression, holes were drilled prior to creating the osteotomy. Consequently, the bones had to be thawed for drilling, before being re-frozen for the osteotomy. The osteotomy procedure could be performed swiftly, and all bones were returned to the freezer before any noticeable thawing occurred. Despite wrapping the bones in moist towels, thawing in small groups, and keeping the bones moist while handling and drilling, the repeated freeze–thaw process may have contributed to the high occurrences of thread hole stripping. However, it must be noted that it was possible to place at least four repairs in six of twenty-one cadaver specimens. Ideally, drilling holes in fresh samples before freezing them in preparation for the osteotomy and fixation would have eliminated the need for multiple thaws. However, logistical constraints meant this approach was not feasible. Nonetheless, the tendency for thread holes to strip at the proximal screw hole underscores the crucial role of precise surgical technique to avoid unnecessary repetition. It must be acknowledged that changes to the bone were likely to occur as a result of the repeated use of the same sample. However, repetition fatigue through use of the same sample was shown to have only a weak influence on the interfragmentary contact area, as shown by the sensitivity findings of the BN model (Table 3).

In this study, Screws were used, until burring of the screw-driver seat was noted. This resulted in screws being used an

inconsistent number of times. Clinically, it is not recommended to reuse screws. The effect of repeated tightening of screws through the bone samples on interfragmentary compression was considered weak, however the effect of multiple uses of each screw was not analyzed. The inconsistency in screw cycle usage should be taken into account when considering the results of this study. The repeated use of screws may have contributed to the high rate of thread hole stripping noted in this study. However, as each screw was tightened to a consistent torque the interfragmentary compression is relative for each repair and the results of this study should be considered valid.

In the present study, interfragmentary compression was evaluated using Prescale® film, a pressure measurement system that has been employed in various veterinary orthopedic investigations (37, 38). Prescale® film was chosen for its flexibility, thinness, and capacity to be cut into different shapes (39). The Low pressure (LLW) pressure film utilized in this study operates in the range of 2.5–10 MPa. When comparing each construct, we considered the area pressed, as it provided the most precise measurement that enabled comparisons in this scenario. Load was unable to be calculated in this investigation, because, once force surpassed the upper threshold of the pressure-sensitive film (10 MPa), the accuracy of the film diminished, and all values above 12.5 MPa were recorded as 12.75 MPa (40). Grouping all pressures above 12.75 MPa prevented the precise calculation and comparison of load between constructs. Based on the results of this study, we determined that a single Prescale® film that can assess all pressures exerted across the osteotomy during fixation is not available. Using a dynamic digital film pressure measurement system would have allowed for the evaluation of the entire range of contact pressures and facilitated the assessment of any dynamic reduction in preload during the sequential tightening experiment. However, the digital sensor technology is expensive, and punching holes in the digital film sensor can be challenging and cause sensor damage (41). The cost of the digital pressure mapping system was beyond the financial capacity of this investigation.

5. Conclusion

This investigation assessed the interrelationships between several different fixation techniques and interfragmentary compression, when repairing simulated lateral condylar fractures. Moderate evidence was found to suggest that triangular repairs result in greater interfragmentary compression when compared to linear repairs. Employing a sequential tightening sequence and the addition of a washer resulted in reduced mean interfragmentary compression when compared to alternate screw tightening and a linear repair without a washer, respectively. However, the impact of these factors can be considered weak. The greater interfragmentary compression provided by triangular repairs, may provide greater stability in lateral condylar fracture repair. The increased surgical difficulty and possible impacts of placing screws near the articular surface should be kept in mind when considering the potential clinical advantages of triangular repair. This study provides a valuable piece of evidence towards building a generalized understanding of interfragmentary compression achieved with triangular repair. However, the previously stated study limitations must be considered and further research is required to evaluate the effect of triangular repair in clinical cases.

Data availability statement

The raw data supporting the conclusions of this article will be made available by the authors, without undue reservation.

Ethics statement

The animal study was approved by Animal Care and Ethics Charles Sturt University. The study was conducted in accordance with the local legislation and institutional requirements.

Author contributions

AB designed the study and wrote the first draft of the manuscript. KH and RL contributed to the review of the study design and manuscript and approve the submitted version.

Funding

AB was supported by an Australian Research Training Program Scholarship from Charles Sturt University.

Acknowledgments

The authors thank Gang Xie for his assistance with the development of the Bayesian Network model.

Conflict of interest

The authors declare that the research was conducted in the absence of any commercial or financial relationships that could be construed as a potential conflict of interest.

Publisher's note

Supplementary material

The Supplementary material for this article can be found online at: https://www.frontiersin.org/articles/10.3389/fvets.2023.1233921/full#supplementary-material

References

1. Parkin TDH, Clegg PD, French NP, Proudman CJ, Riggs CM, Singer ER, et al. Risk of fatal distal limb fractures among thoroughbreds involved in the five types of racing in the United Kingdom. *Vet Rec*. (2004) 154:493–4. doi: 10.1136/vr.154.16.493

2. Wright IM, Nixon AJ. Fractures of the condyles of the third metacarpal and metatarsal bones. In: AJ Nixon, editor. *Equine Fracture Repair*. 2nd edn. Hoboken, NJ, USA: John Wiley & Sons, Inc (2019). p. 378–424.

3. Wongchai B. effect of the screw torque level on the interfragmentary strain and the interfragmentary modulus. *Am J Appl Sci*. (2013) 10:853–6. doi: 10.3844/ajassp.2013.853.856

4. Buckley RE, Moran CG, Apivatthakakul T. *Section 1 Ao philosophy and basic principles:1.5 soft-tissue injury: Pathophysiology, evaluation, and classification. Third Edition.* ed. Stuttgart: Georg Thieme Verlag (2018).

5. Buckley RE, Moran CG, Apivatthakakul T. *Taha we. Ao principles of fracture management: Vol. 1: Principles, Vol. 2: Specific fractures*. New York, Germany: Thieme Medical Publishers, Incorporated (2017).

6. Lewis AJ, Sod GA, Burba DJ, Mitchell CF. Compressive forces achieved in simulated equine third metacarpal bone lateral condylar fractures of varying fragment thickness with Acutrak plus screw and 4.5 mm Ao cortical screws. *Vet Surg*. (2010) 39:78–82. doi: 10.1111/j.1532-950X.2009.00612.x

7. Galuppo LD, Stover SM, Jensen DG, Willits NH. A biomechanical comparison of headless tapered variable pitch and Ao cortical bone screws for fixation of a simulated lateral condylar fracture in equine third metacarpal bones. *Vet Surg*. (2001) 30:332–40. doi: 10.1053/jvet.2001.24386

8. Johnson KA, Smith FW. Axial compression generated by cortical and cancellous lag screws in the equine distal phalanx. *Vet J*. (2003) 166:159–63. doi: 10.1016/S1090-0233(03)00041-8

9. Grant WPDPM, Rubin LGDPM, Pupp GRDPM, Vito GDPM, Jacobus DDPM, Jerlin EADPM, et al. Mechanical testing of seven fixation methods for generation of compression across a Midtarsal osteotomy: a comparison of internal and external fixation devices. *J Foot Ankle Surg*. (2007) 46:325–35. doi: 10.1053/j.jfas.2007.05.010

10. Richardson DW, Ortved KF. Chapter 93 - third metacarpal and metatarsal bones In: JA Auer, JA Stick, JM Kümmerle and T Prange, editors. *Equine Surgery*. Fifth edn. St. Louis, Missouri, United States of America: W.B. Saunders (2019). p. 1618–35.

11. Martin GS. Factors associated with racing performance of thoroughbreds undergoing lag screw repair of condylar fractures of the third metacarpal or metatarsal bone. *J Am Vet Med Assoc*. (2000) 217:1870–7. doi: 10.2460/javma.2000.217.1870

12. Constant C, Zderic I, Arens D, Pugliese B, Gehweiler D, Gueorguiev-Rüegg B, et al. Influence of screw head diameter on ex vivo fixation of equine lateral condylar fractures with 5.5mm cortical screws. *Vet Surg*. (2022) 51:576–91. doi: 10.1111/vsu.13797

13. Gueorguiev-Rüegg B, Stoddart M. Ao principles of fracture management In: CG Moran and T Apivatthakakul, editors. *Buckley RE*. Germany: Thieme Medical Publishers, Incorporated (2017). 3–51.

14. Labens R, Khairuddin NH, Murray M, Jermyn K, Ahmad RS. In vitro comparison of linear vs triangular screw configuration to stabilize complete Uniarticular parasagittal fractures of the proximal phalanx in horses. *Vet Surg*. (2019) 48:96–104. doi: 10.1111/vsu.13123

15. Findley JA, O'Neill HD, Bladon BM. Outcome following repair of 63 sagittal fractures of the proximal phalanx in UK thoroughbreds using either a triangular or linear screw configuration. *Equine Vet J*. (2020). doi: 10.1111/evj.13304

16. Nuñez F, Fricker R, Kastelec M, Axelrod T. (2023). Ao Surgery Reference. Available at: https://surgeryreference.aofoundation.org/orthopedic-trauma/adult-trauma/hand-proximal-phalanges/proximal-articular-shearing/lag-screw-fixation#reduction [Accessed April 14, 2023].

17. Nixon AJ, Auer JA, Watkins JP. Principles of fracture fixation. *Equine Fract Repair*. 2nd edn. (2019). p. 127–55.

18. Haahr M. (1998-2018). Random.Org: True Random Number Service: Randomness and Integrity Services Ltd. Available at: https://www.random.org [Accessed November 05, 2022].

19. R Core Team (2022). R: A language and environment for statistical computing (version 4.2.2). R foundation for statistical computing, Vienna, Austria.

20. Norsys Software Corp (2021). Netica 64 Bit (for Windows 7 to 10). 6.09 ed. Vancouver, BC, Canada: Norsys Software Corp p. Computer Software.

21. Kjærulff UB, Madsen AL. *Bayesian networks and influence diagrams: A guide to construction and analysis. 2nd ed. 2013. Ed*. Springer New York: New York, NY (2013).

22. Upton GJG, Cook I. *A dictionary of statistics. 3rd Edn*. ed. Oxford: Oxford University Press (2014).

23. Norsys, Software, Corp (2023). Netica 6.09 Online Help Manual. Available at: https://www.norsys.com/WebHelp/NETICA.html. [Accessed May 9, 2023].

24. Kruschke JK. Bayesian analysis reporting guidelines. *Nat Hum Behav*. (2021) 5:1282–91. doi: 10.1038/s41562-021-01177-7

25. Korb KB, Nicholson AE. *Bayesian artificial intelligence. 2nd* edn. CRC Press (2010).

26. Nixon AJ, Auer JA, Watkins JP. Fractures of the condyles of the third metacarpal and metatarsal bones. In: AJ Nixon, editor. *Equine Fracture Repair. 2nd* edn. Hoboken, NJ, USA: John Wiley & Sons, Inc. (2019). p. 378–424.

27. Ito K, Perren SM. *Section 1 Ao philosophy and basic principles:1.2 biology and biomechanics in bone healing. Third Edition.* ed. Stuttgart: Georg Thieme Verlag (2018).

28. Bishop JA, Behn AW, Castillo TN. The biomechanical significance of washer use with screw fixation. *J Orthop Trauma*. (2014) 28:114–7. doi: 10.1097/BOT.0b013e31829f9805

29. Braithwaite J, Mehmanparast A. Analysis of tightening sequence effects on preload behaviour of offshore wind turbine M72 bolted connections. *Energies (Basel)*. (2019) 12:4406. doi: 10.3390/en12234406

30. Richardson DW. Fractures of the proximal phalanx. *Equine Fract Repair*. (2019):295–319. doi: 10.1002/9781119108757.ch19

31. Council CW (2023). Csa 086 Engineering Design in Wood 2017. Available at: https://cwc.ca/en/how-to-build-with-wood/codes-standards/wood-standards/csa-o86-engineering-design-in-wood/ [Accessed April 14, 2023].

32. Peirone B. (2023). Lag Screw Fixation: AO surgery reference. Available at: https://surgeryreference.aofoundation.org/vet/cat/femoral-shaft/further-reading/lag-screw-fixation?searchurl=%2fsearchresults#screw-insertion [Accessed April 14, 2023].

33. Rick MC, O'Brien TR, Pool RR, Meagher D. Condylar fractures of the third metacarpal bone and third metatarsal bone in 75 horses: radiographic features, treatments, and outcome. *J Am Vet Med Assoc*. (1983) 183:287–96.

34. Bassage LH 2nd , Richardson DW. Longitudinal fractures of the condyles of the third metacarpal and metatarsal bones in racehorses: 224 cases (1986-1995). *J Am Vet Med Assoc*. (1998) 212:1757–64.

35. Richardson DW In: AJ Nixon, editor. *Fractures of the proximal phalanx* (2019). 295–319.

36. Drum MG, Kawcak CE, Norrdin RW, Park RD, McIlwraith CW, Les CM. Comparison of gross and histopathologic findings with quantitative computed tomographic bone density in the distal third metacarpal bone of racehorses. *Vet Radiol Ultrasound*. (2007) 48:518–27. doi: 10.1111/j.1740-8261.2007.00289.x

37. Yuwen P, Sun W, Guo J, Chang W, Wei N, Wang H, et al. Femoral-Tibial contact stresses on fixed rotational femur models. *Front Surgery*. (2022) 9:1016707. doi: 10.3389/fsurg.2022.1016707

38. Yoo Y-H, Lee S-J, Jeong S-W. Effects of quadriceps angle on patellofemoral contact pressure. *J Vet Sci*. (2020) 21:e69–e. doi: 10.4142/JVS.2020.21.E69

39. Tekscan Inc. (2013). Comparison of Interface Pressure Measurement Options Nashville: Endeavor Business Media. Available at: https://ezproxy.csu.edu.au/login?url=https://www.proquest.com/trade-journals/comparison-interface-pressure-measurement-options/docview/1662436517/se-2?accountid=10344https://primo.csu.edu.au/discovery/openurl?institution=61CSU_INST&vid=61CSU_INST:61CSU&aufirst=&aulast=&atitle=Comparison+of+Interface+Pressure+Measurement+Options&title=Comparison+of+Interface+Pressure+Measurement+Options&volume=&date=2013&spage=&issn=00249114 [Accessed November 22, 2017].

40. FUJIFILM. *Operations manual. Fujifilm pressure distribution mapping system for Prescale, Fpd-8010e. 2.7* ed. Japan: Fujifilm (2009).

41. Inc T. (2023). Pressure Mapping, Force Measurement & Tactile Sensors. Available at: https://www.tekscan.com/blog/flexiforce/how-trim-flexiforce-sensor [Accessed April 20, 2023].

frontiers | Frontiers in Veterinary Science

TYPE Original Research
PUBLISHED 20 September 2023
DOI 10.3389/fvets.2023.1250147

OPEN ACCESS

EDITED BY
Alessia Di Giancamillo,
University of Milan, Italy

REVIEWED BY
Zbigniew Adamiak,
Vet Clinic Białystok, Poland
Regina Zavodovskaya,
VDx Veterinary Diagnostics and Preclinical Research Services, United States

*CORRESPONDENCE
Tobias Per Otto Lundin
✉ tobias.lundin@blastjarnan.se

RECEIVED 06 July 2023
ACCEPTED 04 September 2023
PUBLISHED 20 September 2023

CITATION
Lundin TPO, Pujari-Palmer M, Svensson G and Höglund OV (2023) Canine *ex vivo* tarsal arthrodesis: fixation by using a new bone tissue glue.
Front. Vet. Sci. 10:1250147.
doi: 10.3389/fvets.2023.1250147

Canine *ex vivo* tarsal arthrodesis: fixation by using a new bone tissue glue

Tobias Per Otto Lundin[1]*, Michael Pujari-Palmer[2], Gustaf Svensson[1] and Odd Viking Höglund[2]

[1]Department of Surgery, Blå Stjärnans Djursjukhus, Gothenburg, Sweden, [2]Department of Clinical Sciences, Swedish University of Agricultural Sciences, Uppsala, Sweden

Introduction: Arthrodesis, performed as a salvage surgical procedure to treat intractable joint conditions in dogs and cats, is associated with a high incidence of complications intra and postoperative, proving the need for improved and new techniques in arthrodesis surgery. Adding a new resorbable bone glue to the arthrodesis could potentially add fixation strength and lower complications. The objectives of this experimental *ex vivo* biomechanical study were therefore to develop a biomechanical test model of partial tarsal arthrodesis and to determine whether the new resorbable bone glue (phosphoserine modified cement) produced measurable fixation strength in canine calcaneoquartal arthrodesis, without orthopedic implants.

Methods: Four biomechanical test models with a total of 35 canine tarsal joints were used. Soft tissues were dissected to 4 different test models with variable contributions from soft tissues. The calcaneoquartal joint was prepared as *in vivo* arthrodesis and the glue was applied to joint surfaces as a liquid/putty (0.4 cc). After curing for 24 h, a shear force was applied to the joint (1 mm per minute) and the failure strength was recorded.

Results: Calcaneoquartal joints, where all soft tissues had been completely resected and fixated with glue (1–1.5 cm^2 joint surface), withstood 2–5 mm of displacement and an average of 100 ± 58 N/cm^2 of shear force (Model 1). Similar adhesive fixation strengths were obtained in Model 2 and 3 with increasing contributions from soft tissues (80 ± 44 and 63 ± 23 N/cm^2, $p = 0.39$, ANOVA).

Conclusion: The developed biomechanical model was sensitive enough to measure differences in fixation strengths between different glue formulations. The average fixation strength (60–100 N/cm^2) should be strong enough to support short-term load bearing in medium sized canines (20 kg). The developed cadaver biomechanical test model is of potential use for other arthrodesis studies. The new resorbable glue can potentially contribute to stability at arthrodesis surgery, acting as a complement to today's standard fixation, metal implants.

KEYWORDS

arthrodesis, fixation, stability, biomechanical model, glue, adhesive, resorbable

1. Introduction

Arthrodesis of the tarsal joint is a delicate surgery performed as a salvage surgical procedure, used in dogs and cats to treat intractable tarsal conditions. Examples are fractures, ligament ruptures, shearing injuries, osteochondral diseases, infections, malformations, and injuries to the Achilles mechanism (1–6). Arthrodesis is associated with a high incidence of complications (up to 80%)

ranging from minor complications like cast complications, difficult wound closure and dehiscence, limb swelling and gastrocnemius tendinopathy, to major complications like plantar necrosis, infections, implant failure and misplacement, varus/valgus/rotational malunion and delayed or non-union of the arthrodesis (6–9). Pantarsal arthrodesis, fusion of the talocrural, intertarsal and tarsometatarsal joints, have higher incidences of major complications than partial tarsal arthrodesis (ParTA), fusion of the intertarsal and/or tarsometatarsal joints (6).

The high incidence of postoperative complications and intraoperative difficulties, show the need for new and improved techniques that may enable lower complication rates in arthrodesis surgery. An adhesive that facilitates implant placement and joint alignment, and adds strength to the internal fixation, could potentially be a useful complementary clinical tool to reduce the risk of complications. Furthermore, cases where postoperative external coaptation still are deemed necessary may potentially be reduced (2, 6–8, 10, 11).

In this experimental *ex vivo* study a new bone glue was evaluated as a subchondral bone adhesive (12–16). The glue is composed of natural materials that are present in the body, calcium, silicate, and the amino acid phosphoserine. Prior testing *ex vivo* and *in vivo*, has shown that the glue bonds to cortical bone, with an average bond strength of 100–400 N cm^{-2} (14, 16). The glue is resorbable *in vivo* when implanted into cancellous bone, and maintains bonding and fixation strength as it is actively reabsorbed by the body and turned into new bone, without excessive or pathological inflammation (14). The components of the glue can be sterilized by gamma irradiation and will react and function comparably. Depending on the formulation mix, the glue can be tailored to quicker solidification/hardening (30 s) or slower (10 min), with full strength after 2–4 h or 12–24 h, respectively, and with identical bond strength (Data on file). We hypothesized that adding the glue to an arthrodesis of the calcaneoquartal joint would increase the stability intra and postoperatively. This could potentially facilitate alignment, implant placement and reduce complications post operatively.

No similar, non-synthetic, degradable subchondral bone glue is approved for clinical use. Furthermore, there is no already-existing biomechanical test model, where a glue is applied directly at the arthrodesis joint, which can be used to evaluate an adhesive force. The first objective of this study was therefore to develop a cadaver biomechanical test model of canine ParTa, aimed at detecting loading forces during failure of a glue. Our second objective was to use the biomechanical model to determine whether the glue produced measurable, fixation strength (24 h) in an arthrodesis of the calcaneoquartal joint, without additional orthopedic fixation.

2. Methods

2.1. Materials

Canine cadaver hind limbs (left and right), from dogs euthanized for reasons unrelated to this study, showing no macroscopic signs of musculoskeletal diseases, were used. The cadavers were donated by owners via a signed consent form (at the time for the dog's euthanasia). Ethical approval for use of cadavers was obtained from the Uppsala Animal Ethics Committee, 15533-2018, 04682-2020.

The adhesive was prepared from calcium silicate (AB Sigma-Aldrich Sweden, Stockholm, Sweden) and phosphoserine (Flamma SpA, Chignolo D'isola BG, Italy), and mixed with deionized water.

2.2. Sample preparation

Canine hind limbs were stored at −20°C wrapped in plastic bags and thawed (4°C) for 48 h prior to use. On the day of testing the limbs were kept in room temperature until they reached ambient temperature (21–22°C). The limbs were disarticulated at the talocrural joints. The skin was dissected from the calcaneoquartal and tarsometatarsal 4–5 joints. Tarsometatarsal joint 4–5 were completely disarticulated to prevent interference with movement in the calcaneoquartal joint. In arthrodesis of the calcaneoquartal joint *in vivo*, depending on type of injury, varying degrees of soft tissues are intact. To imitate this, the joints were randomly divided into 4 models where soft tissues were partially, or completely dissected.

In Model 1 the proximal intertarsal joints were completely disarticulated. Model 1 represents a "purely shear" test, without contributions from any soft tissues. In Model 2 the lateral collateral, calcaneoquartal, long plantar and calcaneocentral ligaments, tarsal extensor retinaculum and flexor tendons were cut with the joint capsule of the calcaneoquartal joint. In Model 3 the lateral collateral ligament was cut off the calcaneoquartal joint (Figure 1A).

Since both proximal and distal ends were fixated in a test rig for Model 2 and Model 3, the trochlea of the talus was cut off with a band saw to create a level surface, for gripping. For comparison between the biomechanics of intact joints and our models 1–3, a completely intact tarsal joint (no resection of any soft tissue) was tested (Model 4). Then the calcaneoquartal joint was exposed, only by a minimal dorsal approach preserving all medial, lateral and plantar ligaments (Model 4-Glue), to determine whether the presence of intact soft tissues masked the effects of the glue (e.g., load sharing). In all models a high-speed 2–3 mm burr (Medtronic Integrated Power Control EC 300, Medtronic, Fort Worth, Texas), depending on the size of the dog, was used to meticulously remove cartilage from the calcaneoquartal joint surfaces (Figure 1B). Cartilage and bone remnants were flushed away and the diameter of the calcaneus and quartal bone surfaces where measured, tissues were then stored at −20°C until use.

The adhesive was prepared from pre-mixed kits, containing calcium silicate and phosphoserine (70% calcium silicate by molar percentage). Deionized water was added to start the adhesive reaction (0.5 cc per 2 grams of pre-mixed powders), and the adhesive was mixed manually for 30 s, before applying (0.4 cc) as a thick paste to the calcaneoquartal joint (Figure 1C). The joint was manually fixated for 90 s, then placed onto a flat surface to continue curing for 24 h at 21°C. The Model 1 group also included group with a weaker glue formulation (85% calcium silicate by molar percentage, Model 1-Weak), to serve as model validation if the present cadaver test model was sensitive enough to detect differences in glue strength.

In Model 3 the contributions of soft tissue to the failure strength, and to how the tissue dispersed load at and above the failure point of the glue, were evaluated by testing the joint first with glue (Model 3), then without glue (Model 3-without).

2.3. Mechanical testing

After curing for 24 h, the entire joint was loaded into a custom designed test rig, a 1 cm wide impactor was positioned over calcaneus (Model 1) or the quartal bone (Model 2–4), a shear force was applied via the impactor, and the failure strength was recorded from

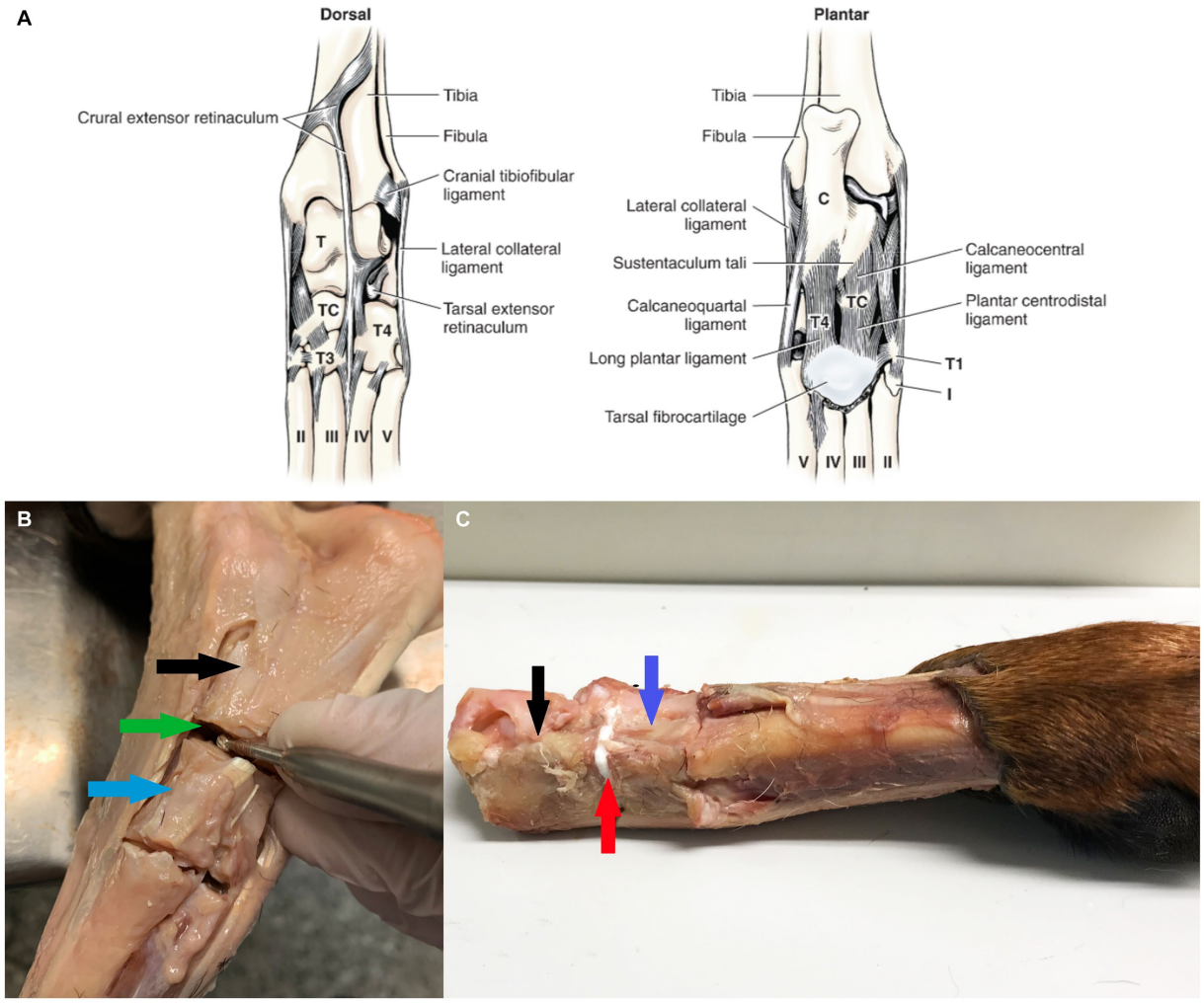

FIGURE 1
Overview of tarsal anatomy and tissue preparation. **(A)** Ligaments of left tarsus (From Evans and de Lahunta (17), with permission). **(B)** The soft tissues surrounding the calcaneal-quartal joint was resected, the joint debrided of cartilage. Black arrow highlights the calcaneus, blue arrow quartal bone and green arrow the calcaneal-quartal joint. **(C)** Glue was applied to the calcaneal-quartal joint, white colored adhesive is visible as bond line, highlighted by red arrow.

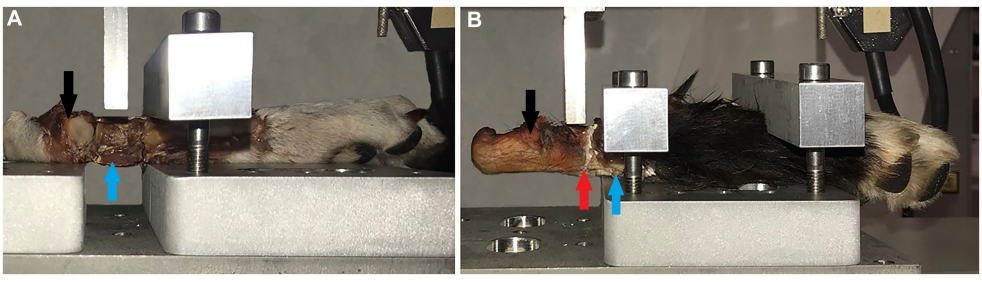

FIGURE 2
Mechanical testing rig and sample positioning. **(A)** The test rigg with a tarsal joint fixated in the test rig for shear testing. The impactor is positioned over the quartal bone (blue arrow), where the shear force was applied (Model 2–4). **(B)** Shows how tissues were prepared and tested for Model 1, with the metal impactor directly over calcaneus (black arrow) and the glued calcaneoquartal joint (red arrow). Backgrounds were edited using Photoshop, for increased visibility to the reader.

force-displacement curves (Figure 2). Data were obtained on an AGS-H, Shimadzu (Shimadzu Europa Gmbh, Duisburg, Germany) mechanical testing machine, using a displacement speed of 1 mm per minute, and a 5kN load cell. Data were analyzed using the manufacturer software, Trapezium-X Lite, version 1.2.0 (Shimadzu Europa).

To investigate if size of bonding surface affected performance of glue (i.e., differences in bond strength between dogs with differing joint size), all mechanical results were normalized to the average surface area of the two joint surfaces that were glued. Surface area was approximated as a square, by multiplying the diameter in the antero-posterior and medio-lateral directions and plotted in a scatter-plot analysis.

2.4. Statistics

The group means were compared using a one-way ANOVA, on JASP statistical software, version 0.16.0.0.

3. Results

In total, 35 tarsal joints where used (model 1 $n=9$ and $n=8$ "weak" glue, model 2 $n=8$, model 3 $n=9$, Model 4 $n=1$).

In Model 1 the average adhesive strength, was 92.3 N/cm^2, for the normal glue formulation (formulation: 70% calcium silicate by molar percentage). In Model 1-Weak with the weaker glue formulation (formulation: 85% calcium silicate by molar percentage), produced an average of 12.0 N/cm^2 peak bond strength.

Using shear models that included more soft tissues, the average bond strength was slightly lower in both Model 2, at 79.7 N/cm^2, and Model 3 with an average bond strength of 63.1 N/cm^2. The difference in average bond strength, between models 1, 2, and 3 was not statistically significant ($p=0.37$, ANOVA).

The force displacement curves of Model 4/Model 4-Glue showed no point of failure, and there was no difference in force displacement curves (Figure 3).

The average bone diameter (surface area) of calcaneus and quartal surfaces was 1.07 ± 0.23 (Model 1), 0.86 ± 0.21 (Model 2), and 1.01 ± 0.20 (Model 3) cm^2. The correlation strength between the size of the animal (average bone diameter, surface area, of calcaneus and quartal surfaces was used as a proxy measure) and the bond strength of the glue, was poor ($R^2<0.20$). While the average bond strength was slightly stronger for larger animals, when normalized by dividing the adhesive strength by the surface area, roughly equivalent bond strengths, per square centimeter, were obtained for both large and small animals (Figure 4).

4. Discussion

In this study we have developed a cadaveric biomechanical test model for calcaneoquartal arthrodesis sensitive enough to detect differences in glue strength and have shown that a new, phosphoserine modified, bone glue adds strength to the arthrodesis, *ex vivo*. This is the first study to evaluate a glue for fusing together subchondral bone surfaces. Our hypothesis that by adding the glue to an arthrodesis of the calcaneoquartal joint could add stability was confirmed.

Arthrodesis involves meticulous removal of articular cartilage, placement of a cancellous bone graft for its osteoconductive, osteoinductive, and osteogenic properties, and a rigid internal or external fixation to achieve osseous fusion (18, 19). Rigid fixation stability is the primary determinant of arthrodesis success, by promoting intramembranous ossification, while poor fixation leads to formation of fibrocartilage and non-union (20–25). In the human metatarsophalangeal joints, movement of the surfaces by 2 mm after arthrodesis is sufficient to interrupt healing, leading to non-union (26, 27). In the present study, joints treated with glue endured a displacement of 2–3 mm before the glue failed. In a clinical setting, the glue may be sufficient to reduce or prevent micro-movements between joint surfaces held together by orthopedic implants. A technology that reduces the risk of implant failures and non-union, especially in canine tarsal and carpal arthrodesis, where not all parts of the joint are fixated by the implant(s) could potentially be of great clinical value.

Another potential technique, not yet investigated, could be to fixate joints in correct alignment with the glue (solidifies in 60–90 s) before placing the implants during arthrodesis, thereby avoiding post malalignments, or misplacement of implants (6).

Historically the use of an external coaptation, usually a cast, to add rigidity and reduce the load of the internal implants has been advocated (8). The effectiveness of coaptation remains however unclear and recent studies suggest the contrary for tarsal and carpal arthrodesis (2, 28). A glue that adds stability to the fixation could even further diminish the need of an external coaptation, after it reached its full strength in 2–24 h depending on the formulation mix of the glue, in cases where it still is deemed necessary (29).

The glue evaluated in this study is a type of biomaterial: a ceramic glue that resorbs and is replaced by bone. The number of case reports evaluating biomaterials for arthrodesis are few and, to our knowledge, thus far there is no ceramic or polymeric biomaterial that can stabilize, fixate, or bond with subchondral bone (30–36). No resorbable material has achieved regulatory approval for use in gluing or fixating subchondral bone and there are no other case reports of an adhesive that can augment, or improve, arthrodesis procedures.

The developed cadaver model was sensitive enough to distinguish between glues with different strengths, and to identify failure of glue in the presence of some soft tissues, similar to the actual clinical conditions of arthrodesis. However, the presence of intact soft tissues contributed to stability and interfered with measurements in intact joints. We conclude, therefore, that biomechanical models of tarsal joint arthrodesis, which use an adhesive to bond or fixate joint surfaces, require removal of at least proximal soft tissues to identify failure of the glue and measure bond strength. The glue appeared to participate in load sharing with nearby soft tissues, similar to what would occur in fused joints *in vivo*.

After curing, the glue in this study resembles a ceramic material. Flaws or defects, such as pores, limit the structural strength of ceramics (37). The likelihood that defects arise during bonding or setting should increase with increases in the size of the bonding surface. Therefore, it was theoretically possible that the failure strength of the reconstructed joints might be correlated with the size of the joint. However, the bond strengths per square centimeter were similar for both small and large dogs.

The glue appeared strong enough to warrant further testing in joint arthrodesis, pending testing in a chronic (cyclical) loading model to account for premature failure due to fatigue. While it was only possible to evaluate the short term, immediate fixation strength (24 h) in the present model, in a recent study we have demonstrated that the

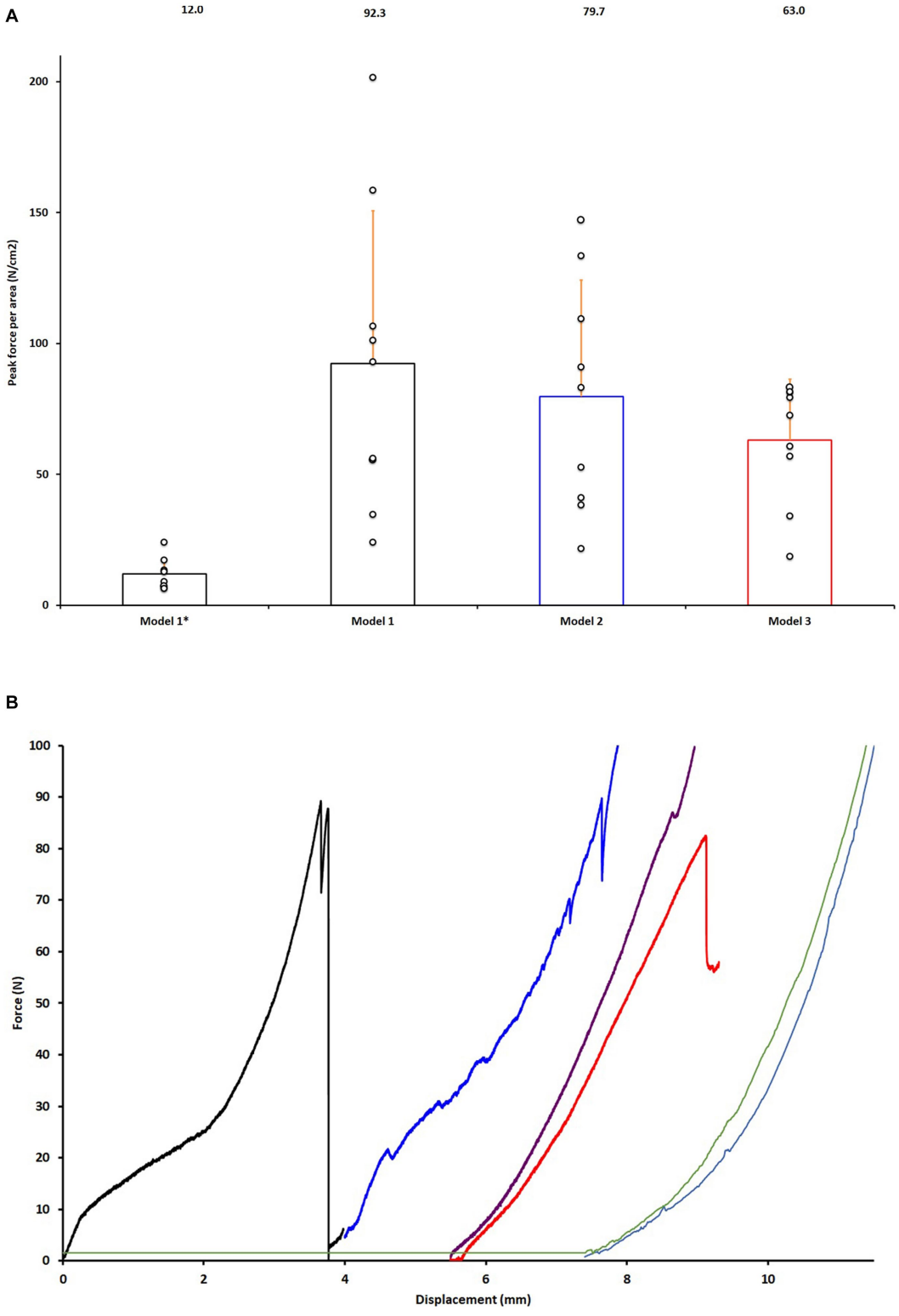

FIGURE 3
Validation and testing of models in glued joints. **(A)** Comparison of adhesive strength of the two glue formulations in Model 1-Weak (Model 1*) and Model 1 for validation of the test model and Model 2–3. Data is normalized to the average size of the two joint surface (force per square centimeter). **(B)** Representative force displacement curves of glued calcaneoquartal joints from data points shown in **(A)**, Model 3-without and Models 4. Black curve representing Model 1, blue curve Model 2, red curve Model 3, purple curve Model 3-without, light blue Model 4 and green Model 4-Glue.

adhesive bonds to live cancellous and cortical bone (*in vivo*) (14) just as strongly as to cadaver bone (13) in rodents and in human bone (38). Therefore, the results of this study are expected to closely predict how the glue will behave in live canines, within 24 h of fixation. However, in this study, rather than using tissue at physiological temperature (37°C), tissues were warmed to ambient temperature (21–22°C) to

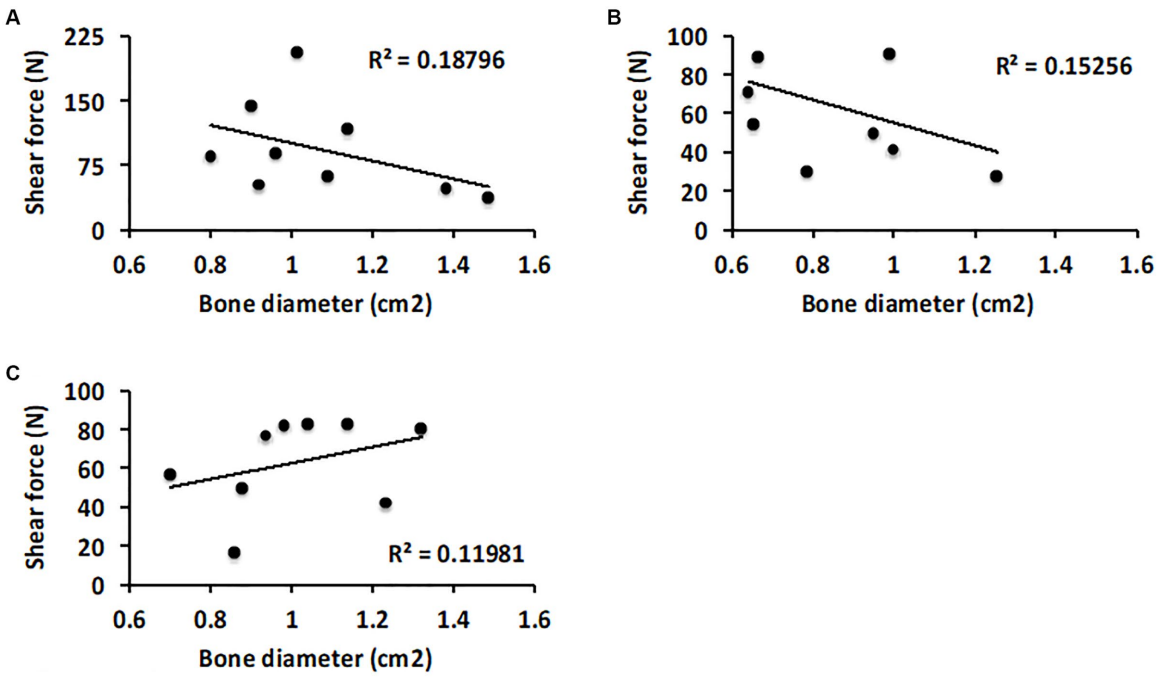

FIGURE 4
Scatter plot analysis of how the size of the tarsal joint surfaces correlate with performance of the glue. **(A)** Comparison of failure strength and average diameter of the calcaneus and quartal bone surfaces in Model 1. **(B)** Model 2 and **(C)** Model 3.

avoid variability. The use of warmed *ex vivo* tissues (37°C) would make the glue performance dependent on confounding variables affecting how quickly the tissues cools down, rather than on how the glue interacted with osteochondral tissue surfaces. Consequently, since the time for curing of the glue, not maximum bond strength, is affected by temperature with colder surfaces slowing the glue reaction, when used *in vivo* the adhesive will react faster and reach maximum strength sooner than in this study.

In laboratory testing, on metals and cortical bone, the average adhesive strength of the glue is typically 400 N/cm^2 (15). This suggests that the joint fusion strength could be increased 2-4-fold (to reach the true strength of the glue) with additional improvements in the handling and fixation technique, or by optimizing the glue to bond with subchondral bone, rather than cortical bone, for future studies.

There were several limitations to the present model and data. First, the present cadaver model represented a compromise, between the need to remove all soft tissues and musculature to achieve a uniaxial loading regimen at a single bone/adhesive interface (e.g., pure shear). There was also a need to reproduce the clinical situation, where the injuries often are more complex, involving several joints and where the surrounding soft tissues and muscle disperse load, thereby preventing an accurate measurement of the biomechanical strength arising only from the bonded joint surfaces. *Ex-vivo* testing also did not consider changes in viscoelasticity between live tissue and cadaver tissue due to decomposition (cadaver), temperature, healing, inflammation, or the presence of fluids that can affect the material properties in live tissue.

Another limitation in the present study was the type of loading forces. A purely shear force was used because this is the most rigorous test for a glue (i.e., most glues are weakest in shear), in addition to being a force that arises during normal locomotion, besides compression, bending and torsion. While tarsal loading has been evaluated in general by using: 1-, 2-, and 3-point bending (26, 39–41); pure torsion (24); compression (42); shear (27) and multi-modal loading using intact (cadaver) ankles (43) there is no clear consensus on which type(s) of loading are sufficient to accurately model forces that arise during locomotion. No other studies have evaluated adhesives for joint fixation, and the magnitude of force(s) that arise during joint movement are poorly characterized in canines. The most comprehensive study thus far in humans, Wang et al. (25) found that the expected peak load in human calcaneocuboidal joints during movement was equivalent to 9% of bodyweight (0.3–0.5 MPa or 40-100 N). Directly translating the results from Wang et al. (25) from human to canine, is impossible due to differences in movement patterns, anatomy, and functional loading angles, between bipeds and quadrupeds. However, a reasonable assumption of loading in canine calcaneoquartal joint is that it would not be greater than in humans. Based upon this assumption the expected peak loading force in a toy breed (weighing 1–3 kg) might be 1–3 N, while a medium sized dog (5–20 kg) might exert up to 20 N on the calcaneoquartal joint during movement. This range of loading forces would be much lower than the measured strength of the glue. Both the joint and surrounding soft tissues disperse load, which may reduce the forces acting upon the joint surfaces, while also complicating analysis of precisely how strong a glue must be to resist displacement/ deformation, and to ensure joint fusion.

Finally, since we evaluated a joint where the surfaces were not visible during testing, failure of the glued joint was confirmed visually when cracks appeared in the bond line. It is possible that smaller, or

partial, failures could have occurred in the glue (e.g., fatigue), when it was subjected to repeated loading. Additional studies are needed to evaluate the fatigue properties of the glue. While not obvious from the data or discussion thus far, the largest challenge in this study was developing a manual fixation method to hold the uneven joint surfaces steady, and avoid disrupting the adhesive while it cured, during the 60–90 s curing/working time. The joint surfaces were not flat, nor perfectly aligned, which is a crucial impediment for any glue, which make the results of this study even more relevant.

5. Conclusion

A cadaver model, of canine calcaneoquartal joint arthrodesis was sensitive enough to measure immediate fixation strength of bone adhesive-type materials. We have also shown that the bone glue produces strong fixation in cadaver tissue with minimal manual fixation time. Finally, the adhesive strength could be sufficient for *in vivo* short-term loading by small and medium breeds (20 kg), supporting future evaluation in live animals.

Author's note

An abstract was presented at the 2022 ACVS Surgery Summit, October 13–15, Portland, Oregon, USA. https://doi.org/10.1111/vsu.13879.

Data availability statement

The original contributions presented in the study are included in the article/supplementary material, further inquiries can be directed to the corresponding author.

Ethics statement

Ethical approval for use of cadavers was obtained from the Uppsala Animal Ethics Committee, 15533-2018, 04682-2020. The cadavers were donated by owners via a signed consent form (at the time for the dog's euthanasia).

Author contributions

TL prepared the specimen, interpreted data and drafted, revised, edited, and completed the manuscript. MP-P prepared specimen, performed and analyzed experiments of mechanical properties, drafted, revised, and edited the manuscript. GS prepared specimen, interpreted data, drafted, revised, and edited the manuscript. OH collected specimen, interpreted data, drafted, revised, and edited the manuscript. All authors contributed to the article and approved the submitted version.

Funding

The study was supported, in part, by the U-Share cross disciplinary grant (SLU 2020.2.5.1-1074). The funding agency did not take part in any experimental planning or analysis.

Acknowledgments

The authors gratefully acknowledge Håkan Engqvist at Uppsala University for generously donating the raw materials for making the adhesive.

Conflict of interest

MP-P declares partial ownership in a company that owns all related intellectual property, GPBio LTD.

The remaining authors declare that the research was conducted in the absence of any commercial or financial relationships that could be construed as a potential conflict of interest.

Publisher's note

References

1. Abrams BE, Wavreille VA, Hettlich BF, Selmic LE. Corrective osteotomy and partial tarsal arthrodesis in two greyhounds with calcaneal malunion. *Vet Surg*. (2020) 49:1600–8. doi: 10.1111/vsu.13517

2. Anesi S, Clarke S, Gemmill T, Oxley B, Pink J, Smith K, et al. Long-term outcomes after pantarsal arthrodesis with medial plate fixation without external coaptation in 30 dogs. *Vet Surg*. (2020) 49:502–11. doi: 10.1111/vsu.13354

3. Franch J, Lafuente P, Diaz-Bertrana MC, Munilla A, Durall I, Pastor J, et al. Management of leishmanial osteolytic lesions in a hypothyroid dog by partial tarsal arthrodesis. *Vet Rec*. (2004) 155:559–62. doi: 10.1136/vr.155.18.559

4. Massimo P, Michela B. Pantarsal arthrodesis to treat a full-thickness lateral trochlear ridge osteochondritis dissecans in a dog. *VCOT Open*. (2019) 2:e27–31. doi: 10.1055/s-0039-1687885

5. Ost PC, Dee JF, Dee LG, Hohn RB. Fractures of the calcaneus in racing greyhounds. *Vet Surg*. (1987) 16:53–9. doi: 10.1111/j.1532-950X.1987.tb00913.x

6. Roch SP, Clements DN, Mitchell RAS, Downes C, Gemmill TJ, Macias C, et al. Complications following tarsal arthrodesis using bone plate fixation in dogs. *J Small Anim Pract*. (2008) 49:117–26. doi: 10.1111/j.1748-5827.2007.00468.x

7. Barnes DC, Knudsen CS, Gosling M, McKee M, Whitelock RG, Arthurs GI, et al. Complications of lateral plate fixation compared with tension band wiring and pin or lag screw fixation for calcaneoquartal arthrodesis. Treatment of proximal intertarsal subluxation occurring secondary to non-traumatic plantar tarsal ligament disruption in dogs. *Vet Comp Orthop Traumatol*. (2013) 26:445–52. doi: 10.3415/VCOT-12-07-0089

8. Klause SE, Piermattei DL, Schwarz PD. Tarso-crural arthrodesis: complications and recommendations. *Vet Comp Orthop Traumatol*. (1989) 2:119–24. doi: 10.1055/s-0038-1633208

9. Choi CJ, Balara JM, Casale SA, Wendelburg KL. Implant removal rate after partial carpal arthrodesis in dogs: a retrospective analysis of 22 cases. *Front Vet Sci*. (2023) 10:10. doi: 10.3389/fvets.2023.1160129

10. Bristow WR. Arthrodesis. *Brit J Surg*. (1928) 15:401–13. doi: 10.1002/bjs.1800155908

11. McKee WM, May C, Macias C, Lapish JP. Pantarsal arthrodesis with a customised medial or lateral bone plate in 13 dogs. *Vet Rec*. (2004) 154:165–70. doi: 10.1136/vr.154.6.165

12. Hulsart-Billström G, Stelzl C, Procter P, Pujari-Palmer M, Insley G, Engqvist H, et al. *In vivo* safety assessment of a bio-inspired bone adhesive. *J Mater Sci-Mater M*. (2020) 31:24. doi: 10.1007/s10856-020-6362-3

13. Procter P, Pujari-Palmer M, Hulsart-Billström G, Wenner D, Insley G, Larsson S, et al. A biomechanical test model for evaluating osseous and osteochondral tissue adhesives. *BMC Biomed Eng*. (2019) 1:11. doi: 10.1186/s42490-019-0011-2

14. Procter PH-BG, Alves A, Pujari-Palmer M, Wenner D, Insley G, Engqvist H, et al. Gluing living bone using a biomimetic bioadhesive: from initial cut to final healing. *Front Bioeng Biotechnol*. (2021) 9:9. doi: 10.3389/fbioe.2021.728042

15. Pujari-Palmer M, Giró R, Procter P, Bojan A, Insley G, Engqvist H. Factors that determine the adhesive strength in a bioinspired bone tissue adhesive. *Chem Eng*. (2020) 4:1–19. doi: 10.3390/chemengineering4010019

16. Pujari-Palmer M, Guo H, Wenner D, Autefage H, Spicer CD, Stevens MM, et al. A novel class of injectable bioceramics that glue tissues and biomaterials. *Materials*. (2018) 11:1–15. doi: 10.3390/ma11122492

17. Evans HE, de Lahunta A. *Miller's anatomy of the dog. 4th* ed. St Louis: Saunders/Elsevier (2013).

18. Ogawa T, Ishii T, Mishima H, Sakai S, Watanabe A, Nishino T, et al. Effectiveness of bone marrow transplantation for revitalizing a severely necrotic small bone: experimental rabbit model. *J Orthop Sci*. (2010) 15:381–8. doi: 10.1007/s00776-010-1459-z

19. Johnson KA, Bellenger CR. Effects of autologous bone grafting on bone healing after carpal arthrodesis in the dog. *Vet Rec*. (1980) 107:126–32. doi: 10.1136/vr.107.6.126

20. Bennett GL, Cameron B, Njus G, Saunders M, Kay DB. Tibiotalocalcaneal arthrodesis: a biomechanical assessment of stability. *Foot Ankle Int*. (2005) 26:530–6. doi: 10.1177/107110070502600706

21. Buda M, Hagemeijer NC, Kink S, Johnson AH, Guss D, DiGiovanni CW. Effect of fixation type and bone graft on tarsometatarsal fusion. *Foot Ankle Int*. (2018) 39:1394–402. doi: 10.1177/1071100718793567

22. Dock CC, Freeman KL, Coetzee JC, McGaver RS, Giveans MR. Outcomes of nitinol compression staples in tarsometatarsal fusion. *Foot Ankle Ortho*. (2020) 5:1–6. doi: 10.1177/2473011420944904

23. Lareau CR, Deren ME, Fantry A, Donahue RMJ, DiGiovanni CW. Does autogenous bone graft work? A logistic regression analysis of data from 159 papers in the foot and ankle literature. *Foot Ankle Surg*. (2015) 21:150–9. doi: 10.1016/j.fas.2015.03.008

24. Riedl M, Glisson RR, Matsumoto T, Hofstaetter SG, Easley ME. Torsional stiffness after subtalar arthrodesis using second generation headless compression screws: biomechanical comparison of 2-screw and 3-screw fixation. *Clin Biomech*. (2017) 45:32–7. doi: 10.1016/j.clinbiomech.2017.04.004

25. Wang Y, Li Z, Wong DW-C, Zhang M. Effects of ankle arthrodesis on biomechanical performance of the entire foot. *PLoS One*. (2015) 10:1–22. doi: 10.1371/journal.pone.0134340

26. Campbell B, Schimoler P, Belagaje S, Miller MC, Conti SF. Weight-bearing recommendations after first metatarsophalangeal joint arthrodesis fixation: a biomechanical comparison. *J Orthop Surg Res*. (2017) 12:23. doi: 10.1186/s13018-017-0525-z

27. Milshteyn MA, Dwyer M, Andrecovich C, Bir C, Needleman RL. Comparison of two fixation methods for arthrodesis of the calcaneocuboid joint: a biomechanical study. *Foot Ankle Int*. (2014) 36:98–102. doi: 10.1177/1071100714552479

28. Bristow PC, Meeson RL, Thorne RM, Butterworth SJ, Rutherford S, Renwick AIC, et al. Clinical comparison of the hybrid dynamic compression plate and the Castless plate for Pancarpal arthrodesis in 219 dogs. *Vet Surg*. (2015) 44:70–7. doi: 10.1111/j.1532-950X.2014.12183.x

29. Meeson RL, Davidson C, Arthurs GI. Soft-tissue injuries associated with cast application for distal limb orthopaedic conditions. *Vet Comp Orthop Traumatol*. (2011) 24:126–31. doi: 10.3415/VCOT-10-03-0033

30. Beuchel MW, Brage M. Bone reconstitution with synthetic bone graft material for osseous defects in revision total ankle arthroplasty. *Foot & Ankle Orthopaedics*. (2016) 1. doi: 10.1177/2473011416S00139

31. Bitterman A, Mathew C, Patel M, Gurtowski JP. Antibiotic spacer arthroplasty for revision MTP arthrodesis: a novel means to build the implant: a case report. *Cureus*. (2016) 8:e537. doi: 10.7759/cureus.537

32. Gonçalves H, Pascal-Moussellard H, Lesoeur J, Schnitzler V, Fellah BH, Wagner NMS, et al. Injection of calcium phosphate apatitic cement/blood composites in intervertebral fusion cages: a simple and efficient alternative to autograft leading to enhanced spine fusion. *Spine*. (2020) 45:E1288–95. doi: 10.1097/BRS.0000000000003598

33. Klos K, Wähnert D, Gueorguiev B, Schwieger K, Hofmann GO, Windolf M, et al. Development of a technique for cement augmentation of nailed tibiotalocalcaneal arthrodesis constructs. *Clin Biomech*. (2010) 25:576–81. doi: 10.1016/j.clinbiomech.2010.03.006

34. Liverneaux P, Khallouk R. Calcium phosphate cement in wrist arthrodesis: three cases. *J Orthop Sci*. (2006) 11:289–93. doi: 10.1007/s00776-006-1008-y

35. O'Donnell SW, Vaughn JJ, Sangeorzan AP, DeFontes KW III, Bluman EM. Surgical strategies: cement spacer for staged first metatarsophalangeal arthrodesis after failed arthroplasty. *Tech Foot Ankle Surg*. (2020) 19:225–9. doi: 10.1097/BTF.0000000000000252

36. Pomeroy G, De Ben S. Ankle arthrodesis with silicate-substituted calcium phosphate bone graft. *Foot Ankle Online J*. (2013) 6:2. doi: 10.3827/faoj.2013.0601.002

37. Pujari-Palmer M, Robo C, Persson C, Procter P, Engqvist H. Influence of cement compressive strength and porosity on augmentation performance in a model of orthopedic screw pull-out. *J Mech Behav Biomed*. (2018) 77:624–33. doi: 10.1016/j.jmbbm.2017.10.016

38. Bojan AJ, Stadelmann VA, Wu D, Pujari-Palmer M, Insley G, Sundh D, et al. A new bone adhesive candidate- does it work in human bone? An *ex-vivo* preclinical evaluation in fresh human osteoporotic femoral head bone. *Injury*. (2022) 53:1858–66. doi: 10.1016/j.injury.2022.04.007

39. Aiyer A, Russell NA, Pelletier MH, Myerson M, Walsh WR. The impact of nitinol staples on the compressive forces, contact area, and mechanical properties in comparison to a claw plate and crossed screws for the first tarsometatarsal arthrodesis. *Foot Ankle Spec*. (2015) 9:232–40. doi: 10.1177/1938640015620655

40. Rodriguez R, Dun S, He JK, McKissack H, Fleisig GS, Jain M, et al. Biomechanical comparison of plantar-to-dorsal and dorsal-to-plantar screw fixation strength for subtalar arthrodesis. *Foot & Ankle Orthopaedics*. (2019) 4. doi: 10.1177/2473011419S00363

41. Wininger FA, Kapatkin AS, Radin A, Shofer FS, Smith GK. Failure mode and bending moment of canine pancarpal arthrodesis constructs stabilized with two different implant systems. *Vet Surg*. (2007) 36:724–8. doi: 10.1111/j.1532-950X.2007.00326.x

42. Jastifer JR, Alrafeek S, Howard P, Gustafson PA, Coughlin MJ. Biomechanical evaluation of strength and stiffness of subtalar joint arthrodesis screw constructs. *Foot Ankle Int*. (2015) 37:419–26. doi: 10.1177/1071100715619680

43. Simons P, Sommerer T, Zderic I, Wahl D, Lenz M, Skulev H, et al. Biomechanical investigation of two plating systems for medial column fusion in foot. *PLoS One*. (2017) 12:e0172563. doi: 10.1371/journal.pone.0172563

frontiers | Frontiers in Veterinary Science

TYPE Original Research
PUBLISHED 25 September 2023
DOI 10.3389/fvets.2023.1183223

OPEN ACCESS

EDITED BY
Remo Lobetti,
Veterinary Specialists Ireland, Ireland

REVIEWED BY
Cord Brundage,
University of Wisconsin–La Crosse, United States
Gareth Edward Zeiler,
University of Pretoria, South Africa

*CORRESPONDENCE
Carla Zamora-Perarnau
✉ carla.zamora@ucv.es

RECEIVED 09 March 2023
ACCEPTED 04 September 2023
PUBLISHED 25 September 2023

CITATION
Zamora-Perarnau C, Malvè M and Fernández-Parra R (2023) Computational fluid dynamics comparison of the upper airway velocity, pressure, and resistance in cats using an endotracheal tube or a supraglottic airway device.
Front. Vet. Sci. 10:1183223.
doi: 10.3389/fvets.2023.1183223

Computational fluid dynamics comparison of the upper airway velocity, pressure, and resistance in cats using an endotracheal tube or a supraglottic airway device

Carla Zamora-Perarnau[1,2,3]*, Mauro Malvè[4,5] and Rocío Fernández-Parra[2,3]

[1]Doctoral School, Catholic University of Valencia San Vicente Mártir, Valencia, Spain, [2]Department of Small Animal Medicine and Surgery, Faculty of Veterinary Medicine, Catholic University of Valencia San Vicente Mártir, Valencia, Spain, [3]Veterinary Referral Hospital UCV, Catholic University of Valencia San Vicente Mártir, Valencia, Spain, [4]Department of Engineering, Public University of Navarre (UPNA), Pamplona, Spain, [5]Biomedical Research Networking Center in Bioengineering, Biomaterials, and Nanomedicine (CIBER-BBN), Madrid, Spain

Intoduction: In veterinary medicine, airway management of cats under general anesthesia is performed with an endotracheal tube (ETT) or supraglottic airway device (SGAD). This study aims to describe the use of computational fluid dynamics (CFD) to assess the velocities, pressures, and resistances of cats with ETT or SGAD.

Methods: A geometrical reconstruction model of the device, trachea, and lobar bronchi was carried out from computed tomography (CT) scans that include the head, neck, and thorax. Twenty CT scans of cats under general anesthesia using ETT ($n = 10$) and SGAD ($n = 10$) were modeled and analyzed. An inspiratory flow of 2.4 L/min was imposed in each model and velocity (m/s), general and regional pressures (cmH_2O) were computed. General resistance (cmH_2O/L/min) was calculated using differential pressure differences between the device inlet and lobar bronchi. Additionally, regional resistances were calculated at the device's connection with the breathing circuit (region A), at the glottis area for the SGAD, and the area of the ETT exit (bevel) (region B) and the device itself (region C).

Results: Recirculatory flow and high velocities were found at the ETT's bevel and at the glottis level in the SGAD group. The pressure gradient (Δp) was more enhanced in the ETT cases compared with the SGAD cases, where the pressure change was drastic. In region A, the Δp was higher in the ETT group, while in regions B and C, it was higher in the SGAD group. The general resistance was not statistically significant between groups ($p = 0.48$). Higher resistances were found at the region A ($p = <0.001$) in the ETT group. In contrast, the resistance was higher in the SGAD cases at the region B ($p = 0.001$).

Discussion: Overall, the provided CT-based CFD analysis demonstrated regional changes in airway pressure and resistance between ETT and SGAD during anesthetic flow conditions. Correct selection of the airway device size is recommended to avoid upper airway obstruction or changes in flow parameters.

KEYWORDS

***in silico*, airway management, v-gel®, feline, general anesthesia, ETT, flow**

1. Introduction

Airway management in veterinary medicine is vital when patients are unable to maintain airway patency autonomously, especially in emergencies and during an anesthesia. Orotracheal intubation with an endotracheal tube (ETT) maintains airway patency, allows positive pressure ventilation, ss aspiration of any material entering the oropharynx, and allows delivery of inhaled anesthetic gasses and oxygen to the patient (1). In cats, however, laryngeal spasm (2), soft tissue swelling (3), tracheal ruptures (1, 3, 4), sublaryngeal tracheal injury and ulceration (5) or trauma to arytenoid cartilages (1, 3) have been reported. Alternatively, a laryngeal mask or supraglottic airway device (SGAD) has been developed for airway management during anesthesia. These devices seal the upper airways above the rima glottidis and are associated with an increased risk of gastro-esophageal reflux and possible aspiration in human (2) and veterinary patients (6). They were first developed for humans (7) and then for rabbits and cats (6, 8, 9). The SGAD used in cats is positioned above the rima glottidis, seal the esophageal entrance, and an inflatable dorsal adjuster that can increase seal pressure allowing spontaneous or mechanical ventilation (9). Insertion problems have been described, including multiple attempts to correct placement, dislodgement, coughing during insertion, causing upper airway obstruction, stimulus for regurgitation and vomiting (3, 6) and fresh gas flow leakages during mechanical ventilation (3).

Computational fluid dynamics (CFD) is a non-invasive *in silico* technique that uses numerical algorithms to solve the governing equations of fluid dynamics and characterize the flow in numerous clinical situations (10, 11). This technique uses images from computed tomography (CT) or magnetic resonance imaging (MRI) scans of patients to create reconstructions of specific anatomical geometries. CFD is used in many fields like scientific research, clinical practice, industry or biomedical engineering. Normal and diseased human breathing and flow behavior have been largely studied in the last decades (10, 12). This is a relatively new technique in the veterinary sciences. It has been recently applied to the canine upper airways to compare upper airway pressure and resistance in brachycephalic, mesocephalic, and dolichocephalic dogs (13) and nasal flow resistance in English bulldogs (14). It has been used to compare respiratory function in brachycephalic patients (before and after surgery for the brachycephalic obstructive airway syndrome) (15, 16) and the evaluation of transport, distribution, and deposition of inhaled salbutamol particles in upper and lower airways in cats (15). Other studies focused on respiratory anatomy and respiratory physiology of animals, for example in bats (16), rabbits (17, 18), rats (19–21), pigs (22), mice (23), wild cats (24), dogs (25, 26), deer (27) and monkeys (19, 28) or for setting up animal models for human medicine (29, 30).

Understanding airway fluid dynamics is important for studying drug delivery, particle inhalation, airway disease, ventilation, and breath sound generation (22). The upper airways contribute to most flow resistance of the respiratory tract, and thus, abnormal anatomy of the upper airways can have consequences on the flow, like in brachycephalic syndrome (31). In general, the relationship among flow, pressure and resistance can be expressed through the analogy of the Ohm's law as pressure difference or pressure gradient (Δp) = flow × resistance. Hence, resistance = pressure difference (cmH_20)/flow (L/min). Flow is defined as the quantity of a fluid passing through a specific location per unit time and it can develop different regimes, depending on several aspects related to the fluid properties, to the geometry and to the velocity (32). During the passage of the air across the glottis, a physiological Δp occurs, caused by anatomical changes in the larynx cross-section (33) which leads to increased flow velocity. When an individual inhales, the laminar flow becomes turbulent in the larynx and tends to be laminar in the lower airways (34). The flow regime (turbulent or laminar) is determined by the Reynolds number. When de Reynolds number is less than 2000, flow is predominantly laminar, and when it is greater than this number, turbulent flow dominates (32) (see Suplemmentary material – Supplementary Text: physics). When the tube wall can be considered rigid, the flow is governed by the Poiseuille's Law that states the proportionality between the Δp and the flow ϕ times the resistance R ($\Delta p \propto R\,\phi$). The resistance is proportional to the dynamic viscosity of the fluid and the length of the tube while it is inversely proportional to the fourth power of the tube radius (see Suplemmentary material – Supplementary Text: physics). These variables can be computed in different clinical situations starting from CT or MRI images (33), using numerical algorithms to solve the Reynolds-averaged Navier–Stokes equations that describe the flow motion in different conditions with complex geometries (for furter details see Suplemmentary material – Supplementary Text: physics).

In our veterinary teaching hospital, we observed that cats under general anesthesia in which we used SGAD presented CT images with a partial or complete rima glottidis closure and esophageal aerophagy, during respiratory work-ups. As well, signs of airway obstruction were clinically observed with the capnogram (phase II slope upward with a blunted α angle in the capnograph) and, in some cases, reintubation was needed by our anesthesiolgist. These clinical situation led us to the aim of this study that was to use CFD for the investigation of the airway velocity, pressure between different regions and resistances in the upper airways of cats intubated with ETT compared to SGAD. We hypothesized that SGAD would cause more airway resistance and pressure compared with ETT, specifically at the glottis region, with more areas of recirculatory flow because of its morphology.

2. Materials and methods

2.1. Animal use and ethical approval

In this retrospective and comparative study, cats that underwent head, neck, and thorax CT scans as part of a diagnostic protocol at the Veterinary Referral Hospital UCV, Catholic University of Valencia San Vicente Mártir from 2018 to 2022 were enrolled for further analysis. All patients were part of the hospital's clinical cases for which CT scans had to be performed as part of their diagnostic protocol. All enrolled cats required anesthesia for CT examination, and they were either intubated with an ETT or had their airway patency maintained with a SGAD (v-gel® for cats sizes C1-C6, Docsinnovent Ltd., Hertfordshire, United Kingdom). Anesthesia protocol was adapted to each cat, and food (but no water) was withdrawn 12 h before the procedure. Information such as breed, sex, neutered status, age, weight, size of the device used in the procedure, and the presence or absence of clinical respiratory signs (coughing, sneezing, tachypnea), was also recorded. The presence of bronchial or tracheal intraluminal obstruction or collapse, incomplete CT scan studies, and/or any technical image acquisition issue, such as motion artifacts, were exclusion criteria. All

procedures were conducted as part of standard veterinary clinical practice with the owner's consent, and approval from the institutional ethical committee (CEEAUCV2101) was obtained. Twenty cats, either with an ETT ($n = 10$) or with a SGAD ($n = 10$), were included.

2.2. Image acquisition and analysis

All CT scans were performed using a multidetector 16-slice CT scanner (Siemens Somatom Scope, Munich, Germany) in helical scan mode. All cats were positioned in sternal recumbency, and scans of the head, neck, and thorax were performed (entire study or for regions acquired separately), including from the connection of the breathing circuit to the most cranial part of the liver. Computed tomography acquisition protocols and technique settings for CT scans included: 512 × 512 matrix, a pitch of 0.65 with scan thickness of 0.75–1.5 mm, 220 mAs, 130 kV, and a patient size adjusted display field of view. At the end of the CT examination, the cats were supervised until they recovered or remained anesthetized for further procedures.

Images were viewed using two DICOM (Digital Imaging and Communications in Medicine) viewers (Aycan Workstation PRO software v3.16.010 SW and Horos v4.0.0 RC5) with a lung (window width [WW] = 1,400 HU (Hounsfield units) and window level [WL] = −500 HU), soft tissue (WW = 120 HU; WL = 40 HU) and bone (WW = 1,500 HU; WL = 300 HU) reconstruction algorithms.

In the CT images, the ETT bevel's orientation to the tracheal wall was described in all cases as ventral, lateral, dorsal, or aligned to it. In the SGAD cases, a classification for rima glottidis closure based on 3 grades was proposed for this study (grade 0 = open glottis; grade 1 = glottis partially closed; grade 2 = closed glottis) (see Figure 1). In this article, we refer to rima glottidis as the opening between the vocal cords and as part of the glottis, which is the anatomical section itself.

2.3. Geometrical reconstruction and numerical discretization

The DICOM files derived from the CT scans were imported into the image-based geometry reconstruction software (MIMICS, Materialise Software, Leuven, Belgium). Manual reconstruction of the device (ETT and SGAD), larynx in the case of SGAD, trachea, mainstem bronchi, and each lobar bronchus geometry were conducted for each cat (Figure 2). A stereolithography (STL) file was exported in each case.

STL files for the patient-specific models were imported to the commercial software package Rhinoceros (v. 5 SR14 32-bit, Robert McNeel and Associates, Seattle, WA, United States), and the ETT and SGAD geometries were added to the cat models. Inlet and outlet sections were created, and all the surfaces building the 3D volumes were exported again as STL files. These files were imported in the software package Ansys IcemCFD (v. 22.2, Ansys Inc., Canonsburg, PA, United States), where the volume of each model was subdivided into tetrahedral elements. At this stage, the minimum size of all tetrahedral edge lengths was specified to control the number of elements. Near-wall regions required a denser mesh with more elements to increase the accuracy of the geometry of the small airways and the laryngeal region in the SGAD cases. The element minimum edge length required varied depending on the size and morphology of the airway region or device, generating slightly different computational grids for the spatial resolution (see Figure 3). Before the final mesh creation, a mesh-independent study was performed to ensure adequate grid sizes. The study, conducted on the airway velocity profiles inside the trachea and the main bronchi with both devices, demonstrated that for both devices, computational grids over 2 million provided similar results in terms of velocity profiles (relative difference between profiles less than 2%). Considering that the Δp, as widely demonstrated in the literature, are relatively unaffected by the element size (25) we concluded that grids ranging from 2 to 5 million elements (Suplemmentary material – Supplementary Table 1), depending on the model geometry, were sufficient for describing the flows within the patient-specific models.

2.4. CFD analysis

The numerical grids from the 20 cats were imported into the commercial software package ANSYS CFX, v.22.2 (Ansys Inc.,

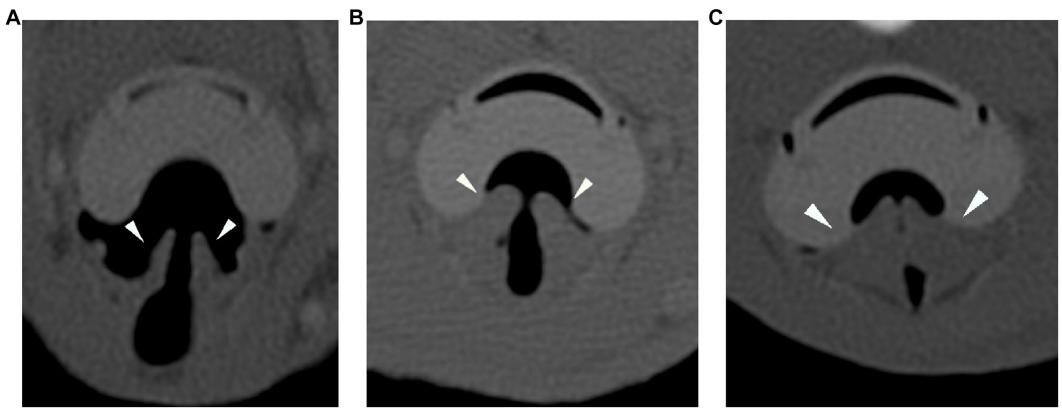

FIGURE 1
Transverse plane of the CT-scan in bone reconstruction algorithm for the three degrees of rima glottidis closure (arrowheads). Grade 0 = open glottis **(A)**, grade 1 = glottis partially closed **(B)**, and grade 2 = closed glottis **(C)**. CT: computed tomography.

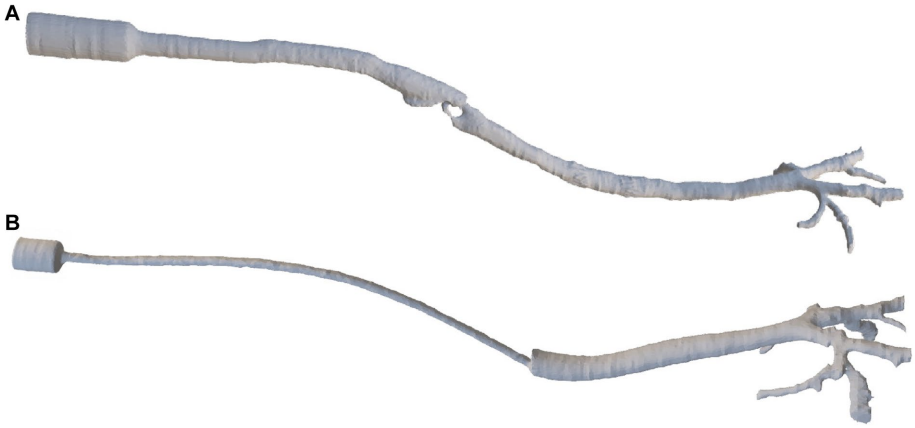

FIGURE 2
The final reconstruction of a SGAD (Case #5) **(A)** and an ETT (Case #4) **(B)** via image-based geometry reconstruction software (MIMICS, Materialise Software). ETT: endotracheal tube; SGAD: supraglottic airway device.

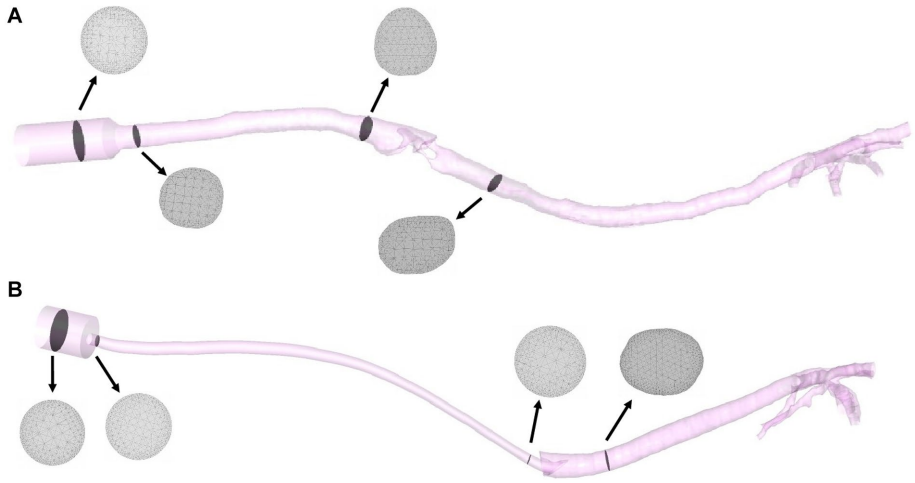

FIGURE 3
Final models of a SGAD (Case #5) **(A)** and an ETT (Case #4) **(B)** with four planes (gray) representing the computational grids. ETT: endotracheal tube; SGAD: supraglottic airway device.

Canonsburg, PA, United States). This software uses numerical algorithms to solve the Reynolds-averaged Navier–Stokes equations that describe the flow motion in different conditions within the geometrical grids. In particular, the Ansys CFX software adopts the finite volume method. The software manual provides the exact mathematical formulations and the solving algorithms used by Ansys CFX (Ansys, 2022).

For boundary conditions, a peak inspiratory flow of 2.4 L/min was imposed at the inlet of each model and, at the outlets, a zero-pressure condition was given. The flow value was obtained using the peak value of different spirometry curves (Carescape Monitor B650, General Electric, Boston, MA, United States with the spirometer module E-sCAiOV and pitot sensor Pedi-Lite) in cats under general anesthesia. To dampen the effect of the boundary conditions, 5-diameter inlet and outlet extensions were added to the model (see Figure 4). The simulation used the following fluid properties: air density 1.225 kg/m^3, viscosity 1.83·10^{-5} kg/(m·s) and 25°C. The flow was considered steady (constant inspiratory peak flow) (35, 36) and turbulent (Reynolds number > 2,000). The k-ω SST (Shear Stress Transport) turbulence model was used with an initial turbulence intensity value of 5%. The numerical discretization and computational cost of each mesh are summarized in the Suplemmentary material (see Supplementary Table 1).

2.5. Resistance evaluation

General resistance was calculated using the pressure gradient of the whole model with the following equation:

$$Resistance\left(cmH_2O/L/\min\right) = \frac{\Delta p\left(cmH_2O\right)}{flow\left(L/\min\right)}$$

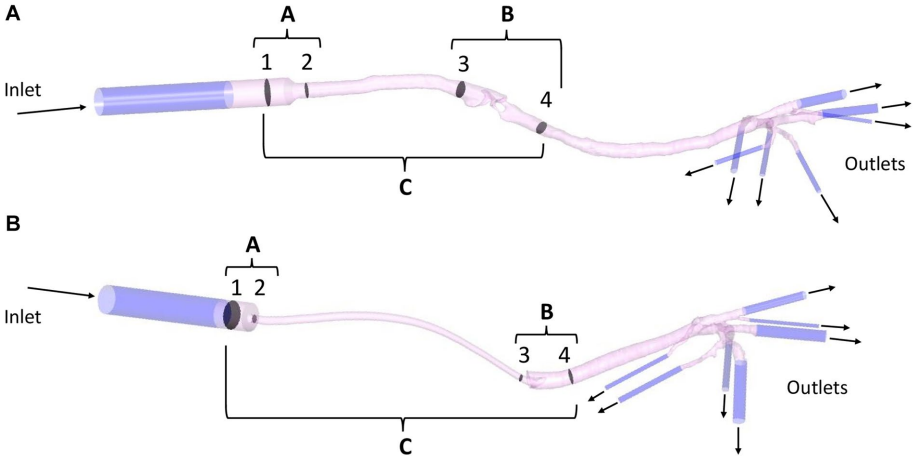

FIGURE 4
Example of a SGAD (Case #5) **(A)** and an ETT (Case #4) **(B)** model with regions A, B, and C formed by planes 1–2, 3–4, and 1–4, respectively. Regional pressure, pressure gradient, and resistance were calculated in three sections, between planes 1–2 (region A), 3–4 (region B), and 1–4 (region C). Representation of inlet and outlet extensions (dark blue) added to each model (pink). ETT: endotracheal tube; SGAD: supraglottic airway device.

where Δp is the pressure gradient between maximum and minimum general pressure. The flow (2.4 L/min) was the same in all cases.

Regional resistance evaluation was determined using the simulation results. The flow and pressure maps were evaluated by looking for areas of flow recirculation and/or abrupt Δp, respectively. The higher flow recirculation and Δp was localized at the glottis area in the SGAD group. At the ETT group, two areas were observed, at the ETT connection to the breathing circuit and where bevel contacts the tracheal wall. The model was divided into sections for further analysis. Section 1 was the proximal connection of the device to the breathing circuit, section 2 the proximal region where the device's diameter decreases. Sections 3 and 4 are, 2 cm cranial and caudal to the glottis in the SGAD and 1 cm cranial and caudal to the ETT bevel, respectively. Then the regional Δp was computed at three regions (A, B, and C) of each anatomical model with the previously mentioned equation. The Δp at the device's entrance at sections 1 and 2 (region A), at sections 3 and 4 (region B), and between sections 1 and 4 (region C, the entire device) were computed (see Figure 4).

2.6. Statistical analysis

Sample size calculations indicated that 10 cats per group was sufficient to detect a decrease in resistance of 25%, mean of 38.7 $cmH_2O/L/s$, and standard deviation (± SD) of 7.8 (pilot study (37)). A statistical power of 0.8 and α value of 0.05 (two-tailed analysis for paired data was input into the online sample size calculator https://clincalc.com/stats/samplesize.aspx). The measured data were analyzed using the IBM® SPSS® Statistics software version 27 (Chicago, IL, United States). A *Shapiro–Wilk* test was used to test the normal distribution of Δp values (general and regional), resistance (general and regional), and velocities. The results are expressed as medians (maximum and minimum range). *Mann–Whitney U* tests compared general and regional Δp values, general and regional resistance, and velocities between groups (ETT/SGAD). Values of $p < 0.05$ were considered statistically significant.

3. Results

A total of 40 cat CT scans were obtained and reviewed. Thirteen SGAD and 16 ETT cases were selected and 9 cats were excluded. One SGAD case was excluded because of bronchial collapse, another because of a tracheal mass, and the other case did not have the airways wholly included in the CT scan. In the ETT group, two cases were excluded because the presence of soft tissue in the bronchi, and one was incorrectly positioned in the CT scan making difficult correct reconstruction. Three ETT cases did not have the airways wholly included in the CT scan. Twenty CT studies, either with an ETT ($n = 10$) or a SGAD ($n = 10$), were finally included.

The ETT group age range was between 3 months and 19 years with a mean age of 7 years, and in the SGAD group, the age range was between 1 to 8 years with a mean age of 4 years. The breeds included Turkish mohair, Siamese (two), Persian, and Domestic Shorthair (16). Body weight, ETT internal diameter (ID) in mm, the SGAD sizes, the orientation of the bevel, the slice thickness of the CT and the glottic closure grade in the SGAD cases are represented in Table 1.

The all bevels were, located at the level of the thoracic inlet. All ETTs included were PVC tubes with inflated cuff and had Murphy's eye. No complete occlusion of the bevel's tube or Murphy's eye was observed. The tubes with a smaller diameter (ID 2.5–3 mm in cases #4 and #10, respectively) did not show higher values of velocity, pressure, and general resistance, but there was higher regional resistance in region A for case #4. Cases #1 and #3 had the largest diameter of ETT (ID = 4.5 mm). Case #1 showed the lowest general Δp, regional (A), and general resistance.

The flow maps depict the flow streamlines that represent the structure of the flow colored with the intensity of the velocity (red = high velocity, dark blue = low velocity) in m/s (see Figure 5). The flow streamlines of an ETT and a SGAD model (case #4 and case #5, respectively) are represented in Figure 5 at steady peak inspiratory flow. The rest of the cases can be found in the Suplemmentary material (Supplementary Figures 1, 2). In the ETT cases, the location with the highest velocities was the bevel of the tube contacting the wall of the trachea (9/10). In this region, the most pronounced flow recirculation

TABLE 1 Results for the ETT and SGAD groups.

ETT Group					SGAD Group				
Case	ID (mm)	Weight (kg)	Bevel orientation	CT-scan slice thickness (mm)	Case	Size	Weight (kg)	Grade glottis closure	CT-scan slice thickness (mm)
1	4.5	5.2	Ventral wall	1	1	C5	5	0	0.75
2	4	5.2	Straight	1.5	2	C4	4.5	0	0.75
3	4.5	6.9	Ventral wall	0.75	3	C3	3.8	2	1
4	2.5	1.5	Ventral wall	0.75	4	C4	4.8	0	0.75
5	3.5	5.2	Ventral wall	1.5	5	C5	4.8	2	0.75
6	3.5	3	Lateral wall	1.5	6	C4	3.5	1	1.5
7	4	6.5	Ventral wall	1	7	C2	2.8	0	1.5
8	4	6.5	Dorsal wall	1.5	8	C2	2.5	1	1
9	4	5.6	Ventral wall	1	9	C6	6.5	2	1
10	3	4.4	Ventral wall	1	10	C4	3.8	2	0.75

For the ETT group, ID is the internal diameter of the ETT tube (mm), the weight of the patient in kg, the bevel orientation of the ETT related to the tracheal wall, and the slice thickness (mm) of the CT scan. For the SGAD group, the size of the device (C2 corresponds to the smallest size and C6 corresponds to the largest size), the weight of the patient in kg, grade of glottis closure (grade 0 = open glottis; grade 1 = glottis partially closed; and grade 2 = closed glottis) and slice thickness (mm) of the CT scan.
ETT, endotracheal tube; SGAD, supraglottic airway device; CT, computed tomography; ID, internal diameter.

was found. In all cases, a change in the velocity was seen in region A, where the diameter of the tube decreases with respect to the diameter of the tube connection to the breathing circuit. The velocities were higher as the diameter of the connection decreased. Mild outflow with minimal recirculation through Murphy's eye was observed in all cases. Case #4 showed the maximum velocity (10.96 m/s). Only in one case (case #2) the bevel was aligned to the tracheal lumen. In the SGAD cases, the point with the highest velocities and flow recirculation lines were at the rima glottidis and caudal to it, consistent with CT image findings. In 6 cases, the glottis was partially ($n = 2$) or completely closed ($n = 4$). Cases #3, #5, #9, and #10 of the SGAD, classified as grade 2, showed the highest velocities (22.4 m/s, 21.1 m/s, 17.4 m/s, and 10.8 m/s, respectively). The median, maximum and minimum values of maximum velocity for the ETT and the SGAD groups are represented in Table 2. No statistically significant differences were observed between devices ($p = 1.00$).

The pressure maps of the device, trachea, and bronchi are represented for two examples of ETT and SGAD cases (case #4 and #5, respectively) in Figure 6 (negative and positive values represent increase and decrease with respect to the atmospheric pressure). The Δp was more staggered in the ETT case compared with the marked pressure change visible in the SGAD case. The rest of the pressure maps can be found in the Suplemmentary material (Supplementary Figures 3, 4). Higher pressures were observed cranial to the glottis in all SGAD cases, especially in cases #3, #5, #9, and #10. Case #3 of the SGAD had the highest maximum pressure value (2.09 cmH_2O), and case #5 had the lowest minimum pressure value (−2.32 cmH_2O). Both were classified as grade 2 glottic closures. The maximum pressures did not show statistically significant differences ($p = 0.09$), while the minimum pressures were statistically significant ($p = 0.015$) between both devices.

The median, maximum, and minimum values of general and regional Δp for the ETT and the SGAD groups (Table 2). The Δp in region A ($p < 0.001$) and B ($p = 0.001$) were statistically significant between groups but not in region C ($p = 0.63$). In region A, the Δp was higher in the ETT group, while in regions B and C, it was higher in the SGAD group. The maximum pressure value in region A was observed in case #4 of the ETT (ID = 2.5 mm). For regions B and C, the maximum pressure values (0.46 cmH_2O) were for case #3 of the SGAD classified as grade 2 (2.05 cmH_2O and 2.12 cmH_2O, respectively).

The general resistance was not statistically significant between groups ($p = 0.48$). The maximum and minimum values were seen in the SGAD group. Higher values were observed in cases #3 and #5 (1.68 and 1.82 cmH_2O/L/min, respectively), and the lowest value was observed in case #1 (0.05 cmH_2O/L/min) and classified as grade 2 and 0, respectively. The resistance in region A was higher in the ETT group, and a statistically significant difference was found between devices ($p < 0.001$). The maximum value was observed in case #4 of the ETT (0.19 cmH_2O/L/min). The resistance in region B was also statistically significant between groups ($p = 0.001$). In this region, higher values were obtained in the SGAD group, specifically in cases #3 and #5 (0.85 and 0.82 cmH_2O/L/min, respectively). Case #10 (ID = 3 mm) showed the highest value in the ETT group in this region (0.04 cmH_2O/L/min). The resistance in region C was not statistically significant ($p = 0.63$) between devices. High values were seen in the ETT group, but the highest resistance was observed in case #3 of the SGAD (0.88 cmH_2O/L/min), classified as grade 2. The median, maximum, and minimum values of general and regional resistances for the ETT and the SGAD groups are represented in Table 2.

4. Discussion

This study computationally evaluated the performances of two devices for managing a cat's airways: ETT and SGAD. We have found differences in Δp and resistances between the ETT and the SGAD groups at different device locations. The area of rima glottidis presented variable Δp and significantly higher values of resistance compared with the ETT group, as this device bypassed this region. However, in the case of the ETT, the region where the device connects to the breathing circuit has the highest resistance in this device. In any

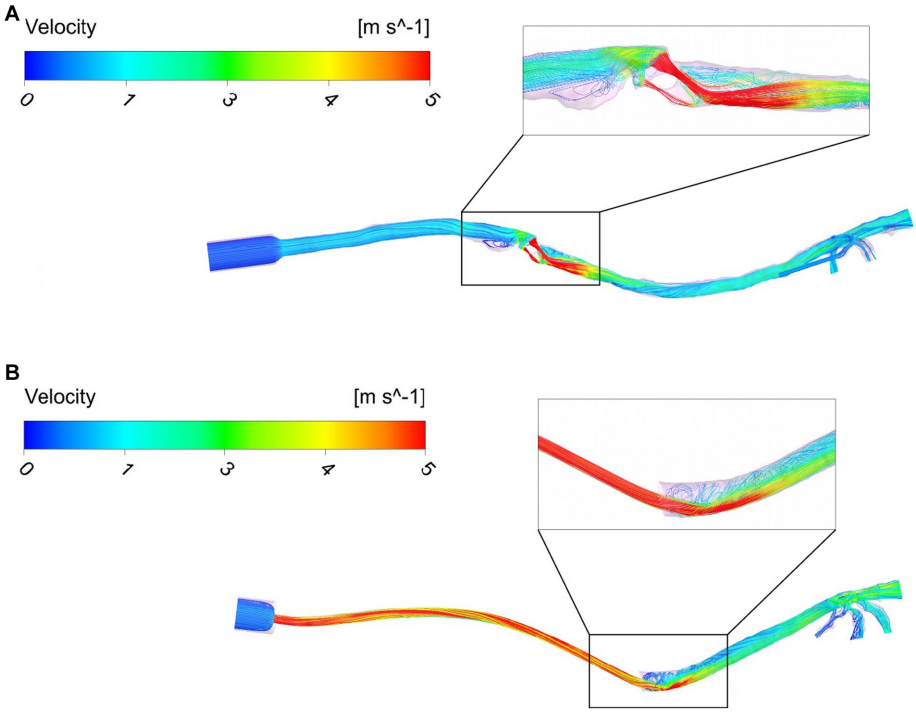

FIGURE 5
Flow maps using streamlines and colored with the velocity intensity (m/s) for a SGAD case (Case #5) **(A)** and an ETT case (Case #4) **(B)**. ETT: endotracheal tube; SGAD: supraglottic airway device. Flow streamlines represent the flow direction depicted with the intensity of the velocity (red = high velocity, dark blue = low velocity) at stationary peak inspiratory flow.

TABLE 2 **Results of each measured parameter (Ansys CFX software) represented by median [minimum value – maximum value] and the statistical significance represented by *p*-value (values of $p < 0.05$ were considered statistically significant).**

Measured parameters	ETT group	SGAD group	*p*-value
Maximal velocity (m/s)	7.48 [4.01–10.96]	6.37 [3.32–22.4]	1.00
Maximal pressure (cmH_2O)	1.07 [0.39–2.19]	0.39 [0.12–2.09]	0.09
Minimal pressure (cmH_2O)	−0.01 [−0.04–0]	−0.07 [−2.32–0]	0.015
General Δp (cmH_2O)	1.09 [0.4–2.19]	0.46 [0.13–4.37]	0.48
Region A Δp (cmH_2O)	0.19 [0.07–0.46]	0.02 [0.01–0.05]	<0.001
Region B Δp (cmH_2O)	0.02 [0.001–0.1]	0.23 [0.02–2.05]	0.001
Region C Δp (cmH_2O)	0.95 [0.34–2.07]	0.33 [0.1–2.12]	0.63
Resistance A (cmH_2O/L/min)	0.08 [0.03–0.2]	0.009 [0.005–0.23]	<0.001
Resistance B (cmH_2O/L/min)	0.009 [0.0003–0.04]	0.09 [0.01–0.85]	0.001
Resistance C (cmH_2O/L/min)	0.4 [0.15–0.86]	0.14 [0.04–0.88]	0.63
General resistance (cmH_2O/L/min)	0.45 [0.16–0.91]	0.19 [0.05–1.82]	0.48

ETT, endotracheal tube; SGAD, supraglottic airway device; Δp, pressure gradient. Region A: consists of an area between two sections, localized where the proximal portion connects the device to the breathing circuit and the distal region where the device's diameter decreases. Region B: consists of the area around the glottis in the SGAD group and, in the ETT group, consists in the point where the bevel contacts the tracheal wall. Region C: consists of the entire device.

case, with these geometrical models and these flows, we could not see any differences in the general resistance in the device and airway models.

There is no consensus and poor knowledge in the veterinary field regarding whether different airway devices induce different flow patterns, Δp, and resistances. Physiological flows of 4–8 L/min (38) and 6 L/min (37) have been reported in awake cats. The inspiratory flow used in this study was smaller as we simulated the ventilation under general anesthesia (2.4 L/min). Consequently, the resistance, pressure, and velocity results are lower than other studies (34). Our results are based in CFD simulations. A comparison in the same patient with both devices was not performed. So it is unknown if changes in velocity, pressure and resistance are due to the devices alone or could be also caused by inter individual patient anatomical characteristics.

In our study, the ETT group's highest velocity and pressure values were seen at the bevel. The ETTs used in this study are tubes for

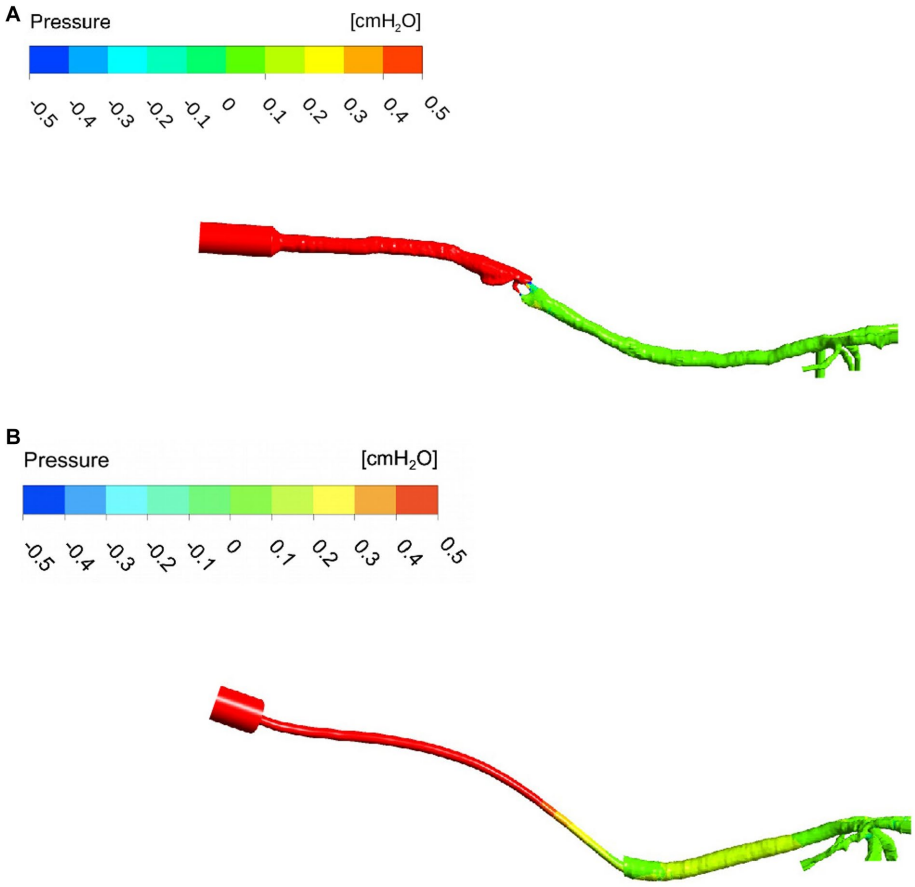

FIGURE 6
Pressure map of a SGAD (Case #5) **(A)** and an ETT (Case #4) **(B)**. The pressure gradient is staggered, from higher values (cmH_2O) at the inlet to lower values at the outlets (bronchi). ETT: endotracheal tube; SGAD: supraglottic airway device; pressure values in cmH_2O. The intensity of the pressure is represented at stationary peak inspiratory flow (red = high pressure, dark blue = low pressure).

neonatal or pediatric human patients. Additionally, the intubation technique differs when compared with cats. The non-physiological ETT conformation for the cat resulted in the bevel impinging on the trachea's wall in most cases, causing changes in the flow behavior. In humans, CFD studies have shown that the ETT induces swirls at the outlet of the straight ETT ending and is related to a jet flow effect (39). This effect may induce high flow rates in the trachea, creating a recirculation zone and the transition to turbulent flow (40). Lumb et al. pointed out that the position and direction of this jet can influence the distribution of the fresh gas flow in patients during general anesthesia with inhalant anesthetics (41). They described that the gas hits the carina or airway wall immediately, perturbing the laminar flow and generating recirculation near the large airways (41). In our study, multiple recirculatory streamlines and higher velocity in the ETT group were seen when the tube was closed to the tracheal wall, as described in humans (41). The same research group later studied the role of Murphy's eye, finding that in a normally positioned ETT, most parts of the flow exited the tube through the bevel, and only a tiny fraction passed through Murphy's eye (42). These results are similar to our findings.

In the SGAD cases, the largest number of recirculatory streamlines, higher velocity, and pressure values were seen at the glottis. Our CT scans showed the glottis wholly or partially closed in 6 of 10 SGAD cases. However, no relation was seen between SGAD size, glottis closure, and increased resistance. During this study, 3 of the 10 cases in the SGAD group needed a change in size of the device and/or orotracheal intubation resulting from obstruction problems during the anesthesia, none in the ETT group. We believe this complication was related to the sealing size, which is likely too big or not perfectly adaptable to all types of feline larynx size and morphology.

The area where the ETT is connected to the breathing circuit demonstrated a significant difference in Δp and resistance compared with the SGAD. This was expected as these connectors have a standardized 15 mm diameter, and the diameter change within the tube is abrupt. This connection is more abrupt for ETT than SGAD. However, we observed a lower Δp within each ETT model, as the flow can adapt to geometrical changes such as constriction and expansion (43). In any case, the diameter change is gradual in this region, so no recirculating streamlines were observed, although there was an increased velocity as the diameter decreased. In contrast, in the SGADs, the pressure maps clearly showed an abrupt Δp across the rima glottidis. Marków et al. reported that, in humans, the resistance to flow depends on the area of the rima glottidis opening, and it is independent of its shape (33). Our findings have partially relation with this study because cases with complete or partially occluded rima glottidis showed high velocities and Δp. In neonatal and pediatric human medicine, an association between ETT diameter and resistance has been reported (44). When the diameter of the ETT decreases, the

resistance increases with significantly more work during breathing (44). However, in this study, the cases with smaller diameters of ETT did not show the highest values and no clear association between ETT size and the cat's weight was seen.

We found similar values of resistances in the device itself and the whole model. In the ETT cases, the resistances in the device were higher than in the SGAD, likely because of the small diameter of the tube compared with the tracheal diameter. General resistance values of the SGAD group were twice as high as the ETT cases, but no statistical significance was observed. Moreover, the SGAD general resistances were uneven compared with the ETT cases, probably because of the regular diameter of the ETT. In the SGAD, patient anatomy and interindividual morphologic variability of the cats, especially at the laryngeal region, play an essential role in the studied flow parameters. This aspect may explain the heterogeneity of the data presented in this group. The general resistance values were dependent on the degree of rima glottidis closure, but not with the ETT connection system. The airway resistance falls with increasing airway bifurcations, and multiple factors play a role, including flow velocity, airway diameter, lung volume, and flow type (laminar or turbulent) (45).

This study has some limitations. Firstly, because of its retrospective and clinical nature, the CT studies have different slice thicknesses, and some were obtained for different regions (head, neck, and thorax). Secondly, intubation was carried out by all the anesthesia staff, interns, and students. The size of the ETT in some cases was smaller than expected for the size of the trachea or the cat's weight. Another limitation is that the model includes the upper airways till the lobar bronchi so that the influence of the lower airways and alveoli was not evaluated. Further studies comparing healthy and diseased animals would be necessary to analyze velocity, pressure, or resistance changes. Finally, a patient-specific flow would provide precise information for accurate simulations and corresponding pressure and flow patterns. However, a comparison between two groups would be more difficult to be conducted, and ultimately that was the objective of this study. Studies comparing different flow parameters are required to relate resistance, velocity, and pressure values between different peaks in inspiratory flows and comparing *in silico* and *in vivo* data of the same patient using both devices.

In conclusion, we have proposed a CT-based CFD study for evaluating changes in airway velocity, pressure, and resistance between two airway management devices under general anesthesia. Their use in this study has showed a differences in resistance, pressure, and velocity at the ETT connector and outflow section and across the rima glottidis in the SGAD. So, selection of the correct device size is necessary to avoid airway obstructions or changes in the upper airway flow. This non-invasive technique can provide physiological and clinical information, as in human studies, but further investigations are needed to evaluate the specific application in veterinary medicine.

Data availability statement

The original contributions presented in the study are included in the article/Supplementary material, further inquiries can be directed to the corresponding author.

Ethics statement

The animal studies were approved by the Ethical committee of the Catholic University of Valencia (CEEAUCV2101). The studies were conducted in accordance with the local legislation and institutional requirements. Written informed consent was obtained from the owners for the participation of their animals in this study.

Author contributions

CZ-P: data curation, formal analysis, investigation, resources, visualization, and writing – original draft. MM: conceptualization, formal analysis, investigation, methodology, project administration, resources, supervision, validation, visualization, and writing – review and editing. RF-P: conceptualization, data curation, formal analysis, investigation, methodology, project administration, supervision, validation, visualization, and writing – review and editing. All authors contributed to the article and approved the submitted version.

Funding

MM and RF-P are supported by the grants PID2021-125731OB-C31 and PID2021-125731OB-C33, respectively, which are financed by the Spanish Ministry of Science and Innovation MCIN/AEI/10.13039/501100011033/ and FEDER ("A way to build Europe").

Acknowledgments

The support of the Institute of Health Carlos III (ISCIII) through the CIBER-BBN initiative and the vice-rectorate for research of the Catholic University of Valencia and the office for the transfer of research results (OTRI), is highly appreciated.

Conflict of interest

The authors declare that the research was conducted without any commercial or financial relationships that could be construed as a potential conflict of interest.

Publisher's note

Supplementary material

The Supplementary material for this article can be found online at: https://www.frontiersin.org/articles/10.3389/fvets.2023.1183223/full#supplementary-material

References

1. Hofmeister EH, Trim CM, Kley S, Cornell K. Traumatic endotracheal intubation in the cat. *Vet Anaesth Analg*. (2007) 34:213–6. doi: 10.1111/j.1467-2995.2006.00314.x

2. Cassu RN, Luna SP, Teixeira FJ, Braz JR, Gasparini SS, Crocci AJ. Evaluation of laryngeal mask as an alternative to endotracheal intubation in cats anesthetized under spontaneous or controlled ventilation. *Vet Anaesth Analg*. (2004) 31:213–1. doi: 10.1111/j.1467-2987.2004.00195.x

3. Prasse SA, Schrack J, Wenger S, Mosing M. Clinical evaluation of the v-gel supraglottic airway device in comparison with a classical laryngeal mask and endotracheal intubation in cats during spontaneous and controlled mechanical ventilation. *Vet Anaesth Analg*. (2016) 43:55–62. doi: 10.1111/vaa.12261

4. Mitchell SL, McCarthy R, Rudloff E, Pernell RT. Tracheal rupture associated with intubation in cats: 20 cases (1996-1998). *J Am Vet Med Assoc*. (2000) 216:1592–5. doi: 10.2460/javma.2000.216.1592

5. Phaneuf LR, Barker S, Groleau MA, Turner P. Tracheal injury after endotracheal intubation and anesthesia in rabbits. *J Am Assoc Lab Anim Sci*. (2006) 45:67–72.

6. Hecker-Turkovic K, Hartmann K, Dörfelt R. Success of placement and complications during v-gel placement and maintenance of anaesthesia. *J Feline Med Surg*. (2021) 24:800–5. doi: 10.1177/1098612X211050612

7. Vaida SJ, Gaitini D, Ben-David B, Somri M, Hagberg CA, Gaitini LA. A new supraglottic airway, the Elisha airway device: a preliminary study. *Anesth Analg*. (2004) 99:124–7. doi: 10.1213/01.ANE.0000123492.26499.63

8. Engbers S, Larkin A, Rousset N, Prebble M, Jonnalagadda M, Knight CG, et al. Comparison of a supraglottic airway device (v-gel®) with blind orotracheal intubation in rabbits. *Front Vet Sci*. (2017) 4:49. doi: 10.3389/fvets.2017.00049

9. Crotaz IR. Initial feasibility investigation of the v-gel airway: an anatomically designed supraglottic airway device for use in companion animal veterinary anaesthesia. *Vet Anaesth Analg*. (2010) 37:579–0. doi: 10.1111/j.1467-2995.2010.00566.x

10. Faizal WM, Ghazali NN, Khor CY, Badruddin IA, Zainon MZ, Yazid AA, et al. Computational fluid dynamics modelling of human upper airway: a review. *Comput Methods Prog Biomed*. (2020) 196:105627. doi: 10.1016/j.cmpb.2020.105627

11. Bates AJ, Schuh A, Amine-Eddine G, McConnell K, Loew W, Fleck RJ, et al. Assessing the relationship between movement and airflow in the upper airway using computational fluid dynamics with motion determined from magnetic resonance imaging. *Clin Biomech*. (2019) 66:88–96. doi: 10.1016/j.clinbiomech.2017.10.011

12. Leong SC, Chen XB, Lee HP, Wang DY. A review of the implications of computational fluid dynamic studies on nasal airflow and physiology. *Rhinology*. (2010) 48:139–5. doi: 10.4193/Rhin09.133

13. Fernández-Parra R, Pey P, Zilberstein L, Malvè M. Use of computational fluid dynamics to compare upper airway pressures and airflow resistance in brachycephalic, mesocephalic, and dolichocephalic dogs. *Vet J*. (2019) 253:105392. doi: 10.1016/j.tvjl.2019.105392

14. Hostnik ET, Scansen BA, Zielinski R, Ghadiali SN. Quantification of nasal airflow resistance in English bulldogs using computed tomography and computational fluid dynamics. *Vet Radiol Ultrasound*. (2017) 58:542–1. doi: 10.1111/vru.12531

15. Fernández-Parra R, Pey P, Reinero C, Malvè M. Salbutamol transport and deposition in the upper and lower airway with different devices in cats: a computational fluid dynamics approach. *Animals*. (2021) 11:1–20. doi: 10.3390/ani11082431

16. Eiting TP, Perot JB, Dumont ER. How much does nasal cavity morphology matter? Patterns and rates of olfactory airflow in phyllostomid bats. *Proc Royal Soc B*. (2014) 282:2161. doi: 10.1098/rspb.2014.2161

17. Xi J, Talaat M, Si X, Dong H, Donepudi R, Kabilan S, et al. Ventilation modulation and nanoparticle deposition in respiratory and olfactory regions of rabbit nose. *Animals*. (2019) 9:1107. doi: 10.3390/ani9121107

18. Xi J, Si XA, Kim J, Zhang Y, Jacob RE, Kabilan S, et al. Anatomical details of the rabbit nasal passages and their implications in breathing, air conditioning, and olfaction. *Anat Rec*. (2016) 299:853–8. doi: 10.1002/ar.23367

19. Corley RA, Kabilan S, Kuprat AP, Carson JP, Minard KR, Jacob RE, et al. Comparative computational modeling of airflows and vapor dosimetry in the respiratory tracts of rat, monkey, and human. *Toxicol Sci*. (2012) 128:500–6. doi: 10.1093/toxsci/kfs168

20. Yang GC, Scherer PW, Mozell MM. Modeling inspiratory and expiratory steady-state velocity fields in the Sprague-Dawley rat nasal cavity. *Chem Senses*. (2007) 32:215–3. doi: 10.1093/chemse/bjl047

21. Zhao K, Dalton P, Yang GC, Scherer PW. Numerical modeling of turbulent and laminar airflow and odorant transport during sniffing in the human and rat nose. *Chem Senses*. (2006) 31:107–8. doi: 10.1093/chemse/bjj008

22. Gamage PP, Khalili F, Khurshidul Azad MD, Mansy HA. Modeling inspiratory flow in a porcine lung airway. *J Biomech Eng*. (2018) 140:0610031–311. doi: 10.1115/1.4038431

23. Kolanjiyil A, Kleinstreuer C, Kleinstreuer NC, Pham W, Sadikot RT. Mice-to-men comparison of inhaled drug-aerosol deposition and clearance. *Respir Physiol Neurobiol*. (2019) 260:82–94. doi: 10.1016/j.resp.2018.11.003

24. Pang B, Yee KK, Lischka FW, Rawson NE, Haskins ME, Wysocki CJ, et al. The influence of nasal airflow on respiratory and olfactory epithelial distribution in felids. *J Exp Biol*. (2016) 219:1866–74. doi: 10.1242/jeb.131482

25. Craven BA, Paterson EG, Settles GS, Lawson MJ. Development and verification of a high-fidelity computational fluid dynamics model of canine nasal airflow. *J Biomech Eng*. (2009) 131:091002–11. doi: 10.1115/1.3148202

26. Craven BA, Neuberger T, Paterson EG, Webb AG, Josephson EM, Morrison EE, et al. Reconstruction and morphometric analysis of the nasal airway of the dog (Canis familiaris) and implications regarding olfactory airflow. *Anat Rec*. (2007) 290:1325–40. doi: 10.1002/ar.20592

27. Ranslow AN, Richter JP, Neuberger T, van Valkenburgh B, Rumple CR, Quigley AP, et al. Reconstruction and morphometric analysis of the nasal airway of the white-tailed deer (Odocoileus virginianus) and implications regarding respiratory and olfactory airflow. *Anat Rec*. (2014) 297:2138–47. doi: 10.1002/ar.23037

28. Bastir M, Sanz-Prieto D, Burgos M. Three-dimensional form and function of the nasal cavity and nasopharynx in humans and chimpanzees. *Anat Rec*. (2022) 305:1962–73. doi: 10.1002/ar.24790

29. Xi J, Kim JW, Si XA, Corley RA, Zhou Y. Modeling of inertial deposition in scaled models of rat and human nasal airways: towards in vitro regional dosimetry in small animals. *J Aerosol Sci*. (2016) 99:78–93. doi: 10.1016/j.jaerosci.2016.01.013

30. Eiting TP, Smith TD, Perot JB, Dumont ER. The role of the olfactory recess in olfactory airflow. *J Exp Biol*. (2014) 217:1799–03. doi: 10.1242/jeb.097402

31. Hoffman AM. Airway physiology and clinical function testing. *Vet Clin North Am Small Anim Pract*. (2007) 37:829–3. doi: 10.1016/j.cvsm.2007.05.013

32. Levitzky MG. *Pulmonary physiology. 7th* ed. New York: McGraw-Hill Medical (2007).

33. Marków M, Janecki D, Orecka B, Misiolek M, Warmuzinski K. Computational fluid dynamics in the assessment of patients' postoperative status after glottis-widening surgery. *Adv Clin Exp Med*. (2017) 26:947–2. doi: 10.17219/acem/64235

34. Gemci T, Ponyavin V, Chen Y, Chen H, Collins R. Computational model of airflow in upper 17 generations of human respiratory tract. *J Biomech*. (2008) 41:2047–54. doi: 10.1016/j.jbiomech.2007.12.019

35. Xi J, Yuan JE, Yang M, Si X, Zhou Y, Cheng YS. Parametric study on mouth–throat geometrical factors on deposition of orally inhaled aerosols. *J Aerosol Sci*. (2016) 99:94–6. doi: 10.1016/j.jaerosci.2016.01.014

36. Sheu TW, Wang SK, Tsai SF. Finite element analysis of particle motion in steady inspiratory airflow. *Comput Methods Appl Mech Eng*. (2002) 191:2681–98. doi: 10.1016/s0045-7825(02)00209-8

37. Epstein A, Godfrey S, Bar-Yishay E, Putilov A, Bark H. Non-invasive measurement of total respiratory compliance and resistance in cats. *Respir Physiol Neurobiol*. (2007) 156:179–6. doi: 10.1016/j.resp.2006.09.006

38. Caro-Vadillo A, Montoya-Alonso JA, García-Guasch L. Impact of obesity on lung function in cats with bronchoconstriction. *Vet Sci*. (2022) 9:278. doi: 10.3390/vetsci9060278

39. Krenkel L, Wagner C, Wolf U, Scholz A, Terekhov M, Rivoire J, et al. Protective artificial lung ventilation: impact of an endotracheal tube on the flow in a generic trachea In: A Dillmann, G Heller, M Klaas, HP Kreplin, W Nitsche and W Schröder, editors. *New results in numerical and experimental fluid mechanics VII*. Berlin: Springer-Verlag (2010)

40. van Rhein T, Alzahrany M, Banerjee A, Salzman G. Fluid flow and particle transport in mechanically ventilated airways. Part I. fluid flow structures. *Med Biol Eng Comput*. (2016) 54:1085–96. doi: 10.1007/s11517-015-1407-3

41. Lumb AB, Burns AD, Figueroa Rosette JA, Gradzik KB, Ingham DB, Pourkashanian M. Computational fluid dynamic modelling of the effect of ventilation mode and tracheal tube position on air flow in the large airways. *Anaesthesia*. (2015) 70:577–4. doi: 10.1111/anae.13003

42. Hall EJ, Burns AD, Ng AC, Lumb AB. Does the Murphy's eye perform its role? *Anaesthesia*. (2015) 70:1326–9. doi: 10.1111/anae.13262

43. Brouns M, Jayaraju ST, Lacor C, De Mey J, Noppen M, Vincken W, et al. Tracheal stenosis: a flow dynamics study. *J Appl Physiol*. (2007) 102:1178–84. doi: 10.1152/japplphysiol.01063.2006

44. Manczur T, Greenough A, Nicholson GP, Rafferty GF. Resistance of pediatric and neonatal endotracheal tubes: influence of flow rate, size, and shape. *Crit Care Med*. (2000) 28:1595–8. doi: 10.1097/00003246-200005000-00056

45. Hill EP, Power GG, Longo LD. Mathematical simulation of pulmonary O2 and CO2 exchange. *Am J Phys*. (1973) 224:904–7. doi: 10.1152/ajplegacy.1973.224.4.904

frontiers | Frontiers in Veterinary Science

TYPE Original Research
PUBLISHED 04 January 2024
DOI 10.3389/fvets.2023.1275013

OPEN ACCESS

EDITED BY
Pamela Murison,
University of Glasgow, United Kingdom

REVIEWED BY
David Bardell,
University of Liverpool, United Kingdom
Rocio Fernandez-Parra,
Catholic University of Valencia San Vicente Mártir, Spain

*CORRESPONDENCE
Olivia Brabant
✉ oliviabrabant22@gmail.com

RECEIVED 09 August 2023
ACCEPTED 07 November 2023
PUBLISHED 04 January 2024

CITATION
Brabant O, Karpievitch YV, Gwatimba A, Ditcham W, Ho HY, Raisis A and Mosing M (2024) Thoracic electrical impedance tomography identifies heterogeneity in lungs associated with respiratory disease in cattle. A pilot study. *Front. Vet. Sci.* 10:1275013. doi: 10.3389/fvets.2023.1275013

Thoracic electrical impedance tomography identifies heterogeneity in lungs associated with respiratory disease in cattle. A pilot study

Olivia Brabant[1]*, Yuliya V. Karpievitch[2,3], Alphons Gwatimba[2], William Ditcham[3], Ho Yin Ho[2], Anthea Raisis[1] and Martina Mosing[4]

[1]School of Veterinary Medicine, Murdoch University, Perth, WA, Australia, [2]Wal-yan Respiratory Research Centre, Telethon Kids Institute, Perth, WA, Australia, [3]School of Biomedical Sciences, University of Western Australia, Perth, WA, Australia, [4]Anesthesiology and Perioperative Intensive Care, Department for Companion Animals and Horses, University of Veterinary Medicine Vienna, Vienna, Austria

Respiratory disease in cattle is a significant global concern, yet current diagnostic methods are limited, and there is a lack of crush-side tests for detecting active disease. To address this gap, we propose utilizing electrical impedance tomography (EIT), a non-invasive imaging technique that provides real-time visualization of lung ventilation dynamics. The study included adult cattle from farms in Western Australia. The cattle were restrained in a crush. A standardized respiratory scoring system, which combined visual, auscultation, and clinical scores, was conducted by two non-conferring clinicians for each animal. The scores were blinded and averaged. During assessment, an EIT electrode belt was placed around the thorax. EIT recordings of ten suitable breaths were taken for analysis before the cattle were released back to the herd. Based on the combined examination scoring, the cattle were categorized as having healthy or diseased lungs. To allow visual interpretation of each breath and enable the creation of the quartile ventilation ratio (V_{QR}), Flow/Tidal Impedance Variation curves (F/TIV) were generated for each breath. The analysis focused on two EIT variables: The novel V_{QR} over time during inhalation and exhalation and global expiratory impedance (TIV_{EXP}) adjusted by breath length. A mixed effects model was used to compare these variables between healthy and diseased cattle. Ten adult cattle of mixed ages were used in the current analysis. Five cattle were scored as healthy and five as diseased. There was a significant difference in the examination scores between the healthy and diseased group ($P = 0.03$). A significant difference in V_{QR} during inhalation ($P = 0.03$) was observed between the healthy and diseased groups. No difference was seen in V_{QR} over time during exhalation ($P = 0.3$). The TIV_{EXP} was not different between groups ($P = 0.36$). In this study, EIT was able to detect differences in inhalation mechanics when comparing healthy and diseased cattle as defined via clinical examination, highlighting the clinical utility of EIT.

KEYWORDS

electrical impedance tomography, cattle, imaging, respiratory disease, thorax

1 Introduction

Respiratory disease in cattle is of global importance, with significant production and financial implications. In Australia, the significant economic impact equates to losses in the feedlot industry of $40 AUS million annually (1). Bovine respiratory disease syndrome (BRDS) has a multifactorial pathophysiology combining host, environment, and agent interactions. This syndrome impacts both the beef and dairy industry, affecting up to 10% of immature cattle and 2.5% adult cattle (2). Bovine respiratory disease syndrome is responsible for 60–90% of morbidity and mortality in feedlots and is the most common disease syndrome in cattle (3–6).

Current diagnostic methods for BRDS are predominantly limited to a thorough history and clinical examination. However, studies have shown that 35–50% of cattle exhibiting lesions in the lungs at slaughter had no history of disease and 64% with lesions at slaughter had received no treatment for BRDS (7–9). Methods to try and improve clinical diagnosis have been developed to include scoring scales such as the Wisconsin calf scoring scale and biomarkers for disease (10–12). However, with these methods specificity and sensitivity remains low (6, 13).

Imaging techniques for identifying lung disease is mainly limited to ultrasound, but in small calves there is the potential to use radiography and computed tomography (CT) (14–16). CT is not possible in adult cattle due to issues of the size of the gantry and is cost prohibitive in young and adult cattle (17–19). Although ultrasound can be utilized in both young and adult cattle, identification of lesions is limited to the pleural surface and superficial lung parenchyma, leaving deeper lesions undiagnosed (18).

More recently there have been developments in alternative monitoring tools to investigate lung ventilation in calves and adult cattle using electrical impedance tomography (EIT) (20, 21). These studies have shown that EIT can monitor ventilation in cattle, although assessment of changes in regional ventilation in the presence of respiratory disease has not been performed.

EIT is a non-invasive imaging modality that uses imperceptible alternating currents to detect impedance changes where there is an alteration in electrical conductivity in the body. Such alterations are due to changes in regional distribution of ventilation within the lung, or changes in blood flow (22, 23). These impedance changes can be reconstructed into real-time images of ventilation distribution, and perfusion, through the presence of gas or blood and tissue stretch, influences those impedance changes (22–24). Numerous studies support its use for investigating lung pathology, such as pneumothorax in humans (25), pathologic ventilatory incidents created in porcine models (26), and acute respiratory distress syndrome (27, 28), including that associated with the recent COVID-19 outbreak (29, 30).

Thus far, there have been studies in veterinary medicine to explore ventilation and perfusion dynamics in healthy conscious and anesthetized animals (20, 31–34). Respiratory studies in horses have used the steepness of the flow/tidal impedance variation curve (F/TIV) and intercept on the expiratory F/TIV curve before and after histamine provocation and salbutamol nebulization to explain differences in the shape of the curve. However, there has only been one study investigating pathology in horses suffering from left-sided cardiac volume overload (35) and no investigation to date of lung pathology in cattle.

The aim of this paper is to evaluate if EIT variables can detect a difference in the homogeneity of ventilation between healthy cattle and cattle with respiratory disease. Our hypothesis is that, by employing EIT, we will assess respiratory mechanics in cattle that can be associated with disease develop EIT-based classification metrics that will correlate with standard clinical examinations and provide additional lung ventilation information.

2 Methods

2.1 Ethics statement

This prospective experimental study was performed with the approval of the Murdoch University Animal Ethics Committee (R3275/20). The Australian code for the care and use of animals for scientific purposes was followed.

2.2 Animals

Data were collected from two dairies and three beef suckler units in the Perth metropolitan and Southwest regions of Western Australia. The farms were contacted prior to the study; they were a mixture of veterinary teaching farms, clients of the university practice, and external contacts. They were provided with an overview of the study and proposed outcomes and agreed to participate prior to commencement of the study. The farms were selected to cover diversity in conformation using a mixture of beef and dairy cattle. Suitability of participation was assessed prior to commencement of the study to ensure all animals were used to being handled and spending time restrained in a crush.

The participating farms sourced animals with and without suspected respiratory disease based on their observations. Five healthy animals (no previous treatment for respiratory disease) and five animals exhibiting clinical signs of respiratory disease were selected to participate in the initial pilot study from a larger cohort of 83 animals. The cattle were assigned a letter from A through to J and categorized into the diseased or healthy group post examination, prior to the analysis. Prior to the study, the animals were on pasture and subject to routine management on the prospective farms before being brought to the handling facilities. Each animal was restrained in a standing position within a crush and hosed down with water before EIT electrode belt placement. All animals tolerated belt placement well to allow reliable data to be collected.

2.3 Instrumentation and data collection

The stretchable EIT belt, with 32 electrodes mounted equidistantly, was prepared by placing low-conductive ultrasound gel (Aquasonic®, Fairfield, USA) onto each electrode prior to placement on the animal. The belt was placed circumferentially on the animal at the level of the 5th intercostal space (ICS) and

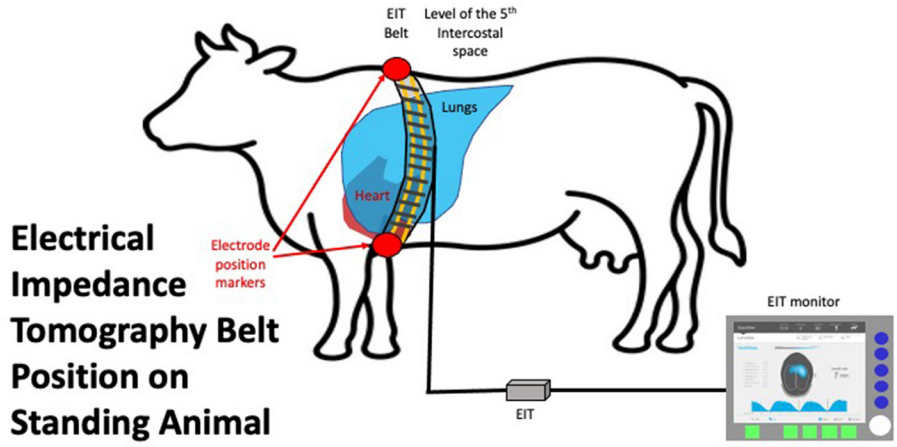

FIGURE 1
EIT belt *in situ* on an animal in standing position placed vertically at the level of the 5th intercostal space. The connector to the EIT control unit is shown on the **left** of the image. The EIT control unit is connected to a laptop with data recording and basic analysis software.

fastened on the ventral aspect. Care was taken to ensure the belt was vertical and the middle of the belt between electrode 16 and 17 was at the point of the withers. The belt was connected to the EIT device (Sentec, Landquart, Switzerland), which was connected to a laptop to allow data recording using BBVet Software (Sentec, Landquart, Switzerland) (Figure 1). All cattle were subject to at least 2 min of measurements to allow 10 consecutive breaths to be collected without movement artifacts or failing electrodes. After completion, the recording was saved to be analyzed retrospectively. The belt was removed and the animal was released from the crush and returned to the herd.

2.4 Data analysis

2.4.1 Clinical examination analysis

The circumference, weight, and body condition score (thin-obese: 1–5 using quarter scores) of each animal was measured prior to placement of the belt. Respiratory clinical examinations were performed in accordance with a modified Wisconsin calf scoring scale modified for adult cattle by Blakebrough-Hall et al. (10). Two experienced veterinarians who were blinded to healthy or diseased status, and each other, completed the examinations. Separate recording sheets were used with no conferring. The order in which each veterinarian examined each animal was randomized. A number was drawn out of a blinded envelope for each animal, stating either one or two to indicate which veterinarian should examine the animal first. A clinical examination was conducted in three parts. The visual clinical signs (Part A), including head carriage, labored breathing, nasal discharge, ocular discharge, rumen fill, and lethargy, were allocated a score of 0–3 (unremarkable-profound changes for each parameter). A diseased animal was classified as having an averaged visual score $\geq$3.5 out of a possible total of 25. A separate lung auscultation (Part B) scored 0–3 (no abnormalities-abnormal lung sounds throughout the entire lung fields and prolonged respiratory sounds). A diseased animal was classified as having a lung auscultation $\geq$1 from an average of both examiners. The final part of the examination was the clinical score (Part C), where rectal temperature ($0 < 40–1 \geq 40^{\circ}$C) and respiratory rate (0 < 40 breaths per minute-1 > 40 breaths per minute) were scored. A diseased animal was classified as having a clinical score $\geq$1 with a maximum of two. The cut off for a diseased animal was a visual score $\geq$3.5, a lung auscultation score of $\geq$1, and a clinical score $\geq$1. Scores from both examiners were averaged to give a visual and clinical diagnosis and categorized into healthy or diseased.

2.4.2 EIT analysis

EIT recordings were taken from all cattle and retrospectively analyzed using reconstruction software (IBEX, Sentec Landquart, Switzerland) to find 10 representative breaths. At least three representative, movement artifact-free breaths from each animal were used for further analysis (36). The EIT analysis was initially performed with the researcher blinded to the results of the clinical examination to eliminate sampling bias of breath selection.

The EIT data from ten cattle were further analyzed using a custom script [written in Python 3.10.8, (CreateSpace, Scotts Valley, California)] and visualized using R 4.2.2 (Development Core Team 2020, GNU, Public license, USA) with all pixels within the image used in the analyses. First, the EIT files for all cattle were opened in IBEX and the impedance data corresponding to the appropriate breaths (up to 10 breaths per EIT file) were exported as .MAT files for external processing. These .MAT files were then processed using Python scripts using packages SciPy (37), NumPy (38), Pandas (39), and Matplotlib (40). Specifically, the impedance and rate of change of impedance across time for each breath was computed to generate Flow/Tidal impedance variation (F/TIV) curves which were exported as .CSV files for statistical analysis in R.

2.4.3 EIT variables

1) Flow/Tidal impedance variation curve (F/TIV)

F/TIV describes the impedance and rate of change in impedance across time in a single breath. The global TIV is given, rather than volume, as no calibration of impedance change to a corresponding change in air to volume has been determined in cattle. Linear relationships between change in impedance and change in the volume of air in the lungs have been seen (31, 41). It is assumed that impedance change correlates to changes in volumes of gas in the lung regions over a single breath (42). To generate a flow parameter, we have used impedance change as a surrogate for volume, to allow the first derivative of which to be analogous to flow (F). The curve is generated by plotting the average impedance value of all pixels in each 2-D EIT frame during the entire breath (TIV) against the 1st derivate of the TIV, flow (F) over time, measured in arbitrary units, as no calibration to volume has been conducted. The shape of this curve was used to identify differences between lung disease states. Scaling was employed where the total impedance change was smaller, to allow visualization and description of the curve. A smooth semicircular curve with few or no peaks/troughs in inhalation and exhalation was observed in healthy animals and irregular-shaped curves that showed multiple peaks in both inhalation and exhalation were noted in diseased cattle (Figure 2).

2) Global expiratory impedance variation (TIV_{EXP})

TIV_{EXP} describes the impedance change of all pixels between the beginning and end of expiration of all pixels within the lung region of interest (ROI). The TIV_{EXP} is calculated for each breath by subtracting the impedance at the beginning of exhalation from the impedance at the end of exhalation in all pixels, is normalized to breath length, and is displayed in arbitrary units.

3) Quartile ventilation ratio (V_{QR})

To describe the changes in the shape of the F/TIV curves, we developed a novel numerical measure, V_{QR}, to describe the inhomogeneity in lung filling over time. V_{QR} is the ratio of total impedance change between the first 25% and last 25% of inhalation or exhalation with the middle 50% of inhalation or exhalation: The F/TIV curves were divided into quartiles (0–25% = Q1, 25–50% = Q2, 50–75% = Q3, 75–100% = Q4) and the median point (Figure 3) on the F/TIV curve of each quartile was used to create a ratio of the sum of Q1 and Q4 and the sum of Q2 and Q3. The V_{QR} was measured for all breaths for that individual to create a fractional rate of change (Equation 1) (Figure 3). The V_{QR} was calculated for inhalation V_{QRi} and exhalation V_{QRe}.

$$V_{QR} = \frac{(Q1 + Q4)}{(Q2 + Q3)}$$

2.5 Statistical analysis

Statistical analysis of the veterinary scores were performed using R statistical software version 4.2.2 (Development Core Team 2020, GNU, Public license, USA). Descriptive statistics (median IQR) of visual scores, lung auscultation scores, temperature, respiratory rate, weight, circumference, and body condition scores are shown in Table 1. Agreement between the two scorers was conducted. Non-parametric tests were used to analyse the data that was not normally distributed. Wilcoxon Rank Sum Test and multiple testing adjustment using Banjamini-Hochberg adjustment were used to describe the differences between diseased and healthy visual scoring, lung auscultation, and clinical score (Table 1). The EIT data was analyzed using a linear mixed effects model to explore differences between the diseased and healthy groups, using R statistical software and the ImerTest package (43). Wilcoxon Rank Sum Test was used for the V_{QRe} and V_{QRi} statistical analysis after averaging V_{QR} for each breath within each animal. A p-value of <0.05 was considered significant.

3 Results

Ten cattle were examined, respiratory disease assessment was conducted, EIT images taken, and results displayed as median (IQR). Nine adult female cows and one male steer of mixed ages [2.5 (0.55) years], with a weight of [552 (430) kg] and body condition score of [1.75 (2)], were included in the study. Of the ten animals, five were classified as diseased, namely cattle B, C, D, E, and G, and five cattle were classified as healthy, namely cattle A, F, H, I, and J. Diseased cattle had a visual score equal to or more than 3.5, a lung auscultation equal to or more than 1, and a clinical score more than 1. The maximum total score including visual score lung auscultation and clinical score in the healthy animals was 2.5 with a variance ($s^2 = 0.14$) and the maximum in the diseased animals was 15.5 ($s^2 = 15.88$) out of a possible 25. Agreement between the two scorers was conducted with correlation of scores for visual score ($R = 0.93$) and lung auscultation ($R = 0.82$), respectively.

An overall difference was observed between the healthy and diseased cattle ($p = 0.03$). Differences were observed from visual score ($p = 0.03$), lung auscultation ($p = 0.03$), and clinical score ($p = 0.03$), respectively. No difference was seen for weight, thorax circumference, or body condition score between healthy and diseased cattle (Table 1).

There was no statistical difference in TIV_{EXP} between healthy and diseased cattle ($p = 0.36$) (Figure 4). Exhalation V_{QRe} ($p = 0.3$) also did not show a difference between healthy and diseased cattle (Figure 5; Table 2). By comparison, inhalation V_{QRi} ($p = 0.03$) did show a difference between healthy and diseased cattle (Figure 5; Table 2).

4 Discussion

In this study, we utilized existing knowledge of lung pathology and physiology in cattle to investigate alterations in the homogeneity of ventilation using EIT that may be associated with respiratory disease. We showed that expiratory tidal impedance variation adjusted to breath length illustrated no difference between healthy and diseased populations. However, inhomogeneous ventilation and filling was detected between the two populations of cattle when comparing quartile ventilation ratio (V_{QRi}) during inhalation. Thus, our study is the first to report the ability of EIT to detect differences between healthy and animals known to be

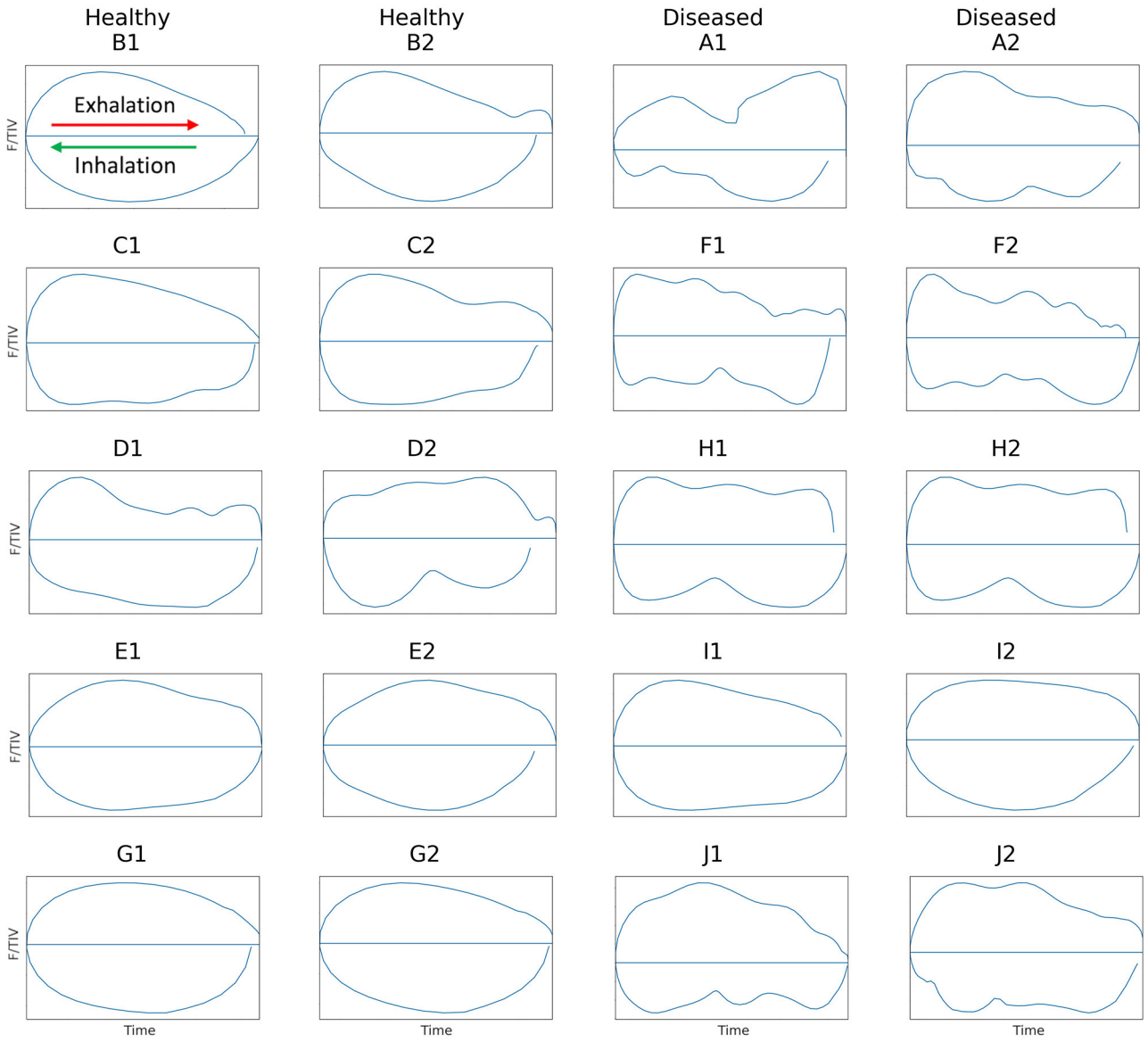

FIGURE 2
Flow/tidal impedance variation (F/TIV) curves in ten cattle illustrating two breaths from each animal. Inhalation is shown in the **bottom** curve of each breath moving **right to left** (green arrow) and exhalation is shown in the **top** half of each breath moving **left to right** (red arrow). Healthy cattle are shown in the first two columns on the **left** with smooth F/TIV curves and diseased cattle are in the last two columns to the **right** with irregular curves illustrating multiple peaks in each breath.

diseased, when compared to the results from standardized clinical examination of cattle.

Due to both the unique anatomy cattle possess compared with other species, and the fact that the majority of lung disease occurs as a result of inhaled pathogens, it was expected that we would observe inhomogeneous lung ventilation and filling rates in the diseased cattle. Our results reflect this inhomogeneity in filling over time. Anatomically, cattle lungs contain separate lung lobules with well-developed interlobular septa, preventing pathogens from passing easily from one lobe to the next (44). Cattle, unlike small animals such as dogs, have reduced collateral ventilation (45, 46). This reduces the ability of the lungs to shift ventilation to other lobes, especially when pathology is present (47–49), leading to inhomogeneous filling.

Respiratory disease of the lung tissue causes a decrease in the ability of alveoli to open, requiring elevated opening pressures to fill (50). This can also change the time constants of lung units, where one lung unit is opening more slowly than others when pathology is present. This is especially true in cattle due to their unique anatomy of the lung, as described above. Based on these physiologic facts, it is not surprising that a significant difference was found between healthy and diseased cattle for a variable describing the homogeneity of lung filling rate. Conversely, expiration is considered passive, and therefore disease of the lung tissue is less

likely to lead to variation in emptying times (51). In this study no difference in the expiratory EIT variables was found.

We observed significant differences between healthy and diseased cattle populations when comparing clinical respiratory disease scoring to novel algorithms detecting the inhomogeneity of filling using EIT.

In one animal (D) deemed healthy, the inhalation curve had more troughs than the other four healthy cattle, suggesting that this animal may have been diseased. On the other hand, for an animal (I) considered diseased, the inhalation and exhalation of both breaths F/TIV curves were smooth, suggesting that this animal was healthy (Figure 2). This suggests that F/TIV curves may be more sensitive than the clinical examination, or not as representative in cattle as in horses (42). Reviewing the clinical examination, there was no evidence to suggest that animal D was unhealthy, however, the V_{QR} suggested this animal did show evidence of respiratory disease. The results of the examination of data for animal I data confirmed significant nasal discharge and a low head carriage with labored breathing and a positive auscultation and clinical score, yet the V_{QRi} and V_{QRe} were more representative of a healthy animal or an animal with focused upper respiratory tract disease. Clinical scoring has limited sensitivity, as explained in the introduction (7, 9) however, one explanation for the lower V_{QR} could be disease contained within the upper respiratory tract, such as chronic granular rhinitis or Infectious Bovine Rhinotracheitis (IBR), that predominantly affects the upper airways (52, 53). If these conditions were chronic or recrudesced as part of a carrier status, then the animal in question may have compensated for this and was able to inhale effectively despite the increase in resistance to the airways. Another reason could be environmental: heavy dust loads during summer in West Australia may cause nasal discharge, lowered head carriage, and labored breathing yet there may be no underlying lung pathology. Analysis of further animals will allow further explanation of these outliers in future studies.

Examination of a novel EIT variable in this study is the first step to establish EIT as a diagnostic tool to define lung disease states. Human medicine has used forced expiratory volume over maximal expiration to explain differences in global and regional ventilation before and after bronchospasmolysis (54–56). Respiratory studies in horses have used the steepness of the flow/Tidal impedance variation (F/TIV) curve and inflection point of the expiratory F/TIV curve before and after histamine provocation and salbutamol nebulization to explain differences (42). We used the peaks and troughs of the curve during inhalation and exhalation to create a ratio illustrating the differences in filling and emptying over the course of a breath. In our study we did not observe a difference in the shape of the F/TIV curves between healthy and diseased cattle during exhalation and could not gather forced expiration due to patient compliance. However, we did observe variations in the shape of the F/TIV curve during inhalation and used the quartile ventilation ratio (V_{QR}) to describe those changes in the shape of the curve and filling inhomogeneities numerically.

Tidal impedance variation over one breath in another study has been shown to have a linear relationship with tidal volume in cattle (21), however, no conversion factor from impedance change to volume exists. In this study the tidal impedance change during expiration was used to define expiratory volume over time. There was no difference in TIV_{EXP} between diseased and sick cattle, therefore any differences in the fractions of ventilation relating to inhomogeneity in filling are more likely to be a true difference and not differences arising from changes in total volume or breath length.

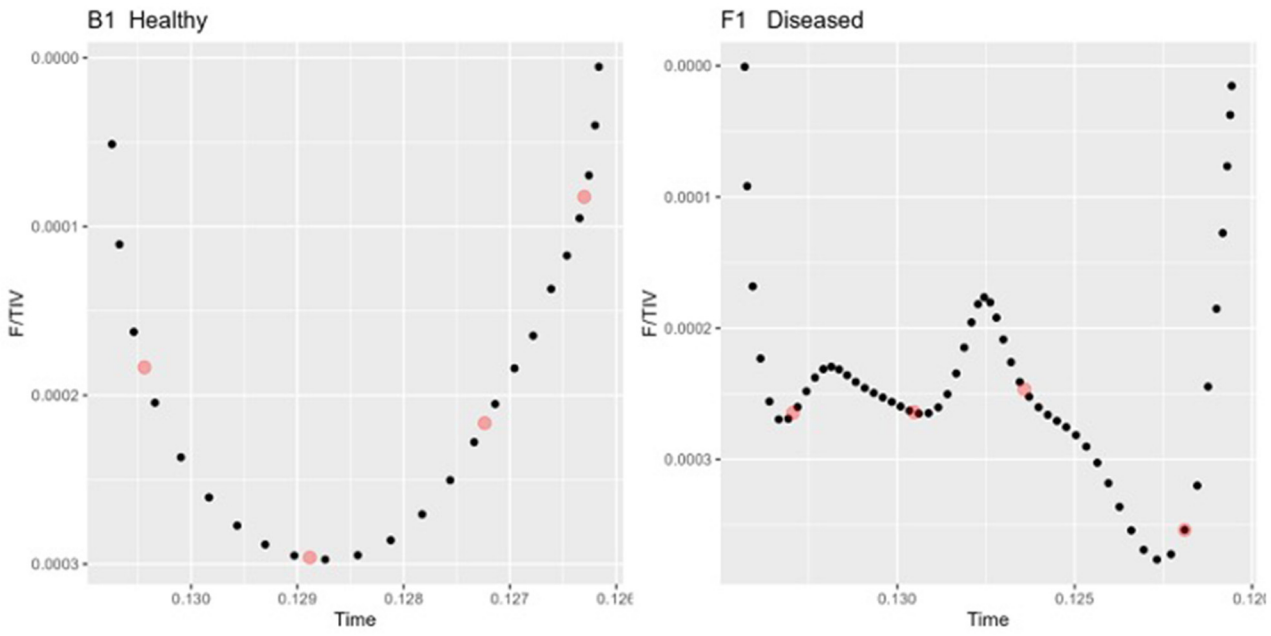

FIGURE 3
Two inhalation sections of the Tidal impedance variation (TIV) curves over time in one healthy **(left)** and one diseased animal **(right)**. The dots (red) indicate the points taken as the medians of each quartile Q1-Q4 used to compute the Quartile Ventilation Ratio (V_{QR}).

10.3389/fvets.2023.1275013

TABLE 1 Median and Interquartile range (IQR) of the ten analyzed cattle, showing the visual and respiratory scores, temperature, respiratory rate, weight, circumference of the thorax, and body condition score of healthy and diseased cattle.

Cows analyzed $N = 10$	Visual score (0–21)	Lung auscultation (0–3)	Clinical score (0–2)	Temperature (°C)	Respiratory rate (BPM)	Weight (Kg)	Circumference of thorax (cm)	Body condition score (1–5)
Healthy ($n = 5$) (IQR)	2 (0.5)*	0 (0)*	0 (0)*	38.9 (0.5)	32 (0)	610 (72)	210 (15)	2.75 (0.25)
Diseased ($n = 5$) (IQR)	6 (1)*	1.5 (0.5)*	1 (0)*	39.1 (0.7)	46 (4)	471 (151)	189 (22)	2.5 (1)
P-values	(p-0.03)	(p-0.03)	(p-0.03)	(p-0.4)	(p-0.05)	(p-0.06)	(p-0.06)	(p-0.06)

*$p < 0.05$.

We observed a significant difference in filling time when comparing the V_{QRi} during inhalation. Healthy cattle have a lower V_{QRi} of filling when compared to diseased cattle, suggesting that in a healthy lung filling takes place over a shorter portion of the breath compared to diseased cattle. The shortened filling time is visible at 0–25% and 75–100% of the filling where minimal impedance change was measured (Figure 6). This suggests that in healthy cattle most of the filling of the lungs happens within the second and third quartile of the breath. In diseased cattle, impedance changes were observed in each quartile of the whole breath. There was no significant difference seen in the V_{QRe} (Figure 7); this may be due to the passive nature of exhalation compared to active inhalation, leading to less change. However, we would expect changes in exhalation dynamics due to airway resistance and air trapping from obstructive disease. To fully investigate this further, a larger cohort of animals would be required and further investigation into the inhomogeneity of breathing and rate of change of impedance globally and regionally over time.

With obstructive diseases such as asthma in horses the work of breathing increases due to overinflation of the lung, reduction in the expired volume, and higher inspiratory filling pressures (57, 58), leading to extended inhalation times to reach adequate filling. In our results, we observed the majority of ventilatory changes occurring during the middle portion of the breath in healthy cattle. In comparison, diseased cattle had ventilatory changes throughout the whole breath, which suggests a similar increased work of breathing where pathology may be present. Airway diameter may also be a contributing factor to ventilation changes and filling times. Cattle have increased resistance in the nares and trachea, evident in diseases such as infectious bovine rhinotracheitis, where inflammation narrows the trachea; this may further contribute to increased inhalation time and flow due to the increased resistance in the upper airway (52, 59, 60).

The shape of the inhalation F/TIV curve appeared subjectively smoother in healthy cattle with less observable peaks, which is in agreement with Lekeux, who described inhalation flow/volume curves, using mask-Fleisch pneumotachography, as more rounded (61). The flow/volume curves were derived from maximal inhalation and exhalation plotted against volume. Lekeux noted more changes in the expiratory curve in diseased cattle, which differs from the findings in our study where changes were associated with inhalation (61). The difference noted in our results may be explained by the position of measurement. EIT measures at the level of the thorax, making changes in impedance as a surrogate for volume potentially easier to detect than a pneumotachograph connected to a breathing mask measuring at the nares. The significance of these differences in the shape of the F/TIV curve are not fully understood. Initial observations do indicate a difference between cattle and horses, which contrasts from previous work. To fully understand the mechanics of breathing in cattle, we will perform further analyses on a larger cohort of animals.

4.1 Limitations

A limitation of this study was the small sample size, but we note that significant differences were seen in both the healthy and

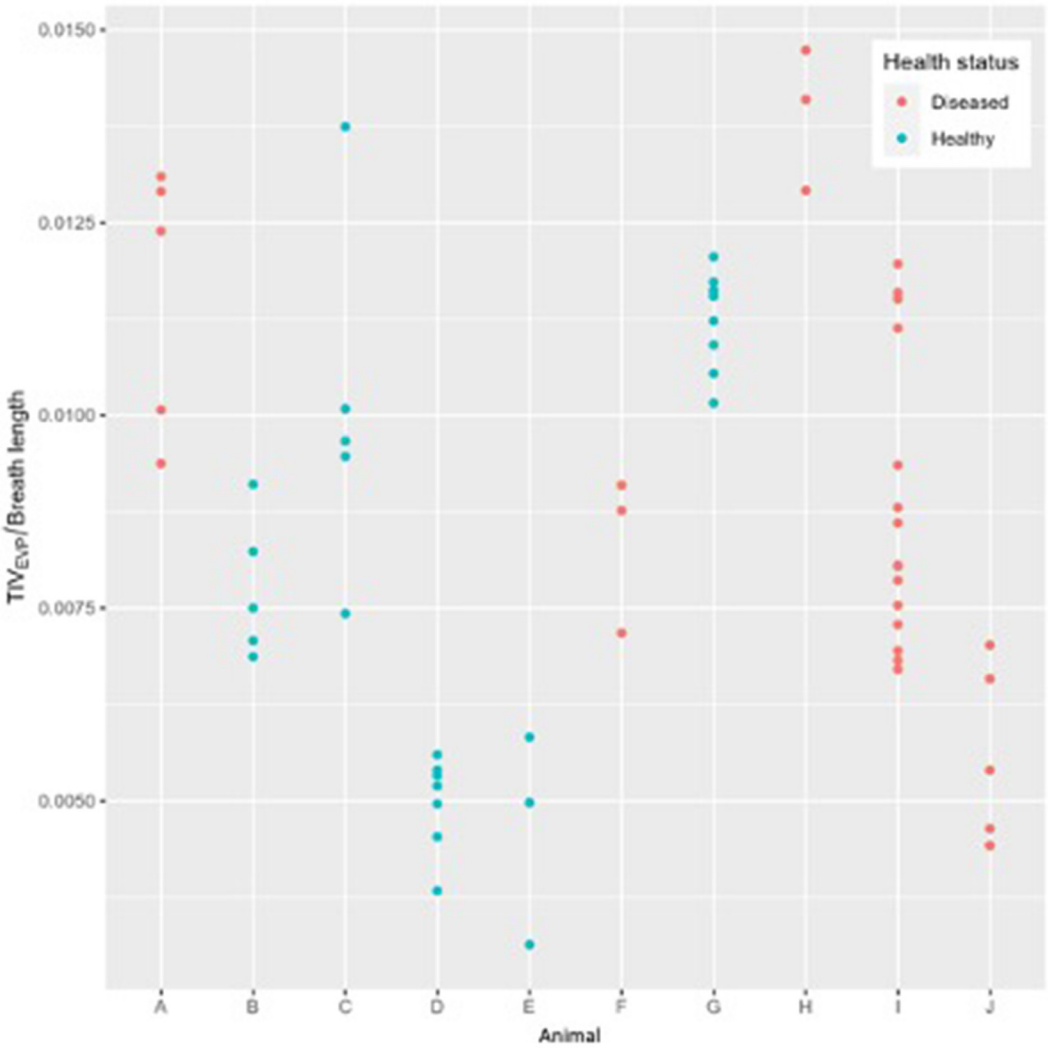

FIGURE 4
Expiratory tidal impedance variation (TIV$_{EXP}$) by breath length (arbitrary units) for five healthy cattle (green) and five diseased cattle (red) examining up to ten breaths from each animal.

diseased group when comparing clinical respiratory scores and specific EIT variables. In the EIT analysis, one animal appeared to be an outlier for the V_{QRi}, while in in the F/TIV curves one healthy and one diseased animal appeared to be outliers. Data from a larger cohort of animals would improve the robustness of the analysis, and comparison of EIT to other diagnostics including histology, ultrasound, and post-mortem would allow more accurate confirmation of findings.

Comparison to clinical examination is limited, as 35–50% of respiratory disease is not detected via clinical examination (8, 62); therefore the sensitivity of detection is reduced. The scoring system structured the clinical examination however, this was not a validated system and therefore the health status determination is limited from this approach. Further testing including blood testing and post-mortem analysis would improve the robustness of the system, however, this was beyond the scope of the study.

In our study, global images were examined using all pixels in the obtained image including those outside of the lungs. To provide a more accurate analysis of pixels derived from lung tissue and not heart or ruminal gas will require further delineation of regions of interest. In initial studies, creation of a global measure negates the issue of using regions of interest, however, future studies would benefit from delineation to allow more accurate analysis. In addition, regional areas and individual pixels have not been examined in this study, so there are potential regional changes which may influence the overall categorization of disease. With a single plain EIT, a lens-shaped ellipse of data is gathered and reconstructed and the position of the 5th intercostal space is used to allow the maximal area of lung tissue to be gathered, however the cranial and caudal tips of the lung will not be included in the data collected, therefore these areas will not be represented in the analysis. In future studies, development of a 3-D belt will improve data capture of the entire lung region, and improved definition of the region of interest, individual pixel analysis, and investigation of the slope of the F/TIV curve may provide greater detail to define disease.

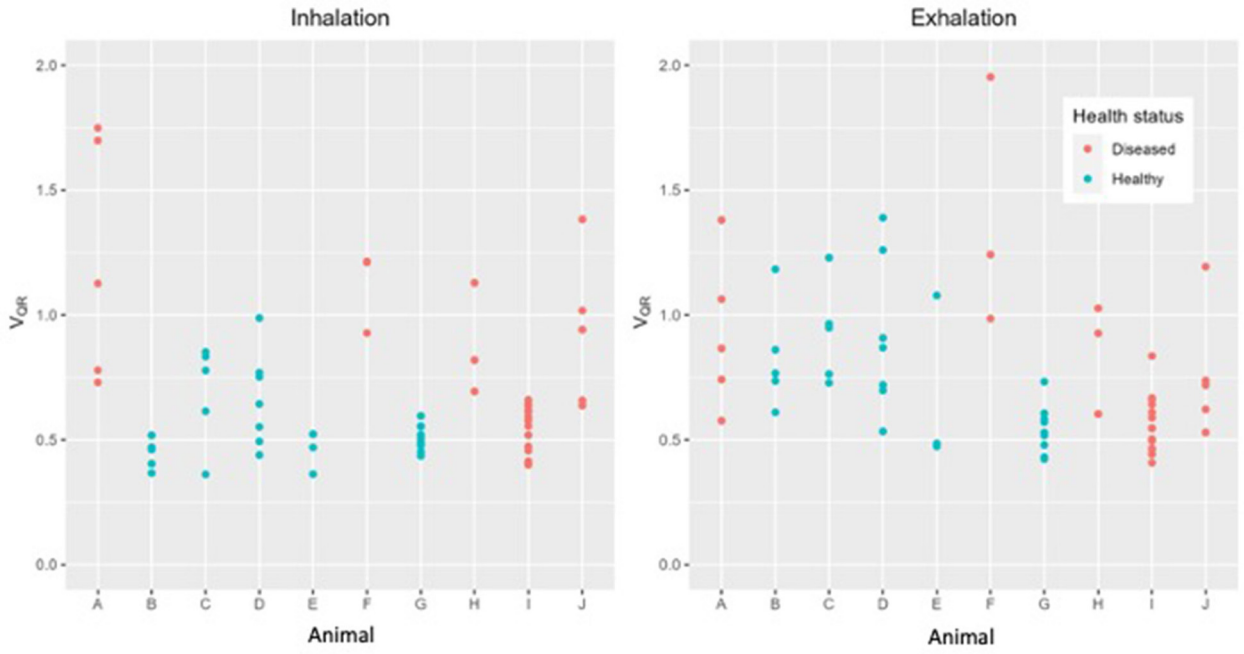

FIGURE 5
Quartile ventilation ratio (V_{QR}) in ten cattle during inhalation **(left)** and exhalation **(right)**. During inhalation V_{QR} differentiates between healthy (green) and diseased (red) cattle. Each dot represents a single breath, up to ten breaths have been analyzed in each animal.

TABLE 2 Results of the mixed-effects model comparison of diseased vs. healthy cattle using the quartile ventilation ratio (V_{QR}) during inhalation and exhalation.

Cows analyzed $N = 10$	Estimate	Std. error	Degrees of freedom (df)	*t*-value	Pr (>|t|)
V_{QRi} ($n = 10$) inhalation	−0.351	0.128	8.421	−2.755	0.03*
V_{QRe} ($n = 10$) exhalation	−0.136	0.181	7.76	−0.755	0.3

*$p < 0.05$.

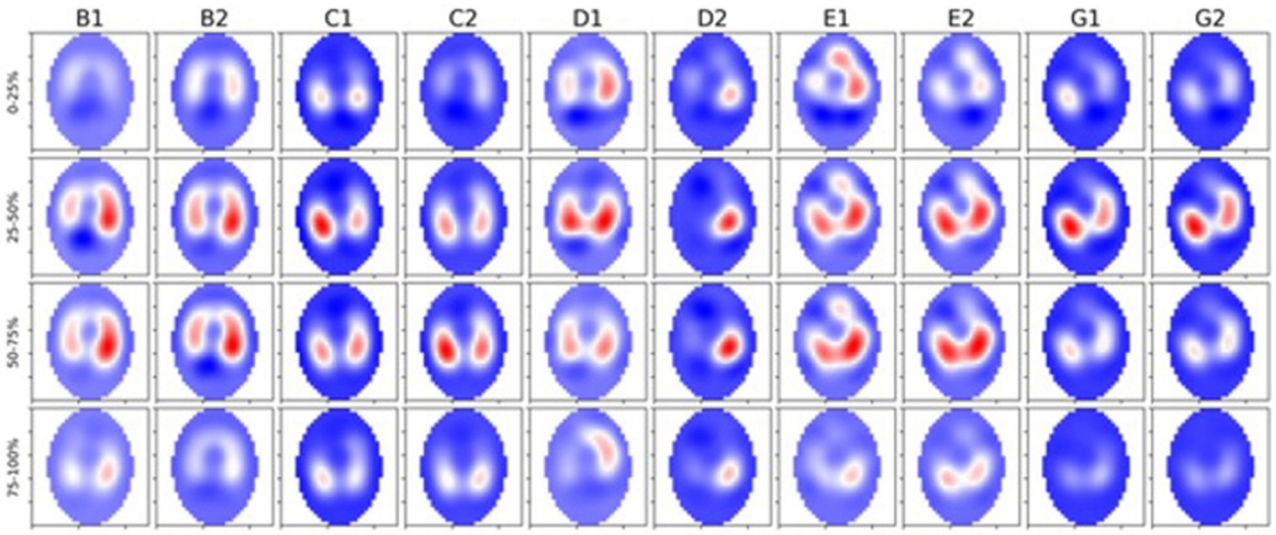

FIGURE 6
Five healthy cattle (B, C, D, E, and G) showing global images of total impedance variation over time during inhalation at 0–25%, 25–50%, 50–75%, and 75–100% of total impedance change **(top-bottom)**. Two breaths are displayed from each animal (1 and 2 preceded by the letter of each animal). The color gradient illustrates areas of no impedance change (dark blue) scaled up to areas of maximal impedance change (red).

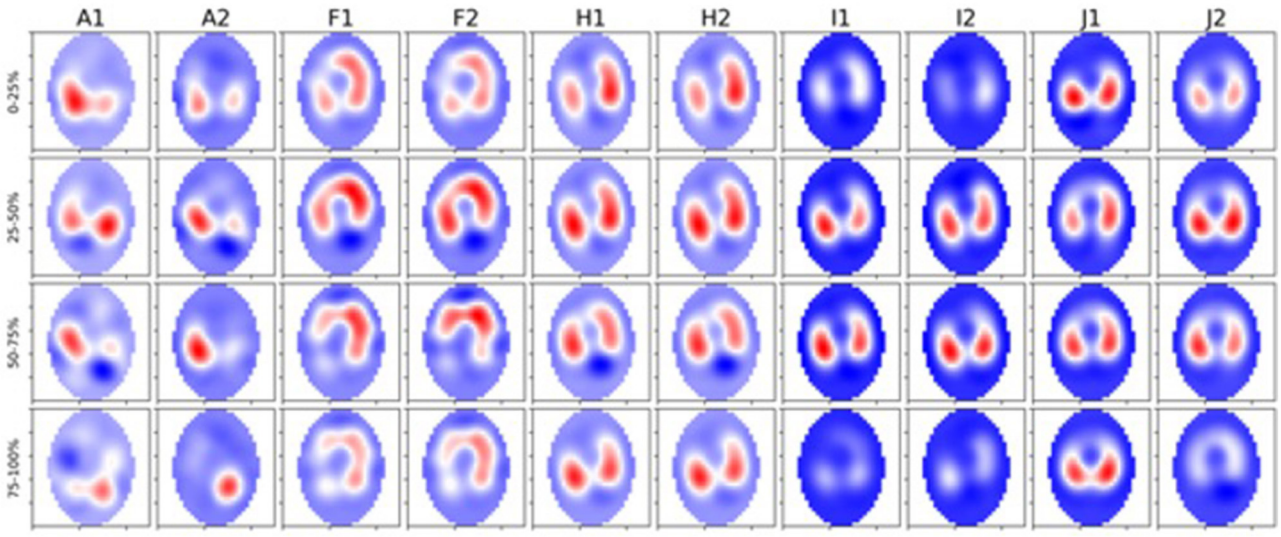

FIGURE 7
Five diseased cattle (A, F, H, I, and J) showing global images of total impedance variation over time during inhalation at 0–25%, 25–50%, 50–75%, and 75–100% of total impedance change **(top-bottom)**. Two breaths are displayed from each animal (1 and 2 preceded by the letter of each animal). The color gradient illustrates areas of no impedance change (dark blue) scaled up to areas of maximal impedance (red).

5 Conclusions

Electrical impedance tomography is able to detect differences in the inhalation portion of the breath when comparing healthy and diseased cattle defined via clinical examination. These initial findings highlight the potential of EIT as a useful imaging tool for the diagnosis of respiratory disease in cattle. Future studies should involve larger cohorts and compare to other diagnostic imaging methods as well as post-mortem samples when available to confirm EIT findings.

Data availability statement

The raw data supporting the conclusions of this article will be made available by the authors, without undue reservation.

Ethics statement

The animal studies were approved by Murdoch University Animal Ethics Committee R3275/20. The studies were conducted in accordance with the local legislation and institutional requirements. Written informed consent was obtained from the owners for the participation of their animals in this study.

Author contributions

OB: Data curation, Formal analysis, Investigation, Methodology, Writing—original draft, Writing—review & editing. YK: Formal analysis, Software, Writing—review & editing. AG: Formal analysis, Software, Writing—review & editing. WD: Formal analysis, Writing—review & editing. HH: Formal analysis, Software, Writing—review & editing. AR: Supervision, Writing—review & editing. MM: Conceptualization, Investigation, Methodology, Project administration, Supervision, Writing—review & editing.

Funding

The author(s) declare that no financial support was received for the research, authorship, and/or publication of this article.

Acknowledgments

The authors would like to thank the participating farms for agreeing to participate in this study and special thanks to Dr. Annika Carbonnier and Dr. Sarah Loroesch for their assistance with data collection.

Conflict of interest

The authors declare that the research was conducted in the absence of any commercial or financial relationships that could be construed as a potential conflict of interest.

Publisher's note

All claims expressed in this article are solely those of the authors and do not necessarily represent those of their affiliated organizations, or those of the publisher, the editors and the reviewers. Any product that may be evaluated in this article, or claim that may be made by its manufacturer, is not guaranteed or endorsed by the publisher.

References

1. Infographic AE. Preview: economic effects of bovine respiratory disease. *J Anim Sci.* (2020) 98:skaa042. doi: 10.1093/jas/skaa042

2. Smith DR. Risk factors for bovine respiratory disease in beef cattle. *Anim Health Res Rev.* (2020) 21:149–52. doi: 10.1017/S1466252320000110

3. Hanzlicek GA, Renter DR, White BJ, Wagner BA, Dargatz DA, Sanderson MW, et al. Management practices associated with the rate of respiratory tract disease among preweaned beef calves in cow-calf operations in the United States. *J Am Vet Med Assoc.* (2013) 242:1271–8. doi: 10.2460/javma.242.9.1271

4. Callan RJ, Garry FB. Biosecurity and bovine respiratory disease. *Vet Clin.* (2002) 18:57–77. doi: 10.1016/S0749-0720(02)00004-X

5. Smith RA. Impact of disease on feedlot performance: a review. *J Anim Sci.* (1998) 76:272. doi: 10.2527/1998.761272x

6. Timsit E, Dendukuri N, Schiller I, Buczinski S. Diagnostic accuracy of clinical illness for bovine respiratory disease (BRD) diagnosis in beef cattle placed in feedlots: a systematic literature review and hierarchical Bayesian latent-class meta-analysis. *Prev Vet Med.* (2016) 135:67–73. doi: 10.1016/j.prevetmed.2016.11.006

7. Potter T. Early detection and treatment for bovine respiratory disease. *Livestock.* (2020) 25:254–60.

8. Wittum T, Woollen N, Perino L, Littledike E. Relationships among treatment for respiratory tract disease, pulmonary lesions evident at slaughter, and rate of weight gain in feedlot cattle. *J Am Vet Med Assoc.* (1996) 209:814–8.

9. Baptiste KE, Kyvsgaard NC. Do antimicrobial mass medications work? A systematic review and meta-analysis of randomised clinical trials investigating antimicrobial prophylaxis or metaphylaxis against naturally occurring bovine respiratory disease. *Pathog Dis.* (2017) 75:7. doi: 10.1093/femspd/ftx083

10. Blakebrough-Hall C, Dona A, D'occhio MJ, McMeniman J, González LA. Diagnosis of Bovine Respiratory Disease in feedlot cattle using blood 1H NMR metabolomics. *Sci Rep.* (2020) 10:115. doi: 10.1038/s41598-019-56809-w

11. McGuirk SM, Peek SF. Timely diagnosis of dairy calf respiratory disease using a standardized scoring system. *Anim Health Res Rev.* (2014) 15:145–7. doi: 10.1017/S1466252314000267

12. Aly SS, Karle BM, Williams DR, Maier GU, Dubrovsky S. Components of a risk assessment tool for prevention and control of bovine respiratory disease in preweaned dairy calves. *Anim Health Res Rev.* (2020) 21:153–9. doi: 10.1017/S1466252320000201

13. Potter T, Barrett D, Cutler K, Hart K, Biggs A. Clinical forum: bovine respiratory disease. *Livestock.* (2017) 22:6–11. doi: 10.12968/live.2017.22.1.6

14. Rhodes V, Ryan EG, Hayes CJ, McAloon C, O'Grady L, Hoey S, et al. Diagnosis of respiratory disease in preweaned dairy calves using sequential thoracic ultrasonography and clinical respiratory scoring: temporal transitions and association with growth rates. *J Dairy Sci.* (2021) 104:11165–75. doi: 10.3168/jds.2021-20207

15. Buczinski S, Forté G, Francoz D, Bélanger A-M. Comparison of thoracic auscultation, clinical score, and ultrasonography as indicators of bovine respiratory disease in preweaned dairy calves. *J Vet Int Med.* (2014) 28:234–42. doi: 10.1111/jvim.12251

16. Fowler J, Stieger-Vanegas SM, Vanegas JA, Bobe G, Poulsen KP. Comparison of thoracic radiography and computed tomography in calves with naturally occurring respiratory disease. *Front Vet Sci.* (2017) 4:101. doi: 10.3389/fvets.2017.00101

17. Ollivett T, Hewson J, Shubotz R, Caswell J, editors. Ultrasonographic progression of lung consolidation after experimental infection with Mannheimia haemolytica in Holstein bull calves. In: *Proceedings of the Forty-Sixth Annual Conference. American Association of Bovine Practitioners.* Milwaukee, WI (2013).

18. Scott PR. Clinical presentation, auscultation recordings, ultrasonographic findings and treatment response of 12 adult cattle with chronic suppurative pneumonia: case study. *Irish Vet J.* (2013) 66. doi: 10.1186/2046-0481-66-5

19. Cuevas-Gómez I, McGee M, McCabe M, Cormican P, O'Riordan E, McDaneld T, et al. Growth performance and hematological changes of weaned beef calves diagnosed with respiratory disease using respiratory scoring and thoracic ultrasonography. *J Anim Sci.* (2020) 98:skaa345. doi: 10.1093/jas/skaa345

20. Bleul U, Wey C, Meira C, Waldmann A, Mosing M. Assessment of postnatal pulmonary adaption in bovine neonates using electric impedance tomography (EIT). *Animals.* (2021) 11:3216. doi: 10.3390/ani11113216

21. Brabant O, Crivellari B, Hosgood G, Raisis A, Waldmann AD, Auer U, et al. Effects of PEEP on the relationship between tidal volume and total impedance change measured via electrical impedance tomography (EIT). *J Clin Monit Comp.* (2021) 36:1–10. doi: 10.1007/s10877-021-00651-x

22. Adler A, Holder D. *Electrical Impedance Tomography: Methods, History and Applications.* London: Institute of Physics Publishing (2021).

23. Frerichs I, Amato MBP, van Kaam AH, Tingay DG, Zhao Z, Grychtol B, et al. Chest electrical impedance tomography examination, data analysis, terminology, clinical use and recommendations: consensus statement of the TRanslational EIT developmeNt stuDy group. *Thorax.* (2017) 72:83. doi: 10.1136/thoraxjnl-2016-208357

24. Frerichs I, Dargaville P, Dudykevych T, Rimensberger P. Electrical impedance tomography: a method for monitoring regional lung aeration and tidal volume distribution? *Intens Care Med.* (2003) 29:2312–6. doi: 10.1007/s00134-003-2029-z

25. Morice A, Harris N, Campbell J, Zhang F, Brown B. EIT in the investigation of chest disease. *Clin Physiol Appl Elect Imped Tomogr.* (1993) 236–41.

26. Reinartz SD, Imhoff M, Tolba R, Fischer F, Fischer EG, Teschner E, et al. EIT monitors valid and robust regional ventilation distribution in pathologic ventilation states in porcine study using differential DualEnergy-CT (ΔDECT). *Sci Rep.* (2019) 9:1–10. doi: 10.1038/s41598-019-45251-7

27. Bachmann MC, Morais C, Bugedo G, Bruhn A, Morales A, Borges JB, et al. Electrical impedance tomography in acute respiratory distress syndrome. *Crit Care.* (2018) 22:1–11. doi: 10.1186/s13054-018-2195-6

28. Zhao Z, Lee L-C, Chang M-Y, Frerichs I, Chang H-T, Gow C-H, et al. The incidence and interpretation of large differences in EIT-based measures for PEEP titration in ARDS patients. *J Clin Monit Comput.* (2020) 34:1005–13. doi: 10.1007/s10877-019-00396-8

29. Pulletz S, Krukewitt L, Gonzales-Rios P, Teschendorf P, Kremeier P, Waldmann A, et al. Dynamic relative regional strain visualized by electrical impedance tomography in patients suffering from COVID-19. *J Clin Monit Comp.* (2021) 13:1–11. doi: 10.1007/s10877-021-00748-3

30. Perier F, Tuffet S, Maraffi T, Alcala G, Victor M, Haudebourg A-F, et al. Electrical impedance tomography to titrate positive end-expiratory pressure in COVID-19 acute respiratory distress syndrome. *Crit Care.* (2020) 24:1–9. doi: 10.1186/s13054-020-03414-3

31. Mosing M, Waldmann A, Raisis A, Böhm S, Drynan E, Wilson K. Monitoring of tidal ventilation by electrical impedance tomography in anaesthetised horses. *Equine Vet J.* (2018). doi: 10.1111/evj.12998

32. Raisis AL, Mosing M, Hosgood GL, Secombe CJ, Adler A, Waldmann AD. The use of electrical impedance tomography (EIT) to evaluate pulse rate in anaesthetised horses. *Vet J.* (2021) 273:105694. doi: 10.1016/j.tvjl.2021.105694

33. Ambrosio AM, Carvalho-Kamakura TPA Ida KK, Varela B, Andrade FSRM, Facó LL, et al. Ventilation distribution assessed with electrical impedance tomography and the influence of tidal volume, recruitment and positive end-expiratory pressure in isoflurane-anesthetized dogs. *Vet Anaesth Analg.* (2017) 44:254–63. doi: 10.1016/j.vaa.2016.06.003

34. Auer U, Schramel JP, Moens YP, Mosing M, Braun C. Monitoring changes in distribution of pulmonary ventilation by functional electrical impedance tomography in anaesthetized ponies. *Vet Anaesth Analg.* (2019) 46:200–8. doi: 10.1016/j.vaa.2018.09.048

35. Sacks M, Byrne DP, Herteman N, Secombe C, Adler A, Hosgood G, et al. Electrical impedance tomography to measure lung ventilation distribution in healthy horses and horses with left-sided cardiac volume overload. *J Vet Int Med.* (2021) 35:2511–23. doi: 10.1111/jvim.16227

36. Brabant OA, Byrne DP, Sacks M, Martinez FM, Raisis AL, Araos JB, et al. Thoracic electrical impedance tomography—The 2022 Veterinary Consensus Statement. *Front Vet Sci.* (2022) 9:946911. doi: 10.3389/fvets.2022.946911

37. Virtanen P, Gommers R, Oliphant TE, Haberland M, Reddy T, Cournapeau D, et al. SciPy 10: fundamental algorithms for scientific computing in Python. *Nat Methods.* (2020) 17:261–72. doi: 10.1038/s41592-020-0772-5

38. Harris CR, Millman KJ, Van Der Walt SJ, Gommers R, Virtanen P, Cournapeau D, et al. Array programming with NumPy. *Nature.* (2020) 585:357–62. doi: 10.1038/s41586-020-2649-2

39. Zenodo. *pandas-dev/pandas:Pandas* [Internet]. (2020). doi: 10.5281/zendo.3509134

40. Hunter JD. Matplotlib: A 2D graphics environment. *Comput Sci Eng.* (2007) 9:90–5. doi: 10.1109/MCSE.2007.55

41. Frerichs I, Hahn G, Hellige G. Thoracic electrical impedance tomographic measurements during volume controlled ventilation-effects of tidal volume and positive end-expiratory pressure. *IEEE Trans Med Imaging.* (1999) 18:764–73. doi: 10.1109/42.802754

42. Secombe C, Adler A, Hosgood G, Raisis A, Mosing M. Can bronchoconstriction and bronchodilatation in horses be detected using electrical impedance tomography? *J Vet Int Med.* (2021) 35:2035–44. doi: 10.1111/jvim.16152

43. Kuznetsova A, Brockhoff PB, Christensen RH. lmerTest package: tests in linear mixed effects models. *J Stat Softw.* (2017) 82:1–26. doi: 10.18637/jss.v082.i13

44. Dyce KM. *Essentials of Bovine Anatomy*. Philadelphia, PA: Lea & Febiger (1971).

45. Parent RA. *Comparative Biology of the Normal Lung*. 2nd ed. London: Academic Press (2015).

46. Amoroso EC, Scott P, Williams K. The pattern of external respiration in the unanaesthetized animal. *Proc R Soc London Ser B Biol Sci.* (1964) 159:325–47. doi: 10.1098/rspb.1964.0006

47. Verhoeff J, Cruijsen AL, Kremer WD. Mismatching of ventilation and perfusion in calves with natural bovine respiratory syncytial virus infection. *Vet Record.* (1988) 123:131. doi: 10.1136/vr.123.5.131

48. Meyer H, Kästner SBR, Beyerbach M, Rehage J. Cardiopulmonary effects of dorsal recumbency and high-volume caudal epidural anaesthesia with lidocaine or xylazine in calves. *Vet J.* (2010) 186:316–22. doi: 10.1016/j.tvjl.2009.08.020

49. Desmecht DJM, Linden AS, Lekeux PM. Pathophysiological response of bovine pulmonary function to gastric distension. *J Comp Pathol.* (1995) 112:11–25. doi: 10.1016/S0021-9975(05)80086-6

50. Muylle E, Oyaert W. Lung function tests in obstructive pulmonary disease in horses. *Equine Vet J.* (1973) 5:37–44. doi: 10.1111/j.2042-3306.1973.tb03191.x

51. Gallivan GJ, McDonell WN, Forrest JB. Comparative ventilation and gas exchange in the horse and the cow. *Res Vet Sci.* (1989) 46:331–6. doi: 10.1016/S0034-5288(18)31175-5

52. Muylkens B, Thiry J, Kirten P, Schynts F, Thiry E. Bovine herpesvirus 1 infection and infectious bovine rhinotracheitis. *Vet Res.* (2007) 38:181–209. doi: 10.1051/vetres:2006059

53. Gallagher P. Chronic granular rhinitis (nasal catarrh) of cattle. *N Z Vet J.* (1972) 20:40. doi: 10.1080/00480169.1972.33999

54. Sang L, Zhao Z, Lin Z, Liu X, Zhong N, Li Y. A narrative review of electrical impedance tomography in lung diseases with flow limitation and hyperinflation: methodologies and applications. *Ann Transl Med*. (2020) 8:24. doi: 10.21037/atm-20-4984

55. Ngo C, Lehmann S, Verjans E, Tenbrock K, Leonhardt S. Assessing global and regional pulmonary function with electrical impedance tomography in pediatric patients: the EIT-derived flow-volume loops. *Eur Respir Soc.* (2020). doi: 10.1183/13993003.congress-2020.1239

56. Ngo C, Dippel F, Tenbrock K, Leonhardt S, Lehmann S. Flow-volume loops measured with electrical impedance tomography in pediatric patients with asthma. *Pediatr Pulmonol.* (2018) 53:636–44. doi: 10.1002/ppul.23962

57. Couëtil L, Cardwell J, Gerber V, Lavoie JP, Léguillette R, Richard E. Inflammatory airway disease of horses—revised consensus statement. *J Vet Int Med.* (2016) 30:503–15. doi: 10.1111/jvim.13824

58. Robinson N, Olszewski M, Boehler D, Berney C, Hakala J, Matson C, et al. Relationship between clinical signs and lung function in horses with recurrent airway obstruction (heaves) during a bronchodilator trial. *Equine Vet J.* (2000) 32:393–400. doi: 10.2746/042516400777591147

59. Gallivan G. *Comparative Pulmonary Structure and Function in Two Large Mammals, the Horse and the Cow*. ProQuest Dissertations Publishing, McMaster University, Hamilton, Ontario (1981).

60. Grissett G, White B, Larson R. Structured literature review of responses of cattle to viral and bacterial pathogens causing bovine respiratory disease complex. *J Vet Int Med.* (2015) 29:770–80. doi: 10.1111/jvim.12597

61. Lekeux P, Art T, Amory H. The effect of common bovine respiratory diseases on tidal breathing flow-volume loops. *Vet Res Commun.* (1988) 12:463–73. doi: 10.1007/BF01075476

62. Maillard R, Assié S, Douart A, editors. Respiratory Disease in Adult Cattle. In: *Conference Proceedings from World Buiatrics Conference*. Nice (2006).

frontiers | Frontiers in Veterinary Science

TYPE Methods
PUBLISHED 24 January 2024
DOI 10.3389/fvets.2023.1181036

OPEN ACCESS

EDITED BY
Rocío Fernández-Parra,
Catholic University of Valencia San Vicente Mártir, Spain

REVIEWED BY
Mauro Malvè,
Public University of Navarre, Spain
Jason Bourke,
New York Institute of Technology, United States

*CORRESPONDENCE
Alejandro Pérez-Ramos
✉ pera@uma.es

†These authors have contributed equally to this work

RECEIVED 06 March 2023
ACCEPTED 26 December 2023
PUBLISHED 24 January 2024

CITATION
Burgos M, Pérez-Ramos A, Mulot B, Sanz-Prieto D, Esteban F and Bastir M (2024) Advancements in veterinary medicine: the use of Flowgy for nasal airflow simulation and surgical predictions in big felids (a case study in lions).
Front. Vet. Sci. 10:1181036.
doi: 10.3389/fvets.2023.1181036

Advancements in veterinary medicine: the use of Flowgy for nasal airflow simulation and surgical predictions in big felids (a case study in lions)

Manuel Burgos[1†], Alejandro Pérez-Ramos[2*†], Baptiste Mulot[3], Daniel Sanz-Prieto[4], Francisco Esteban[5] and Markus Bastir[4]

[1]Dpto. de Ingeniería Térmica y de Fluidos, Universidad Politécnica de Cartagena, Murcia, Spain, [2]Dpto. de Ecología y Geología, Facultad de Ciencias, Universidad de Málaga, Málaga, Spain, [3]ZooParc de Beauval and Beauval Nature, Saint-Aignan, France, [4]Department of Paleobiology, Museo Nacional de Ciencias Naturales, Madrid, Spain, [5]Servicio Andaluz de Salud, Hospital Universitario Virgen del Rocío, Servicio de Otorrinolaringología, Sevilla, Spain

Flowgy is a semi-automated tool designed to simulate airflow across the nasal passage and detect airflow alterations in humans. In this study, we tested the use and accuracy of Flowgy in non-human vertebrates, using large felids as the study group. Understanding the dynamics of nasal airflow in large felids such as lions (*Panthera leo*) is crucial for their health and conservation. Therefore, we simulated airflow during inspiration through the nasal passage in three lions (*Panthera leo*), two of which were siblings (specimens ZPB_PL_002 and ZPB_PL_003), without breathing obstructions. However, one of the specimens (ZPB_PL_001) exhibited a slight obstruction in the nasal vestibule, which precluded the specimen from breathing efficiently. Computed tomography (CT) scans of each specimen were obtained to create detailed three-dimensional models of the nasal passage. These models were then imported into Flowgy to simulate the airflow dynamics. Virtual surgery was performed on ZPB_PL_001 to remove the obstruction and re-simulate the airflow. In parallel, we simulated the respiration of the two sibling specimens and performed an obstructive operation followed by an operation to remove the obstruction at the same level and under the same conditions as the original specimen (ZPB_PL_001). Thus, we obtained a pattern of precision for the operation by having two comparable replicas with the obstructed and operated specimens. The simulations revealed consistent airflow patterns in the healthy specimens, demonstrating the accuracy of Flowgy. The originally obstructed specimen and two artificially obstructed specimens showed a significant reduction in airflow through the right nostril, which was restored after virtual surgery. Postoperative simulation indicated an improvement of >100% in respiratory function. Additionally, the temperature and humidity profiles within the nostrils showed marked improvements after surgery. These findings underscore the potential of Flowgy in simulating nasal airflow and predicting the outcomes of surgical interventions in large felids. This could aid in the early detection of respiratory diseases and inform clinical decision-making, contributing to improved veterinary care and conservation efforts. However, further research is needed to validate these findings in other species and explore the potential of integrating Flowgy with other diagnostic and treatment tools in veterinary medicine.

KEYWORDS

airflow, virtual surgery, *Panthera leo*, zoology, wild mammals

Introduction

The study of airflow in the nasal passage of felines, particularly large felids such as lions, is a multidisciplinary field of critical importance that intersects veterinary medicine, wildlife conservation, and computational fluid dynamics (1, 2). Nasal airways, a marvel of biological engineering, are complex and intricate structures that play several vital roles in the life of felines, and their importance is often understated (3, 4).

The primary function of the nasal passage is to facilitate respiration. It acts as the first point of contact for air entering the body and is responsible for filtering, warming, and humidifying the inhaled air before it reaches the lungs (5, 6). This process is crucial for maintaining the delicate balance of the respiratory system and ensuring the efficient exchange of gases in the lungs. The nasal passage, which is lined with cilia and mucus, traps dust, allergens, and pathogens, preventing them from reaching the lungs. Any alteration in the structure or function of the nasal airway, such as obstructions or inflammation, can significantly affect the efficiency of this filtration system, leading to difficulties in breathing and increased susceptibility to respiratory infections (7).

In addition to its role in respiration, the nasal cavity houses the olfactory epithelium, which is responsible for the sense of smell (3, 4). The sense of smell is a primary sense in felines that is far more developed than in humans. It plays crucial roles in various aspects of life, including hunting, territory marking, mate selection, and social interaction. Felines rely heavily on their sense of smell to detect prey, recognize territorial boundaries, and communicate with other members of their species. Therefore, any airflow disruption that affects olfactory capabilities can have far-reaching consequences on a feline's behavior and survival (1).

Moreover, the nasal airways also play a significant role in thermoregulation (5, 6). Large felids such as lions inhabit diverse environments, from the scorching heat of the African savannah to the freezing temperatures of the Siberian taiga. The intricate structure of the nasal passage, with its extensive vascular network, helps dissipate heat and maintain body temperature, which is crucial for survival under extreme conditions. Any alteration in the nasal passage that affects this thermoregulatory function can affect a feline's ability to adapt to its environment, thereby affecting its survival (1, 5, 6).

These complications can have severe consequences in the wild. Difficulties in breathing can reduce a feline's hunting efficiency, affecting its ability to catch prey and leading to malnutrition (1, 2). Reduced olfactory capabilities can affect the ability to mark territory, find mates, or avoid predators, thereby increasing vulnerability. Furthermore, the inability to effectively regulate body temperature can affect adaptability to environmental changes, increasing susceptibility to diseases (3, 4).

The lion population is estimated to have declined by approximately 43% over the past two decades, with an estimated 20,000–25,000 lions remaining in the wild (1, 2). The causes of this decline in wild lion populations include a variety of factors, from poaching to climate change and habitat loss. An increase in intensive cattle farming linked to the growing human population and the introduction of domestic animals, such as cats, have led to an increase in bovine pleuropneumonia (8, 9) and feline AIDS virus in lion populations (10, 11).

In addition, the incidence of respiratory disease due to COVID-19 in domestic and farm animals has increased since the 2020 pandemic (12, 13). There has been an increase in cases of respiratory problems in zoo animals in recent years, which are thought to be largely the result of COVID-19 infections (12–14). All these problems generate the need for new actions and vaccination protocols for professionals such as veterinarians and personnel specialized in handling large mammals to control contagions among domestic, farm, and zoo animals (12, 15, 16). Given this situation, human-animal infections and vice versa have increased in recent years. Therefore, a correct respiratory diagnosis, enabling one to distinguish between respiratory problems that are due to the action of COVID-19 and those that are due to other respiratory pathologies, is essential (17, 18). Using Flowgy software as a tool to detect pathologies and conduct virtual surgeries has become indispensable (19–21). In this study, we aimed to demonstrate the potential of Flowgy in large mammals using large felids, such as *Panthera leo*.

Understanding airflow dynamics in the nasal cavities of felines is critical (3, 4). This will provide insights into their physiological adaptations, inform veterinary practices, and contribute to their conservation efforts. By studying the airflow in the nasal cavities, we can better understand how these animals adapt to their environment, communicate, and hunt. Additionally, we can identify and treat respiratory conditions more effectively, thereby improving health and quality of life. Moreover, by understanding how changes in their environment might affect their nasal airflow and, consequently, their ability to regulate body temperature, hunt, and communicate, we can better predict and mitigate the impacts of environmental changes on these animals.

There has been a great demand for non-domestic animals such as wild cats, skunks, possums, and raccoons in recent years (22, 23). These new animals require new protocols for surgical practice and pose a considerable danger to veterinary professionals (24–26).

In the context of veterinary medicine, the application of computational fluid dynamics (CFD) has been a game changer, particularly in the study of respiratory systems in various animals. The respiratory system, with its intricate network of airways and blood vessels, presents a complex fluid flow environment. Understanding airflow dynamics in this system is crucial for diagnosing and treating various respiratory conditions (3–6).

CFD enables non-invasive detailed analysis of airflow patterns within the respiratory system. It can provide valuable data on various parameters, such as pressure, velocity, and turbulence, which can be used to gain insights into the structure–function relationships in the respiratory system. For instance, it can help us to understand how the shape and size of the nasal airways affect airflow and, consequently, the animal's ability to warm, humidify, and filter inhaled air (3–6).

Moreover, CFD can be used to simulate the effects of certain diseases or conditions that alter the structure of the nasal passage (19–21). Conditions such as polyps, tumors, or congenital deformities can disrupt normal airflow, leading to various complications (7, 17, 18). By simulating these conditions using CFD, veterinarians can better understand the impact on animal respiration and overall health. This can aid in the diagnosis of these conditions and the planning of appropriate treatment strategies.

Furthermore, CFD can be used to predict surgical intervention outcomes. For instance, it can simulate the effects of removing a polyp or tumor or correcting a congenital deformity on the airflow in the nasal passage (7–11). This can provide valuable information for clinical decision-making, helping veterinarians predict the likely outcomes of surgery and plan the best course of action.

In conclusion, applying CFD in veterinary medicine represents a significant advancement in this field. It is a powerful tool for understanding the complex dynamics of airflow in the respiratory system, aiding in diagnosing and treating various conditions. As technology advances, its application in veterinary medicine will likely expand, opening new avenues for research and clinical practice.

Flowgy software was selected to perform all preprocessing, airflow simulations, and post-processing.[1] It is an innovative semi-automated tool designed to simulate and analyze airflow across nasal passages (19–21). Its primary function is to apply highly accurate CFD analysis to models in a short time. Over the last few years, the analytical capabilities of Flowgy have been improved at different levels, from generating more accurate virtual models to the analytical power of CFD and adding the capability of virtual surgeries (27–32). The last aspect was to focus on this study, which used large carnivores to demonstrate the versatility of Flowgy in the fields of veterinary medicine and zoology.

The main goals of this study were to test (i) virtual surgery tools by detecting perturbations in healthy cases (small intentional obstructions), (ii) the computational limits of Flowgy using large mammals with complex nasopharyngeal topology, and (iii) the results of the analysis using hyperbolic curves and compare them with the standard curves of efficient and inefficient hyperbolic functions.

Materials and methods

The study material consisted of three *Panthera leo krugeri* specimens, of which two were siblings (ZPB_PL_002 and ZPB_PL_003), and the other specimen (ZPB_PL_001) was a subadult individual. They were captive specimens from the ZooParc de Beauval and Beauval Nature. The specimens were anesthetized for a tomographic study for a veterinary protocol review. One of the measures of the protocol is to carry out medical studies (medical checkups) to detect possible pathologies and to conduct routine follow-ups on the health of the animals. The acronyms used to register the study specimens were based on the provenance, i.e., Zooparc de Beauval (ZPB), and the species (PL, *Panthera leo*).

Data acquisition

The study material was tomographed at the Beauval Veterinary Institute. The acquisition parameters were 120 kV and 499 mA. The data obtained from the three specimens at the cranial level were in 16-bit format with a 512 × 512 pixel size. The reconstruction of the images of each specimen gave the following voxel sizes with their specific image numbers: ZPB_PL_001 had 460 slices with a slice thickness of 0.6 mm and a voxel size of 0.375 mm (X, Y) and 0.600 mm (Z); ZPB_PL_002 had 591 slices with a slice thickness of 0.6 mm and a voxel size of 0.527 mm (X, Y) and 0.600 mm (Z); and ZPB_PL_003 had 454 slices with a slice thickness of 0.8 mm and a voxel size of 0.516 mm (X, Y) and 0.804 mm (Z).

Computational CFD workflow

Pre-processing

We used Flowgy software (see text footnote 1) for virtual morphological three-dimensional image preparation, semi-automatic segmentation of the CT dataset, and quantitative simulations of the physical properties of nasal airflow dynamics (27, 28) (see Figure 1).

The data obtained were imported into Flowgy. The first step was the isometric conversion of the voxels to a size of 0.4 (29). This method of resampling using a binary process is essential for generating virtual models for CFD analyses.

The CT scans were segmented to create three-dimensional models of the face (yellow), nasal airways, paranasal sinuses, nasopharynx (green), and spherical external region (blue) to simulate the natural inflow of air during inspiration (inlet). The final section of the nasopharyngeal passage represents the outflow domain of the inspired flow (light blue) and the outlet. The details of the computational domains are presented in Figure 1A. Thus, we used a non-truncated computational domain, which consists of all or part of the subject's head, surrounded by an atmosphere from which air is inhaled through the nasal passage (27, 28, 30, 31) (see Figure 1A).

Experimental and boundary conditions

Virtual surgery

The advent of virtual surgery software, particularly Flowgy, has offered unprecedented possibilities for veterinary surgical planning. In this report, three cases were examined (ZPB_PL_001 [Case 01], ZPB_PL_002 [Case 02], and ZPB_PL_003 [Case 03]), each requiring distinct surgical interventions in the nasal area. This study aimed to provide a comprehensive overview of how virtual surgery can aid in unblocking and intentionally obstructing specific nasal passages for various medical necessities (Figure 2).

Case 01: unblocking nasal passages (ZPB_PL_001)

In Case 01, the focus was on eliminating an obstruction in the nasal vestibule (3, 4). The module used for this operation was replete with a set of virtual tools that mimicked the real-world surgical environment (Figure 2A). A notable tool is the virtual scalpel, which facilitates the removal of material from a three-dimensional model representing the anatomical structure of the subject animal. The scalpel was calibrated to ensure precision in the incisions and to minimize the removal of non-target tissues (27, 28, 30, 31). In addition, the module incorporates polyline technology, which enables the user to manipulate partitions or augment materials in a manner that adheres to the septum and meatus anatomical patterns. In the case of ZPB_PL_001, the obstruction was successfully excised by carefully maneuvering the virtual scalpel tool along a planned polyline path, as shown in Figure 2B. The result showed a clear frontal nasal meatus, making it a suitable candidate for subsequent simulations analyzing fluid dynamics and other variables of interest (Tables 1–8).

1 https://www.flowgy.com/

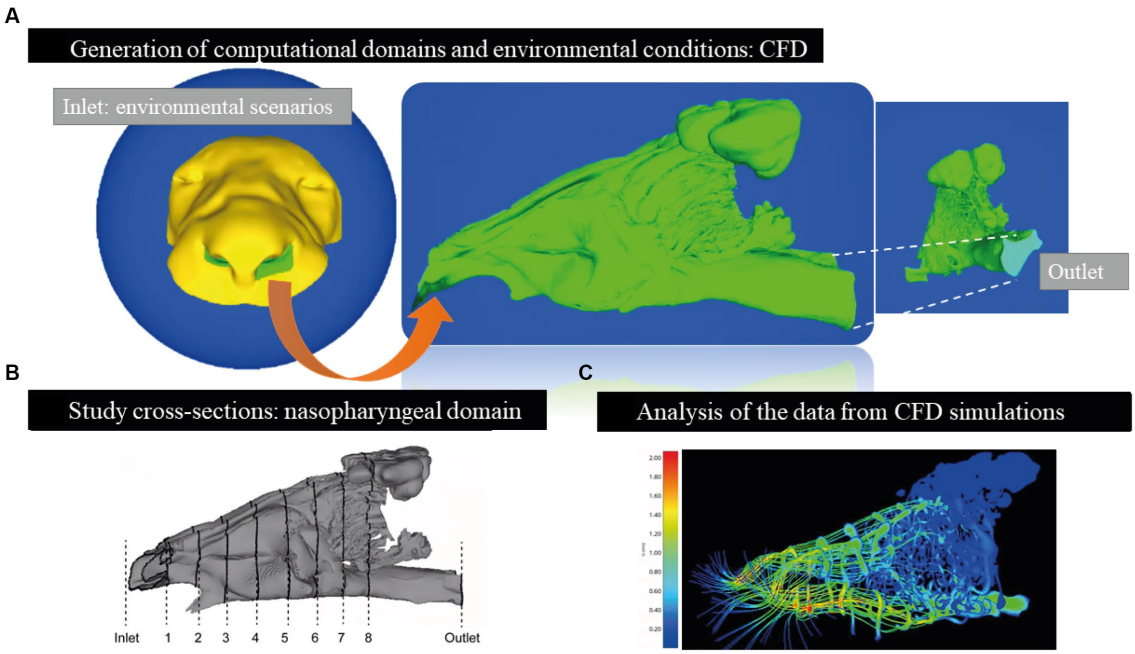

FIGURE 1
Virtual surgical process in *Panthera leo* specimens. **(A)** Import of tomographic data and generation of computational domains from the produced meshes. Input (in blue) in a spherical shape represents the external boundary conditions for simulating environmental scenarios. Surface domain 1 (in yellow) represents the external topology of the model where the air will interact when entering through the nostrils. Domain 2 (study of the nasopharyngeal tract; in green) represents where the airflow will be simulated. Domain 3 (output; in light blue) represents the system's simulated outflow. At this point, the computational fluid dynamics (CFD) analysis was conducted. **(B)** Study planes cut along the nasopharyngeal tract for the subsequent analysis of the simulated flow. The first cut (inlet) is the air inlet (representing the atmosphere) and is generated in the cutting plane closest to the nostrils from the outside, and the last cut plane (outlet) is the air outlet from the nasopharyngeal tract. The remaining eight cuts are generated anatomically in a homologous manner, with the first one (cut 1) behind the nostrils and cut 8 in the proximal position of the choana. The remaining six cuts are added equidistantly. **(C)** Quantification of pressure, temperature, and humidity variables in the air simulated by CFD. In this example, airflow speed maps or streamline lines (m/s) are applied, where blue represents low speeds or stationary air, and red represents high speeds.

TABLE 1 Data on *Panthera leo* specimen ZPB_PL_001.

Study slices	Distance	Temp. 28	Temp. 40	Temp. 5	Average temp.	Humid. 60	Humid. 05	Humid. 10	Average H.
1	0.0000	−1.0000	−1.0000	−1.0000	−1.0000	−1.0000	−1.0000	−1.0000	−1.0000
2	0.1806	−0.5035	−0.5027	−0.5058	−0.5040	−0.5143	−0.5159	−0.5166	−0.5156
3	0.2977	−0.0961	−0.0953	−0.0978	−0.0964	−0.0988	−0.1012	−0.1032	−0.1011
4	0.4147	−0.0193	−0.0193	−0.0196	−0.0194	−0.0137	−0.0169	−0.0177	−0.0161
5	0.5318	−0.0017	−0.0020	−0.0017	−0.0018	0.0085	0.0049	0.0047	0.0061
6	0.6488	−0.0002	0.0000	−0.0001	−0.0001	0.0108	0.0074	0.0069	0.0084
7	0.7659	0.0000	0.0000	0.0000	0.0000	0.0111	0.0076	0.0073	0.0087
8	0.8829	0.0000	0.0000	−0.0001	0.0000	0.0111	0.0074	0.0071	0.0085
9	1.0000	−0.0133	−0.0133	−0.0129	−0.0132	−0.0026	−0.0061	−0.0063	−0.0050

Standardization of temperature and humidity data obtained from the three simulations (28°C at 60% RH, 40°C at 5% RH, and 5°C at 10% RH) applying the method described by Burgos (32).

Cases 02 and 03: inducing controlled obstructions (ZPB_PL_002 and ZPB_PL_003)

In contrast to Case 01, Cases 02 and 03 required the intentional obstruction of specific nasal regions (Figure 1C). This is often required for many reasons, including, but not limited to, experimental trials on obstructive respiratory conditions. In these cases, a complementary set of tools was used, prominently featuring contour master polylines and an alternate setting on the virtual scalpel to add rather than remove material (28, 31). This procedure was methodological. Contour master polylines were initially used to delineate the region where the obstruction was introduced. These polylines function as dynamic guides for the virtual scalpel, which adds material to the three-dimensional model in this particular mode. The integrity of the three-dimensional model was maintained throughout, ensuring that the added material coherently followed the topological and anatomical patterns of the existing structures. The operations for Cases 02 and 03

TABLE 2 Data on the operated *Panthera leo* specimen ZPB_PL_001.

Study slices	Distance	Temp. 28	Temp. 40	Temp. 5	Average temp.	Humid. 60	Humid. 05	Humid. 10	Average H.
1	0.0000	−1.0000	−1.0000	−1.0000	−1.0000	−1.0000	−1.0000	−1.0000	−1.0000
2	0.1806	−0.4338	−0.4327	−0.4356	−0.4340	−0.4431	−0.4453	−0.4460	−0.4448
3	0.2977	−0.0669	−0.0660	−0.0681	−0.0670	−0.0662	−0.0693	−0.0708	−0.0688
4	0.4147	−0.0122	−0.0120	−0.0125	−0.0122	−0.0042	−0.0076	−0.0082	−0.0067
5	0.5318	−0.0011	−0.0013	−0.0011	−0.0012	0.0101	0.0065	0.0063	0.0076
6	0.6488	−0.0001	0.0000	−0.0001	−0.0001	0.0117	0.0081	0.0078	0.0092
7	0.7659	0.0000	0.0000	0.0000	0.0000	0.0121	0.0083	0.0080	0.0095
8	0.8829	0.0000	0.0000	0.0000	0.0000	0.0121	0.0083	0.0080	0.0095
9	1.0000	−0.0151	−0.0153	−0.0147	−0.0151	−0.0036	−0.0072	−0.0076	−0.0061

Standardization of temperature and humidity data obtained from the three simulations (28°C at 60% RH, 40°C at 5% RH, and 5°C at 10% RH) applying the method described by Burgos (32).

TABLE 3 Data on *Panthera leo* specimen ZPB_PL_003.

Study slices	Distance	Temp. 28	Temp. 40	Temp. 5	Average temp.	Humid. 60	Humid. 05	Humid. 10	Average H.
1	0.0000	−1.0000	−1.0000	−1.0000	−1.0000	−1.0000	−1.0000	−1.0000	−1.0000
2	0.2143	−0.2496	−0.2470	−0.2535	−0.2501	−0.2595	−0.2610	−0.2645	−0.2616
3	0.3265	−0.0785	−0.0772	−0.0804	−0.0787	−0.0802	−0.0828	−0.0844	−0.0825
4	0.4388	−0.0200	−0.0200	−0.0205	−0.0202	−0.0140	−0.0171	−0.0179	−0.0163
5	0.5510	−0.0049	−0.0047	−0.0047	−0.0048	0.0059	0.0025	0.0022	0.0035
6	0.6633	−0.0031	−0.0033	−0.0030	−0.0032	0.0075	0.0043	0.0039	0.0052
7	0.7755	−0.0034	−0.0033	−0.0033	−0.0034	0.0075	0.0043	0.0039	0.0052
8	0.8878	−0.0066	−0.0067	−0.0064	−0.0065	0.0049	0.0016	0.0011	0.0025
9	1.0000	−0.0171	−0.0173	−0.0166	−0.0170	−0.0049	−0.0083	−0.0086	−0.0073

Standardization of temperature and humidity data obtained from the three simulations (28°C at 60% RH, 40°C at 5% RH, and 5°C at 10% RH) applying the method described by Burgos (32).

TABLE 4 Data on the obstructed *Panthera leo* specimen ZPB_PL_003.

Study slices	Distance	Temp. 28	Temp. 40	Temp. 5	Average temp.	Humid. 60	Humid. 05	Humid. 10	Average H.
1	0.0000	−1.0000	−1.0000	−1.0000	−1.0000	−1.0000	−1.0000	−1.0000	−1.0000
2	0.2143	−0.6733	−0.6718	−0.6738	−0.6730	−0.6802	−0.6822	−0.6809	−0.6811
3	0.3265	−0.1785	−0.1764	−0.1818	−0.1789	−0.1842	−0.1863	−0.1895	−0.1867
4	0.4388	−0.0432	−0.0426	−0.0450	−0.0436	−0.0401	−0.0430	−0.0451	−0.0427
5	0.5510	−0.0056	−0.0053	−0.0056	−0.0055	0.0055	0.0020	0.0015	0.0030
6	0.6633	−0.0032	−0.0033	−0.0031	−0.0032	0.0085	0.0047	0.0043	0.0058
7	0.7755	−0.0034	−0.0033	−0.0033	−0.0034	0.0085	0.0049	0.0045	0.0060
8	0.8878	−0.0066	−0.0067	−0.0064	−0.0065	0.0059	0.0022	0.0017	0.0033
9	1.0000	−0.0171	−0.0173	−0.0166	−0.0170	−0.0039	−0.0076	−0.0080	−0.0065

Standardization of temperature and humidity data obtained from the three simulations (28°C at 60% RH, 40°C at 5% RH, and 5°C at 10% RH) applying the method described by Burgos (32).

are illustrated in Figure 2C. The objective was to perform an induced obstructive operation with the same characteristics (Cases 02 and 03) and at the same location within the nasal tract as the diseased specimen (Case 01), scaling the obstruction (orange object in Figure 2) to the proportional size of the healthy specimens (Figure 1C; Table 9).

Specimens ZPB_PL_003 and ZPB_PL_002 were twin brothers; therefore, they were ideal specimens for a replicate study. Based on this genetic approach, we performed a mock operation on these two specimens and validated the success of the operation and its accuracy. In these cases, virtual obstructive operations were performed in the same nasal region where the obstruction was detected in specimen ZPB_PL_001. The next phase was the operation of such an obstruction so that the two specimens (siblings) could return to their initial state of respiratory function. The results are shown in Figure 2C. The data for the materials extracted from the different specimens were similar. It must be considered that specimen ZPB_PL_001 is a subadult;

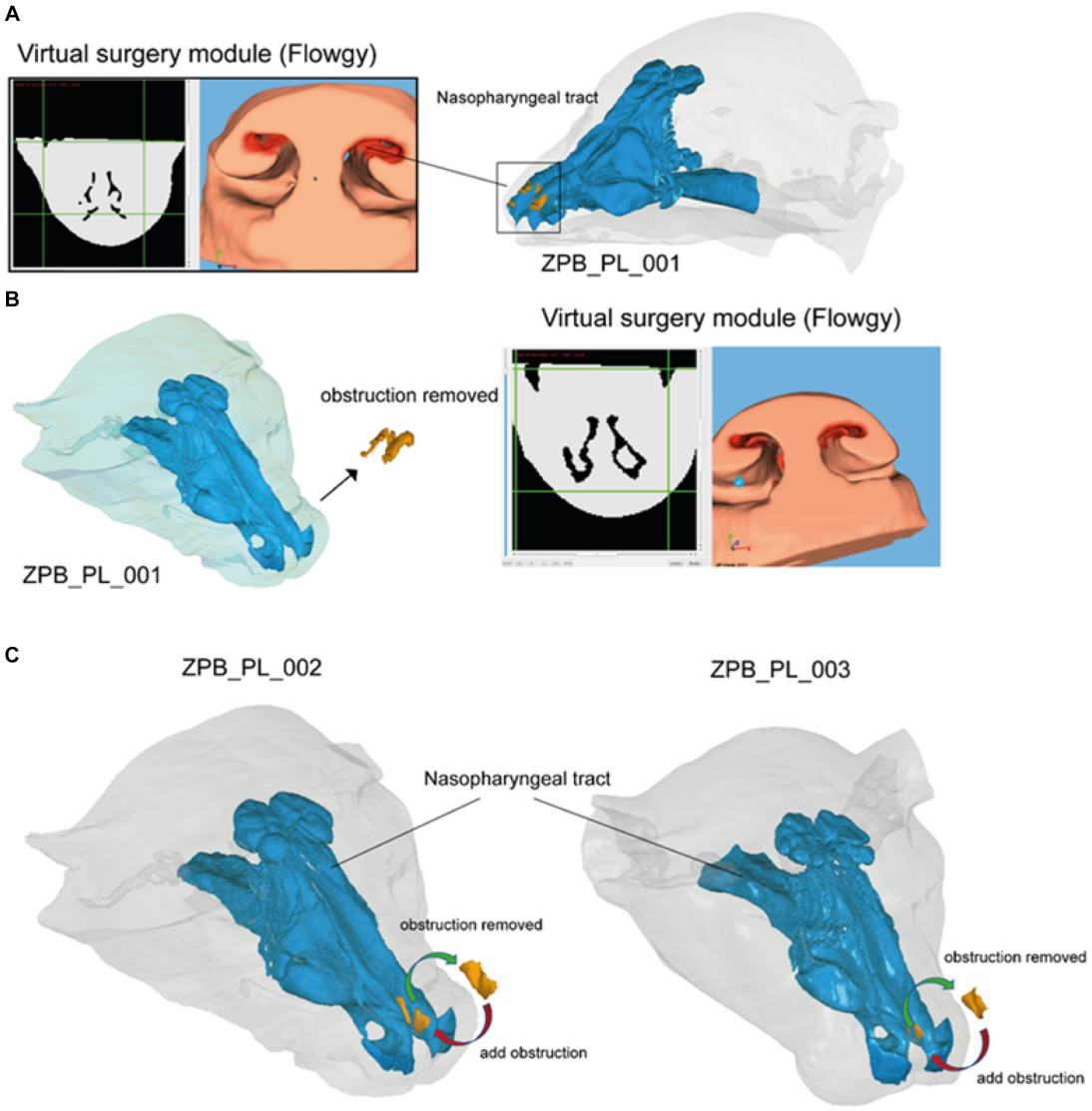

FIGURE 2
The process of using the virtual surgery module of the Flowgy program. **(A)** Case 01 (ZPB_PL_001): exploration of the frontal nasal meatus obstruction using the Flowgy software module tools. **(B)** Operation using the virtual surgery module tools to remove the obstruction. This resulted in Case 01 after the operation and without the obstruction. **(C)** Obstructive operation of Cases 02 (ZPB-PL_002) and 03 (ZPB-PL_003) by adding material in the frontal nasal meatuses using a virtual scalpel and virtual surgery module polylines. In this step, the red arrows indicate the process. The second step is to reoperate on Cases 02 and 03 by means of a de-obstructive surgery using the same Flowgy module tools, but in this process, removing, instead of adding, material (green arrows).

therefore, the extracted material that caused the obstruction was smaller than that in the replicate study. However, the same conditions were used based on the location and form of the obstruction. The results are summarized in Table 9.

In summary, unblocking and controlled blocking surgeries were executed using the virtual surgery module of the Flowgy software. The results demonstrated high levels of accuracy and feasibility for both intervention types. Importantly, these simulations will pave the way for future surgical plans and additional simulations to improve patient outcomes.

Fluid dynamics simulation

To simulate inspiration, the input to the computational domain was outside the surroundings of the subject's head, where the value of a known atmospheric pressure (101,325 Pa) was set. We modeled the efficiency of the nasal airflow in three different environmental scenarios: a temperate forest region (28°C, 60% RH), a warm desert region (40°C, 5% RH), and a cold or high mountain region (5°C, 10% RH). (5). Boundary conditions within the nasal passage, i.e., the area between the internal part of the nostrils and the nasopharynx, were defined and set to 100% relative humidity and 311.65 K (38.5°C) (5, 6) (Figure 1A). The Navier–Stokes equations were solved in a steady state with laminar and compressible flows using the open-source CFD software Open FOAM.[2] An appropriate pressure drop was applied

2 https://www.openfoam.com/

10.3389/fvets.2023.1181036

TABLE 5 Data on the operated *Panthera leo* specimen ZPB_PL_003.

Study slices	Distance	Temp. 28	Temp. 40	Temp. 5	Average temp.	Humid. 60	Humid. 05	Humid. 10	Average H.
1	0.0000	−1.0000	−1.0000	−1.0000	−1.0000	−1.0000	−1.0000	−1.0000	−1.0000
2	0.2143	−0.3153	−0.3129	−0.3189	−0.3157	−0.3250	−0.3267	−0.3299	−0.3272
3	0.3265	−0.0890	−0.0879	−0.0910	−0.0893	−0.0903	−0.0934	−0.0950	−0.0929
4	0.4388	−0.0224	−0.0220	−0.0230	−0.0225	−0.0160	−0.0193	−0.0203	−0.0185
5	0.5510	−0.0049	−0.0047	−0.0048	−0.0048	0.0068	0.0029	0.0026	0.0041
6	0.6633	−0.0034	−0.0033	−0.0033	−0.0034	0.0081	0.0045	0.0043	0.0057
7	0.7755	−0.0036	−0.0033	−0.0035	−0.0035	0.0085	0.0047	0.0043	0.0058
8	0.8878	−0.0067	−0.0067	−0.0065	−0.0066	0.0059	0.0020	0.0017	0.0032
9	1.0000	−0.0174	−0.0180	−0.0170	−0.0175	−0.0042	−0.0079	−0.0084	−0.0068

Standardization of temperature and humidity data obtained from the three simulations (28°C at 60% RH, 40°C at 5% RH, and 5°C at 10% RH) applying the method described by Burgos (32).

TABLE 6 Data on *Panthera leo* specimen ZPB_PL_002.

Study slices	Distance	Temp. 28	Temp. 40	Temp. 5	Average temp.	Humid. 60	Humid. 05	Humid. 10	Average H.
1	0.0000	−1.0000	−1.0000	−1.0000	−1.0000	−1.0000	−1.0000	−1.0000	−1.0000
2	0.2143	−0.2650	−0.2633	−0.2687	−0.2657	−0.2764	−0.2783	−0.2804	−0.2784
3	0.3265	−0.0736	−0.0727	−0.0755	−0.0739	−0.0740	−0.0767	−0.0784	−0.0764
4	0.4388	−0.0173	−0.0173	−0.0179	−0.0175	−0.0111	−0.0142	−0.0149	−0.0134
5	0.5510	−0.0031	−0.0033	−0.0031	−0.0032	0.0075	0.0043	0.0039	0.0052
6	0.6633	−0.0133	−0.0133	−0.0129	−0.0132	−0.0026	−0.0061	−0.0063	−0.0050
7	0.7755	−0.0008	−0.0007	−0.0007	−0.0007	0.0101	0.0067	0.0065	0.0078
8	0.8878	−0.0047	−0.0047	−0.0045	−0.0046	0.0068	0.0036	0.0032	0.0046
9	1.0000	−0.0205	−0.0207	−0.0198	−0.0203	−0.0081	−0.0115	−0.0119	−0.0105

Standardization of temperature and humidity data obtained from the three simulations (28°C at 60% RH, 40°C at 5% RH, and 5°C at 10% RH) applying the method described by Burgos (32).

TABLE 7 Data on the obstructed *Panthera leo* specimen ZPB_PL_002.

Study slices	Distance	Temp. 28	Temp. 40	Temp. 5	Average temp.	Humid. 60	Humid. 05	Humid. 10	Average H.
1	0.0000	−1.0000	−1.0000	−1.0000	−1.0000	−1.0000	−1.0000	−1.0000	−1.0000
2	0.2143	−0.6881	−0.6887	−0.6890	−0.6886	−0.2751	−0.6995	−0.6969	−0.5572
3	0.3265	−0.1763	−0.1720	−0.1770	−0.1751	−0.0759	−0.1802	−0.1835	−0.1466
4	0.4388	−0.0409	−0.0400	−0.0424	−0.0411	−0.0104	−0.0400	−0.0421	−0.0309
5	0.5510	−0.0038	−0.0040	−0.0040	−0.0039	0.0088	0.0038	0.0032	0.0053
6	0.6633	−0.0141	−0.0133	−0.0130	−0.0135	−0.0023	−0.0056	−0.0058	−0.0046
7	0.7755	−0.0008	−0.0007	−0.0007	−0.0007	0.0111	0.0074	0.0071	0.0085
8	0.8878	−0.0047	−0.0047	−0.0045	−0.0046	0.0078	0.0043	0.0039	0.0053
9	1.0000	−0.0210	−0.0207	−0.0198	−0.0205	−0.0075	−0.0108	−0.0112	−0.0098

Standardization of temperature and humidity data obtained from the three simulations (28°C at 60% RH, 40°C at 5% RH, and 5°C at 10% RH) applying the method described by Burgos (32).

between the atmosphere and the nasopharynx in each case to obtain an approximate flow rate of 15 L/min (31, 32) (see Figure 1A).

We generated unstructured tetrahedral meshes with sizes ranging from 7 to 30 million tetrahedral cells to solve the governing equations of the fluid flow and performed a mesh convergence study to evaluate the accuracy of the values in the simulations (see Table 10) (27, 28, 30–32). The numerical solutions of the equations included temperature (provided in Kelvin units but converted to degrees Celsius for a correct understanding of the study), velocity (m/s), and absolute humidity (Kg/m^3). Specifically, we estimated absolute and standardized (relative) values of temperature, humidity, and velocity and compared them at specific sections between the external environment and the choanae, represented by different functional regions of the entire nasal airway (Figure 1A). These sections or cuts were equidistant and homologous in all three specimens. Eight anatomical sections and the inlet section represented the atmosphere

TABLE 8 Data on the operated *Panthera leo* specimen ZPB_PL_002.

Study slices	Distance	Temp. 28	Temp. 40	Temp. 5	Average temp.	Humid. 60	Humid. 05	Humid. 10	Average H.
1	0.0000	−1.0000	−1.0000	−1.0000	−1.0000	−1.0000	−1.0000	−1.0000	−1.0000
2	0.2143	−0.3307	−0.3293	−0.3341	−0.3314	−0.3419	−0.3440	−0.3459	−0.3439
3	0.3265	−0.0841	−0.0833	−0.0861	−0.0845	−0.0841	−0.0873	−0.0889	−0.0868
4	0.4388	−0.0197	−0.0193	−0.0204	−0.0198	−0.0130	−0.0164	−0.0173	−0.0156
5	0.5510	−0.0031	−0.0033	−0.0031	−0.0032	0.0085	0.0047	0.0043	0.0058
6	0.6633	−0.0136	−0.0133	−0.0132	−0.0134	−0.0020	−0.0058	−0.0058	−0.0045
7	0.7755	−0.0010	−0.0007	−0.0009	−0.0008	0.0111	0.0072	0.0069	0.0084
8	0.8878	−0.0048	−0.0047	−0.0046	−0.0047	0.0078	0.0040	0.0039	0.0053
9	1.0000	−0.0208	−0.0213	−0.0202	−0.0208	−0.0075	−0.0110	−0.0117	−0.0101

Standardization of temperature and humidity data obtained from the three simulations (28°C at 60% RH, 40°C at 5% RH, and 5°C at 10% RH) applying the method described by Burgos (2014) (32).

TABLE 9 Data on the obstructive material extracted from each specimen and nasopharyngeal length measurements of each specimen.

Specimens	ZPB_ PL_001	ZPB_ PL_002	ZPB_ PL_003
Length (nostrils-choana) mm	80.28	155.57	157.24
Material obstructed	ZPB_PL_001	ZPB_PL_002	ZPB_PL_003
Length mm	18.95	26.66	21.23
Width mm	6.98	19.4	19.21
Surface mm^2	336.49	763.85	610.92
Volume mm^3	695.55	984,11	856.89

Data on the size of the nasopharyngeal tract (nasal entrance or nostril to the exit or choana). Measurements of the material extracted in specimen ZPB_PL_001 as well as those added in the replicate specimens (ZPB_PL_002 and ZPB_PL_003) to simulate the obstruction.

and the outlet section of the nasopharyngeal tract (Figure 1B) (27, 28, 30–32).

Results

The results supported the reliability and accuracy of the operation using large felids, such as *Panthera leo*, as a case study (Figures 1C, 2). As shown in Figure 3A, the obstruction in ZPB_PL_001 (Case 01) was very high, reducing the inhalation of air through the right nostril. Once operated on, the flow through the right nostril was restored. Regarding the replicate lions (Figure 3B), the comparison between the initial situation, before the obstructive surgery, and the final operating situation showed that the flow was the same, both in topology and velocity. With regard to the obstructive situation, an increase in velocity at the level of the obstruction was observed. This was because the same volume of flow must pass through a narrower channel, which generates regions with high velocities. This indicated the high accuracy of the Flowgy software in detecting small obstructions in detail. With respect to the data obtained, the temperature and humidity graphs in Figure 4 show that the data for the operated situation (orange) improved from those of the initial situation (blue). The data for Cases 02 and 03 in Figure 4 indicate that the obstruction (gray) generated a greater negative response in the respiratory function. This is because the two specimens used were two adult lions with a larger allometry and size than *Panthera leo* Case 01. Nevertheless, the operation on the two lions (orange) resulted in the return of respiratory function very close to or equal to the initial situation (blue). We followed the principle of similarity in the resolution of the flow during the acclimation process, detailed by Burgos (32), to observe changes in the acclimation function based on the temperature and absolute humidity of each specimen. This equation is expressed as follows:

$$T\left(average\ of\ each\ cut\right) - T\left(internal\ body\right) / T\left(internal\ body\right) - T\left(external\right).$$

Each slice from the standardized and homologous coordinates was divided by the final slice to convert the distance into values from 0 to 1 as a distance index to represent the standardized temperature and humidity data based on the expressed formula. Following the nomenclature of Burgos et al. (32), the average temperature and absolute humidity data were collapsed into a hyperbolic function. The x-axis represents the dimensionless distance d* = d/dc, where dc is the distance from the nares to the choana. The y-axis represents dimensionless temperature and humidity:

$$\theta = \left(T - Tw\right) / \left(Tw - To\right),$$

where T is the average temperature at each study point, Tw is the average nasopharyngeal wall temperature, and To is the average outlet temperature.

$$\theta = \left(H - Hw\right) / \left(Hw - Ho\right),$$

where H is the average humidity at each study point, Hw is the average nasopharyngeal wall humidity, and Ho is the average outlet humidity.

Subsequently, the data were fitted to a hyperbolic function by means of the differences in the sum of the squares with two values that acted as operators (α and β), as in the study by Burgos (2014) (32). This formula was used so that the collapsed average data matched the minimum square of the data to the function of the hyperbolic curve:

Hyperbolical formula: $$TANH\left(\frac{d^* + \alpha}{\beta} - 1\right),$$

TABLE 10 A mesh convergence test was performed using the specimen from Case 01 (similar to Burgos, (32)).

Mesh size	Volumetric elements (approx.)	Nr V (m/s)	RE (%)	Nr P (Pa)	RE (%)	Nl V (m/s)	RE (%)	Nl (Pa)	RE (%)	Ch V (m/s)	RE (%)	Ch P (Pa)	RE (%)
Coarse	1.5 million	0.305	4.98	101,312	0.16	0.735	0.97	101,311	0.11	0.270	2.31	101,302	0.02
Medium	3.5 million	0.317	1.24	101,311	0.08	0.740	0.30	101,310	0.04	0.275	0.51	101,301	0.01
Finest	7.0 million	0.321	–	101,310	–	0.742	–	101,309	–	0.276	–	101299.992	–

Three mesh resolutions were applied in this specimen: coarse (approximately 1.5 million elements), medium (approximately 3.5 million elements), and fine (approximately 7 million elements, approximately half of that used in this study). Pressure (Pa) and velocity (m/s) measurements were obtained at common locations (right and left nostrils and choana) and compared between mesh sizes. Relative error (RE) as a percentage, velocity (V), pressure (P), nostril right (Nr), nostril left (Nl), Choana (Ch).

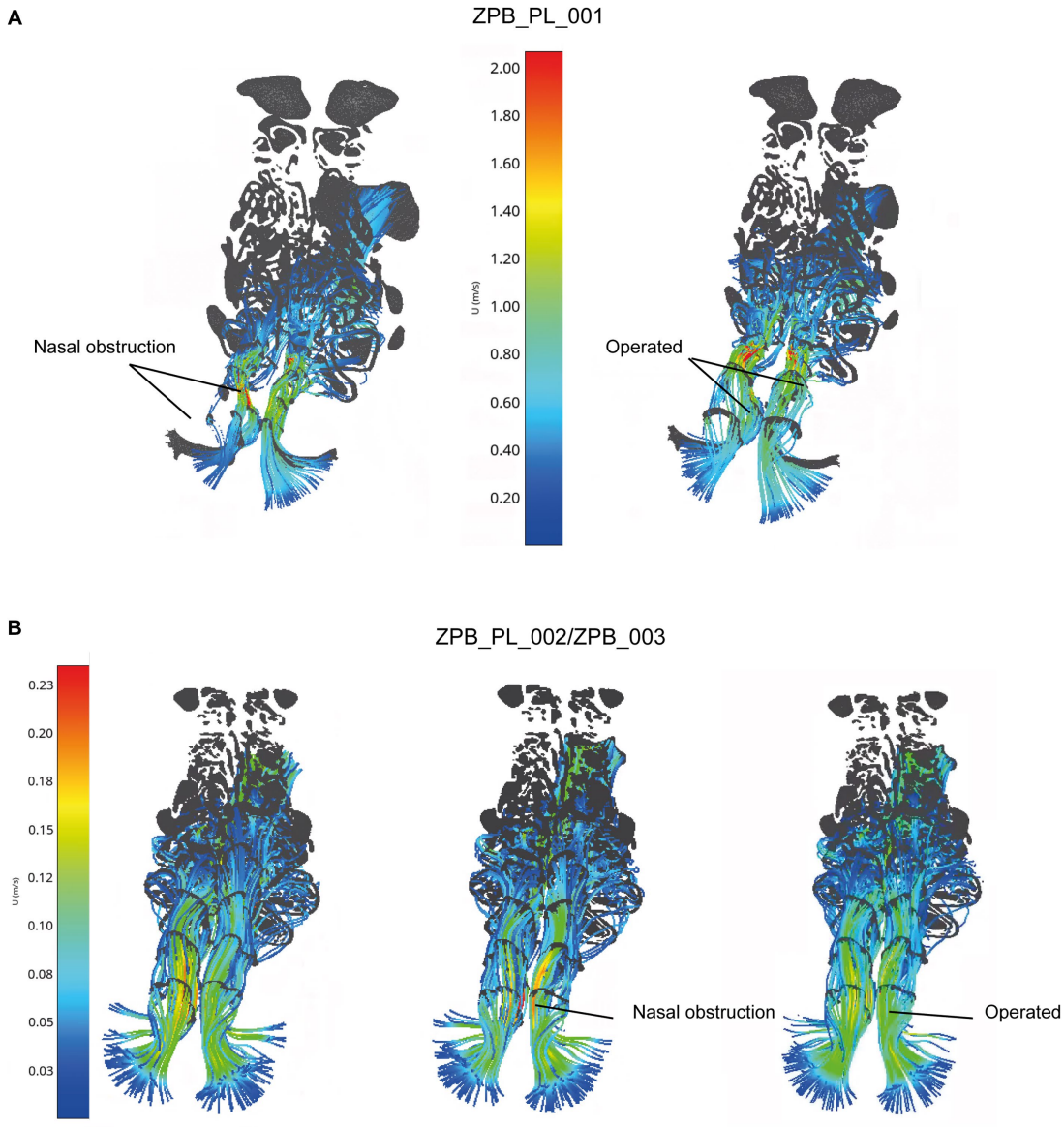

FIGURE 3
CFD simulations for the three specimens (Case 01 [ZPB_PL_001], Case 02 [ZPB_PL_002], and Case 03 [ZPB_PL_003]). The airflow lines (streamlines) are represented in all cases with a color pattern based on the velocity values (m/s), i.e., low velocities represented using cold colors and high velocities represented using warm colors. Nasal obstruction is indicated, where airflow is minimal or velocities are high due to reduced air passage. Operated nasal passages increase the airflow through a larger opening of the nasal passages, returning the airflow velocities to normal values.

This principle is highly dependent on the airflow topology. Therefore, the average data on the temperature and absolute humidity variables were collapsed to fit a hyperbolic function, generating a unique hyperbolic curve and providing a robust signal for the nasal airway (Figures 5, 6). In Figures 5, 6, a loss of hyperbolic function was observed when ZPB_PL_003 was obstructed (Figures 3B, 4). This

10.3389/fvets.2023.1181036

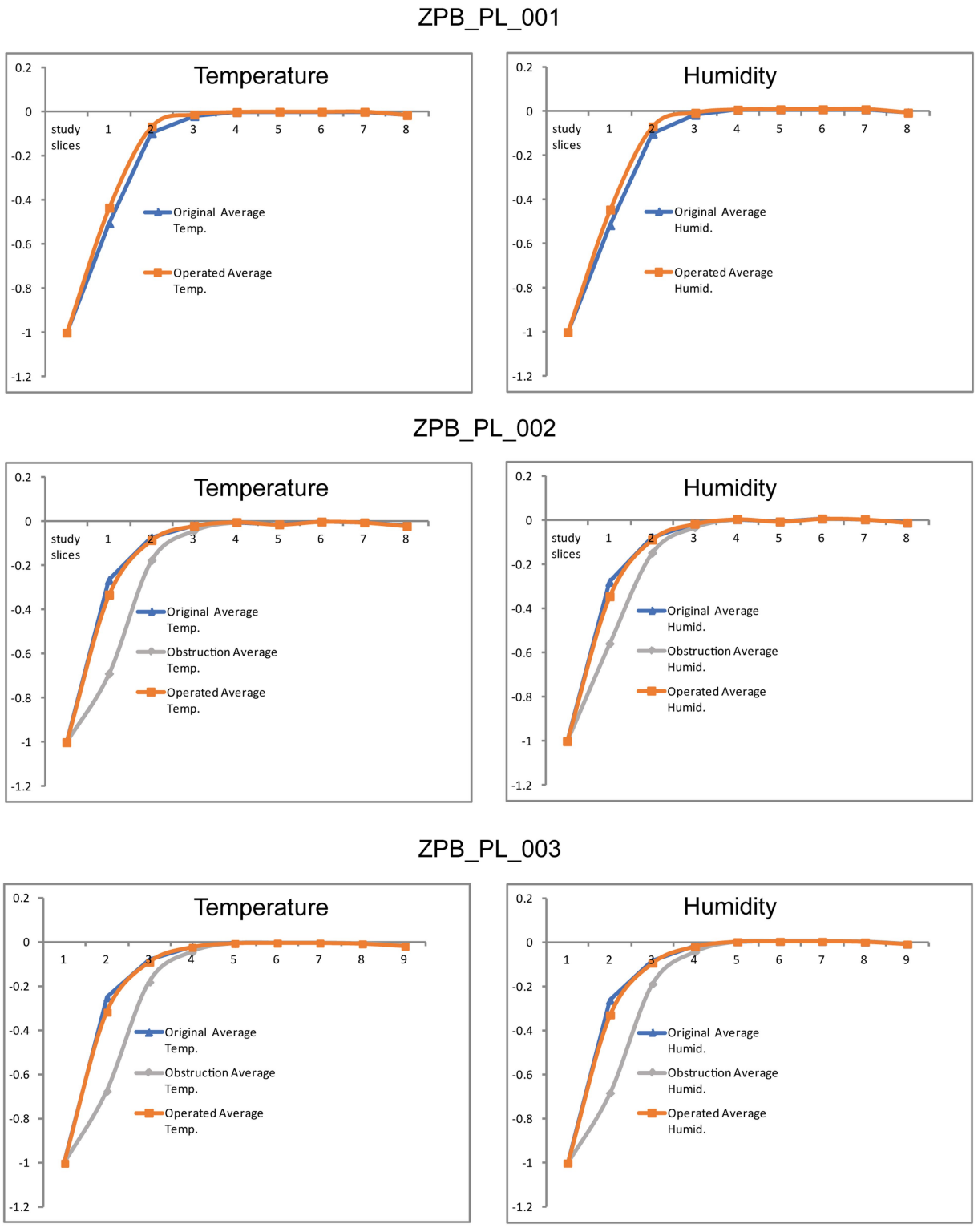

FIGURE 4
Plots of the results obtained from the CFD simulations in the three scenarios (28°C at 60% RH, 40°C at 5% RH, and 5°C at 10% RH) from the standardized data in Tables 1–8, following the study by Burgos, 2014 (32). Case 01 (ZPB_PL_001), Case 02 (ZPB_PL_002), and Case 03 (ZPB_PL_003) are shown.

indicated that the obstruction induced in Cases 03 and 02 negatively affected the resolution of the flow during acclimatization. Our results confirm that Flowgy has the analytical ability to resolve and detect small nasal obstructions. We developed a method to validate the efficiency of this function using hyperbolic curves and the obtained data, (32). A mesh convergence test was performed using the specimen

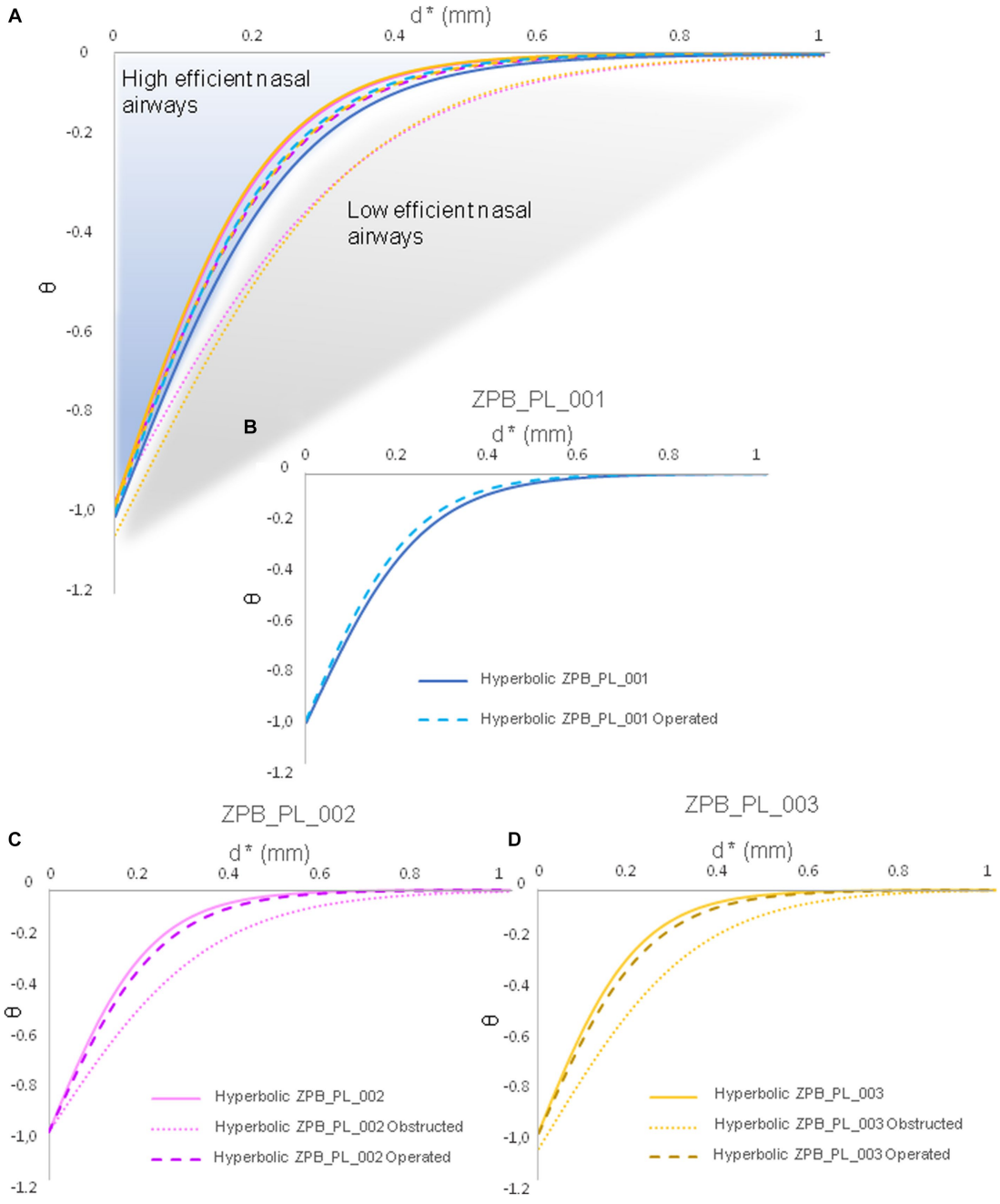

FIGURE 5
Temperature data collapsed into a hyperbolic function. These hyperbolic functions are generated based on the functions used by Burgos, 2014 (32). The average temperature data are from Tables 1–8. These hyperbolic functions describe the acclimation function specific to each nasal airway of each specimen. **(A)** General cases of all specimens. **(B)** Functional hyperbola of specimen ZPB_PL_001. **(C)** Functional hyperbola of specimen ZPB_PL_002. **(D)** Functional hyperbola of specimen ZPB_PL_003. Case 01 (ZPB_PL_001), Case 02 (ZPB_PL_002), and Case 03 (ZPB_PL_003) are shown.

from Case 01 [similar to Burgos (32)] to test the independence of the results with respect to mesh size. Three mesh resolutions were applied to this specimen: coarse (approximately 1.5 million elements), medium (approximately 3.5 million elements), and fine (approximately 7 million elements, approximately half of those used in this study). Pressure and velocity measurements were obtained at common locations (right and left nostrils and choana) and compared between mesh sizes (see Table 10). The relative error (RE) was calculated using the following formula:

$$RE = \left| \frac{\text{Value finest mesh} - \text{Value coarse mesh}}{\text{value finest mesh}} \right| x100\%$$

In all cases, the relative error decreased from 50 to 78% when moving from a low mesh size to a medium mesh size. In all cases, when moving to a fine mesh size (high density of elements), the flow field was accurately represented, achieving convergence for these variables (temperature, humidity, pressure, and velocity; Table 10).

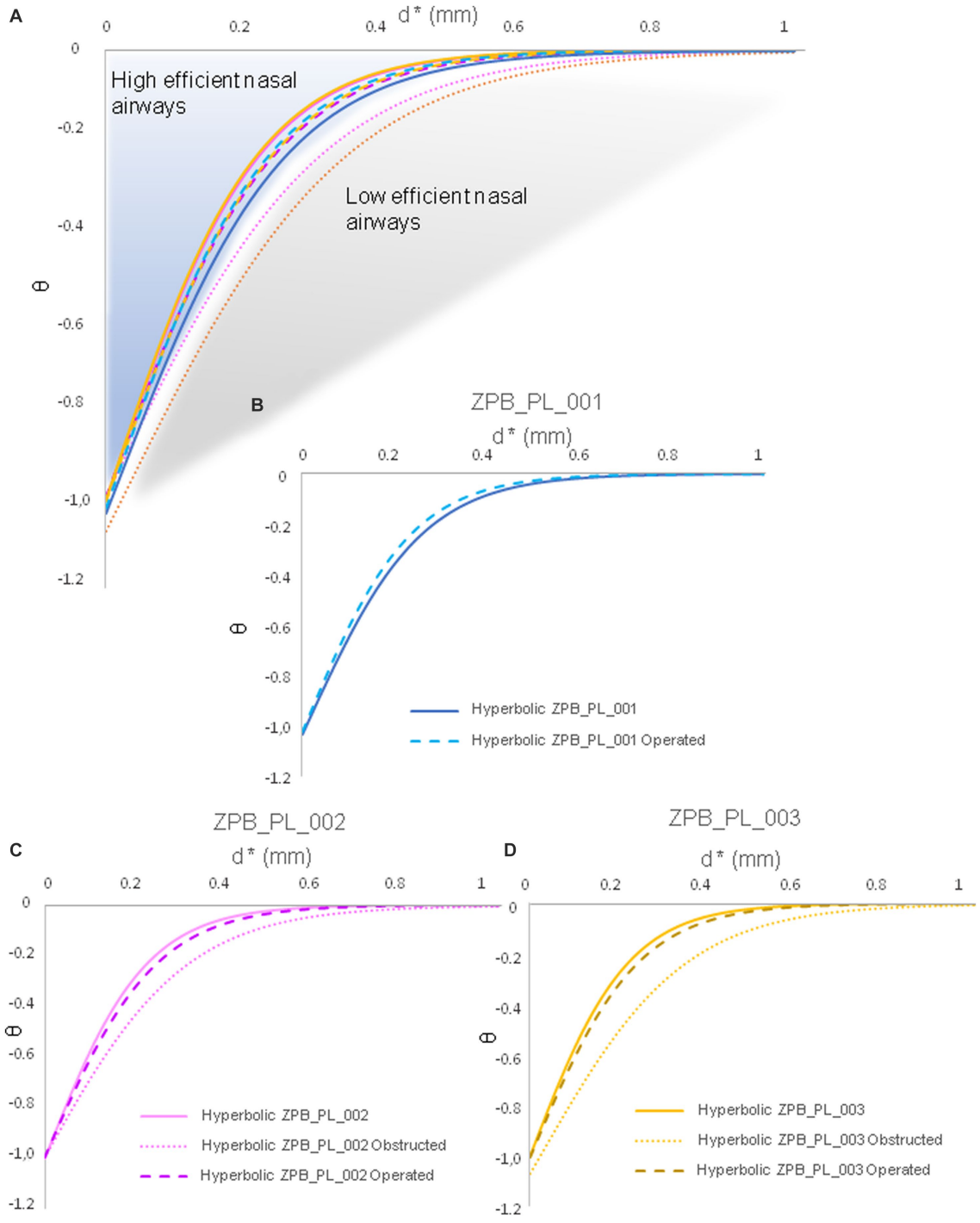

FIGURE 6
Humidity data collapsed into a hyperbolic function. These hyperbolic functions are generated based on the functions used by Burgos, 2014 (32). The average humidity data are from Tables 1–8. These hyperbolic functions describe the acclimation function specific to each nasal airway of each specimen. **(A)** General cases of all specimens. **(B)** Functional hyperbola of specimen ZPB_PL_001. **(C)** Functional hyperbola of specimen ZPB_PL_002. **(D)** Functional hyperbola of specimen ZPB_PL_003. Case 01 (ZPB_PL_001), Case 02 (ZPB_PL_002), and Case 03 (ZPB_PL_003) are shown.

Statistical analysis

In this study, the Wilcoxon test was used to quantify the effects of surgery. The Wilcoxon test (a non-parametric test) for related samples (also known as the Wilcoxon signed-rank test) could be a suitable option for comparing measurements in the same case before and after the operation, especially if the sample size is small (no more than 10 samples). The data on which the statistical analyses were performed are the mean data (θ) for both temperature and humidity obtained by applying Burgos (32). The data in Supplementary Table S1; Figure S1 indicate that the unobstructed operation in Case 01 had a statistically significant loss on the normal function of acclimatizing air in the nasopharynx. In the discussion on functional hyperbolics. The data from Case 01 post-operation aligned with that of other cases post-operation, suggesting a

restoration of nasopharyngeal function and successful adaptation to air acclimatization. Based on an experiment with replicates to test the significance of the effect of the operation on these large felids, we started by testing the correlation between the genetically related data of Cases 02 and 03. Using the ordinary least squares (OLS) method with linear regression, the regression slope was almost 1 (slope = 0.99) with a Pearson correlation coefficient of $r = 0.99$. This indicated that the variables behaved similarly and supported the fact that they are two sibling specimens or even twins (Supplementary Table S2; Figure S2A). The operation in Cases 02 and 03 consisted of eliminating the induced obstruction and replicating the original obstruction from Case 01, both in size and anatomical position (Table 9). The statistical data for the Wilcoxon test in both the original cases and the cases after the operation, collected in Supplementary Tables S3–S5, indicated no significant differences between the operation and original states. Supplementary Figure S2B indicates a linear regression with r = 0.99 between Cases 02 and 03 after the operation. Supplementary Figures S4, S5 show very similar violin and box distributions between the operated and original cases. The operated case with the highest data dispersion was used.

Conclusion

In conclusion, our results confirmed that Flowgy has the analytical ability to resolve and detect small nasal obstructions. Using the obtained data, we developed a method to validate the efficiency of this function using hyperbolic curves (32). The integration of engineering tools such as CFD and Flowgy in veterinary medicine represents a significant leap forward in our ability to understand and treat respiratory conditions in animals (3–6). These tools provide a non-invasive, detailed, and accurate analysis of airflow dynamics, significantly enhancing our ability to diagnose and manage these conditions (7–18). This improves the health and well-being of these animals and contributes to our broader understanding of their physiology and adaptations, thereby informing conservation efforts (1–6). As we continue to explore and develop these tools, we expect further advances in this exciting field.

Discussion

This study demonstrated the power of virtual surgery and CFD virtual computation (33–36). The results based on small operations on the replicate lions have shown that the Flowgy software has the power and definition to detect these small obstructions and quantify them through the modeling resulting from the simulations. In the detection and virtual operation presented by Flowgy software, this tool will help visualize possible pathological diseases in large mammals, specifically those that are not easy to handle due to their aggressive and dangerous behavior, such as large felids.

Using sibling specimens (subjects with high genetic relatedness) provides a way to test the potential of virtual surgery and the analytical computing capabilities of Flowgy. Very minor operations or very small obstructions provide interesting results regarding the functional stability of airways (33, 34). As observed with the results from obstructions and virtual obstructive surgery in lions, small variations in the operation result in variations in the hyperbolic function. This indicated that Flowgy has the computational resolution to detect small disturbances in the topologies of the specimens and can precisely predict whether the alterations affect airway function compared with its normal hyperbolic function. Furthermore, in all instances, the hyperbolic functions of the treated cases overlapped with the normal hyperbolic function of the healthy cases before the obstructive intervention. This includes ZPB_PL_001 (Case 01), in which only the natural obstruction was treated. Although we do not have an initial healthy case for comparison with the new hyperbolic function of Case 01, it was in the same region as the other healthy and treated hyperbolic functions of Cases 02 and 03. In addition, the hyperbolic function of ZPB_PL_001 has a larger slope and is above the base hyperbola. This indicates that the operation improved the respiratory function by more than 100%.

This study demonstrates the power of the Flowgy program for detecting small anomalies in the nasal airways and computing complex nasal topologies, such as those of great felids such as *Panthera leo* (3–6). Additionally, it shows that Flowgy is a highly effective tool for routinely diagnosing and preventing respiratory diseases. This will help us to achieve control over respiratory diseases, in the preventive diagnosis for veterinary specialists, and in the conservation of large mammals in zoos and extensive natural reserves.

Data availability statement

The original contributions presented in the study are included in the article/Supplementary material, further inquiries can be directed to the corresponding author.

Ethics statement

Ethical review and approval were not required for the study on animals in accordance with the local legislation and institutional requirements. Written informed consent was obtained from the owners for the participation of their animals in this study.

Author contributions

AP-R and MBu conceived and designed the study. BM scanned the specimens. AP-R and MBu analyzed the data. AP-R and MBu wrote the paper with the input of FE, DS-P, and MBa. All authors contributed to the article and approved the submitted version.

Funding

This study was funded by the Spanish Ministry of Science and Innovation and the European Union (PID2019-105097RB-I00/MCIN/AEI/10.13039/501100011033 to MBu and PID2020-115854GB-I00/MCIN/AEI/10.13039/501100011033 to MBa).

Acknowledgments

We thank BF (Researcher in carnivore specialist, University of Málaga) for reviewing the manuscript and the collaboration and participation of the team of Baptiste Mulot (Veterinary Director of the Veterinary Officer Zooparc de Beauval and Research Director of Beauval Nature) for providing tomographic data on specimens from his institution.

Conflict of interest

MBu is the developer of Flowgy©.

The remaining authors declare that this study was conducted in the absence of any commercial or financial relationships that could be construed as potential conflicts of interest.

Publisher's note

All claims expressed in this article are solely those of the authors and do not necessarily represent those of their affiliated organizations, or those of the publisher, the editors and the reviewers. Any product that may be evaluated in this article, or claim that may be made by its manufacturer, is not guaranteed or endorsed by the publisher.

Supplementary material

The Supplementary material for this article can be found online at: https://www.frontiersin.org/articles/10.3389/fvets.2023.1181036/full#supplementary-material

References

1. Ham A. *The last lions of Africa: Stories from the frontline in the battle to save a species*. Sydney, London: Allen & Unwin (2020).

2. Bauer H, Chapron G, Nowell K, Henschel P, Funston P, Hunter LT, et al. Lion (*Panthera leo*) populations are declining rapidly across Africa, except in intensively managed areas. *P Natl Acad Sci USA*. (2015) 112:14894–9. doi: 10.1073/pnas.1500664112

3. Van Valkenburgh B, Smith TD, Craven BA. Tour of a labyrinth: exploring the vertebrate nose. *Anat Rec*. (2014) 297:1975–84. doi: 10.1002/ar.23021

4. Van Valkenburgh B, Pang B, Bird D, Curtis A, Yee K, Wysocki C, et al. Respiratory and olfactory turbinals in feliform and caniform carnivorans: the influence of snout length. *Anat Rec*. (2014) 29:2065–79. doi: 10.1002/ar.23026

5. Collier RJ, Baumgard LH, Zimbelman RB, Xiao Y. Heat stress: physiology of acclimation and adaptation. *Anim Front*. (2019) 9:12–9. doi: 10.1093/af/vfy031

6. Morrison SF, Nakamura K, Madden CJ. Central control of thermogenesis in mammals. *Exp Physiol*. (2008) 93:773–97. doi: 10.1113/expphysiol.2007.041848

7. Michiels L, Day MJ, Snaps F, Hansen P, Clercx C. A retrospective study of non-specific rhinitis in 22 cats and the value of nasal cytology and histopathology. *J Feline Med Surg*. (2003) 5:279–85. doi: 10.1016/S1098-612X(03)00044-5

8. Ayele WY, Neill SD, Zinsstag J, Weiss MG, Pavlik I. Bovine tuberculosis: an old disease but a new threat to Africa. *Int J Tuberc Lung Dis*. (2004) 8:924–37.

9. Cleaveland S, Packer C, Hampson K, Kaare M, Kock R, Craft M, et al. "The multiple roles of infectious diseases in the Serengeti ecosystem" in *Serengeti III: Human Impacts on Ecosystem Dynamics*. ARE Sinclair, S Mduma, J Fryxell eds. Chicago, Ill, USA: Chicago University Press. (2008) 209–239.

10. Troyer JL, Pecon-Slattery J, Roelke ME, Black L, Packer C, O'Brien SJ. Patterns of feline immunodeficiency virus multiple infection and genome divergence in a free-ranging population of African lions. *J Virol*. (2004) 78:3777–91. doi: 10.1128/JVI.78.7.3777-3791.2004

11. Roelke ME, Brown MA, Troyer JL, Winterbach H, Winterbach C, Hemson G, et al. Pathological manifestations of feline immunodeficiency virus (FIV) infection in wild African lions. *Virology*. (2009) 390:1–12. doi: 10.1016/j.virol.2009.04.011

12. Leroy EM, Gouilh MA, Brugère-Picoux J. The risk of SARS-CoV-2 transmission to pets and other wild and domestic animals strongly mandates a one-health strategy to control the COVID-19 pandemic. One. *Health*. (2020) 10:100133. doi: 10.1016/j.onehlt.2020.100133

13. Murphy HL, Ly H. Understanding the prevalence of SARS-CoV-2 (COVID-19) exposure in companion, captive, wild, and farmed animals. *Virulence*. (2021) 12:2777–86. doi: 10.1080/21505594.2021.1996519

14. Haider N, Rothman-Ostrow P, Osman AY, Arruda LB, Macfarlane-Berry L, Elton L, et al. COVID-19—zoonosis or emerging infectious disease? *Front Public Health*. (2020) 8:763. doi: 10.3389/fpubh.2020.596944

15. Chavda VP, Feehan J, Apostolopoulos V. A veterinary vaccine for SARS-CoV-2: the first COVID-19 vaccine for animals. *Vaccine*. (2021) 9:631. doi: 10.3390/vaccines9060631

16. Valencak TG, Csiszar A, Szalai G, Podlutsky A, Tarantini S, Fazekas-Pongor V, et al. Animal reservoirs of SARS-CoV-2: calculable COVID-19 risk for older adults from animal to human transmission. *GeroScience*. (2021) 43:2305–20. doi: 10.1007/s11357-021-00444-9

17. Wehausen JD, Kelley ST, Ramey RR. Domestic sheep, bighorn sheep, and respiratory disease: a review of the experimental evidence. *California Fish and Game*. (2011) 97:7–24.

18. Mach N, Baranowski E, Nouvel LX, Citti C. The airway Pathobiome in complex respiratory diseases: a perspective in domestic animals. *Front Cell Infect Microbiol*. (2021) 11:583600. doi: 10.3389/fcimb.2021.583600

19. Burgos MA, Sanmiguel-Rojas E, Del Pino C, Sevilla-García MA, Esteban-Ortega F. New CFD tools to evaluate nasal airflow. *Eur Arch Oto-Rhino*. (2017) 274:3121–8. doi: 10.1007/s00405-017-4611-y

20. Sanmiguel-Rojas E, Burgos MA, Del Pino C, Sevilla-García MA, Esteban-Ortega F. Robust nondimensional estimators to assess the nasal airflow in health and disease. *Int J Numerical Methods Biomedical Engineer*. (2018) 34:e2906. doi: 10.1002/cnm.2906

21. Burgos MA, García MAS, Rojas ES, Del Pino C, Vélez CF, Piqueras F, et al. Virtual surgery for patients with nasal obstruction: use of computational fluid dynamics (MeComLand®, Digbody® & Noseland®) to document objective flow parameters and optimise surgical results. *Acta Otorrinolaringologica (English Edition)*. (2018) 69:125–33. doi: 10.1016/j.otoeng.2017.05.001

22. Harrington L, Macdonald D, D'Cruze N. Popularity of pet otters on YouTube: evidence of an emerging trade threat. *Nature Conservation*. (2019) 36:17–45. doi: 10.3897/natureconservation.36.33842

23. McMillan SE, Dingle C, Allcock JA, Bonebrake TC. Exotic animal cafes are increasingly home to threatened biodiversity. *Conserv Lett*. (2021) 14:e12760. doi: 10.1111/conl.12760

24. Bell D, Roberton S, Hunter PR. Animal origins of SARS coronavirus: possible links with the international trade in small carnivores. *Philos T Roy Soc B*. (2004) 359:1107–14. doi: 10.1098/rstb.2004.1492

25. Nienhaus A, Skudlik C, Seidler A. Work-related accidents and occupational diseases in veterinarians and their staff. *Int Arch Occup Environ Health*. (2005) 78:230–8. doi: 10.1007/s00420-004-0583-5

26. Chomel BB, Belotto A, Meslin FX. Wildlife, exotic pets, and emerging zoonoses. *Emerg Infect Dis*. (2007) 13:6–11. doi: 10.3201/eid1301.060480

27. Burgos MA, Sanmiguel-Rojas E, Singh N, Esteban-Ortega F. DigBody®: a new 3D modeling tool for nasal virtual surgery. *Comput Biol Med*. (2018) 98:118–25. doi: 10.1016/j.compbiomed.2018.05.016

28. Burgos MA, Sanmiguel-Rojas E, Rodríguez R, Esteban-Ortega F. A CFD approach to understand nasoseptal perforations. *Eur Arch Oto-Rhino-L*. (2018) 275:2265–72. doi: 10.1007/s00405-018-5073-6

29. Pérez-Ramos A, Figueirido B. Toward an "ancient" virtual world: improvement methods on X-ray CT data processing and virtual reconstruction of fossil skulls. *Front Earth Sci*. (2020) 8:345. doi: 10.3389/feart.2020.00345

30. Burgos MA, Pardo A, Rodríguez R, Rodríguez-Balbuena B, Castro D, Piqueras F, et al. Linking chronic otitis media and nasal obstruction: a CFD approach. *Laryngoscope*. (2021) 132:1224–30. doi: 10.1002/lary.29882

31. Chantre T, Oliveira R, Burgos MA, Cunha B, Barroso M, Oliveira M, et al. Computational fluid dynamics applied to study the impact of septal perforations on nasal physiology. *Portuguese J Otorhinolaryngol - Head and Neck Surgery*. (2022) 60:3.

32. Burgos MA, Sanmiguel-Rojas E, Martín-Alcántara A, Hidalgo-Martínez M. Effects of the ambient temperature on the airflow across a Caucasian nasal cavity. *Int J Numer Meth Bio*. (2014) 30:430–45. doi: 10.1002/cnm.2616

33. Gleason HE, Phillips H, Fries R, Keating S, Hamel P, McCoy A. Ala vestibuloplasty improves cardiopulmonary and activity-related parameters in brachycephalic cats. *Vet Surg*. (2023) 52:575–86. doi: 10.1111/vsu.13948

34. Zamora-Perarnau C, Malvè M, Fernández-Parra R. Computational fluid dynamics comparison of the upper airway velocity, pressure, and resistance in cats using an endotracheal tube or a supraglottic airway device. Frontiers in veterinary. *Science*. (2023) 10. doi: 10.3389/fvets.2023.1183223

35. Barchilon M, Reinero CR. Breathe easy: inhalational therapy for feline inflammatory airway disease. *J Feline Med Surg*. (2023) 25:1098612X231193054. doi: 10.1177/1098612X231193054

36. Pavletic MM, Trout NJ. Successful correction of stenotic nares using combined alar fold lift-up and sulcus pull-down techniques in brachycephalic cats: 8 cases (2017–2022). *J Am Vet Med Assoc*. (2023) 1:1–5. doi: 10.2460/javma.23.01.0054

Frontiers in Veterinary Science

Transforms how we investigate and improve animal health

The third most-cited veterinary science journal, bridging animal and human health with a comparative approach to medical challenges. It explores innovative biotechnology and therapy for improved health outcomes.

Discover the latest Research Topics

See more →

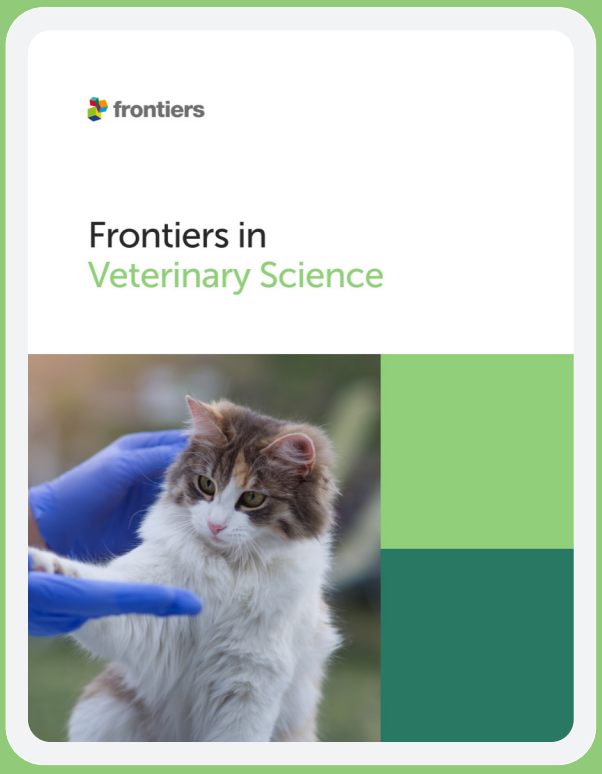

Frontiers

Avenue du Tribunal-Fédéral 34
1005 Lausanne, Switzerland
frontiersin.org

Contact us

+41 (0)21 510 17 00
frontiersin.org/about/contact